Edited by
L. Andrew Lyon and Michael Joseph Serpe

Hydrogel Micro and Nanoparticles

Related Titles

Tadros, T. F.

Dispersion of Powders in Liquids and Stabilization of Suspensions

2012

ISBN: 978-3-527-32941-0

Tadros, T. F. (ed.)

Topics in Colloid and Interface Science

2012

ISBN: 978-3-527-31991-6

Fernandez-Nieves, A., Wyss, H., Mattsson, J., Weitz, D. A. (eds.)

Microgel Suspensions

Fundamentals and Applications

2011

ISBN: 978-3-527-32158-2

Tadros, T. F. (ed.)

Self-Organized Surfactant Structures

2011

ISBN: 978-3-527-31990-9

Tadros, T. F.

Rheology of Dispersions

Principles and Applications

2010

ISBN: 978-3-527-32003-5

Tadros, T. F. (ed.)

Colloids and Interface Science Series

6 Volume Set

2008

ISBN: 978-3-527-31461-4

Platikanov, D., Exerowa, D. (eds.)

Highlights in Colloid Science

2009

Hardcover

ISBN: 978-3-527-32037-0

Edited by L. Andrew Lyon and Michael Joseph Serpe

Hydrogel Micro and Nanoparticles

WILEY-VCH Verlag GmbH & Co. KGaA

The Editors

Prof. L. Andrew Lyon
Georgia Inst. of Technology
School of Chemistry & Biochem.
901 Atlantic Dr. NW
Atlanta GA 30332-0400
USA

Prof. Michael Joseph Serpe
University of Alberta
Department of Chemistry
11227 Saskatchewan Drive
Edmonton, Alberta T6G 2G2
Canada

All books published by **Wiley-VCH** are carefully produced. Nevertheless, authors, editors, and publisher do not warrant the information contained in these books, including this book, to be free of errors. Readers are advised to keep in mind that statements, data, illustrations, procedural details or other items may inadvertently be inaccurate.

Library of Congress Card No.: applied for

British Library Cataloguing-in-Publication Data
A catalogue record for this book is available from the British Library.

Bibliographic information published by the Deutsche Nationalbibliothek
The Deutsche Nationalbibliothek lists this publication in the Deutsche Nationalbibliografie; detailed bibliographic data are available on the Internet at http://dnb.d-nb.de.

© 2012 Wiley-VCH Verlag & Co. KGaA,
Boschstr. 12, 69469 Weinheim, Germany

All rights reserved (including those of translation into other languages). No part of this book may be reproduced in any form – by photoprinting, microfilm, or any other means – nor transmitted or translated into a machine language without written permission from the publishers. Registered names, trademarks, etc. used in this book, even when not specifically marked as such, are not to be considered unprotected by law.

Print ISBN: 978-3-527-33033-1
ePDF ISBN: 978-3-527-64645-6
ePub ISBN: 978-3-527-64644-9
mobi ISBN: 978-3-527-64643-2
oBook ISBN: 978-3-527-64642-5

Cover Design Grafik-Design Schulz, Fußgönheim
Typesetting Thomson Digital, Noida, India
Printing and Binding Markono Print Media Pte Ltd, Singapore

Contents

List of Contributors *XIII*
Foreword *XIX*
Preface *XXIII*

1 Thermally Sensitive Microgels: From Basic Science to Applications *1*
He Cheng and Guangzhao Zhang
1.1 Introduction *1*
1.2 Theoretical Background *2*
1.2.1 Thermodynamics of Volume Phase Transition *2*
1.2.2 Internal Motion *3*
1.2.3 Dynamics of Microgel *4*
1.2.4 Kinetics Calculation of Reversible Aggregation *6*
1.3 Basic Physics of Microgels *7*
1.3.1 Volume Phase Transition *7*
1.3.2 Internal Motion *9*
1.3.2.1 Internal Motions in Good Solvent *9*
1.3.2.2 Internal Motions in Θ and Poor Solvents *11*
1.3.3 Dynamics of Cation-Induced Aggregation of Thermally Sensitive Microgels *14*
1.3.3.1 Salt-Induced Complexation *14*
1.3.3.2 Complexation Between Microgels and Protein *18*
1.3.3.3 Aggregation of Spherical Microgels *18*
1.3.4 Non-Ergodic and Ergodic Phenomena of Physical Crosslinked Gel *21*
1.4 Applications *25*
1.5 Conclusions *27*
References *29*

2 Thermosensitive Core–Shell Microgels: Basic Concepts and Applications *33*
Yan Lu and Matthias Ballauff
2.1 Introduction *33*
2.2 Volume Transition in Single Particles *35*

2.3 Concentrated Suspensions: 3D Crystallization *40*
2.4 Particles on Surfaces: 2D Crystallization *41*
2.5 Concentrated Suspensions: Rheology *42*
2.6 Core–Shell Particles as Carriers for Catalysts *45*
2.6.1 Metal Nanoparticles *45*
2.6.2 Enzymes *50*
2.7 Conclusion *53*
References *54*

3 Core–Shell Particles with a Temperature-Sensitive Shell *63*
Haruma Kawaguchi
3.1 Introduction *63*
3.2 Preparation of Core–Shell Particles with a Temperature-Sensitive Shell *63*
3.2.1 Spontaneous Formation of the Core–Shell Structure via Emulsion Polymerization and Soap-Free Emulsion Polymerization *63*
3.2.2 Formation of a Temperature-Sensitive Shell by Seeded Polymerization *66*
3.3 Preparation of Hairy Particles with Temperature-Sensitive Hair *66*
3.3.1 Hairy Particle Formation from Block Copolymer Micelles *67*
3.3.2 Hairy Particle Formation Through *In Situ* Formation of Surface Active Material *68*
3.3.3 Hairy Particle Formation Through Hair Growth on Core Particles *68*
3.3.3.1 Hairy Particle Formation Through Hair Growth on Rigid Core Particles *69*
3.3.3.2 Hairy Particle Formation Through Hair Growth on Microgels *70*
3.3.3.3 Graft Polymerization of NIPAM from a CMC Microgel Using the Ceric Ion Redox System *71*
3.3.4 Hairy Particle Formation Through the Attachment of Hydrophilic Polymer Chains to the Surface of Core Particles (Grafting-to Method) *73*
3.4 Properties, Functions and Applications of Core–Shell Particles with a Temperature-Sensitive Shell *75*
3.4.1 Volume Phase Transition of the Temperature-Sensitive Shell and Accompanying Changes in Physical Properties of the Particles *75*
3.4.2 Two-Dimensional Assembly of Hairy Particles and Optical Properties *76*
3.4.3 Other 2D Assembly – Temperature-Sensitive Pickering Emulsion by PNIPAM Hairy Particles *77*
3.4.4 Fluorescence Resonance Energy Transfer (FRET) Particles Tuned by Temperature *77*
3.5 Conclusions *78*
References *79*

4 pH-Responsive Nanogels: Synthesis and Physical Properties *81*
Beng Hoon Tan, Jeremy Pang Kern Tan, and Kam Chiu Tam
4.1 Introduction *81*
4.2 Preparation Techniques for pH-Responsive Nanogels *82*
4.2.1 Emulsion Polymerization *82*
4.2.2 Physical Self-Assembly of Interactive Polymers *84*
4.3 Structural Properties of pH-Responsive Nanogels *85*
4.3.1 Distribution of Crosslinking Monomers *85*
4.3.2 Kinetic Modeling of Functional Group Distributions in Nanogels *86*
4.4 Swelling of pH-Responsive Nanogels *87*
4.4.1 Mechanism of pH-Responsive Swelling *87*
4.4.2 Theory of Swelling and Elasticity of pH-Responsive Nanogels *91*
4.4.3 Effect of Ionic Strength *93*
4.5 Rheological Behavior of pH-Responsive Nanogels *96*
4.6 Approach to Model pH-Responsive Nanogel Properties *97*
4.7 Osmotic Compressibility of pH-Responsive Nanogels in Colloidal Suspensions *106*
4.8 Conclusions and Future Perspectives *109*
References *110*

5 Poly(*N*-Vinylcaprolactam) Nano- and Microgels *117*
Cheng Cheng and Andrij Pich
5.1 Introduction *117*
5.2 Poly(*N*-Vinylcaprolactam): Synthesis, Structure and Properties in Solution *117*
5.3 Thermal Behavior of Poly(*N*-Vinylcaprolactam) in Water *120*
5.4 PVCL Nano- and Microgels *123*
5.4.1 Homopolymer PVCL Microgels *125*
5.4.2 Copolymer PVCL Microgels *129*
5.4.3 Composite and Hybrid Microgels *133*
5.5 Conclusions *137*
References *137*

6 Doubly Crosslinked Microgels *141*
Brian R. Saunders
6.1 Introduction *141*
6.1.1 Definitions and Classifications of SX and DX Microgels *141*
6.1.2 A Brief History of Doubly Crosslinked Microgels *142*
6.1.3 Stimulus-Responsive DX Microgels *143*
6.1.4 General Equations Governing Hydrogel Swelling *143*
6.1.5 General Equations Governing Hydrogel Mechanical Properties *144*
6.2 Methods of Preparation *145*
6.2.1 DX Microgel Aggregates *146*

6.2.2 Microgel Crosslinked Hydrogels *146*
6.2.3 Microgel-Reinforced Hydrogels *146*
6.2.4 DX Microgel Crystals by Small Molecule Addition *147*
6.2.5 Self-Crosslinked DX Microgel Crystals *147*
6.2.6 Interpenetrating DX Microgels *148*
6.3 Methods of Characterization *148*
6.3.1 ^{1}H Nuclear Magnetic Resonance *148*
6.3.2 Confocal Microscopy *149*
6.3.3 Scanning Electron Microscopy *150*
6.3.4 Swelling Experiments *150*
6.3.5 Optical *152*
6.3.6 Dynamic Rheology *153*
6.3.7 Compression Modulus Measurements *154*
6.3.8 Tensile Testing *154*
6.4 Morphology *155*
6.4.1 Morphology Types *155*
6.4.2 Morphology Control *156*
6.5 Properties *157*
6.5.1 Swelling Properties of DX Microgels and Control *157*
6.5.2 Optical Tuning *158*
6.5.3 Mechanical Properties of DX Microgels and Control *158*
6.5.4 Comparison of Properties with Microgels *161*
6.5.5 Comparison of Properties with Conventional Hydrogels *162*
6.6 Potential Applications *162*
6.6.1 Photonic Applications *162*
6.6.2 Biomedical Applications *163*
6.7 Conclusion *165*
References *166*

7 ATRP: A Versatile Tool Toward Uniformly Crosslinked Hydrogels with Controlled Architecture and Multifunctionality *169*
Jeong Ae Yoon, Jung Kwon Oh, Wenwen Li, Tomasz Kowalewski, and Krzysztof Matyjaszewski
7.1 Incorporating Crosslinking Reactions into Controlled Radical Polymerization *169*
7.2 Effect of Network Homogeneity on Thermoresponsive Hydrogel Performance *171*
7.2.1 Performance of Macroscopic Hydrogels *172*
7.2.2 Molecular Level Dehydration Kinetics *175*
7.3 Gel Networks Containing Functionalized Nanopores *176*
7.3.1 Enhanced Swelling Ratios *178*
7.3.2 Accelerated Deswelling Kinetics *178*
7.4 Toward Micro- and Nano-Sized Hydrogels by ATRP *180*
References *184*

8 Nanogel Engineering by Associating Polymers for Biomedical Applications *187*
Yoshihiro Sasaki and Kazunari Akiyoshi
8.1 Introduction *187*
8.2 Preparation of Associating Polymer-Based Nanogels *188*
8.2.1 Hydrophobically Modified Polysaccharide *188*
8.2.2 Photoresponsive Molecule-Modified Polysaccharides *190*
8.2.3 Thermoresponsive Polymer-Grafted Polysaccharide *191*
8.2.4 Metal–Ligand Modified Polysaccharides *192*
8.2.5 Siloxane-Modified Polysaccharides *193*
8.2.6 Protein-Crosslinked Nanogels *193*
8.3 Functions of Self-Assembled Nanogels *194*
8.3.1 Nano-Encapsulation of Proteins by the Nanogel: Nanogels as Macromolecular Hosts *194*
8.3.2 Artificial Molecular Chaperones *195*
8.3.3 Nanogel Chaperones in Cell-Free Protein Synthesis *196*
8.4 Application of Polysaccharide Nanogels to DDS *197*
8.4.1 Protein Delivery *198*
8.4.2 Nucleic Acid Delivery *199*
8.5 Integration of Nanogels *199*
8.6 Conclusion and Perspectives *202*
References *202*

9 Microgels and Biological Interactions *209*
Michael H. Smith, Antoinette B. South, and L. Andrew Lyon
9.1 An Introduction to Polymer Biomaterials *209*
9.1.1 Hydrogels *210*
9.1.2 Hydrogels as Particles *211*
9.1.3 Hydrogel Particle Synthesis *212*
9.2 Drug Delivery *213*
9.2.1 Nanoparticles and the Mononuclear Phagocytic System *214*
9.2.2 Nanoparticle Size and Surface Modification for Enhanced Delivery *214*
9.2.3 Nanogel Cellular Targeting *216*
9.2.3.1 Passive Targeting: The Enhanced Permeability and Retention Effect *216*
9.2.3.2 Active Targeting: Nanoparticle Bioconjugation *217*
9.2.4 Degradation and Release of Encapsulated Cargo *220*
9.2.4.1 Release by Reduction *220*
9.2.4.2 Release by pH Changes *220*
9.3 Biomaterial Films *221*
9.3.1 The Foreign Body Response *222*
9.3.2 Hydrogels as a Biomaterial Interface *223*
9.3.3 Antifouling Surfaces *224*
9.3.4 Cellular Adhesion *225*

9.3.5 Drug Release *227*
9.4 Conclusion *228*
References *229*

10 Oscillating Microgels Driven by Chemical Reactions *237*
Daisuke Suzuki
10.1 Introduction *237*
10.2 Types of Oscillating Microgels *238*
10.3 Synthesis and Fabrication of Oscillating Microgels *240*
10.4 Control of Oscillatory Behavior *241*
10.4.1 Effect on Induction Period *242*
10.4.2 Effect on Oscillation Amplitude *244*
10.4.3 Effect on Oscillation Period and Waveforms *247*
10.5 Flocculating/Dispersing Oscillation *251*
10.6 Concluding Remarks *254*
References *254*

11 Smart Microgel/Nanoparticle Hybrids with Tunable Optical Properties *257*
Matthias Karg and Thomas Hellweg
11.1 Introduction *257*
11.2 Synthesis of Hybrid Gels *258*
11.3 Characterization of Hybrid Gels *260*
11.4 Hybrid Microgels with Plasmon Properties *261*
11.5 Photoluminescent Hybrid Microgels *269*
11.6 Summary *272*
References *274*

12 Macroscopic Microgel Networks *281*
Todd Hoare
12.1 Introduction and Motivation *281*
12.2 Preparation of Microgel Networks *284*
12.2.1 Networking Strategies *284*
12.2.2 Direct Microgel Crosslinking *285*
12.2.2.1 Hydrophobic Assembly *285*
12.2.2.2 Ionic Assembly *287*
12.2.2.3 Covalent Assembly *289*
12.2.3 Microgel-Mediated Crosslinking *290*
12.2.3.1 Initiator-Grafted Microgels *290*
12.2.3.2 Surface-Polymerizable Microgels *291*
12.2.3.3 Surface-Reactive Microgels *293*
12.2.4 Physical Microgel Entrapment *295*
12.2.4.1 Entrapment to Form 3D Hydrogels *295*
12.2.4.2 Entrapment to Form 2D Films *299*
12.3 Applications of Microgel Networks *301*

12.3.1 Drug Delivery *301*
12.3.2 Cell Adhesion-Directing Coatings *304*
12.3.3 Tissue Engineering *304*
12.3.4 Biosensors *307*
12.3.5 Optical Materials *309*
12.3.6 Biomolecule Separation and Purification *309*
12.3.7 DNA Sequencing *310*
12.4 Conclusions and Future Outlook *310*
References *311*

13 Color-Tunable Poly (*N*-Isopropylacrylamide) Microgel-Based Etalons: Fabrication, Characterization, and Applications *317*
Michael J. Serpe, Courtney D. Sorrell, Matthew C.D. Carter, Ian N. Heppner, Janelle B. Smiley-Wiens, and Liang Hu
13.1 Introduction *317*
13.2 Microgel-Based Photonic Materials *319*
13.2.1 Microgel-Based Etalons *320*
13.2.2 Tuning the Reflection Order *323*
13.2.3 Mechanism of Etalon Deswelling *324*
13.2.4 Applied Sensing *329*
13.3 Conclusions and Future Directions *330*
References *332*

14 Crystals of Microgel Particles *337*
Juan José Liétor-Santos, Urs Gasser, Jun Zhou, Zhibing Hu, and Alberto Fernández-Nieves
14.1 Introduction *337*
14.2 Theoretical Background and Experimental Methods *339*
14.2.1 Crystal Nucleation and Growth *339*
14.2.2 Crystalline Structure *340*
14.2.2.1 Body-Centered Cubic *340*
14.2.2.2 Face-Centered Cubic *341*
14.2.2.3 Hexagonal and Hexagonal Close-Packed *342*
14.2.2.4 A15 *343*
14.2.3 Scattering of Waves from Crystals *343*
14.2.4 Small-Angle Neutron Scattering *345*
14.2.5 Experimental Details *351*
14.2.6 Experimental System *352*
14.3 Determining and Modeling the Particle Form Factor *353*
14.4 Structure Factor of Concentrated Suspensions *357*
14.4.1 Phase Behavior *357*
14.4.2 Analysis of the Structure Factor for Crystalline Samples *358*
14.4.3 Tuning Polydispersity *361*
14.5 Final Remarks and Future Directions *365*
References *366*

15 Dynamical Arrest and Crystallization in Dense Microgel Suspensions *369*
Priti Mohanty, Divya Paloli, Jerome Crassous, and Peter Schurtenberger
15.1 Introduction *369*
15.2 Methods *372*
15.3 Synthesis and Responsive Properties *374*
15.4 Structural and Dynamic Properties of Neutral Microgels *379*
15.5 Structural and Dynamic Properties of Soft and Weakly Charged Microgels *388*
15.6 Conclusions and Outlook: Probing Anisotropic Interactions *391*
References *394*

Index *397*

List of Contributors

Kazunari Akiyoshi
Kyoto University
Department of Polymer Chemistry
Katsura Campus, Room 317, Bldg. A3
Kyoto daigaku-katsura
Nishikyo-ku
Kyoto 615–8530
Japan

Matthias Ballauff
Helmholtz-Zentrum Berlin für
Materialien und Energie
Soft Matter and Functional Materials
Hahn-Meitner-Platz 1
14109 Berlin
Germany

Matthew C.D. Carter
University of Alberta
Department of Chemistry
11227 Saskatchewan Drive
Edmonton
Alberta T6G 2G2
Canada

Cheng Cheng
RWTH Aachen
DWI an der RWTH Aachen e.V.
Pauwelsstraße 8
52056 Aachen
Germany

He Cheng
State Key Laboratory of Polymer Physics
and Chemistry
Joint Laboratory of Polymer Science
and Materials
Beijing National Laboratory for
Molecular Sciences
Institute of Chemistry
CAS, Beijing 100190
P. R. China

Jerome Crassous
Lund University
Physical Chemistry Chemical Center
P. O. Box 124
22100 Lund
Sweden

Alberto Fernández-Nieves
Georgia Institute of Technology
School of Physics
Atlanta
GA
USA

Urs Gasser
Paul Scherrer Institut
Laboratory for Neutron Scattering
5232 Villigen PSI
Switzerland

Thomas Hellweg
Universität Bielefeld
Fakultät für Chemie, Biophysikalische Chemie (PC III)
33501 Bielefeld
Germany

Ian N. Heppner
University of Alberta
Department of Chemistry
11227 Saskatchewan Drive
Edmonton
Alberta T6G 2G2
Canada

Todd Hoare
McMaster University
Department of Chemical Engineering
1280 Main St. W.
Hamilton
Ontario L8S 4L7
Canada

Liang Hu
University of Alberta
Department of Chemistry
11227 Saskatchewan Drive
Edmonton
Alberta T6G 2G2
Canada

Zhibing Hu
University of North Texas
Department of Physics
Denton
TX
USA

Matthias Karg
Universität Bielefeld
Fakultät für Chemie, Biophysikalische Chemie (PC III)
33501 Bielefeld
Germany

Haruma Kawaguchi
Kanagawa University
Faculty of Engineering
3-27-1 Rokkakubashi
Kanagawa-ku
Yokohama 221-8686
Japan

Tomasz Kowalewski
Carnegie Mellon University
Department of Chemistry
4400 Fifth Avenue
Pittsburgh
PA 15213
USA

Wenwen Li
Carnegie Mellon University
Department of Chemistry
4400 Fifth Avenue
Pittsburgh
PA 15213
USA

Juan José Liétor-Santos
Georgia Institute of Technology
School of Physics
Atlanta
GA 30332–0430
USA

Yan Lu
Helmholtz-Zentrum Berlin für Materialien und Energie
Soft Matter and Functional Materials
Hahn-Meitner-Platz 1
14109 Berlin
Germany

L. Andrew Lyon
Georgia Institute of Technology
School of Chemistry and Biochemistry
& Petit Institute for Bioengineering
and Bioscience
Atlanta
Georgia 30332-0400
USA

Krzysztof Matyjaszewski
Carnegie Mellon University
Department of Chemistry
4400 Fifth Avenue
Pittsburgh
PA 15213
USA

Priti Mohanty
Lund University
Physical Chemistry
Chemical Center
P.O. Box 124
22100 Lund
Sweden

and

University of Fribourg
Adolphe Merkle Institute
Route de l'Ancienne Papeterie CP 209
1723 Marly 1
Switzerland

Jung Kwon Oh
Concordia University
Department of Chemistry and
Biochemistry
7141 Sherbrooke Street West,
Montreal
Quebec H4B 1R6
Canada

Divya Paloli
University of Fribourg
Adolphe Merkle Institute
CH-1723 Marly
Switzerland

and

Lund University
Physical Chemistry
Department of Chemistry
SE-221 00 Lund
Sweden

Andrij Pich
RWTH Aachen
DWI an der RWTH Aachen e.V.
Pauwelsstraße 8
52056 Aachen
Germany

Yoshihiro Sasaki
Kyoto University
Department of Polymer Chemistry
Katsura Campus, Room 317, Bldg. A3
Kyoto daigaku-katsura
Nishikyo-ku
Kyoto 615–8530
Japan

Brian R. Saunders
The University of Manchester
Polymer Science and Technology
Group, School of Materials
Grosvenor Street
Manchester M13 9PL
UK

Peter Schurtenberger
Lund University
Physical Chemistry
Chemical Center
P.O. Box 124
22100 Lund
Sweden

Michael J. Serpe
University of Alberta
Department of Chemistry
11227 Saskatchewan Drive
Edmonton
Alberta T6G 2G2
Canada

Janelle B. Smiley-Wiens
University of Alberta
Department of Chemistry
11227 Saskatchewan Drive
Edmonton
Alberta T6G 2G2
Canada

Michael H. Smith
Georgia Institute of Technology
School of Chemistry and Biochemistry
& Petit Institute for Bioengineering
and Bioscience
Atlanta
Georgia 30332-0400
USA

Courtney D. Sorrell
University of Alberta
Department of Chemistry
11227 Saskatchewan Drive
Edmonton
Alberta T6G 2G2
Canada

Antoinette B. South
Georgia Institute of Technology
School of Chemistry and Biochemistry
& Petit Institute for Bioengineering
and Bioscience
Atlanta
Georgia 30332-0400
USA

Daisuke Suzuki
Shinshu University
Faculty of Textile Science & Technology
3-15-1, Tokida, Ueda
Nagano 386-8567
Japan
Daisuke Suzuki
Shinshu University
International Young Researchers
Empowerment Center
3-15-1, Tokida, Ueda
Nagano 386-8567
Japan

K.C. Tam
Waterloo Institute for Nanotechnology,
University of Waterloo
Department of Chemical Engineering
200 University Avenue West
Waterloo
Ontario N2L 3G1
Canada

B.H. Tan
Institute of Materials Research and
Engineering (IMRE)
A*STAR (Agency for Science,
Technology & Research)
3 Research Link
Singapore 117602

J.P.K. Tan
Institute of Bioengineering and
Nanotechnology (IBN)
A*STAR (Agency for Science,
Technology and Research)
3 Research Link
Singapore 117602
Jeong Ae Yoon
Carnegie Mellon University
Department of Chemistry
4400 Fifth Avenue
Pittsburgh
PA 15213
USA

Guangzhao Zhang
University of Science and Technology of China
The Hefei National Laboratory for Physical Sciences at Micro-scale
Department of Chemical Physics
Hefei 230026
China

Jun Zhou
University of North Texas
Department of Physics
Denton
TX
USA

Foreword

In the unlikely event that you have opened this book without knowing anything about microgels, we start with a definition. Microgels are solvent swollen polymer networks (i.e. a type of gel) present as discrete particles with average diameters in the range 20 nm to 50 μm. Although Baker's first explicit description of microgels in 1949, describes solvent swellable polybutadiene particles, most of the microgel literature concentrates on aqueous microgels (hydrogels) in the size range 100 to 1000 nm. Generalizing more, most of the aqueous microgel publications involve crosslinked poly(N-isopropylacrylamide), PNIPAM, or related polymers showing lower critical solution temperature (LCST) behaviors. Microgel technologies have their roots in latex emulsion polymerization, which is one of the most important historical advances in polymer technology. I mention emulsion polymerization because of the parallels between latex and microgel technologies. Both involve colloidally stable, nano-scale particles with very high specific surface areas and low viscosities. Instrumentation, techniques, and colloidal theories perfected with the advent of monodisperse latexes in the 1960–1980 period are now used to characterize microgels. The ability to apply microelectrophoresis, light scattering, particulate rheology, high performance titrations and small angle neutron scattering to microgel characterization gives researchers a much larger characterization toolbox compared to those working with macrogels.

Microgel research dramatically expanded with the advent of PNIPAM microgels. We made the first PNIPAM microgel in 1978 and we were allowed to publish the work 1986, followed by the first description of a polystyrene-core-PNIPAM shell latex or microgel in 1988 – the definitions blur when considering solid core-gel shell particles. In my opinion, the large number of subsequent microgel publications arises for two reasons. First, microgels based on LCST polymers are extremely easy to make, modify and purify - one does not have to be a highly skilled synthetic polymer chemist to prepare microgels. Second, easy to measure properties including electrophoretic mobility and hydrodynamic particle size from dynamic light scattering, are sensitive functions of temperature, pH, and the presence of surfactants, proteins and other solutes.

The ease of PNIPAM microgel synthesis is a direct consequence of the LCST behavior of PNIPAM. Indeed, I believe that this link to microgel synthesis is the most important consequence of the temperature sensitivity of PNIPAM and related

polymers – there are few applications that actually exploit the temperature sensitivity. The importance of the LCST, or more correctly cloud behavior, in microgel preparation is illustrated by comparing the synthesis of PNIPAM microgels to polyacrylamide microgels. When polymerizing N-isopropylacrylamide in water above the cloud point, the growing polymer chains phase separate (coil-to-globule transition) leading to homogeneous nucleation of dispersed, microgel particles. The PNIPAM particle formation mechanism is analogous to the surfactant-free polymerization of styrene. By contrast, there are very few publications involving cross-linked polyacrylamide microgels because they are difficult to make, and nearly impossible to make as uniform particles. Polyacrylamide is water soluble and does not spontaneously yield microgels. Instead, polyacrylamide microgels must be prepared by a more complex procedure, such as pre-emulsification of aqueous monomer in oil followed by polymerization.

In 2000 I published a review summarizing microgel science and technology – this would be a daunting task now because of the volume of work in the last decade. The ranges of activities summarized in the following chapters highlight the breadth and complexity of the microgel landscape. I finish this essay with my biased view of the main trends in microgel research, and as well, some unanswered questions that have nagged me over they years.

Trend 1 – Applications: In line with the general trends in modern chemistry/material science, microgel publications include a strong emphasis on potential applications. In many cases the potential applications appear to be added as an afterthought, presumably to justify the work; in a few cases the application is the main emphasis and microgels are a means to an end. From my earliest days working with microgels, I have believed there must exist some good applications for microgels. In view of the volume of microgel literature with links to potential applications, many others must feel the same. Some early outstanding examples are Pichot's body of work using microgels as platforms for bioassays, and Asher's concept of responsive microgel-based colloidal arrays. Many clever and more recent examples are found in the following chapters. Nevertheless, one can argue that a "killer application" has yet to surface. To the best of my knowledge, aqueous synthetic microgels are not manufactured in large scale and they do not appear in consumer products. Of course there are food hydrocolloids, nano-particulate starch and other examples of commodities that could be considered as microgels – definitions are always controversial.

Trend 2 – Biodegradable Microgels: I suspect that the largest number of proposed microgel applications is biomedical, and most of those involve controlled drug release. For implanted microgels, biodegradability is an issue. *In vivo* decomposition requires that PNIPAM and other vinyl polymers must be replaced by polyesters, polyamides and other degradable backbones. In many cases biodegradability comes with the cost of losing the exquisite control of composition and particle size achievable with vinyl polymerization.

Trend 3 – Complex Functionalization: The original PNIPAM microgels offered little more than temperature sensitive swelling and a few sulfate or amidine groups. One can find microgel examples of all the popular forms of conjugation from

biotinylation to click chemistry. Because microgels can be dialyzed, filtered, and centrifuged, purification and multi-step reactions are easier with microgels than with the corresponding soluble polymers. In most cases, the starting point for functionalization is the inclusion of carboxyls or amine groups in the parent microgels. With PNIPAM and related microgels, the topochemical distribution of these attachment points within the microgel particles is controlled by the polymerization kinetics.

Trend 4 – Organic/inorganic Composite Microgels: Magnetic microgels, quantum dot-loaded gels, and virtually any other nanoparticle-load microgel one can imagine has been reported. The synthesis either involves growing nanoparticles within the microgels or loading gels with existing particles. These systems should greatly expand the application space for microgels. Hellweg in Chapter 2 describes examples of composite microgels.

Trend 5 – Assembled Microgels: In my view, one of the most promising areas for microgels involves the assembly of microgels in much larger and complex structures. The early papers by Sandy Asher, Zhibing Hu and Andrew Lyon focused on exploiting the environmentally sensitive photonic properties of microgel based colloidal crystals. Microgels are readily printed by ink jet and other water-based printing technologies, facilitating roll-to-roll manufacturing of patterned surfaces. Surely the "killer application" is coming.

Microgel science is mature. With a thirty plus year history and the accumulated knowledge in hundreds of publications, it is possible to synthesize and characterize almost any microgel structure one could imagine. Nevertheless, there are some gaps. With the exception of neutron scattering, there are few (no?) tools to measure the mass and functional group distribution within microgel particles. Compared to our structural knowledge of proteins such as enzymes or other synthetic systems such as self-assembled monolayers, we know little about the detailed organization of microgels. Controlled radical polymerizations should give better control of microgel structure, facilitating characterization – see Matyjaszewski, Chapter 9.

The polymer reaction engineering aspects of microgels have received little attention. Hoare's work is the only significant kinetic modeling and there have been few measurements of microgel polymerization kinetics. Such work will be required to transform impractical academic microgel recipes (dilute solution, long reaction times, and purification by ultracentrifugation) into a commercial process when large scale applications emerge.

In closing, microgels are an established subset of the materials toolbox. The chapters herein describe fascinating phenomena that point to a multitude of potential applications. In my view, microgel science will not evolve as a separate field but will continue to occupy an important position in the hierarchy of nano-colloidal dispersed systems.

Robert Pelton
McMaster University

Preface

The idea of polymers, or more colloquially "plastics", was initially met with scrutiny at the time of the initial experiments of Staudinger and Carothers. Despite this scrutiny, their ideas were eventually accepted, and these days one would be hard pressed to live one day (possibly one minute) without having contact with polymer-based materials. Whereas countless varieties of polymers, and polymer-based materials exist, this book focuses solely on colloidally stable hydrogel particles. Hydrogel particles, often referred to as microgels or nanogels depending on the length scale of their smallest dimension, are composed of a cross-linked hydrophilic polymer network. Because of the hydrophilicity of the polymer, and the cross-linked nature of the structure, the particles swell with water, typically taking on a spherical shape. Hydrogel particles have found their way into numerous applications ranging from lubricants in machinery to targeted/controlled drug delivery. Looking forward, there are still many potential applications that could benefit tremendously from new, enabling microgel-based materials. With the prospect of revolutionizing specific technologies, comes basic research; this book is meant to highlight the most exciting and impactful current research in the fields of microgels and nanogels. The volume was assembled to highlight the newest synthetic routes, characterization methods, and applications emergent in the area. Leaders in the field have contributed chapters representative of their most recent results from their respective labs, thereby shedding light on the enormous potential of this unique class of matter.

In editing this book the authors owe a great deal of thanks to our respective group members for volunteering their time to aid with the review process of the submitted chapters. We also owe a great deal of gratitude to Anja Tschörtner and Martin Preuss of Wiley for allowing us the opportunity to edit this volume, and for their assistance along the way.

L. Andrew Lyon
Michael J Serpe

1
Thermally Sensitive Microgels: From Basic Science to Applications

He Cheng and Guangzhao Zhang

1.1
Introduction

A thermally sensitive microgel is a microscopic three-dimensional gel network (10^2 nm) consisting of crosslinked macromolecular chains that can undergo volume "phase" transitions in response to temperature. Since the first thermally sensitive microgel – poly(*N*-isopropylacrylamide) (PNIPAM) microgel – was synthesized in 1986 via precipitation polymerization [1], microgels have received increasing interest because of their applications in hollow thermosensitive capsules, heat storage, thermoregulated textiles [2], *in vivo* diagnostics [3], and gene or drug delivery [4]. Moreover, since a microgel can vary in size from tens of nanometers to several micrometers, it exhibits unique physical properties between those of a polymer coil and a macroscopic gel [5]. In fact, because the swelling or shrinking of a microgel is caused by conformational changes of the subchains between two neighboring crosslinking points inside the gel network, the coil-to-globule transition of individual linear polymer chains can help us to understand the swelling/shrinking of a thermally sensitive microgel.

In terms of the mean field theory of Flory [6], the coil-to-globule region in the phase diagram is sandwiched between the θ-region and the phase boundary [7]. Stockmayer predicted that a flexible linear homopolymer chain can switch its conformation from an expanded coil to a collapsed globule if the solvent quality gradually changes from good to poor but will still remain in the one-phase region [8]. However, the coil-to-globule transition of single chain is difficult to observe experimentally because of the very narrow temperature window resolved [9–18]. Grosberg and Kuznetsov [19] predicted a two-stage kinetic for the collapse of a single chain, namely, a fast crumpling of the unknotted chain followed by a slow knotting of the collapsed polymer chain. The two-stage kinetic was experimentally observed by Chu and coworkers [20, 21] in the study of the collapse of single polystyrene chain. In 1996, Wu *et al.* [22, 23] successfully observed the coil-to-globule transition of thermally sensitive PNIPAM homopolymer chains in water, which has a lower critical solution temperature (LCST) at ∼32 °C. The study provides fundamentals for studying PNIPAM microgels.

Hydrogel Micro and Nanoparticles, First Edition. Edited by L. Andrew Lyon and Michael Joseph Serpe.
© 2012 Wiley-VCH Verlag GmbH & Co. KGaA. Published 2012 by Wiley-VCH Verlag GmbH & Co. KGaA.

The mechanisms for volume phase transition, internal motion, aggregation, and non-ergodic phenomena are fundamental problems in gel systems. We will introduce the developments in the fields by using microgel as a model system. Section 1.2 is about the theoretical background. Section 1.3 deals with the basic physics of microgels. The applications of microgels are presented in Section 1.4.

1.2 Theoretical Background

1.2.1 Thermodynamics of Volume Phase Transition

The swelling or shrinking of polymer gels is a fundamental and classic problem in polymer physics. Dusek and coworkers [24, 25] showed that certain polymer gels can undergo a discontinuous volume change or the so-called volume phase transition with temperature. Supposing the chemical potential of the solvent is in equilibrium with that of the swollen gel,

$$\frac{\Delta\mu_1}{RT} = \ln a_1 = \ln(1-\varphi_2) + \varphi_2 + \chi_T\varphi_2^2 + \zeta(\varphi_2^{1/3} < \alpha^2>_0 - \kappa\varphi_2) \tag{1.1}$$

the chemical potential per equivalent segment ($\Delta\mu_2/n$) of the network polymer is,

$$\frac{\Delta\mu_2}{nRT} = -\varphi_1 + \chi_T\varphi_1^2 + \zeta\left[< \alpha^2>_0 \left(\frac{\varphi_2^{-2/3}}{2} + \varphi_2^{-1/3} - \frac{3}{2}\right) - \kappa(\ln\varphi_2 + \varphi_1)\right] \tag{1.2}$$

where the subscripts 1 and 2 denote the solvent and the polymer, respectively, $n = V_2/V_1$ with V being the partial molar volume, φ is the volume fraction, χ_T is the Flory–Huggins polymer–solvent interaction parameter depending on the temperature T, $\zeta = \varrho V_1/M_c$, where ϱ and M_c are respectively the density of the dry gel and the average molar mass of the subchain between two neighbor crosslinking points. The isotropic deformation factor of the gel network $<\alpha^2>_0$ is defined as the ratio of the mean square end-to-end distance of the chains in a dry network to that of unperturbed free chains. $0 < \kappa < 1$, depending on the models [26–28].

When two phases with different concentrations coexist, the equations $\mu_1 = \mu'_1$ and $\mu_2 = \mu'_2$ have a solution outside the unstable region wherein $\partial\Delta\mu_2/\partial\varphi_2 > \partial\Delta\mu_1/\partial\varphi_2$. Inserting Equations 1.1 and 1.2 into $\mu_1 = \mu'_1$ and $\mu_2 = \mu'_2$, one can calculate the curves describing the composition of the gel, namely χ_T versus φ_2. The coexistence of the swollen and the collapsed phases requires that χ_T is sufficiently high but $<\alpha^2>_0$ and M_c are sufficiently low. However, a low M_c means a high crosslinking density or a high $<\alpha^2>_0$. Therefore, it is practical to choose a gel system with a strong interaction between the polymer network and solvent (i.e., a higher χ_T) to study the volume phase transition.

Hydrogels are often used to test the theoretical prediction in experiments because of their higher χ_T values. Lightly crosslinked PNIPAM gels show a sharp volume

change at ~33 °C, which was taken as the discontinuous volume phase transition [29–34]. However, a continuous volume change was also observed for PNIPAM and other hydrogels [35–38]. Clearly, on the basis of Equations 1.1 and 1.2, a discontinuous volume phase transition is expected as long as the equations $\mu_1 = \mu'_1$ and $\mu_2 = \mu'_2$ have a solution outside the unstable region. It should be noted that Li and Tanaka [35] showed that as the crosslinking density of a bulk PNIPAM gel decreases, a continuous volume change transits into a discontinuous one.

1.2.2 Internal Motion

Pecora showed that when an infinitely dilute polymer solution is illuminated by a coherent and monochromatic laser light beam, the spectral distribution of the light scattered from a flexible polymer chain can be written as [39]

$$S(q,\varpi) = (1/2\pi)\int \mathrm{e}^{-i\varpi t}\mathrm{e}^{-q^2 D|t|}S(q,t)\mathrm{d}t \tag{1.3}$$

where ω is the angular frequency difference between the scattered and the incident light, D is the translational diffusion coefficient of individual chains, and $S(q,t)$ is generally expressed as

$$S(q,t) = < (1/N^2)\sum_{i=0}^{N}\sum_{j=0}^{N}\mathrm{e}^{-iq\cdot[r_i(0)-r_j(t)]} > \tag{1.4}$$

which is due to the interference of the scattered light from different segments within a long polymer chain made of N such segments, where $\boldsymbol{r}_i(0)$ is the position of the ith segments at time 0 and $\boldsymbol{r}_j(t)$ is the position of the jth segment at time t, both referred to the center of mass of the polymer.

To perform the ensemble average in $S(q,t)$, a model for the internal motion of a chain is needed. By incorporating the Oseen–Kirkwood–Riseman hydrodynamic interaction into the bead-and-spring model, Perico, Piaggio, and Cuniberti have shown [40, 41]

$$\begin{aligned} S(q,\varpi) = {} & P_0(x)L(\varpi, q^2 D) + \sum_{\alpha=1}^{N} P_1(x,\alpha)L(\varpi, q^2 D + \Gamma_\alpha) \\ & + \sum_{\alpha=1}^{N}\sum_{\beta=1}^{N} P_2(x,\alpha,\beta)L(\varpi, q^2 D + \Gamma_\alpha + \Gamma_\beta) \\ & + \sum_{\alpha=1}^{N}\sum_{\beta=1}^{N}\sum_{\gamma=1}^{N} P_3(x,\alpha,\beta,\gamma)L(\varpi, q^2 D + \Gamma_\alpha + \Gamma_\beta + \Gamma_\gamma) + \cdots \end{aligned} \tag{1.5}$$

where $x = (qR_g)^2$, and the function

$$L(\varpi,\Gamma) = \frac{2\Gamma}{2\pi(\varpi^2 + \Gamma^2)} \tag{1.6}$$

This represents the ω-normalized Lorentzian distribution with Γ being the half-width at half-height, that is, the line width, and P_n ($n = 0,1,\ldots$) determines the contribution of each Lorentzian to the line width distribution $G(\Gamma)$ of the scattered light. The zeroth-order of $P_0(x)$ represents the contribution from the translational diffusion, $P_1(x,\alpha)$ is the first-order contribution of the αth internal mode, $P_2(x,\alpha,\beta)$ is the second-order contribution of the αth and βth internal modes, and so on. When $x < 1$, the spectral distribution is measured in the long-wavelength regime and the polymer chain is viewed as a point. Accordingly, $P_0(x)$ is dominant in $S(q,\omega)$. As x increases, the light probes a portion of the chains and the contributions from $P_1(x,\alpha)$, $P_2(x,\alpha,\beta)$, and other higher order terms become more important. Perico and coworkers have numerically shown that $P_2(x,1,1)$ is the largest contribution to $S(q,\omega)$ among all Lorentzian terms associated with the internal modes [40, 41].

According to the theories for a flexible polymer coil in the free-draining [42] and nondraining limits [40, 41], When $x > 1$, $S(q,t)$ mainly depends on the first five relaxation processes, namely, a pure translational term plus four principal internal motions. In decreasing order of the contributions to the spectrum, Equation 1.5 in the time domain at $x > 1$ can be written as

$$S(q,t) = \sum_{n=0}^{\infty} P_n \mathrm{e}^{-\Gamma_n t} \tag{1.7}$$

where P_n (the numeric values) in the range of $1 \leq x \leq 10$ have been calculated by Perico and coworkers [40, 41]. On the basis of the Zimm model [43],

$$\Gamma_n/(Dq^2) = \frac{0.293RT\lambda_n' R_g^2}{xD\eta_0 M[\eta]}. \tag{1.8}$$

where $RT/(D\eta_0) = 6\pi R_h N_A$ (the Stokes–Einstein equation) so that

$$\Gamma_n/(Dq^2) = \frac{5.52\lambda_n' R_g^2 R_h}{xM[\eta]} = \frac{5.52\lambda_n'(R_g/R_h)^2}{x}\frac{R_h^3}{M[\eta]} \tag{1.9}$$

where $[\eta]$ is the intrinsic viscosity, λ'_n are the eigenvalues in the Zimm model [44], $M[\eta]$ is a measure of hydrodynamic volume, $M[\eta]/R_h{}^3 = \Phi$ (the Flory constant), which is widely used as the universal calibration in gel permeation chromatography (GPC), and R_g/R_h depends weakly on the nature of polymer and solvent for flexible linear polymer chains in a good solvent.

In a modern dynamic laser light scattering (DLS) experiment, the intensity–intensity time correlation function of the scattered light can be measured from which $S(q,t)$, and the Fourier transform of $S(q,\omega)$ is determined.

1.2.3 Dynamics of Microgel

In static laser light scattering (SLS), the angular dependence (15–150°) of the excess absolute time-averaged scattered intensity, that is, the Rayleigh ratio $R_{vv}(q)$, which leads to the weight-averaged molar mass M_w and the z-averaged root mean square

radius of gyration $<R_g{}^2>_z{}^{1/2}$ (or written as $<R_g>$) of scattering objects and the scattering vector q as [45],

$$\frac{Kc}{R_{vv}(q)} = \frac{1}{M_w}\left(1 + \frac{1}{3} < R_g^2 > q^2 - \cdots\right) + 2A_2c - \cdots \tag{1.10}$$

In DLS, the intensity–intensity time correlation function $g^{(2)}(t,q)$ in the self-beating mode was measured, where t is the decay time. The $g^{(2)}(t,q)$ function can be related to the normalized first-order electric field time correlation function $|g^{(1)}(t,q)|$ via the Siegert relation as $g^{(2)}(t,q) = B[1 + \beta|\, g^{(1)}(t,q)|^2]$ where B ($\equiv <I(0)>^2$) is the measured baseline. For the broadly distributed relaxation spectrum, $|g^{(1)}(t,q)|$ is related to a characteristic relaxation time distribution $G(\tau)$, that is, $|g^{(1)}(t,q)| \equiv <E(0,q)E^*(t,q)>/<E(0,q)E^*(0,q)> = \int G(\tau)e^{-t/\tau}d\tau$, where $G(\tau)$ can be calculated from the Laplace inversion of the measured $g^{(2)}(t,q)$ [51]. For a pure diffusive relaxation, the characteristic decay time, $\Gamma = 1/\tau$, can be related to the translational diffusion coefficient D by $(\Gamma/q^2)_{C\to 0, q\to 0} = D$ or a hydrodynamic radius $R_h = k_BT/6\pi D\eta$ with k_B, T, and η being the Boltzmann constant, the absolute temperature and the solvent viscosity, respectively [46, 47].

In a semi-dilute solution or a solution undergoing the crosslinking reaction, $|g^{(1)}(t,q)|$ can also be analyzed by a single-exponential function combined with a stretched exponential function to take care of the additional slow relaxation as follows [48–51],

$$\left|g^{(1)}(t,q)\right| = A_f \exp\left(-\frac{\tau}{<\tau_c>_f}\right) + A_s \exp\left(-\frac{\tau}{<\tau_c>_s}\right)^b \tag{1.11}$$

where A and $<\tau_c>$ are the intensity weighting and the average characteristic decay time, respectively; subscripts "s" and "f" denote the fast and slow modes, respectively; and $0 < b < 1$, a constant related to the distribution width of the characteristic decay time. Note that $A_f + A_s = 1$. Strictly speaking, when using Equation 1.11, we have assumed that the two relaxation modes are "monodisperse," which is not true in reality [52].

For a non-ergodic system, the time-averaged scattered light intensity, $<I>_T$, is different from the position-averaged ones, and it contains both static and dynamic contributions, $<I>_s$ and $<I>_d$, namely [53],

$$<I>_T = <I>_s + <I>_d \tag{1.12}$$

where $<I>_d$ is independent of the sample position but $<I>_s$ not. Therefore, at a given q, for each chosen sample position, we can measure one $<I>_T$ and one normalized intensity–intensity time correlation function $g^{(2)}(t,q)$. $g^{(2)}(t,q)$ can be written as [53–56],

$$\begin{aligned}\left|g^{(2)}(t,q)\right| = &\left(\frac{<I>_d}{<I>_T}\right)^2 \exp\left(-2Dq^2t\right) \\ &+ 2\left(\frac{<I>_d}{<I>_T}\right)\left[1 - \left(\frac{<I>_d}{<I>_T}\right)\right]\exp\left(-Dq^2t\right)\end{aligned} \tag{1.13}$$

For a non-ergodic system at a given q, one can measure the time-averaged scattered intensity from different sample positions to obtain an ensemble-averaged scattered intensity, $<I>_E$. Note that for a given q, $<I>_T$ depends on the sample position, but not $<I>_E$ by its definition: $<I>_E = \Sigma <I>_{T,i}/N$, where I=1,2,. . .,N, and N is the number of the positions measured. Only in an ergodic system, $<I>_E$=$<I>_T$. In the dynamic measurement, the initial slope of each $\ln g^{(2)}(t,q)$ vs. t leads to an apparent diffusion coefficient D_A in the range of $D/2 < D_A < D$. It is known that D and $<I>_d$ are related to D_A and $<I>_T$ as [53, 54]

$$\frac{<I>_T}{D_A} = \frac{2<I>_T}{D} - \frac{<I>_d}{D} \tag{1.14}$$

Experimentally, for each chosen sample position at a given q, one can measure one $<I>_T$ from SLS and calculated one D_A from $g^{(2)}(t,q)$ measured in DLS. Therefore, on the basis of Equation 1.13, D and $<I>_d$ can be respectively obtained from the slope and the intercept of the plot of $<I>_T/D_A$ vs. $<I>_T$ by measuring at a number of sample positions.

1.2.4
Kinetics Calculation of Reversible Aggregation

Diffusion-limited cluster–cluster aggregation (DLCA) follows a second-order growth kinetics, and the coagulation kernel is independent of the size of resultant aggregates [57–59]. On the other hand, the fragmentation follows first-order kinetics, and its rate is also independent of the size of the aggregates [57]. Assuming that at any given time t, $N(t)$ is the total number of the microgel clusters, including individual microgels in which the aggregation number is only one, we can write the changing rate of $N(t)$ as [60]

$$\frac{dN(t)}{dt} = -k_a[N(t)]^2 + k_f\left[N_{microgel} - N(t)\right] \tag{1.15}$$

where $N_{microgel}$ is the total molar number of initial microgels in the dispersion, a constant for a given microgel concentration, and k_a and k_f are the rate constants of aggregation and fragmentation, respectively. As $t \to \infty$, $dN(t)/dt \to 0$ for a system at a dynamic equilibrium. In this way, the ratio k_a/k_f can be solved in terms of $N(\infty)$ and $N_{microgel}$, that is, $k_a/k_f = [N_{microgel} - N(\infty)]/N^2(\infty)$. Using the two boundary conditions, $N(0)$ and $N(\infty)$, we can analytically solve Equation 1.15 as

$$\ln \frac{[N(t)-N(\infty)][N_{microgel}N(0) - N(0)N(\infty) + N_{microgel}N(\infty)]}{[N(0)-N(\infty)][N_{microgel}N(t) - N(t)N(\infty) + N_{microgel}N(\infty)]} = -st \tag{1.16}$$

where $s = k_f[(2N_{microgel} - N(\infty))/N(\infty)]$. Experimentally, $N(0)$ and $N(\infty)$ can be determined from the weight-averaged molar masses of the microgel clusters ($M_{w,c}(0)$ and $M_{w,c}(\infty)$) at $t \to 0$ and $t \to \infty$, respectively. This is because the total microgel mass

(M_{total}) for a given dispersion is a constant, namely, $M_{total}=M_{w,m}N_{microgel}=M_{w,c}(t)\ N(t)$. Since $N(t)$ is proportional to the reciprocal of $M_{w,c}(t)$, Equation 1.16 can be rewritten as

$$\frac{[M_{w,c}(t)-M_{w,c}(\infty)][M_{w,c}(\infty)+M_{w,c}(0)-M_{w,m}]}{[M_{w,c}(0)-M_{w,c}(\infty)][M_{w,c}(\infty)+M_{w,c}(t)-M_{w,m}]}=\exp(-st) \tag{1.17}$$

The left side of Equation 1.17 can be measured experimentally.

1.3 Basic Physics of Microgels

A thermally sensitive microgel provides a model system in polymer physics. On one hand, its three-dimensional crosslinked polymer network shows typical viscoelastic property. On the other hand, a microgel with a dimension between polymer coil and gel shows a combination of their physical properties.

1.3.1 Volume Phase Transition

The volume phase transition theory states that the phase transition temperature depends on the length of the subchain between two neighboring crosslinking points inside the gel, so it is helpful to compare the results for linear chains and spherical microgels [61–64].

Figure 1.1 shows the temperature dependence of the expansion factor α_h [$\equiv<R_h>/<R_h>_\Theta$], where $<R_h>_\Theta$ is the hydrodynamic radius at $T=\Theta$. The volume change associated with the temperature dependence of the hydrodynamic

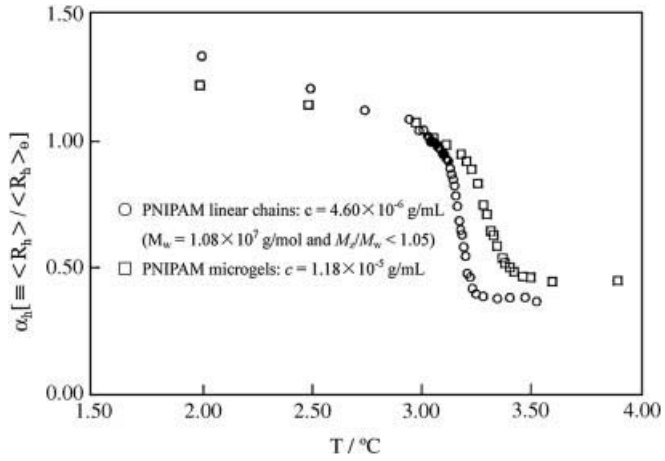

Figure 1.1 Expansion factor α_h [$\equiv<R_h>/<R_h>_\Theta$] as a function of temperature for the PNIPAM microgels and individual chains, where $<R_h>_\Theta$ is the hydrodynamic radius at $T=\Theta$. Reprinted with permission from [64], Wu, C. *Polymer* 39, 4609, 1998. © 1998 Elsevier Science.

radii of both the linear chains and the spherical microgels is continuous. It is well known that for a linear polymer chain in solution its phase transition temperature has molecular weight dependence [6]. For a given polymer solution with a LCST, the higher the molecular weight, the lower the phase transition temperature. For a polydisperse sample, polymer chains with different lengths undergo phase transition at different temperatures, leading to a continuous transition. Figure 1.1 shows that the microgels swell less than the linear chains in the good solvent region. The phase transition temperature of the microgel is ~1.5 °C higher than that of the PNIPAM linear chains. At a low temperature, either the microgels or the linear chains are swollen. As temperature increases, the segment–segment interaction becomes strong, and they start to collapse. However, the detailed mechanism is different. When a gel is swollen, the elasticity would retard the chain expansion in good solvent. In a poor solvent, the elasticity prevents its collapse. Therefore, a linear chain collapses easier than a gel.

Figure 1.1 also indicates that linear chains have a sharper volume change than microgels. Tanaka *et al.* [29] attributed this to the polydispersity of microgels. However, according to Equations 1.1 and 1.2, the phase transition temperature or χ_T is not related to the gel dimension but the subchain length or M_c because the temperature is a thermodynamic intensive property.

Figure 1.2 shows a simulation of χ_T vs. φ based on Equations 1.1 and 1.2, where χ_T decreases as ζ decreases, that is, as M_c decreases. Therefore, the transition temperature decreases as M_c increases. Clearly, the linear chains have a lower transition temperature because of their much higher average molecular weight ($M_w = 1.08 \times 10^7\,g\,mol^{-1}$) compared to the subchains ($M_c \sim 10^4\,g\,mol^{-1}$) inside the microgels.

Normally, the subchains inside a polymer gel have a broad molecular weight (length) distribution and a gel network can be visualized as a set of subnetworks with different M_c. As temperature varies, the subnetwork with a longer subchain undergoes phase transition before that with a shorter subchain. Thus, different parts of the

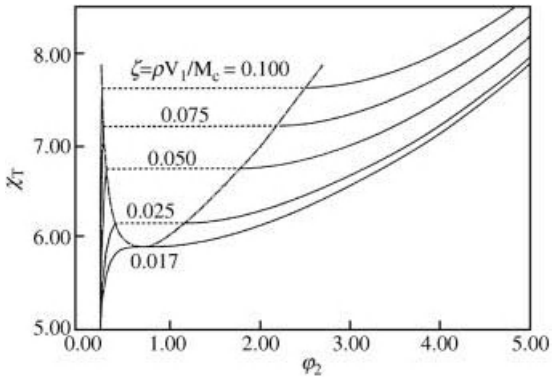

Figure 1.2 Plot of χ_T versus φ_2 for a polymer gel based on Equations 1.1 and 1.2, where we have chosen $\kappa = 0.5$, $<\alpha^2>_0 = 0.04$, and $\zeta = \varrho V_1/M_c$. Reprinted with permission from [65], Wu, C. and Zhou, S.Q. *Macromolecules* 30, 574, 1997. © 1997 American Chemical Society.

gel network experience phase transition at different temperatures. The fact that a transparent PNIPAM gel changes into a milky gel in phase transition indicates the microscopic inhomogeneity. Therefore, the volume phase transition of a polymer gel should be practically continuous because the subchains normally have a broad chain length distribution. With the subchain inhomogeneity concept, it is also possible to explain that higher homogeneity gels with a lower crosslinking density display a discontinuous volume phase transition.

In principle, the discontinuous volume phase transition predicted on the basis of Equations 1.1 and 1.2 is correct if M_c is a constant or the subchains have a uniform chain length. However, it will be extremely difficult to prepare such a gel, if not impossible. Note that the use of one average M_c in Equations 1.1 and 1.2 is very successful in many other predictions; for example, the relation between a shear modulus G and M_c, that is, $G = RT\varrho\Phi/M_c$, where Φ is the volume ratio of the dry and swollen gels.

The discontinuous volume phase transition of bulk PNIPAM gel can be explained as follows. As discussed above, longer subchains inside the gel undergo phase transition before shorter subchains. Then, the shrinking of a small amount of longer subchains initially cannot alter the overall dimensions of a bulk gel because of its shear modulus, but can build up stress inside the gel. The stress will gradually increase until the shear modulus cannot maintain the macroscopic shape of the gel, and the overall dimension of the gel will change abruptly, leading to a discontinuous macroscopic volume change with temperature. As for the microgels with an average radius of $\sim$0.1–0.2 μm, the shear modulus plays a minor role so that its dimension changes continuously when the stress increases. Generally, it takes several days for a bulk gel to attain the swelling or shrinking equilibrium [66]. In the process, unless the temperature is kept to be a constant with a fluctuation less than $\pm$0.01 °C and the incremental temperature is less than 0.1 °C, a continuous volume phase change can be taken to be a discontinuous one. In contrast, it takes less than one second for microgels to reach equilibrium, so the study of microgels is more straightforward.

1.3.2 Internal Motion

Dynamics of linear flexible chains such as polystyrene (PS), polyisoprene (PIP), and PNIPAM in solution have been examined. Here, we focus on the internal motion in PNIPAM linear chains and microgels in good and Θ solvents [67].

1.3.2.1 Internal Motions in Good Solvent

Figure 1.3 shows typical plots of $G(\Gamma/q^2)$ vs. Γ/q^2 for individual PNIPAM linear chains at 15 °C and different x. $G(\Gamma/q^2)$ changes with x: at $x < 1$, there exists only a single narrow peak which corresponds to the Brownian motion of PNIPAM linear chains in solution. When $x \sim 1$, a second peak appears at larger Γ/q^2, while the first peak basically retains its position. This second small peak is related to the internal motions of PNIPAM chains. The first peak becomes broader and shifts to larger Γ/q^2

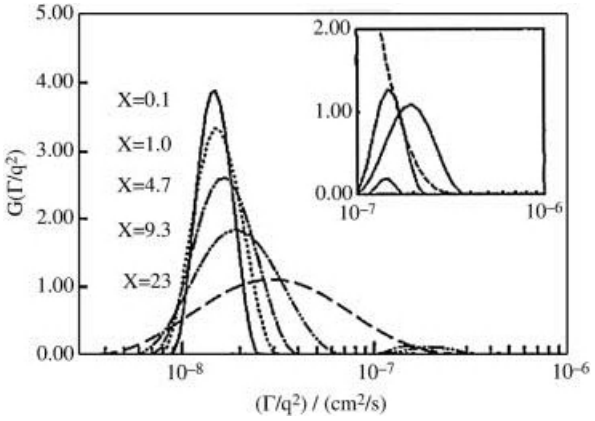

Figure 1.3 Typical line width distributions $G(\Gamma/q^2)$ of the PNIPAM linear chains at 15 °C. The insert shows a 10-fold enlargement of the second peak in the range of $10^{-7} < \Gamma/q^2 < 10^{-6}\,\mathrm{cm^2\,s^{-1}}$. Reprinted with permission from [68], Wu, C. and Zhou, S.Q. *Macromolecules* 29, 1574, 1996. © 1996 American Chemical Society.

with x. This is understandable because the observation length scale ($1/q$) is much shorter than R_g at larger x and the observation is well inside the microgel particle. More internal motions with larger Γ contribute to the relaxation and mix with the translational diffusion in the measured spectrum. Finally, two peaks merge into one broader peak because the line width associated with D increases with q, while the line widths related to the internal motions are independent of q.

Figure 1.4 shows a plot of $<\Gamma>_{peak2}/(Dq^2)$ vs. x, where $<\Gamma>_{peak2}$ is the average line width of the second peak in Figure 1.3. For comparison, previous experimental data

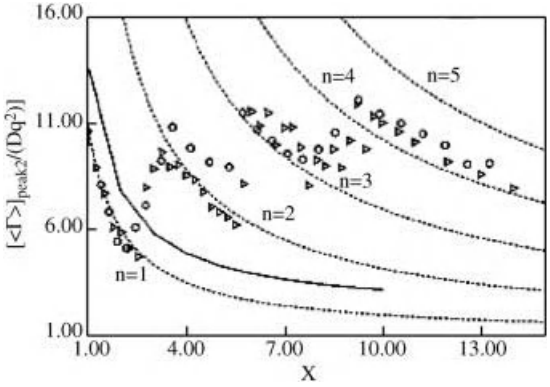

Figure 1.4 Plots of the reduced average line width $<\Gamma>_{peak2}/(Dq^2)$ vs. x. Open circles: PNIPAM linear chains in water at T=15 °C; triangles: polystyrene in toluene at T = 20 °C [108]. The dashed lines are predicted in [108], and the full lines are calculated from Equations 1.7 and 1.8. Reprinted with permission from [68], Wu, C. and Zhou, S.Q. *Macromolecules* 29, 1574, 1996. © 1996 American Chemical Society.

about polystyrene are also plotted here [69]. Clearly, the two plots follow a similar pattern. The dotted lines in Figure 1.4 show the predicted $[1 + 2\Gamma_n/(Dq^2)]$ dependence on x for polystyrene in toluene [69]. As discussed in Section 1.2, Equation 1.9 predicts that Γ_n is independent of polymer and solvent for polymers in good solvents. Equation 1.9 also reveals that $\Gamma_n/(Dq^2)$ decreases as x increases for a given temperature, which explains the shift of the average position of the second peaks. Figure 1.4 shows that the two sets of results from completely different polymer/solvent systems follow a very similar pattern, which indicates that the prediction of Equation 1.9 is essentially correct.

The average line width $<\Gamma>_{int}$ associated with the internal motions can be calculated by using the numeric values of P_n in Refs [40, 41] and the values of Γ_n calculated from Equation 1.8 for polystyrene in toluene at 20 °C [69]. The plot of $<\Gamma>_{int}/(Dq^2)$ vs. x (the solid line) is illustrated in Figure 1.4. If Equation 1.7 was right, $<\Gamma>_{int}/(Dq^2)$ would follow the solid line. But Figure 1.4 shows a clear deviation between the data and the solid line. On the other hand, Figure 1.4 shows that the experimental data have a tendency to respectively follow the dotted lines of $n = 1$ in $1 < x < 3$; $n = 2$ in $3 < x < 6$; $n = 3$ in $6 < x < 10$; $n = 4$ in $10 < x < 15$. Thus, Γ_1, Γ_2, Γ_3, and Γ_4 in different ranges of x can be estimated by analyzing $<\Gamma>_{int}/(Dq^2)$ in Figure 1.4 with an assumption of $<\Gamma>_{int}/(Dq^2) = 1 + 2<\Gamma>_n/(Dq^2)$. For $x > 15$, two peaks in Figure 1.3 merge into a broader peak, which makes it difficult to get a precise $<\Gamma>_{peak2}$ value from the spectral distribution $G(\Gamma)$. So we stopped the second peak analysis at $x > 15$ to avoid any ambiguity. It shows the internal motion in either polystyrene or PNIPAM is related to $2\Gamma_n$ or $\Gamma_n + \Gamma_n$ dominates the relation measured in DLS in different range of x. $\Gamma_n + \Gamma_n$ relaxation implies a self-coupling of nth order internal motion based on Equations 1.5 and 1.7. So far, the nature of the internal motion remains unclear. Energetically, it is easier to excite the internal motions associated with Γ_1 and $4\Gamma_1$ than those with $2\Gamma_2$, $2\Gamma_3$, and $2\Gamma_4$. What is observed is $2\Gamma_2$ instead of Γ_1 and $4\Gamma_1$, indicating that DLS can only measure a certain kind of internal motion because of the observation length scale $1/q$. Therefore, not all internal motions can be observed by DLS in a certain range of x, although they do exist.

A similar phenomenon is also observed in PNIPAM microgels. Figure 1.5 shows $G(\Gamma/q^2)$ vs. Γ/q^2 plot for the spherical PNIPAM microgel particles as a function of x at 15 °C. $G(\Gamma/q^2)$ is independent of x at $x < 13$ and only a single, narrow peak is observed. When $x > 13$, a very small second peak associated with the internal motions of the microgel network appears. By comparison with Figure 1.3, we can see that the internal motions for the linear chains start to contribute to $G(\Gamma)$ when $1/q \sim R_g$, while the internal motions for the particles appear only when $1/q \sim R_g/(13)^{1/2} \sim R_g/3.6$. Thus the former involve the entire chain, while the latter are only related to a fraction of the microgel network.

1.3.2.2 Internal Motions in Θ and Poor Solvents

Figure 1.6 shows that the extrapolation of time-averaged scattered light intensity at different temperatures to zero angle leads to an identical value, indicating no change in the weight-averaged molar mass, or collapse of individual linear PNIPAM chains

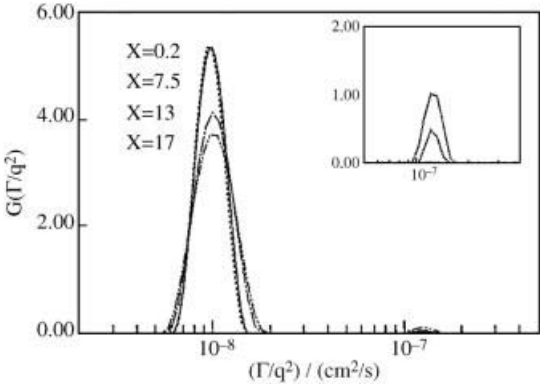

Figure 1.5 Typical plots of $G(\Gamma/q^2)$ vs. Γ/q^2 for the microgel particles at 15 °C. The insert shows a 10-fold enlargement of the second peak at $\Gamma/q^2 \sim 10^{-7}\,\mathrm{cm^2\,s^{-1}}$. Reprinted with permission from [68], Wu, C. and Zhou, S.Q. *Macromolecules* 29, 1574, 1996. © 1996 American Chemical Society.

without interchain association. Thus, the internal motions of individual chains at different temperatures can be studied, especially under the Θ temperature and in poor solvent conditions.

Figure 1.7 shows how the internal motions vary with the relative observation length scale (x) at 31.0 °C (Θ temperature) where the chains are not fully collapsed yet, and the line width (Γ) is scaled with translational diffusion coefficient (D) and scattering vector (q). It is worth noting that here $1/q$ is compared with R_g. For $x < 1$, that is, $1/q > R_g$, each chain behaves just like a structureless point so that we only see its Brownian motion. When $x \geq 1$, a second peak related to the internal motions appears in the measured line width distribution, which relaxes 10–20 times faster than the translational diffusion.

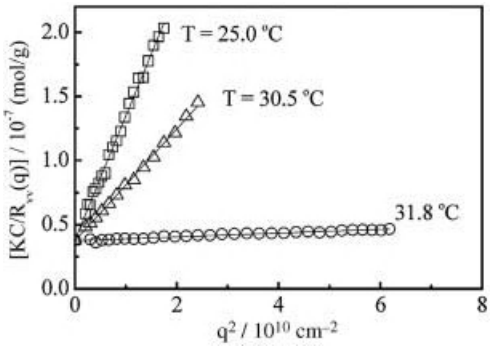

Figure 1.6 Scattering vector (angular)-dependent time-averaged scattered light intensity (Rayleigh ratio) of PNIPAM linear chains in water at three different temperatures. Reprinted with permission from [70], Dai, Z.J. and Wu, C. *Macromolecules* 43, 10064, 2010. © 2010 American Chemical Society.

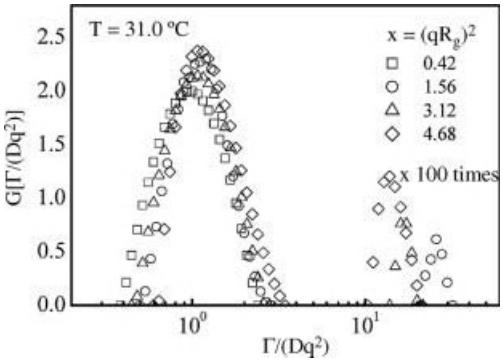

Figure 1.7 x-dependent Dq^2-scaled line width distributions $G(\Gamma/Dq^2)$ of PNIPAM linear chains in water, where the peak related to internal motions is enlarged by a factor of 100 times for a better view. Reprinted with permission from [70], Dai, Z.J. and Wu, C. *Macromolecules* 43, 10064, 2010. © 2010 American Chemical Society.

A parallel study of PNIPAM spherical microgels has also been conducted. The microgel collapses much less than the linear chains, presumably due to the crosslinking. In contrast to linear chains where internal motion is observed at $x \sim 1$, the second peak related to the internal motion of the microgels is much weaker and appears only when $x \geq 8$ at 25.0 °C; thus we can only observe their internal motions when $1/q \sim 50\,\text{nm} \leq \langle R_g \rangle/3$, instead of at $1/q \sim \langle R_g \rangle$, implying that the thermal energy can excite the entire linear chain with its longest normal mode, but only a small portion of a gel network with a dimension of ~50 nm.

Figure 1.8 shows that the internal motion at a smaller x (~5–6) can be observed at 31.5 °C, implying that the thermal energy excites a large portion of the gel

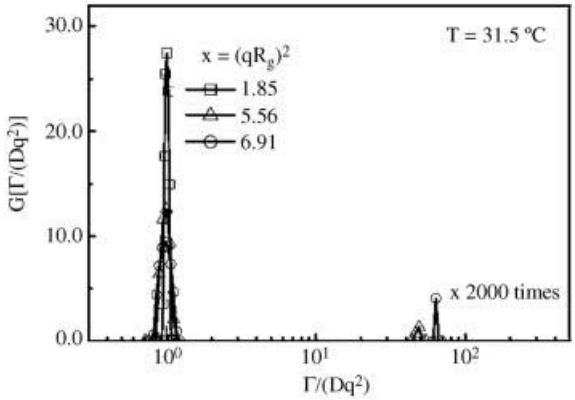

Figure 1.8 x-dependent q^2-scaled line width distributions $G(\Gamma/Dq^2)$ of PNIPAM microgels in water, where the peak related to internal motions is enlarged by a factor of 2000 for a better view. Reprinted with permission from [70], Dai, Z.J. and Wu, C. *Macromolecules* 43, 10064, 2010. © 2010 American Chemical Society.

network to undergo the internal motion and the microgel becomes softer. If we imagine that the gel network is made of small uniform meshes with a dimension of ~10 nm on the basis of the crosslinking density, we can estimate that the internal motions only involve about $\sim 10^2$ of such meshes from the minimum $1/q$. Note that such measured internal motions are slower than the relaxation of the subchains ("blobs") of a macroscopic gel network with a similar crosslinking density but faster than the translational diffusion of individual microgels in the dispersion.

1.3.3
Dynamics of Cation-Induced Aggregation of Thermally Sensitive Microgels

Despite a great deal of effort, the kinetics and dynamics of complex formation among polyelectrolytes and cations or protein are still poorly understood due to the complexity of the systems. These complex systems exhibit quite different responses to various experimental conditions. Here, we present the kinetics and dynamics of cation-induced aggregation of microgels in dilute solution, and the complexation between microgels and protein. The effects of temperature, pH, and ionic strength have been examined [71, 72].

1.3.3.1 Salt-Induced Complexation

Microgels made of poly(*N*-vinylcaprolactam) (PVCL) and a few per cent of sodium acrylate (SA) were used as a model system to study the cation-induced reversible and controllable aggregation of colloid particles because PVCL exhibits continuous shrinking in the range of 25–40 °C. The presence of SA can increase the extent of its swelling and shifts the temperature at which it shrinks to a higher level [73, 74]. It is known that certain alkaline earth ions and heavy metal ions can specifically interact with carboxylic groups [75, 76], which can lead to cation–polyanion complexation, even at a very low cation concentration [77]. This is probably because the addition of metal ions to an aqueous solution of polyanions alters the hydration or disrupts oriented water molecules near the chain [78–80].

Figure 1.9 shows the temperature dependence of the average hydrodynamic radius $\langle R_h \rangle$ and apparent weight-averaged molar mass ($M_{w,app}$) of linear P(VCL-*co*-SA) chains and microgels in 0.03 M $CaCl_2$ aqueous solution. In the range 25–31.8 °C, the microgels shrink with temperature but $M_{w,app}$ stays constant, indicating no inter-microgel aggregation. At ~32 °C, $\langle R_h \rangle$ and $M_{w,app}$ increase sharply, revealing a clear inter-microgel aggregation. Linear chains can entangle and complex with each other via the interaction between Ca^{2+} and COO^- to form a hyperbranched structure. For the microgels, when the transition temperature is reached, PVCL becomes hydrophobic and the microgel starts to collapse but the hydrophilic COO^- groups tend to stay on the periphery of the microgel. The complexation between Ca^{2+} and COO^- sticks the microgels together.

Figure 1.10 shows the effects of different cations on the P(VCL-*co*-SA) microgels as a function of temperature [81, 82]. Clearly, Na^+ has the weakest effect on microgels, while Hg^{2+} leads to profound shrinking. This is understandable because the

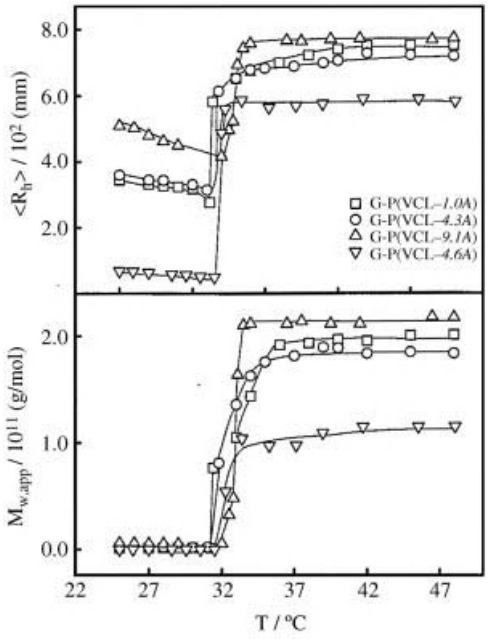

Figure 1.9 Temperature dependence of the average hydrodynamic radius $\langle R_h \rangle$ and apparent weight-averaged molar mass ($M_{w,app}$) of linear P (VCL-*co*-SA) chains and spherical microgels with the presence of Ca^{2+}, where $[Ca^{2+}] = 0.03$ M. Reprinted with permission from [71], Peng, S.F. and Wu, C.J. *Phys. Chem. B* 105, 2331, 2001. © 2001 American Chemical Society.

presence of monovalent Na^+ can only increase the ionic strength and reduce electrostatic repulsion between carboxylic groups. However, divalent cations can also pull two carboxylic groups together so that they can induce greater shrinking of the microgels. The fact that the molar mass of the microgels ($M_{w,\,microgel}$) remains a constant indicates that there is no interparticle complexation. In other words, the interaction between cations and microgels at 25 °C is intra-microgel. Figure 1.10 shows that in terms of the effect of different cations on the shrinking of the microgel, $Hg^{2+} > Cu^{2+} > Ca^{2+}$. This is related to the ion-specificity.

We have also studied the sorting of oppositely charged microgels, P(NIPAM-*co*-SA) and poly(*N*-isopropylacrylamide-*co*-vinylbenzyl trimethylammonium chloride) (P(NIPAM-*co*-VT)). In the absence of salt, P(NIPAM-*co*-SA) and P(NIPAM-*co*-VT) microgels in the mixture do not aggregate but shrink upon heating. The addition of monovalent cations does not affect the aggregation. In the presence of divalent metal ions, the heating leads to the association of P(NIPAM-*co*-SA) microgels via the complexation of metal ions and carboxyl groups on the microgel surface when the temperature approaches the LCST. Further increasing the temperature over the LCST results in the adsorption of P(NIPAM-*co*-VT) microgels on the P(NIPAM-*co*-SA) aggregate via the electrostatic attraction so that a core–shell structure, with a

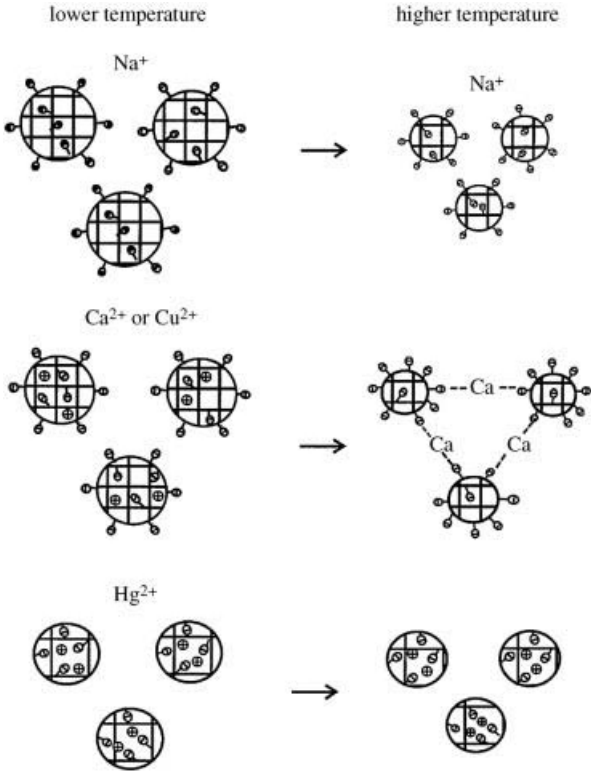

Figure 1.10 Schematic of effects of different cations and temperature on P(VCL-*co*-SA) microgels. Reprinted with permission from [82], Peng, S.F. and Wu, C. *Polymer* 42, 6871, 2001. © 2001 Elsevier Science.

P(NIPAM-*co*-SA) core and a P(NIPAM-*co*-VT) shell forms, resembling the biological cell-sorting.

Figure 1.11 shows the hydrodynamic radius distributions $f(R_h)$ of P(NIPAM-*co*-SA) and P(NIPAM-*co*-VT) microgels and their mixture in the presence of $CaCl_2$ at 51 °C, $\langle R_h \rangle$ values are ~40, 120, and 420 nm, respectively. The larger size of the mixture clearly indicates that the oppositely charged microgels form mixed aggregates with a narrow size distribution.

The structure of the microgel aggregates has been directly observed by high-resolution transmission electron microscopy (TEM) (Figure 1.12). Since metal ions can enhance the electron density contrast, the Ca^{2+} complexed with carboxyls makes a contrast between P(NIPAM-*co*-SA) and P(NIPAM-*co*-VT) domains. Clearly, the aggregates have a core–shell structure. The inset shows the image of the aggregates stained by iodine vapor. A boundary can be clearly observed. It is formed by P(NIPAM-*co*-VT) microgels because iodine can bind with $[N(CH_3)_3]^+$ but cannot with Ca^{2+}. Thus, P(NIPAM-*co*-SA) and P(NIPAM-*co*-VT) microgels form the core and shell of an aggregate, respectively. The core–shell structure indicates that the

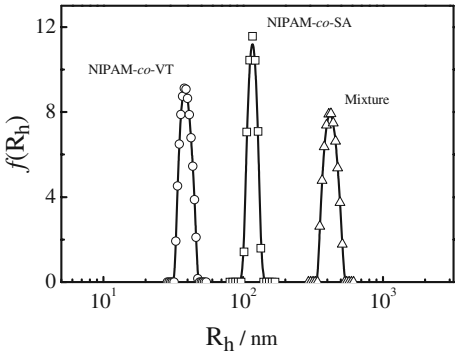

Figure 1.11 Hydrodynamic radius distributions $f(R_h)$ of P(NIPAM-*co*-SA) and P (NIPAM-*co*-VT) microgels and their mixture (1/1, w/w) in the presence of Ca^{2+} at 51 °C, where the concentrations of microgels and Ca^{2+} are 5.0×10^{-5} g mL^{-1} and 0.03 M, respectively. Reprinted with permission from [83], Hou, Y., Ye, J., Wei, X.L., and Zhang, G.Z. *J. Phys. Chem. B* 113, 7457, 2009. © 2009 American Chemical Society.

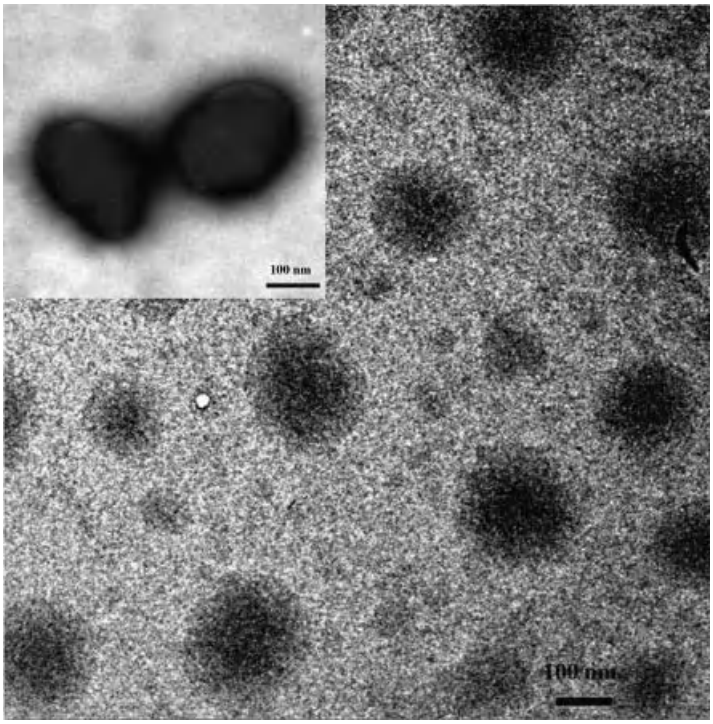

Figure 1.12 TEM image of P(NIPAM-*co*-SA) and P(NIPAM-*co*-VT) microgel aggregates at 51 °C. The inset shows the image of the aggregates stained by I_2 vapor. Reprinted with permission from [83], Hou, Y., Ye, J., Wei, X.L., and Zhang, G.Z. *J. Phys. Chem. B* 113, 7457, 2009. © 2009 American Chemical Society.

oppositely charged microgels exhibit sorting behavior during the aggregation, which is determined by the difference in Ca^{2+} adhesion between the unlike microgels.

1.3.3.2 Complexation Between Microgels and Protein

Complexation of a polyelectrolyte and a protein can provide an insight into its physicochemical properties, such as biocompatibility for other applications [84, 85]. In biopolymers, the complexation can modify their biological activities such as blood clotting and muscular contraction [86, 87]. In spite of a great deal of effort, the details of the complexation and stabilization are still missing because of its complex nature.

Figure 1.13 shows that when the gelatin/microgel molar ratio [G]/[M] is less than $\sim 3.4 \times 10^4$ and in the absence of Ca^{2+}, both $\langle R_h \rangle$ and $M_{w,app}$ of the microgel/gelatin complexes only slightly increase at about 32 °C, revealing that each complex contains at most two microgels on average. Further increasing temperature leads to a gradual decrease of $\langle R_h \rangle$, but $M_{w,app}$ is nearly independent of temperature in the same range, indicating the shrinking of the microgels without inter-microgel association. For mixtures with a higher molar ratio, $\langle R_h \rangle$ decreases monotonously with temperature in the whole temperature range studied. The increase in the average chain density ($\langle \varrho \rangle$) of the microgel/gelatin complexes with temperature in the range ~32–45 °C reflects the shrinking of the microgels inside the complex. Note that at high temperatures, $\langle \varrho \rangle$ increases as the [G]/[M] ratio decreases, further indicating that more microgels inside each complex can provide a stronger shrinking force and lead to a more compact structure at high temperatures.

Figure 1.14 shows that the complexation is more profound in the presence of Ca^{2+} compared with that shown in Figure 1.13. Both $\langle R_h \rangle$ and $M_{w,app}$ increase as the [G]/[M] ratio decreases, indicating that gelatin chains act as a stabilizer, presumably because of the absorption of gelatin chains on the microgel surface. Note that the complexation occurs at a similar temperature regardless of the gelatin concentration. This clearly shows that when the microgel is in its shrunk state (hydrophobic), most of the carboxylic groups are forced to locate on the microgel surface so that Ca^{2+} can bind the microgels and gelatin chains through the carboxylic groups. On average, each complex contains 20–70 microgels and the average density of the complexes is in the range 0.13–0.22 g cm^{-3} at temperatures higher than ~32 °C. The deceases in N_{agg} [$\equiv M_{w,aggregate}/M_{w,microgel}$] and $\langle \varrho \rangle$ with [G]/[M] further indicate that the adsorption of gelatin chains on the microgel surface reduces the compexation of the microgels.

1.3.3.3 Aggregation of Spherical Microgels

Aggregation of colloidal particles in dispersion has been extensively studied because it is important in both theory and practice; for example, in the production of chemical toners and the treatment of wastewater [89–96]. Two limiting regimes have been identified: the diffusion-limited cluster–cluster aggregation (DLCA) and the reaction-limited cluster–cluster aggregation (RLCA) [97, 98]. One of the features distinguishing between them is the different fractal dimensions (ν) of the resultant aggregates, that is, different scaling between the mass (M) and size (R) of the aggregates, $M \sim R^{\nu}$. The regime is essentially governed by the sticking efficiency between two collided

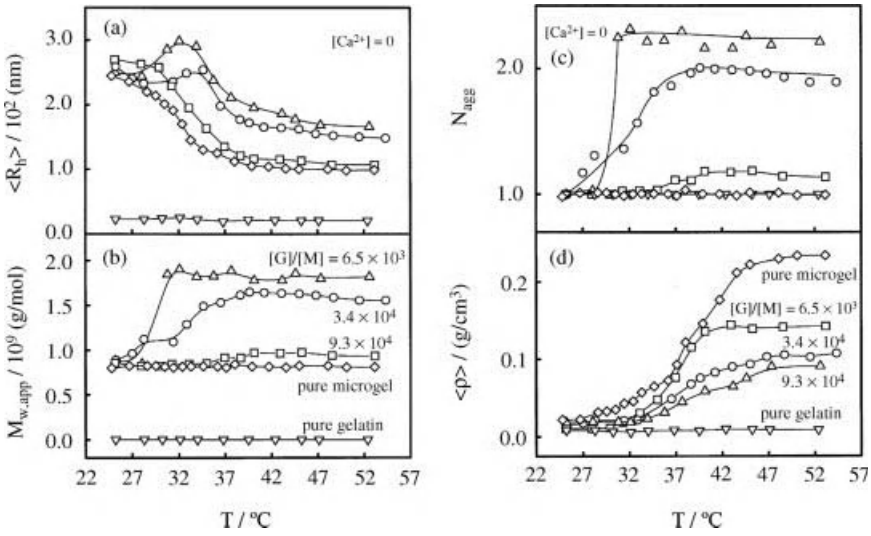

Figure 1.13 Temperature dependence of (a) average hydrodynamic radius $\langle R_h \rangle$; (b) apparent weight-averaged molar mass ($M_{w,app}$); (c) average aggregation number (N_{agg}); and (d) average chain density $\langle \varrho \rangle$ of the microgel/gelatin complexes, where [G]/[M] is the initial gelatin/microgel molar ratio and $\langle \varrho \rangle$ is defined as $M_{w,app}/[(4/3)\pi\langle R_h \rangle^3]$. Reprinted with permission from [88], Peng, S.F. and Wu, C. *Polymer* 42, 7343, 2001. © 2001 Elsevier Science.

particles. Experimentally, a combination of different scattering techniques allows us to study the formation and structures of colloidal aggregates over a wide size range [99–101].

The Ca^{2+}/COO^- complexation can induce a fractal aggregate at 32.5 °C. As expected, the extent of the aggregation for a given Ca^{2+} concentration increases with the ionic content because each COO^- group acts as a "sticker" in the interparticle or interchain aggregation via the $Ca^{2+}(COO^-)_2$ complexation. Figure 1.15 shows that the scattering intensity $I(q)$ of the resultant aggregates is dependent on the scattering vector q as $I(q) \sim q\alpha$ with α=1.7–1.9 for spherical microgels and α=2.4–2.5 for linear chains, indicating that the aggregation of spherical microgels follows the DLCA process, but the aggregation of linear chains might be described by the RLCA mechanism. For spherical microgels, the slight decrease of α with the COO^- groups indicates that the structure of the aggregates made of microgels with fewer COO^- groups is relatively more open and less uniform.

Note that the reversible processes of aggregation or fragmentation happen simultaneously. Therefore, a kinetic model should be established. As we know, Ca^+-induced spherical P(VCL-*co*-SA) microgel aggregation is a DLCA process, and it follows a second-order growth kinetics, whose coagulation kernel is independent of the size of the resultant aggregates. On the other hand, fragmentation is a first-order kinetics whose rate is also independent of the size of the aggregates. Therefore, Equation 1.17 can be used to fit both the heating and cooling data.

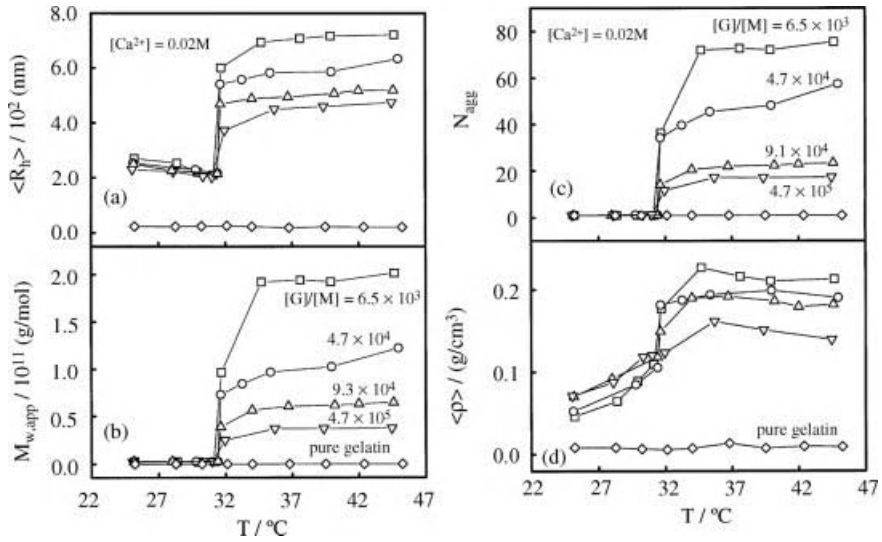

Figure 1.14 Temperature dependence of (a) average hydrodynamic radius $\langle R_h \rangle$; (b) apparent weight-averaged molar mass ($M_{w,app}$); (c) average aggregation number (N_{agg}); and (d) average chain density $\langle \varrho \rangle$ of the microgel/gelatin complexes. Reprinted with permission from [88], Peng, S.F. and Wu, C. *Polymer* 42, 7343, 2001. © 2001 Elsevier Science.

Figure 1.16 shows that aggregation dominates the initial process at higher temperatures but the fragmentation rate gradually increases with time. Note that each cluster contains ~230 microgels on average when $t \to \infty$. Such an aggregation process is reversible if the temperature decreases to ~35 °C. At lower temperatures each cluster contains only about two and about four microgels on average,

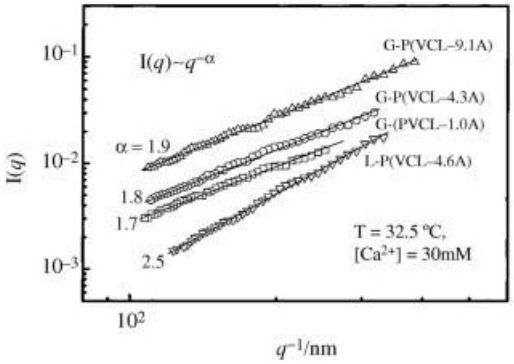

Figure 1.15 Double-logarithmic plots of scattering intensity I(q) vs. scattering vector q for resultant aggregates made of different spherical microgels and linear chains, where $[Ca^{2+}]$=30 mM and T=32.5 °C. Reprinted with permission from [81], Peng, S.F. and Wu, C. *Macromolecules* 34, 6795, 2001. © 2001 American Chemical Society.

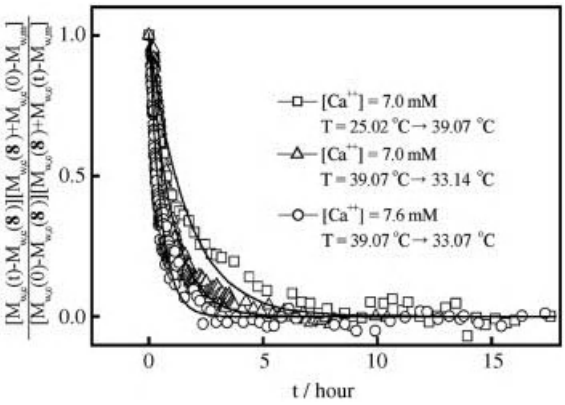

Figure 1.16 Time dependence of function $\{[M_{w,c}(t)-M_{w,c}(\infty)][M_{w,c}(\infty)+M_{w,c}(0)-M_{w,m}]\}/\{[M_{w,c}(0)-M_{w,c}(\infty)][M_{w,c}(\infty)+M_{w,c}(t)-M_{w,m}]\}$ after a microgel dispersion ($c=2.6\times10^{-6}\,\mathrm{g\,mL^{-1}}$) was heated or cooled to different temperatures. The solid lines represent the best fitting on the basis of Equation 1.17. Reprinted with permission from [60], Cheng, H., Wu, C., and Winnik, M.A. *Macromolecules* 37, 5127, 2004. © 2004 American Chemical Society.

respectively, indicating that the microgel clusters formed at higher temperature are essentially redissolved.

1.3.4
Non-Ergodic and Ergodic Phenomena of Physical Crosslinked Gel

The network structure of a gel can be formed by either a chemical or a physical gelation process. In a chemical process, linear chains gradually turn into branched clusters, and then clusters are interconnected by covalent bonds to form a network structure. In a physical process, various forces such as van der Waals forces, electrostatic attraction, and hydrogen bonding can be employed to bind polymer chains to form a network. Therefore, the sol–gel transition in physical gels is often reversible [102–105].

It is well known that in the formation of normal chemical gels short linear chains are first formed, then large branched clusters, and finally a network, where the clusters ("islands") are interconnected to form a "continent," while the solvent "sea" is changed into "lakes" [106–109]. In principle, such an inhomogeneous clustering structure could be avoided if long polymer chains uniformly distributed in a solution are randomly associated to form a physical gel. Recently, DLS has been used to study a non-ergodic solid-like medium such as polymer gels or colloidal glasses [110], wherein the Brownian motions of scattering elements are limited around fixed average positions. One obvious characteristic of the non-ergodicity is the appearance of speckles; thus, the scattered intensity depends on the sample position. It is now generally known that the concentration fluctuation inside a gel comprises both static and dynamic parts. The inhomogeneous static part represents a frozen structure,

while the dynamic fluctuation presumably reflects diffusive relaxation [111–119]. The concept of non-ergodicity has led to the development of several relevant methods for the analysis of the dynamic properties of gels [54, 120, 121].

A novel hydrogel, in which billions of small spherical swollen PNIPAM microgels (~100 nm) in a concentrated dispersion are close-packed into a macroscopic three-dimensional gel network, has been developed. Inside each microgel, the polymer chains were chemically crosslinked, but the microgels were close-packed by physical interaction. This is why we named it a "hybrid" gel. It resembles a glass in which atoms or small molecules are replaced by "large" spherical microgels. There are several advantages of using this hybrid gel as a model system to study the volume–concentration-induced sol–gel transition and structures of physical gels. For example, the structural inhomogeneity resulting in the microgel preparation is limited in volume ($\sim 100 \times 100 \times 100\ nm^3$), and it is so small in comparison with the wavelength of light that it does not show up in laser light scattering. Also, as building blocks, these microgels are narrowly distributed and well characterized. Moreover, such a gelation is completely thermally reversible without any hysteresis. Using a combination of SLS and DLS, we studied a series of such hybrid gels formed at different gelling rates and temperatures. The main finding is that the observed static non-ergodicity is not intrinsic but strongly depends on how the microgels (clusters) are packed. Therefore, it can be completely suppressed if there are no large voids among the microgels. On the other hand, the dynamic fluctuation is almost not influenced by the static non-ergodicity.

Figure 1.17 shows that in the gel state, the time-averaged scattered intensity $\langle I \rangle_T$ randomly varies with sample position [122]. In contrast, the scattering speckle pattern disappears at 30 °C because the bulk hybrid gel melts into microgel dispersion (i.e.,

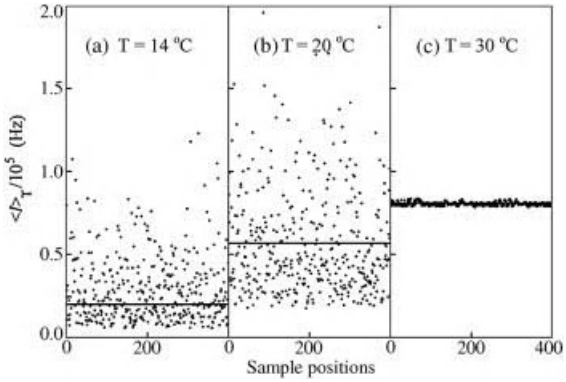

Figure 1.17 Sample position dependence of time-averaged scattered light intensity $\langle I \rangle_T$ of hybrid PNIPAM gel after the microgel dispersion was quickly cooled from 40 °C to different gelling temperatures, where the scattering angle (θ) is 90°, and each solid line represents an ensemble-averaged scattered light intensity $\langle I \rangle_E$ defined as $\sum \langle I \rangle_{T,i}/N$ with N being the total number of randomly chosen sample positions. Reprinted with permission from [122], Zhao, Y., Zhang, G.Z., and Wu, C. *Macromolecules* 34, 7804, 2001. © 2001 American Chemical Society.

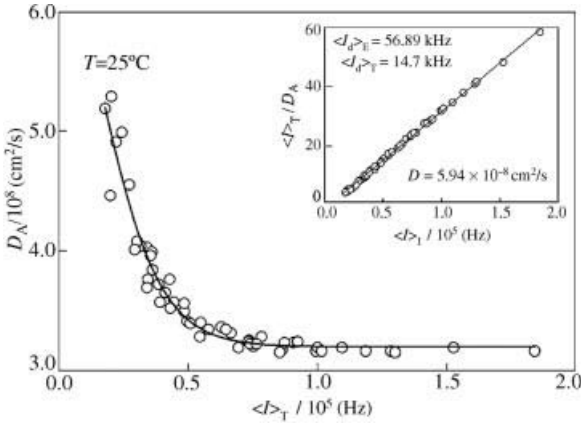

Figure 1.18 Time-averaged scattered light intensity $\langle I\rangle_T$ dependence of apparent diffusion coefficient D_A of the hybrid gel formed at 20 °C, where $\theta = 90°$ and D_A was obtained from the initial slope of $g^{(2)}(t,q)$. The inset shows a plot on the basis of Equation 1.14, in which the intercept and the slope are D and $\langle I_d\rangle_T$, respectively. Reprinted with permission from [122], Zhao, Y., Zhang, G.Z., and Wu, C. *Macromolecules* 34, 7804, 2001. © 2001 American Chemical Society.

the sol state) due to the shrinking of individual microgels. It is worth noting that in the temperature range 15–33 °C the microgels in a dilute dispersion can reversibly swell and shrink with a size change between ~45 nm and ~106 nm, corresponding to a 13-times variation in volume. This is why the swelling could induce the sol–gel transition. Note that $\langle I\rangle_E$ increases with temperature, which is very different from previous observations in which $\langle I\rangle_E$ decreased when a physical gel melted into individual, less scattered polymer chains [123], but similar to a concentration-induced sol–gel transition. This difference can be attributed to the fact that individual collapsed microgels are stronger scattering objects than the swollen gel network in this study, especially when the temperature approaches its LCST.

For each chosen sample position at a given q, we can measure $\langle I\rangle_T$ from static LLS and calculate one D_A from $g^{(2)}(t,q)$ measured in dynamic LLS [130]. Figure 1.18 shows that D_A decreases as $\langle I\rangle_T$ increases and approaches a constant when $\langle I\rangle_T$ is sufficiently high. The inset is a corresponding plot on the basis of Equation 1.14. A least-square fitting of the data leads to D and $\langle I_d\rangle_T$, respectively, from its slope and intercept.

In the present case, individual microgels shrink so that non-jammed microgels diffuse quickly with temperature. Above the melting temperature, the gel network breaks into slowly diffused large clusters so that D decreases. Note that the value of D is close to that of individual microgels in a dilute dispersion. Since individual swollen microgels are transparent to the light used, the inhomogeneities observed in Figure 1.17 must come from an imperfect packing of the microgels when they are suddenly jammed together. Therefore, if we slow down the cooling process, the swollen microgels would have time to arrange themselves into a more uniform structure. Ideally, if individual collapsed microgels could be closely stacked together at a high temperature before cooling them down, we might be able to

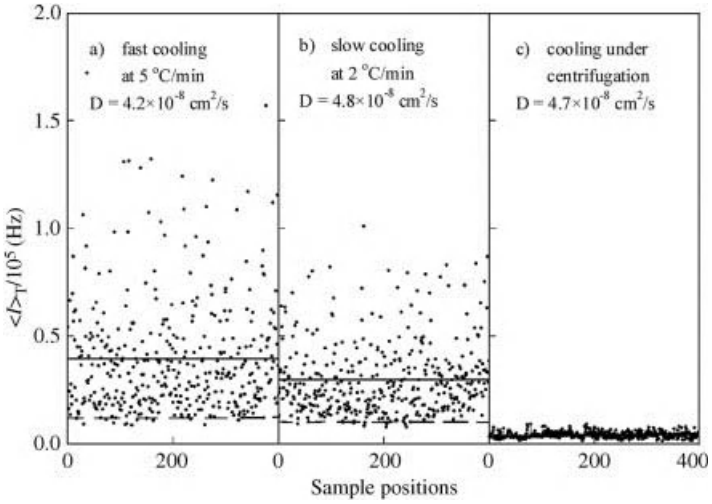

Figure 1.19 Sample position dependence of time-averaged scattered light intensity $\langle I \rangle_T$ of hybrid PNIPAM gel after the microgel dispersion was cooled down from 40 to 15 °C under different conditions, where the solid and dashed lines represent $\langle I \rangle_E$ and $\langle I_d \rangle_T$, respectively. Reprinted with permission from [122], Zhao, Y., Zhang, G.Z., and Wu, C. *Macromolecules* 34, 7804, 2001. © 2001 American Chemical Society.

obtain a uniform hybrid gel [124]. It should be stated that the hybrid gel prepared under centrifugation showed a color if a white light was shone on it even if it could not completely disperse the white light as a prism or a crystal. This imperfect dispersion might be attributed to the polydispersity in the microgel size and a low refractive index contrast between water and swollen microgel networks, but it clearly indicates a certain degree of ordering of the microgels inside the hybrid bulk gel.

Figure 1.19 shows that different cooling processes lead to different extents of inhomogeneity, reflected in the difference between $\langle I \rangle_E$ and $\langle I_d \rangle_T$. Note that Figures 1.17c and 1.19c are similar. Both display an ergodic behavior, that is, $\langle I \rangle_E = \langle I_d \rangle_T$. However, it is worth noting that they were obtained from two completely different states; namely, Figure 1.17c shows a measurement of a uniform and ergodic microgel dispersion in which individual collapsed microgels are under random Brownian motion in water, while Figure 1.19c is from a uniform hybrid gel.

Figure 1.19 clearly demonstrates that the static inhomogeneity of thermally reversible physical gels is not intrinsic but strongly dependent of the gelation process. It is also interesting to note that D is nearly a constant, indicating that the voids inside the gel network are much larger than the microgels and the gel network does not affect the relaxation of individual non-jammed microgels. As expected, for a given temperature, individual non-jammed microgels with the same size relax at the same rate. How the gel network is formed can only affect the static part, that is, $\langle I_d \rangle_T$ but not D. This point has been overlooked in the past.

1.4 Applications

Despite having a variety of interesting physical and chemical properties, synthetic gels currently find application in only a few areas, such as foods, water adsorbents, and soft contact lenses. Two main obstacles, namely, the gel shrinking/swelling speed and mechanical strength, limit their application. Much effort has been paid in the last two decades to overcome these obstacles. It is reported that the slow shrinking rate can be attributed to the formation of a hard skin layer at the very initial stage of gel shrinking, which prevents further diffusion and outflow of solvent molecules such as water molecules from inside the gel [125–127]. Using another hydrophobic polymer to modify thermally sensitive polymer gels via an interpenetrating polymer network (IPN) structure has also been reported [128, 129]. Such a gel is mainly used in drug delivery. Yoshida *et al.* [129] reported that a hydrogel modified by grafting also shows an increased shrinking rate. However, preparation of such a comb-type grafted hydrogel is not a simple task. Simple approaches are desirable to prepare polymer gel/microgel composition, which has improved shrinking rate and strength characteristics [130–133].

Spherical PNIPAM microgels with a diameter of 0.3–1.0 μm in the swollen state are embedded into a gelatin network. The shrinking of the microgels can lead the gelatin gel to shrink quickly. The embedded microgels were attached to the gelatin gel network by physical adhesion and not by chemical bonding. Therefore, it is expected that the shrunken microgels could slowly detach themselves from the gelatin gel network and be absorbed by normal tissue mechanisms, because the shrunken microgels have a diameter of only 0.1–0.3 μm. The product used here is a polymer in the form of a soft gel as shown in Figure 1.20.

The *in vivo* biological responses to the polymer gel had to be tested carefully before it could be accepted as a surgical implant. Different tissues that were likely to be put in contact with the implant when used surgically were chosen. Different tissues might have different responses to the polymer, and how the polymer would degrade with time also needed to be clarified. The tissues included subcutaneous tissues, nerve, artery, tendon, and muscle. The animals used included adult male Wistar rats and guinea pigs. Short-term and medium-term observations were made and the implant sites were inspected after periods of 3, 10, 20, and 90 days.

Polymer gel–gelatin sheet was used to wrap the cut ends of the sciatic nerve of the rat, so as to form a bridging tube. The rats were euthanized after 3, 10, 20, and 90 days to retrieve the repaired nerve for gross and histological study, as shown in Figure 1.21.

The femoral artery of the rat was used for the study of arterial repair. After cutting through, the arterial ends were prevented from separating by putting two 10 "0" stitches to sling the edges together while leaving a gap of about 1 mm open. Then the approximated site was wrapped around with a thin sheet of thermally sensitive polymer gel. The rats were euthanized on days 3, 10, 20, and 90 for the inspection and retrieval of the bridged artery (Figure 1.22).

The gel material is nontoxic. Both rats and guinea pigs survived well after the gel implantations. When the implantation sites were inspected, there was neither gross

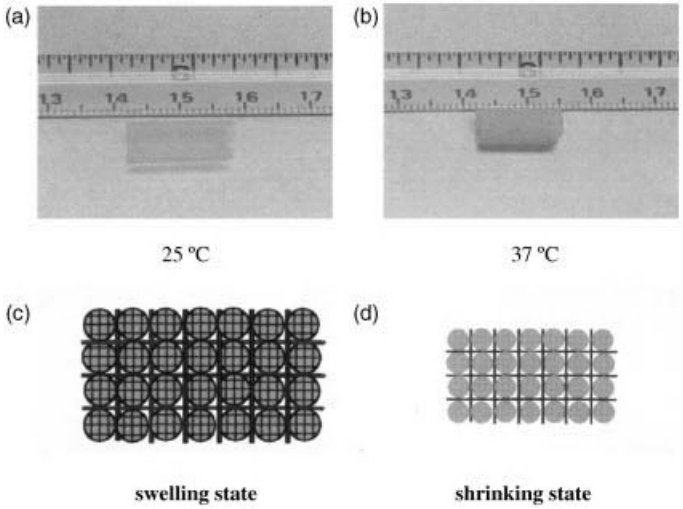

Figure 1.20 (a) Thermally sensitive polymer at 25 °C. (b) Same polymer at 37 °C. (c) Polymer at 25 °C. (d) Same polymer at 37 °C. Reprinted with permission from [134] Leung, P.C., Yew, D., Wu, C., and Peng, S.F. *Microsurgery* 23, 123, 2003. © 2003 Wiley-Liss, Inc.

nor histological suggestion of toxicity. The tissues around the implanted polymer gel were inspected for inflammatory changes and at the same time the degradation of the gel material was recorded.

The thermally sensitive polymer microgel sheet used was the product of multiple early tests, using polymers of different protein concentrations and different

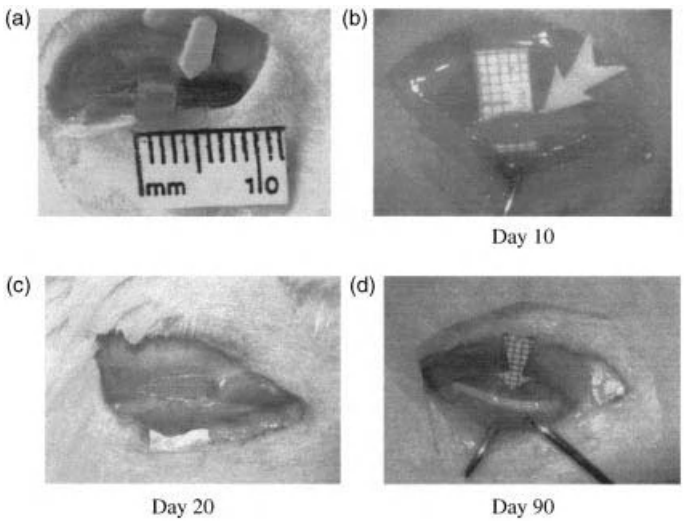

Figure 1.21 (a) Sciatic nerve of rat, bisected across, and cut ends wrapped with thermally sensitive gel. (b) Day 10. (c) Day 20. (d) Day 90. Reprinted with permission from [134], Leung, P.C., Yew, D., Wu, C., and Peng, S.F. *Microsurgery* 23, 123, 2003. © 2003 Wiley-Liss, Inc.

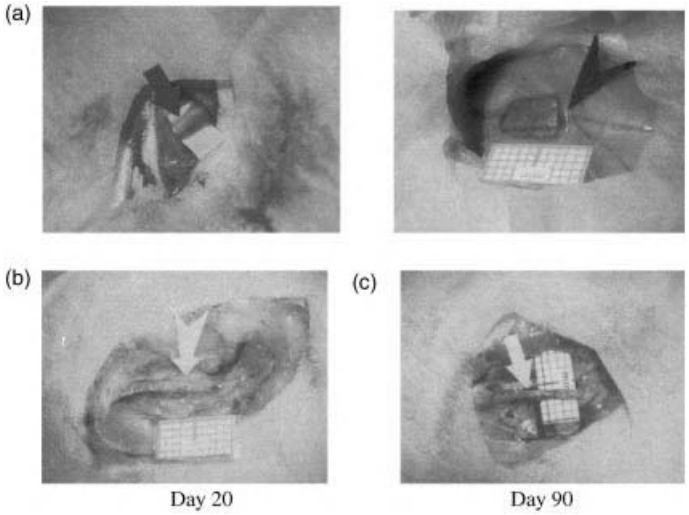

Figure 1.22 (a) Femoral artery of rat, bisected across, cut ends wrapped with thermosensitive gel. (b) Day 20. (c) Day 90. Reprinted with permission from [134], Leung, P.C., Yew, D., Wu, C., and Peng, S.F. *Microsurgery* 23, 123, 2003. © 2003 Wiley-Liss, Inc.

morphological forms, which included preformed tubes and fluid forms. The unique property of the polymer microgel is that it gives extra binding power when it is wrapped around cylindrical biological structures. The experiments on arteries and peripheral nerves showed that wrapping facilitated the maintenance of arterial patency and allowed natural nerve regeneration, while the foreign body reaction to the implanted polymer was mild.

Two more potential uses of this polymer could be considered for muscle and tendon repair. When muscle tissues are disrupted, repair by ordinary suturing gives very poor results because of extensive fibrosis around the repaired site and replacement of the damaged muscle with fibrous tissues, which leads to a gross loss of muscle function. If a tissue wrap could be applied to the damaged site to bring about approximation while minimizing fibrosis, the functional results might be better.

1.5 Conclusions

Microgels exhibit unique physical properties between those of a polymer coil and a macroscopic gel. By using a microgel as a model system, we have studied volume phase transition, internal motion, aggregation, and non-ergodic phenomena. The reason for the volume phase transition of a polymer gel is that the subchains normally have a broad chain length distribution. However, a higher homogeneity gels with a lower crosslinking density display a discontinuous volume phase transition because of the subchain inhomogeneity. The internal motion of a linear polymer chain or

microgel can be observed in good and Θ solvents at a certain observation lengths. Its nature still remains elusive but it is associated with the thermal motion of subchains.

Cations can induce the aggregation of microgels because of the interaction between the cations and anionic groups (e.g., carboxylic groups). Such a cation–polyanion complex leads to the sorting of oppositely charged microgels in a mixture; they form core–shell structures with one microgel as the core and the oppositely charged one as the shell. These cation–polyanion complexes can also induce fractal aggregates of microgels following a diffusion-limited cluster–cluster aggregation (DLCA) process. Charged microgels can form complexes with proteins, and the properties of the complexes depend on the molar ratio of protein to microgels. Thus, thermally sensitive microgels can be used in protein adsorption and separation.

The studies on the non-ergodic and ergodic phenomena of gel formed by close-packed microgels via physical interaction reveal that the observed static non-ergodicity is not intrinsic but strongly depends on how the microgels (clusters) are packed, and the dynamic fluctuation is slightly influenced by the static non-ergodicity.

The studies also show that thermally sensitive microgels have potential uses for muscle and tendon repair.

Abbreviations

Φ: Flory constant
Γ: Half-width at half-height
θ: Scattering angle
χ_T: Flory–Huggins polymer–solvent interaction parameter
$[\eta]$: Intrinsic viscosity
$<\alpha^2>_0$: Isotropic deformation factor of the gel network
D: Translational diffusion coefficient
DLCA: Diffusion-limited cluster–cluster aggregation
$g^{(2)}(t,q)$: Intensity–intensity time correlation function
IPN: Interpenetrating polymer network
LCST: Lower critical solution temperature
M_c: Average molar mass of subchain between two neighbor crosslinking points
q: Scattering vector
R_g: Radius of gyration
R_h: Hydrodynamic radius
RLCA: Reaction-limited cluster–cluster aggregation

Acknowledgments

The financial support of the National Distinguished Young Investigator Fund (20725414), National Basic Research Program of China (973 Program, 2012CB821500), and Ministry of Science and Technology of China (2012CB933800) is gratefully acknowledged. We are also indebted to Professor Chi Wu of the Chinese

University of Hong Kong, Professor Shuiqin Zhou of the City University of New York, and to Drs. Peng SF, Zhao Y, Jiang SH, Dai ZJ, and Hou Y.

References

1 Pelton, R.H. and Chibante, P. (1986) *Colloids Surf.*, **20**, 247.
2 Crespy, D. and Rossi, R.M. (2007) *Polym. Int.*, **56**, 1461.
3 Nayak, S. and Lyon, L.A. (2005) *Angew. Chem. Int. Ed.*, **44**, 7686.
4 Prokop, A., Kozlov, E., Carlesso, G., and Davidson, J.M. (2002) *Adv. Polym. Sci.*, **160**, 119.
5 Baker, W.O. (1949) *Ind. Eng. Chem.*, **41**, 511.
6 Flory, P.J. (1953) *Principles of Polymer Chemistry*, Cornell University Press, Ithaca, NY.
7 Williams, C., Brochard, F., and Frisch, H.L. (1981) *Annu. Rev. Phys. Chem.*, **32**, 433.
8 Stockmayer, W.H. (1960) *Makromol. Chem.*, **35**, 54.
9 Ptitsyn, O.B., Kron, A.K., and Eizner, Y.Y. (1993) *J. Polym. Sci. Part C*, **16**, 3509.
10 Yamakawa, H. (1971) *Modern Theory of Polymer Solutions*, Harper & Row, New York.
11 Post, C.B. and Zimm, B.H. (1979) *Biopolymers*, **18**, 1487. 21, 2123, 1982.
12 Tanaka, F. (1985) *J. Chem. Phys.*, **85**, 4707.
13 Park, I.H., Wang, Q.W., and Chu, B. (1987) *Macromolecules*, **20**, 1965.
14 Chu, B., Park, I.H., Wang, Q.W., and Wu, C. (1987) *Macromolecules*, **20**, 2883.
15 Tanaka, F. and Ushiki, H. (1988) *Macromolecules*, **21**, 1041.
16 Grosberg, A.Y. and Kuznetsov, D.V. (1992) *Macromolecules*, **25**, 1996.
17 Chu, B., Yu, J., and Wang, Z.L. (1993) *Prog. Colloid Polym. Sci.*, **91**, 142.
18 Yamakawa, H. (1993) *Macromolecules*, **26**, 5061.
19 Grosberg, A.Y. and Kuznetsov, D.V. (1993) *Macromolecules*, **26**, 4249.
20 Yu, J., Wang, Z.L., and Chu, B. (1992) *Macromolecules*, **25**, 1618.
21 Chu, B., Ying, Q.C., and Grosberg, A.Y. (1995) *Macromolecules*, **28**, 180.
22 Wu, C. and Zhou, S.Q. (1995) *Macromolecules*, **28**, 5388.
23 Wu, C. and Zhou, S.Q. (1996) *Phys. Rev. Lett.*, **77**, 3053.
24 Dusek, K. and Patterson, D. (1968) *J. Polym. Sci. Polym. Phys. Ed.*, **6**, 1209.
25 Dusek, K. and Prins, W. (1969) *Adv. Polym. Sci.*, **6**, 1.
26 Flory, P.J. (1956) *J. Am. Chem. Soc.*, **78**, 191.
27 Hermans, J.J. (1956) *J. Polym. Sci.*, **59**, 191.
28 James, H.M. and Guth, E. (1953) *J. Chem. Phys.*, **21**, 1048.
29 Tanaka, T., Sato, E., Hirokawa, Y., Hirotsu, S., and Peetermans, J. (1985) *Phys. Rev. Lett.*, **55**, 2455.
30 Hirotsu, S. (1987) *J. Phys. Soc. Jpn*, **56**, 233.
31 Hirose, Y., Hirokawa, Y., and Tanaka, T. (1987) *Macromolecules*, **20**, 1342.
32 Marchetti, M., Prager, S., and Cussler, E.L. (1990) *Macromolecules*, **23**, 3445.
33 Inomata, H., Goto, S., and Saito, S. (1990) *Macromolecules*, **23**, 4888.
34 Kokufuta, E., Zhang, Y., and Tanaka, T. (1993) *Macromolecules*, **26**, 1053.
35 Li, Y. and Tanaka, T. (1989) *J. Chem. Phys.*, **90**, 5161.
36 Shibayama, M., Morimoto, M., and Nomura, S. (1994) *Macromolecules*, **27**, 5060.
37 Park, T.G. and Hoffman, A.S. (1994) *J. Appl. Polym. Sci.*, **52**, 85.
38 Yu, H. and Grainger, D.W. (1994) *Macromolecules*, **27**, 4554.
39 Pecora, R. (1965) *J. Chem. Phys.*, **43**, 1762.
40 Perico, A., Piaggio, P., and Cuniberti, C. (1975) *J. Chem. Phys.*, **62**, 2690.
41 Perico, A., Piaggio, P., and Cuniberti, C. (1975) *J. Chem. Phys.*, **62**, 4911.
42 Sorlie, S.S. and Pecora, R. (1988) *Macromolecules*, **21**, 1437.

43 Zimm, B.H. (1956) *J. Chem. Phys.*, **24**, 269.

44 Zimm, B.H. and Roe, G.M. (1956) *J. Chem. Phys.*, **24**, 279.

45 Wang, J., Wang, Z.L., Peiffer, D.G., Shuely, W.J., and Chu, B. (1991) *Macromolecules*, **24**, 790.

46 Wu, C. and Xia, K. (1994) *Q. Rev. Sci. Instrum.*, **65**, 587.

47 Wu, C. and Zhou, S.Q. (1996) *J. Polym. Sci. Polym. Phys.*, **34**, 1597.

48 Adam, M., Delsanti, M., Munch, J.P., and Durand, D. (1988) *Phys. Rev. Lett.*, **61**, 706.

49 Martin, J.E. and Wilcoxon, J. (1988) *Phys. Rev. Lett.*, **61**, 373.

50 Shibayama, M. (1998) *Macromol. Chem. Phys.*, **199**, 1.

51 Shibayama, M. and Norisuye, T. (2002) *Bull. Chem. Soc. Jpn.*, **75**, 641.

52 Ngai, T., Wu, C., and Chen, Y. (2004) *Macromolecules*, **37**, 987.

53 Pusey, P.N. and van Megen, W. (1989) *Physica A*, **157**, 705.

54 Joosten, J.G.H., Mccarthy, J.L., and Pusey, P.N. (1991) *Macromolecules*, **24**, 6690.

55 Tanaka, T., Hocker, L.O., and Benedek, G.B. (1973) *J. Chem. Phys.*, **59**, 5151.

56 Horkay, F., Burchard, W., Hecht, A.M., and Geissler, E. (1993) *Macromolecules*, **26**, 3375.

57 Asnaghi, D., Carpineti, M., Giglio, M., and Sozzi, M. (1992) *Phys. Rev. A*, **45**, 1018.

58 Fernandez-Barbero, A., and Vincent, B. (2000) *Phys. Rev. E*, **63**, 011509.

59 Robinson, D.J. and Earnshaw, J.C. (1992) *Phys. Rev. A*, **46**, 2045.

60 Cheng, H., Wu, C., and Winnik, M.A. (2004) *Macromolecules*, **37**, 5127.

61 Wu, C., Zhou, S.Q., Au-yeung, S.C.F., and Jiang, S.H. (1996) *Die Angew. Makromol. Chem.*, **240**, 123.

62 Wu, C. and Zhou, S.Q. (1997) *J. Macromol. Sci. Phys. B*, **36**, 345.

63 Gao, J. and Wu, C. (1997) *Acta Polym. Sin.*, **3**, 324.

64 Wu, C. (1998) *Polymer*, **39**, 4609.

65 Wu, C. and Zhou, S.Q. (1997) *Macromolecules*, **30**, 574.

66 Wu, C. and Yan, C.Y. (1994) *Macromolecules*, **27**, 4516.

67 Dai, Z.J., Ngai, T., and Wu, C. (2011) *Soft Matter*, **7**, 4111.

68 Wu, C. and Zhou, S.Q. (1996) *Macromolecules*, **29**, 1574.

69 Wu, C., Chan, K.K., and Xia, K. (1995) *Macromolecules*, **28**, 1032.

70 Dai, Z.J. and Wu, C. (2010) *Macromolecules*, **43**, 10064.

71 Peng, S.F. and Wu, C. (2012) In *Handbook of Polyelectrolytes and Their Applications*, Vol. 2: *Polyelectrolytes: their Characterization and Polyelectrolyte Solutions* (eds S.K. Tripathy, J. Kumar, and H.S. Nalwa), American Scientific Publishers, CA, chapter 7, pp. 189–225.

72 Peng, S.F. and Wu, C. (2001) *J. Phys. Chem. B*, **105**, 2331.

73 Stockmayer, W.H., and Schmidt, M. (1982) *Pure Appl. Chem.*, **54**, 407.

74 Hirokawa, Y. and Tanaka, T. (1984) *J. Chem. Phys.*, **81**, 6379.

75 Ershov, B.G. and Henglein, A. (1998) *J. Phys. Chem. B*, **102**, 10663.

76 Ikeda, Y., Beer, M., Schmidt, M., and Huber, K. (1998) *Macromolecules*, **31**, 728.

77 Heitz, C. and Francois, J. (1999) *Polymer*, **40**, 3331.

78 Frank, H.S. and Wen, W.Y. (1978) *Discuss. Faraday Trans.*, **74**, 583.

79 James, D.W. and Frost, R.L. (1978) *J. Chem. Soc., Faraday Trans.*, **74**, 583.

80 Hindman, J.C. (1962) *J. Chem. Phys.*, **36**, 1000.

81 Peng, S.F. and Wu, C. (2001) *Macromolecules*, **34**, 6795.

82 Peng, S.F. and Wu, C. (2001) *Polymer*, **42**, 6871.

83 Hou, Y., Ye, J., Wei, X.L., and Zhang, G.Z. (2009) *J. Phys. Chem. B*, **113**, 7457.

84 Kabanov, V.A. and Zezin, A.B. (1985) *Pure Appl. Chem.*, **56**, 343.

85 Thomas, J.L., Brian, P.D., and Tirrell, D.A. (1996) *Biochim. Biophys. Acta*, **1278**, 73.

86 Bondeson, J. and Sundler, R. (1990) *Biochim. Biophys. Acta*, **1026**, 186.

87 Kuber, K. (1993) *J. Phys. Chem.*, **97**, 9825.

88 Peng, S.F. and Wu, C. (2001) *Polymer*, **42**, 7343.

89 Meakin, P. (1983) *Phys. Rev. Lett.*, **51**, 1119.

90 Martin, J.E. and Ackerson, B. (1985) *J. Phys. Rev. A*, **31**, 1180.

91 Jullien, R., Botet, R., and Mors, P.M. (1987) *Faraday Disuss. Chem. Soc.*, **83**, 125.

92 Reinecke, H., Fazel, N., Dosiere, M., and Guenet, J.M. (1997) *Macromolecules*, **30**, 8360.

93 Aubert, C. and Cannell, D.S. (1986) *Phys. Rev. Lett.*, **56**, 738.

94 Lin, M.Y., Lindsay, H.M., Weitz, D.A., Ball, R.C., Klein, R., and Meakin, P. (1989) *Nature*, **40**, 4665.

95 Micali, N., Mallamace, F., Romeo, A., Purrello, R., and Scolaro, L. (2000) *J. Phys. Chem. B*, **104**, 5897.

96 Magazu, S., Maisano, G., Mallamace, F., and Micali, N. (1989) *Phys. Rev. A*, **39**, 4195.

97 Botet, R., Kolb, M., and Jullien, R. (1985) *Physics of Finely Divided Matter*, Springer-Verlag, New York.

98 Zhou, Z. and Chu, B. (1991) *J. Colloid Interface Sci.*, **143**, 356.

99 Aymard, P., Nicolai, T., Durand, D., and Clark, A. (1999) *Macromolecules*, **32**, 2542.

100 Kim, A.Y. and Berg, J.C. (2000) *Langmuir*, **16**, 2101.

101 Takata, S., Norisuye, T., Tanaka, N., and Shibayama, M. (2000) *Macromolecules*, **33**, 5470.

102 Larson, R.G. (1999) *The Structure and Rheology of Complex Fluids*, Oxford University Press, New York, chapter 5, pp. 232–258.

103 Lapasin, R. and Pricl, S. (1998) In *Progress and Trends in Rheology Vol. V the Fifth European Rheology Conference* (eds Emri, I. and Cvelbar, R.), Springer, Berlin, pp. 22.

104 Winter, H.H. (2007) In *Encyclopedia of Polymer Science and Engineering*, Third Edition, John Wiley & Sons, Inc., New York, pp. 507.

105 Almdal, K., Dyre, J., Hvidt, S., and Kramer, O. (1993) *Polym. Gels Networks*, **1**, 5–17.

106 Wu, C., Zuo, J., and Chu, B. (1989) *Macromolecules*, **22**, 633.

107 Sato-Matsuo, E., Orkisz, M., Sun, S.T., Li, Y., and Tanaka, T. (1994) *Macromolecules*, **27**, 6791.

108 Wu, C., Chu, B., and Stell, G. (1989) *Makromol. Chem., Macromol. Symp.*, **45**, 75.

109 Norisuye, T., Inoue, M., Shibayama, M., Tamaki, R., and Chujo, Y. (2000) *Macromolecules*, **33**, 900.

110 Brown, W. (1993) *Dynamic Light Scattering, the Methods and Applications;*, Clarendon Press, Oxford.

111 Panyukov, S. and Rabin, Y. (1996) *Macromolecules*, **29**, 7690.

112 Panyukov, S. and Rabin, Y. (1996) *Phys. Rep.*, **269**, 1.

113 Horkay, F., Hecht, A.M., Mallam, S., Geissler, E., and Renie, A.R. (1991) *Macromolecules*, **24**, 2896.

114 Shibayama, M., Tanaka, T., and Han, C.C. (1992) *J. Chem. Phys.*, **97**, 6892.

115 Rouf, C., Bastide, J., Pujol, J.M., Schosseler, F., and Munch, J.P. (1994) *Phys. Rev. Lett.*, **73**, 830.

116 Bastide, J. and Leibler, L. (1988) *Macromolecules*, **21**, 2647.

117 Hecht, A.M., Duplessix, R., and Geissler, E. (1985) *Macromolecules*, **18**, 2167.

118 Mallam, S., Horkay, F., Hecht, A.M., and Geissler, E. (1989) *Macromolecules*, **22**, 3356.

119 Cohen, Y., Ramon, O., Kopelman, I.J., and Mizrahi, S.J. (1992) *Polym. Sci., Polym. Phys. Ed.*, **30**, 1055.

120 Joosten, J.G.H., Gelade, E., and Pusey, P.N. (1990) *Phys. Rev. A*, **42**, 2161.

121 Fang, L. and Brown, W. (1992) *Macromolecules*, **25**, 6897.

122 Zhao, Y., Zhang, G.Z., and Wu, C. (2001) *Macromolecules*, **34**, 7804.

123 Ikkai, F. and Shibayama, M. (1999) *Phys. Rev. Lett.*, **82**, 4946.

124 Zhao, Y. and Wu, C. (2002) *Chinese J. Polym. Sci.*, **20**, 269.

125 Gutowska, A., Bae, Y.H., Feijen, J., and Kim, S.W. (1992) *J. Controlled Release*, **22**, 95.

126 Yoshida, R., Sakai, K., Okano, T., and Sakurai, Y. (1994) *J. Biomater. Sci. Polymer Ed.*, **6**, 585.

127 Kim, Y.H., Bae, Y.H., and Kim, S.W. (1994) *J. Controlled Release*, **28**, 143.

128 Gutowska, A., Bae, Y.H., Jacobs, H., Feijen, J., and Kim, S.W. (1994) *Macromolecules*, **27**, 4167.

129 Yoshida, R., Uchida, K., Kaneko, Y., Sakai, K., Kikuchi, A., Sakurai, Y., and Okano, T. (1995.) *Nature*, **374**, 240.
130 Wu, C. and Jiang, S.H. (2000) U.S. Patent No. 6,030,634. Approved on February 29.
131 Wu, C. and Jiang, S.H. (2001) U.S. Patent No. 6,238,688. Approved on May 29.
132 Wu, C. and Jiang, S.H. (2003) Chinese Patent No. 97 1 80823.6. Approved on March 5.
133 Wu, C. and Jiang, S.H. (2003) HK Standard Patent No. 1025585. Approved on September 19.
134 Leung, P.C., Yew, D., Wu, C., and Peng, S.F. (2003) *Microsurgery*, **23**, 123.

2
Thermosensitive Core–Shell Microgels: Basic Concepts and Applications

Yan Lu and Matthias Ballauff

2.1
Introduction

Networks composed of thermoresponsive polymers have been a central topic in polymer research for the last 40 years [1–4]. Thus, networks of poly(*N*-isopropylacrylamide) (PNIPAM) can undergo a volume transition. In cold water these networks swell by uptake of the solvent. Raising the temperature leads to a phase transition in which most of the water is expelled. Many years ago, Tanaka and coworkers pointed out that the volume transition in PNIPAM networks represents a polymeric analog to the gas-to-liquid transition of a van der Waals gas [2, 5]. Thus, by adding charge co-units and an appropriate degree of crosslinking, the continuous transition referring to a supercritical isotherm can be driven into the two-phase region. Here a discontinuous shrinkage of the network takes place [4]. If the respective parameters are chosen correctly, a critical isotherm can be adjusted in such a network and critical phenomena can be investigated by measuring the scattering intensity around the critical point [5, 6]. In this way PNIPAM networks present a classical case for soft matter systems that provide models for the phenomena observed in conventional matter.

Tanaka and coworkers were also the first to study the kinetics of this volume transition. Downsizing the macroscopic gels to the colloidal domain, they found that the characteristic time needed for deswelling scales with the square of the overall size of the gels, as is to be expected by a process limited by diffusion [4]. These investigations opened a new field devoted to the synthesis and analysis of microgels, that is, thermosensitive gels with dimensions between 50 nm and a few micrometers [7–12]. Smaller particles can be made by conventional colloidal techniques while particles in the range of micrometers are now conveniently prepared by microfluidic techniques [13, 14]. Microgels have been studied intensively recently and a number of comprehensive reviews are available [7–15].

Core–shell microgels consisting of a spherical or ellipsoidal core of a solid material such as, for example, polystyrene or silica present systems of particular interest with properties that differ markedly from those of conventional microgels [16–25].

Hydrogel Micro and Nanoparticles, First Edition. Edited by L. Andrew Lyon and Michael Joseph Serpe.
© 2012 Wiley-VCH Verlag GmbH & Co. KGaA. Published 2012 by Wiley-VCH Verlag GmbH & Co. KGaA.

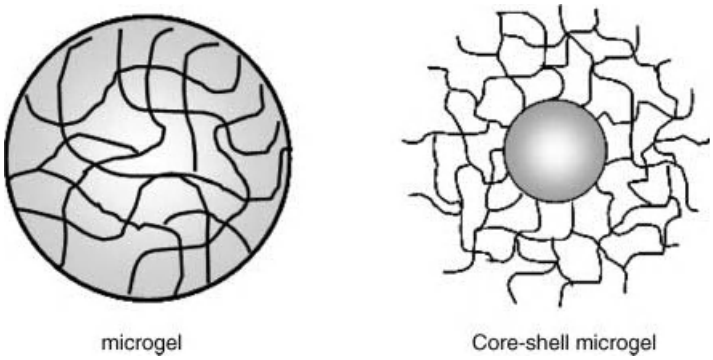

Figure 2.1 Schematic comparison of microgels with core–shell microgels.

Figure 2.1 shows a comparison of both systems in a systematic fashion. In the case of core–shell microgels, the network is affixed to a solid surface. Hence, it can swell only along the radial direction; hardly any expansion is possible along the perpendicular directions. If the degree of swelling of an unbound network is given by α, the respective quantity of a core–shell system should be of the order of $\alpha^{1/3}$ only, which is indeed obtained. This raises the question how much the volume transition of such particles and the critical phenomena within their shell is affected by this effect. Hence, single core–shell microgels present interesting objects for thermodynamic studies of finite size effects [26, 27].

Moreover, affixing the network to a solid core leads to particles of an extraordinary colloidal stability. Therefore these particles can be used as model colloids with variable volume fraction. At higher temperatures the shell is in a shrunken state and the volume fraction ϕ that scales with the third power of the hydrodynamic radius R_h of the particles is small. Decreasing the temperature leads to a strong increase of ϕ and colloidal suspensions with a high volume fraction can be easily adjusted. The stability of the core–shell particles allows us to reverse the process and core–shell particles have become highly valuable model systems for questions related to colloid physics. Hence, these particles have been used for studies of colloidal crystallization [28–31] and of the flow behavior of concentrated suspensions [32–39]. The results derived from these investigations can be directly compared with data obtained from conventional microgels [40–42]. Moreover, two-dimensional crystallization of microgels [10, 43–45] and of core–shell microgels [46] on planar surfaces has recently become an interesting field of research. Thus, it is fair to state that microgels and in particular core–shell systems have become true model systems for colloid physics that allow us to perform experimental studies that are not available through the use of conventional particles.

In this chapter we first review recent work related to basic investigations of these systems. The synthesis and characterization of core–shell particles are discussed by Kawaguchi in Chapter 3. At first, the properties and the thermodynamics of single particles will be reviewed [47–52]. Then properties related to assemblies of particles, such as crystallization and rheology, for example, will be reviewed. Special emphasis

is put on recent work using core–shell particles as model colloids. In a second part, the consequences of the thermosensitive behavior for possible applications will be reviewed. Here we focus on the recent use of core–shell particles as colloidal carriers of metallic nanoparticles [53–56] and enzymes [57].

2.2
Volume Transition in Single Particles

The volume transition in core–shell microgels in aqueous solution has been studied in great detail by various methods. Cryogenic transmission electron microscopy (cryo-TEM)[58, 59] is one of the best means to investigate these structures directly *in situ*. A thin layer with a thickness of 300–500 nm of the sample is shock-frozen at the temperature of liquid nitrogen. The aqueous phase is thereby converted into hyperquenched glassy water (HGW)[60, 61] and the particles are thus embedded in an amorphous water phase. This treatment circumvents possible disturbance of the particles by the crystallization of water.

Figure 2.2 shows the particles in a schematic fashion together with the respective cryo-TEM micrographs of the swollen and the shrunken state [47]. The cores made

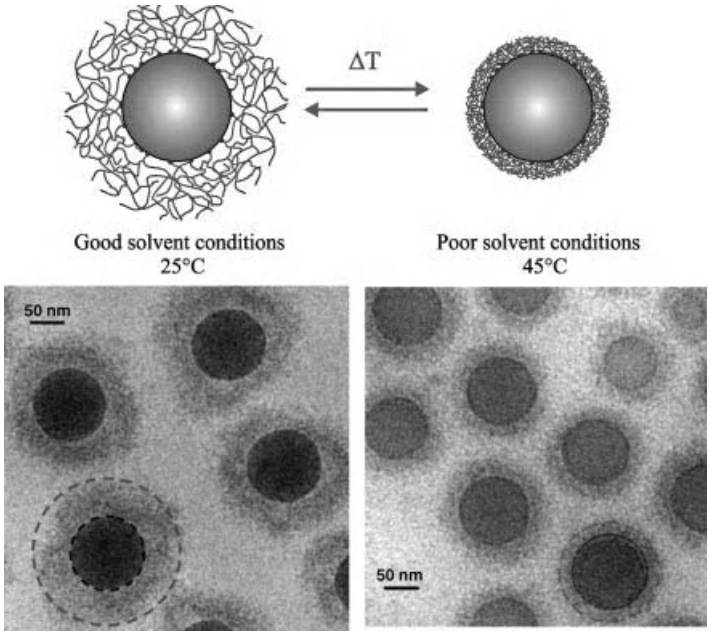

Figure 2.2 Cryo-TEM images of PS–PNIPAM core–shell particles. The sample was stored at 23 °C (left) and 45 °C (right) before vitrification. The circle around the core marks the core radius determined by dynamic light scattering (DLS) in solution. The circle around the entire particle that marks the entire particle gives the hydrodynamic radius R_h of the core–shell particles as determined by DLS (Figure 2.3). Taken with permission from [47].

from polystyrene and the PNIPAM shells are directly visible. Moreover, these micrographs demonstrate that the shell is rather dense and well-ordered in the shrunken high-temperature state. However, swelling at lower temperature leads to a rather irregular shape. For some particles even a buckling of the shell can be seen. This is due to the fact that the swelling can only take place along the radial direction and not in three dimensions as in an unbound gel. If the network is not fully affixed to the core, it will buckle off. This buckling was first observed by Tanaka and coworkers on macroscopic networks (see review in [62]) and the observation using cryo-TEM [47] was the first proof of this effect in colloidal systems.

The irregular shape leads also to a finite optical anisotropy that can be used to monitor shape fluctuations by depolarized dynamic light scattering (DDLS) [52]. This method measures the rotational and translational diffusion coefficients of the particles in dilute solution [63, 64]. For homogeneous spheres, both coefficients must be related to the same hydrodynamic radius. Figure 2.2 demonstrates that this is the case for the high-temperature state. However, in case of the swollen state the rotational diffusion seems to be faster than that inferred from the hydrodynamic radius of translation. This result could be explained by an addition decorrelation due to the internal fluctuations of the network in the shell of the particles.

It should be noted that the gray scale of the cryo-TEM pictures can be evaluated quantitatively to yield the local excess electron density of the particles, that is, the difference between the particles and the surrounding HGW phase [49]. This information can directly be converted into the scattering intensity to be observed by small-angle X-ray scattering (see below). In this way a comparison between a microscopic method and small-angle scattering becomes possible.

Scanning transmission X-ray microscopy (STXM) has recently become an excellent technique that allows us to analyze samples in direct space with high chemical sensitivity. Fujii *et al.* [65, 66] have described the real space characterization of swollen pH-responsive microgel particles in aqueous solution using STXM. These authors combined STXM with near-edge X-ray absorption fine structure spectroscopy (NEXAFS) and presented images of submicrometer-sized swollen microgel particles. This analysis simultaneously leads to the determination of the chemical state of the microgels in the aqueous phase. Since the resolution of X-ray microscopy has been much improved recently [67, 68], this method is expected to become an indispensable tool for the analysis of microgels *in situ*.

Dynamic light scattering (DLS) is certainly the technique applied mostly for the characterization of microgels in aqueous solution. Figure 2.3 displays a typical example of a swelling curve obtained from the microgels discussed already in conjunction with Figure 2.2. The sharp volume transition around 31 °C is clearly visible. The precision of these data is high enough to state that this volume transition is continuous. Moreover, the data can be evaluated further and compared to a theoretical modeling (see the discussion of Figure 2.4 below). The precision of DLS is underscored further by the fact that the hydrodynamic radius derived by this method agrees rather well with the overall size estimated from cryo-TEM. The dashed circles in Figure 2.2 indicate the size of the particles measured by DLS. Hence, the hydrodynamic radius is sensitive to the smallest detail of the surface structure and the

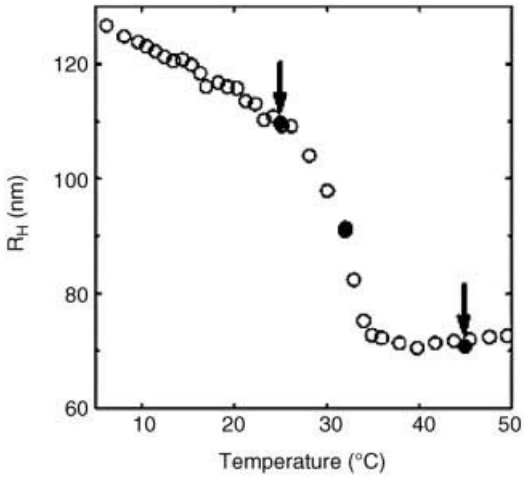

Figure 2.3 Hydrodynamic radius of thermosensitive core–shell particles, as measured by dynamic light scattering (90° scattering angle) as the function of temperature (see Figure 2.2). Solid circles mark the temperatures where measurements have been done at angles ranging from 45 to 150° in steps of 15°. Arrows indicate the temperatures at which the cryo-TEM measurements shown in Figure 2.2 were made. Taken with permission from [47].

hydrodynamic radius presents the largest extension of the object under consideration. This is in sharp contrast to small-angle scattering methods, as discussed further below.

The theory of macroscopic thermosensitive networks can now be regarded as entirely understood and reviews thereof may be found in early reviews of this subject [69, 70]. It is now clear that the salient features of the swelling equilibrium can be modeled in terms of conventional Flory–Rehner theory, that is, the final degree of swelling results from the osmotic pressure inside the network and the retrieving force of the polymer chains. This leads to a full description of classical phase diagrams in which continuous supercritical swelling curves can be driven to the subcritical state by adding increasing amounts of charged groups (see the discussion of figures 5 and 6 in the review by Shibayama and Tanaka [4]). This approach has been adapted for the description of microgels recently [26] and applied successfully to the core–shell systems described above [48]. Figure 2.4 shows the respective phase diagrams in plots of T vs. the volume fraction of the polymer in the network of the shell. Here the overall size determined by dynamic light scattering (DLS) has been used since it provides a good measure for the size of the particles (see above). The degree of swelling depends sensitively on the degree of crosslinking of the network as expected. The agreement of theory and experiment is quite satisfactory and the parameters deriving from these fits allow us a detailed discussion of the systems (see the discussion of table 2 in [48]). Interestingly, these fits lead to the conclusion that the volume fraction of the polymer in the shrunken state is about

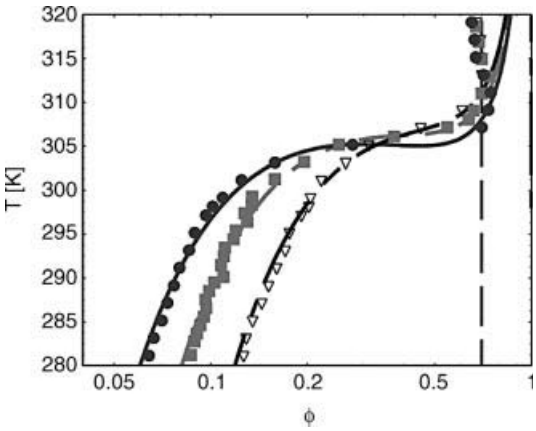

Figure 2.4 Experimental phase diagram T–ϕ of core–shell particles for different degrees of crosslinking (full circles: 1.25 mol%, hollow triangles: 2.5 mol%, full squares: 5 mol%). Lines present the fits obtained from the thermodynamic modeling by a Flory–Rehner-type approach. The volume fraction ϕ of the polymer in the network has been calculated from the hydrodynamic radii of the particles. The vertical dashed line marks the reference volume fraction $\phi_0 = 0.7$ in the collapsed state. Taken with permission from [48].

0.7 (see Figure 2.4). This finding is in good agreement with the direct evidence by cryo-TEM (see Figure 2.2 and further discussions in [48, 49]).

Small-angle X-ray scattering (SAXS) [71] and small-angle neutron scattering (SANS) [72] supply additional interesting information. These techniques are ideally suited for studying microgels with sizes below 200 nm. For such particles the scattering intensity $I(q)$ (where q is the magnitude of the scattering vector $q = (4\pi/\lambda)\sin(\theta/2)$, λ is the wavelength of the radiation used, and θ is the scattering angle) contains information about the size of the particles and their interaction if $1/q$ is of the order of their size and smaller [73]. The intermediate q-range leads to the analysis of the core–shell structure of the particles. Finally, network fluctuations can be analyzed quantitatively using the range of large scattering angles in which small-scale details are probed. Up to now, there has been a large number of studies on microgels and on core microgels by SAXS and SANS [40, 41, 50, 51]. Here it will suffice to focus the attention on a recent comparison of SAXS with cryo-TEM [15, 49].

Figure 2.5 displays the central result of this analysis, which is related to the inhomogeneities of the network [15]. It shows a comparison between a SAXS scattering curve and a cryo-TEM micrograph in which the contrast was strongly enhanced by false colorization. In principle, there are two types of inhomogeneities in a network [62, 74]: (i) the static inhomogeneities caused by the freezing of thermal density fluctuations through the crosslinks; and (ii) the thermal fluctuations of the network density (dynamic inhomogeneities). The latter are expected to increase dramatically near the phase transition; they should diverge at the critical point which has been seen in macroscopic PNIPAM networks in the classical work of Han,

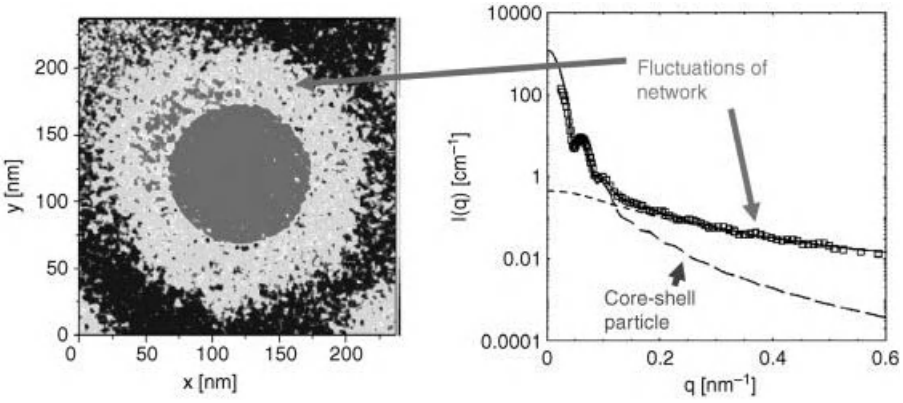

Figure 2.5 Fluctuations of the thermosensitive network as revealed by cryo-TEM (left-hand side) and by SAXS measurements ([51]; right-hand side). The long-dashed line in the right panel displays the fit of the overall core–shell structure whereas the short-dashed line shows the contribution of the density fluctuations in the network. The contrast in the cryo-TEM micrograph has been much enhanced by false coloration to show the local inhomogeneities of the network in the shell. The approximate size of these inhomogeneities is of the order of a few nanometers which agrees with correlation length ξ deduced from SAXS data. Taken from [15].

Tanaka, and Shibayama [6]. Analysis of the SAXS data of this part of the scattering curve of core–shell particles is shown in Figure 2.5: SAXS "sees" the local inhomogeneities of and the fluctuation-induced scattering $I_{\text{fluct}}(q)$ can be modeled by an Ornstein–Zernicke expression

$$I_{\text{fluct}}(q) \propto \frac{\xi^2}{1 + q^2\xi^2}$$

The short-dashed line in Figure 2.5 suggests that this expression provides a good description of the scattering intensity at higher scattering angles. The correlation length ξ is the characteristic length of the density fluctuations. The analysis in [51] demonstrated that ξ decreases linearly with the volume fraction of the polymer in the shell (see figure 10 of [51]). No indication of any criticality of ξ in the vicinity of the transition was found in the course of this analysis. Hence, we only see static inhomogeneities built into the network by synthesis. This conclusion is directly supported by cryo-TEM. The left-hand side of Figure 2.5 shows the swollen state of the particles in a cryo-TEM micrograph. Cryo-TEM visualizes these static inhomogeneities that originate from the synthesis of the shell. Evidently, these inhomogeneities are much more pronounced than any critical fluctuation and the core–shell systems under consideration are not suited to study these phenomena in the vicinity of the phase transition. The inhomogeneities may also be responsible for the observation that the transition is always found to be continuous (see the discussion of Figures 2.3 and 2.4 above). However, much work is needed to come to firm conclusions on this subtle problem.

2.3
Concentrated Suspensions: 3D Crystallization

Suspensions of colloidal spheres are now important model systems for condensed matter [75–77]. If the concentration of spherical particles is increased beyond a volume fraction of 0.494, crystallization sets in. This is directly evident from the iridescent colors caused by the Bragg reflections of visible light by colloidal crystallites. Thermosensitive core–shell particles are uniquely suited to the study of these phenomena inasmuch as they may be "inflated" by lowering the temperature in the system. Thus, thermosensitive suspensions have become the basis of a number of recent studies devoted to colloidal crystallization [28–30, 78–80]. A review of work devoted to core–shell systems has been presented recently [15].

Figure 2.6 displays a typical example for the crystallization in such a system [34]. Here the volume fraction is increased from left to right by lowering the temperature. The biphasic gap ranges from 0.49 to 0.55. This finding indicates that the core–shell particles discussed in conjunction with Figures 2.2–2.5 behave as hard spheres, at least up to these volume fractions. This result can be easily rationalized as follows: The modulus of the densely crosslinked network can be estimated by kT/ξ^3 where ξ denotes the correlation length of the network. Since ξ is of the order of a few nanometers only, the modulus of the network is much higher than the shear modulus of a crystal of spheres in simplest approximation through $G_0 \sim kT/R^3$ where R is the radius of the spheres [76]. It should be noted, however, that this approximation is only valid at low frequencies. Measurements of the high-frequency viscosity [81] and of the

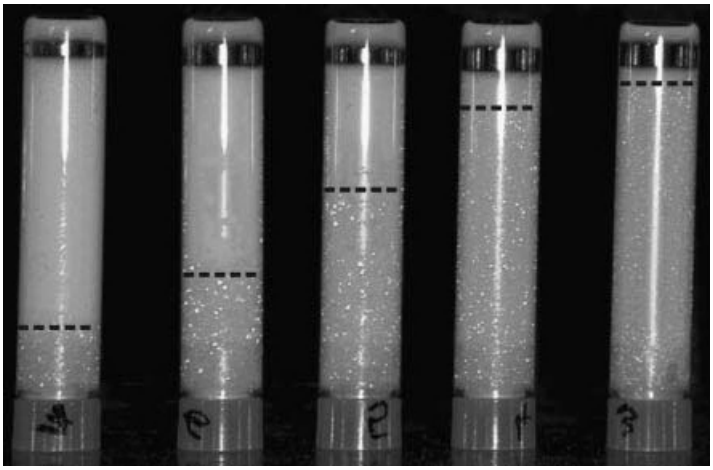

Figure 2.6 Fluid-crystal equilibria in aqueous suspensions of core–shell microgels. The volume fraction increases from left to right. The system is in the two-phase region and the crystalline fraction, seen from the iridescent colors, is slightly denser than the coexisting fluid phase and fills the lower parts of the tubes. Increasing the volume fraction of the spheres leads finally to an entire crystalline system. The phase diagram thus obtained coincides with the one predicted for hard spheres. Taken with permission from [34].

high-shear viscosity [37] have clearly revealed marked deviations from this behavior (see below).

The small modulus $G_0 \sim kT/R^3$ leads to an extreme softness of the crystals ("soft matter"). A small shearing force suffices to melt them [76]. Concomitantly, the motions in such a system are drastically slowed down when compared to molecular systems. This can be seen by calculating the Brownian time τ needed by one sphere to diffuse over its own size R. Given the Stokes–Einstein diffusion coefficient $D = kT/(6\pi\eta R)$ with η being the viscosity of the suspending medium, the Brownian time can be estimated to $\tau \sim R^2/D \sim \eta R^3$. For a given viscosity of the suspending medium, the increase of the size by 10^3 leads to a slowing down of motions by at least 10–11 orders of magnitude. Processes which take place in atomic systems within picoseconds are therefore shifted to the range of milliseconds. In this way colloidal systems allow us to study dynamic phenomena using simple mechanical spectroscopy.

2.4
Particles on Surfaces: 2D Crystallization

Assemblies of colloidal spheres (including organic or inorganic particles) into 2D or 3D ordered structures have attracted considerable attention, and are useful for applications in optical switches [82], chemical sensors [83], or photonic devices [84]. Hard spheres, such as silica and polystyrene, have been used most often for studying the self-organization processes because of their easy availability [85]. Meanwhile, increasing attention has been directed towards the assembling of polymer microgel particles with regard to their soft-sphere characters and stimuli-sensitive behaviors [10]. Materials prepared using ordered colloids change color when the lattice distance is varied. This can be achieved for microgel particles by changing the particle size through thermal deswelling. Most of these microgel systems are based on PNIPAM or copolymers of PNIPAM with a charged comonomer [7]. For example, Lyon *et al.* [86] achieved colloidal crystals with tunable color by the assembly of water-swollen PNIPAM-*co*-acrylic acid (AA) microgels via centrifugation. Kumacheva *et al.* [87] have used hybrid core–shell particles, in which the PNIPAM-AA-hydroxyethyl acrylate (HEA) core is doped with CdS nanoparticles as the building blocks as photonic crystals with interesting optical properties.

The formation of the loosely ordered 2D structure of PNIPAM microgel particles was first observed by Pelton *et al.* [88] in 1986. Since then, several groups have studied 2D assemblies of microgel particles. Kawaguchi *et al.* [44] reported that a 2D superlattice can be formed for the PNIPAM hydrogel or particles with PNIPAM graft chains on the surface when they are dried and self-assembled on the substrates. They explained that the array formation is caused by the balance between capillary forces and sterical hindrance of PNIPAM layer. The interparticle distance was determined by the hydrodynamic diameters as well as the concentration of the particles. Moreover, films formed from the periodic microstructures of the PNIPAM particles produced iridescent colors due to diffraction when polystyrene (PS) was used as substrate [89]. Von Klitzing *et al.* [45, 90, 91] have also confirmed that

PNIPAM-*co*-AA microgel particles form well-organized 2D structures at solid surfaces. The possible parameters, such as pH, pre-coating of the substrate and preparation technique, which will influence the packing density of microgel particles on precoated Si wafers have been investigated. They have found that for the adsorption density the electrostatic contribution of the particle-particle interaction play a more pronounced role than that of the particle-surface interaction. Horecha *et al.* [92, 93] have prepared ordered periodic loosely packed (PLP) 2D arrays from PNIPAM-based microgels with core–shell structures via self-assembly. Such microgel arrays can be used as masks for different patterns.

In our study, the formation of core–shell microgel particles into 2D arrays has been investigated by depositing the diluted microgel dispersion on various substrates [46]. Microgel particles with different surface charges have been made by using various initiators during polymerization. Dependent on the electrostatic interactions between microgel particles and charged substrate surface, ordered 2D patterns of microgel particles can be formed on the substrate as shown in Figure 2.7. As discussed in the previous section, an electrostatic repulsion of the microgels leads to a superlattice in microgel solution (see Section 2.3), which are precipitated on the substrate surface during water evaporation. When microgel particles bear a surface charge opposite to that of the substrate, a well-ordered arrangement on the surface will be achieved due to the mutual repulsion and attractive interaction with the surface. In contrast, when microgel particles are deposited onto a substrate surface with a similar charge, no long-range 2D order is formed on the surface. This may be because of the strong electrostatic repulsion between the particles and the surface, which precludes any sticking of the particles to the surface. Thus, the capillary forces operative upon drying destroy the preformed superlattice structure of the microgel particles in the solution. This finding agrees well with the results on the formation of 2D structures based on the electrostatic interaction between charged spheres and charged substrates reported by Gliemann *et al.* [94].

In addition, 2D arrays with tunable interparticle spacing are still a major challenge in the self-assembly of colloidal particles. Here, core–shell microgel particles using a microgel shell as a flexible spacer for controlled assembly of the core particles will definitely be a promising candidate. As shown by Karg *et al.* [95] recently, 2D arrays of Au-PNIPAM core–shell particles can be fabricated using convective deposition and spin-coating. Removal of the microgel shell by annealing at 700 °C leads to ordered 2D arrays of Au nanocrystals with tunable interparticle spacings.

2.5
Concentrated Suspensions: Rheology

Another important feature directly related to the slowing down of the dynamics in these suspension (see above) is transition from the fluid to a glassy state [75–77]. Above a volume fraction of about 0.58, the constraints of the motion of the colloidal spheres by their neighbors leads to a freezing-in of the motion (i.e., to the formation of a colloidal glass). A given sphere is now densely surrounded and confined by a

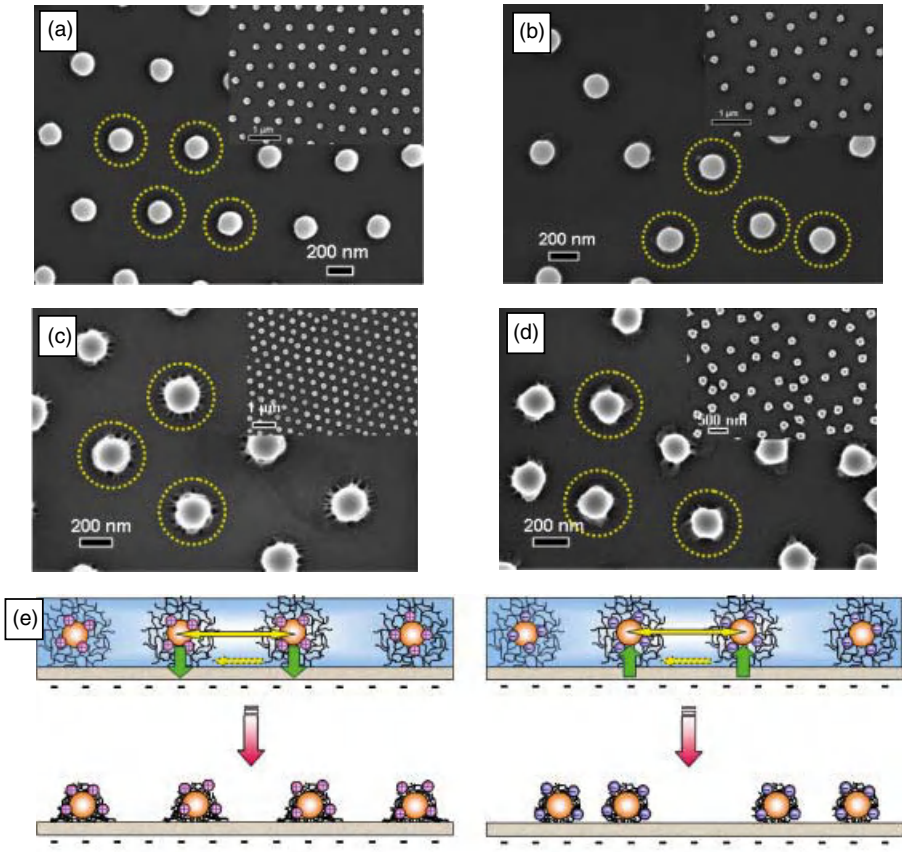

Figure 2.7 Field emission scanning electron microscope (FESEM) images of positive microgel particles assembled on mica substrate (a) and Si wafer (c); and negative microgel particles assembled on mica substrates (b) and Si wafer (d), respectively. The dashed circles shown in the FESEM images indicate the size of the microgel particles in the wet state. Schematic images (e) are shown of the mechanism of self-assembly of positive microgel particles and negative microgel particles on negatively charged substrates during water evaporation, respectively. Taken with permission from [46].

rather dense cage of other spheres. On a short timescale on the order of the Brownian time τ, a relaxation can only take place within the cage (β-relaxation) that amounts to a "rattling in the cage" of the spheres. Motion over longer length scales (α-relaxation) can take place only by a total rearrangement or breaking of the cage. This process can take place in a timescale much longer than τ. In quiescent suspension, the cage effect can be seen directly by the suppression of the α-relaxation above a volume fraction of 0.58 (see the discussion in [75, 76, 96]). Suppression of this relaxation is thus the signature of the glass transition.

Evidently, the glass transition must have a strong impact on flowing suspensions [96]. Thermosensitive suspensions have a distinct advantage when studying the

flow behavior of concentrated suspensions. Immersed in water above temperatures of 25 °C the particles will be shrunken and exhibit a small volume fraction. Hence, they will flow easily and local equilibrium in this fluid state can be achieved without problems. Cooling down this suspension to lower temperature will be followed by a marked increase of the hydrodynamic radius and hence of the effective volume fraction ϕ_{eff}. If ϕ_{eff} is raised above 0.58, the system is in the glassy state and the dynamics of the suspension will be slowed down dramatically. After performing the rheological experiments in this state, the temperature can be raised again and the entire system is brought into the fluid and mobile state again. In this way all traces of the previous shearing of the sample can be wiped out. Thus, these "reversibly inflatable spheres" present a model system since the glassy state can be easily reached through change of the temperature. It should be kept in mind, however, the flow behavior is solely governed by the control parameter ϕ_{eff} [47].

The obvious advantages of thermosensitive suspensions have led to an appreciable number of rheological studies so far [32, 34–38, 78–80]. Several reviews of this work have been presented recently [15]. Here it suffices to present the main points of this analysis. As already discussed above, the modulus of concentrated suspension is expected to be of the order of kT/R^3 whereas the Brownian timescales as $\tau \sim \eta R^3$. This suggests plotting the shear modulus σ of the suspension in units of kT/R^3 as a function of the Péclet number Pe_0 obtained through normalization of the shear rate or the oscillation frequency by τ.Figure 2.8 displays the flow curves, that is, the shear modulus as function of the shear stress. A parameter of the different curves is the effective volume fraction of the spheres in suspension. In this rendition the flow curves taken in the fluid regime, that is, below the glass transition, have a characteristic S-shape: At lowest Pe_0 there is a first Newtonian regime in which the viscosity is independent of the shear rate. Here $\sigma = \eta\dot{\gamma}$, where η is the viscosity. However, at

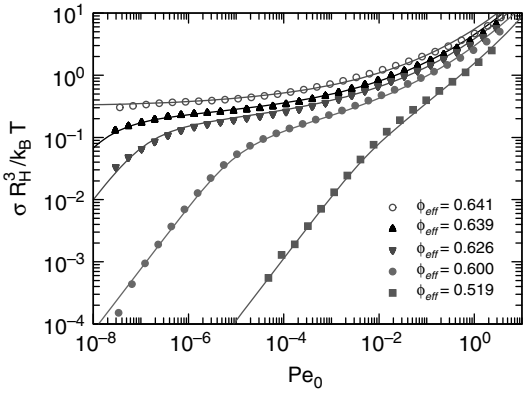

Figure 2.8 Flow curves of concentrated suspensions of thermosensitive particles. The reduced shear stress $\sigma {R_h}^3/k_BT$ is plotted against the Péclet number $Pe_0 = (6\pi\eta_S {R_h}^3/k_BT)\dot{\gamma}$ for suspensions differing in the volume fraction indicated in the graph. The effective volume fractions which are also given in the graph have been calculated from the hydrodynamic radii at a given temperature. The lines give the fits by mode-coupling theory. Adapted from [37].

slightly higher shear rates, shear thinning sets in. For $Pe_0 > 1$ there is an onset of a second Newtonian region. Going to higher and higher volume fractions leads to the fluid-to-glass transition. This transition can be seen in Figure 2.8 as the vanishing of the first Newtonian region of the flow curves. It should be kept in mind that the change of volume fraction has been brought about by a lowering of the temperature of the suspension. Hence, the effective volume fraction can be adjusted precisely and reproducibly to a given value.

All investigations done on thermosensitive core–shell suspension have revealed that the effective volume fraction deriving from dynamic light scattering (see above) is the sole control parameter that governs the flow behavior; no parameter related to the network in the shell needs to be taken into account. This finding follows directly from the fact that these particles behave as hard spheres in experiments that probe their low-frequency-behavior, that is, their flow behavior at low Péclet number $Pe \ll 1$ (cf. Figure 2.8). However, the high-shear viscosity resulting for $Pe \gg 1$ is considerably smaller than the value deduced for particles that consist of, for example, a solid polymer [97]. The same result is found for the high-frequency viscosity, which is much lower than that expected from the effective volume fraction (see [81] and the discussion in [37]). Under these conditions the solvent in the network is no longer fully immobilized and partial draining takes place.

However, at low *Pe* the data may serve for a full text of mode-coupling theory (MCT; see [96]). This theory models the slowing down of particle dynamics in the quiescent state when approaching the glassy state. Moreover, it gives a full treatment of the flow curves as a function of *Pe* as shown in Figure 2.8, together with the linear viscoelastic behavior. The solid lines in Figure 2.8 have been calculated by this approach and good agreement between theory and experiment is seen for all volume fractions under consideration. The set of parameters deriving from this fit may then be used to model the linear viscoelastic behavior [37] as well as the transition from this regime to the nonlinear flow behavior [39]. It is hence fair to state that recent work done on thermosensitive core–shell suspensions has demonstrated that MCT provides a full description of the rheology of concentrated suspensions. Given the fact that these particles have been equally useful in studies of colloidal crystallization, it is evident that thermosensitive microgels have become the most versatile model system in colloid physics [15].

2.6
Core–Shell Particles as Carriers for Catalysts

2.6.1
Metal Nanoparticles

Polymer–inorganic hybrid microgels comprising metal nanoparticles have become an important focus of current research since the development of new pathways in the synthesis of various hybrid materials with advanced and tailored properties [22, 98–100]. Using microgel particles as carrier systems for metal nanoparticles

may have several advantages over other systems, namely, ease of synthesis, colloidal stability and easy functionalization with stimulus-sensitive behavior [101]. By combining polymeric microgels with inorganic nanoparticles it is possible to introduce optical [102], magnetic [103], and catalytic [104] features into the hybrid materials. These features are also tunable due to the stimuli-responsive behavior of the microgel particles. Thus, these hybrid particles exhibit a combination of "inorganic" and "organic" characteristics.

The deposition of metallic nanoparticles into microgel particles can be realized by an *in situ* approach, that is, by the chemical reduction of metal ions immobilized into microgel networks using $NaBH_4$ as the reducing agent [105]. Similarly, magnetic nanoparticles can be synthesized in microgels *in situ* through the oxidation of immobilization Fe^{3+} ions [106, 107]. Antonietti *et al.* [108, 109] were the first to synthesize gold nanoparticles in the presence of polystyrene sulfonate microgels. Kroll and Winnik [110] reported the fabrication of magnetic alginate that utilizes the crosslinking ion as the reaction center for the *in situ* formation of nanocrystalline iron oxides. The resulting spherical beads of gel are superparamagnetic and stable indefinitely at room temperature. Suzuki and Kawaguchi [111] have used a thermosensitive core–shell microgel as a template for the synthesis of hybrid core–shell particles via *in situ* gold nanoparticle formation. The core consists of a water-insoluble polymer containing reactive sites to bind gold ions. Thus synthesized gold nanoparticles are located entirely between the rigid core and a thermosensitive PNIPAM shell.

Instead of chemical reduction, other methods such as microwave-assisted synthesis and photo-reduction, have been applied to synthesize metal nanoparticles using microgel particles as carriers as well. These methods are essential for biological applications of hybrid microgels because they avoid the use of $NaBH_4$ or N_2H_4 as reducing agent. Khan *et al.* [112] have prepared silver nanoparticles using PNIPAM-co-AA microgels as a template with glucose as a mild reducing agent under microwave irradiation. Silver nanoparticles with diameter of about 8.5 nm have been homogeneously immobilized in microgel particles, which show excellent colloidal stability over months. Zhang and Kumacheva [113] have synthesized stable silver nanoclusters in the interior of PNIPAM-AA-2-hydroxyethyl acrylate (HEA) microgel particles through a fast photoactivated process. The silver nanoclusters obtained in this way are fluorescent in a particular pH window which is bound by the value of the solubility product AgOH and efficient ionization of AA residues.

The electrostatic interactions between charged microgel carriers and metal nanoparticles will also facilitate the immobilization of metal nanoparticles [114, 115]. Bradley and Garcia-Risueno [116] have investigated the adsorption of the carboxylic acid-stabilized gold nanoparticles into a poly(NIPA-*co*-*N*-[3-(dimethylamino)propyl] methacrylamide (DMAPMA)) microgel network as a function of pH. It is found that gold nanoparticles are adsorbed asymmetrically onto microgels by adsorption of nanoparticles onto microgel-stabilized oil-in-water emulsions from the aqueous phase. Feiler *et al.* [117] have investigated the uptake of anionic gold nanoparticles (2-mercaptoethanesulfonate (MES) stabilized gold) by pH-responsive poly(2-vinylpyridine) (P2VP) microgels deposited on a quartz surface in both swollen and

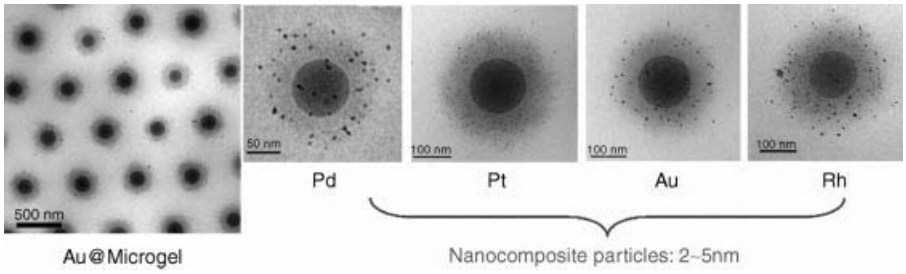

Figure 2.9 Cryo-TEM images of different metal nanoparticles immobilized in thermosensitive core–shell microgels, respectively. Adapted from [56].

collapsed states. The uptake of Au-MES nanoparticles into adsorbed microgel layers showed quantitative correlation with the uptake in microgel dispersion. However, there was a systematic reduction in the total adsorbed amount due to the microgel particles being constrained at the surface. Karg *et al*. [118] have modified Au-nanorods (Au-NRs) with polyelectrolyte layers to affix a positive charge onto their surface, which can be then affixed to thermosensitive PNIPAM microgel with negative charges. Recently, these authors have demonstrated that a denser and more homogeneous Au-NR coating can be achieved by using PNIPAM-*co*-allylacetic acid (AAA) microgel as the carrier [119].

In our work, thermosensitive PS–PNIPAM core–shell microgels were applied as the "microreactor" for the immobilization of different kinds of metal nanoparticles [104]. Due to complexation at the nitrogen atoms of the PNIPAM chains, metal ions are strongly localized within the microgel [120]. Reduction of these ions leads to nearly monodisperse metallic nanoparticles that are only formed within the microgel shell. Figure 2.9 shows cryo-TEM images for composite particles. As shown in Figure 2.9, the dark spherical particle indicates the PS core, and the bright corona around it is the microgel shell. The metal nanoparticles seen as small black dots are homogeneously immobilized in the PNIPAM network. This demonstrates that thermosensitive core–shell microgel particles can work efficiently as "microreactors" for the generation and immobilization of metal nanoparticles. The metal nanoparticles are in the size range 2–5 nm in diameter, which differs slightly with metal species.

Although in recent years a lot of work has been reported on the use of microgels as nanoreactors for the immobilization of metal nanoparticles, the control of nanoparticle size, shape, and size-dependent properties still remain a synthetic challenge. More recently, we have demonstrated that bimetallic Au-Pt-nanorods can be grown *in situ* into thermosensitive core–shell microgel particles by a novel two-step approach as shown schematically in Figure 2.10 [121]. Based on our previous work, spherical gold nanoparticles are first immobilized into thermosensitive microgel particles. These preformed gold nanoparticles, which act as seeds, direct the growth of Au-NRs (seed-mediated growth) inside the microgel carrier system. In the first step, Au-NRs with an average width of 6.6 ± 0.3 nm and length of 34.5 ± 5.2 nm (aspect ratio 5.2 ± 0.6) were homogeneously embedded into the shell of the PNIPAM

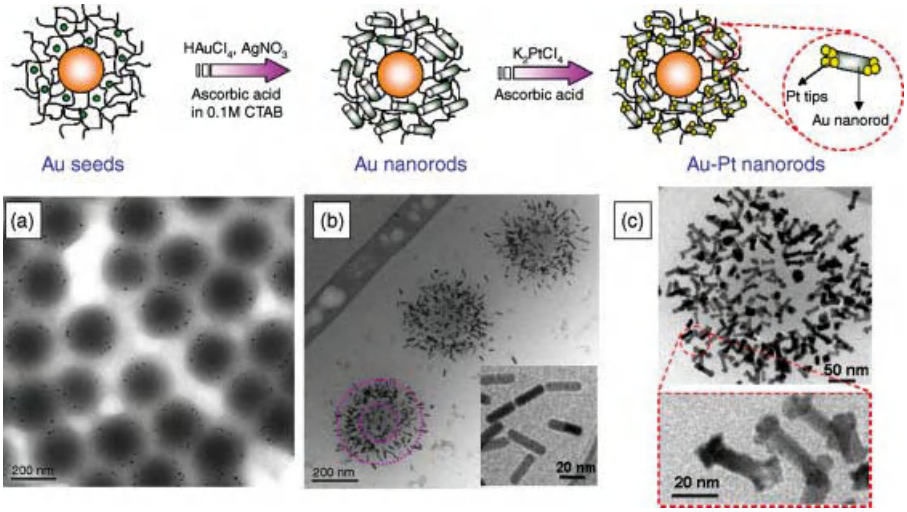

Figure 2.10 Schematic illustration of the *in situ* generation of bimetallic Au–Pt nanorods in the thermosensitive core–shell microgels by means of a seed-mediated growth method. (a) TEM image of Au seeds embedded in microgel particles; (b) cryo-TEM image of Au-NRs grown in the presence of thermosensitive core–shell microgels. (Dashed circles indicate the size of PS core and microgel particles in swollen state measured by DLS, respectively ($R_h^{PSCore} = 87.8$ nm, $R_h^{Microgel} = 198.4$ nm at 25 °C). The inset shows the morphology of embedded Au-NRs.); (c) cryo-TEM image and the enlarged views of Pt tips grown on the Au-NRs in water. Adapted from [121].

network. In the second step, platinum was preferentially deposited onto the tips of the Au-NRs to form dumbbell-shaped bimetallic nanoparticles. Analysis of the cryo-TEM images shown in Figure 2.10 indicates that the obtained metallic Au-Pt-NRs have an average width (middle) of 7.4±0.8 nm and length of 39.5±6.5 nm (aspect ratio 5.3±0.6). No secondary platinum nanoparticles were observed either in the microgel template or in the solution. Hence, this synthesis forms bimetallic Au-Pt-NRs immobilized in microgels without impeding their colloidal stability. This demonstrates for the first time that core–shell microgels can be used as "smart nanoreactors" for the *in situ* growth of bimetallic nanoparticles with controlled morphology and high colloidal stability.

One of the most attractive properties for metal nanoparticles is their strong surface plasmon resonance absorption due to the high electronic polarizability of nanoparticles. Using a stimuli-responsive microgel as the carrier, the optical properties of composite particles can be modulated by the volume transition of the microgel template. Suzuki and Kawaguchi [122] have reported a color change with temperature for thermosensitive hybrid core–shell particles, which is due to the change of interparticle distance of gold nanoparticles in the thermosensitive microgel phase with temperature. Similar behavior has been also reported by Das *et al.* [123] and Karg *et al.* [118, 119]. Liz-Marzán and coworkers [124, 125] have developed core–shell colloidal system comprising gold nanoparticles with a thermosensitive PNIPAM

microgel. The fluorescence intensity of adsorbed chromophores can be modulated as a function of temperature. In addition, they have shown that the immobilized gold nanoparticles can work as seeds for the growth of a thin layer of magnetically responsive nickel [103]. The hybrid core–shell microgels show an optical response induced by swelling–deswelling of the PNIPAM shell, and the hybrid particles can be also manipulated through external magnetic fields. More recently, they have simplified the preparation procedure by using butenoic acid as the reducing agent for the gold nanoparticles, which brings a vinyl functionality on the gold core that could be used for the PNIPAM polymerization directly [126]. Increasing the gold core size or the growth of silver shells on gold cores may improve the plasmonic performance of the gold particles significantly.

In our study, a red shift of the longitudinal plasmon resonance of Au-NRs immobilized in core–shell microgels can be clearly observed with increasing temperature, which can be correlated to the volume transition of the microgel carrier [121]. This transition is fully reversible upon cooling down to room temperature. The shift to longer wavelengths and the broadening of the surface plasmon absorption band are attributed to the increase of local refractive index near Au-NRs during the collapse of microgel particles [118]. A similar shift induced by the collapse of the microgel has also been found in silver nanoparticles embedded in microgels [54]. However, a much higher sensitivity is observed for the Au-NRs here: The shift of plasmon band is around 30 nm by increasing the temperature from 20 to 40 °C, while the respective shift for the microgel–silver nanocomposites is only 6 nm.

One of the most important applications for metal nanoparticles is catalysis. Biffis *et al*. [127, 128] have studied the application of microgel-stabilized metal nanoclusters as catalysts for different reactions. Palladium nanoclusters have shown enhanced catalytic activity in Heck reactions of activated aryl bromides. In our study, it is found that the catalytic activity of immobilized metal nanoparticles can be switched "on" and "off" by the swelling and collapse of thermosensitive microgels [53, 121]. This has been first confirmed by using the catalytic reduction of 4-nitrophenol in the presence of $NaBH_4$ as the model reaction [129]. More recently, we have shown that this reaction can be modeled in terms of the Langmuir–Hinshelwood kinetics [130]. The induction time of this reaction is related to a substrate-induced surface restructuring that is necessary to render the facetted gold nanoparticles into an active catalyst [131]. It is found that the rate constant k_{app} of the catalytic reaction does not follow a typical Arrhenius-type dependence on temperature when thermosensitive core–shell microgels are used as the carrier, as shown in Figure 2.11 [55]. When the reaction temperature is higher than 25 °C, the PNIPAM network shrinks markedly, leading to a concomitant slowing down of the diffusion of reactants within the network. This in turn decreases the rate constant k_{app} of the metal nanoparticles immobilized in the microgel particles. Similar phenomena have also been observed by other groups for metal nanoparticles immobilized in thermosensitive polymers [132, 133]. Carregal-Romero *et al*. [126] observed this behavior for gold nanoparticles encapsulated in PNIPAM microgels as a catalyst for the electron-transfer reaction between hexacyanoferrate (III) and borohydride [134]. They found that systems with a

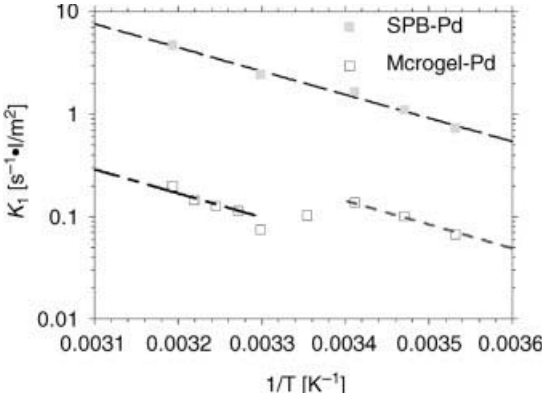

Figure 2.11 Dependence of the rate constant k_1 on the temperature T for different systems: Arrhenius plot of k_1 measured in the presence of the non-thermosensitive composite particles SPB-Pd (filled squares). In the case of the microgel–Pd system (open squares), we obtained an S-curve. Adapted from [55].

thermoresponsive shell with limited crosslinking allow for particularly efficient control of catalysis.

On the other hand, the influence of temperature on catalytic activity has been studied for two-phase reactions by oxidation of benzyl alcohol. In this case, the hydrophilicity of the microgels is reduced dramatically with increasing temperature [135]. We found that the change of polarity plays a more important role in the catalytic activity of hybrid core–shell microgels than that of the diffusional barrier. The catalytic activity of metal nanocomposites increases more than exponentially with increasing temperature. A significantly smaller catalytic activity has been observed only in the immediate vicinity of the volume transition [56].

2.6.2 Enzymes

Microgel particles can also work as carriers for enzymes with high catalytic efficiency. In general, the driving force for the adsorption of proteins on microgels is hydrophobic and electrostatic interactions. The physicochemical properties of microgels and proteins under certain conditions (pH, ionic strength, nature of buffer) play an important role in this process. Using thermosensitive microgels with a lower critical solution temperature (LCST) as carrier is of great interest, since the adsorption–desorption of proteins, which depends strongly on their physicochemical properties, can be controlled by the temperature, pH, and salinity of the medium.

Kawaguchi *et al.* [136] reported that the adsorption of proteins onto PNIPAM microgels depends on temperature. When the thermosensitive surface of PNIPAM microgel became hydrophobic (above the LCST), microgels favor the adsorption of protein (human gamma globulin). Elaïssari and Bourrel [137] studied the adsorption and desorption of protein (human serum albumin, HSA) onto the magnetic

core–shell microgels with a magnetic PS core and a PNIPAM shell. They found that the adsorption of HSA protein above the LCST of the microgel was governed by hydrophobic interactions. The maximal desorption of protein was obtained at pH > IEP (isoelectric point of the protein), high salinity and at 20 °C, that is, when the microgel is in a hydrophilic state. Huber *et al.* [138] investigated the adsorption of proteins on PNIPAM thin layers using a microfluidic device that consists of a 4-nm-thick end-tethered monolayer of PNIPAM. It is possible to adsorb proteins and release them again by thermally switching.

Functionalization of PNIPAM microgels with ionizable groups can facilitate faster phase transition when heated through the LCST or generate sensitivity to additional stimuli [139–141]. Duracher *et al.* [142] have synthesized positively charged thermosensitive core–shell microgels by copolymerization of NIPAM with aminoethyl methacrylate hydrochloride (AEMH) for the adsorption of bovine serum albumin (BSA). Below the LCST, the adsorption of BSA is nearly negligible due to the hydration capacity of the microgel shell, while it is much higher above the LCST. Chen *et al.* [143] found that a pH-responsive PNIPAM-*co*-AA microgel was an excellent sorbent for the selective isolation of specific protein species from complex sample matrices, for example, hemoglobin from human blood. Hoare and Pelton [144, 145] have synthesized different kinds of PNIPAM-based microgels via the copolymerization of acrylic acid (AA), methacrylic acid (MAA), vinylacetic acid (VAA), and fumaric acid (FA). The functional group distribution in the microgels strongly influenced the performance of different microgels as drug uptake vehicles. Maximum uptake for cationic drugs has been found for microgels containing a core-localized functional group distribution. Kim *et al.* [146] have developed bioresponsive hydrogel microlenses via Coulombic assembly of anionic stimuli-responsive PNIPAM-*co*-AA microgels functionalized with biotin on a positively charged glass substrate. The intrinsic bioresponsivity of the hydrogels is completely insensitive to simple adsorption via nonspecific protein binding from reconstituted human serum.

Recently, we have studied the adsorption of β-D-glucosidase onto thermosensitive core–shell PS–PNIPAM microgels [57]. A Langmuir isotherm has been used to describe the adsorption behavior of β-D-glucosidase, which shows excellent fit of the data as shown in Figure 2.12. The adsorption was performed in MOPS buffer at pH 7.2. Under this condition, the enzyme is negatively charged (the isoelectric point of β-D-glucosidase from almonds is 4.4). PS–PNIPAM microgel is also weakly negatively charged due to the rest of the initiator ($K_2S_2O_8$) on the PS core particle [56]. This leads to an overall repulsion between negatively charged enzyme and microgel particles, which indicates that the hydrogen bonds between the backbone of the enzyme and the amide side chains of the microgel as well as hydrophobic bonding are the main driving forces for immobilization [147]. This has been further confirmed by Fourier transform infrared (FTIR) spectroscopy. Recent measurements by isothermal titration calorimetry (ITC) showed that protein adsorption was entropy-driven in the case of spherical polyelectrolyte brushes (SPB) as carriers. This gain of entropy could be explained by the release of counter-ions from the protein molecules and the charged polyelectrolyte brushes ("polyelectrolyte mediated protein adsorption"

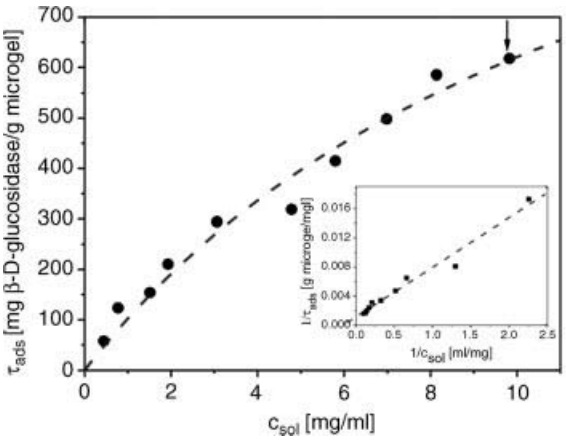

Figure 2.12 The adsorbed amount of β-D-glucosidase per gram microgel τ_{ads} is plotted versus the concentration of free enzyme c_{sol} in solution. The dashed line represents the fit of the experimental data by Langmuir isotherm. The arrow marks the amount of entrapped enzyme used for kinetic investigation (620 mg β-D-glucosidase per gram microgel). The inset displays the data as a linear Langmuir plot. The adsorption was conducted at 4 °C in 10 mM MOPS buffer solution (pH = 7.2) and with a microgel concentration of 1 wt%. The immobilized enzymes do not prevent the microgel from shrinking above the LCST. Taken with permission from [57].

(PMPA)) [148]. Similar ITC experiments are being performed for microgels as well in order to arrive at a better understanding of the driving forces for adsorption.

Until now, most of the research work has focused on using microgel particles as substrates for the immobilization of enzymes retaining their catalytic efficiency [149]. Less work has been reported on the regulation of catalytic efficiency of immobilized enzymes by extrinsic stimulation, for instance temperature or pH. Huang *et al.* [150] have introduced glutathione peroxidase (GPx) into thermosensitive PNIPAM microgels. They found that changing the temperature turns the enzyme activity on and off reversibly, which is due to a change of pore size as well as the hydrophobicity of the microgel induced by the temperature. The highest GPx-like activity is achieved at 32 °C. On the other hand, the GPx-like activity is almost lost when the temperature is above 50 °C.

In our study we have also shown that the catalytic properties of immobilized enzymes can be modulated by the swelling and collapse behavior of the microgel [57]. The enzymatic activity of adsorbed and native β-D-glucosidase has been tested using *o*-nitrophenyl-β-D-glucopyranoside (*o*NPG) as substrate. As shown in Figure 2.13, a slowing down of the catalytic rate has been observed for the adsorption of the enzyme at temperatures at which the volume transition of PNIPAM occurs. Moreover, the activation energy for the catalyzed reaction above the LCST is smaller than that of the free enzyme. These can be attributed to the volume phase transition of the PS–PNIPAM microgel. Therefore the reduction of the pore sizes of the PNIPAM network must lead to an increase of the diffusional barrier of *o*NPG, which is followed by a slight decrease in k_{cat} until the microgel is totally collapsed. Then, when the

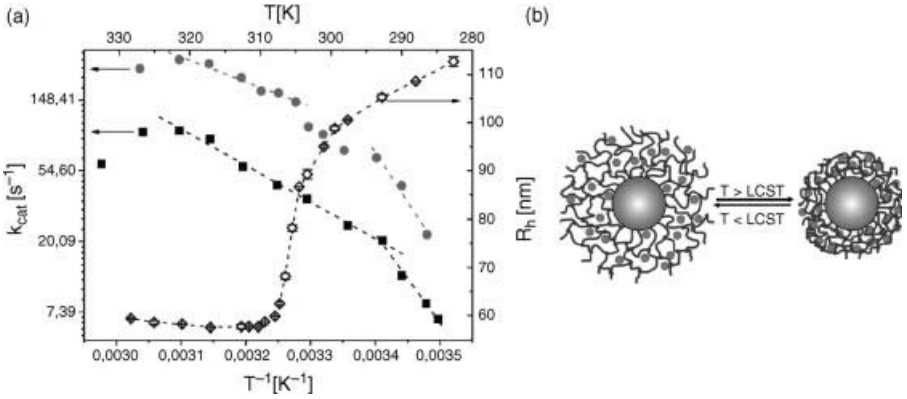

Figure 2.13 (a) Arrhenius plots of native (filled squares) and immobilized (filled circles) β-D-glucosidase (620 mg enzyme per g microgel) in MOPS buffer solution (pH=7.2). The turnover number k_{cat} for each temperature was determined by performing a whole Michaelis–Menten curve. The enzyme concentration was located between 0.005 and 0.01 g l^{-1} (native enzyme) and 0.0035–0.01 g l^{-1} (immobilized enzyme), respectively, and the substrate concentration varied between 1.0 and 20.0 mM. The dashed lines are linear fits of the experimental data according to the Arrhenius equation to determine the activation energies of the rate-limiting steps of the reaction. In addition, the swelling curve (diamonds) of the carrier particles is plotted. (b) Scheme of the enzymes (β-D-glucosidase) immobilized in the thermosensitive core–shell microgel template at different temperatures. Taken with permission from [57].

temperature increases further, a linear relation between ln k_{cat} with T^{-1} is recovered again. The lower E_a above the LCST indicates that in the collapsed state of the microgel the catalytic rate is affected by diffusional limitation. In general, thermosensitive core–shell microgels can serve as excellent carriers for enzymes and their catalytic activity may be modulated by the volume transition. Hence, these microgels present a novel class of "active" carriers for biocatalysis.

2.7 Conclusion

We review recent research work in the field of core–shell microgels, which consist of a well-defined solid core onto which thermosensitive PNIPAM networks are directly grafted. The morphology of microgels has been investigated *in situ*, that is, in their swollen state, by means of cryo-TEM. In addition, the cryo-TEM micrographs have been evaluated in a quantitative manner, which can be compared directly to the data deriving from scattering methods. Microgel particles act as "reversibly inflatable spheres." The fundamental studies of crystallization and the rheology of concentrated colloidal suspensions based on microgel particles have been discussed. Recently, these microgels particles have become model systems for reversible association and hydrophobic attraction [151]. Moreover, recent attention has been focused on the 2D self-assembly of polymer microgel particles. Finally, core–shell

microgel can work practically as an "active" carrier system for the immobilization of metal nanoparticles and enzymes.

Acknowledgment

Financial support by the Deutsche Forschungsgemeinschaft, SPP "Intelligente Hydrogele" is gratefully acknowledged.

References

1 Dusek, K. and Patterson, D. (1968) Transition on swollen polymer networks induced by intramolecular condensation. *J. Polym. Sci. Part A-2*, **6**, 1209–1216.
2 Heskins, M. and Guillet, J.E. (1968) Solution properties of poly(n-isopropylacrylamide). *J. Macromol. Sci. Chem.*, **2**, 1441–1455.
3 Tanaka, T. (1978) Collapse of gels and the critical endpoint. *Phys. Rev. Lett.*, **40**, 820–823.
4 Shibayama, M. and Tanaka, K. (1993) Volume phase transition and related phenomena of polymer gels. *Adv. Polym. Sci.*, **109**, 1–62.
5 Tanaka, T., Ishiwata, S., and Ishimoto, C. (1977) Critical behavior of density fluctuations in gels. *Phys. Rev. Lett.*, **37**, 771–774.
6 Shibayama, M., Tanaka, T., and Han, C.C. (1992) Small angle neutron scattering study on poly(N-isopropylacrylamide) gels near their volume-phase transition. *J. Chem. Phys.*, **97**, 6829–6841.
7 Pelton, R. (2000) Temperature-sensitive aqueous microgels. *Adv. Colloid Interface Sci.*, **85**, 1–33.
8 Kawaguchi, H. (2000) Functional polymer microspheres. *Prog. Polym. Sci.*, **8**, 1171–1210.
9 Nayak, S. and Lyon, L.A. (2005) Soft nanotechnology with soft nanoparticles. *Angew. Chem. Int. Ed.*, **44**, 7686–7708.
10 Lyon, L.A., Meng, Z., Singh, N., Sorrell, C.D., and St. John, A. (2009) Thermoresponsive microgel-based materials. *Chem. Soc. Rev.*, **38**, 865–874.
11 Karg, M. and Hellweg, Th. (2009) New "smart" poly(NIPAM) microgels and nanoparticles hybrids: Properties and advances in characterization. *Curr. Opin. Colloid Interface Sci.*, **14**, 438–450.
12 Motornov, M., Roiter, Y., Tokarev, I., and Minko, S. (2010) Stimuli-responsive nanoparticles, nanogels, and capsules for integrated multifunctional intelligent systems. *Prog. Polym. Sci.*, **35**, 174–211.
13 Zhang, H., Tumarkin, E., Sullan, R.M.A., Walker, G.C., and Kumacheva, E. (2007) Exploring microfluidic routes to microgels of biological polymers. *Macromol. Rapid Commun.*, **28**, 527–538.
14 Seiffert, S. and Weitz, D.A. (2010) Microfluidic fabrication of smart microgels from macromolecular precursors. *Polymer*, **51**, 5883–5889.
15 Lu, Y. and Ballauff, M. (2011) Thermosensitive core-shell microgels: From colloidal model systems to nanoreactors. *Prog. Polym. Sci.*, **36**, 767–792.
16 Pelton, R.H. (1988) Polystyrene and polystyrene-butadiene latexes stabilized by poly(N-isopropylacrylamide). *J. Polym. Sci. A*, **26**, 9–18.
17 Makino, K., Yamamoto, S., Fujimoto, K., Kawaguchi, H., and Oshima, H. (1994) Surface structure of latex particles covered with temperature-sensitive hydrogel layers. *J. Colloid Interface Sci.*, **166**, 251–258.
18 Okubo, M. and Ahmad, H. (1996) Adsorption behaviors of emulsifiers and biomolecules on temperature-sensitive polymer particles. *Colloid Polym. Sci.*, **274**, 112–116.
19 Dingenouts, N., Norhausen, Ch., and Ballauff, M. (1998) Observation of the

volume transition in thermosensitive core–shell latex particles by small-angle X-ray scattering. *Macromolecules*, **31**, 8912–8917.

20 Kim, J.H. and Ballauff, M. (1999) The volume transition in thermosensitive core-shell particles containing ionizable groups. *Colloid Polym. Sci.*, **277**, 1210–1218.

21 Ballauff, M. and Lu, Y. (2007) Smart nanoparticles: Preparation, characterization and applications. *Polymer*, **48**, 1815–1823.

22 Karg, M. and Hellweg, F.Th. (2009) Smart inorganic/organic hybrid microgels: Synthesis and characterization. *J. Mater. Chem.*, **19**, 8714–8727.

23 Karg, M., Pastoriza-Santos, I., Liz-Marzán, L.M., and Hellweg, Th. (2006) A versatile approach for the preparation of thermosensitive PNIPA core-shell microgels with nanoparticle cores. *Chem. Phys. Chem.*, **7**, 2298–2301.

24 Hoffmann, M., Siebenbürger, M., Harnau, L., Hund, M., Hanske, Ch., Lu, Y., Wagner, C.S., Drechsler, M., and Ballauff, M. (2010) Thermoresponsive colloidal molecules. *Soft Matter*, **6**, 1125–1128.

25 Dagallier, C., Dietsch, H., Schurtenberger, P., and Scheffold, F. (2010) Thermoresponsive hybrid microgel particles with intrinsic optical and magnetic anisotropy. *Soft Matter*, **6**, 2174–2177.

26 Fernandez-Barbero, A., Fernández-Nieves, A., and López-Carbarcos, E. (2002) Structural modifications in the swelling of inhomogeneous microgels by light and neutron scattering. *Phys. Rev. E*, **66**, 051803.

27 Keerl, M., Pedersen, J.S., and Richtering, W. (2009) Temperature sensitive copolymer microgels with nanophase separate structure. *J. Am. Chem. Soc.*, **131**, 3093–3097.

28 Tang, S., Hu, Z., Cheng, Z., and Wu, J. (2004) Crystallization kinetics of thermosensitive colloids probed by transmission spectroscopy. *Langmuir*, **20**, 8858–8864.

29 Alsayed, A.M., Islam, M.F., Zhang, J., Collings, P.J., and Yodh, A.G. (2005) Premelting at defects within bulk colloidal crystals. *Science*, **309**, 1207–1210.

30 Meng, Z., Cho, J.K., Breedveld, V., and Lyon, L.A. (2009) Physical aging and phase behavior of multiresponsive microgel colloidal suspensions. *J. Phys. Chem. B*, **113**, 4590–4599.

31 Hertle, Y., Zeiser, M., Hasenöhrl, Ch., Busch, P., and Hellweg, Th. (2010) Responsive poly(NIPAM-co-NtBAM) microgels: Flory-Rehner description of the swelling behaviour. *Colloid Polym. Sci.*, **288**, 1047–1059.

32 Senff, H., Richtering, W., Norhausen, Ch., Weiss, A., and Ballauff, M. (1999) Rheology of a thermosensitive core-shell latex. *Langmuir*, **5**, 102–106.

33 Fuchs, M. and Ballauff, M. (2005) Flow curves of dense colloidal dispersions: schematic model analysis of the shear-dependent viscosity near the colloidal glass transition. *J. Chem. Phys.*, **122**, 094707.

34 Crassous, J.J., Siebenbürger, M., Ballauff, M., Drechsler, M., Henrich, O., and Fuchs, M. (2006) Thermosensitive core-shell particles as model systems for studying the flow behavior of concentrated colloidal dispersions. *J. Chem. Phys.*, **125**, 204906.

35 Crassous, J.J., Siebenbürger, M., Ballauff, M., Drechsler, M., Hajnal, D., Henrich, O., and Fuchs, M. (2008) Shear stresses of colloidal dispersions at the glass transition in equilibrium and in flow. *J. Chem. Phys.*, **128**, 204902.

36 Tan, B.H. and Tam, K.C. (2008) Review on the dynamics and micro-structure of pH-responsive nano-colloidal systems. *Adv. Colloid Interface Sci.*, **136**, 25–44.

37 Siebenbürger, M., Fuchs, M., Winter, H.H., and Ballauff, M. (2009) Viscoelasticity and shear flow of concentrated, noncrystallizing colloidal suspensions: Comparison with mode-coupling theory. *J. Rheol.*, **53**, 707–726.

38 Winter, H.H., Siebenbürger, M., Hajnal, D., Henrich, O., Fuchs, M.,

and Ballauff, M. (2009) An empirical constitutive law for concentrated colloidal suspensions in the approach of the glass transition. *Rheol. Acta*, **48**, 747–753.

39 Brader, J.M., Siebenbürger, M., Ballauff, M., Reinheimer, K., Wilhelm, M., Frey, S.J., Weysser, F., and Fuchs, M. (2010) Nonlinear response of dense colloidal suspensions under oscillatory shear: Mode-coupling theory and Fourier transform rheology experiments. *Phys. Rev. E*, **82**, 061401.

40 Stieger, M., Richtering, W., Pedersen, J.S., and Lindner, P. (2004) Small-angle neutron scattering study of structural changes in temperature sensitive microgels. *J. Phys. Chem.*, **120**, 6197–6206.

41 Eckert, Th. and Richtering, W. (2008) Thermodynamic and hydrodynamic interaction in concentrated microgel suspensions: Hard or soft sphere behaviour? *J. Chem. Phys.*, **129**, 124902.

42 Mohanty, P.S. and Richtering, W. (2008) Structural ordering and phase behavior of charged microgels. *J. Phys. Chem. B*, **112**, 14692–14697.

43 Nerapusri, V., Keddie, J.L., Vincent, B., and Bushnak, I.A. (2006) Swelling and deswelling of adsorbed microgel monolayers triggered by changes in temperature, pH, and electrolyte concentration. *Langmuir*, **22**, 5036–5041.

44 Tsuji, S. and Kawaguchi, H. (2005) Self-assembly of poly(N-isopropylacrylamide)-carrying microspheres into two-dimensional colloidal arrays. *Langmuir*, **21**, 2434–2437.

45 Schmidt, S., Hellweg, T., and von Klitzing, R. (2008) Packing density control in P(NIPAM-co-AAc) microgel monolayers: Effect of surface charge, pH, and preparation technique. *Langmuir*, **24**, 12595–12602.

46 Lu, Y. and Drechsler, M. (2009) Charge-induced self-assembly of 2-dimensional thermosensitive microgel particle patterns. *Langmuir*, **25**, 13100–13105.

47 Crassous, J.J., Ballauff, M., Drechsler, M., Schmidt, J., and Talmon, Y. (2006) Imaging the volume transition in thermosensitive core-shell particles by cryo-transmission electron microscopy. *Langmuir*, **22**, 2403–2406.

48 Crassous, J.J., Wittemann, A., Siebenbürger, M., Schrinner, M., Drechsler, M., and Ballauff, M. (2008) Direct imaging of temperature-sensitive core-shell latexes by cryogenic transmission electron microscopy. *Colloid Polym. Sci.*, **286**, 805–812.

49 Crassous, J.J., Rochette, C.N., Wittemann, A., Schrinner, M., Ballauff, M., and Drechsler, M. (2009) Quantitative analysis of polymer colloids by cryo-transmission electron microscopy. *Langmuir*, **25**, 7862–7871.

50 Dingenouts, N., Seelenmeyer, S., Deike, I., Rosenfeld, S., Ballauff, M., Lindner, P., and Narayanan, T. (2001) Analysis of thermosensitive core-shell colloids by small-angle neutron scattering including contrast variation. *Chem. Phys. Phys. Chem.*, **3**, 1169–1174.

51 Seelenmeyer, S., Deike, I., Rosenfeldt, S., Norhausen, Ch., Dingenouts, N., Ballauff, M., Narayanan, T., and Lindner, P. (2001) Small-angle X-ray and neutron scattering studies of the volume phase transition in thermosensitive core-shell colloids. *J. Chem. Phys.*, **114**, 10471.

52 Bolisetty, S., Hoffmann, M., Lekkala, S., Hellweg, Th., Ballauff, M., and Harnau, L. (2009) Coupling of rotation motion with shape fluctuations of core-shell microgels having tunable softness. *Macromolecules*, **42**, 1264–1269.

53 Lu, Y., Mei, Y., Drechsler, M., and Ballauff, M. (2006) Thermosensitive core-shell particles for Ag-nanoparticles: Modulating the catalytic activity by the volume transition in networks. *Angew. Chem. Int. Ed.*, **45**, 813–816.

54 Lu, Y., Mei, Y., Drechsler, M., and Ballauff, M. (2006) Thermosensitive core-shell particles as carrier systems for metallic nanoparticles. *J. Phys. Chem. B*, **110**, 3930–3937.

55 Mei, Y., Lu, Y., Polzer, F., Ballauff, M., and Drechsler, M. (2007) Catalytic activity of palladium nanoparticles encapsulated in spherical polyelectrolyte brushes and core-shell microgels. *Chem. Mater.*, **19**, 1062–1069.

56 Lu, Y., Proch, S., Schrinner, M., Drechsler, M., Kempe, R., and Ballauff, M. (2009) Thermosensitive core-shell microgel as a "nanoreactor" for catalytic active metal nanoparticles. *J Mater Chem.*, **19**, 3955–3961.

57 Welsch, N., Wittemann, A., and Ballauff, M. (2009) Enhanced activity of enzymes immobilized in thermoresponsive core-shell microgels. *J. Phys. Chem. B*, **113**, 16039–16045.

58 Li, Z., Kesselman, E., Talmon, Y., Hillmyer, M.A., and Lodge, T.P. (2004) Multicompartment micelles from ABC miktoarm stars in water. *Science*, **306**, 98–101.

59 Cui, H., Hodgon, T.K., Kaler, E.W., Abegauz, L., Danino, D., Lubovsky, M., Talmon, Y., and Pochan, D.J. (2007) Elucidating the assembled structure of amphiphiles in solution via cryogenic transmission electron microscopy. *Soft Matter*, **3**, 945–955.

60 Sceats, M.G. and Rice, S.A. (1982) *Water*, Vol. 7, Plenum Press, New York.

61 Sciortino, F., Poole, P.H., Essmann, U., and Stanley, H.E. (1997) Line of compressibility maxima in the phase diagram of supercooled water. *Phys. Rev. E*, **55**, 727–737.

62 Shibayama, M. (1998) Spatial inhomogeneity and dynamic fluctuations of polymer gels. *Macromol. Chem. Phys.*, **199**, 1–30.

63 Degiorgio, V., Piazza, R., Corti, M., and Stavans, J. (1991) Dynamic light scattering study of concentrated dispersions of anisotropic spherical colloids. *J. Chem. Soc. Faraday Trans.*, **87**, 431–434.

64 Schmitz, K.S. (1990) *An Introduction to Dynamic Light Scattering by Macromolecules*, Academic Press, London.

65 Fujii, S., Armes, S.P., Araki, T., and Ade, H. (2005) Direct imaging and spectroscopic characterization of stimulus-responsive microgels. *J. Am. Chem. Soc.*, **127**, 16808–16809.

66 Fujii, S., Dupin, D., Araki, T., Armes, S.P., and Ade, H. (2009) First direct imaging of electrolyte-induced deswelling behavior of pH-responsive microgels in aqueous media using scanning transmission x-ray microscopy. *Langmuir*, **25**, 2588–2592.

67 Ade, H. and Hitchcock, A.P. (2008) NEXAFS microscopy and resonant scattering: Composition and orientation probed in real and in reciprocal state. *Polymer*, **49**, 643–675.

68 Schneider, G., Guttmann, P., Heim, S., Rehbein, S., Mueller, F., Nagashima, K., Heymann, J.B., Muller, W.G., and McNally, J.G. (2010) Three-dimensional cellular ultrastructure resolved by X-ray microscopy. *Nat. Methods*, **7**, 985–987.

69 Onuki, A. (1993) Theory of phase transition in polymer gels. *Adv. Polym. Sci.*, **109**, 64–121.

70 Khokhlov, A.R., Starodubtzev, S.G., and Vasilevskaya, V.V. (1993) Conformal transitions in polymer gels: Theory and experiment. *Adv. Polym. Sci.*, **109**, 123–172.

71 Guinier, A. and Fournet, G. (1955) *Small Angle Scattering of X-Ray*, John Wiley & Sons, Inc., New York.

72 Higgins, J.S. and Benoit, H. (1994) *Polymers and Neutron Scattering, Oxford Series on Neutron Scattering*, Oxford University Press, New York, p. 436.

73 Pötschke, D. and Ballauff, M. (2002) Analysis of polymer latexes by small-angle X-ray scattering, in *Structure and Dynamics of Polymer and Colloidal Systems* (eds R. Borsali and R. Pecora), Kluwer Academic Publishers, Dordrecht.

74 Panyukow, S.V. and Rabin, Y. (1996) Statistical physics of polymer gels. *Phys. Rep.*, **269**, 1–131.

75 Pusey, P.N. and van Megen, W. (1986) Phase behaviour of concentrated suspensions of nearly hard colloidal spheres. *Nature*, **320**, 340–342.

76 Poon, W.C.K. and Pusey, P. (1991) Phase transitions of spherical colloids, in *Observation, Prediction and Simulation of Phase Transitions* (eds M. Baus, L.F. Rull, and J.P. Ryckaert), North-Holland, Amsterdam.

77 Pusey, P.N. (2008) Colloidal glasses. *J. Phys.: Condens. Matter*, **20**, 494202.

78 Senff, H. and Richtering, W. (1999) Temperature sensitive microgel suspensions: Colloidal phase behaviour and rheology of soft spheres. *J. Chem. Phys.*, **111**, 1705–1711.

79 Senff, H. and Richtering, W. (2000) Influence of cross-link density on rheological properties of temperature-sensitive microgel suspensions. *Colloid Polym. Sci.*, **278**, 830–840.

80 Stieger, M., Pedersen, J.S., Lindner, P., and Richtering, W. (2004) Are thermosensitive microgels model systems for concentrated suspensions? A rheology and small-angle neutron scattering study. *Langmuir*, **20**, 7283–7292.

81 Deike, I., Ballauff, M., Willenbacher, N., and Weiss, A. (2001) Rheology of thermosensitive latex particles including the high-frequency limit. *J. Rheol.*, **45**, 709–720.

82 Lumsdon, S.O., Kaler, E.W., and Velev, O.D. (2004) Two-dimensional crystallization of microspheres by a coplanar AC electric field. *Langmuir*, **20**, 2108.

83 Holtz, J.H.. and Asher, S.A. (1997) Polymerized colloidal crystal hydrogel films as intelligent chemical sensing materials. *Nature*, **389**, 829.

84 Miguez, H., Yang, S.M., Tetreault, N., and Ozin, G.A. (2002) Oriented free-standing three-dimensional silicon inverted colloidal photonic crystal microfiber. *Adv. Mater.*, **14**, 1805.

85 Dutta, J. and Hofmann, H. (2004) Self-organization of colloidal nanoparticles, in *Encyclopedia of Nanoscience and Nanotechnology*, American Scientific Publishers, Valencia, CA, Vol. 9, p. 617.

86 Debord, J.D. and Lyon, L.A. (2000) Thermoresponsive photonic crystals. *J. Phys. Chem. B*, **104**, 6327–6331.

87 Xu, S.Q., Zhang, J.G., Paquet, C., Lin, Y.K., and Kumacheva, E. (2003) From hybrid microgels to photonic crystals. *Adv. Funct. Mater.*, **13**, 468–472.

88 Pelton, R.H. and Chibante, P. (1986) Preparation of aqueous latices with N-isopropylacrylamide. *Colloids Surf.*, **20**, 247–256.

89 Tsuji, S. and Kawaguchi, H. (2005) Colored thin film prepared from hydrogel microspheres. *Langmuir*, **21**, 8439–8442.

90 Schmidt, S., Motschmann, H., Hellweg, Th., and von Klitzing, R. (2008) Thermoresponsive surfaces by spin-coating of PNIPAM-co-PAA microgels: A combined AFM and ellipsometry study. *Polymer*, **49**, 749–756.

91 Burmistrova, A. and von Klitzing, R. (2010) Control of number density and swelling/shrinking behavior of P (NIPAM-AAc) particles at solid surface. *J. Mater. Chem.*, **20**, 3502–3507.

92 Horecha, M., Senkovakyy, V., Synytska, A., Stamm, M., Chervanyov, A.I., and Kiriy, A. (2010) Ordered surface structures from PNIPAM-based loosely packed microgel particles. *Soft Matter*, **6**, 5980–5992.

93 Horecha, M., Senkovskyy, V., Schneider, K., Kiriy, A., and Stamm, M. (2011) Swelling bahavior of PNIPAM-polyisoprene core-shell microgels at surface. *Colloid Polym. Sci.*, **289**, 603–612.

94 Gliemann, H., Mei, Y., Ballauff, M., and Schimmel, Th. (2006) Adhesion of spherical polyelectrolyte brushes on mica: An in situ AFM investigation. *Langmuir*, **22**, 7254–7259.

95 Jaber, S., Karg, M., Morfa, A., and Mulvaney, P. (2011) 2D assembly of gold-PNIPAM core-shell nanocrystals. *Phys. Chem. Chem. Phys.*, **13**, 5576–5578.

96 Fuchs, M. (2010) Nonlinear rheological properties of dense colloidal dispersions close to a glass transition under steady shear. *Adv. Polym. Sci.*, **236**, 55–115.

97 Larson, R.G. (1999) *The Structure and Rheology of Complex Fluids*, Oxford University Press, New York.

98 Hendrickson, G.R., Smith, M.H., South, A.B., and Lyon, L.A. (2010) Design of multiresponsive hydrogel particles and assemblies. *Adv. Funct. Mater.*, **20**, 1697–1712.

99 Thorne, J.B., Vine, G.J., and Snowden, M.J. (2011) Microgel applications and commercial considerations. *Colloid Polym. Sci.*, **289**, 625–646.

100 Ho, K.M., Li, W.Y., Wong, C.H., and Li, P. (2010) Amphiphilic polymeric particles with core-shell structures: emulsion-based syntheses and potential applications. *Colloid Polym. Sci.*, **288**, 1503–1523.

101 Das, M., Zhang, H., and Kumacheva, E. (2006) Microgels: Old materials with new applications. *Annu. Rev. Mater. Res.*, **36**, 117–142.

102 Álvarez-Puebla, R.A., Contreras-Cáceres, R., Pastoriza-Santos, I., Pérez-Juste, J., and Liz-Marzán, L.M. (2009) Au-pNIPAM colloids as molecular traps for surface-enhanced, spectroscopic, ultra-sensitive analysis. *Angew. Chem. Int. Ed.*, **48**, 138–143.

103 Sánchez-Iglesias, A., Grzelczak, M., Rodríguez-González, B., Guardia-Girós, P., Pastoriza-Santos, I., Pérez-Juste, J., Prato, M., and Liz-Marzán, L.M. (2009) Synthesis of multifunctional composite microgels via in situ Ni growth on pNIPAM-coated Au nanoparticles. *ACS Nano*, **3**, 3184–3190.

104 Welsch, N., Ballauff, M., and Lu, Y. (2011) Microgels as nanoreactors: applications in catalysis. *Adv. Polym. Sci.*, **234**, 129–163.

105 Thomas, V., Namdeo, M., Murali Mohan, Y., Bajpai, S.K., and Bajpai, M. (2008) Review on polymer, hydrogel and microgel metal nanocomposites: a facile nanotechnological approach. *J. Macromol. Sci. A*, **45**, 107–119.

106 Zhang, J., Xu, S., and Kumacheva, E. (2004) Polymer microgels: Reactors for semiconductor, metal, and magnetic nanoparticles. *J. Am. Chem. Soc.*, **126**, 7908–7914.

107 Bhattacharya, S., Eckert, F., Boyko, V., and Pich, A. (2007) Temperature-, pH-, and magnetic-field-sensitive hybrid microgels. *Small*, **3**, 650–657.

108 Antonietti, M., Groehn, F., Hartmann, J., and Bronstein, L. (1997) Nonclassical shapes of noble-metal colloids by synthesis in microgel nanoreactors. *Angew. Chem. Int. Ed.*, **36**, 2080–2083.

109 Whilton, N.T., Berton, B., Bronstein, L., Henze, H., and Antonietti, M. (1999) Organized functionalization of mesoporous silica supports using prefabricated metal-polymer modules. *Adv. Mater.*, **11**, 1014–1018.

110 Kroll, E. and Winnik, F.M. (1996) In situ preparation of nanocrystalline γ-Fe_2O_3 in iron (II) cross-linked alginate gels. *Chem. Mater.*, **8**, 1594–1596.

111 Suzuki, D. and Kawaguchi, H. (2005) Gold nanoparticle localization at the core surface by using thermosensitive core–shell particles as a template. *Langmuir*, **21**, 12016–12024.

112 Khan, A., El-Toni, A.M., Alrokayan, S., Alsalhi, M., Alhoshan, M., and Aldwayyan, A.S. (2011) Microwave-assisted synthesis of silver nanoparticles using poly-N-isopropylacrylamide/acrylic acid microgel particles. *Colloids Surf. A*, **377**, 356–360.

113 Zhang, J., Xu, S., and Kumacheva, E. (2005) Photogeneration of fluorescent silver nanoclusters in polymer microgels. *Adv. Mater.*, **17**, 2336–2340.

114 Das, M., Sanson, N., Fava, D., and Kumacheva, E. (2007) Microgels loaded with gold nanorods: photothermally triggered volume transitions under physiological condictions. *Langmuir*, **23**, 196–201.

115 Wong, J.E., Gaharwar, A.K., Müller-Schulte, D., Bahadurand, D., and Richtering, W. (2008) Dual-stimuli responsive PNIPA microgel achieved via layer-by-layer assembly: Magnetic and thermoresponsive. *J. Colloid Interface Sci.*, **324**, 47–54.

116 Bradley, M. and Garcia-Risueno, B.S. (2011) Symmetric and saymmetric adsorption of pH-responsive gold nanoparticles onto microgel particles and dispersion characterisation. *J. Colloid Interface Sci.*, **355**, 321–327.

117 Feiler, A.A., Davies, P.T., and Vincent, B. (2011) Adsorption of anionic gold nanoparticles by a layer of cationic microgel particles deposited on a gold-coated, quartz surface: studied by quartz crystal microbalance and atomic force microscopy. *Soft Matter*, **7**, 6660–6670.

118 Karg, M., Pastoriza-Santos, I., Pérez-Juste, J., Hellweg, Th., and Liz-Marzán, L.M. (2007) Nanorod-coated

PNIPA microgels: Thermoresponsive optical properties. *Small*, **7**, 1222–1229.

119 Karg, M., Lu, Y., Carbó-Argibay, E., Pastoriza-Santos, I., Pérez-Juste, J., Liz-Marzán, L.M., and Hellweg, T. (2009) Multiresponsive hybrid colloids based on gold nanorods and poly(NIPAM-co-allylacetic acid) microgels: Temperature- and pH tunable plasmon resonance. *Langmuir*, **25**, 3163–3167.

120 Frattini, A., Pellegri, N., Nicastro, D., and de Sanctis, O. (2005) Effect of amine groups in the synthesis of Ag nanoparticles using aminosilanes. *Mater. Chem. Phys.*, **94**, 148–152.

121 Lu, Y., Yuan, J., Polzer, F., Drechsler, M., and Preussner, J. (2011) In-situ growth of catalytic active Au-Pt bimetallic nanorods in thermo-responsive core-shell microgels. *ACS Nano*, **4**, 7078–7086.

122 Suzuki, D. and Kawaguchi, H. (2006) Hybrid microgels with reversibly changeable multiple brilliant color. *Langmuir*, **22**, 3818–3822.

123 Das, M., Mordoukhovski, L., and Kumacheva, E. (2008) Sequestering gold nanorods by polymer microgels. *Adv. Mater.*, **20**, 2371–2375.

124 Contreras-Cácares, R., Sánchez-Iglesias, A., Karg, M., Pastoriza-Santos, I., Pérez- Juste, J., Pacifico, J., Hellweg, T., Fernández-Barbero, A., and Liz-Marzán, L.M. (2008) Encapsulation and growth of gold nanoparticles in thermoresponsive microgels. *Adv. Mater.*, **20**, 1666.

125 Álvarez-Puebla, R.A., Contreras-Cáceres, R., Pastoriza-Santos, I., Pérez-Juste, J., and Liz-Marzán, L.M. (2009) Au-pNIPAM colloids as molecular traps for surface-enhanced, spectroscopic, ultra-sensitive analysis. *Angew. Chem. Int. Ed.*, **48**, 138–143.

126 Carregal-Romero, S., Buurma, N.J., Pérez-Juste, J., Liz-Marzán, L.M., and Hervés, P. (2010) Catalysis by Au-pNIPAM nanocomposites: Effect of the cross-linking density. *Chem. Mater.*, **22**, 3051–3059.

127 Biffis, A. and Sperotto, E. (2003) Microgel-stabilized metal nanoclusters: Improved solid-state stability and catalytic activity in suzuki couplings. *Langmuir*, **19**, 9548–9550.

128 Biffis, A., Cunial, S., Spontoni, P., and Prati, L. (2007) Microgel-stabilized gold nanoclusters: Powerful "quasi-homogeneous" catalysts for the aerobic oxidation of alcohols in water. *J. Catal.*, **251**, 1–6.

129 Pradhan, N., Pal, A., and Pal, T. (2002) Silver nanoparticle catalyzed reduction of aromatic nitro compounds. *Colloids Surf. A*, **196**, 247–257.

130 Wunder., S., Polzer, F., Lu, Y., Yu, M., and Ballauff, M. (2010) Kinetic analysis of catalytic reduction of 4-nitrophenol by metallic nanoparticles immobilized in spherical polyelectrolyte brushes. *J. Phys. Chem. C*, **114**, 8814–8820.

131 Wunder, S., Lu, Y., Abrecht, M., and Ballauff, M. (2011) Catalytic activity of facetted gold nanoparticles studied by a model reaction: Evidence for substrate-induced surface restructuring. *ACS Catal.*, **1**, 908–916.

132 Hain, J., Schrinner, M., Lu, Y., and Pich, A. (2008) Design of multicomponent microgels by selective deposition of nanomaterials. *Small*, **4**, 2016–2024.

133 Wang, Y., Wei, G., Wen, F., Zhang, X., Zhang, W., and Shi, L. (2008) Synthesis of gold nanoparticles stabilized with poly (N-isopropylacrylamide)-co-poly(4-vinyl pyridine) colloid and their application in responsive catalysis. *J. Mol. Catal. A: Chem.*, **280**, 1–6.

134 Carregal-Romero, S., Pérez-Juste, J., Hervés, P., Liz-Marzán, L.M., and Mulvaney, P. (2010) Colloidal gold-catalyzed reduction of ferrocyanate (III) by borohydride ions: A model system for redox catalysis. *Langmuir*, **26**, 1271–1277.

135 Pelton, R. (2010) Poly(N-isopropylacrylamide) (PNIPAM) is never hydrophobic. *J. Colloid Interface Sci.*, **348**, 673–674.

136 Kawaguchi, H., Fujimoto, K., and Mizuhara, Y. (1992) Hydrogel microspheres III Temperature-dependent adsorption of proteins on poly-N-isopropylacryamide hydrogel

microspheres. *Colloid Polym. Sci.*, **270**, 53–57.

137 Elaïssari, A. and Bourrel, V. (2001) Thermosensitive magnetic latex particles for controlling protein adsorption and desorption. *J. Magn. Magn. Mater.*, **225**, 151–155.

138 Huber, D.L., Manginell, R.P., Samara, M.A., Kim, B.I., and Bunker, B.C. (2003) Programmed adsorption and release of proteins in a microfluidic device. *Science*, **301**, 352–354.

139 Alvarez-Lorenzo, C., and Concheiro, A. (2002) Reversible adsorption by a pH- and temperature-sensitive acrili hydrogel. *J. Controlled Release*, **80**, 247–257.

140 Lee, C.F., Lin, C.C., Chien, C.A., and Chiu, W.Y. (2008) Thermosensitive and control release bahavior of poly(N-isopropylacrylamide-co-acrylic acid)/ nano-Fe3O4 magnetic composite latex particle that is synthesized by a novel method. *Eur. Polym. J.*, **44**, 2768–2776.

141 Huo, D., Li, Y., Qian, Q., and Kobayashi, T. (2006) Temperature-pH sensitivity of bovine serum albumin protein-microgels based on cross-linked poly(N-isopropylacrylamide-co-acrylic acid). *Colloids Surf. B Biointerfaces*, **50**, 36–42.

142 Duracher, D., Veyret, R., Elaïssari, A., and Pichot, C. (2004) Adsorption of bovine serum albumin protein onto amino-containing thermosensitive core-shell latexes. *Polym. Int.*, **53**, 618–626.

143 Chen, X., Chen, S., and Wang, J. (2010) A pH-responsive poly(N-isopropylacrylamide-co-acrylic acid) hydrogel for the selective isolation of haemoglobin from human blood. *Analyst*, **135**, 1736–1741.

144 Hoare, T. and Pelton, R. (2006) Titrametric characterization of pH-induced phase transitions in functionalized microgels. *Langmuir*, **22**, 7342–7350.

145 Hoare, T. and Pelton, R. (2008) Impact of micro gel morphology on functionalized micro gel-drug interactions. *Langmuir*, **22**, 7342–7350.

146 Kim, J., Singh, N., and Lyon, L.A. (2007) Influence of ancillary binding and nonspecific adsorption on bioresponsive hydrogel microlenses. *Biomacromolecules*, **8**, 1157–1161.

147 Lindman, S. (2007) Systematic investigation of the adsorption of HAS N-isi-propylacrylamide/N-tert-butylacrylamide copolymer nanoparticles. Effects of particle size and hydrophobicity. *Nano Lett.*, **7**, 914–920.

148 Henzler, K., Haupt, B., Lauterbach, K., Wittemann, A., Borisov, O., and Ballauff, M. (2010) Adsorption of β-lactoglobulin on spherical polyelectrolyte brushes: Direct proof of counterion release by isothermal titration calorimetry. *J. Am. Chem. Soc.*, **132**, 3159–3163.

149 Wang, Q.G., Yang, Z.M., Wang, L., Ma, M.L., and Xu, B. (2007) D-Glucosamine-based supramolecular hydrogels to improve wound healing. *Chem. Commun.*, 1032–1034.

150 Huang, X., Yin, Y., Tang, Y., Bai, X., Zhang, Z., Xu, J., Liu, J., and Shen, J. (2009) Smart microgel catalyst with modulatory glutathione peroxidase activity. *Soft Matter*, **5**, 1905–1911.

151 Zaccone, A., Crassous, J.J., Béri, B., and Ballauff, M. (2011) Quantifying the reversible association of thermosensitive nanoparticles. *Phys. Rev. Lett.*, **107**, 168303-1–168303-4.

3
Core–Shell Particles with a Temperature-Sensitive Shell

Haruma Kawaguchi

3.1
Introduction

Core–shell particles are defined as particles with inner and outer phases (the core and shell, respectively) that are composed of different materials. These materials include polymers, ceramics, metals, and carbon. This chapter exclusively deals with core–shell particles with a temperature-sensitive shell. The temperature-sensitive polymers can comprise, for example, acrylamide derivatives, caprolactone, vinylalkyl ether, and cellulose derivatives. Because poly(*N*-isopropylacrylamide) (PNIPAM) is the most typical temperature-sensitive polymer [1, 2], the majority of particles described here include PNIPAM. There have been various applications of PNIPAM shell-carrying particles, such as drug carriers, micro-reactors, micro-sensors, adsorbents, and photonic devices [3–6].

When the PNIPAM shell is not crosslinked, and the particles are dispersed in water at a temperature lower than the lower critical solution temperature (LCST) of PNIPAM, PNIPAM chains extend into the aqueous phase owing to a high degree of hydration. Particles in this state, referred to as hairy particles, have sharper responsiveness to changes in environmental conditions than crosslinked shell particles and may find more applications [7, 8].

3.2
Preparation of Core–Shell Particles with a Temperature-Sensitive Shell

3.2.1
Spontaneous Formation of the Core–Shell Structure via Emulsion Polymerization and Soap-Free Emulsion Polymerization

Emulsion polymerization is a representative method for forming submicron-sized polymeric particles. Polymerization is carried out in an aqueous medium that can alleviate any problems resulting from heat of polymerization and viscosity evolution in the reaction system. When two or more monomers with different hydrophilicity

Hydrogel Micro and Nanoparticles, First Edition. Edited by L. Andrew Lyon and Michael Joseph Serpe.
© 2012 Wiley-VCH Verlag GmbH & Co. KGaA. Published 2012 by Wiley-VCH Verlag GmbH & Co. KGaA.

are used for emulsion copolymerization, the resulting particles are apt to have a radial gradient of polymer composition. In general, more hydrophilic monomer units preferentially localize on the outside and more hydrophobic monomer units on the inside [9, 10]. Sometimes even core–shell particles are obtained.

In general emulsion polymerization, emulsifiers contribute to efficient formation of particles and stabilization of latex (dispersion of polymer particles); however, emulsifiers have serious drawbacks. Emulsifiers are regarded as an undesirable contaminant in the latex and weaken the water resistance of the latex film. To overcome these drawbacks, soap-free emulsion polymerization has been developed. Particles are generated via homogeneous nucleation from a soap-free aqueous medium [11, 12]. The resulting particles are stabilized by charged groups at the polymer chain ends that originate from initiator fragments, although sometimes the stability might be insufficient. In such cases, several hydrophilic co-monomers such as acrylamide, vinyl pyridine, and acrylic acid have been used to increase the stability of particles [13–16]. The polymerization kinetics of soap-free emulsion copolymerization of hydrophobic and hydrophilic monomers using a water-soluble initiator is controlled by the monomer reactivity and solubility of the two monomers in water. The morphology of the resulting particle is generally a core–shell-type – that is, the particles have a shell rich in hydrophilic monomer units and a core rich in hydrophobic monomer units. In the soap-free emulsion copolymerization of styrene and acrylamide, for example, the latter polymerizes preferentially during the beginning stage of polymerization, and the resulting acrylamide-abundant hydrophilic polymer chains preferentially localize at the particle surface. This is also the case when styrene and acrylamide derivatives, for example, acryloylpyrrolidone (APr), are copolymerized in an emulsifier-free aqueous medium (Figure 3.1) [17–19].

The latex of poly-APr shell–polystyrene core particles exhibits temperature-sensitive stability. The copolymer particle dispersion is stable at temperatures below

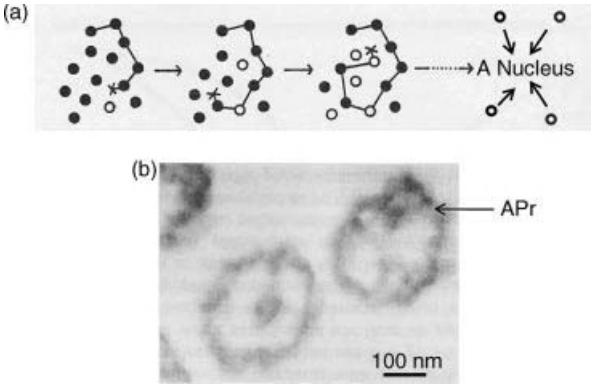

Figure 3.1 Mechanism of particle formation (a) and TEM of thin section of polystyrene core–PAPr shell particles (b). Filled circles: APr monomer; open circles: styrene monomer; cross: radical. Polymerization recipe: styrene/APr/water/V50 (initiator) = 24/6/180/0.5 (g). Polymerization was carried out at 60 °C under nitrogen for 24 h.

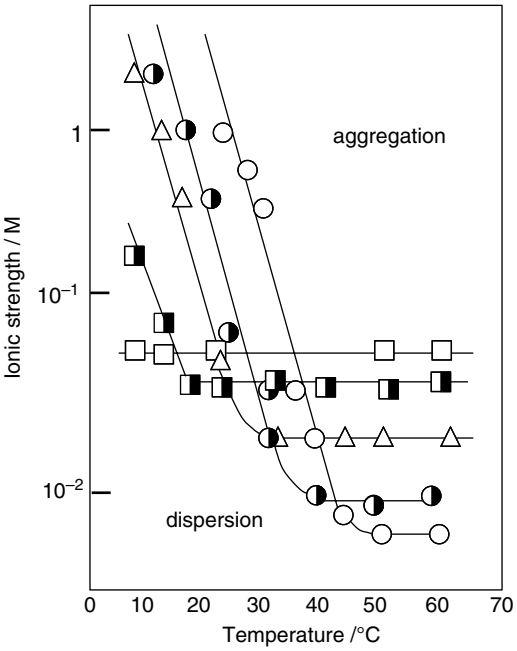

Figure 3.2 Boundary between dispersion and aggregation of latex in terms of temperature and ionic strength APr/APp. Open circles: 4/0, half-filled circle: 3/1, open triangles: 2/2, half-filled squares: 1/3, open squares: 0/4. Polymerization recipe: styrene/(APr + APp)/water/V50 = 26/4/180/0.50 (g). Polymerization was carried out at 60 °C under nitrogen for 24 h.

55 °C and at ionic strength 0.01, but it loses this stable state and is aggregated by increasing temperature and/or salt concentration. The boundary conditions for stable dispersion and aggregate formation are presented in Figure 3.2. The temperature effect on dispersion stability can be explained by the transition of poly-*N*-acryloylpyrrolidine (PAPr). The PAPr shell layer maintains a swollen state below PAPr's transition temperature of 55 °C. This swollen shell makes the dispersion stable due to a steric stabilization effect. However, the PAPr shell shrinks above 55 °C and loses its steric stabilization force. The salt concentration effect on dispersion stability can be explained by the ionic strength contribution. An increase in ionic strength causes loss of the electrorepulsive force between particles and brings about aggregation above a critical salt concentration [20]. A series of particles with an APr/APp (acryloylpiperidine) copolymer shell with different APr/APp ratios displays varied dispersion stability, as shown by the dotted lines in Figure 3.2, because the transition temperature of APp is about 5 °C and the transition temperature of the copolymer shell shifts according to the composition of shell – that is, the APr/APp ratio. Temperature-sensitive aggregation of PNIPAM shell-carrying particles is still an attractive research subject that leads to practical applications [21, 22].

3.2.2
Formation of a Temperature-Sensitive Shell by Seeded Polymerization

"Seeded polymerization" is defined as polymerization that is carried out within the dispersion of particles [23]. The existing particles are used as a seed – that is, the particles absorb monomers and allow *in situ* polymerization. If the monomer is less hydrophobic than the seed particle, the resulting polymers are apt to localize at the outermost phase of the seed particles and, as a result, core–shell particles are formed. To ensure efficient shell construction, seed particles with a pre-adjusted structure are used that include a small amount of monomer units for the seeded polymerization. This process accelerates the absorption of monomers during the seeded polymerization and suppresses the formation of new particles. For the copolymerization of polystyrene (PS) and PNIPAM, for example, a second shot of NIPAM was added after soap-free emulsion copolymerization of styrene with a small amount of NIPAM, with the aim of forming polystyrene core–PNIPAM shell particles efficiently [22].

3.3
Preparation of Hairy Particles with Temperature-Sensitive Hair

As defined in the previous section, hairy particles refer to particles with linear polymer chains extending from the surface to the medium. Methods that have been used to prepare hairy particles are presented in Figure 3.3. In Figure 3.3a1, an amphiphilic block copolymer is prepared by solution polymerization, usually by living radical polymerization in which two monomers are added sequentially to a

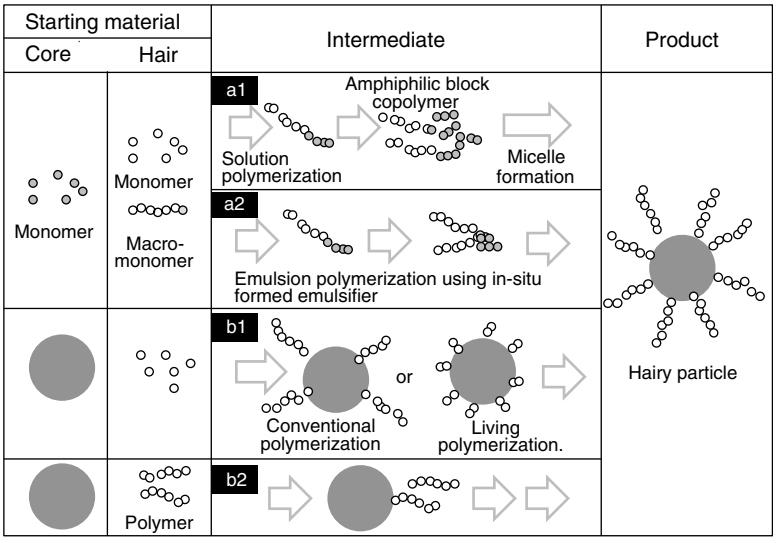

Figure 3.3 Methods to prepare hairy particles.

polymerization vessel. The block copolymer molecules are then assembled to form micelles, and the hydrophobic interior of the micelles is crosslinked if necessary [24].

On the other hand, the method in Figure 3.3a2 relies on the *in situ* formation of surface active material during the polymerization [25]. In a mixture of hydrophilic and hydrophobic monomers in an aqueous medium, the former preferentially polymerizes; however, the gradual elongation of chains and the occasional incorporation of more hydrophobic monomers into the growing chain results in the formation of amphiphilic molecules. These then assemble to give particle nuclei. After that, the polymerization proceeds in a manner similar to general emulsion polymerization.

Figure 3.3b1 and b2 show grafting-from and grafting-to methods, respectively, and are discussed further below.

3.3.1
Hairy Particle Formation from Block Copolymer Micelles (Figure 3.3a1)

The development of living radical polymerization enabled the formation of block copolymers with well-defined structure. The chain length of each block can be uniform and easily regulated. After the preparation of such block copolymers, the copolymers are exposed to different conditions in terms of temperature, pH, and solvent, after which they assemble and form micelles [24, 26]. Crosslinking is necessary to prevent re-dissolution in general. When the inner phase of the micelle is crosslinked, hairy particles are formed.

For example, PNIPAM-block-poly(glycerol methacrylate) (PGLM) was prepared by sequential living radical polymerization starting from the polymerization of GLM. In this study, an "iniferter" was used as a living radical species instead of a nitroso group, ATRP species, or RAFT reagent. The iniferter was invented by Otsu [27]; its name comes from its performance as an initiator, transfer reagent, and terminator, The molecular equation of the iniferter, *N,N*-diethyldithiocarbamate acetic acid (DCAA), used in this study and its reaction is presented in Scheme 3.1.

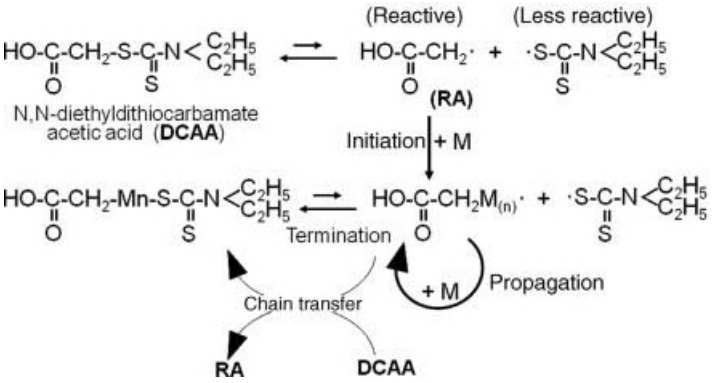

Scheme 3.1 Living radical polymerization using DCAA.

Inversion of the order of polymerization of the two monomers resulted in a failure of block copolymer formation. Amide group-carrying radical seems to be inactive to GLM monomer. An increase in temperature of the aqueous solution of the block copolymer generated micelles with a PNIPAM core–PGLM hair because PNIPAM collapses above its LCST, whereas PGLM retains its high affinity with water even at such a temperature [28]. PNIPAM-block-poly(ethylene-oxide) (PEO) forms hairy particles by the same methodology [29, 30]. A physical stimulus other than temperature must be applied in order to prepare PGLM core–PNIPAM shell micelles. This stimulus is solvent exchange; for example, the target micelles were obtained by adding tetrahydrofuran to a methanol solution of block copolymer. In the case of PEO-block-poly(4-vinylpyridinium cation), SO_4^- ion was used as an assembler for the polymer to form a PEO hair–poly(vinylpyridinium salt) core [31].

3.3.2
Hairy Particle Formation Through *In Situ* Formation of Surface Active Material (Figure 3.3a2)

The mechanism of this method is illustrated in Figure 3.4 [32]. Although it has not been used for the preparation of PNIPAM hair particles, it is an interesting method for preparing smart particles with sharp temperature sensitivity.

3.3.3
Hairy Particle Formation Through Hair Growth on Core Particles (Figure 3.3b1)

This methodology has been used by many researchers. Some researchers have prepared sparsely haired particles, while others have made densely haired particles referred to as brush particles. The core particles can be rigid particles or soft microgels.

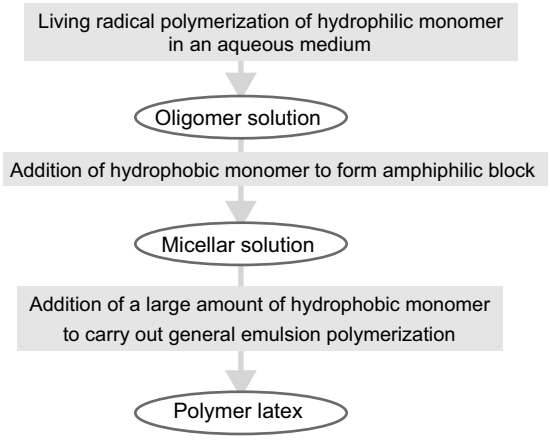
Living radical polymerization of hydrophilic monomer in an aqueous medium
Oligomer solution
Addition of hydrophobic monomer to form amphiphilic block
Micellar solution
Addition of a large amount of hydrophobic monomer to carry out general emulsion polymerization
Polymer latex

Figure 3.4 Modified emulsifier-free emulsion polymerization [32].

3.3.3.1 Hairy Particle Formation Through Hair Growth on Rigid Core Particles

Surface graft polymerization is the most effective method of preparing hairy particles. In this case, initiation of polymerization starts from active or activated sites on the surface of core particles. For example, after the preparation of core particles with OH groups on their surface, the ceric ion can be charged into the dispersion of core particles in order to initiate polymerization via a redox initiation system [33].

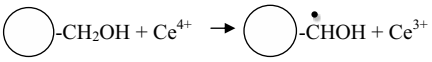

(3.1)

This polymerization using ceric ions results in the formation of particles whose surface is covered with a number of linear grafted chains. If the grafted chains have high affinity with water, they extend into the water phase and sway in water. Hairy particles are thus obtained. The number of hairs on the particles increases but the degree of polymerization of each chain, once it is formed, remains unchanged during the course of polymerization. In this system, the chain length – that is, the degree of polymerization – has broad distribution.

Another type of surface grafting polymerization relies on a living radical mechanism. The products have hairs with a narrow distribution of chain length, whereas the number of chains remains unchanged throughout the polymerization. The narrow distribution of hair chain length results because the chains grow at the same pace. The difference between conventional and living radical polymerizations can be clearly seen when two kinds of monomers are grafted sequentially. As shown in Figure 3.5, the former polymerization gives two kinds of polymer hairs with a broad chain length distribution. In contrast, the latter polymerization gives block copolymer hairs with a narrow distribution of hair length.

A hairy particle with double transition temperatures has been prepared by two-step living radical graft polymerization [34]. The hair was composed of a block copolymer in which one block was PNIPAM and the other was poly(NIPAM

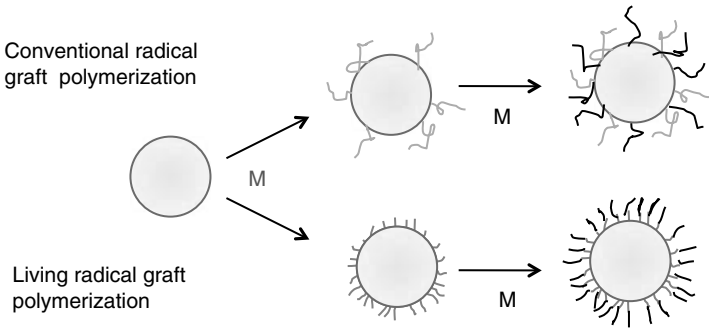

Figure 3.5 Two types of graft polymerizations and the structure of resulting hairy particles.

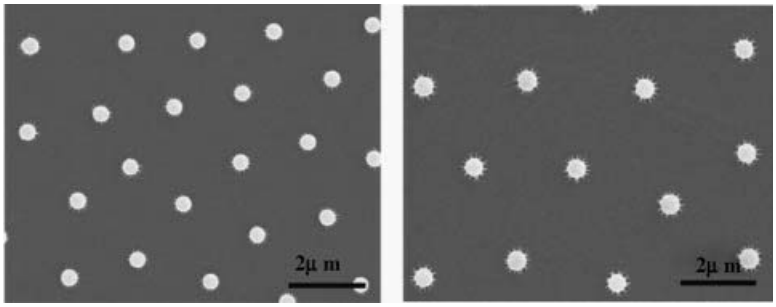

Figure 3.6 Arrays of hairy particles with hairs of different lengths on a substrate. Core particle preparation: styrene/VBC/KPS/water = 2.85/0.15/0.10/70 (g). Polymerization at 70 °C under nitrogen for 24 h. DCAA immobilization: particle/DCAA/water = 2/0.74/80 (g). Reaction proceeded under mild stirring. Hairy particle preparation: DCAA particle/NIPAM/water = 0.5/2.0/200 (g). Polymerization was started by UV irradiation.

(99%)-*co*-methacrylic acid(1%)). The transition temperature of the latter is about 38 °C, which is 6 degrees higher than that of PNIPAM, and the plot of hydrodynamic diameter versus temperature described a two-step curve.

The extent of hair growth can be estimated by determining the chain length. The chain length determination should be done for chains that are cut at the base of the chain on the particle surface. Separating the chain from the particle is not easy because cutting the chain at the base is difficult. Fukuda and coworkers have shown that the hairy polymer obtained by graft polymerization and the free polymer obtained by solution polymerization using the same initiating species are expected to have similar weights and polydispersity in controlled living radical polymerization [35, 36].

The relation between the [hydrodynamic diameter (d_h) of the hairy particle) – (d_h of core particle)]/2, which corresponds to the thickness of the hair layer, and the expected molecular weight of the hair polymer is linear, as shown in Figure 3.6. Quantitative analysis has revealed that the thickness of the hair layer (e.g., 160 nm for a hair polymer of MW 500 000) is much shorter than the length of the fully extended chain (ca. 800 nm for a polymer of MW 500 000), but only slightly longer than the end-to-end distance of a randomly coiled chain (ca. 100 nm) [37]. According to this result, each hair chain seems to have little restriction from neighboring chains. This is reasonable judging from the graft density on the particle surface, 0.0235 chain nm^{-2}. In the case of brush particles, the hydrodynamic thickness is close to the extended chain length [38]. As shown in Figure 3.6, the hairy particles form a two-dimensional colloidal crystal in which the particles make an array that keeps a constant inter-particle distance when samples for electron microscopy are prepared at room temperature. This distance is discussed with reference to the thickness of the hair layer in Section 4.2.

3.3.3.2 Hairy Particle Formation Through Hair Growth on Microgels

A carboxymethylcellulose (CMC) microgel has been used as a core particle for PNIPAM hair-carrying composite microgel formation. An aqueous solution of CMC

was titrated with an aqueous solution of dodecyl-trimethylammonium bromide (DTAB) until the solution became turbid, because turbidity is the sign of micro-aggregate formation [39, 40]. The aggregation occurred via electrostatic interactions between anionic CMC and the cationic micelle. Other cationic materials can be used as aggregating reagents. Multi-valence metal ions, such as Fe^{2+} and Fe^{3+}, can also contribute to aggregation. For example, incubation of an aqueous solution of CMC after Fe^{2+} and Fe^{3+} addition, followed by pH elevation of the solution, resulted in the formation of a magnetite nanoparticle-containing CMC microgel. A typical recipe for magnetite/CMC composite microgel formation is: 1.0 wt% CMC solution/0.02 M $FeCl_2 \cdot 4H_2O$/0.02 M $FeCl_3 \cdot 6H_2O$/1.0 M NaOH/water = 7.5 g/1.6 ml/2.3 ml/1.25 ml/17.35 g [40].

In this procedure, ferric and ferrous ions served as an aggregate reagent to form CMC aggregates embedded with ferric/ferrous ions. Incubation in an alkaline solution was necessary to convert the ferric/ferrous ions to magnetite nanoparticles via *in situ* oxidation [39]. In this case, the sizes of the magnetite nanoparticle and microgel were about 5–10 nm and 50–100 nm, respectively. Chitosan, a cationic polymer, has also been used successfully for the formation of a chitosan–CMC composite microgel.

The micro-aggregate was crosslinked using divinyl sulfone (DVS). The CMC microgel thus obtained exhibited pH-sensitive swelling/shrinking behavior. To give temperature sensitivity to this pH-sensitive CMC microgel, incorporation of PNIPAM into the CMC microgel was attempted by the two following methods:

1) graft polymerization of NIPAM from a CMC microgel using the ceric ion redox system;
2) grafting of amine-terminated PNIPAM to a CMC microgel.

Method (1), a grafting-from method, is discussed in this section, whereas method (2), a grafting-to method, will be described in the next section.

3.3.3.3 Graft Polymerization of NIPAM from a CMC Microgel Using the Ceric Ion Redox System

In this method, graft polymerization took place via redox initiation when the ceric ion was added to the solution of CMC and NIPAM at 40 °C:

$$\text{Cellulose-CHOH} + Ce^{4+} \rightarrow -\dot{C}OH + H^+ + Ce^{3+}$$

However, there was a serious drawback with the resulting CMC–PNIPAM composite microgel, which lost pH sensitivity. This problem was observed at the beginning of graft polymerization. The CMC micogel shrank immediately when the ceric ion was introduced into the CMC microgel dispersion because of an ionic interaction between the carboxyl group of CMC and a ceric ion, as shown in Figure 3.7. The hydrodynamic diameter began to increase soon after the graft polymerization of NIPAM began. Successful graft polymerization of NIPAM was confirmed by an apparent increase in hydrodynamic size. The CMC–PNIPAM composite microgel was swollen at room temperature and showed a volume phase

transition around 32 °C, above which the composite microgel shrank. However, the microgel did not show pH sensitivity and the hydrodynamic diameter did not change from pH 3 to pH 9. Transmission electron microscopy (TEM) views (not shown) of the microgel before and after its contact with ceric ion suggested a reason for the insensitivity of the CMC-*g*-PNIPAM microgel. The TEM image of the original microgel was thin due to high electron transparency, whereas that of the microgel treated with ceric ion was thicker and smaller than the former. This indicates that the microgel held a significant amount of heavy metal ions and was shrunken. This condition did not change even after continual dialysis of the microgel dispersion. Strong binding of ceric ion to CMC resulted in loss of the weakly acidic property of the carboxyl groups in CMC. This was the reason why the CMC–PNIPAM microgel exhibited no pH sensitivity. These results led us to the conclusion that ceric ion quickly permeates in the CMC microgel, strongly blocks COO^- ion, and makes the microgel shrink. Therefore, it would be reasonable to conclude that graft polymerization of NIPAM must take place only at the surface of the shrunken microgel to produce a PNIPAM hair–CMC core microgel. The two scanning electron microscopy (SEM) views in Figure 3.7 show the CMC microgel (left) and the PNIPAM hair–CMC core microgel (right). The latter seems spherical with some height, but the former looks flattened. The latter is smaller than the former, although the hydrodynamic diameter of the latter (820 nm) is larger than that of the former (650 nm). These

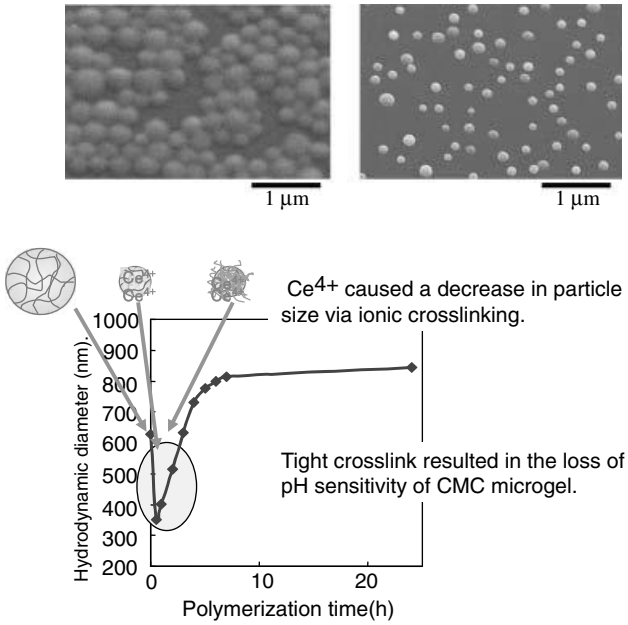

Figure 3.7 PNIPAM hair growth from CMC microgel initiated by CMC-CH_2OH/Ce^{4+} redox system. CMC microgel formation: CMC/DTAB/water=0.25/0.23/200 (g). PNIPAM-grafted CMC microgel formation: CMC microgel/NIPAM/$Ce(NH_4)_2(NO_3)$/buffer solution (pH 2.8) = 0.01/1.03/0.02/14 (g).

results are explained by the invisible PNIPAM hairy layer, which exists in the space between the CMC core microgels.

3.3.4
Hairy Particle Formation Through the Attachment of Hydrophilic Polymer Chains to the Surface of Core Particles (Grafting-to Method, Figure 3.3b2)

In the "grafting-to" method, hair-forming polymer chains and core particles are made in advance, and the chains are attached to the particle at their chain ends. To illustrate this, in this section we describe an example in which the core particle was a microgel. The polymer chain used was amine-terminated PNIPAM and the core was a CMC microgel.

The product described in the previous section had no pH-dependence, despite being composed of CMC. Thus, the challenge was to construct a pH- and temperature-sensitive microgel from the CMC microgel. The next method examined was the so-called "grafting-to" technique, which involved a coupling reaction between an amino end group-carrying PNIPAM molecule and the carboxyl group of CMC. The first step in this method was the preparation of amino end group-carrying PNIPAM. The following reactions were carried out at room temperature [41]:

$$K_2S_2O_8 + 2Cl^-NH_3{}^+-CH_2-CH_2-SH(AET) \rightarrow 2KHSO_4 + 2Cl^-NH_3{}^+ -CH_2-CH_2-S\bullet \quad (3.2)$$

$$Cl^-NH_3{}^+-CH_2-CH_2-S\bullet + M \rightarrow Cl^-NH^{3+}-CH_2-CH_2-S-M\bullet \quad (3.3)$$

$$Cl^-NH_3{}^+-CH_2-CH_2-S-M\bullet + M \rightarrow \rightarrow \rightarrow Cl^-NH_3{}^+-CH_2-CH_2-S-PNIPAM\bullet \quad (3.4)$$

Here, AET (aminoethanethiol-hydrofloride) contributed a component of the redox system, a chain transfer reagent, and an amino group supplier. The product of reaction (3.4) would suffer a termination or chain transfer reaction, and would give rise to amino end group-carrying PNIPAM that should have one or two amino group(s) at the chain end(s). These reactions took place at room temperature; therefore, the following reaction, which forms PNIPAM with no amino chain end, was negligible.

$$K_2S_2O_8 \rightarrow 2\,K^+ + 2^-SO_4\bullet \quad {}^-SO_4\bullet + M \rightarrow {}^-SO_4M\bullet \quad (3.5)$$

The reaction was carried out at different concentrations of AET. The molecular weight of PNIPAM was inversely proportional to the concentration of AET (data not shown), showing the typical performance of a chain transfer reagent.

The amino end group-carrying PNIPAM molecule was then attached to the carboxyl group of CMC by the aid of a coupling reagent, 1-(3-(dimethylamino) propyl)- 3-ethyl-carbodiimide (EDC). The progress of the "grafting-to" reaction was confirmed by measuring the hydrodynamic size and electrophoretic mobility of the microgels before and after the reaction. The results are shown in Table 3.1.

Table 3.1 Physical properties of core particle and core–shell particle.

	Hydrodynamic diameter (nm)[a)]	Electrophoretic mobility ($\mu m\, s^{-1}\, cm^{-1}\, V^{-1}$)
CMC core	614	−4.4
CMC core–PNIPAM shell	680	−0.8

a) At 25 °C, pH was not adjusted.

The hydrodynamic diameter and electrophoretic mobility of the CMC core–PNIPAM shell microgel as compared with the CMC core microgel changed significantly when the reaction was carried out in the presence of coupling reagent, whereas neither property changed when the system contained no coupling reagent (data is not shown) – in other words, the increase in hydrodynamic diameter of the CMC core–PNIPAM shell microgel indicated attachment of the PNIPAM hair to the CMC microgel, and the decrease in electrophoretic mobility indicated masking of the anionic character of CMC by the bulky PNIPAM hairy layer. Fourier transform infrared (FTIR) measurements also supported formation of the expected structure (not shown). It is reasonable to suppose that only the surface carboxyl groups of CMC react with the PNIPAM chain because bulky PNIPAM chains hardly diffuse into the inside of the microgel; thus, the original property of the carboxyl groups in the CMC microgel should be maintained. As expected, CMC-*g*-PNIPAM exhibited pH sensitivity, as well as temperature sensitivity (Figure 3.8). It would be worth mentioning

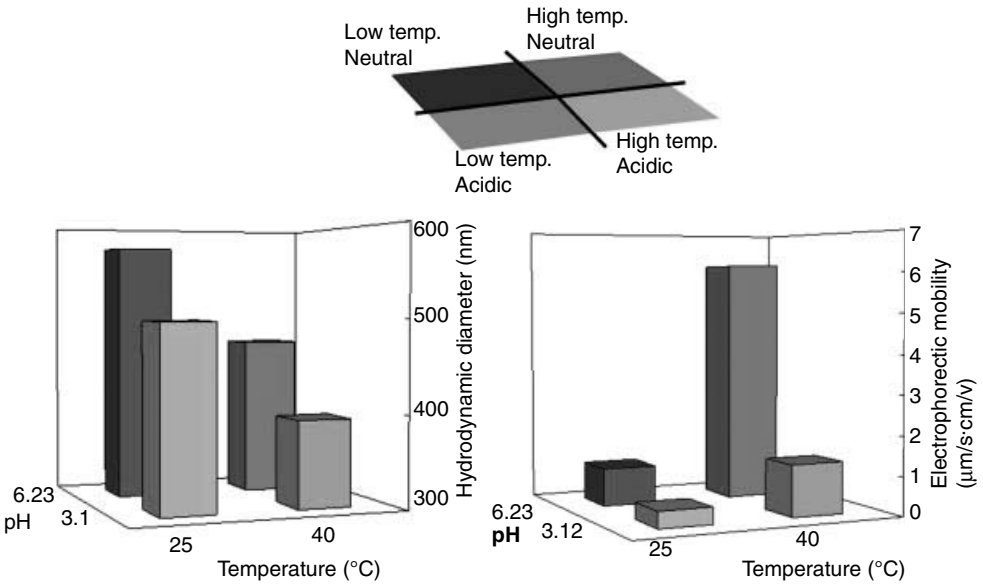

Figure 3.8 Temperature- and pH-dependence of hydrodynamic diameter and electrophoretic mobility (EPM) of CMC core–PNIPAM shell microgel.

that, as can be supposed from the above-mentioned facts, ceric ion is effective for the assembly of CMC molecules from aqueous solution.

Another example of the grafting-to method is a temperature-sensitive bioreactor hair particle [42, 43]. Two kinds of hairs have been grafted to the particle. One is trypsin-carrying PNIPAM hair and the other is free-end PNIPAM hair. The two kinds of hairs have a different transition temperatures, 38 °C and 31 °C, respectively. Above 31 °C, the enzyme is exposed in the aqueous phase because the free-end PNIPAM shrinks. This promotes the encounter of enzyme and substrate and increases the reaction rate.

3.4
Properties, Functions and Applications of Core–Shell Particles with a Temperature-Sensitive Shell

3.4.1
Volume Phase Transition of the Temperature-Sensitive Shell and Accompanying Changes in Physical Properties of the Particles

As expected, temperature-sensitive shell-carrying particles respond to temperature change. The particle size or thickness of the shell changes discontinuously around the volume phase transition temperature (VPTT), which is close to the LCST of the polymer. An example is shown in Figure 3.9. Detailed examination of the temperature-sensitive phase of the particle revealed that, in the temperature range just below the VPTT, clustering of the temperature-sensitive polymer chains takes place, although a significant change in hydrodynamic size is not observed [44]. The shape of the plot of hydrodynamic size versus temperature changes as follows:

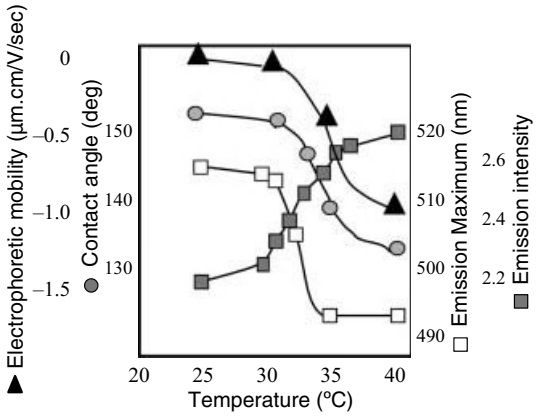

Figure 3.9 Temperature dependence of various properties of PNIPAM microgel. Filled triangles: electrophoretic mobility; filled circles: contact angle; open squares: emission maximum wavelength of ANS; gray squares: emission intensity.

the transition temperature becomes obscure but seems to shift to a higher temperature when a hydrophilic co-monomer is incorporated in the temperature-sensitive polymer preparation [45]. Jones and Lyon reported that core–shell particles in which both core and shell are temperature-sensitive, modification of the PNIPAM phase with acrylic acid influenced the temperature sensitivity of not only the modified phase but also the unmodified one [46].

Not only hydrodynamic size but other physical properties change discontinuously with temperature. Electrophoretic mobility is very small at a temperature lower than the LCST because the charged groups on the temperature-sensitive chains are buried inside the swollen shell and do not affect the surface charge. The surface of the shell – that is, the interface between the polymer and aqueous phase – is not clear for the gel or hairs. Therefore, no zeta potential is identified [47]. At a temperature higher than the LCST, the absolute value of electrophoretic mobility becomes significantly large because most of the charged groups condense near the surface and contribute to the potential. The hydrophilicity/hydrophobicity of the shell of particles can be estimated by using a fluorescent dye. For example, the fluorescence of ANS (8-anilino-1-naphthalenesulfonic acid magnesium(II) salt) reflects the hydrophilicity/hydrophobicity of the microenvironment surrounding the ANS molecules. When ANS was added to PNIPAM hairy particles, the ANS molecules migrated to and remained near the PNIPAM phase because of its hydrophobic nature. The peak of the fluorescence spectrum shifts from 520 to 460 nm when the temperature of dispersion changes from 25 to 45 °C [48, 49]. Among several organic solvents, acetone shows strong fluorescence at 460 nm; therefore, the microenvironment of shrunken PNIPAM is estimated to have almost the same degree of hydrophilicity/hydrophobicity as acetone.

Protein adsorption is another characteristic event for temperature-sensitive hairy particles [50, 51]. The amount of adsorption increases gradually, but not discontinuously, with increasing temperature [52]. This behavior is explained by the gradual increase in the hydrophobicity of the surface with temperature. The adsorption is reversible if the experiment is done in a short time and the protein is not strongly hydrophobic.

3.4.2
Two-Dimensional Assembly of Hairy Particles and Optical Properties

PNIPAM hairy particles can self-assemble into two-dimensional colloidal crystals when the dispersion is poured on a substrate and dried at a temperature below the LCST of PNIPAM [48]. The effect of the dispersion concentration on self-assembly has been studied. Three dispersions with different concentrations of hairy particles were prepared and dropped on a shale. The patterns observed after drying are presented in Figure 3.10. A dispersion with a high concentration of hairy particles gave a spot of dull color, a dispersion with a moderate concentration of particles gave a circle of brilliant structural color, whereas a dispersion with a low concentration of particles gave a partially colored circle. The last dispersion was the result of a lack of particles, which made it impossible to form a complete circle of structural color.

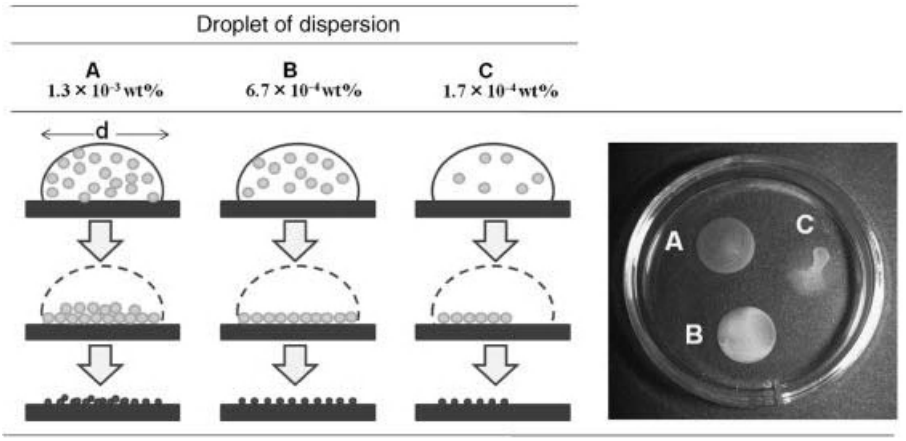

Figure 3.10 Two-dimensional array formation from dried droplet of microgel dispersion.

The partial structural color development is evidence of the self-assembly of particles. The structural color area is made as wide as possible by self-assembly during medium evaporation.

3.4.3
Other 2D Assembly – Temperature-Sensitive Pickering Emulsion by PNIPAM Hairy Particles

Li and Ngai used a polystyrene core–PNIPAM shell particle to form a porous membrane through a Pickering emulsion [53]. PNIPAM seems to be able to stabilize a oil/water interface if the couple has a suitable value of work of adhesion (W_a):

$$W_a = \gamma_{oa} + \gamma_{aw} - \gamma_{ow} \tag{3.6}$$

where γ_{oa} is tension at the air/oil interface, γ_{aw} is tension at the air/water interface, and γ_{ow} is tension at the oil/water interface. If W_a is small, the oil/water interface is incapable of retaining the particles and, if W_a is large, the oil/water interface rejects permeation of the particles [54].

Not only polystyrene core–PNIPAM shell particles but also PNIPAM hairy particles have excellent ability to form a Pickering emulsion. Moreover, the Pickering emulsion made by PNIPAM particles exhibits temperature-induced inversion from oil/water to water/oil states when a selected solvent is used that has W_a=60–65 mJ m^{-2} [55].

3.4.4
Fluorescence Resonance Energy Transfer (FRET) Particles Tuned by Temperature

Core–shell particles with controllable thickness will find special applications as a sensing tool. A novel core–shell particle with a shell composed of PNIPAM molecules

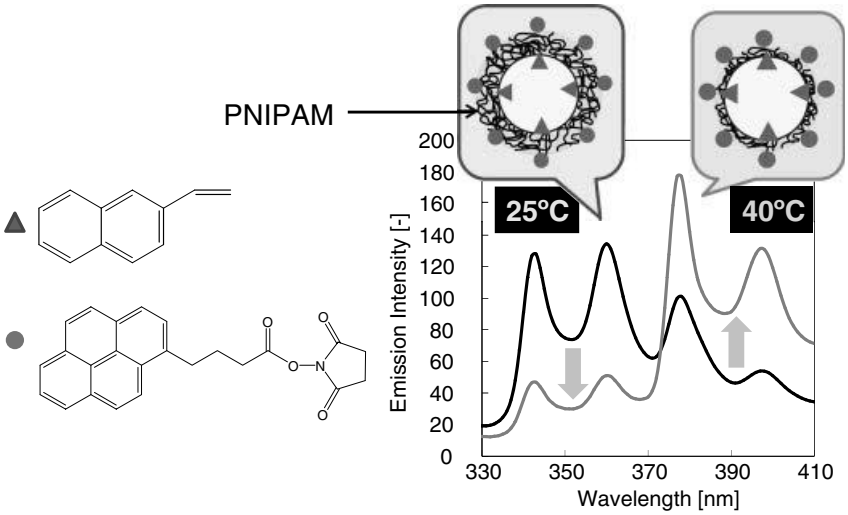

Figure 3.11 Temperature-sensitive FRET particle. Shell is composed of PNIPAM. Thickness of swollen shell <50 nm. Excitation 250 nm.

with a 10 nm thickness that is sandwiched by a donor and an acceptor has been created [56]. The thickness of 10 nm is crucial as it is sufficient to prevent fluorescence energy transfer (FRET) between the donor and the acceptor [57]. The PNIPAM shell maintains this thickness under its transition temperature. However, the shell shrinks above the transition temperature and allows FRET. In other words, this core–shell particle is a temperature-tunable FRET particle.

The donor and acceptor used in this study were vinyl naphthalene (VN) and 1-pyrenebutyric acid *N*-hydroxysuccinimide ester (PBHS), respectively. The fluorescent wave range of VN overlaps with the excitation wave range of PBHS. The shell thickness was adjusted by controlled radical polymerization. The experimental result on FRET tuned by temperature is presented in Figure 3.11. The fluorescence of VP was dominant at 25 °C, whereas that of PBHS became dominant at 40 °C. This result shows that FRET was tuned by temperature – in other words, the swollen PNIPAM shell prevented FRET, whereas the shrunken shell allowed it. The principle of this temperature-tunable FRET system can be applied to other systems using different materials that are sensitive to stimuli such as pH, ionic strength, and specific biomolecules, among others.

3.5 Conclusions

Core–shell particles with a temperature-sensitive shell that can be prepared by several methods have been described. The shell of these particles might be a hairy layer. Changes in the temperature of the aqueous dispersion of the particles cause

discontinuous changes in the physical properties of the particles, such as the degree of swelling, electrophoretic mobility, and hydrophilicity, among others. Such properties can be used for practical applications including temperature-sensitive bioreactors, biosensors, 2D colloidal crystals, tunable colored materials, and Pickering emulsions.

References

1 Schild, H.G. (1992) *Prog. Polym. Sci.*, **17**, 163.
2 Pelton, R. (2000) *Adv. Colloid Interface Sci.*, **85**, 1–33.
3 Lu, Y., Mei, Y., and Ballauff, M. (2006) *J. Phys. Chem. B*, **110**, 3930–3937.
4 Kawaguchi, H., Fujimoto, K., and Mizuhara, Y. (1992) *Colloid Polym. Sci.*, **270**, 53–57.
5 Yu, Z.Y., Chen, L., and Chen, S. (2010) *J. Mater. Chem.*, **20**, 6182–6188.
6 Wei, H., Cheng, S.X., Zhang, X.Z., and Zhuo, R.X. (2009) *Prog. Polym. Sci.*, **34**, 693–910.
7 Schrinner, M., Polzer, F., Mei, Y., Lu, Y., Haupt, B., Ballauff, M., Goldel, A., Drechsler, M., and Preussner, J. (2007) *Macromol. Chem. Phys.*, **208**, 1542–1547.
8 Tsuji, S. and Kawaguchi, H. (2005) *Langmuir*, **21**, 8175–8179.
9 Yeliseyeva, V.I., Petrova, S.A., and Zuikov, A.V. (1973) *J. Polym. Sci. (Symp.)*, **42**, 63.
10 Ceska, G.W. (1976) *J. Appl. Polym. Sci.*, **20**, 1745.
11 Goodall, A.R., Wilkinson, M.C., and Hearn, I. (1977) *J. Polym. Sci., Polym. Chem. Ed.*, **15**, 2193.
12 Goodwin, J.W., Hearn, JI., Ho, C.C., and Ottewill, R.H. (1973) *Br. Polym. J.*, **5**, 347.
13 Juang, M.S. and Krieger, I.M. (1976) *J. Polym. Sci., Polym. Chem. Lett.*, **14**, 2089.
14 Sakota, K. and Okaya, T. (1976) *J. Appl. Polym. Sci.*, **20**, 2583–3265.
15 Vijayendran, B.R. (1979) *J. Appl. Polym. Sci.*, **23**, 893.
16 Ohtsuka, Y., Kawaguchi, H., and Sugi, Y. (1981) *J. Appl. Polym. Sci.*, **26**, 1637–1647.
17 Kawaguchi, H., Hoshino, F., and Ohtsuka, Y. (1986) *Macromol. Chem., Rapid Commun.*, **7**, 109–114.
18 Hoshino, F., Fujimoto, T., Kawaguchi, H., and Ohtsuka, Y. (1987) *Polym. J.*, **19**, 241–247.
19 Hoshino, F., Kawaguchi, H., and Ohtsuka, Y. (1987) *Polym. J.*, **19**, 1157–1164.
20 Lv, S., Liu, L., and Yang, W. (2010) *Langmuir*, **26**, 2076–2082.
21 Ye, J., Hou, Y., Zhang, G.Z., and Wu, C. (2008) *Langmuir*, **24**, 2727–2731.
22 Kawaguchi, H. (1998) *Biomedical Functions and Biotechnology of Natural and Artificial Polymers* (ed. M. Yalpani), ATL Press, Shrewsbury, MA, pp. 157–166.
23 Vandezande, G.A. and Rudin, A. (1992) *Polymer Latexes* (eds E.S. Daniels, E.D., Sudol and M.S. Ei-Aasser), ACS Symposium Series 492, American Chemical Society, Washington, DC, p. 134.
24 Xu, X., Smith, A.E., Kirkland, S.E., and MacCormick, C.L. (2008) *Macromolecules*, **41**, 8429–8435.
25 Ferguson, C.J., Gilbert, R.G. *et al*. (2002) *Macromolecules*, **35**, 9243–9245.
26 Lobb, E.J., Ma, I., Billingham, N.C., and Armes, S.P. (2001) *J. Am. Chem. Soc.*, **123**, 7913.
27 Otsu, T., Nayatani, K., Muto, I., and Imai, M. (1958) *Makromol. Chem.*, **27**, 142–148.
28 Sato, T., Tsuji, S., and Kawaguchi, H. (2008) *Ind. Eng. Chem. Res.*, **47**, 6358–6361.
29 Topp, M.D.C., Dijkstra, P.J., Talsma, H., and Feijien, J. (1997) *Macromolecules*, **30**, 8518–8520.
30 Virtanen, J., Holapps, S., Lemmetyinen, H., and Tenhu, H. (2002) *Macromolecules*, **35**, 4763–4769.
31 Wu, K., Shi, L., Zhang, W., An, Y., Zhang, X., Li, Z., and Zhu, X.X. (2006) *Langmuir*, **22**, 1474–1477.
32 Bontempo, D. (2002) *Macromol. Rapid Commun.*, **23**, 417.

33 Matsuoka, H., Fujimoto, K., and Kawaguchi, H. (1999) *Polym. J.*, **31**, 1139–1144.

34 Tsuji, S. and Kawaguchi, H. (2004) *Langmuir*, **20**, 2449–2455.

35 Tsujii, Y., Ejaz, M., Sato, K., Goto, A., and Fukuda, T. (2001) *Macromolecules*, **34**, 8872–8878.

36 Kizhakke ndathu, J.N., Norris-Jones, R., and Brooks, D.E. (2004) *Macromolecules*, **37**, 734–743.

37 Tsuji, S. and Kawaguchi, H. (2006) *Macromolecules*, **39**, 4338–4344.

38 Ohno, K., Monnaga, T., Takeno, S., Tujii, Y., and Fukuda, T. (2007) *Macromolecules*, **40**, 9143–9150.

39 Trabelsi, S., Raspaud, E., and Langevin, D. (2007) *Langmuir*, **23**, 10053.

40 Kawaguchi, H., Hattori, S., and Kato, M., in Emulsion Polymerization and Functional Polymeric Microspheres–Science and Technology ed. By Kim, J. (2012, Yonsei University Press, Korea) pp. 37–49.

41 Pourbaix, M. (1966) *Atras of Electrochemical Equilibria*, Pergamon Press, London, p. 312.

42 Shiroya, T., Yasui, M., Fujimoto, K., and Kawaguchi, H. (1995) *Colloids Surf. B.*, **4**, 275–285.

43 Yasui, M., Shiroya, T., Fujimoto, K., and Kawaguchi, H. (1997) *Colloids Surf. B.*, **8**, 311–319.

44 Zhu, P.W. and Napper, D.H. (1996) *Colloids Surf. A.*, **113**, 145–153.

45 Zhou, S. and Chu, B. (1998) *J. Phys. Chem. B*, **102**, 1364–1371.

46 Jones, C.D. and Lyon, L.A. (2003) *Langmuir*, **19**, 4544–4547.

47 Ohshima, H., Makino, K., Kato, T., Fujimoto, K., Kondo, T., and Kawaguchi, H. (1993) *J. Colloid Interface Sci.*, **159**, 512–514.

48 Fujimoto, K., Nakajima, Y., and Kawaguchi, H. (1993) *Polym. Int.*, **30**, 237–241.

49 Matsumura, Y. and Iwai, K. (2006) *J. Colloid Interface Sci.*, **296**, 102–109.

50 Kawaguchi, H., Fujimoto, K., and Mizuhara, Y. (1992) *Colloid Polym. Sci.*, **270**, 53–57.

51 Janzen, J., Kizhakkedathu, Y., and Brooks, D.E. (2004) *J. Biomat. Sci. Polym. Ed.*, **15**, 1121–1135.

52 Tsuji, S. and Kawaguchi, H. (2005) *Langmuir*, **21**, 2434–2437.

53 Li, Z. and Ngai, T. (2010) *Langmuir*, **26**, 5088–5092.

54 Binks, B.P. and Lumsdon, S.O. (2000) *Phys. Chem. Chem. Phys.*, **2**, 2959–2967.

55 Tsuji, S. and Kawaguchi, H. (2009) *Langmuir*, **24**, 3300–3305.

56 (a) Ashida, A. (2010) Temperature sensitive fluorescent nano-particle for microenvironmental biosensor. Master's thesis. Keio University; (b) Ashida, A. and Kawaguchi, H. (2009) Gel Sympo (Osaka, Japan, 2009), Abstracts, p. 83.

57 Jones, C.D., Jonathan, J.G., McGrath, G., and Lyon, L.A. (2004) *J. Phys. Chem. B*, **108**, 12652–12657.

4
pH-Responsive Nanogels: Synthesis and Physical Properties[1)]

Beng Hoon Tan, Jeremy Pang Kern Tan, and Kam Chiu Tam

4.1
Introduction

The rediscovery of the utility of colloidal systems consisting of soft matter with nano size range is becoming an important field of research because of their potential applications in biological and chemical sciences, such as vesicles, bilayers, membranes, and living cells. An understanding of the behavior of these complex nanosized soft colloidal systems is critical for their engineering applications, hence simpler model systems have been developed to enable the development of fundamental understanding into these interesting and emerging systems. Moreover, simpler model colloidal systems provide a good basis to elucidate the physical interaction forces controlling their properties in solution. Thus, the synthesis of narrowly distributed stimulus-responsive nanogels offers the opportunity to study model systems, so that the knowledge gained can be applied in the development of better systems for applications in diverse fields, such as drug delivery [1–6], biological sensing [7–9], separation and purification technologies [10]. Many different applications of nanogels have been made possible as a result of the stimulus-responsive nature and ability of nanogels to undergo reversible volume phase transitions in response to environmental stimuli, such as pH [11, 12], temperature [11], ionic strength [13], solvent quality [14], and external electromagnetic fields [15]. This chapter focuses on monodispersed, internally crosslinked, alkali-swellable nanogels containing carboxylic acids, whose properties display extreme pH sensitivity in water.

In the last 20 years, advanced synthetic, experimental, and theoretical methodologies have provided important understanding in the microstructure, physicochemical properties, and their relationship to bulk property (e.g., rheological property) of pH-responsive nanogels containing carboxylic acid functionalities. During the neutralization of these aqueous nanogel dispersions, the viscosity and shear-thinning increase dramatically, making this class of materials useful for rheology control

1) Parts of this article have been published before in Tan, Beng H., and Tam, C. Kam, Advances in Colloid and Interface Science, *Review on the dynamics and micro-structure of pH-responsive nanocolloidal systems* **2008**, 136, 25–44. Printed with permission by Elsevier.

Hydrogel Micro and Nanoparticles, First Edition. Edited by L. Andrew Lyon and Michael Joseph Serpe.
© 2012 Wiley-VCH Verlag GmbH & Co. KGaA. Published 2012 by Wiley-VCH Verlag GmbH & Co. KGaA.

applications [16, 17]. The pronounced increase in viscosity and shear-thinning has been attributed to the swelling of colloids induced by electrostatic repulsion between polymer chains, and osmotic pressure effect within the nanogels [18]. In this chapter, we discuss the synthesis and preparation of pH-responsive nanogels, their physicochemical properties, and their impact on bulk properties, such as rheology.

4.2
Preparation Techniques for pH-Responsive Nanogels

Current approaches used for the preparation of pH-responsive nanogels can be classified into two main categories: (i) emulsion polymerization; and (ii) physical self-assembly of interactive polymers. In this section we discuss these methods, where the synthetic technique employed is dictated by the desired application or the types information required to better understand the system.

4.2.1
Emulsion Polymerization

Because of its well-controlled particle size distribution and structure, emulsion polymerization is among the most popular synthetic routes for preparing vinyl-based pH-responsive nanogel systems that employ radical chain polymerization methodology. Emulsion polymerization systems are commonly composed of monomer(s), water-soluble/oil-soluble initiator, and surfactant (emulsifier), where the synthesis can be performed in either oil/water (o/w) or water/oil (w/o) emulsions as shown in Figure 4.1 [19]. The o/w emulsion (Figure 4.1b) involves emulsification of a relatively hydrophobic monomer in water by an oil-in-water emulsifier followed by initiation reaction with either a water-soluble initiator (e.g., sodium persulfate (NaPS)) or an oil-soluble initiator (e.g., 2–20-azobisisobutyronitrile (AIBN)) through batch polymerization [20–25]. A large oil–water interfacial area is generated as particle nuclei form and grow in size with the progress of polymerization. Thus, an effective stabilizer, such as ionic and non-ionic surfactants and protective colloids (e.g., hydroxyethyl cellulose and polyvinyl alcohol) that can be physically adsorbed or chemically incorporated onto the particle surface, is required to prevent the interactive latex particles from coagulating. Typical monomers used in o/w emulsion polymerization include butadiene, styrene, acrylonitrile, acrylate ester and methacrylate ester monomers. In industry, a semi-batch emulsion polymerization technique has been used to produce latexes with high solid content. For example, commercial hydrophobically modified alkali-soluble/swellable emulsions (HASE) were synthesized via semi-batch emulsion polymerization using Aerosol OT surfactant [26, 27]. The alkali-soluble polymers contain a polymer backbone comprising methacrylic acid (MAA) and ethyl acrylate (EA) with up to 1–5 mol% of hydrophobic macromonomers grafted to its backbone [26, 28]. At low pH, they are in the form of colloidal particles, while at high pH they are soluble, and the hydrophobic macromonomers associate to form a viscous solution. In the case of hydrophobically modified alkali-swellable polymers, small amounts of crosslinker are introduced, and

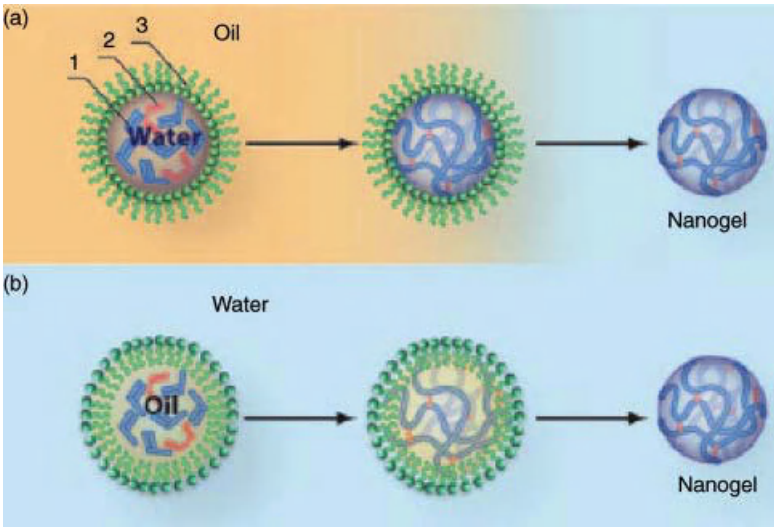

Figure 4.1 Chemical synthesis of nanogels by copolymerization in colloidal environments. (a) Copolymerization of monomers (1) and bifunctional crosslinkers (2) in w/o emulsions stabilized by surfactants (3) produces nanogels that can then be transferred into aqueous media after removal of the surfactants and organic solvent. (b) Copolymerization reactions can also be carried out in o/w emulsions that can be additionally stabilized by surfactants. Reprinted with permission from [19].

the swelling/deswelling behaviors can be controlled by MAA and crosslinker contents. Seeded semi-batch emulsion polymerization under monomer-starved feeding conditions can be used to prepare well-defined core–shell nano-particles [29, 30]. The core–shell particles containing poly(methyl methacrylate) (PMMA) core and P(MAA-*co*-EA) shell have been synthesized [31]. The PMMA core was first synthesized through conventional seeded emulsion polymerization, and then pre-emulsified monomers and small amounts of initiator were introduced slowly under monomer-starved feeding conditions to grow the pH-responsive shell layer. Other systems, such as those composed of poly(methacrylic acid) (PMAA) and poly(*N*,*N*,-diethylaminoethyl methacrylate) (PDEA) chains, have recently been reported [32]. In contrast to the PMAA or polyacrylic acid (PAA) system, such latex is swellable at low pH due to the protonization of amine functionalities.

Unlike the o/w emulsion, w/o emulsion polymerization (inverse emulsion polymerization) is best for water-soluble monomers; an aqueous solution of all the monomers is added to an appropriate amount of oil and surfactant that is stirred to form thermodynamically stable reverse micelles (Figure 4.1a). Polymerization can be initiated by having the initiator either in the aqueous phase (reverse micelles) or in the oil phase. This method has been used to synthesize nanogels with high wt% of ionic monomers, for example, PHEMA [33], PAA [34], PAAm [33], nanogels of PNIPAM that are hollow [35] and zwitterionic [13], and core–shell nanocapsules with hydrophobic shell and hydrophilic interior [36]. Neyret and Vincent prepared zwitterionic PNIPAM microgels using a UV-activated photo-initiator dissolved in

the organic phase [13]. McAllister *et al*. used the same technique to synthesize a highly cationic hydrogel that is able to bind to DNA and can potentially be used in gene delivery applications [37]. The Matyjaszewski research group used atom-transfer radical polymerization (ATRP) in an inverse microemulsion to synthesize stable biodegradable nanogels of water-soluble polymers containing a disulfide-functionalized crosslinker [38, 39].

In both o/w and w/o emulsion polymerization, the size of the nanogels can be controlled by varying the amount of surfactant. To synthesize smaller nanogels, the precursor particles must be stabilized earlier in the reaction, where surfactant can be added to impart colloidal stability. Similarly, larger particles can be obtained by decreasing the surfactant concentration [40]. However, the presence of surfactants is one of the major shortcomings in emulsion polymerization, which should be removed at the end of the polymerization reaction. The removal of surfactant, either by dialysis or desorption, may lead to coagulation or flocculation of the latex. To solve this problem, surfactant-free emulsion polymerization (SFEP) was adopted, using persulfate initiator. A characteristic of SFEP is that the particle number is generally lowered by up to 2 orders of magnitude compared to the typical emulsion polymerization process. SFEP has been widely used to prepare poly(*N*-isopropylacrylamide) (PNIPAM), polystyrene (PS), and PMAA nanogel systems [41–43].

4.2.2
Physical Self-Assembly of Interactive Polymers

Nanogels that are pH-responsive can also be formed using amphiphilic block copolymers that self-assemble into micelles via noncovalent interactions, such as van der Waals, hydrogen bonding, stereocomplexation, charge transfer, and polyelectrolyte complexation [44]. During the self-assembly process, small molecular drugs and macromolecular therapeutics, such as genes and proteins, can be incorporated into the micellar nanostructures. The most widely used self-associating polymers are amphiphilic block copolymers, synthesized by living radical polymerization techniques, for example, ATRP, RAFT, and nitroxide-mediated polymerization (NMP), which have a hydrophobic and a hydrophilic block that can self-associate in selective solvents to form submicron micelles (nanogels). The micellization of amphiphilic block copolymers can be tailored by changing the block nature, block lengths, composition, or architecture of the amphiphilic copolymers [45–47]. In addition, external parameters (i.e., change in temperature/solvent or addition of additives, such as electrolytes, co-solvents) provide extra degrees of freedom to tune the micellar behavior of the amphiphilic block copolymers [48–52]. Moreover, the chemistry of the surface can be manipulated for conjugation of a targeting signal that can recognize specific tissues or cells, and the functionalities of the core of nanogels can be tuned through advanced chemical approaches to improve drug-loading capacity.

Researchers have taken a step further by combining the controlled self-assembly of polymeric micelles and crosslinking techniques which has provided opportunities for the control of spatial distribution of polymeric chains at the nanoscale. Wooley and coworkers have used crosslinked block copolymer micelles to form nanogels,

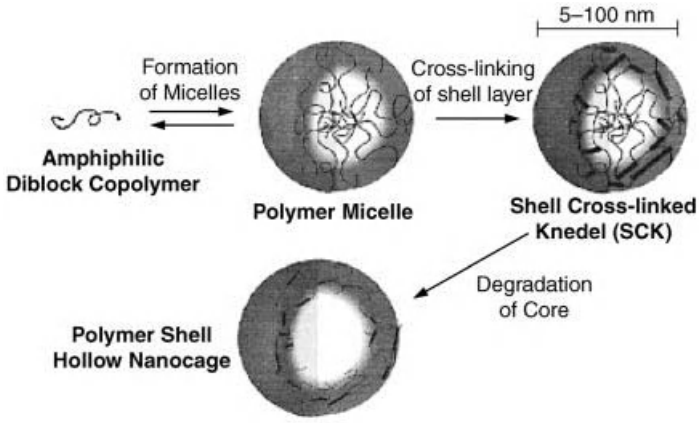

Figure 4.2 General synthetic approach for synthesizing shell crosslinked knedel (SCK) nanoparticles. The degradation step is used for the preparation of hollow particles. Reprinted with permission from [55].

which is widely referred to as shell crosslinked knedels (SCK) [44, 53–58]. The size range of SCKs is around 5–200 nm, and they are prepared from amphiphilic block copolymers that self-assemble into polymeric micelles. The micelles are further stabilized by crosslinking of side chain functional groups located on the shell of the micelles (Figure 4.2). The first pH-responsive SCK reported was fabricated from a polystyrene and poly(4-vinylpyridine) block copolymer [53]. Other examples of pH-responsive SCKs prepared by the Wooley group include hydrogel-coated particles using polystyrene-*b*-PAA copolymer [57], SCKs with degradable cores based on poly (ε-caprolactone)-*b*-PAA copolymers [56], hollow SCKs using poly(isoprene-*b*-acrylic acid) [54] as well as entirely hydrophilic SCKs have been reported [58].

4.3
Structural Properties of pH-Responsive Nanogels

4.3.1
Distribution of Crosslinking Monomers

The distribution of the crosslinking monomer as a function of distance from the particle center is an important parameter that influences the swelling properties of pH-responsive nanogels. Although the theories of nanogel swelling described in Section 4.4 below assume uniform swelling, that is, a uniform crosslinked density, this situation is highly unlikely. A more likely situation for nanogel particles prepared by emulsion polymerization is that the crosslinked density decreases from the center of the particles toward the periphery. This viewpoint is supported by the work of Nieuwenhuis *et al.*, who examined PMMA nanogel particles crosslinked with divinylbenzene (DVB) and ethylene glycol dimethacrylate (EGDM) dispersed in benzene. Light-scattering and viscometry measurements displayed variation in the

nanogel particle diameters [59], which suggest that the particles contained an inhomogeneous crosslinked distribution. By measuring the efficiency of incorporation of crosslinking monomers into growing particles during SFEP, McPhee *et al.* concluded that a large proportion of the crosslinks were incorporated during the initial growth of the particles [60]. This is not surprising as the solubility of a polymer chain decreases with increasing molecular weight, and the addition of crosslinking monomers leads to a substantial increase in its length. Accordingly, one is more likely to obtain uniform swollen nanogel particles by performing the polymerization reaction in a good solvent. The improved homogeneity of the structure would be at the expense of a monodispersed particle size distribution.

4.3.2
Kinetic Modeling of Functional Group Distributions in Nanogels

The design of nanogels with specific functional groups is complicated because both the total number and the nature of the functional group distribution within the nanogel play a critical role in controlling its swelling behavior [61]. The first available analytical method to semi-quantitatively predict and control the reactivities and functional group distributions of acid-functionalized nanogel systems was reported by Hoare and coworkers [62]. In the kinetic model developed, the mole fractions of each monomer within the gel were used to estimate the average numbers of each monomer incorporated between functional monomer residues using the expression

$$d_{cc} = b_0\left(\frac{n_1 + n_2 + n_3}{n_4}\right) \tag{4.1}$$

where n_i is the number of moles of each monomer component incorporated into the volume and b_0 is the effective length of a monomer unit. Alternatively, the average volumetric spacing between charged monomers can be calculated based on this shell-specific radial functional group density. The equivalent radius required to pack the model-estimated number of charged sites into a close-packed configuration within the calculated shell volume can be estimated using Equation 4.2:

$$\mathrm{d} = 2\mathrm{r}_{\mathrm{sphere}} = 2\left(\phi \mathrm{V}_{\mathrm{c}}\frac{3}{4\pi}\right)^{1/3} \tag{4.2}$$

where d is the average charge–charge separation distance, ϕ is the packing fraction of equivalent spheres (0.74 in their closest-packed configuration), and V_c is the volume per unit charge in the nanogel, equal to the total volume of the shell divided by the total number of charged monomers incorporated within the shell [62].

Multimodal functional group distributions can be predicted theoretically and verified experimentally using the kinetics model when two different carboxylic acid-containing monomers with different copolymerization kinetics are used to prepare a functionalized nanogel. Hoare and coworkers observed a correlation between the radial functional group distribution in functionalized nanogels and the copolymerization kinetics of the functional monomer; the slower the functional

monomer reacts relative to NIPAM, the more localized the functional groups are on the nanogel surface [63]. They discussed the synthesis of carboxylic acid-containing nanogels via free-radical copolymerization for four different functional monomers: acrylic acid (AA), MAA, vinylacetic acid (VAA), and acrylamide (AM), and discovered significant differences in the relative hydrophobicities, kinetic and chemical reactivities of these four monomers with the other gel components [63, 64]. While AA, MAA, and AM all react via standard free radical propagation, VAA reacts primarily via slow chain transfer, creating a "hairy", lightly crosslinked surface with a high concentration of carboxy-terminated chain ends [63]. Based on these physical properties and experimental results, functional group distribution models for each functionalized nanogel were proposed; a uniform charge distribution in hydrolyzed AM–NIPAM, a NIPAM-rich core/carboxylic acid-rich shell morphology in AA–NIPAM, a carboxylic acid-rich core/NIPAM-rich shell in MAA–NIPAM, and an "extreme" core–shell microstructure in VAA–NIPAM with highly surface localized charges. The radial and chain distributions were calculated via copolymerization kinetics modeling [62, 65] and were confirmed experimentally via transmission electron microscopy (TEM) [62, 65] electrophoresis mobility [66], potentiometric titration [67], dimensionless plot analysis [68], and differential scanning calorimetry [69]. The strategies developed to control and characterize the number and approximate distributions of carboxylic acid groups within nanogel systems should improve our knowledge concerning the selection of acid-based copolymer systems to best fit a wide variety of applications, for example the glucose swelling responses in NIPAM-based nanogels [70].

4.4
Swelling of pH-Responsive Nanogels

4.4.1
Mechanism of pH-Responsive Swelling

The mechanism of swelling of nanogels containing pH-responsive groups is governed by the internal osmotic pressure due to mobile counter-ions contained within the particles that balances the internal electrostatic repulsion [71]. The extent of swelling depends on the ionization degree, quality of solvent, crosslinked density, and ionic strength as illustrated by the example in Figure 4.3, which shows the effect of pH on the hydrodynamic diameter of P(MMA-*co*-MAA) particles [71]. On increasing pH, the swelling increases due to the ionizing of carboxylic acid groups followed by a leveling off in the rate of swelling at around pH 8 as the ionization attains a maximum value. In addition, the increase in ionic strength screens the internal repulsion or reduces the osmotic pressure difference inside and outside of the nanogel particles. Similar trends were observed for poly(ethyl acrylate-*co*-MAA) [28], P(MMA-*co*-AA) [72, 73] and poly(methacrylic acid-*co*-ethylene glycol) (P(MAA-*co*-EG)) [74], where swelling increased with increasing extents of neutralization.

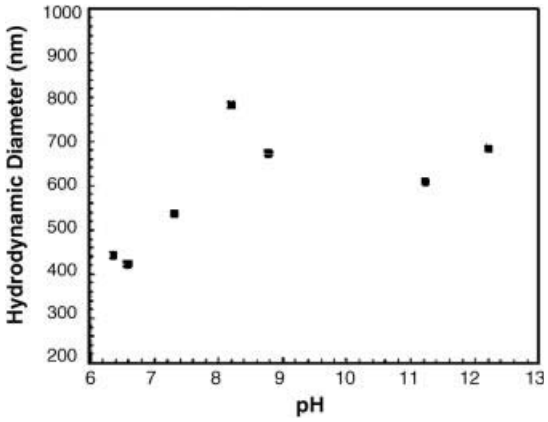

Figure 4.3 Effect of pH on the hydrodynamic diameter of PMMA–PMAA nanogel particles [71].

Tan *et al*. investigated the swelling characteristics of model pH-responsive nanogel systems consisting of PMAA–PEA crosslinked with diallyl phthalate (DAP) as depicted in Figure 4.4 [28]. The swelling at neutralization degree, $\alpha < 0.4$ is fairly similar for all the nanogel systems with 20 mol% MAA but different crosslinked densities. However, the R_h values begin to deviate from each other when α exceeds 0.4, which suggests a change in the microstructure of the nanogels during the neutralization process. The hydrophobic attraction between the EA blocks preserves the existing particle structure, whereas the osmotic pressure exerted by the counter-

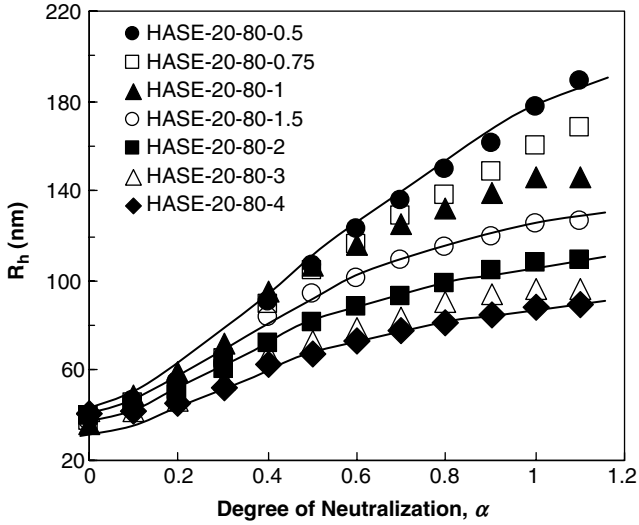

Figure 4.4 Dependence of hydrodynamic radius, R_h, on neutralization degree, α, for microgels with 20 mol% MAA crosslinked at different DAP density (wt% DAP) in salt-free solutions [28].

ions attracted to the charged carboxylate groups expands the particles. Consequently, a transition region reflecting the conformational change of nanogels induced by the competition of these two types of interactions was observed. Below this transition point, the increase in R_h is smaller because the osmotic pressure exerted by the counter-ions is insufficient to overcome the hydrophobic attraction between the PEA blocks. As α increases beyond this transition point, the osmotic pressure exceeds the hydrophobic attraction, resulting in a rapid increase in R_h at $\alpha > 0.4$. As anticipated, nanogels of lower crosslinked density exhibit larger swelling behaviors.

Nanogels that are pH-responsive with both positive and negative charges along the polymer chain are known as polyampholyte nanogels [32, 75–79]. Such systems are interesting because they maintain a robust internal microstructure under all pH conditions. Schulz *et al.* [76] and Harding and Healy [77] prepared and characterized a series of spherical latex particles with functionalized zwitterionic (amphoteric) groups on the surface, resulting in a range of isoelectric points (IEP). Amalvy *et al.* reported the synthesis and characterization of acid-swellable PDEA nanogels, which are sterically stabilized with reactive macromonomers to achieve colloidal stability [80]. Recently, Das and Kumacheva prepared polyampholyte nanogels with different fractions of acrylic acid (AA) and vinyl imidazole (VI) monomers where the nanogel exhibited marked swelling at both high and low pH values, but shrank at $4.0 < \text{pH} < 7.0$ due to electrostatic attraction between charged AA and VI, moieties as shown in Figure 4.5 [79]. The largest contraction occurred at the IEP (zeta-potential $= 0$). As the pK_a values of AA and VI are 4.25 and 6.99, respectively, within the range corresponding to nanogel shrinkage, the particles possessed both positive and negative charges, corresponding to a zwitterionic behavior which was also corroborated by zeta-potential measurements (Figure 4.5a′ to d′). An increase in the molar ratio of anionic-to-cationic residues caused the IEP to shift towards lower values of pH because the number of COO^- groups exceeded the number of NH^+ groups. Thus, increased acidity was required to protonate the excess COO^- groups (that were not neutralized by NH^+ moieties) to achieve the IEP.

In a separate study, pH-responsive polyampholyte nanogels consisting of PMAA–PDEA of 200–300 nm in diameter were synthesized by Tan *et al.* [32] These nanogels showed enhanced hydrophilic behavior in aqueous medium at low and high pH, but formed large aggregates of approximately 2500 nm at intermediate pH due to overall charge neutralization. To achieve colloidal stability at intermediate pH, nanogels were synthesized and grafted with monomethoxy-capped poly(ethylene glycol)methacrylate (PEGMA) on the surface of these particles. Dynamic light scattering (DLS) and TEM revealed the absence of large aggregates at the IEP region, unlike nanogels without steric stabilizers as depicted in Figure 4.6.

Wolfe and coworkers studied the changes in the internal polymer segment density and particle swelling during the alkalization of internally crosslinked PMAA–PEA nanogels using static and dynamic light scattering. Upon neutralization with a base, pronounced negative deviations of the ratio of the radius of gyration, R_g, to hydrodynamic radius, R_h, from a known value of between 0.75 and 0.78 for homogeneous spheres (Figure 4.7) indicated a non-uniform polymer segment density distribution within the nanogels [81, 82]. To explain the non-uniform

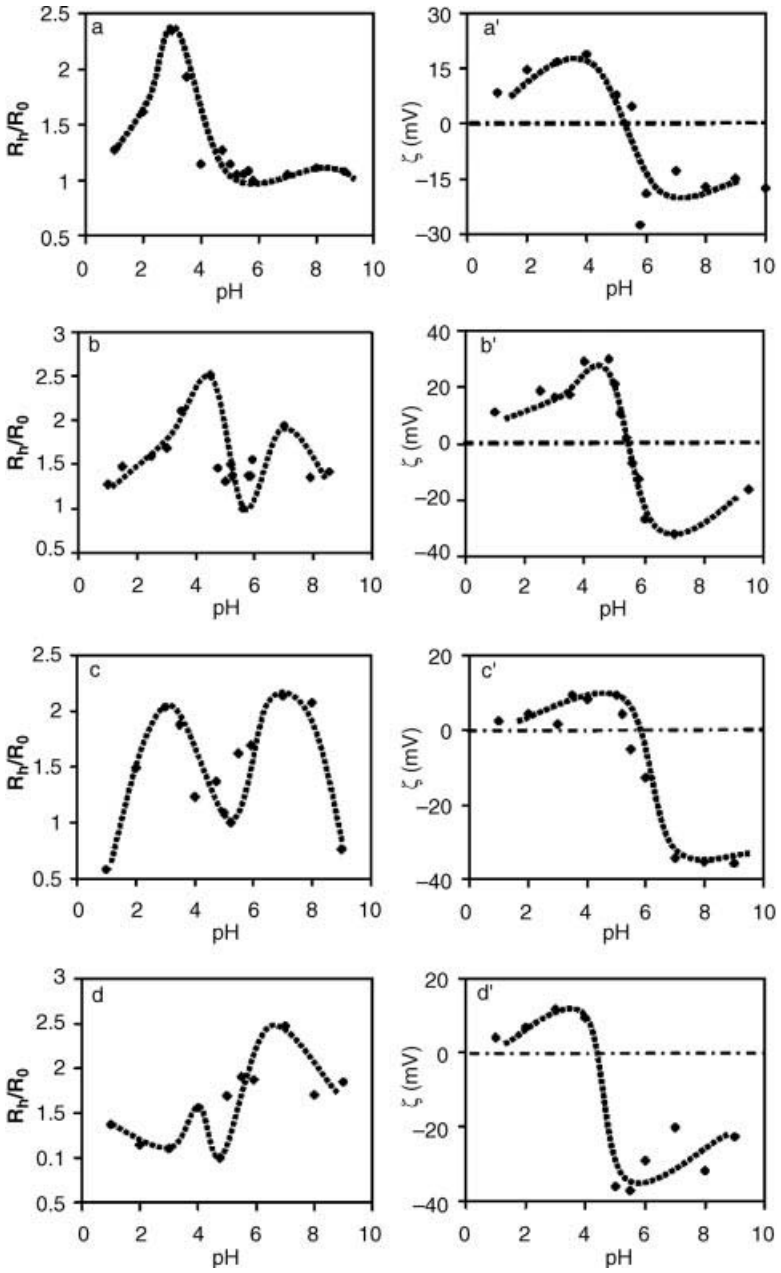

Figure 4.5 Effect of pH on the variation in R_h/R_0 (a–d) and zeta-potential (a′–d′) for polyampholyte nanogels in 0.01 M KCl solution at 25 °C. (a, a′) PA-0.46, $R_0 = 79$ nm; (b, b′) PA-0.9, $R_0 = 73.8$ nm; (c, c′) PA-1.25, $R_0 = 59.6$ nm; (d, d′) PA-1.65, $R_0 = 57.2$ nm. Dashed lines are drawn as eye guidelines. The horizontal dashed line indicates zeta-potential = 0 [79].

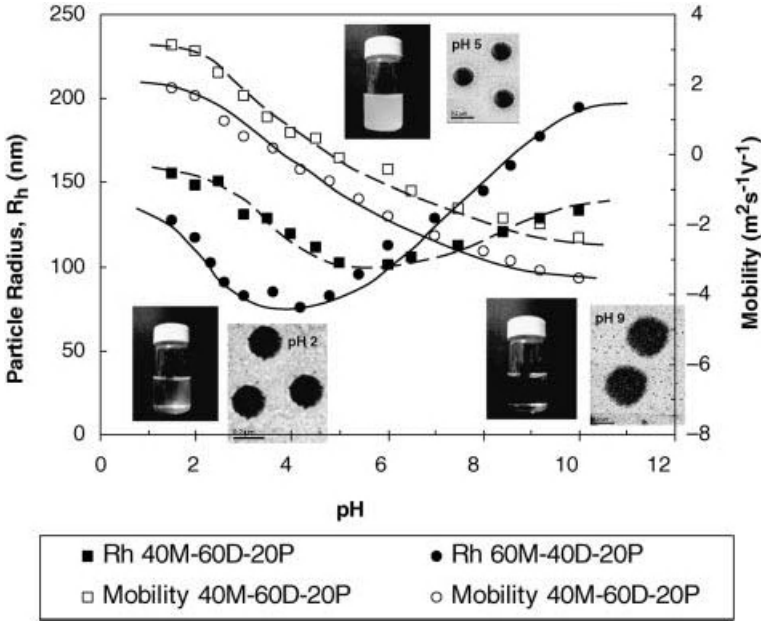

Figure 4.6 The hydrodynamic radius, R_h, and electrophoretic mobility of 0.1 wt% nanogel concentration of sterically stabilized 60M-40D (open circles) and 40M-60D (squares) at different pH values at 25 °C obtained from light-scattering measurements. Filled symbol represents R_h and open symbol represents electrophoretic mobility. Digital photographs and TEM micrographs of 0.1 wt% 60M-40D nanogel at three different pHs, that is, 2, 5, and 9 are shown to illustrate the change in solution transmittance and the morphology of the nanogel [32].

swelling, the nanogels were modeled in terms of a core–shell structure composed of a crosslinked core and an outer shell of dangling chains, with uniform polymer densities within each region.

4.4.2
Theory of Swelling and Elasticity of pH-Responsive Nanogels

The equation of swelling of nanogels is determined by the balance between the osmotic pressure inside and outside the nanogels as described by Equation 4.3:

$$\Pi_{in} + \Pi_{el} = \Pi_{out} \tag{4.3}$$

where Π_{in} and Π_{out} are the osmotic pressures of mobile ions inside the nanogels and in the bulk solution, respectively [83], Π_{el} is the elastic pressure of the polymeric network described by Equation 4.4:

$$\Pi_{el} = -\frac{RTc_0}{2N_x Q^{1/3}} \tag{4.4}$$

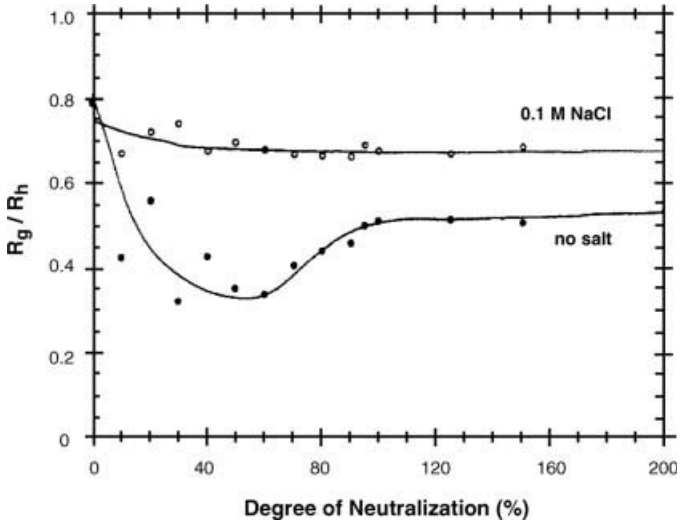

Figure 4.7 (a) R_g/R_h for PMAA–PEA nanogels as a function of the degree of neutralization and added salt. (b) Hypothetical polymer density as a function of the distance from the microgel center: (a) uniform density; (b) long polymeric tail [81].

where $Q = (R_\alpha / R_{\alpha=0})^3$ is the swelling ratio of nanogels, N_x is the crosslinked density, and c_0 is the polymer concentration in the particles at collapsed state. R_α represents the hydrodynamic radius of the particle at a particular α and $R_{\alpha=0}$ represents the hydrodynamic radius of the uncharged ($\alpha = 0$) particle, both measured using DLS technique. The terms Π_{in} and Π_{out} can be described by:

$$\Pi_{in(out)} = RTC_{in(out)} \tag{4.5}$$

where C_{in} and C_{out} are the concentrations of the ions inside and outside the nanogels.

Recently, Cloitre and coworkers showed that the theoretical prediction of the relative swelling of polyelectrolyte nanogels agreed with experimental data [83]. In the absence of salt, that is, $C_{out} = 0$, all the counter-ions associated with the ionized units are trapped inside the polymeric network by electrostatic attraction exerted by fixed charges, $C_{in} = \alpha c_0 \gamma / Q$, where c_0 is the polymer concentration inside the particles at collapsed state, γ is the molar fraction of acidic units, and α is the neutralization degree. By combining Equations 4.3 to 4.5, the swelling ratio Q of the nanogels as a function of neutralization degree, α, and crosslinked density, N_x, can be described by the scaling relation below:

$$Q \propto (\alpha N_x)^{3/2} \tag{4.6}$$

which assumes that all the counter-ions are trapped inside the nanogels. They compared this prediction with the experimental data and showed that the data measured for different crosslinked densities collapsed onto a master curve, in good agreement with theoretical prediction in Figure 4.8.

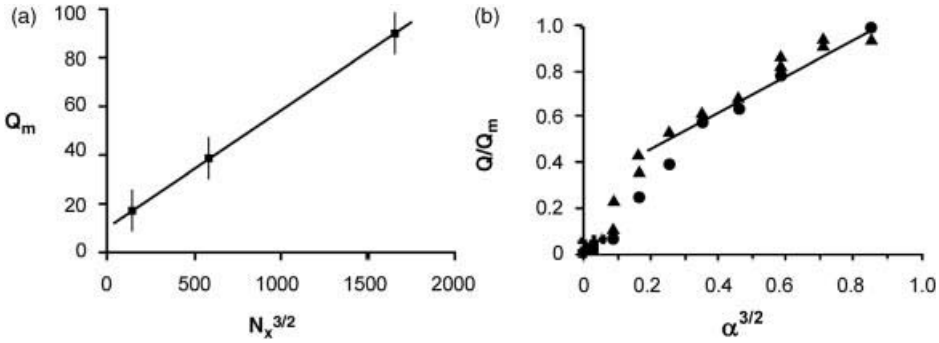

Figure 4.8 (a) Variation of the swelling ratio at maximum swelling versus the crosslinked density. (b) Variation of the swelling ratio with the neutralization degree for $N_x = 140$ (filled circle), $N_x = 70$ (filled diamond), $N_x = 28$ (filled triangle) [83].

4.4.3
Effect of Ionic Strength

Because of their relatively simple molecular structure, pH-responsive nanogels have often been used as models for many complex biological systems for elucidating the effect of salt on macromolecular conformations. Since pH-responsive nanogels exhibit different equilibrium degrees of swelling in response to various kinds of salts and concentrations, they can be used to measure the effects of solvent environment on the polymer chain conformation [84]. The swelling behavior of charged gels in electrolyte solutions has been successfully predicted using the Donnan equilibrium [85–87]. Salt-induced phase transition in a hydrolyzed (ionic) polyacrylamide gel was reported in a water–organic solvent mixture [88]. A discrete volume phase transition has been observed in response to mono- or divalent electrolytes only in the region of high acetone concentration. This phase transition behavior in the relatively hydrophilic gel could be caused by van der Waals interactions in the low dielectric medium. Saunders *et al*. investigated the effect of pH on the hydrodynamic diameter of crosslinked PAA–PEA nanogels in the presence of different background electrolyte concentrations (Figure 4.9). The data showed that the swollen diameter decreased with increasing electrolyte concentration, and the salt concentrations were too low to cause particle collapse through competitive hydration for water [89].

In addition, the swelling of carboxylic-containing nanogels decreased with increasing salt concentration as a result of the reduced osmotic pressure inside the nanogels, which was attributed to a charge-shielding effect of counter-ions (salt) on the negatively charged carboxylate groups, as reported by Tan *et al*. for the MAA–EA nanogels [90]. In this work, there are two types of counter-ions present in the nanogel solution: K^+ from the added salt KCl, which was used as the background electrolyte, and Na^+ from NaOH which was used to neutralize the nanogels. Electromotive measurements using ion-selective electrodes confirmed that not all the counter-ions

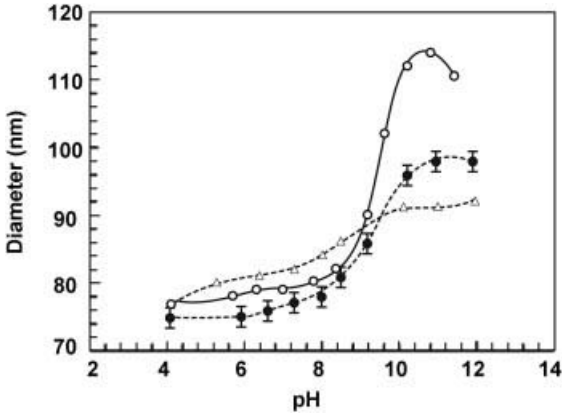

Figure 4.9 The influence of NaCl concentration on the pH dependence of the particle size for crosslinked PAA–PEA nanogel. The NaCl concentrations used were 0.1 mM (open circle), 1 mM (filled diamond), and 10 mM (open tringle). The error bars correspond to one standard deviation of the mean diameter [89].

(i.e., K^+) remained mobile but a fraction of these ions could penetrate the porous nanogel particles to shield the negatively charged carboxylate groups. A consequence of this was that some of the Na^+ counter-ions inside the particles were expelled, regaining their translational entropy and becoming mobile Na^+ ions in the bulk solution [90]. These researchers developed a new scaling law that relates the swelling ratio Q of the nanogels as a function of neutralization degree, α, crosslinked density, N_x, molar fraction of acidic units, y, and concentration of mobile counter-ions, C_{K+} and C_{Na+},

$$\frac{N_x}{c_0}(C_{K^+} + C_{Na^+})Q + Q^{2/3} \propto y\, N_x \alpha$$

where all the data fall on a master curve as depicted in Figure 4.10 [90]. The new scaling law no longer assumed that all the counter-ions were trapped inside the nanogels. The proportionality reduced to the form $Q \propto (y\,\alpha\, N_x)^{3/2}$ in the absence of salt, that is, $C_{K+} + C_{Na+} \approx 0$.

The effects of ionic strength on the swelling properties of pH-responsive polyelectrolyte and polyampholyte nanogels in different concentrations of KCl solutions were also examined by Kumacheva *et al.* [79] Figure 4.11a shows the variation in normalized size, R_h/R_0, of P(NIPAM–AA) nanogels (pH = 7) and P(NIPAM–VI) nanogels (pH = 4) as a function of KCl concentration. In both dispersions, an increase in the concentration of KCl from 10^{-5} M to 2.0 M resulted in a contraction of the size of nanogels. The total shrinkage observed for P(NIPAM–AA) and P(NIPAM–VI) nanogels was 75 and 50%, respectively. Such polyelectrolyte behavior was typical of polyelectrolytes in salt solutions [91]. No particle aggregation was observed up to KCl concentrations of 1 M. The volume transitions of polyampholyte nanogels were studied at their respective IEP values [79]. Figure 4.11b shows the swelling profiles

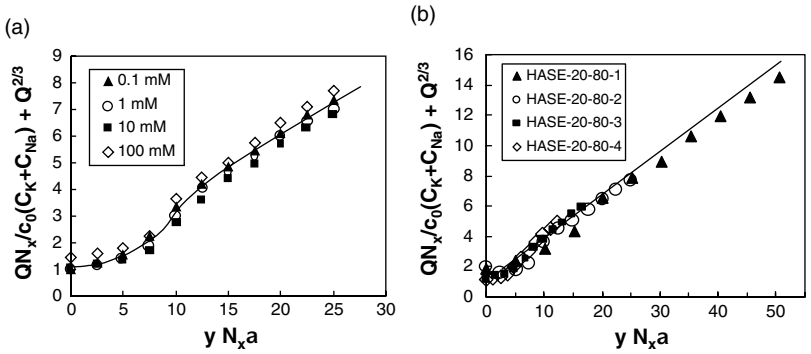

Figure 4.10 Variations of $N_x/c_0\,(C_{K+} + C_{Na+})Q + Q^{2/3}$ as a function of $\gamma N_x\alpha$ for (a) HASE-20-80-2 at different salt concentrations, [KCl], and (b) HASE-20-80 with different crosslinked density at salt concentration of 100 mM KCl. The master curve is represented by the solid line [90].

of polyampholyte nanogels of different compositions as a function of KCl concentration. At salt concentrations below 0.005 M, no significant change in the nanogel size was observed. A notable swelling peak occurred at higher salt concentrations for all polyampholyte nanogels, indicating their anti-polyelectrolyte behavior. The large increase in the nanogel size was not due to particle flocculation because the light scattering data showed relatively narrow size distributions and negligible change in scattering intensity. At higher concentrations of KCl, the nanogels aggregated because of the suppressed electrostatic interactions between them.

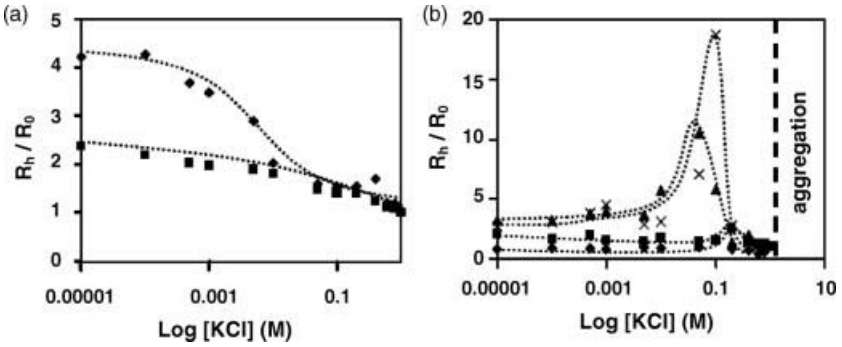

Figure 4.11 (a) Variation in normalized hydrodynamic radius (R_h/R_0) as a function of KCl concentration for polyelectrolyte nanogels: (filled diamonds) P(NIPAM–AA), pH = 7.0, $T = 25\,^{\circ}C$, $R_0 = 22.6$ nm; (filled squares) P (NIPAM–VI), pH = 4.0, $T = 25\,^{\circ}C$, $R_0 = 91$ nm. (b) Variation in normalized hydrodynamic radius (R_h/R_0) as a function of KCl concentration for polyampholyte nanogels: (filled diamonds) PA-0.46, $R_0 = 24.5$ nm; (filled sqaures) PA-0.9), $R_0 = 44.2$ nm; (filled triangles) PA-1.25, $R_0 = 28.6$ nm; (crosses) PA-1.65, $R_0 = 24.5$ nm; pH = pI, $T = 25\,^{\circ}C$ [79].

4.5
Rheological Behavior of pH-Responsive Nanogels

In most applications, these nanogels are subjected to hydrodynamic forces and their rheological behavior should be elucidated and monitored. The main parameters that control such rheology are particle surface charge, particle size and distribution, nanogel phase volume fraction, and particle internal structure. Under shear flow, both the plateau viscosity and shear-thinning behaviors of the crosslinked nanogels deviate appreciably from those of hard spheres, depending on the crosslinking density [92]. The influence of crosslinking density on the bulk rheology of monodisperse, internally crosslinked, carboxylic-containing nanogel particles was elucidated by Wolfe [92]. He demonstrated that the viscosity decreased with increasing crosslinked density as depicted in Figure 4.12, and that the observed changes in the viscosity (which is dependent on nanogel concentration, crosslinked density, and solvent quality) could be correlated with the effective volume fraction of the nanogel.

Tan *et al.* investigated the effect of crosslinked density on the rheological behavior of model pH-responsive MAA–EA nanogels crosslinked with DAP [28]. Figure 4.13 illustrates the conformational transition of the crosslinked nanogel with 20 mol% MAA as a function of crosslinked density by comparing the molecular weight and relative viscosity at 5 wt% nanogel concentration. The viscosity exhibited a maximum at approximately 1 wt% DAP and it decreased to a steady value at 4 wt% DAP, which was independent of pH and particle concentrations. Below the optimum level of 1 wt% DAP, there were insufficient crosslinked junctions to produce a stable and compact nanogel particle. In addition to particle swelling, there was substantial expulsion of polymer chains from the nanogel particles as confirmed by the reduction in the

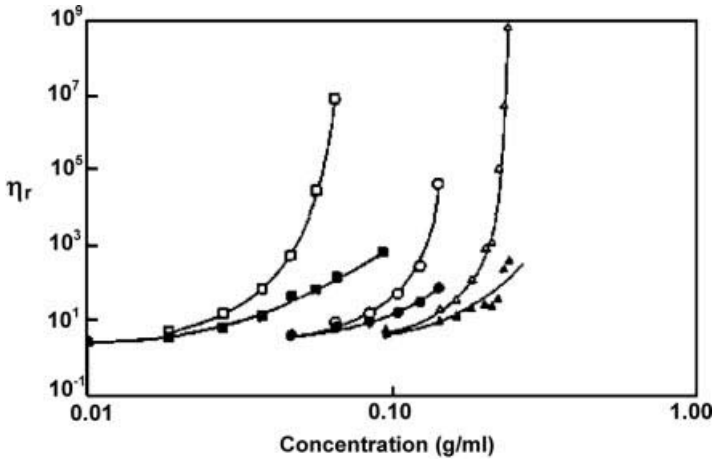

Figure 4.12 Zero and infinite shear rate-limiting viscosities as a function of concentration for PMMA nanogels of different crosslinked densities. Dispersions were in butyl carbitol acetate at 20 °C. Open symbol are for η_0 and filled symbols are for η_∞. Crosslinker contents in wt% are: (open squares) 0.25; (open circles) 1.0; and (open triangles) 4.0 [92].

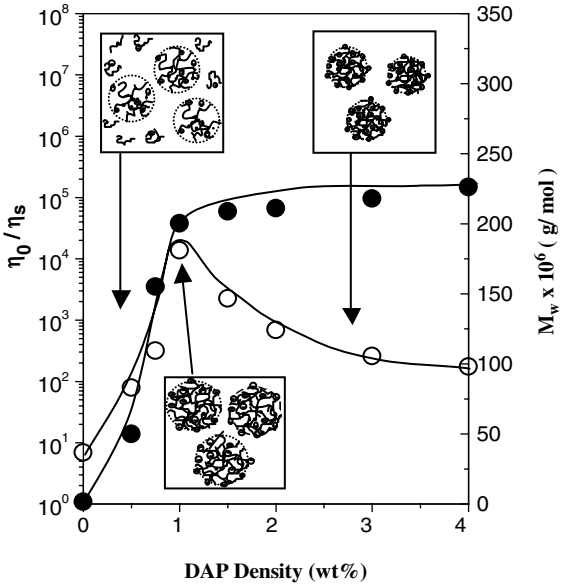

Figure 4.13 Illustration of the conformational transition for the crosslinked nanogel particle with 20 mol% MAA as function of crosslinked density (wt% DAP). The filled circles represents M_w and the open circles represent the low-shear relative viscosity at 5 wt% polymer concentration [28].

molecular weight, M_w, upon neutralization. The large increase in A_2 upon neutralization suggested that the polymer–solvent interaction was enhanced due to exposure of negatively charged carboxylate groups to the solvent environment when the particle swelled and the chains expelled from the swollen particles. Thus, 1 wt% DAP was the critical point at which sufficient crosslink points were present to produce permanent junctions that permitted optimal swelling of the nanogel particles.

4.6 Approach to Model pH-Responsive Nanogel Properties

Based on the above review, the characteristics of pH-responsive nanogels and their corresponding interaction potentials can be manipulated by varying the following: degree of ionization of acid/basic groups (α), salt concentration, nanogel crosslinked density and the mole composition of acid/basic groups, which have a significant impact on the nanogel particle size and their bulk rheological property. These interesting findings have motivated researchers to propose a semi-empirical approach for predicting the viscosity of dilute and concentrated soft condensed particles, by taking into account the physics of compressible soft nanogel particles. To date, the most significant contribution in the field of stimuli-responsive nanogels can be attributed to the pioneering work of Ballauff and coworkers [93–96]. Although their initial findings were based on a thermoresponsive system, they were

successfully extended to various pH-responsive nanogels [97–104]. These studies reported the behavior of thermosensitive core–shell particles with a monodispersed polystyrene grafted with a layer of crosslinked PNIPAM and a pH-responsive shell consisting of PAA. A simple method for treating the viscosity data was to determine the effective volume fraction of particles, where the volume fraction ϕ was replaced by the effective volume fraction, ϕ_{eff}, using the Batchelor equation for hard spheres:

$$\frac{\eta_0}{\eta_s} = 1 + 2.5\phi_{\text{eff}} + 5.9\phi_{\text{eff}}^2 \tag{4.7}$$

The effective volume fraction ϕ_{eff} can be substituted by the term kc (where c is the mass concentration of the dispersion in g ml^{-1} and k is the specific volume in ml g^{-1}) to convert the mass concentration to the effective volume fraction. Hence, Equation 4.7 can be rewritten as:

$$\frac{\eta_0}{\eta_s} = 1 + 2.5(kc) + 5.9(kc)^2 \tag{4.8}$$

where the constant k is the only adjustable parameter.

The relative viscosity of dilute PNIPAM nanogel solutions is shown in Figure 4.14a as a function of the mass concentration, c, for different temperatures. The lines represent fittings according to Equation 4.8 with the effective volume fraction ϕ_{eff} substituted by $\phi_{\text{eff}} = kc$. Strong temperature dependence was evident, which was caused by the shrinkage of particles. The relative viscosity of PNIPAM nanogel dispersion was plotted against ϕ_{eff} calculated from the constant k determined from Equation 4.8. All the data determined at different temperatures seemed to fall onto a single master curve as shown in Figure 4.14b [94]. This showed that the shear viscosity was only a function of the effective volume fraction of the nanogel particles even at high concentration. Also plotted in Figure 4.14b is a line representing the relative zero-shear viscosity of model hard sphere suspensions as provided by Meeker *et al.* [103]. Obviously, the nanogel resembled hard sphere behavior up to effective volume fractions, ϕ_{eff}, approximately 0.5. However, above $\phi_{\text{eff}} = 0.5$ the viscosity was lower as compared to hard sphere model systems and the deviation was not caused by polydispersity effects, but by a soft sphere interaction potential that becomes noticeable when the particles are close to each other. The deviation from the Batchelor prediction suggests that the specific volume, k, obtained in a dilute solution regime is not representative of the "true" effective volume of soft particles in regions where interparticle repulsion is present.

Tan *et al.* postulated that interparticle distance decreased with increasing concentration of soft particles [31, 105, 106]. At a critical particle concentration the concentration of free counter-ions in the solution can be sufficiently large to induce osmotic deswelling of soft particles, resulting in the shrinkage of the particles. Thus the specific volume, k, should be a function of volume fraction of particles. A pictorial representation on the changes in the specific volume k is given in Figure 4.15a–c, where k should decrease with increasing nanogel concentration. Figure 4.15a illustrates the crosslinked soft nanogel particle in the swollen state, impregnated with large amounts of solvent, rendering them "soft" and porous, unlike hard spheres. In the dilute solution regime, interparticle interaction is absent and k is

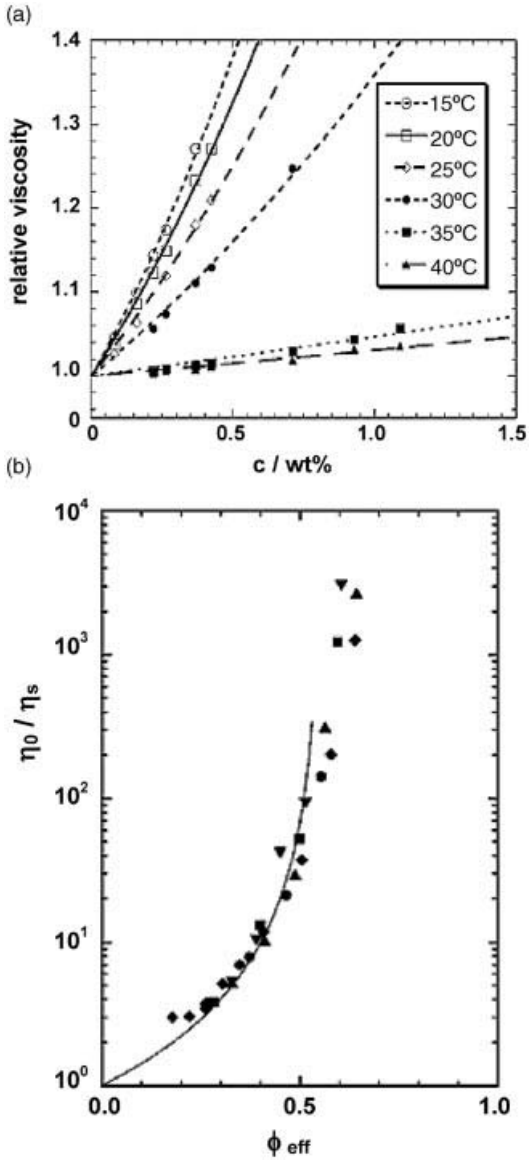

Figure 4.14 Relative zero-shear viscosity, η_0/η_s of PNIPAM nanogels at different temperatures as a function of (a) polymer concentration (wt%) and (b) effective volume fraction. The lines in (a) display fits according to Equation 4.8 and in (b) represent the master curve of hard sphere suspensions (Equation 4.7) [94].

a constant. With increasing concentration, the interparticle distance between nanogels is reduced and the concentration of free counter-ions in the solution can be large enough to induce an osmotic deswelling of soft particles (Figure 4.15b). Increasing interparticle interactions cause the nanogel to shrink, resulting in a corresponding

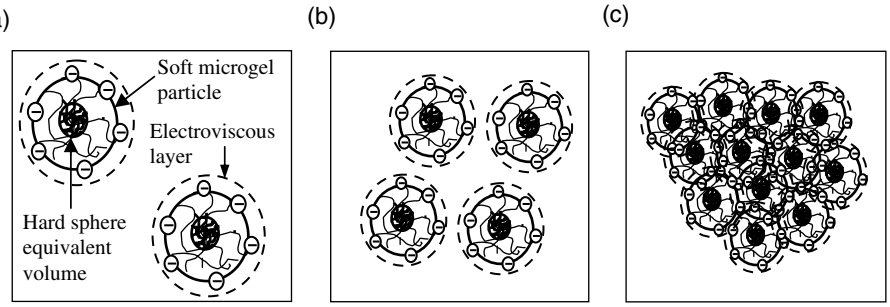

Figure 4.15 A pictorial representation of the changes in the specific volume, k, at three different concentration regimes: (a) dilute; (b) semi-dilute; and (c) concentrated region [105].

decrease in k, until it approaches the hard sphere limit (indicated by the black core). If we do not take into account the changes in the specific volume k and overlap of the electroviscous layer of soft particles (Figure 4.15c), $\phi_{\text{eff}} = kc$ will exceed the maximum packing limit of 0.63 and can even approach 1.5 [105].

A generalized semi-empirical approach to model soft condensed particles was proposed by taking into account the physics of compressible soft nanogel particles where k is inversely proportional to volume fraction [105]. The specific volume, k, depends on concentration of particles, c, neutralization degree, α, of acid groups (MAA), salt concentration, crosslinked density, and the molar ratio of acid groups. The values of k were determined from the mathematical fitting of the data to the form of the modified Krieger–Dougherty equation shown in Equation 4.9.

$$\frac{\eta_0}{\eta_s} = \left(1 - \frac{kc}{\phi_m}\right)^{-[\eta]\phi_m} \tag{4.9}$$

Figure 4.16a–d shows the specific volume, k, as a function of concentration of particles for four different systems: (a) degree of neutralization (α) of MAA groups; (b) salt concentration; (c) nanogel crosslinked density; and (d) molar ratio of MAA groups. The general trend of specific volume, k, can be described by a mathematical expression given in Equation 4.10:

$$\frac{k - k_{\min}}{k_0 - k_{\min}} = \left[1 + \left(\frac{c}{c_0}\right)^2\right]^{-m} \tag{4.10}$$

with $k_{\min}$ describing the limiting condition when the soft particles are compressed to the hard sphere equivalent volume at high concentration. The constant c_0 denotes the critical concentration at which the concentration of free counter-ions in the solution is large enough to induce an osmotic deswelling of the soft particle, resulting in a smaller k. The rate of decrease in k with particle concentration is described by the parameter m, which can also be obtained from the slope of the $(k - k_{\min})/(k_0 - k_{\min})$ versus c curve on a log–log plot.

Depending on the nature of soft particles and surrounding environment, the rate of decrease in k with volume fraction varies. Equation 4.10 permits the determination of

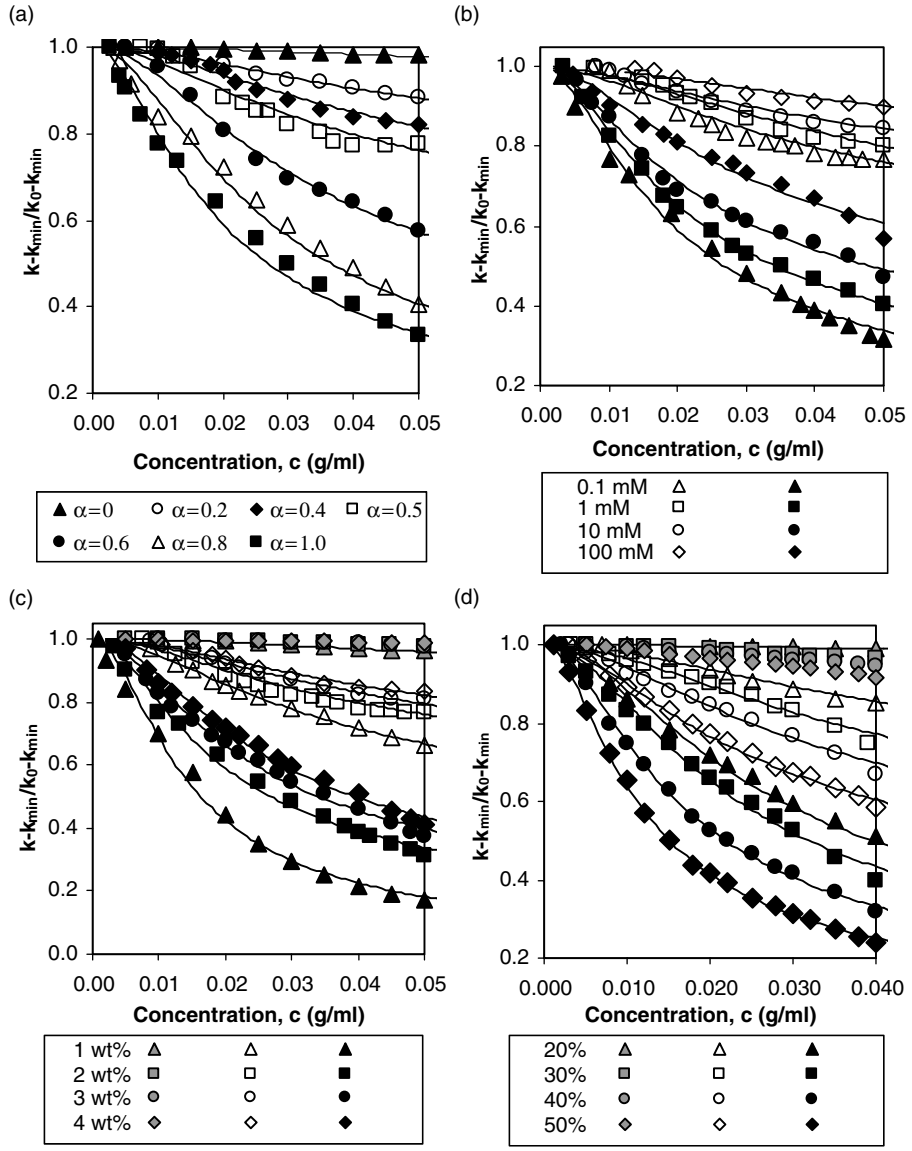

Figure 4.16 Specific volume, *k*, as a function of concentration of crosslinked MAA–EA microgel at 5 wt% polymer concentration and four different conditions: (a) varying neutralization degree, α of HASE-20-80-2 in salt-free solution; (b) varying salt concentrations (mM KCl) of HASE-20-80-2; (c) varying crosslinked density (wt% DAP) of nanogels with 20 mol% MAA in salt-free solution; and (d) varying molar ratio of MAA groups (% MAA) of 4 wt% crosslinked nanogels in salt-free solution. The solid lines denote mathematical fittings according to Equation 4.10 [105]. For (b) to (d), grey, open and black symbols correspond to α of 0, 0.5 and 1.0 respectively.

k, once the parameters c_0, m, and k_0 are known for a given system. The dependence of k on c for different systems, such as degree of neutralization (Figure 4.16a), salt concentrations (Figure 4.16b), crosslinked density (Figure 4.16c), and MAA contents (Figure 4.16d) is suitably described by Equation 4.10. Nanogel particles are highly swollen in conditions of large α, low salt environment, low crosslinked density, and high content of MAA. Such particles exhibit strong dependence of k on polymer concentration, where (k/k_0) may decrease from 1.0 to 0.2. From the dependence of k on c, the effective volume fraction, ϕ_{eff}, of soft nanogels at various polymer concentrations can be determined from Equation 4.11. This expression corrects for the changes in the volume fraction of soft particles to that of the equivalent hard sphere.

$$\phi_{\text{eff}} = k_{\min} + (k_0 - k_{\min})\left[1 + \left(\frac{c}{c_0}\right)^2\right]^{-m} * c \tag{4.11}$$

The applicability of the generalized approach was evaluated by plotting the viscosity data using the modified ϕ_{eff} determined from Equation 4.11 (Figure 4.17a–d). Excellent agreement with the modified Krieger–Dougherty's model prediction was observed for moderate to high volume fraction, which strongly suggests that the physics of soft nanogels has been captured. At a volume fraction less than 0.1, good agreement with the Batchelor's equation is evident (see insets of Figure 4.17a–d). This semi-empirical model provides us with the capability to predict the viscosity, and describes the physics of compressibility of soft particles as a function of polymer concentration.

Another major contribution was credited to Cloitre *et al.* [83], who successfully computed the volume fraction of pH-responsive nanogels using the values calculated in Equation 4.6 for the swelling ratio. The Debye length associated with the counter-ions at concentration C_{in} was compared with the characteristic size of the nanogels:

$$\kappa_{\text{in}}^{-1} = (4\pi l_B N_A C_{\text{in}})^{-1/2} \tag{4.12}$$

where l_B is the Bjerrum length and N_A Avogadro's number. Only counter-ions in a peripheral shell of thickness κ_{in}^{-1} can leave the nanogels and diffuse in the solution, and the fraction of those counter-ions is:

$$\Gamma \cong 3\kappa_{\text{in}}^{-1}/R_h \tag{4.13}$$

At a higher nanogel concentration, the concentration of free counter-ions in the solution can be large enough to induce an osmotic deswelling of the nanogels and this phenomenon can be quantified using Equation 4.3–4.5, where C_{in} and C_{out} now take into account the existence of free counter-ions. The new expressions for C_{in} and C_{out} are given below [107]:

$$C_{\text{in}} = \alpha(1-\Gamma)\gamma c_0/\tilde{Q} \text{ and } C_{\text{out}} = \alpha\Gamma\gamma c_0\phi/\tilde{Q}(1-\phi) \tag{4.14}$$

where $\tilde{Q}$ is the swelling at finite concentration and ϕ is the volume fraction of nanogels in the solution. Solving Equations 4.4,4.5 and 4.14, the expression for the

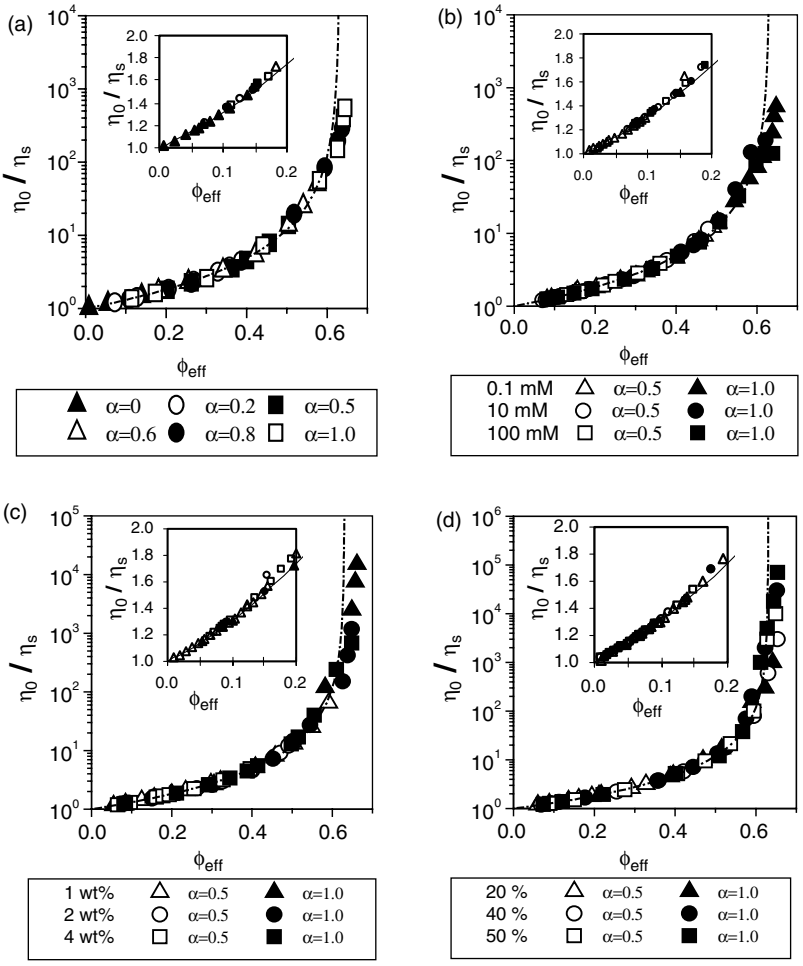

Figure 4.17 Relative low-shear viscosity versus effective volume fraction of crosslinked MAA-EA nanogel at 5 wt% polymer concentration and four different conditions: (a) varying neutralization degree, α of HASE-20-80-2 in salt-free solution; (b) varying salt concentrations (mM KCl) of HASE-20-80-2; (c) varying crosslinked density (wt% DAP) of nanogels with 20 mol% MAA in salt-free solution; and (d) varying molar ratio of MAA groups (% MAA) of 4 wt% crosslinked nanogels in salt-free solution. The solid lines and dotted lines denote the hard sphere behavior according to Equations 4.7 and 4.9, respectively [105].

swelling ratio at finite concentration, $\tilde{Q}$, as a function of the swelling ratio at infinite dilution Q is described by:

$$\frac{\tilde{Q}}{Q} = \left[1 - \frac{\Gamma}{1-\phi}\right]^{3/2}. \tag{4.15}$$

The volume of nanogels can reduce by one third near close packing ($\phi = 0.6$) and thus osmotic deswelling has important consequences on the flow behavior of

nanogels at high concentration. The mass concentration, c, of the dispersion in g ml^{-1} and ϕ are related through the simple relation:

$$\phi = \frac{\tilde{Q}}{V_m c_0}\frac{\varrho_s}{\varrho_p}c \tag{4.16}$$

where V_m is the molar volume of monomeric units, ϱ_s and ϱ_p are the specific mass of the suspension and polymer, respectively. Cloitre and coworkers [83] investigated the variations of the low-shear viscosity, η_0, with the concentration, c, of nanogels containing three different crosslinked densities as depicted in Figure 4.18a. The value of η_0 initially increases slowly with concentration, then rises sharply at a certain concentration, above which it is no longer accessible. The volume fraction of nanogels can be easily computed using the values calculated for the swelling ratio. In Figure 4.18b, the variation of the relative viscosity η_0/η_s with ϕ for the nanogels investigated (η_s is the viscosity of the solvent) was plotted and the data collapsed nicely onto a single curve, which is very close to the analytical form expected for a polydisperse hard sphere [99], $\eta_0/\eta_s=(1-\phi/\phi_m)^{-2}$. They emphasized that it is crucial to use $\tilde{Q}$ to calculate the volume fraction of nanogels whereas using Q would lead to an overestimation of the volume fraction by a large factor.

Tan *et al.* proposed a more accurate method, determining Γ by measuring the concentration of free counter-ions as a function of nanogel concentration using an ion-selective electrode (ISE) [106]. Measurements were conducted for MAA–EA nanogels and the values of Γ measured using ISE were compared with the values calculated from Equations 4.12 and 4.13. It is observed that Γ increased with nanogel concentration, thus the assumption that the variations of Γ with the swelling ratio

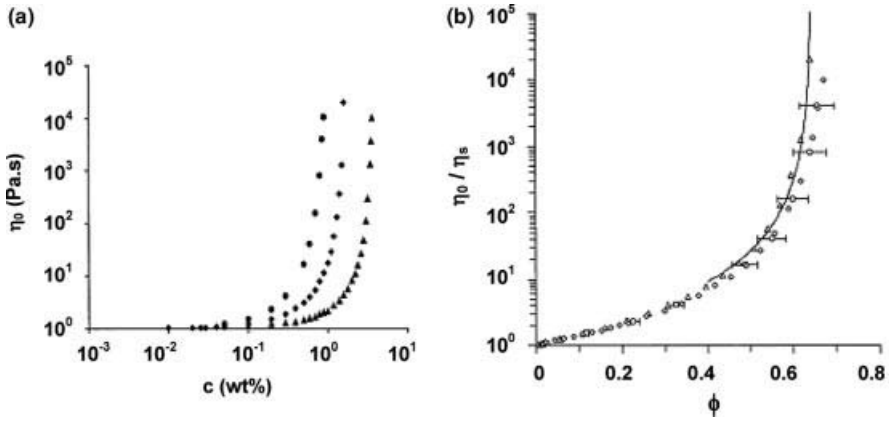

Figure 4.18 (a) Variations of the low-shear viscosity of nanogel suspensions with the polymer concentration for $N_x = 140$ (filled circles), $N_x = 70$ (filled diamonds), $N_x = 28$ (filled triangles). (b) Variations of the low-shear viscosity with the volume fraction of nanogels (open circles): $N_x = 140$; (open diamonds): $N_x = 70$ and (open triangles): $N_x = 28$. The solid line represents the variation expected for polydisperse brownian hard spheres [83].

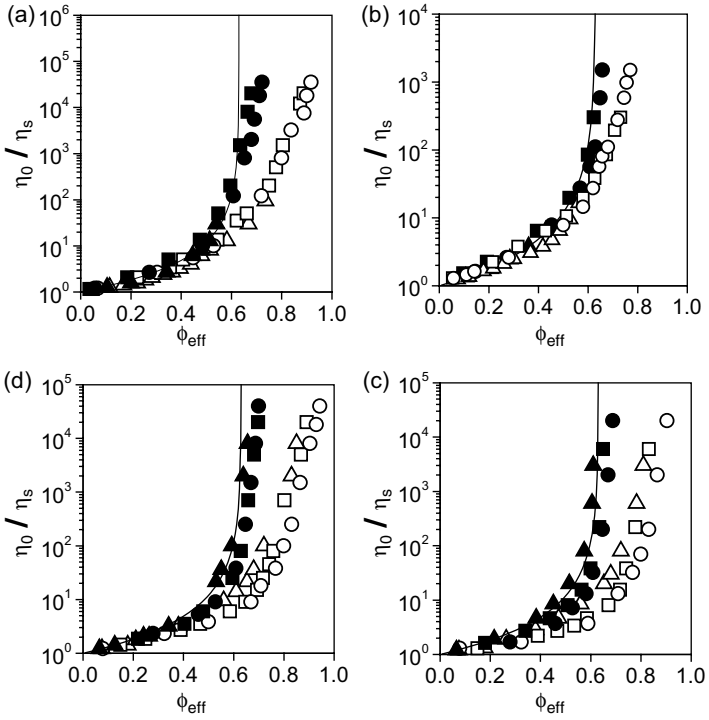

Figure 4.19 Relative low-shear viscosity versus effective volume fraction calculated from Equation 4.16 for crosslinked MAA–EA nanogel systems with varying crosslinked densities: (a) 1 wt%, (b) 2 wt% and varying MAA content; (c) 40 mol%, and (d) 50 mol% at three different α values (open triangles: $\alpha = 0.5$; open squares: $\alpha = 0.8$; open circles: $\alpha = 1.0$). The open symbols represent ϕ_{eff} determined when Γ was calculated from Equation 4.12 and 4.13, whereas the filled symbols represent ϕ_{eff} calculated from the values of Γ measured using Na^+ ion-selective electrodes. The solid line denotes the hard sphere behavior according to Equation 4.9 [106].

($\Gamma \sim Q^{1/6}$) were small at infinite dilution is no longer valid at higher nanogel concentration [83]. As discussed earlier, nanogel particles are highly swollen at large α, low crosslinked density, and high content of MAA, thus exhibiting strong dependence of Γ on particle concentration. The larger fraction of free counter-ions, Γ, resulted in stronger osmotic deswelling effect as described by Equation 4.15, which confirmed the earlier hypothesis that the specific volume, k, should decrease with increasing nanogel concentration. Figure 4.19 displays the corrected viscosity data with ϕ_{eff} determined from Equation 4.16 using Γ measured by ISE [106]. Within the experimental accuracy, the data agree well with the Krieger–Dougherty's model (Equation 4.9) for dilute to high volume fraction, unlike the deviation observed when Γ was calculated from Equations 4.12 and 4.13 (open symbols). It is critical to use Γ measured at different concentrations instead of that determined by Equations 4.12 and 4.13, as this will lead to an overestimation of the volume fraction.

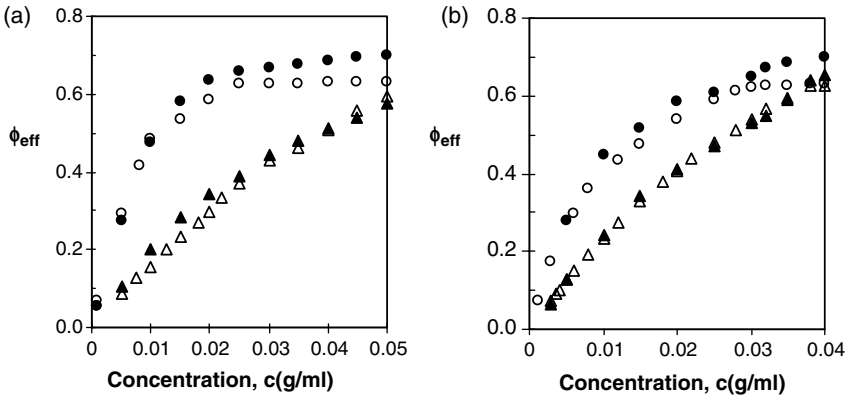

Figure 4.20 Comparison of values of ϕ_{eff} determined using the semi-empirical approach (Equation 4.11) (open symbols) with the theoretical approach (Equation 4.16), where values of Γ was measured using Na^+ ion-selective electrodes (filled symbols) of nanogel systems: (a) HASE-20-80-1 and (b) HASE-50-50-4 at two different α values (open triangles: $\alpha = 0.5$; open circles: $\alpha = 1.0$) [106].

The validity of the semi-empirical approach against the theoretical approach originally proposed by Cloitre and coworkers was evaluated [106]. The ϕ_{eff} determined using the semi-empirical approach (open symbols) proposed by Tan *et al.* (Equation 4.11) was compared with the theoretical approach (closed symbols) proposed by Cloitre and coworkers (Equation 4.16), for two MAA–EA nanogel systems as depicted in Figure 4.20. The ϕ_{eff} values determined from these two methods are in good agreement, which strongly suggests that the semi-empirical approach is able to capture the physics of soft nanogel particles and the form of Equation 4.11 has the ability to predict the relative viscosity of different systems. This is important evidence that the present model is valid for describing the physics of soft particles, which can then be used to predict the viscosity behavior of dilute and concentrated soft sphere systems.

4.7
Osmotic Compressibility of pH-Responsive Nanogels in Colloidal Suspensions

Previous discussion demonstrated that pH-responsive nanogel particles undergo osmotic deswelling with increasing particle concentration where the volume of nanogels can decrease significantly, depending on the nature of the soft particles and surrounding environment [31, 105, 106]. Thus, knowledge on the structural properties of nanogels is of specific importance since they are intimately connected to the particle interaction potentials. Understanding of these parameters permits us to quantitatively evaluate the factors governing particle osmotic compressibility as well as colloidal stability [108–110]. It was shown previously that turbidimetry is a suitable technique for the study of particle interactions in dilute and concentrated soft

colloidal suspensions since this method is practically insensitive towards multiple scattering, unlike light scattering techniques [111–115].

The turbidity, τ, is defined as the attenuation (weakening) of a light beam by scattering when passing through a sample. Thus, $\tau = l^{-1} \ln(I_0/I_t)$ with I_0 being the incident intensity of the light, I_t the transmitted intensity and l the length of the optical path. When absorption can be excluded, the intensity of the scattered light and the turbidity are related through the following relation:

$$\tau = 2\pi \int_0^{\pi} R(q) \sin\theta \, \mathrm{d}\theta \tag{4.17}$$

where $R(q)$ is the Rayleigh ratio for unpolarized light, $\mathrm{q} = (4\pi n_0/\lambda_0)\sin(\theta/2)$ is the magnitude of the scattering vector, θ the scattering angle, n_0 the refractive index of the medium, and λ_0 the wavelength in vacuum [111–113]. With the assumption that the size parameter $n_0\pi d/\lambda_0$, where d is the diameter of particles, is below unity, it is permissible to use the Rayleigh–Debye (RD) theory for the theoretical evaluation of turbidity, which is expected to provide a very good approximation [116]. The Rayleigh ratio, $R(q)$, is defined as $R(q) \propto cP(q)S(q,\phi)$, where c and ϕ are the mass concentration and volume fraction of the colloidal particles, respectively. In the region of low qR, the form factor, $P(q)$, and the structure factor, $S(q,\phi)$, can be approximated by $P(q) = 1 - 1/3(qR)^2 + 0(q^4R^4)$ and $S(q,\phi) = S(0,\phi) + \gamma(\phi)(qR)^2 + 0(q^4R^4)$ [108, 109]. Ballauff *et al.* tested these approximations by comparing the integrated structure factor calculated using the above approximations with the exact result obtained by integrating Equation 4.17 with the Percus–Yevick (PY) structure factor, $S_{PY}(0)$, given as $S_{PY}(0) = (1-\phi)^4/(1+2\phi)^2$, with ϕ being the volume fraction of hard spheres [111–113]. The calculations were carried out for 120 nm hard spheres, and there was good agreement between both methods for wavelengths greater than 500 nm. Insertion of $P(q)$ and $S(q,\phi)$ into $R(q)$ and subsequent integration of Equation 4.17 leads to [111, 115]:

$$\tau \propto cQ(\lambda^2)Z(\lambda^2, c) \tag{4.18}$$

where $Q(\lambda^2)$ is an integrated form factor and $Z(\lambda^2,c)$ is an integrated structure factor, $Z(\lambda^2,c) = S(0,c) + 0(1/\lambda^2)$. In the region of low concentrations, $Z(\lambda^2,c) \rightarrow 1$ (interparticle interferences are negligible). Hence, $(\tau/c)_{c=0} \propto Q(\lambda^2)$ and

$$Z(\lambda^2, c) = (\tau/c)/(\tau/c)_{c=0} \tag{4.19}$$

Equation 4.19 suggests that $Z(\lambda^2,c)$ can be calculated from a plot of (τ/c) as a function of c at fixed λ when the concentration is extrapolated to zero. Zukoski *et al.* plotted $Z(\lambda^2,c)$ as a function of $1/\lambda^2$ for 100 nm silica spheres and the intercept at each concentration is the structure factor $S(0)$ as depicted in Figure 4.21 [115].

Tan *et al.* utilized the turbidimetric analysis above to investigate the particle interaction of model pH-responsive PMAA–PEA nanogels in concentrated colloidal suspensions [117]. They reported that the osmotic compressibility of nanogels at various crosslinked densities and ionic strength falls onto a master curve when plotted against the effective volume fraction, which clearly suggests that particle

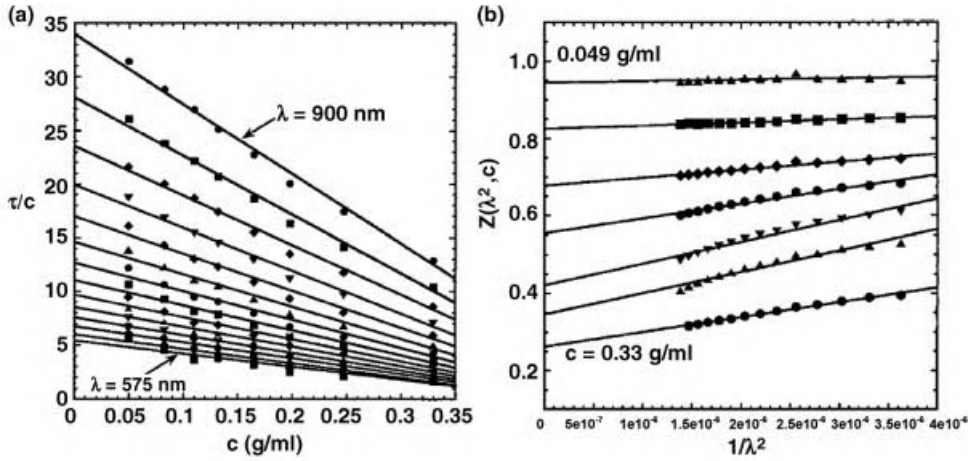

Figure 4.21 (a) Specific turbidity as a function of concentration for octadecyl silica in toluene without added polymer for different wavelengths. The solid lines are linear curve fits to the data to extract the intercept. (b) Integrated structure factor of the silica spheres as a function of $1/\lambda^2$ in the absence of polymer for different concentrations. The solid lines are linear curve fits to the data to extract the intercept, which equals the structure factor of the colloidal particles in the zero angle limit ($S_{cc}(0)$) [115].

interaction potential and osmotic compressibility is a function of volume fraction of nanogels. In addition, they examined the deviation, μ, of the osmotic compressibility, $S(0)$ of the PMAA–PEA nanogel systems from the hard sphere structure factor where the $S(0)$ of the nanogels was normalized against the osmotic compressibility of hard spheres, $S_{PY}(0)$ obtained from the PY theory to give Equation 4.20:

$$\mu = S(0) - S_{PY}(0)/(S_{PY}(0))_{\phi \to 0} \tag{4.20}$$

where $(S_{PY}(0))_{\phi \to 0}$ represents the structure factor of hard sphere when the volume fraction, ϕ, approaches zero [117]. When the deviation, μ, of nanogels at various crosslinked densities and salt concentrations was plotted against the volume fraction, all the data collapsed onto a single master curve (represented by the solid line in Figure 4.22), which clearly suggest that the deviation of $S(0)$ from the theoretical hard sphere structure factor, $S_{PY}(0)$ is a function of the volume fraction of nanogels. The maximum point at $\phi_{eff} \sim 0.2$ observed in Figure 4.22 further confirmed the hypothesis that points to the change in the conformation of nanogel particles with increasing volume fraction as depicted by the pictorial diagrams in Figure 4.22 [105, 106]. The osmotic pressure exerted by counter-ions trapped in large amounts of solvent impregnated in these soft nanogels contributed to the osmotic force inside the soft particle, thereby maintaining the particle conformation, whereas the free counter-ions in the solution induce an osmotic deswelling of the particle. Consequently, a critical volume fraction, ϕ_0 (~0.2), reflecting the conformational change of nanogel particles caused by the competition of these two kinds of interactions is observed [117].

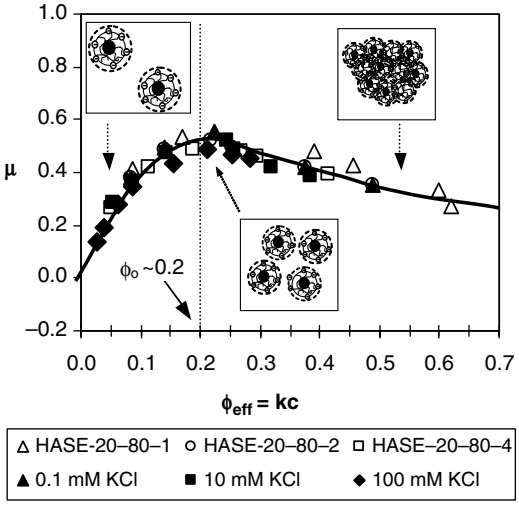

Figure 4.22 The deviation, μ, as a function of effective volume fraction, ϕ_{eff}, of fully neutralized nanogels with 20 mol% MAA at various crosslinked densities and salt concentrations. The solid line represents the master curve, which shows the trend of μ as a function of ϕ_{eff} [17].

4.8 Conclusions and Future Perspectives

Nanogel systems that are pH-responsive have been extensively studied, both from theoretical and from applied perspectives. Such colloidal systems can be synthesized through either emulsion polymerization or physical self-assembly of interactive polymers. Depending on the external conditions, the size of nanogels can vary significantly, from a swollen state at highly charged to a collapsed state in neutral conditions. The swelling characteristics can be modeled adequately by considering the osmotic pressure induced by counter-ions inside and outside the nanogels. Such physical insights can be extended to describe the bulk rheological properties, where the deswelling of nanogels as a function of particle concentration adequately describes the physics that is responsible for the bulk rheological properties.

The pH-responsive nanogels can be used for a wide range of applications. They are widely used as thickeners in coatings, food, and personal care product formulations. Encapsulation of active compounds, such as small molecular drugs, food additives, etc. are being explored. Potential use of these materials as stabilizers, colloidal scaffolds for preparing inorganic nanoparticles, gene and drug delivery are being actively explored. We envisage that increasing use of these materials in many disciplines will be realized once the systems are well understood and characterized.

References

1 Lopez, V.C. and Snowden, M.J. (2003) Colloidal microgels as potential control release devices. *Drug Deliv. Syst. Sci.*, **3**, 19–25.

2 Nayak, S., Lee, H., Chmielewski, J., and Lyon, L.A. (2004) Folate-mediated cell targeting and cytotoxicity using thermoresponsive microgels. *J. Am. Chem. Soc.*, **126** (33), 10258–10259.

3 Nolan, C.M., Reyes, C.D., Debord, J.D., Garcia, A.J., and Lyon, L.A. (2005) Phase transition behavior, protein adsorption, and cell adhesion resistance of poly (ethylene glycol) crosslinked microgel particles. *Biomacromolecules*, **6** (4), 2032–2039.

4 Varma, M.V.S., Kaushal, A.M., and Garg, S. (2005) Influence of micro-environmental pH on the gel layer behavior and release of a basic drug from various hydrophilic matrices. *J. Control. Release*, **103** (2), 499–510.

5 Lopez, V.C., Castro, H.J., and Snowden, M.J. (2005) The use of colloidal microgels as a (trans)dermal drug delivery system. *Int. J. Pharmac.*, **292** (1–2), 137–147.

6 Murthy, N., Thng, Y.X., Schuck, S., Xu, M.C., and Frechet, J.M.J. (2002) A novel strategy for encapsulation and release of proteins: Hydrogels and microgels with acid-labile acetal cross-linkers. *J. Am. Chem. Soc.*, **124** (42), 12398–12399.

7 Morris, G.E., Vincent, B., and Snowden, M.J. (1997) Adsorption of lead ions onto N-isopropylacrylamide and acrylic acid copolymer microgels. *J. Colloid Interface Sci.*, **190** (1), 198–205.

8 Retama, J.R., Lopez-Ruiz, B., and Lopez-Cabarcos, E. (2003) Microstructural modifications induced by the entrapped glucose oxidase in cross-linked polyacrylamide microgels used as glucose sensors. *Biomaterials.*, **24** (17), 2965–2973.

9 Guo, Z., Sautereau, H., and Kranbuehl, D.E. (2005) Structural evolution and heterogeneities studied by frequency-dependent dielectric sensing in a styrene/dimethacrylate network. *Macromolecules*, **38** (19), 7992–7999.

10 Bromberg, L., Temchenko, M., and Hatton, T.A. (2003) Smart microgel studies. Polyelectrolyte and drug-absorbing properties of microgels from polyether-modified poly(acrylic). *Langmuir.*, **19** (21), 8675–8684.

11 Hoare, T. and Pelton, R. (2004) Highly pH and temperature responsive microgels functionalized with vinylacetic acid. *Macromolecules*, **37** (7), 2544–2550.

12 Amalvy, J.I., Wanless, E.J., Li, Y., Michailidou, V., and Armes, S.P. (2004) Synthesis and characterization of novel pH-responsive microgels based on tertiary amine methacrylates. *Langmuir*, **20** (21), 8992–8999.

13 Neyret, S. and Vincent, B. (1997) The properties of polyampholyte microgel particles prepared by microemulsion polymerization. *Polymer*, **38** (25), 6129–6134.

14 Kaneda, I. and Vincent, B. (2004) Swelling behavior of PMMA-g-PEO microgel particles by organic solvents. *J. Colloid Interface Sci.*, **274** (1), 49–54.

15 Fernandez-Nieves, A. and Marquez, M. (2005) Electrophoresis of ionic microgel particles: From charged hard spheres to polyelectrolyte-like behavior. *J. Chem. Phys.*, **122** (8), 084702.

16 Shay, G.D. (1989) Alkali-swellable and alkali-soluble thickener technology, in *Polymers in Aqueous Media* (ed. J.E. Glass), ACS Advances in Chemistry Series, American Chemical Society, Washington, DC, pp. 457–493.

17 Bradna F P., Stern, P., Quadrat, O., and Snuparek, J. (1990) Thickening effect of dispersions of ethyl acrylate-methacrylic acid copolymer prepared by different polymerization routes. *Colloid Polym. Sci.*, **273** (4), 324–330.

18 Rodriguez, B.E., Wolfe, M.S., and Fryd, M. (1994) Nonuniform swelling of alkali swellable microgels.

Macromolecules, **27** (22), 6642–6647.

19 Kabanov, A.V. and Vinogradov, S.V. (2009) Nanogels as pharmaceutical carriers: finite networks of infinite capabilities. *Angew. Chem. Int. Ed.*, **48**, 5418–5429.

20 Bovey, F.A., Kolthoff, I.M., Medalia, A.I., and Meehan, E.J. (1965) *Emulsion Polymerization*, Interscience Publishers., New York.

21 Blakely, D.C. (1975) *Emulsion Polymerization. Theory and Practice*, Applied Science, London.

22 Eliseeva, V.I., Ivanchev, S.S., Kuchanov, S.I., and Lebedev, A.V. (1981) *Emulsion Polymerization and its Applications in Industry*, Consultants Bureau, New York.

23 Barton, J. and Capek, I. (1994) *Radical Polymerization in Dispersed Systems*, Ellis Horwood., New York.

24 Gilbert, R.G. (1995) *Emulsion Polymerization: A Mechanistic Approach*, Academic Press., London.

25 Fitch, R.M. (1997) *Polymer Colloids: A Comprehensive Introduction*, Academic Press., London.

26 Tirtaatmadja, V., Tam, K.C., and Jenkins, R.D. (1997) Rheological properties of model alkali-soluble associative (HASE) polymers: Effect of varying hydrophobe chain length. *Macromolecules*, **30** (11), 3271–3282.

27 Dai, S., Tam, K.C., Jenkins, R.D., and Bassett, D.R. (2000) Light scattering of dilute hydrophobically modified alkali-soluble emulsion solutions: Effects of hydrophobicity and spacer length of macromonomer. *Macromolecules*, **33** (19), 7021–7028.

28 Tan, B.H., Tam, K.C., Lam, Y.C., and Tan, C.B. (2005) Microstructure and rheology of stimuli-responsive microgel systems – effect of cross-linked density. *Adv. Colloid Interface Sci.*, **113** (2–3), 111–120.

29 Fonseca, T., Relogio, P., Martinho, J.M.G., and Farinha, J.P.S. (2007) Preparation and surface characterization of polymer nanoparticles designed for incorporation into hybrid materials. *Langmuir*, **23** (10), 5727–5734.

30 Jonsson, J., Karlssson, O.J., Hassander, H., and Tornell, B. (2007) Semi-continuous emulsion polymerization of styrene in the presence of poly(methyl methacrylate) seed particles. Polymerization conditions giving core–shell particles. *Eur. Polym. J.*, **43** (4), 1322–1332.

31 Tan, B.H., Tam, K.C., Lam, Y.C., and Tan, C.B. (2005) Microstructure and rheological properties of pH-responsive core-shell particles. *Polymer*, **46** (23), 10066–10076.

32 Tan, B.H., Ravi, P., and Tam, K.C. (2006) Synthesis and characterization of novel pH-responsive polyampholyte microgels. *Macromol. Rapid Commun.*, **27** (7), 522–528.

33 Landfester, K., Willert, M., and Antonietti, M. (2000) Preparation of polymer particles in nonaqueous direct and inverse miniemulsions. *Macromolecules*, **33**, 2370–2376.

34 Kriwet, B., Walter, E., and Kissel, T. (1998) Synthesis of bioadhesive poly(acrylic acid) nano- and microparticles using an inverse emulsion polymerization method for the entrapment of hydrophilic drug candidates. *J. Control. Release*, **56**, 149–158.

35 Sun, Q. and Deng, Y. (2005) *In situ* synthesis of temperature-sensitive hollow microspheres via interfacial polymerization. *J. Am. Chem. Soc.*, **127**, 8274–8275.

36 Liu, J., Zhang, Q., Remsen, E.E., and Wooley, K.L. (2001) Nanostructured materials designed for cell binding and transduction. *Biomacromolecules*, **2**, 362–368.

37 McAllister, K., Sazani, P., Adam, M., Cho, M.J., Rubinstein, M., Samulski, R.J., and DeSimone, J.M. (2002) Polymeric nanogels produced via inverse microemulsion polymerization as potential gene and antisense delivery agents. *J. Am. Chem. Soc.*, **124** (51), 15198–15207.

38 Oh, J.K., Tang, C., Gao, H., Tsarevsky, N.V., and Matyjaszewski, K. (2006) Inverse miniemulsion ATRP: a

new method for synthesis and functionalization of well-defined water-soluble/cross-linked polymeric particles. *J. Am. Chem. Soc.*, **128**, 5578–5584.

39 Oh, J.K., Siegwart, D.J., Lee, H.I., Sherwood, G., Peteanu, L., Hollinger, J.O., Kataoka, K., and Matyjaszewski, K. (2007) Biodegradable nanogels prepared by atom transfer radical polymerization as potential drug delivery carriers: Synthesis, biodegradation, in vitro release, and bioconjugation. *J. Am. Chem. Soc.*, **129**, 5939–5945.

40 Nayak, S. and Lyon, L.A. (2005) Soft nanotechnology with soft nanoparticles. *Angew. Chem. Int. Ed.*, **44**, 7686–7708.

41 Pelton, R.H. and Chibante, P. (1986) Preparation of aqueous lattices with N-isopropylacrylamide. *Colloid Surface*, **20** (3), 247–256.

42 Saunders, B.R. and Vincent, B. (1997) Osmotic de-swelling of polystyrene microgel particles. *Colloid Polym. Sci.*, **275** (1), 9–17.

43 Saunders, B.R., Crowther, H.M., and Vincent, B. (1997) Poly[(methyl methacrylate)-co-(methacrylic acid)] microgel particles: Swelling control using pH, cononsolvency, and osmotic deswelling. *Macromolecules*, **30** (3), 482–487.

44 Wooley, K.L. (1997) From dendrimers to knedel-like structures. *Chem. Eur. J.*, **3** (9), 1397–1399.

45 Booth, C. and Attwood, D. (2000) Effects of block architecture and composition on the association properties of poly (oxyalkylene) copolymers in aqueous solution. *Macromol. Rapid. Commun.*, **21**, 501–527.

46 Riess, G. (2003) Micellization of block copolymers. *Prog. Polym. Sci.*, **28**, 1107–1170.

47 Zamurovic, M., Christodoulou, S., Vazaios, A., Iatrou, E., Pitsikalis, M., and Hadjichristidis, N. (2007) Micellization behavior of complex comblike block copolymer architectures. *Macromolecules*, **40**, 5835–5849.

48 Castro, E., Barbosa, S., Juarez, J., Taboada, P., Katime, I.A., and Mosquera, V. (2008) Influence of external factors on the micellization process and aggregate structure of poly(oxy)styrene-poly(oxy)ethylene block copolymers. *J. Phys. Chem. B*, **112**, 5296–5304.

49 Denkova, A.G., Mendes, E., and Coppens, M.O. (2008) Effects of salts and ethanol on the population and morphology of triblock copolymer micelles in solution. *J. Phys. Chem. B*, **112**, 793–801.

50 Bang, J., Viswanathan, K., Lodge, T.P., Park, M.J., and Char, K. (2004) Temperature-dependent micellar structures in poly(styrene-b-isoprene) diblock copolymer solutions near the critical micelle temperature. *J. Chem. Phys.*, **121**, 11489–11500.

51 Jansson, J., Schillen, K., Olofsson, G., da Silva, R.C., and Loh, W. (2004) The interaction between PEO-PPO-PEO triblock copolymers and ionic surfactants in aqueous solution studied using light scattering and calorimetry. *J. Phys. Chem. B*, **108**, 82–92.

52 Lin, Y.N. and Alexandridis, P. (2002) Cosolvent effects on the micellization of an amphiphilic siloxane graft copolymer in aqueous solutions. *Langmuir*, **18**, 4220–4231.

53 Thurmond, K.B. II, Kowalewski, T., and Wooley, K.L. (1996) Water-soluble knedel-like structures: The preparation of shell-cross-linked small particles. *J. Am. Chem. Soc.*, **118** (30), 7239–7240.

54 Huang, H., Remsen, E.E., Kowalewski, T., and Wooley, K.L. (1999) Nanocages derived from shell cross-linked micelle templates. *J. Am. Chem. Soc.*, **121** (15), 3805–3806.

55 Wooley, K.L. (2000) Shell crosslinked polymer assemblies: Nanoscale constructs inspired from biological systems. *J. Polym. Sci. Polym. Chem.*, **38** (9), 1397–1407.

56 Zhang, Q., Remsen, E.E., and Wooley, K.L. (2000) Shell cross-linked nanoparticles containing hydrolytically degradable, crystalline core domains. *J. Am. Chem. Soc.*, **122** (15), 3642–3651.

57 Huang, H., Kowalewski, T., Remsen, E.E., Gertzmann, R., and Wooley, K.L. (1997) Hydrogel-coated

glassy nanospheres: A novel method for the synthesis of shell cross-linked knedels. *J. Am. Chem. Soc.*, **119** (48), 11653–11659.

58 Ma, Q., Remsen, E.E., Kowalewski, T., Schaefer, J., and Wooley, K.L. (2001) Environmentally-responsive, entirely hydrophilic, shell cross-linked (SCK) nanoparticles. *Nano Lett.*, **1** (11), 651–655.

59 Nieuwenhuis, E.A. and Vrij, A. (1979) Light-scattering of PMMA latex-particles in benzene – structural effects. *J. Colloid Interface Sci.*, **72** (2), 321–341.

60 McPhee, W., Tam, K.C., and Pelton, R. (1993) Poly(N-isopropylacrylamide) latices prepared with sodium dodecyl-sulfate. *J. Colloid Interface Sci.*, **156** (1), 24–30.

61 Pelton, R. (2000) Temperature-sensitive aqueous microgels. *Adv. Colloid Interface Sci.*, **85** (1), 1–33.

62 Hoare, T. and Mclean, D. (2006) Kinetic prediction of functional group distributions in thermosensitive microgels., *J. Phys. Chem. B*, **110** (41), 20327–20336.

63 Hoare, T. and Pelton, R. (2004) Highly pH and temperature responsive microgels functionalized with vinylacetic acid. *Macromolecules*, **37** (1), 2544–2550.

64 Hoare, T. and Pelton, R. (2004) Functional group distributions in carboxylic acid containing poly (N-isopropylacrylamide) microgels. *Langmuir*, **20** (6), 2123–2133.

65 Hoare, T. and Mclean, D. (2006) Multi-component kinetic modeling for controlling local compositions in thermosensitive polymers. *Macromol. Theory Simul.*, **15** (8), 619–632.

66 Hoare, T. and Pelton, R. (2005) Electrophoresis of functionalized microgels: morphological insights. *Polymer*, **46** (4), 1139–1150.

67 Hoare, T. and Pelton, R. (2006) Titrametric characterization of pH-induced phase transitions in functionalized microgels. *Langmuir*, **22** (17), 7342–7350.

68 Hoare, T. and Pelton, R. (2006) Dimensionless plot analysis: A new way to analyze functionalized microgels. *J. Colloid Interface Sci.*, **303** (1), 109–116.

69 Hoare, T. and Pelton, R. (2007) Calorimetric analysis of thermal phase transitions in functionalized microgels. *J. Phys. Chem. B*, **111** (6), 1334–1342.

70 Hoare, T. and Pelton, R. (2007) Engineering glucose swelling responses in poly(N-isopropylacrylamide)-based microgels. *Macromolecules*, **40** (3), 670–678.

71 Saunders, B.R. and Vincent, B. (1999) Microgel particles as model colloids: theory, properties and applications. *Adv. Colloid Interface Sci.*, **80** (1), 1–25.

72 Sawai, T., Yamazaki, S., Ikariyama, Y., and Aizawa, M. (1991) pH-responsive swelling of the ultrafine microsphere. *Macromolecules*, **24** (8), 2117–2118.

73 Eichenbaum, G.M., Kiser, P.F., Dobrynin, A.V., Simon, S.A., and Needham, D. (1999) Investigation of the swelling response and loading of ionic microgels with drugs and proteins: The dependence on cross-link density. *Macromolecules*, **32** (15), 4867–4878.

74 Madeline, T.L. and Peppas, N.A. (1999) Molecular design and in vitro studies of novel pH-sensitive hydrogels for the oral delivery of calcitonin. *Macromolecules*, **32** (20), 6646–6651.

75 Kihara, N., Adachi, Y., Nakao, K., and Fukutomi, T. (1998) Reaction of methyl thioglycolate with chloromethylstyrene microgel: Preparation of core-shell-type microgel by chemical modification. *J. Appl. Polym. Sci.*, **69** (9), 1863–1873.

76 Schulz, S.F., Gisler, T., Borkovec, M., and Sticher, H. (1994) Surface-charge on functionalized latex spheres in aqueous colloidal suspensions. *J. Colloid Interface Sci.*, **164** (1), 88–98.

77 Harding, I.H. and Healy, T.W. (1982) Purification of amphoteric polystyrene latex colloids. *J. Colloid Interface Sci.*, **89** (1), 185–201.

78 Homola, A. and James, R.O. (1977) Preparation and characterization of

amphoteric polystyrene lattices. *J. Colloid Interface Sci.*, **59** (1), 123–134.

79 Das, M. and Kumacheva, E. (2006) From polyelectrolyte to polyampholyte microgels: comparison of swelling properties. *Colloid Polym. Sci.*, **284** (10), 1073–1084.

80 Amalvy, J.I., Wanless, E.J., Li, Y., Michailidou, V., and Armes, S.P. (2004) Synthesis and characterization of novel pH-responsive microgels based on tertiary amine methacrylates. *Langmuir*, **20** (21), 8992–8999.

81 Wolfe, M.S. and Scopazzi, C. (1989) Rheology of swellable microgel dispersions-influence of crosslink density. *J. Colloid Interface Sci.*, **133** (1), 265–277.

82 Antonietti, M., Bremser, W., and Schmidt, M. (1990) Microgels-model polymers for the cross-link state. *Macromolecules*, **23** (16), 3796–3805.

83 Cloitre, M., Borrega, R., Monti, F., and Leibler, L. (2003) Structure and flow of polyelectrolyte microgels: from suspensions to glasses. *C. R. Phys.*, **4** (2), 221–230.

84 Snowden, M.J., Chowdhry, B.Z., Vincent, B., and Morris, G.E. (1996) Colloidal copolymer microgels of N-isopropylacrylamide and acrylic acid: pH, ionic strength and temperature effects. *J. Chem. Soc. Faraday Trans.*, **92** (24), 5013–5016.

85 Ricka, J. and Tanaka, T. (1984) Swelling of ionic gels – quantitative performance of the Donnan theory. *Macromolecules*, **17** (12), 2916–2921.

86 Flory, P.J. and Erman, B. (1982) Theory of elasticity of polymer networks. *Macromolecules*, **15** (3), 800–806.

87 Beltran, S., Baker, J.P., Hooper, H.H., Blanch, H.W., and Prausnitz, J.M. (1991) Swelling equilibria for weakly ionizable, temperature-sensitive hydrogels. *Macromolecules*, **24** (2), 549–551.

88 Ohmine, I. and Tanaka, T. (1982) Potential-energy surfaces for water dynamics – reaction coordinates, transition-states and normal mode analyses. *J. Chem. Phys.*, **91** (10), 6318–6327.

89 Kaggwa, G.B., Carey, M.J., Such, C., and Saunders, B.R. (2003) A new family of water-swellable microgel particles. *J. Colloid Interface Sci..*, **257** (2), 392–397.

90 Tan, B.H., Tam, K.C., Lam, Y.C., and Tan, C.B. (2004) Microstructure and rheology of stimuli-responsive nanocolloidal systems-effect of ionic strength. *Langmuir*, **20** (26), 11380–11386.

91 Crowther, H.M., Saunders, B.R., Mears, S.J., Cosgrove, T., Vincent, B., King, S.M., and Yu, G.E. (1999) Poly (NIPAM) microgel particle de-swelling: A light scattering and small-angle neutron scattering study. *Colloid Surface A*, **152** (3), 327–333.

92 Wolfe, M.S. (1992) Dispersion and solution rheology control with swellable microgels. *Prog. Org. Coat.*, **20** (3–4), 487–500.

93 Senff, H., Richtering, W., Norhausen, A., Weiss, A., and Ballauff, M. (1999) Rheology of a temperature sensitive core-shell latex. *Langmuir*, **15** (1), 102–106.

94 Senff, H. and Richtering, W. (1999) Temperature sensitive microgel suspensions: Colloidal phase behavior and rheology of soft spheres. *J. Chem. Phys.*, **111** (4), 1705–1711.

95 Senff, H. and Richtering, W. (2000) Influence of cross-link density on rheological properties of temperature-sensitive microgel suspensions. *J. Colloid Polym. Sci.*, **278** (9), 830–840.

96 Ballauff, M. (2003) Nanoscopic polymer particles with a well-defined surface: Synthesis, characterization, and properties. *Macromol. Chem. Phys.*, **204** (2), 220–234.

97 Krieger, I.M. (1972) Rheology of monodisperse latices. *Adv. Colloid Interface Sci.*, **3** (2), 111–136.

98 Batchelor, G.K. (1977) Effect of Brownian-motion on bulk stress in a suspension of spherical particles. *J. Fluid Mech.*, **83**, 97–117.

99 Van der Werff, J.C. and De Kruif, C.G. (1989) Hard sphere colloidal dispersions: the scaling of rheological properties with

particle size, volume fraction, and shear rate. *J. Rheol.*, **33** (3), 421–455.

100 Onoda, G.Y. and Liniger, E.G. (1990) Random loose packings of uniform spheres and the dilatancy onset. *Phys. Rev. Lett.*, **64** (22), 2727–2730.

101 Lionberger, R.A. and Russel, W.B. (2010) High-frequency modulus of hard-sphere colloids. *J. Rheol.*, **38** (6), 1885–1908.

102 Shikata, T. and Pearson, D.S. (1994) Viscoelastic behavior of concentrated spherical suspensions. *J. Rheol.*, **38** (3), 601–616.

103 Meeker, S.P., Poon, W.C.K., and Pusey, P.N. (1997) Concentration dependence of the low-shear viscosity of suspensions of hard-sphere colloids. *Phys. Rev. E*, **55** (5), 5718–5722.

104 Horn, F.M., Richtering, W., Bergenholtz, J., Willenbacher, N., and Wagner, N.J. (2000) Hydrodynamic and colloidal interactions in concentrated charge-stabilized polymer dispersions. *J. Colloid Interface Sci.*, **225** (1), 166–167.

105 Tan, B.H., Tam, K.C., Lam, Y.C., and Tan, C.B. (2004) A semi-empirical approach for modeling charged soft microgel particles. *J. Rheol.*, **48** (4), 915–926.

106 Tan, B.H., Tam, K.C., Lam, Y.C., and Tan, C.B. (2004) Dynamics and microstructure of charged soft nano-colloidal particles. *Polymer*, **45** (16), 5515–5523.

107 Borrega, R., Cloitre, M., Betremieux, I., Ernst, B., and Leibler, L. (1999) Concentration dependence of the low-shear viscosity of polyelectrolyte micro-networks: From hard spheres to soft microgels. *Europhys. Lett.*, **47** (6), 729–735.

108 Hunter, R.J. (1991) *Foundations of Colloid Science*, Vol. 1, Clarendon Press, Oxford.

109 Hunter, R.J. (1991) *Foundations of Colloid Science*, Vol. 2, Clarendon Press, Oxford.

110 Candau, F. and Ottewill, R.H. (1990) *An Introduction to Polymer Colloids*, Kluwer Academic Publishers, Dordrecht.

111 Apfel, U., Grunder, R., and Ballauff, M. (1994) A turbidity study of particle interaction in a latex suspensions. *Colloid Polym. Sci.*, **272** (7), 820–829.

112 Apfel, U., Grunder, R., and Ballauff, M. (1995) Precise analysis of the turbidity spectra of a concentrated latex. *Langmuir*, **11** (9), 3401–3407.

113 Weiss, A., Potschke, D., and Ballauff, M. (1996) Study of particle interaction in a highly concentrated latex by turbidimetry. *Acta Polym.*, **47** (8), 333–339.

114 Weiss, A., Horner, K.D., and Ballauff, M. (1999) Analysis of attractive interactions between latex particles in the presence of nonadsorbing polymers by turbidimetry. *J. Colloid Interface Sci.*, **213** (2), 417–425.

115 Ramakrishnan, S., Fuchs, M., Schweizer, K.S., and Zukoski, C.F. (2002) Concentration fluctuations in a model colloid-polymer suspension: Experimental tests of depletion theories. *Langmuir*, **18** (4), 1082–1090.

116 Kerker, M. (1969) Chapter 8, in *The Scattering of Light and Other Electromagnetic Radiation*, Academic Press, New York.

117 Tan, B.H., Tam, K.C., Lam, Y.C., and Tan, C.B. (2005) Osmotic compressibility of soft colloidal systems. *Langmuir*, **21** (10), 4283–4290.

5
Poly(*N*-Vinylcaprolactam) Nano- and Microgels

Cheng Cheng and Andrij Pich

5.1
Introduction

This chapter focuses on the chemical design of multifunctional nano- and microgels based on poly(*N*-vinylcaprolactam) (PVCL). *N*-Vinylcaprolactam belongs to the family of poly(*N*-vinylamides) which have been intensively studied in recent decades because of their interesting physicochemical properties in aqueous solutions and biocompatibility. Here, we describe the basic properties of *N*-vinylcaprolactam and briefly discuss the synthesis of poly(*N*-vinylcaprolactam) by radical precipitation polymerization as well as the relationship of conformational state of the monomer and microstructure of the main chain. The major focus is on the various approaches for synthesis of aqueous PVCL-based colloids with variable chemical composition, size, crosslinking degree, surface charge, and volume phase transition temperature (VPTT).

5.2
Poly(*N*-Vinylcaprolactam): Synthesis, Structure and Properties in Solution

A large variety of water-soluble poly(*N*-vinylamide) polymers have been intensively investigated in recent decades [1]. The main reasons for the increased scientific interest in these is their structural similarity to proteins (amide-containing polymers) and their extraordinary properties in aqueous systems.

The poly(*N*-vinylamide) family includes poly(*N*-vinylformamide) (PVF), poly(*N*-vinylacetamide) (PVAc), and poly(*N*-vinyl-*N*-(alkyl)acetamide). The most important representatives of the cyclic poly(*N*-vinylamides) are poly(vinylpyrrolidone) (PVP) and poly(*N*-vinylcaprolactam) (PVCL), polymers widely used in medical [2], pharmaceutical [3–6], and cosmetic [7] applications.

N-Vinylcaprolactam (VCL) has a ring that consists of seven carbon atoms and cannot have a flat conformation (Figure 5.1a). It is well known [8] that the cycloheptane ring can have various forms, such as the "chair", "bath," and "twist bath" conformations. But the presence of the rigid double bond in the cycloheptene

Hydrogel Micro and Nanoparticles, First Edition. Edited by L. Andrew Lyon and Michael Joseph Serpe.
© 2012 Wiley-VCH Verlag GmbH & Co. KGaA. Published 2012 by Wiley-VCH Verlag GmbH & Co. KGaA.

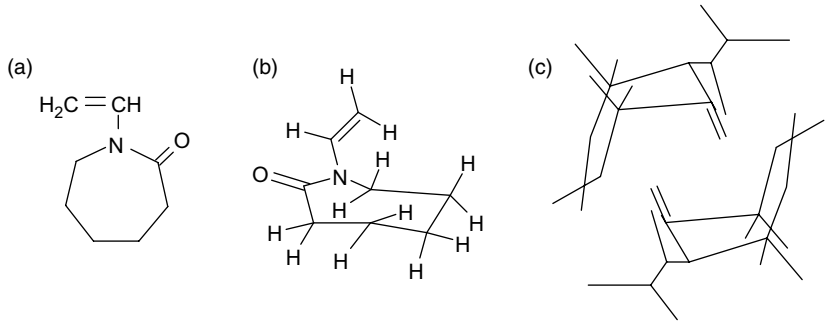

Figure 5.1 Chemical structure of *N*-vinylcaprolactam (a) its structure determined by quantum-chemical calculation (b) and ordering of *N*-vinylcaprolactam molecules in a crystal. Reprinted with permission from [10] by Elsevier.

excludes a pseudo-transformation ("chair"–"bath") and reduces the number of forms. Creation of the conformer "bath" is unprofitable due to repulsion of the carbon atoms on the "nose of the bath" and carbons of the double bonds. The most favorable conformation for the cycloheptene is the "chair" conformation, which is also favorable for the 4-cyclohepten-1-on. In analogy to cycloheptane, a seven-membered ring of VCL which holds a "chair" conformation having a rigid structure attributed to the rigid mid part connecting with double bonds has been proved by theoretical and experimental investigations [9, 10] (Figure 5.1b).

Most poly(*N*-vinylamides) can be polymerized by radical mechanisms using different initiators in bulk or in different solvents. However, some initiators such as benzoyl peroxide are quite ineffective in radical polymerization of VCL in alcohols and lead to polymer yields around 10–30% [11]. The reason for such behavior is the formation of benzoic acid after reaction of primary radicals with alcohol molecules [12]. The appearance of H^+ in the reaction system accelerates side-reactions and leads to formation of *N*-(α-oxyethyl)amides. The polymerization of vinylamides cannot be initiated by persulfates ($Na_2S_2O_8$) in water because of the more probable reaction of oxidation and hydrolysis of the ring [13, 14]. Polymerization of VCL initiated by different agents has been investigated by Solomon *et al.* [15–17]. The most suitable initiators were found to be *tert*-butyl peroxide, cumene hydroxide, and Trigonox A 75 at elevated temperatures (80–100 °C). The most effective initiator is 2,2′- azobisisobutyronitrile (AIBN) which in relatively low concentrations leads to high conversions in the temperature range 60–80 °C. The reaction rate was found to be proportional to $[I]^{0.5}$ and the following equation for the overall reaction rate is applicable:

$$\nu = k\,[I]^{0.5}[M] \tag{5.1}$$

where ν is the rate of polymerization; k is the constant of polymerization; $[I]$, $[M]$ are concentrations of initiator and monomer, respectively. Calculated from experimental data, $k_{70} = 0.07$; $k_{75} = 0.12$; $k_{80} = 0.19\,\mathrm{l\,(mol\,min)^{-1}}$ and the activation energy was $25 \pm 2\,\mathrm{kcal\,mol^{-1}}$. It was reported that the molecular oxygen influences the reaction

by decreasing the polymerization rate and reduction of the molecular weight of the polymer. Eisele *et al*. [18] described polymerization of VCL in benzene and water with AIBN (in the latter case an emulsifier was used). Redox initiating systems ($NaHSO_2 + tert$-butyl peroxide or $NH_3 + H_2O_2$) were also tested. PVCL polymers with molecular weights from $2\times10^4\,g\,mol^{-1}$ to $1\times10^6\,g\,mol^{-1}$ were obtained. Polymers with smaller molecular weights up to $2\times10^4\,g\,mol^{-1}$ can be obtained in *iso*-propanol [19]. In this case the solvent plays a role of a chain-transfer agent. Synthesis of PVCL with high molecular weight by γ-irradiation is also reported [20, 21].

The main chain of PVCL has a syndiotactic structure [22]. This architecture can be well understood after consideration of the structural occupation of molecules in cells of the crystal. Two molecules of VCL in the "chair" conformation create these cells by the packing of these "chairs" in a "seat-on-seat" structure with oppositely directed "backs" (Figure 5.1c) [10]. In this structure the double bonds are far from each other and one can assume that similar structural associations are present in solution and near the growing radical. This means that for the effective addition of the VCL monomer to the growing oligoradical chain, special orientation of the bulky caprolactam ring is required. Accordingly, the syndiotactic microstructure of the PVCL chains provides minimal repulsion between caprolactam rings.

PVCL is soluble in a variety of solvents such as water, alcohols (methanol, ethanol, propanol, etc.), amides (DMF), chlorinated hydrocarbons (CH_2Cl_2, CCl_4) and aromatic hydrocarbons (toluene, benzene, xylol). It is not soluble in hydrocarbons and ketones [22].

Several authors have studied the behavior of PVCL in water by dynamic and static light scattering methods and showed scaling relations of the average radius of gyration and translation diffusion coefficients with weight-average molecular weights, but their results differ. According to Eisele and Burchard [18] these scaling laws are

$$< r^2 >= 1.77 \times 10^{-18}\, M_w^{1.15} \tag{5.2}$$

$$D_z = 1 \times 10^{-4}\, M_w^{-0.52} \tag{5.3}$$

but according to Lau and Wu [23] these relations are

$$R_g = 2.94 \times 10^{-2} M_w^{0.54} \tag{5.4}$$

$$D_z = 7.93 \times 10^{-5} M_w^{-0.505} \tag{5.5}$$

where R_g is the average radius of gyration ($R_g = <s^2>^{1/2}$), D_z is the translation diffusion coefficient, M_w is the weight-average molecular weight.

Different values of refractive index increment dn/dc for determination of M_w were reported in these studies. The refractive index increment was in the range from 0.16 to $0.206\,ml\,g^{-1}$. Eisele and Burchard [18] also showed the independence of dn/dc on

laser wavelength for PVCL. The Kuhn–Mark–Houwink equation for PVCL in water at 25 °C [24] is as follows:

$$[\eta] = 0.0105 M_{\eta}^{0.69} \tag{5.6}$$

where $[\eta]$ is intrinsic viscosity (in $cm^3\,g^{-1}$) and M_η is viscosity-average molecular weight.

The molecular weight and molecular weight distribution of PVCL cannot be correctly determined using size exclusion chromatography in most solvents because of the sorption on the column. However, the determination of molecular weight distribution in chloroform with the addition of LiCl using a special type of column has been reported [10].

5.3 Thermal Behavior of Poly(*N*-Vinylcaprolactam) in Water

PVCL is soluble in water in a temperature range between 0 and 30 °C. The heating of the aqueous PVCL solution above 32 °C (lower critical solution temperature (LCST)) leads to phase separation and precipitation of the polymer [25–27]. The temperature of phase separation of PVCL (cloud point) strongly depends on the molecular weight of the polymer (Figure 5.2a) [28]. The most significant increase of transition temperature happens for polymers with a low molecular weight. In the range 2×10^5–$5\times10^4\,g\,mol^{-1}$, the cloud point increases slightly from 32.5 to 35–36 °C; in the range 5×10^4–$6\times10^3\,g\,mol^{-1}$, T_{tr} increases sharply from 36 to 51 °C.

Tager *et al.* [29] showed for PVCL with $M_w = 5\times10^5\,g\,mol^{-1}$ a change of cloud point from 32 to 34 °C depending on the concentration of the polymer in solution. Meeussen *et al.* [19] estimated phase diagrams for polymers with different molecular weights (Figure 5.2b). The concentration of the PVCL polymer in aqueous solution increases the transition temperature. For PVCL with $M_w < 20\times10^3\,g\,mol^{-1}$ in the concentration range from 0.4 to 30 wt% in water solution there is no influence on

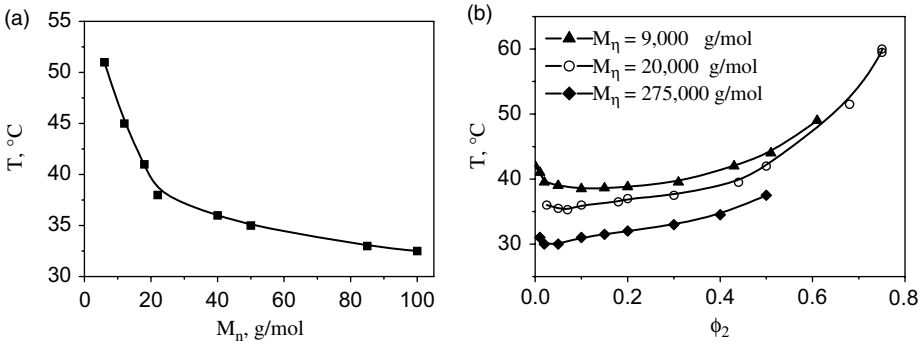

Figure 5.2 (a) Dependence of the cloud temperature of PVCL in water on M_w ($\times 10^3$) of polymer (polymer concentration 0.4%). Reprinted with permission from [28]. (b) Phase diagram PVCL–water for polymers with different molecular weights. Reprinted with permission from [19].

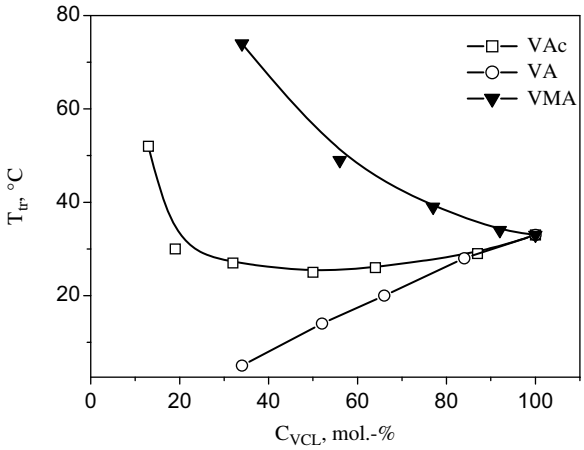

Figure 5.3 Dependence of the phase separation temperature on chemical composition of VCL copolymers with: (1) *N*-vinyl-*N*-methylacetamide (VMA); (2) vinyl alcohol (VA); and (3) vinylacetate (VAc). Reprinted from [27].

transition temperature and it is only in the higher concentration range that this temperature increases.

The incorporation of hydrophilic or hydrophobic monomers in PVCL chains shifts the phase separation temperature to higher or lower values respectively (Figure 5.3) [25, 27]. The presence of *N*-vinyl-*N*-methylacetamide units in the PVCL chain leads to an increase of the phase transition temperature in water up to 75 °C. The incorporation of hydrophobic vinylacetate units decreases the phase separation temperature to 3 °C. For PVCL chains containing monomers with OH groups the change of the phase separation temperature is different. The increase in vinyl alcohol (VA) units in the copolymer structure reduces the phase separation temperature, but if the VCL becomes a minor component in the copolymer the phase separation temperature increases. The minimum in this curve is observed at the equimolar VCL : VA composition, which indicates that the reason for such complex behavior is possibly formation of hydrogen bonds between the OH groups of VA and the C=O groups of VCL.

The hydration mechanism of PVCL chains in water has been investigated using differential scanning calorimetry (DSC) [10, 30] and infrared (IR) spectroscopy [31, 32]. DSC thermograms indicate the absence of an endothermic peak for the melting of ice crystals in the aqueous phase even at extremely low PVCL concentrations (0.15 mol l^{-1}). This behavior is different from other poly(*N*-vinylamides) where such a peak is present up to a polymer concentration of 2 mol l^{-1}. In the case of solid PVCL with $M_n = 21 \times 10^3$ g mol^{-1}, only one peak of the heat capacity in the range of 140–150 °C can be seen in DSC thermograms ($T_g = 147$ °C; $\Delta c_p = 0.11$ J $(g\,K)^{-1}$) [10].

The absence of a melting point characterizes PVCL as a rigid-chain, amorphous polymer. The presence of water molecules leads to rapid reduction of T_g to −38 °C due to the plasticizing action of water molecules (Figure 5.4a). The water molecules

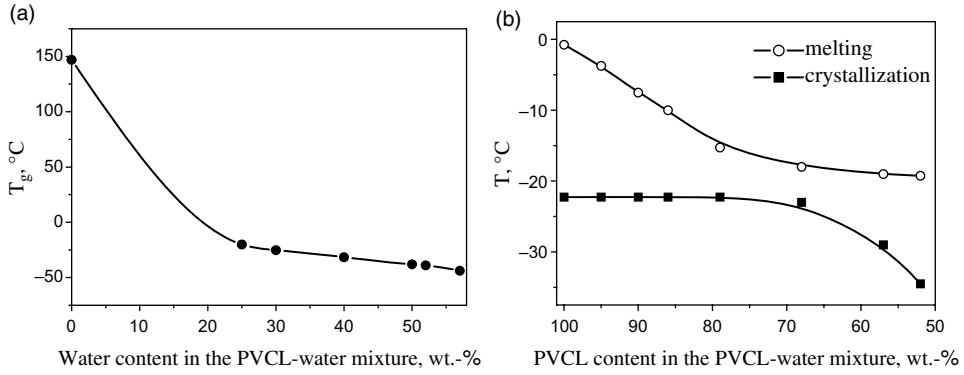

Figure 5.4 (a) Glass temperature of PVCL in the presence of water. (b) Melting and crystallization of water in the presence of PVCL. Reprinted with permission from [10].

interact with carbonyls of amide groups by formation of the hydrogen bonds and thus weaken the dipole–dipole interactions between C=O bonds. Consequently, the dispersive interactions between nonpolar segments of the polymer chains become weaker due to the increase in interchain distance. The phase diagram of the PVCL–water system is shown in Figure 5.4b. The crystalline phase appears in the system starting from a water content of 55 wt% (or 8.1 water molecules per VCL monomer unit). The rapid decrease in T_m and T_{cr} due to the increase of the polymer concentration indicates formation of defects in the ice structures.

Based on the above results, Kirsh *et al.* [10] formulated the mechanism of the interactions between PVCL chains and water molecules. In the presence of a small amount of water, the polymer and water form polymer–hydrate complexes. Each of the dipoles of the carbonyl groups is able to bind a maximum of two molecules of water directly (1 and 3 in Figure 5.5). Other water molecules can be gradually attached via hydrogen bridges with the first water molecules (2 in Figure 5.5). This structure probably dominates in the first water shell surrounding the polymer–water complex. The probability of this structure existing is much higher than that of water molecules forming a chain structure (4 in Figure 5.5). As calculated with a quantum chemical method, the energy of hydrogen bonds between C=O and H_2O is significantly lower than that of hydrogen bonds between water molecules. Second and third hydration shells close to PVCL chains are formed by the interaction of water molecules with dipoles of carbonyls indirectly by interaction with the first hydration shell of the polymer–hydrate complex. It is assumed that at least 15–20 molecules of water near one caprolactam ring are involved in the formation of the complex below the phase transition temperature.

The increase of the temperature in the PVCL–water system leads to the partial dehydration of the water in third and fourth hydration shells. Bridge hydrogen bonds in the first hydration shell are broken at the phase transition temperature. In this situation macromolecules undergo transformation to the unordered conformation state in comparison with the stable state with water interactions. This leads to the formation of contacts between nonpolar parts of caprolactam rings (increased

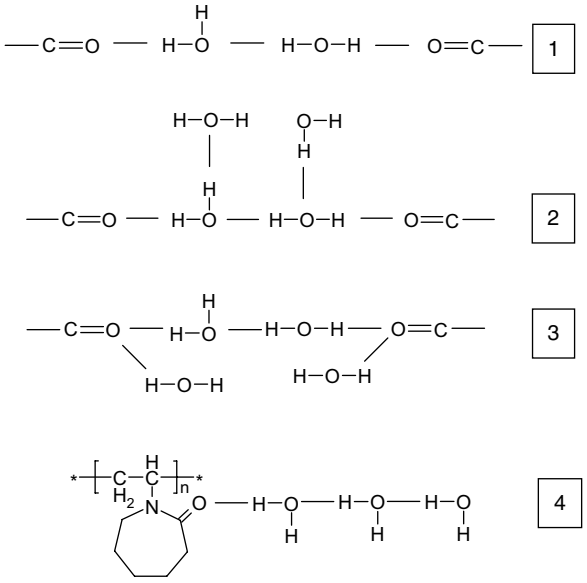

Figure 5.5 Types of interaction of PVCL with water. Reprinted with permission from [4].

hydrophobic interaction). As result, the polymer precipitates from solution; however precipitated polymer chains include a large amount of water, which stays in the polymer even at 90 °C.

Lebedev *et al.* [33] have studied the interaction of PVCL with water by small angle neutron scattering (SANS) and neutron spin echo (NSE) around the coil-to-globule transition. Experimental data from non-elastic neutron scattering of the PVCL solution near 32.5 °C showed anomalies that are caused by memory effects and relaxation of surface tension. The higher amplitude of the molecular movement in globules is the consequence of broken hydrogen bonds of water by the neighboring amide groups. As a result, water effectively lubricates the chain movement in the globular state, while in the coil state water diminishes the mobility of chains. The SANS and NSE data support the conclusion that water has an apparent effect on PVCL glassing.

PVCL is not only thermosensitive but also a biocompatible polymer. In PVCL the hydrophilic amide group is connected to the hydrophobic polymer backbone. Due to this reason the formation of the toxic small amide compounds via hydrolysis of PVCL is strongly inhibited [34]. In addition, it has been reported that the VCL monomer is less cytotoxic than *N*-isopropylacrylamide (NIPAM) [35].

5.4 PVCL Nano- and Microgels

Because of its interesting behavior in aqueous solutions, PVCL has been used for the synthesis of hydrogels [36–42]. The good solubility of VCL in water and the

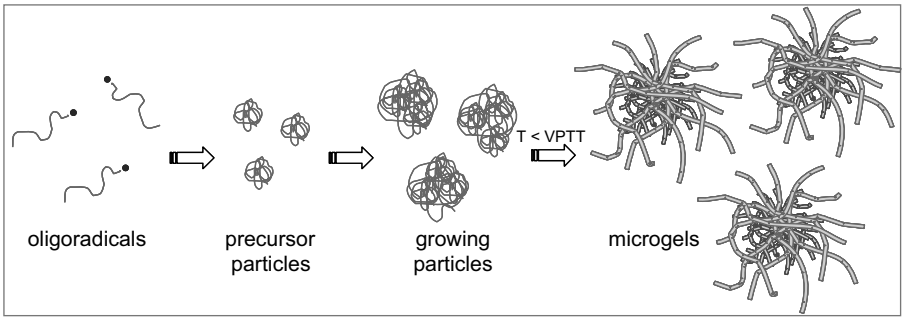

Figure 5.6 Schematic representation of microgel formation by precipitation polymerization.

phase separation of the PVCL above 32 °C in aqueous solution which was first observed by Shostakovski and Sydelkovskaya [43] is the reason why this monomer is suitable for use in precipitation polymerization in the design of nano- and microgels (Figure 5.6).

At the initial stage of precipitation polymerization, monomer(s), crosslinker, and initiator are all dissolved in water. The microgel particles are formed via a homogeneous nucleation mechanism. Polymerization begins after the decomposition of the water-soluble initiator (peroxide- or azo-based compound) and the production of free radicals. The monomers are attacked by these radicals and radical propagation occurs and polymer chains start to grow. In the case of VCL, the polymer chains collapse when they reach a certain length, forming precursor particles. This occurs because the polymerization temperature is normally 50–70 °C, which is far above the LCST of formed polymers. Formed precursor particles may grow in the following ways: (a) aggregation to form large, colloidally stable polymer particles; (b) absorption onto the surface of existing polymer particles; or (c) growth as new monomers or macroradicals are added. Microgel particles are stabilized by electrostatic stabilization mechanisms when they reach a critical size. At this stage microgel particles possess smooth surfaces and are in a collapsed state but still contain some water in their interior. This situation is different to emulsion polymerization, where latex particles such as polystyrene or poly(butylacrylate) have a compact structure [44].

When the reaction is complete, the microgel particles swell after cooling to room temperature (temperature below the VPTT of polymer chains) and become "hairy." At temperatures below the VPTT microgels are stabilized by steric mechanisms due to the formation of hydrogen bonds between the polymer and water molecules. This reaction mechanism of precipitation polymerization was suggested for the synthesis of VCL and NIPAM microgels [45–47]. When VCL is used in precipitation polymerization,crosslinking agents are needed to prevent the microgel dissolving in the water at low temperatures. In contrast, several reports show that PNIPAM chains can be "self-crosslinked" by chain-transfer reactions without the use of a crosslinking agent [48, 49].

The advantages of precipitation polymerization for synthesis of PVCL microgels can be summarized as follows:

- The polymerization process can be carried out as a batch, semi-batch, or continuous process, which makes it possible to optimize reaction conditions and obtain microgels with designed properties.
- Obtained microgel particles have a fairly narrow particle size distribution.
- The size of the microgel can be controlled in a broad range (from 50 nm to 3 μm) by the addition of surfactants or co-monomers.
- Hybrid colloids can be prepared by encapsulation of nanoparticles during microgel formation.
- Different co-monomers can be integrated into the microgel network during the polymerization process.

However, precipitation polymerization has some limitations:

- Nanogels with size below 50 nm are difficult to prepare with this method.
- Only thermostable materials can be used due to the high polymerization temperature, therefore the incorporation of biomacromolecules is not possible.
- After the polymerization process a non-crosslinked sol fraction still exists.

5.4.1 Homopolymer PVCL Microgels

Imaz *et al.* [50] reported surfactant-free synthesis of homopolymer microgels based on PVCL by precipitation polymerization in water using a conventional crosslinker – bisacrylamide (BIS) – and persulfate as initiator. It is reported that the size of microgel particles in the swollen state is 350 nm below the VPTT. The colloidal stability of homopolymer PVCL microgels is rather poor and can be improved by the use of stabilizing agents. The colloidal stability and size distribution of microgel particles are both improved by the use of surfactants. Wu and coworkers synthesized PVCL microgels with and without surfactant and studied the thermal behavior of PVCL microgels in water [51]. The surfactant-free microgels continuously shrunk as the temperature increased, reaching the fully collapsed state above VPTT at ~38 °C. The addition of surfactant led to additional swelling at higher temperatures. Authors attributed this effect to the formation of micelles inside the microgel network.

As an alternative to low-molecular-weight surfactants, polymer tensides have been used for the preparation of PVCL microgels. Boyko and coworkers reported PVCL microgels stabilized by poly(vinyl alcohol) (PVA) with different molecular weights [52]. In this system the hydrodynamic radius of temperature-sensitive PVCL microgels decreased from 280 to 180 nm with increase in PVA concentration from 2 to 10 $g\,l^{-1}$ (Figure 5.7a). The stability of the PVCL microgels at room temperature was improved when PVA of lower molecular weight and lower hydrolysis degree was used.

However, the thermal behavior of PVA-stabilized PVCL microgels was strongly dependent on the type of heating regime. In the first case microgel dispersion was measured by stepwise direct heating. In this case the hydrodynamic radii continuously decreased up to 30 °C and sharply increased at around 32 °C. This increase of

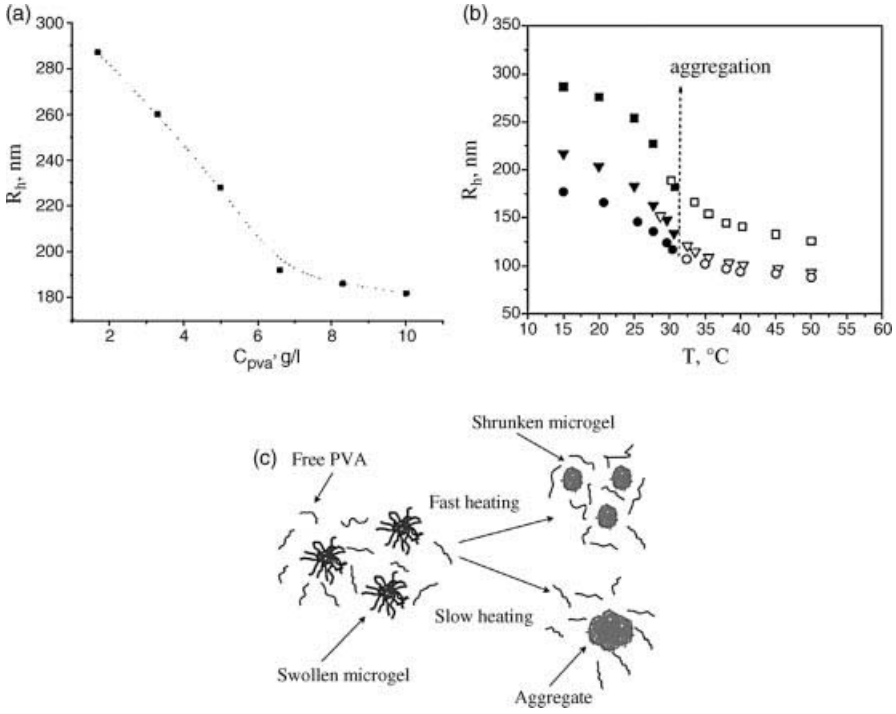

Figure 5.7 (a) Hydrodynamic radius of PVCL microgels as a function of PVA concentration in aqueous phase (PVA: $M_w = 14\,000\ g\ mol^{-1}$, hydrolysis degree 99%; $T = 15\ °C$). (b) Temperature dependence of the hydrodynamic radius R_h (filled symbols – direct slow heating; open – slow cooling after fast heating; squares – the sample prepared at $1.67\ g\ l^{-1}$ of PVA; triangles – $5\ g\ l^{-1}$ of PVA; circles – $8.3\ g\ l^{-1}$ of PVA. PVA ($M_w = 14\,000\ g\ mol^{-1}$, degree of hydrolysis – 99%). (c) Schematic representation of microgel behavior during temperature variation. Reprinted with permission from [52].

size indicates the aggregation of the individual particles (Figure 5.7b). The microgel sample showed a different thermal behavior when it was quickly heated to 50 °C and then step-by-step cooled. In this case, like a normal thermosensitive microgel, no aggregation was observed (the form of swelling–deswelling curve can be described by the Boltzman sigmoidal model). It was also observed that a high concentration of PVA slightly inhibited the microgel from swelling. At room temperature the stability of the microgels is a cooperative effect of free PVCL chains on the particle surface and free PVA chains in solution. After heating, microgels aggregate as PVCL chains shrink and the stabilization effect of PVA is not sufficient. When fast heating to a temperature above LCST, the remaining charged initiator groups on the surface are immobilized and the colloidal stability increases (Figure 5.7c).

The use of alternative crosslinking agents (BIS is used in majority of the microgel systems) allows the synthesis of PVCL microgels with interesting properties. A new crosslinker (cross-PAOS) (Figure 5.8a) was synthesized using vinylethoxy silane as a co-monomer with tetraethoxy silane to obtain branched poly(ethoxysiloxane). Later,

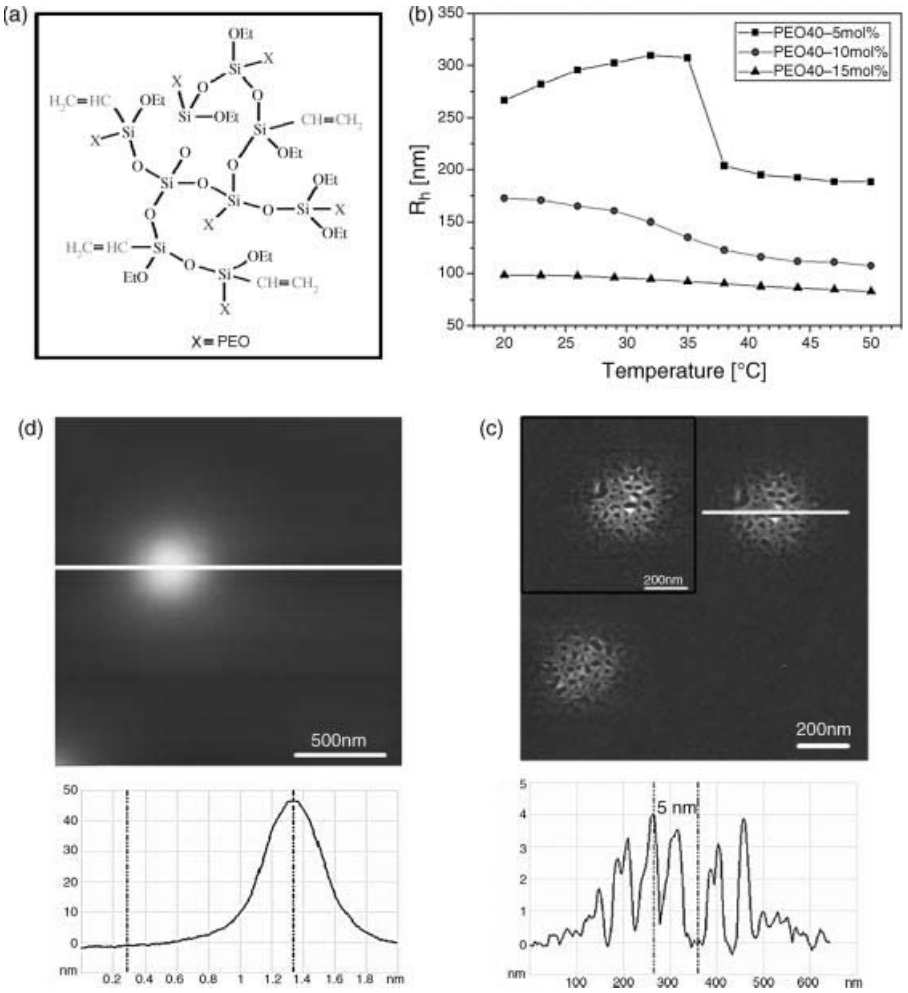

Figure 5.8 (a) Chemical structure of cross-PAOS. (b) Thermal sensitivity of microgel particles synthesized by different amounts of cross-PAOS which has 15% vinyl and 40% PEO end groups. (c,d) AFM images of VL 15–5 mol% microgel particles before (c) and after (d) H_2 plasma treatment. Reprinted with permission from [53].

a certain fraction of vinyl groups of poly(ethoxysiloxane) was reacted with poly (ethylene oxide) (PEO) monomethyl ether to incorporate short PEO chains which makes the crosslinker hydrophilic and water-soluble. Obtained crosslinkers with variable content of PEO segments and vinyl groups were used for synthesis of PVCL microgels. The increase of the crosslinker concentration from 5 to 15 mol% in the reaction mixture reduced the microgel size from 270 to 100 nm and gradual loss of the thermosensitive properties characterized by the difference between swollen (low temperatures) and collapsed (high temperatures) states was observed (Figure 5.8b). To confirm the crosslinker incorporation we did some atomic force microscopy

(AFM) measurements with and without H_2 plasma treatment of PVCL microgels crosslinked by BIS and cross-PAOS. The idea behind it was to see the silica after the removal of organic compound by plasma. After treating PVCL/BIS microgel with H_2 plasma, only some residues were detected. Figure 5.8c and d shows the AFM images of PVCL/cross-PAOS microgel particles before H_2 plasma treatment. The image shows nicely formed microgel particles which are approximately 50 nm in height. A well-defined Si-based network skeleton with height ≈5 nm is found after H_2 plasma treatment, giving almost 90% reduction in height because of the removal of organic material from the microgel particles.

Recently, the incorporation of reactive cyclodextrins (CDs) used as multifunctional crosslinkers in aqueous nanogels based on PVCL was studied [54]. α-, β-, γ-CDs were functionalized with acrylic groups and the average amount of vinyl bonds per CD molecule was adjusted to 2, 4, or 6. The final hydrodynamic radius of nanogels was reduced from 227 to 62 nm as the CD concentration in the reaction mixture increased (Figure 5.9). Smaller nanogels ($R_h = 22.5$ nm) with higher degrees of crosslinking were produced when the vinyl groups number per CD molecule increased. The cyclodextrin-modified nanogels obtained show temperature sensitivity with a volume transition point around 30 °C in aqueous medium.

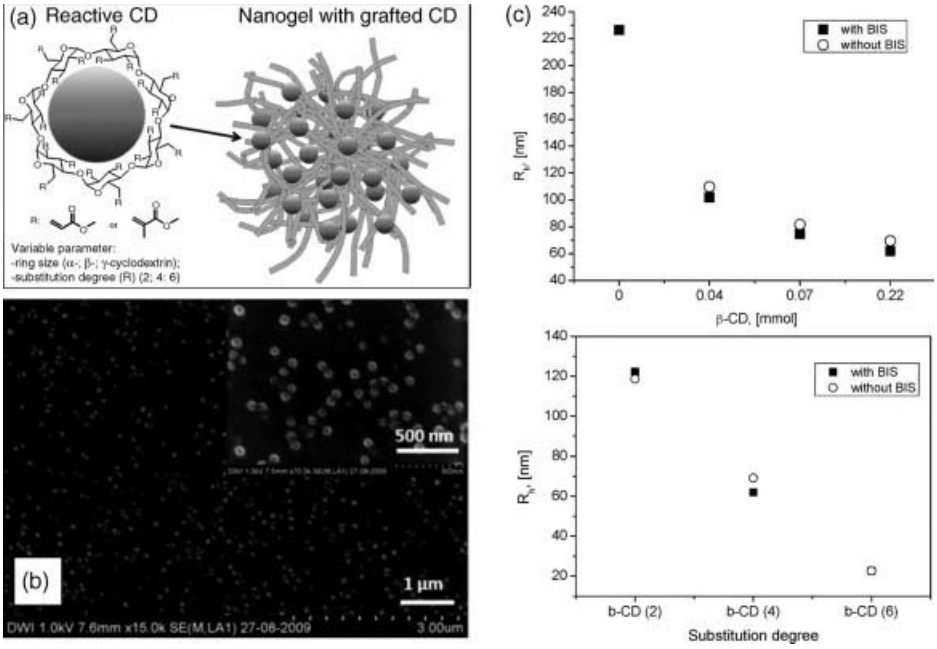

Figure 5.9 (a) Cyclodextrin-modified PVCL nanogels; (b) FESEM image of nanogel sample; (c,d) hydrodynamic radii (R_h) of β-CD-modified nanogels prepared with: (c) variable amounts of β-CD with substitution degree 4 and (d) constant amount of β-CD with variable substitution degree (size measurements performed at 20 °C). Reprinted with permission from [54].

5.4.2
Copolymer PVCL Microgels

As mentioned above, precipitation polymerization allows the use of several monomers in the reaction mixture to obtain copolymer microgels. This makes it possible to vary the chemical composition of polymer chains within microgels and consequently their physical properties in aqueous solution. In addition, in this way microgels with complex morphologies can be prepared.

Boyko *et al*. [55] synthesized microgels by copolymerization of *N*-vinylcaprolactam and *N*-vinylpyrrolidone in aqueous medium. The hydrophilic nature of *N*-vinylpyrrolidone improved the colloidal stability of obtained copolymer microgels at temperatures above the VPTT.

Recently we reported the synthesis of microgels by copolymerization of VCL with *N*-isopropylacrylamide (PVCL–NIPAM) or *N*-isopropylmethacrylamide (PVCL–NIPMAM) [56]. The colloidally stable microgel particles with different dimensions were obtained with variable copolymer compositions (Figure 5.10a). According to nuclear magnetic resonance (NMR) results the authors reported statistical distribution of the monomer units in the polymer chains within the microgels. By using DSC, the VPTT values for PVCL–NIPAM copolymer microgels were detected at 32–34 °C (close to the LCST of PVCL (33 °C) and PNIPAM (32 °C). For PVCL–NIPMAM copolymer microgels the shift of the VPTT from 33 to 45 °C was observed on increase of the amount of NIPMAM units in copolymer chains (the LCST of PNIPMAM in water is around 45 °C) (Figure 5.10b).

Synthesis of microgel particles with core–shell structure can be also achieved by using monomers of different water-solubility or reactivity in batch precipitation polymerization. Besides, seed polymerization technique or stepwise addition of comonomers in reaction mixture also makes it possible to prepare core–shell microgels. Copolymerization of VCL and acetoacetoxy ethyl methacrylate (AAEM) in the aqueous phase results in a core–shell microgel in an aqueous system under surfactant-free conditions [57]. A water-soluble cationic radical initiator was used and water-soluble AAEM and BIS monomers first polymerized and then became

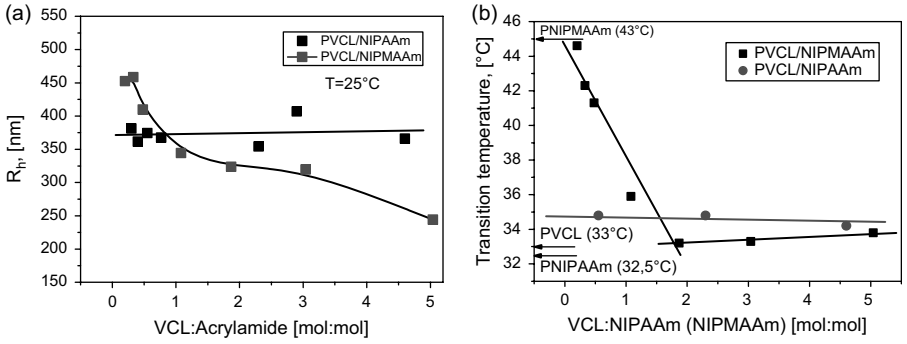

Figure 5.10 Variation of (a) microgel hydrodynamic radius (DLS data) and (b) VPTT (DSC data) with copolymer composition. Reprinted with permission from [56].

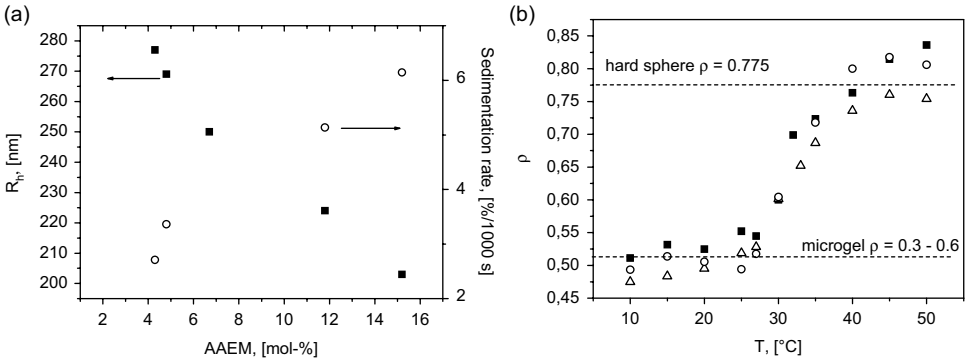

Figure 5.11 (a) Hydrodynamic radii R_h and sedimentation rate as a function of the AAEM content in VCL–AAEM microgels; (b) ratio $R_g/R_h = \varrho$ as a function of the temperature for VCL–AAEM microgels with different composition: 1 (open circles) – 4 mol%; 2 (filled squares) – 6.5 mol%, 3 (open triangles) – 15 mol% AAEM. Reprinted with permission from [57].

precursor particles. PVCL growing chains collapsed on the surface of these precursor nuclei at a polymerization temperature of 70 °C which is far above their LCST and further crosslinked. The VCL–AAEM microgel particles are stabilized by steric mechanisms and partly electrostatic stabilization provided by charged groups of the cationic initiator. The resulting particles consist of a PAAEM-rich core and a PVCL-rich shell structure due to the rapid consumption of highly reactive AAEM in the first stage of reaction.

As shown in Figure 5.11a the variation of the monomer ratio in the reaction mixture allows microgel size to be controlled. The average hydrodynamic radii measured by dynamic light scattering (DLS) and sedimentation velocity for different microgels decrease gradually with increasing AAEM content. The combination of static and dynamic light scattering was used to calculate the $<R_g>/<R_h>$ ratio (ϱ), which reveals the conformation of a polymer chain and the density distribution of a particle and therefore gives valuable information about the internal structure of the microgels. Figure 5.11b shows that as the temperature increases, the mobility of the PVCL chains decreases and the microgel forms a compact structure without internal motion. Thereafter, ϱ increases rapidly and finally approaches the theoretically predicted ϱ value for the homogeneous sphere (0.775). Figure 5.11b also shows that because of the heterogeneous distribution of the monomer units in the microgel no shift of VPTT with chemical composition is observed.

As in the previous example, the copolymerization of glycidyl methacrylate (GMA) with VCL results in the formation of thermoresponsive microgels with core–shell morphology [58]. The microgel particles exhibit a heterogeneous structure, for example, a temperature-sensitive PVCL-rich shell and reactive PGMA-rich core due to the large reactivity difference between VCL and GMA [59] and the more hydrophobic nature of the PGMA obtained. DLS results and Figure 5.12a show that the size of microgels decreases with increasing GMA content but the size distribution of microgel particles remains unaltered. Scanning electron microscopy (SEM) images

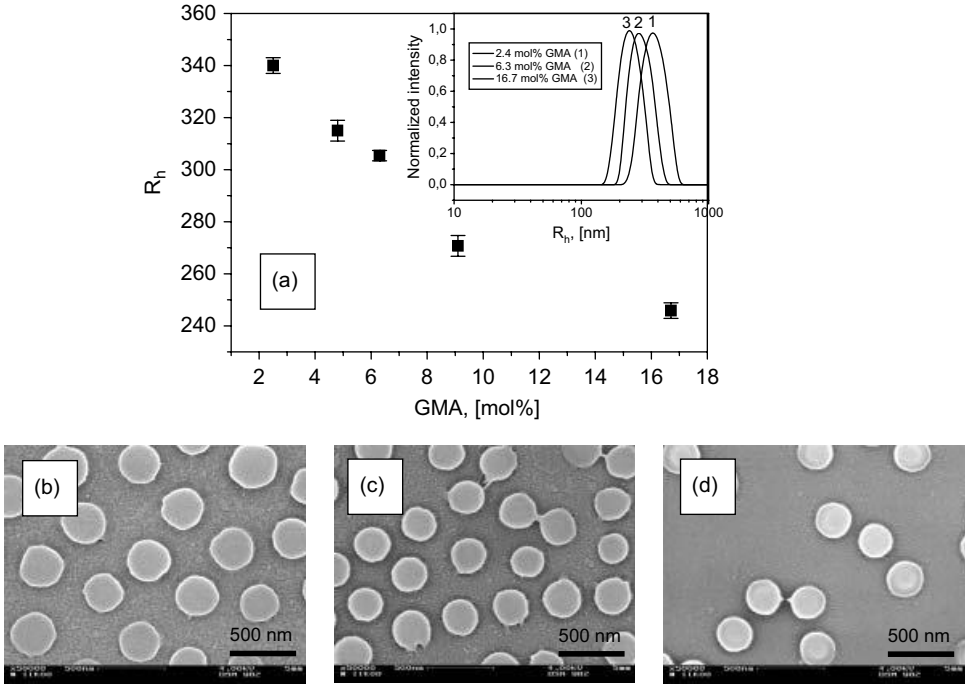

Figure 5.12 (a) Hydrodynamic radii of PVCL–PGMA microgels (inset shows the particle size distribution curves for selected samples; measurements performed at 20 °C). (b,c,d) SEM images of VCL/GMA microgel samples: (b) 4.8 mol%; (c) 9.1 mol%; (d) 16.7 mol% GMA. Reprinted with permission from [58].

(Figure 5.12b–d) indicate smaller size and reduced deformation degree for microgels containing a larger GMA content.

The use of hydrophilic monomers carrying charged groups in precipitation polymerization of VCL allows preparation of temperature- and pH-sensitive microgels. The copolymerization of a few molar percent of ionic sodium acrylate (NaA) into the PVCL microgel slightly raised its VPTT and increased the extent of its swelling [60–63]. In another system VCL was copolymerized with AAEM and vinylimidazole (VIm) by a simple batch polymerization procedure. Colloidally stable pH- and temperature-sensitive core–shell microgel particles were produced [64]. Figure 5.13a shows the influence of VIm content on the particle size of microgels at pH = 6 and a temperature of 20 °C. It indicates that the microgel size increases with linear order while the VIm amount is larger. These results reveal that the incorporation of VIm strongly increases the hydrophilicity of the particles, leading to better solvation by water and higher swelling in continuous medium. Figure 5.13b shows the R_h of different microgel samples as a function of pH. The R_h–pH dependencies for all samples containing VIm exhibit a maximum at pH = 4, which is due to the maximum ionization of VIm units. This effect induces the microgel particles to swell. Figure 5.13b also shows that the swelling at pH = 4 increases gradually with

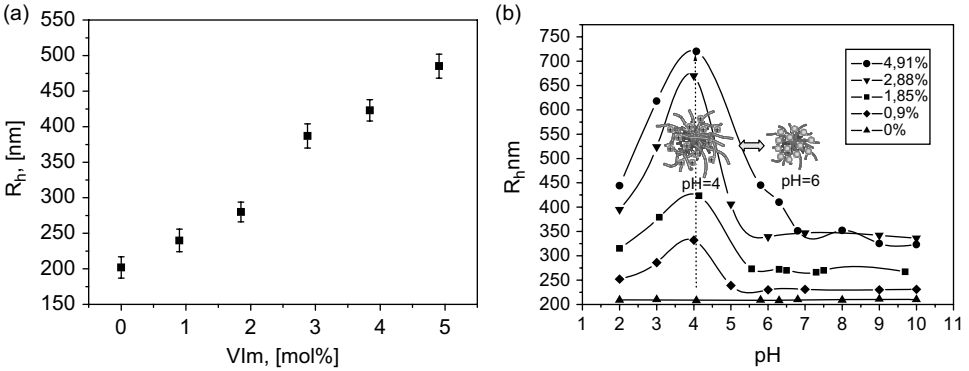

Figure 5.13 (a) Hydrodynamic radii of microgel particles prepared at different VIm contents ($T = 20\,^{\circ}C$; pH = 6); (b) variation of hydrodynamic radii with pH ($T = 20\,^{\circ}C$). Reprinted with permission from [64].

increase of VIm content in the microgel structure, indicating that the electrostatic repulsion forces within the microgel particle became stronger at higher concentrations of charged VIm groups.

Amphoteric PVCL microgels have been synthesized by copolymerization of VCL, itaconic acid dimethylester (IADME), and VIm in a precipitation polymerization process [65]. After hydrolysis of the ester groups of the IADME component, microgels containing acidic and basic groups in their structure were obtained (Figure 5.14).

The internal structure of amphoteric microgels has been investigated with NMR. Proton high-resolution transverse magnetization relaxation under magic angle sample spinning (MAS) was used to measure the dynamic heterogeneity of the chemical structure in amphoteric microgels. The core–shell morphology of

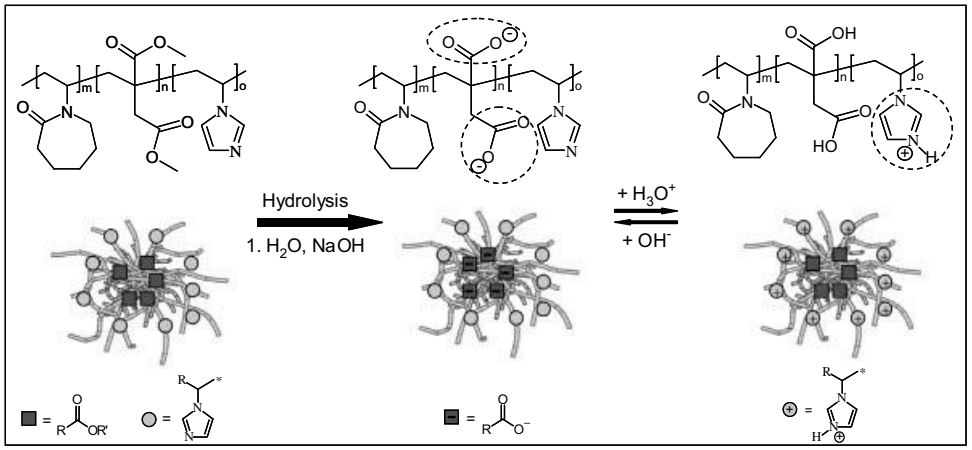

Figure 5.14 Schematic representation of polyampholyte microgels. Reprinted with permission from [65].

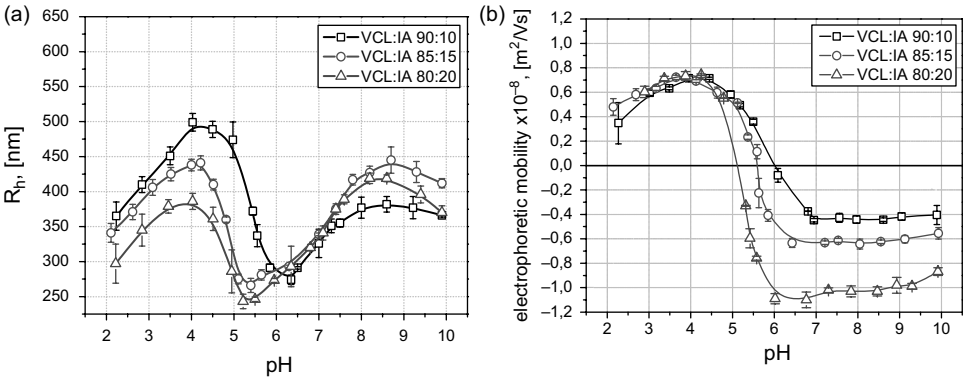

Figure 5.15 (a) Hydrodynamic radii and (b) electrophoretic mobility of amphoteric microgels as a function of pH ($T = 20\,^{\circ}C$). Reprinted with permission from [65].

PVCL-based microgels was proved with imidazole groups localized in the shell and itaconic acid groups (originating from the hydrolyzed IADME component) localized in the core. Variation of the IADME and VIm content in the microgel structure allowed variation of the microgel charge and swelling degree in basic and acidic pH, respectively (Figure 5.15).

PVCL microgels with grafted amphiphilic chains have been prepared using reactive macromonomers consisting of a hydrophilic PEO segment and hydrophobic hydrocarbon segment [66]. The amphiphilic character of the macromonomer and its ability to form micelles in water (critical micelle concentration (CMC) value 0.25 $g\,l^{-1}$ at 20 °C) allowed synthesis of microgels exhibiting very small size (73 nm at 20 °C) and narrow size distribution. Microgel samples prepared with macromonomers showed discontinuous thermal transition at 35 °C, whereas in the case of microgels prepared with SDS as stabilizer the collapse transition occurs over a broad temperature range.

Poly(ethylene glycol) (PEG)-modified PVCL microgels have been synthesized by free radical copolymerization of VCL and AAEM in the presence of methoxy-capped PEG methacrylate macromonomers [67]. The variation of the PEG macromonomer concentration in the reaction mixture or the length of the PEG chain can be used to vary the microgel diameter in the range 60–220 nm (Figure 5.16). In addition, grafting of the PEO chains improves the colloidal stability of the microgels. The incorporation of the PEG macromonomers decreases the swelling degree and shifts the volume phase transition to higher temperatures.

5.4.3
Composite and Hybrid Microgels

Precipitation polymerization can be used for the incorporation of inorganic nanoparticles into microgel structures to obtain composite colloids. Reactive LaF_3:Eu nanoparticles modified with mixed ligand (aminoethyl phosphate (AEP) and

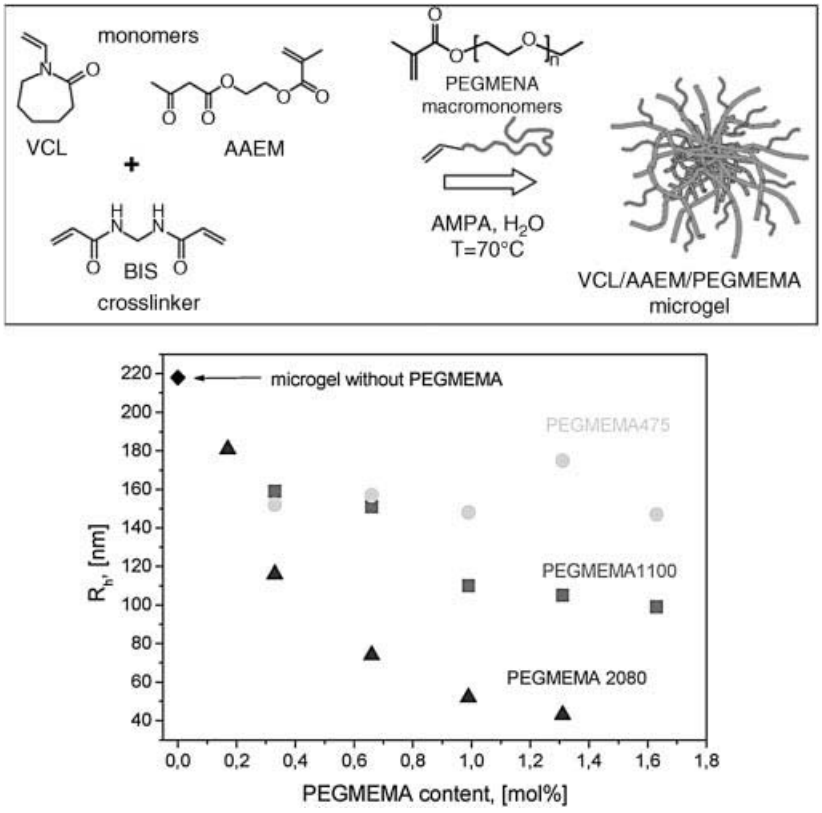

Figure 5.16 Ingredients used for the synthesis of PVCL microgels with grafted PEG chains. Hydrodynamic radii (R_h) of PVCL–AAEM microgel particles as a function of poly(ethylene glycol) methyl ether methacrylate (PEGMEMA) content ($T = 20\,^{\circ}C$). Reprinted with permission from [67].

ethylene glycol methacrylate phosphate (EGMAP); molar ratio 3:1) have been integrated into microgels by this method [68]. In this system AEP improves the stabilization of nanoparticles in water and the introduction of EGMAP covalently fixes the nanoparticles in the microgel. Figure 5.17a shows the hydrodynamic radii (R_h) and radii of gyration (R_g) (measured at 20 °C) for microgels prepared at different nanoparticles concentrations. The size of the microgel is reduced with the increasing nanoparticle concentration in the reaction mixture (from 220 to 80 nm). It is obvious from Figure 5.17a that both R_g and R_h follow similar trends, for example, decrease with increasing nanoparticle content in the microgels. The increase of the R_g/R_h ratio with nanoparticle content indicates a more compact structure of the nanogels. The sample containing the highest nanoparticle content exhibits a R_g/R_h ratio of 0.78 which is very close to the theoretical value for the solid sphere. These data are in good agreement with DLS measurements performed at different temperatures (Figure 5.17b). As shown in Figure 5.17b the increase of the nanoparticle content in the nanogel structure induces two major effects, namely decrease of the swelling

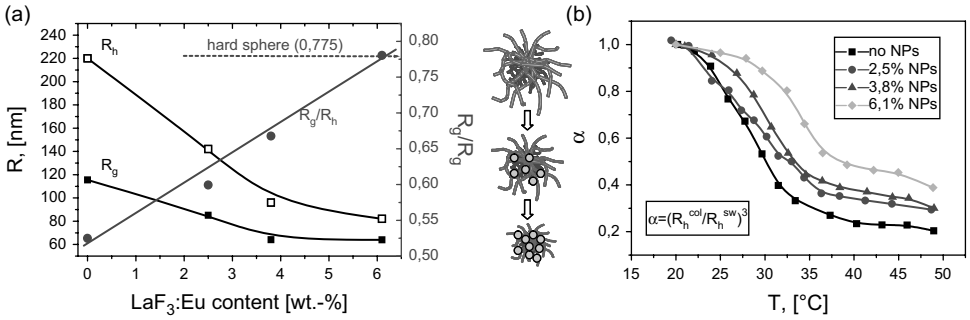

Figure 5.17 (a) R_h, R_g, and R_g/R_h ratio as a function of nanoparticle content in microgels; (b) swelling ratio α as a function of the temperature (inset demonstrates the evolution of microgel morphology with increase of nanoparticle content). Reprinted with permission from [68].

ratio (α) and shift of the VPTT to higher values. The second effect is present due to the amino-groups on the nanoparticle surfaces which increase the hydrophilicity of the nanogels.

The high-resolution transmission electron microscopy (TEM) images in Figure 5.18 clearly indicate the presence of nanoparticles in the microgel core, which suggests that the integration of the nanoparticles into microgel occurs during early nucleation stage. In addition, the presence of nanoparticles has been confirmed by energy-dispersive X-ray (EDX) analysis of the hybrid microgels. Figure 5.18 shows a line scan analysis of the VCL–AAEM (6.1% nanoparticles) sample. The element distribution spectra confirm the presence of La, Eu, and P in the bright areas localized within the microgel particles, indicating the presence of nanoparticles.

Batch surfactant-free precipitation polymerization has been used for the synthesis of microgel-clay composite particles [69]. Laponite nanoparticles in reaction mixture were shown to be encapsulated during the microgel formation process. Microgel samples based on P(VCL-*co*-AAEM) containing different amount of incorporated clay nanoparticles (from 2 wt% to 18 wt%) were synthesized.

Figure 5.19a shows experimental data from flow field flow fractionation (F-FFF) coupled with multi-angle laser light scattering (MALLS) detector presented as distribution curves (cumulative mass fraction vs. R_g) for the different microgel samples. These data indicate that the radius of gyration of microgels decreases and the size distribution becomes narrower while the clay content increases. The hydrodynamic radii obtained by photon correlation spectroscopy as a function of the clay content in the microgels are shown in Figure 5.19b. The reduction of the microgel size (as measured by dynamic and static light scattering techniques) and the narrowing of the size distribution can be explained by the stabilization effect of clay nanoparticles for the newly formed precursor particles at the initial stages of the process. This induces the larger content of stable precursors which leads finally to more microgel particles with smaller size. The clay nanoparticles become effectively encapsulated and mechanically "locked" in the microgel network due to their active participation in the nucleation and polymerization process.

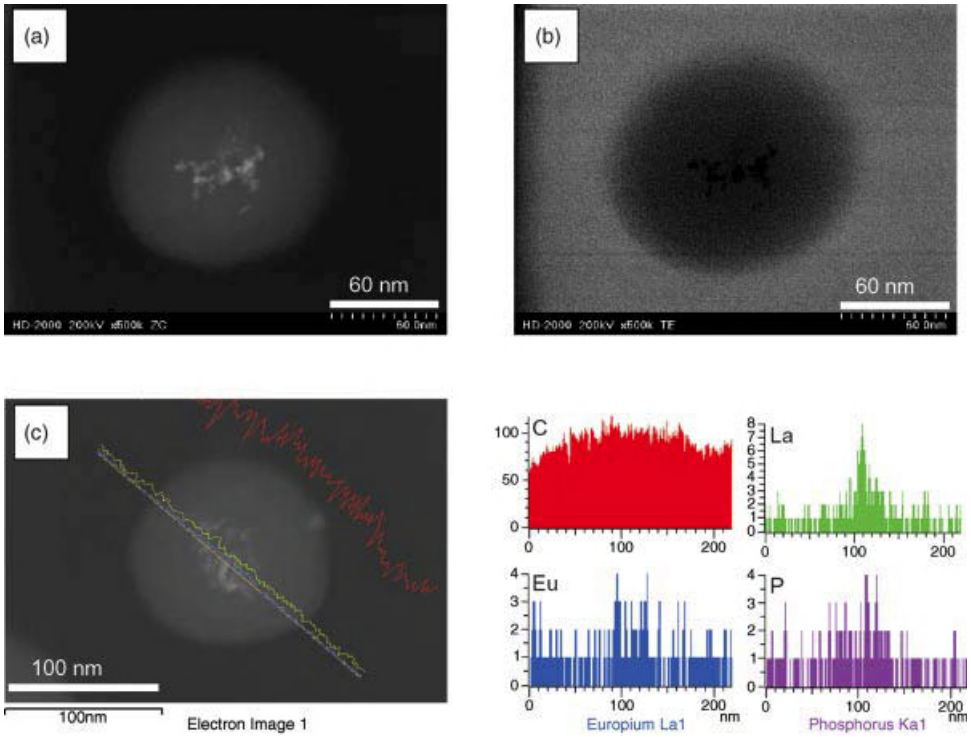

Figure 5.18 High-resolution TEM images of the VCL–AAEM microgel (6.1% nanoparticles): (a) Z-contrast transmission mode and (b) transmission mode; (c) EDX line scan analysis of the single microgel (spectra show the distributions of C, La, Eu, and P along the line scan). Reprinted with permission from [68].

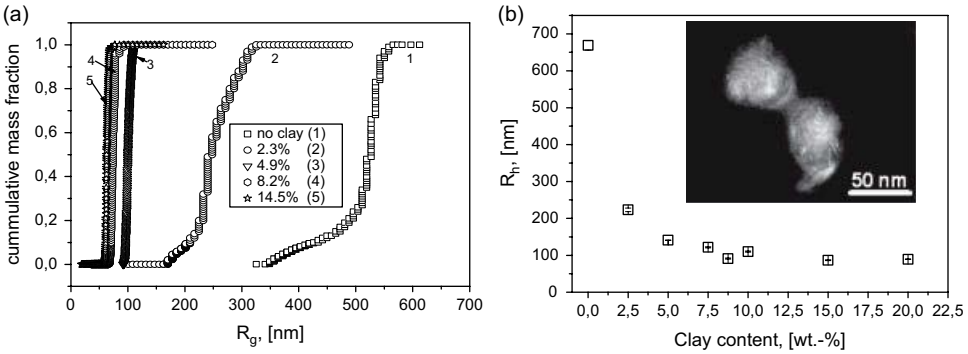

Figure 5.19 Cumulative mass fraction vs. radii of gyration (R_g) (F-FFF data) (a), and intensity-averaged hydrodynamic particle size (PCS data) (b) for microgel samples with different clay loading (inset shows TEM image of microgel particles (9.7 wt% clay)). Reprinted with permission from [69].

5.5 Conclusions

This short review describes the use of VCL for the synthesis of aqueous microgels. This monomer is ideally suited for the synthesis of microgels by precipitation polymerization because its LCST in water is around 32 °C. Microgel synthesis can be realized with commercially available initiator systems and a large variety of other monomers can be copolymerized with VCL in aqueous solutions. This allows the design of microgel particles with various chemical structures, sizes, and charges. The swelling degree of PVCL microgels can be tuned by selection of multifunctional crosslinking agents or the use of reactive nanoparticles. PVCL-based microgels are temperature-sensitive and have a VPTT around 33–34 °C. The VPTT can be flexibly tuned by copolymerization of VCL with other monomers and influencing the hydrophilic/hydrophobic balance within microgels. The biocompatibility of PVCL, as well as its low toxicity and solubility in aqueous solutions make PVCL-based microgels suitable for biomedical applications.

References

1 (a) Molyneux, P. (1984) *Water-Soluble Synthetic Polymers*, CRC Press, Boca Raton; (b) Sidelkovskaya, F.P. (1970) *Chemistry of N-Vinylpirrolidone and its Polymers*, Nauka, Moscow; (c) Kirsh, Y.E. (1993) Water-soluble poly(*N*-vinylamides): microstructure, solvation, conformational state and complex formation in aqueous solutions. *Prog. Polym. Sci*, **18**, 519; (d) Kirsh, Y.E. (1998) *Poly-N-Vinylpyrrolidone and Other N-Vinylamides: Synthesis and Physico-Chemical Properties*, Nauka, Moscow.

2 Wessel, W., Schoog, M., and Winkler, E. (1971) Polyvinylpyrrolidone (PVP), its diagnostic, therapeutic, and technical application and consequences thereof. *Arzneim-Forsch. Drug Res.*, **21**, 1468.

3 Botzolakis, J.E., Small, L.E., and Augsburger, L.L. (1982) Effect of disintegrants on drug dissolution from capsules filled on a dosator-type capsule-filling machine. *Int. J. Pharm.*, **12**, 341.

4 Wan, L.S.C., Heng, P.W.S., and Ling, B.L. (1996) Effect of polyvinylpyrrolidone solutions containing dissolved drug on characteristics of lactose fluidized bed granules. *Int. J. Pharm.*, **141**, 161.

5 Macleod, G.S., Fell, J.T., and Collett, J.H. (1999) An in vitro investigation into the potential for bimodal drug release from pectin/chitosan/HPMC-coated tablets. *Int. J. Pharm.*, **188**, 11.

6 Berggren, J. and Alderborn, G. (2004) Long-term stabilisation potential of poly (vinylpyrrolidone) for amorphous lactose in spray-dried composites. *Eur. J. Pharm. Sci.*, **21**, 209.

7 Goddard, E.D. and Gruber, J.V. (1999) *Principles of Polymer Science and Technology in Cosmetics and Personal Care*, Marcel Dekker, New York.

8 Iliel, E., Allinger, N., Engial, S., and Morrison, T. (1961) *The Conformational Analysis*, Mir, Moscow.

9 Tischenko, G.N., Zukhlistova, N.E., and Kirsh, Yu.E. (1997) Crystal and molecular structure of N-vinylcaprolactam. *Crystallogr. Rep.*, **42**, 626.

10 Kirsh, Yu.E., Yanul, N.A., and Kalninsh, K.K. (1999) Structural transformations and water associate interactions in poly-N-vinylcaprolactam-water system. *Eur. Polym. J.*, **35**, 305.

11 Akashi, M., Yashima, E., and Yamashita, T. (1990) A novel synthetic procedure of vinylacetamide and its free-radical

polymerization. *J. Polym. Sci. Polym. Chem.*, **28**, 3487.
12 Bagdasaryan, X.S. (1966) *Theory of Radical Polymerisation*, Nauka, Moscow, p. 300.
13 House, D.A. (1962) Kinetics and mechanism of oxidations by peroxydisulfate. *Chem. Rev.*, **62**, 185.
14 Ferguson, J. and Rajan, V.S. (1979) Hydropolysis of N-vinylpyrrolidone in the presence of polyacrylic acid and potassium persulfate. *Eur. Polym. J.*, **15**, 627.
15 Solomon, O.F., Corciovei, M., and Boghina, C. (1968) Properties of solutions of poly-N-vinylcaprolactam. *J. Appl. Polym. Sci.*, **12**, 1835.
16 Solomon, O.F., Corciovei, M., and Boghina, C. (1968) Radical bulk polymerization of N-vinylcaprolactam. *J. Appl. Polym. Sci.*, **12**, 1843.
17 Solomon, O.F., Vasilescu, D.S., and Tatarescu, T. (1969) Radical polymerization of N-vinylcaprolactam in homogeneous solution. *J. Appl. Polym. Sci*, **13**, 1.
18 Eisele, M. and Burchard, W. (1990) hydrophobic water-soluble polymers. 1. dilute solution properties of poly(1-vinyl-2-piperidone) and poly(N-vinylcaprolactam). *Macromol. Chem.*, **191**, 169.
19 Meeussen, F., Nies, E., Berghmans, H., Verbrugghe, S., Goethals, E., and Du Prez, F. (2000) Phase behaviour of poly (N-vinylcaprolactam) in water. *Polymer*, **41**, 8597.
20 Kirsh, Yu.E.; Karaputadze, T.M.; Shumskii, V.I.; Timashev, S.F.; Krylova, L.A.; Dobrov, I.V.; Lukhovitskii, V.I.; Popkov, Yu.M.; Shelukhina, G.D.; Polikarpov, V.V. Radiochemical polymerization of N-vinylcaprolactam, U.S.S.R. Patent 1,613,446, 15 Dec 1990
21 Cheng, S.C., Feng, W., Pashkin, I.I., Yuan, L.H., Deng, H.C., and Zhou, Y. (2002) Radiation polymerisation of thermo-sensitive poly(N-vinylcaprolactam). *Radiat. Phys. Chem.*, **63**, 517.
22 Kirsh, Yu.E. (1993) Water-soluble poly(n-vinylamides) microstructure, solvation, conformational state and complex formation aqueous solutions. *Prog. Polym. Sci.*, **18**, 519.
23 Lau, A.C.W. and Wu, C. (1999) Thermally sensitive and biocompatible poly(N-vinylcaprolactam): synthesis and characterization of high molar mass linear chains. *Macromolecules*, **32**, 581.
24 Eisele, M. (1988) Dissertation, Freiburg. Synthesis and solution properties of linear and branched polyvinyllactames
25 Kirsh, Yu.E., Soos, T.A., Karaputadze, T.M., Kobyakov, V.V., Sinitzina, L.A., and Ostrovskii, S.A. (1979) Peculiarities of the complexes formation and conformational transitions of poly(N-vinyllactams) in aqueous solutions. *Vysokomolekularnye Soedineniya*, **21** (12), 519.
26 Kirsh, Yu.E., Soos, T.A., and Karaputadze, T.M. (1983) Poly-N-Vinylamides, complexation and conformational changes in aqueous solution. *Eur. Polym, J.*, **19** (7), 639.
27 Pashkin, I.I., Kirsh, Yu.E., and Zubov, V.P. (1993) Synthesis of water-soluble N-vinylcaprolactam-based copolymers and physico-chemical properties of their aqueous solutions. *Vysokomolekularnye Soedineniya*, **35** (5), 481.
28 Yanul, N.A., Zemljanova, O.Y., Kalninsh, K.K., and Kirsh, Yu.E. (1998) Interaction of aqueous associates with poly-N-vinylcaprolactam in concentrated polymer solutions. *Zh. Fiz. Khim.*, **72** 1037.
29 Tager, A.A., Safronov, A.P., Berezyuk, E.A., and Galaev, I. (1994) Lower critical solution temperature and hydrophobic hydratation in aqueous polymer solutions. *Colloid Polym. Sci.*, **272**, 1234.
30 Kirsh, Yu.E., Yanul, N.A., Karaputadze, T.M., and Timashev, S.F. (1992) Characteristics of melting of poly-N-vinylamides frozen water solutions.. *Zh. Fiz. Khim.*, **66**, 2629.
31 Maeda, Y., Nakamura, T., and Ikeda, I. (2002) Change in solvation of poly(N,N-diethylacrylamide) during phase transition in aqueous solutions as observed by IR spectroscopy. *Macromolecules*, **35**, 217.
32 Maeda, Y., Yamamoto, H., and Ikeda, I. (2001) Effects of ionization of incorporated imidazole groups on the

phase transitions of poly(N-isopropylacrylamide), poly(N,N-diethylacrylantide), and poly(N-vinylcaprolactam) in water. *Langmuir*, **17**, 6855.

33 Lebedev, V.T., Török, Gy., Cser, L., Kali, Gy., Kirsh, Yu.E., Sibilev, A.I., and Orlova, D.N. (2001) NSE-study of poly (N-vinylcaprolactam) by coil-globule transition. *Physica B*, **297**, 50.

34 Lau, A.C.W. and Wu, C. (1999) Thermally sensitive and biocompatible poly(N-vinylcaprolactam): Synthesis and characterization of high molar mass linear chains. *Macromolecules*, **32** (3), 581.

35 Dimitrov, I., Trzebicka, B., Müller, A.H.E., Dworak, A., and Tsvetanov, C.B. (2007) Thermosensitive water-soluble copolymers with doubly responsive reversibly interacting entities. *Prog. Polym. Sci.*, **32**, 1275.

36 Makhaeva, E.E., Thang, L.T.M., Starodubzev, S.G., and Khohlov, A.R. (1996) Thermoshrinking behavior of poly (vinylcaprolactam) gels in aqueous solution. *Macromol. Chem. Phys.*, **197**, 1973.

37 Mikheeva, L.M., Grinberg, N.V., Mashkevich, A.Y., Grinberg, V.Y., Thanh, L.T.M., Makhaeva, E.E., and Khokhlov, A.R. (1997) Microcalorimetric study of thermal cooperative transitions in poly(N-vinylcaprolactam) hydrogels. *Macromolecules*, **30**, 2693.

38 Yanul, N.A., Verbrugghe, S., Goethals, E.J., and Du Prez, F.E. (2001) Thermoresponsive properties of poly(N-vinylcaprolactam)-poly(ethylene oxide) aqueous systems: Solutions and block copolymer networks. *Macromol. Chem. Phys.*, **202**, 1700.

39 Loos, W., Kirsh, Yu.E., Verbrugghe, S., Goethals, E.J., Du Prez, F.E., Bakeeva, I.V., and Zubov, V.P. (2003) Thermo-responsive organic/inorganic hybrid hydrogels based on poly(N-vinyl caprolactam). *Macromol. Chem. Phys.*, **204**, 98.

40 Mamytbekov, G., Bouchal, K., and Ilavsky, M. (1999) Phase transition in swollen gels 26. Effect of charge concentration on temperature dependence of swelling and mechanical behaviour of poly(N-vinylcaprolactam) gels. *Eur. Polym. J.*, **35**, 1925.

41 Ilavsky, M., Mamytbekov, G., Bouchal, K., and Hanykova, L. (1999) Phase transition in swollen gels 27. Effect of negative charge concentration on swelling and mechanical behaviour of poly (N-vinylcaprolactam) gels. *Polym. Bull.*, **43**, 109.

42 Ilavsky, M., Mamytbekov, G., Sedalkova, Z., Hanykova, L., and Dušek, K. (2001) Phase transition in swollen gels-29. Temperature dependences of swelling and mechanical behaviour of poly(N-vinylcaprolactam-co-1-vinyl-2-pyrrolidone) gels in water. *Polym. Bull.*, **46**, 99.

43 Sydelkovskaya, F.P. and Shostakovski, M.F. (1957) *Vesnik Akad. Nauk SSSR*, **7**, 45.

44 Tauer, K., Hernandez, H., Kozempel, S., Lazareva, O., and Nazaran, P. (2008) Towards a consistent mechanism of emulsion polymerization **-** new experimental details. *Colloid Polym. Sci.*, **286**, 499.

45 Pelton, R. (2000) Temperature-sensitive aqueous microgels. *Adv. Colloid Interface Sci.*, **85**, 1.

46 Wu, X., Pelton, R.H., Hamjelec, A.E., and Woods, D.R. (1994) The kinetics of poly(N-isopropylacrylamide) microgel latex formation. *Colloid Polym. Sci.*, **272**, 467.

47 Pelton, R. and Chibante, P. (1986) Preparation of aqueous latices with N-isopropylacrylamide. *Colloids Surf.*, **20**, 247.

48 Gao, J. and Frisken, B.J. (2003) Cross-linker-free N-isopropylacrylamide gel nanospheres. *Langmuir*, **19**, 5212.

49 Gao, J. and Frisken, B.J. (2003) The influence of reaction conditions on the synthesis of self-crosslinked N-isopropylacrylamide microgels. *Langmuir*, **19**, 5217.

50 Imaz, A., Miranda, J.I., Ramos, J., and Forcada, J. (2008) Evidences of a hydrolysis process in the synthesis of N-vinylcaprolactam-based microgels. *Eur. Polym. J.*, **44**, 4002.

51 Gao, Y., Au-Yeng, S.C.F., and Wu, C. (1999) Interaction between surfactant and poly(N-vinylcaprolactam) microgels. *Macromolecules*, **32**, 3674.

52 Boyko, V., Richter, S., Pich, A., and Arndt, K.F. (2003) Poly(N-vinylcaprolactam) microgels polymeric stabilization with poly(vinyl alcohol). *Colloid Polym. Sci.*, **282**, 127.

53 Agrawal, G., Schürings, M., Zhu, X., and Pich, A. (2012) Poly(ethoxysiloane) crosslinkers for synthesis of aqueous microgels. *Langmuir* (submitted).

54 Kettel, M., Möller, M., and Pich, A. (2011) Aqueous nanogels modified with cyclodextrin. *Polymer*, **52**, 1917.

55 Boyko, V., Richter, S., Burchard, W., and Arndt, K.F. (2007) Chain dynamics in microgels: poly(N-vinylcaprolactam-co-N-vinylpyrrolidone) microgels as examples. *Langmuir*, **23**, 776.

56 A. Balaceanu, V. Mallorga, W. Lin, M. Schürings, D.E. Demco, A. Böker, M.A. Winnik, A. Pich, Copolymer Microgels by Precipitation Polymerisation of N-Vinylcaprolactam and N-Isopropylacrylamides in Aqueous Medium, *Colloid Polym. Sci*. 2012, DOI: 10.1007/s00396-012-2659-1.

57 Boyko, V., Pich, A., Lu, Y., Richter, S., Arndt, K.F., and Adler, H.J. (2003) Thermo-sensitive poly(N-vinylcaprolactam–co-acetoacetoxyethyl methacrylate) microgels: I. Synthesis and characterization. *Polymer*, **44**, 7821.

58 Häntzschel, N., Zhang, F., Eckert, F., Pich, A., and Winnik, M.A. (2007) Poly(N-vinylcaprolactam-co-glycidyl methacrylate) aqueous microgels labeled with fluorescent LaF3:Eu nanoparticles. *Langmuir*, **23**, 10793.

59 Qui, X. and Sukhishvili, S. (2006) Copolymerization of N-Vinylcaprolactam and glycidyl methacrylate: Reactivity ratio and composition control. *J. Polym. Sci., Part A: Polym. Chem.*, **44**, 183.

60 Peng, S. and Wu, C. (2001) Ca^{2+}-induced complexation between thermally sensitive spherical poly(N-vinyl-caprolactam-co-sodium acrylate) microgels and linear gelatin chains in water. *Polymer*, **42**, 7343.

61 Peng, S. and Wu, C. (2001) Ca^{2+}-induced thermoreversible and controllable complexation of poly(N-vinylcaprolactam-co-sodium acrylate) microgels in water. *J. Phys. Chem. B*, **105**, 2331.

62 Peng, S. and Wu, C. (2001) Surfactant effect on pH and temperature sensitivities of Poly(N-vinylcaprolactam-co-sodium acrylate) microgels. *Macromolecules*, **34**, 568.

63 Peng, S. and Wu, C. (2003) Influence of initial chain conformation on the formation of mesoglobule phase in a dilute heteropolymer solution. *Polymer*, **44**, 1089.

64 Pich, A., Teissier, A., Boyko, V., Lu, Y., and Adler, H.J. (2006) Synthesis and characterization of poly(N-vinylcaprolactam)-based microgels exhibiting temperature and pH-sensitive properties. *Macromolecules*, **39**, 7701.

65 Schachschal, S., Demco, D., Popescu, C., Eckert, T., Richtering, W., and Pich, A. (2010) Polyampholyte microgels with anionic core and cationic shell. *Macromolecules*, **43**, 4331.

66 Laukkanen, A., Hietala, S., Maunu, S.L., and Tehnu, H. (2000) Poly(N-vinylcaprolactam) microgel particles grafted with amphiphilic chains. *Macromolecules*, **33**, 8703.

67 Pich, A., Berger, S., Ornatsky, O., Baranov, V., and Winnik, M.A. (2009) The influence of PEG macromonomers on the size and properties of thermosensitive aqueous microgels. *Colloid Polym. Sci.*, **287**, 269.

68 (a) Pich, A., Zhang, F., Shen, L., Berger, S., Ornatsky, O., Baranov, V., and Winnik, M.A. (2008) Biocompatible hybrid nanogels. *Small*, **4**, 2171; (b) Berger, S., Ornatsky, O., Baranov, V., Winnik, M.A., and Pich, A. (2010) Hybrid nanogels by encapsulation of lanthanide-doped LaF_3 nanoparticles as elemental tags for detection by atomic mass spectrometry. *J Mater. Chem.*, **20**, 5141.

69 Berger, S., Singh, R., Sudha, J.D., Adler, H.-J., and Pich, A. (2010) Microgel/Clay nanohybrids as responsive scavenger systems. *Polymer*, **51**, 3829.

6
Doubly Crosslinked Microgels

Brian R. Saunders

6.1
Introduction

The purpose of this chapter is to review work concerning a new type of hydrogel: doubly crosslinked microgels (DX microgel). This is a new area of hydrogel research which involves hydrogels formed by the linking together of microgel particles. Microgel particles are crosslinked polymer colloid particles that swell in a good solvent or when the pH approaches [1–4] their pK_a. This review aims to show how DX microgels can be prepared, considers their unique structure–property relationships and demonstrates their importance as a versatile hydrogel system for the future. It will be shown that DX microgels provide a unique colloidal-scale approach for designing advanced hydrogel structures which allows new properties to be obtained. In this review we focus on DX microgels involving permanent covalent bonds. Dynamic DX microgels that have labile bonds between particles, although of considerable interest [5], are beyond the scope of this review.

6.1.1
Definitions and Classifications of SX and DX Microgels

For the purposes of this review, a DX microgel is defined as a hydrogel that comprises singly crosslinked microgels (SX microgel) where these microgels act as the only crosslinking species within the hydrogel. The SX microgels are, themselves, internally crosslinked. There are therefore two types of elastically effective chains within a DX microgel; *intrap*article chains (within the SX microgels) and *interp*article chains (linking neighboring particles). If all of the interparticle chains were to be severed, the DX microgel would redisperse (as a SX microgel dispersion) if it were in a good solvent for the SX microgel. A diagram depicting a DX microgel is shown in Figure 6.1. This figure also shows images of DX microgel based on poly(ethylacrylate-*co*-methacrylic acid-*co*-butanediol diacrylate) microgel, abbreviated as E-BDD. Note how the DX microgel appears blue (top right) and slightly red (bottom right) when viewed, respectively, by scattered and transmitted light. This is because it is composed of covalently linked colloid particles.

Hydrogel Micro and Nanoparticles, First Edition. Edited by L. Andrew Lyon and Michael Joseph Serpe.
© 2012 Wiley-VCH Verlag GmbH & Co. KGaA. Published 2012 by Wiley-VCH Verlag GmbH & Co. KGaA.

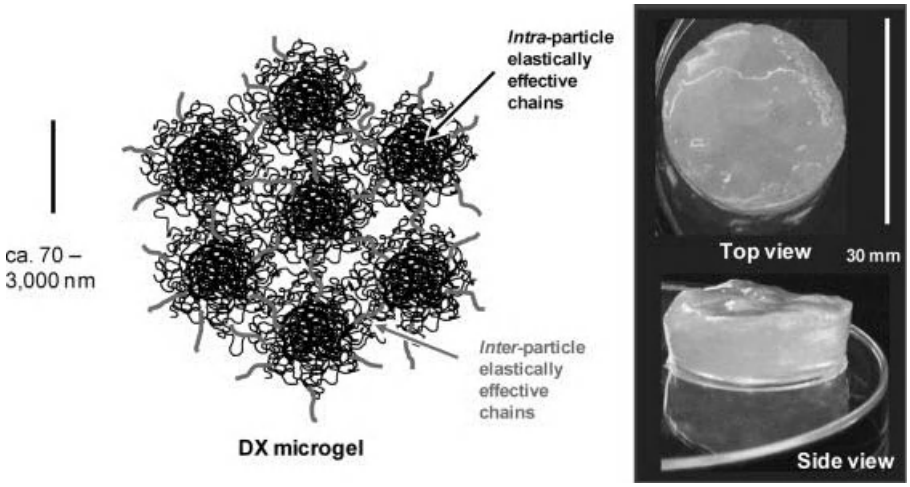

Figure 6.1 Depiction of a DX microgel (left) and images of a pH-responsive DX microgel based on E-BDD (right). See text.

Microgel-reinforced hydrogels [6, 7] are also discussed in this review. They are defined here as hydrogels containing microgel particles that are covalently crosslinked to a hydrogel network. If the microgel particles were detached from the hydrogel network (by severing all chains at the periphery of the microgel particles) the hydrogel would remain intact. These hydrogels are related to DX microgels. For microgel-reinforced hydrogels containing low-volume fractions of microgel particles, these systems approach conventional hydrogels in structure and properties. In the case of very high-volume fractions of microgel particles they approach DX microgels in structure and properties.

6.1.2 A Brief History of Doubly Crosslinked Microgels

According to the authors' literature searches, the first example of a DX microgel was that from the group of Hu *et al.* [8] in 2000. That work used an aggregation method to prepare hydroxypropyl cellulose DX microgels. They noted a fast swelling response of their DX microgels. A subsequent article by the same group was entitled "Hydrogel opals" and demonstrated for the first time the ability to prepare temperature-responsive photonic hydrogels from temperature-responsive microgels [9]. The early major developments in DX microgel preparation came from the Hu group and are discussed in detail below. Other noteworthy developments for DX microgels were (i) the use of an aggregation-based method for poly(NIPAM)-based microgels Cho *et al.* [10, 11], (ii) the preparation of microgel-crosslinked hydrogels by Xia *et al.* [12] in 2010, and, recently, (iii) demonstration of an interpenetration approach for DX microgel preparation [13].

Microgel-reinforced hydrogels appear to have mainly been pursued in the context of biomaterials applications [6, 7, 14] and have all been based on hyaluronic acid. The first publication in this area was by Jia *et al*. [14].

6.1.3
Stimulus-Responsive DX Microgels

Because DX microgels are composed of SX microgels they inherit the responsive behavior of the parent microgels. This was shown elegantly by Hu *et al*. [9] and also Cho *et al*. [10, 11]. To date, most DX microgels studied have been temperature responsive. At Manchester we have reported the first examples of pH-responsive DX microgels [13]. To date SX microgels have been investigated that are responsive to temperature, pH, redox species, and also enzymes [1–4]. It follows that DX microgels could also be prepared that have each of these properties. With the exception of enzyme response, all of these responsive behaviors have now been reported for DX microgels.

6.1.4
General Equations Governing Hydrogel Swelling

The most important property of DX microgels is their ability to swell. Hydrogel swelling theory originates from the original pioneering work of Flory [15], who considered swelling of both neutral and ionic polymer networks. We will briefly outline the key equations in the following. More detail can be found in the original text [15]. Comprehensive swelling equations for ionic hydrogels have been reported in seminal studies by Brannon-Peppas and Peppas [16]. The following equations are simplified versions of more complicated equations. They are shown in this form because they provide general guidance in terms of hydrogel formulation in relation to swelling. The key parameter is the volume swelling ratio, Q. This is the ratio of the swollen to collapsed hydrogel volume.

The following equation describes the swelling ratio, Q, for a non-ionic hydrogel [4]:

$$Q \approx \left[\left(\frac{M_A}{f_B \varrho_A x_B}\right)\frac{(1/2-\chi_{12})}{\nu_1}\right]^{3/5} \tag{6.1}$$

For this equation M_A and ϱ_A are, respectively, the molar mass and density of the main co-monomer from which the hydrogel is composed. Furthermore, f_B, x_B, χ_{12}, and ν_1 are, respectively, the number of elastically effective chains formed per crosslinking monomer unit, mole fraction of crosslinking monomer, Flory interaction parameter, and molar volume of the solvent. The subscripts 1 and 2 refer to the solvent and polymer network, respectively. This equation predicts that Q will increase with decreasing x_B, χ_{12} and f_B.

The equations governing the swelling for ionic hydrogels are complex [16]. Simplified versions that apply in the limit of low electrolyte concentrations are given

below and are based on Flory's work [15]. Equation 6.2 overestimates Q for hydrogels in high electrolyte environments (e.g., *in vivo*).

$$Q \approx \left[\left(\frac{M_A}{f_B Q_A x_B}\right)\frac{\alpha}{v_u}\right]^{3/2} \tag{6.2}$$

For this equation, v_u is the molar volume of the structural unit. It is calculated from the average repeat unit molar mass and density. The parameter α is the degree of neutralization. The value of α for an ideal polyelectrolyte-containing acid groups is given by the following equation.

$$\alpha \approx \left(\frac{1}{1+10^{(pKa-pH)}}\right) \tag{6.3}$$

For this equation [4] the apparent pK_a is used. This corresponds to the point at which half of the acid groups have been neutralized. These two equations show the importance of α and hence the pH in relation to the pK_a for controlling Q for ionic hydrogels. The pK_a is tunable through design. The equations do not consider complications, such as activity coefficients and factors that alter the pK_a, such as ionic strength and intra-segment interactions [17].

The swelling behavior for DX microgels will be complicated by the presence of an additional source of crosslinking, and hence elastically effective chains, that exist between the particles. The overall swelling ratio should be a weighted combination of the swelling contributions from the intra- and interparticle crosslinks. Equations governing this combination, and hence DX microgel swelling, remain to be determined.

6.1.5
General Equations Governing Hydrogel Mechanical Properties

The following equation originates from rubber elasticity theory [18] and can be used to describe the modulus of a hydrogel network [19].

$$G = \frac{\varrho RT}{M_c} \tag{6.4}$$

For this equation G is the shear modulus and ϱ is the density of the polymer that comprises the network. M_c is the average molar mass of the elastically effective chains. R and T have their usual meanings. Generally, the strain at break will be an increasing function of M_c.

An equivalent version of Equation 6.4, that is often used, is

$$G = nRT \tag{6.5}$$

where n is the number density of elastically effective chains. This equation is potentially useful as a starting point for considering DX microgel elasticity because it is possible to consider two contributions for n, one arising from intraparticle chains and the other interparticle chains. The challenge is then to derive an equation with

reasonable weighting for both contributions in terms of the DX microgel composition. That is not within the scope of this review. For now we simply note that n has two contributions and limit our discussions to qualitative considerations.

6.2
Methods of Preparation

A survey of the literature reveals that there are a number of different methods that have been used to prepare hydrogels containing covalently-linked microgels. These are depicted in Figure 6.2 and are discussed in the following. They are classified here based on the structures of the hydrogels. For the purposes of this review DX microgels encompass all of the approaches depicted in Figure 6.2 with the exception of Figure 6.2c.

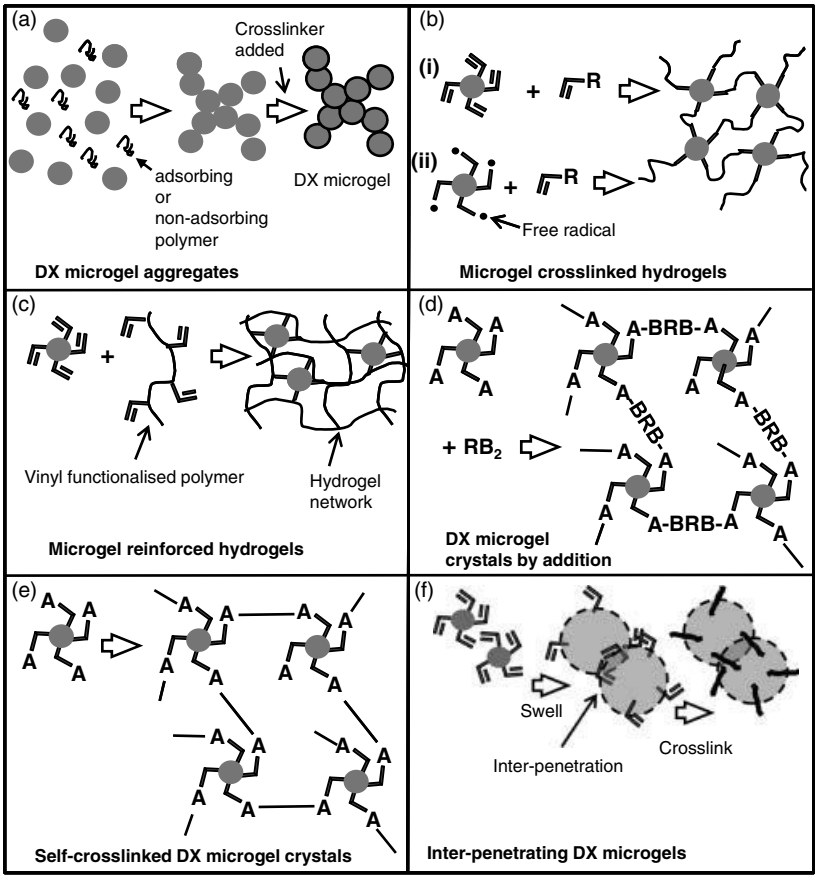

Figure 6.2 Depictions of six general methods for preparing hydrogels containing covalently linked microgels. The size of the SX microgels considered is about 70–3000 nm. For (d) addition of **BRC** can also be used where **B** and **C** react with the **A** functional groups to form covalent bonds.

6.2.1
DX Microgel Aggregates

This method involves triggered aggregation of SX microgels followed by covalent linking. Hu *et al.* first demonstrated this method [8]. Later, DX microgel formation using the aggregation method was investigated by Cho *et al.* [11] (shown in Figure 6.2a). They used 800 nm poly(NIPAM–AAm) microgel dispersions (AAm is allylamine) and then added linear poly(acrylic acid) to cause bridging flocculation. After heating the aggregated dispersion to 65 °C glutaraldehyde crosslinking was used to form permanent DX microgels. The authors also reported that the DX microgels could be prepared using depletion flocculation (with non-adsorbed polymer).

Recently, the same group found that soluble linear poly(NIPAM-*co*-AAm) was also present as a result of microgel preparation [10]. This is not surprising because poly (AAm) is very hydrophilic at pH values less than about 10. The result of the presence of the linear polymer was that the dispersions had a tendency to exhibit depletion flocculation when heated. They found that DX microgels could be prepared by heating 1.4 wt% dispersions at 65 °C for 4 h.

6.2.2
Microgel Crosslinked Hydrogels

This method applies to DX microgels where the SX microgels are the only crosslinking species and there are long elastically effective chains between the microgels. Cai *et al.* [20] constructed thermoresponsive photonic hydrogels by copolymerization of vinyl-functionalized microgels with acrylamide or poly(ethyleneglycol) methacrylate. Linear polymer chains linked the microgel particles. The particles were in the swollen state when crosslinked. They used photocrosslinking to form the hydrogel. This approach is depicted in Figure 6.2b(i).

A different example of the formation of the same general type of DX microgel is given by Xia *et al.* [12]. Linear polymer chains linked collapsed microgel particles. They prepared poly(NIPAM-*co*-acrylic acid) microgel particles. They claim to have converted some of the carboxylic acid groups to per-acid initiators by reaction of the washed microgels with H_2O_2. The authors used XPS spectra of the peroxide-treated microgels to support their claim of per-acid formation. The microgel initiators were then added to NIPAM/acrylic acid solution to form hydrogels. Swelling experiments of the hydrogels provided indirect support for their view that microgel-based initiation had occurred (as shown in Figure 6.2b(ii)).

6.2.3
Microgel-Reinforced Hydrogels

A third approach involves the formation of a hydrogel network in the presence of functionalized (reactive) microgel particles. The functional groups on the microgel particles enable covalent linking of the microgel particles to the hydrogel network. This is shown in Figure 6.2c for the case of vinyl functionalized microgel particles.

Bencherif *et al.* [7] prepared PEG-based microgel particles using inverse mini-emulsion polymerization combined with an ATRP method. They subsequently reacted the surface hydroxyl groups to insert surface vinyl groups. Photocrosslinking of the vinyl-functionalized microgels with hyaluronic acid-glycidyl methacrylate (HAGM) macromonomer produced microgel-reinforced hydrogels.

A related method was used by Jha *et al.* [6] to prepare their hydrogels, which were also based on hyaluronic acid (HA). This work was related to an earlier paper which also involved HA-based hydrogels [14]. In that case the authors prepared HA-based microgel particles. The same chemistry, which involved reaction of aldehyde and hydrazide functional groups, was elegantly used to prepare the microgels and then the hydrogels. The SX microgel particles were first prepared by inverse emulsion polymerization and were in the swollen state upon subsequent crosslinking.

6.2.4
DX Microgel Crystals by Small Molecule Addition

This method is related to that shown in Figure 6.2b; however, in this case it is the reaction of a small difunctional molecule linker that provides the DX microgels. This approach is depicted in Figure 6.2d. Hu *et al.* [9] demonstrated this using two chemistries. Poly(NIPAM-*co*-AA) and poly(NIPAM-*co*-HEA) (hydroxylethyl acrylate) microgels were used. The latter was able to be conducted in water, which is a potential advantage for this system. The approach using poly(NIPAM-*co*-AA) required the use of acetone as a solvent and was further investigated by Zhou *et al.* in 2007 [21].

In 2003 and 2007 the same group [22, 23] applied a related approach using poly (NIPAM-*co*-AAm) microgel particles. In this case the small molecule linker used was glutaraldehyde, which reacted with primary amine groups from the AAm segments. The approach used here was to heat a concentrated dispersion to above the volume phase transition temperature (VPTT) for the microgel, allowing ordered array formation, followed by cooling to bring the interfaces close enough for interparticle crosslinking. The formation of colloidal crystals in this way was established earlier by Lyon *et al.* [24]. The stability of the Schiff base formed by the reaction involving glutaraldehyde should have been limited and an additional reduction reaction could have been beneficial since it would have converted those groups into the more stable amides. An example of this type of reaction is given by Wang *et al.* [25].

6.2.5
Self-Crosslinked DX Microgel Crystals

The group of Hu *et al.* [26] have also demonstrated a self-crosslinking approach to DX microgel formation, which is depicted in Figure 6.2e. Once again the work was motivated by potential photonic applications. The method involved drying poly (NIPAM-*co*-*N*-hydroxymethacrylamide) microgel dispersions to dryness at room temperature. The dispersions self-crosslinked, in the dry state, at room temperature. The reaction, a polycondensation, required three weeks for completion. The product was a swellable colloidal crystal. The obvious benefit of this approach is its simplicity.

It was, understandably, rather slow, and could not be accelerated successfully by heating. Because the linkages between the microgels are the shortest possible it is expected that these hydrogels would be brittle.

6.2.6
Interpenetrating DX Microgels

The final approach discussed was developed at Manchester [13] and is depicted in Figure 6.2f. This also involves crosslinking of vinyl-functionalized microgels. The difference between this approach and those discussed above is that the microgels are pH-responsive and form physical gels prior to crosslinking of the vinyl groups. The physical gel occurs as a consequence of particle swelling and interpenetration of segments at the periphery of the microgel particles. The vinyl functionalization was achieved by reacting glycidyl methacrylate (GM) with some of the methacrylic acid (MAA) units of the microgel particles. No aggregation occurred as a consequence of functionalization.

6.3
Methods of Characterization

DX microgels are characterized by a combination of methods drawn from those usually used for hydrogels. It is essential, however, that the microgel particle precursors are thoroughly characterized. This is particularly important when they are functionalized because functionalization of microgels can be accompanied by a decrease in colloidal stability. If aggregation is present in the precursor microgel it will almost certainly be present in the DX microgel. In the following a discussion of the main techniques currently used to characterize DX microgels is presented.

6.3.1
^{1}H Nuclear Magnetic Resonance

For microgels that have been functionalized with reactive groups the mole fraction of these groups present is an important parameter. That is because these groups will provide crosslinking sites in the final DX microgels. If microgels are based on poly (NIPAM) it is sometimes possible to use ^{1}H nuclear magnetic resonance (^{1}H NMR) of swollen particles to estimate composition [6]. However, one must consider broadening of the signals which can complicate the interpretation. Low-temperature spectra are useful. Jha *et al.* [6] used acid digestion to cleave their vinyl functionalized microgels in an effort to simplify the ^{1}H NMR spectra. Sometimes it is possible to prepare model microgels which are not crosslinked and analyze their NMR spectra in good solvents. However, that approach will not be compatible with functionalization strategies that require microgel swelling. A potentially powerful technique for probing hydrogel composition is magic angle spinning (MAS) ^{1}H NMR. This was used successfully by Bencherif *et al.* [7]. MAS involves acquisition of the NMR

spectrum while a solid sample is rotated about an axis inclined at 54.7° to the magnetic field direction [27]. At this angle the anisotropy in all the interactions vanish, which increases the resolution of the spectral features considerably. However, that technique is not widely available.

6.3.2 Confocal Microscopy

Confocal laser scanning microscopy (CLSM) has been used to investigate the morphology of DX microgels [7, 10, 11]. CLSM images are fluorescence spectral maps of a sample and the technique has been reviewed elsewhere in the context of pharmaceutical systems [28]. In CLSM contrast originates from differences in the concentration and spectral properties (absorption and emission) of the chromophores. In the absence of complications such as photobleaching, the intensity of a given part of an image is proportional to chromophore concentration. If quantitative information is sought from this technique it is important to first check that the fluorescent intensity is proportional to the chromophore concentration.

Cho *et al*. [10, 11] fluorescently labeled their poly(NIPAM-*co*-AAm) particles with methacryloxy thiocarbonyl rhodamine B (Polyfluor 570). This commercially available vinyl-functionalized chromophore was copolymerized within the particles during particle formation. The advantage of this approach was that the aggregated microgels obtained from their aggregation method were clearly visualized using CLSM. A CLSM image from the work of Cho *et al*. [10] is shown in Figure 6.3a. This is a

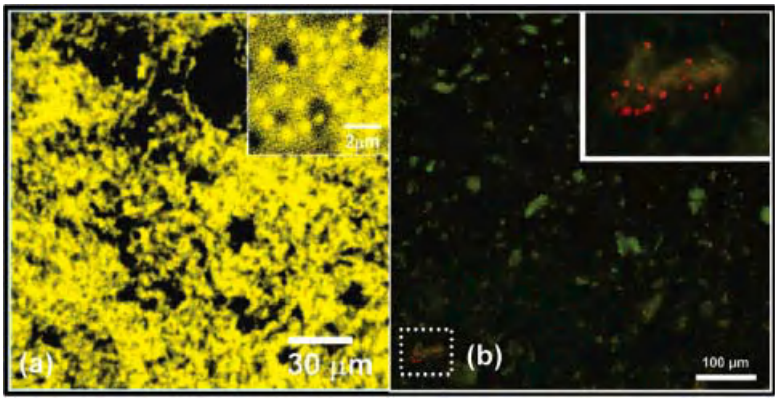

Figure 6.3 CLSM images of microgel-containing hydrogels. (a) Poly(NIPAM)-based DX microgel labeled with Polyfluor 570. (b) HA-based microgel-reinforced hydrogel. For (b) two different fluorescent labels were incorporated. The red dots show aggregated microgels. Reproduced from (a) [10] and (b) [7] with permission of American Chemical Society and Elsevier, respectively.

very useful technique to enhance the contrast of small microgel particle networks and overcomes a problem of using scanning electron microscopy (SEM) which can result in artifacts due to drying (discussed below).

Bencherif *et al.* [7] also used CLSM to examine their HA-based microgel-reinforced hydrogels (Figure 6.3b). They incorporated RITC-dextran during microgel preparation. Interestingly, these authors used FITC-dextran to label the hydrogel network. The result was that the CLSM image showed the HA hydrogel as green and the microgel particles as red (Figure 6.3b). This very useful image showed that their microgels were aggregated within the hydrogel.

6.3.3
Scanning Electron Microscopy

SEM is an experimentally convenient technique for investigating the morphology of hydrogels. It has been used by a number of authors to investigate the morphology of DX microgels [6, 10–14]. Several examples are shown in Figure 6.4. The method most commonly used for sample preparation involves freeze-drying [10, 12, 13]. A potential problem with this technique is the formation of ice crystals and this can, in principle, give artifacts due to the ice crystals. Indeed, Yao *et al.* [29], used directional freeze-drying of oppositely charged microgels to obtain three-dimensional hierarchical morphologies (Figure 6.4d). The morphology of the DX microgels prepared by interpenetration (Figure 6.4e and f) are discussed later. Jha *et al.* [6] used cryogenic SEM (cryo-SEM) to prepare and view their samples (Figure 6.4a and b). This involved samples being rapidly frozen (freezing rate $\geq$10 000 °C s^{-1}) under high pressure ($\geq$ than 2000 bar) followed by freeze-fracturing in liquid nitrogen. The rapid freezing rate was too fast to allow ice formation, simplifying the interpretation.

6.3.4
Swelling Experiments

DX microgels swell in response to an external stimulus such as temperature or pH. Provided the polymer segments that comprise the network are in good solvency conditions the DX microgel will spontaneously swell. The extent of swelling is easily measured for a hydrogel from gravimetric measurements of hydrogel mass as a function of time. These measurements should also be used to determine the sol fraction (SF, soluble fraction) of the hydrogel. This is because the SF value gives a direct measure of the efficiency of network formation. It is normally possible to measure Q and SF from the same series of experiments, which should be conducted in at least triplicate.

The mass swelling ratio for a hydrogel, Q_m, is simply measured as the mass ratio of the swollen (m) to the initial dry hydrogel (m_{dry}) mass. The equation used is:

$$Q_m = \frac{m}{m_{dry}} \tag{6.6}$$

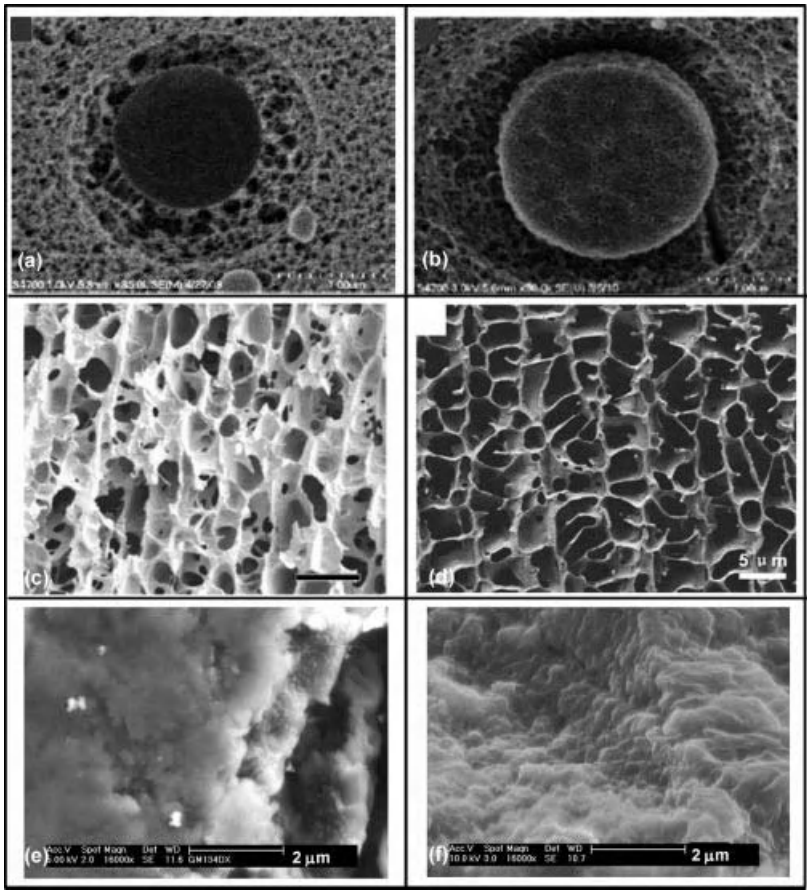

Figure 6.4 Cryo-SEM images for HA-based microgel reinforced hydrogels are shown in (a) and (b). The scales are 1 µm. SEM of freeze-dried DX microgels based on poly(NIPAM) (c) and microgel aggregates using directed ice formation (d) are also shown. The scale bars in (c) and (d) are 50 and 5 µm, respectively. Images (e) and (f) show freeze-dried pH responsive DX microgels based on GM functionalized M-EGD and E-BDD microgels, respectively. (a, b) Reproduced from [6] by permission of the Royal Society of Chemistry. (c) Reproduced from [10] by permission of the American Chemical Society. (d) Reproduced from [29] by permission of the Royal Society of Chemistry. (e, f) Reproduced from [13] by permission of the Royal Society of Chemistry.

If the density of the dried polymer (ϱ_p) and solvent (ϱ_s, e.g., water) are the same then Q_m and Q are equivalent. However, if $\varrho_p \neq \varrho_s$ then the following equation applies.

$$Q = \varrho_p \left(\frac{Q_m}{\varrho_s} + \frac{1}{\varrho_p} \right) - \frac{\varrho_p}{\varrho_s} \tag{6.7}$$

It is recommended that Q, as defined here, is used to quantify swelling of DX microgels. The reason for this is the Q values can then be compared to

those of the parent microgels. The swelling ratio for a microgel particle is given by:

$$Q = \left(\frac{d}{d_{\text{coll}}}\right)^3 \tag{6.8}$$

For equation (6.8) d and d_{coll} are the diameters at a given set of conditions (pH, temperature, etc.) and the collapsed state, respectively. The value for d is usually measured using photon correlation spectroscopy (PCS) and is the hydrodynamic diameter. The choice of the value to use for d_{coll} can be problematic for microgel particles. If the particles are completely collapsed, but not aggregated, at a given pH, temperature, and so on, then PCS measurements can be used for this. If that is not possible, and the particles collapse as spheres in vacuum, then SEM images can be used as an approximation. In that case the z-average diameter may provide a better value for d_{coll} if individual particles are clearly seen. Of course, it is better to use PCS data to obtain Q if that is possible since both diameters should be from the same technique.

The value for SF for hydrogels is obtained using the same measurement technique as for Q combined with the final mass at the end of the swelling experiment ($m_{\text{dry(end)}}$). The equation for the mass SF is:

$$SF = \frac{m_{\text{dry}} - m_{\text{dry (end)}}}{m_{\text{dry}}} \tag{6.9}$$

The formation of a network of infinite molar mass will give an SF of zero. Inefficient network formation results in a loss of mass during swelling and SF will be greater than zero. It is not necessary for all of the crosslinkable groups to have reacted in order to achieve an SF value of zero, which means that this method does not give a direct measure of functional group extent of reaction.

6.3.5 Optical

The optical properties of photonic DX microgel; crystals have been studied extensively [9, 20, 22, 23]. This was performed by examining the hydrogels using UV-visible spectroscopy and varying the particle concentration or temperature. Hu *et al.* [9] showed that these data can be analyzed by application of Bragg's law of diffraction. In that work the wavelength of the shoulder of the absorption (λ_c) was plotted against the calculated interparticle spacing (D) using the assumption of face-centered cubic or hexagonally close-packed lattice. The packing fraction for each lattice is 0.74. They further assumed that the scattering angle corresponding to the absorbance measured by the spectrophotometer was 90° and found a linear relationship between λ_c and D which strongly supported their interpretation of the scattering behavior. This technique is a particularly useful method for characterizing photonic DX microgel crystals where the value for λ_c is less than or equal to D, or, equivalently, D is greater than or equal to λ_c.

6.3.6
Dynamic Rheology

Dynamic rheology is a key method for studying the mechanical properties of gels. To date it has only been reported by our group for the study of DX microgels. The method is simple, powerful, and well suited for hydrogels. The technique has been very well described in detail elsewhere [30]. Briefly, dynamic rheology consists of measurements of the storage modulus (G') and loss modulus (G'') as a function of oscillation frequency (ν). G' is the stress required to shear the elastic component of the gel by unit strain; whereas G'' is the stress required to shear the viscous component by unit strain [31]. Of particular interest are the values for G' and tanδ ($= G''/G'$). In order to be classified as a gel, tanδ < 1.0. However, there is a second criteria that is frequently overlooked in the literature, which is that tanδ should be independent of frequency. This is a Winter–Chambon criterion for a network [32, 33]. We refer to this as ideal gel behavior. This is considered further below.

There are two types of dynamic rheology experiments that should be conducted. The first is a strain sweep. This consists of varying the shear strain (γ) at fixed frequency (e.g., 1 Hz) over a range of strains from about 0.01 to 1000%. (A gap size of about 1000 μm is commonly used.) A plot of G' and tanδ as a function of γ enables identification of the γ values for which G' decreases and tanδ increases. Typical data are shown for a swollen DX microgel from our group [13] in Figure 6.5. Of particular interest here is the yield strain. There are two commonly used yield strains that can be identified. The first is the yield strain at which G' falls to 95% of the value measured at a γ value of 1% [34, 35]. This onset yield strain, γ^*, is shown in Figure 6.5a and corresponds to about 13% for this DX microgel. The value for γ^* is particularly important for potential applications involving load-bearing tissue, because the strain that results in the onset of network breakdown is of paramount importance from the biocompatibility perspective.

A second parameter of interest is the strain at which a gel-to-fluid transition occurs. This yield strain, γ_c, corresponds to an advanced breakdown of the network structure

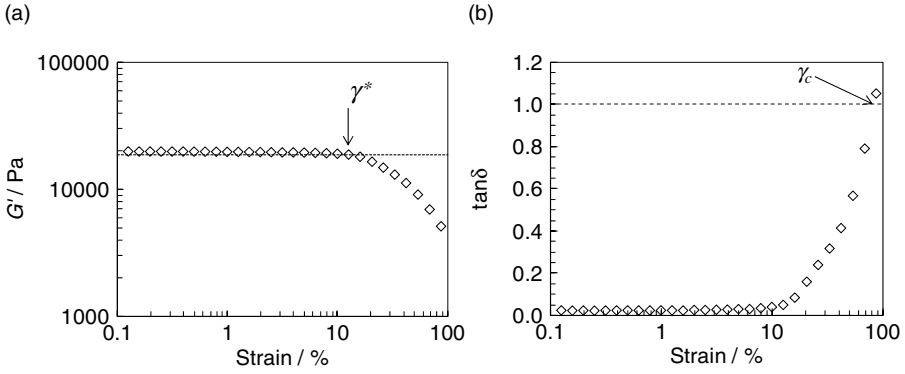

Figure 6.5 Variation of G' (a) and tanδ (b) with strain for a DX microgel based on E-BDD.

responsive for load distribution and mechanical energy storage within the gel. The choice of the yield strain to be used is governed by the fundamental information being sort and/or the potential application (if applicable).

Frequency sweep data are also important to obtain and complement the strain sweep data. For those experiments it is important to use a strain that is within the linear viscoelastic region. That is, a strain should be selected from the strain-sweep measurements to ensure that the strain used for the frequency-sweep measurements corresponds to the region where G' and tanδ ($= G''/G'$) are independent of strain. For the system shown in Figure 6.5, we used $\gamma = 1\%$ for the frequency-sweep experiments [13]. The frequency-sweep data provide useful information about the gel quality. For a gel-forming system a very good method for determining the condition at which an ideal gel is formed is to plot tanδ (at a range of frequencies) as a function of a given experimental parameter (e.g., microgel concentration, pH, temperature). If a critical value is present at which an ideal gel exists then the values for tanδ will intersect [31] and the Winter–Chambon criterion will be satisfied.

6.3.7
Compression Modulus Measurements

The compression modulus (K) is a particularly important property for hydrogels, especially in the context of load support applications in the body. It is determined from the initial gradient of a compressive stress vs. strain plot in the linear region. A number of different approaches have been used to obtain K values. They normally use a cylindrical sample of hydrogel in a laterally unconstrained geometry. This corresponds to uniaxial compression. Zhou *et al.* [21] used compressive stress vs. deformation measurements obtained using a digital force gage. Bencherif *et al.* [7] used a texture analyzer. The equations used by these authors to analyze the applied compressive stress (σ) vs. relative deformation (λ) is the same as those used for conventional hydrogels [36].

$$\sigma = K\left(\lambda - \frac{1}{\lambda^2}\right) \tag{6.10}$$

and

$$\lambda = \frac{L}{L_o} \tag{6.11}$$

where L and L_o are the lengths of the deformed and undeformed samples, respectively.

6.3.8
Tensile Testing

Tensile tests measure the elastic, Young's, modulus (E) and are conducted using "dumbbell" shape samples and a tensile testing instrument. These measurements are widely used for elastomers. However, measurements for hydrogels are more

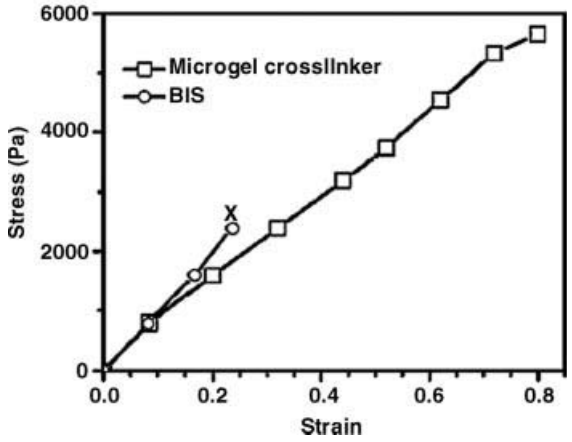

Figure 6.6 Tensile stress vs. strain data for PEG microgel-crosslinked hydrogel (labeled as microgel crosslinker) and microgel-reinforced hydrogel (labeled as BIS). Reproduced from [20] with permission from the American Chemical Society.

difficult, primarily because of the problem of gripping the samples without damaging them. The data are obtained by measuring the σ vs. tensile strain (ε). The ε value is the change in sample length divided by the initial sample length. Of particular interest for hydrogels are the value for E, obtained from the initial gradient in the linear section of the curve, as well as the tensile strength (σ_B) and strain at break (ε_B). The latter can be generally regarded as being related to the molar mass of the elastically effective chains. Tensile data reported by Cai *et al.* [20] for their hydrogels are reproduced in Figure 6.6. The values for E were given as 7 and 10 kPa, respectively, for the microgel-crosslinked and microgel-reinforced hydrogels. The values for σ_B and ε_B can be estimated from their data for the microgel systems as, respectively, about 5.7 kPa and 0.8, respectively. The relatively high ε_B value for the microgel-crosslinked hydrogel is indicative of relatively large M_c values.

6.4 Morphology

6.4.1 Morphology Types

As mentioned above, the morphology of DX microgels is of particular interest because it should provide insights into the mechanical behavior. There are several morphology types that have been reported for the hydrogels considered here. The work using confocal microscopy reported by Bencherif *et al.* [7] (Figure 6.3b) is particularly useful because it showed that aggregation occurred prior to hydrogel formation. Dispersing microgels in polymer solutions always provides opportunity for depletion interactions. The extent to which this will occur will be a function of

particle size, polymer size, and concentration [37] and whether or not the polymer can penetrate the pores of the microgel particles. Although it is not certain that depletion was the cause of aggregation in the work of Bencherif *et al.* [7], it seems a distinct possibility. In the work of Cho *et al.* [10] (Figure 6.3a) aggregation was used as a tool to promote DX microgel formation. In that case CLSM images were invaluable in explaining the rapid swelling transitions observed for their hydogels.

The cryo-SEM images reported by Jha *et al.* [6] (Figure 6.4a and b) provide one of the best examples of using morphology data to explain the properties of microgel-reinforced hydrogels. It was these cryo-SEM images that demonstrated that their vinyl functionalized microgels were attached to the hydrogel network. The image reproduced here in Figure 6.4a clearly shows hydrogel network in contact with the microgel particle periphery. That image was complicated, however, by the unequal deswelling of the microgel and hydrogel network. Nevertheless, the central point that attachment of the hydrogel to the microgel particles occurred was strongly supported by these images. A control image obtained using noncovalently attached microgel particles showed a much greater separation between the microgel and hydrogel network (Figure 6.4b). Cryo-SEM data provided a clear demonstration of a microgel-reinforced hydrogel.

The SEM images reported by our group for DX GM-M-EGD microgels (Figure 6.4e) showed a compact, mostly smooth, morphology with some evidence of the individual microgels. (The microgel particles had a size in the range of about 100 nm in the collapsed state.) This relatively featureless morphology was argued to be the result of microgel interpenetration during DX microgel formation [13]. Closer examination of the image shows some individual particles are also present which may indicate that interpenetration was not complete.

6.4.2
Morphology Control

Establishing methods for control DX microgel is still in its infancy and there are not many examples currently available that unambiguously demonstrate a morphological change through composition. (The work of the Hu group [8, 9, 22] is an exemption to this as particle spacing was tunable.) We have shown that some changes can be achieved through the composition of the microgel particles. Figure 6.4e and f show morphologies for DX GM-M-EGD and DX GM-E-BDD microgels. The latter morphology (Figure 6.4f) had no features that could be identified as particles. It appears that coaleascence of neighboring microgel particles had occurred throughout the surfaces that could be visualized. This was ascribed to a combination of increased interpenetration due to greater swelling of the SX GM-E-BDD microgels prior to DX microgel formation as well as the lower T_g of these microgel particles. Morphology control is expected to become an increasingly important issue for DX microgels because it offers the unique ability to control the hierarchial structure of a hydrogel on a colloidal scale. This was already an aim for the microgel-reinforced hydrogels being studied with a view to cartilage repair [6].

6.5
Properties

6.5.1
Swelling Properties of DX Microgels and Control

For a conventional hydrogel the time required for a swelling or shrinking transition to occur (transition time) is proportional to the square of its size [38]. The swelling kinetics for DX microgels have been reported by Hu *et al.* [8] and later by Cho *et al.* [10, 11]. The latter work used poly(NIPAM)-based systems. They used the modeling approach initially developed by Okajima *et al.* [39] and applied the following equation.

$$D = \left[(D_0 - D_\infty)\exp\left(-\frac{t}{\tau}\right)\right] + D_\infty \tag{6.12}$$

where D, D_o, and D_∞ are, respectively, the diameter of the hydrogels at time t, zero, and equilibrium. The parameter τ is the characteristic swelling relaxation time. Data from their work [11] are shown in Figure 6.7. They showed that τ decreased from about 250 min for a conventional bulk poly(NIPAM) hydrogel to 2.3 min for the DX microgel. This major decrease in swelling time was attributed to increased permeability as a consequence of the high porosity of the DX microgels. The effect of the highly porous morphology is to make the smallest dimension approach the size of the microgel particle building blocks [8]. In contrast (non-microporous) DX microgels prepared by interpenetration [13] do not show fast swelling kinetics because in that case the hydrogel was formed from a non-aggregated, expanded, microgel system where the particles were effectively occupying all of the volume of the gel. Comparison of these two approaches suggests that the swelling kinetics can be controlled

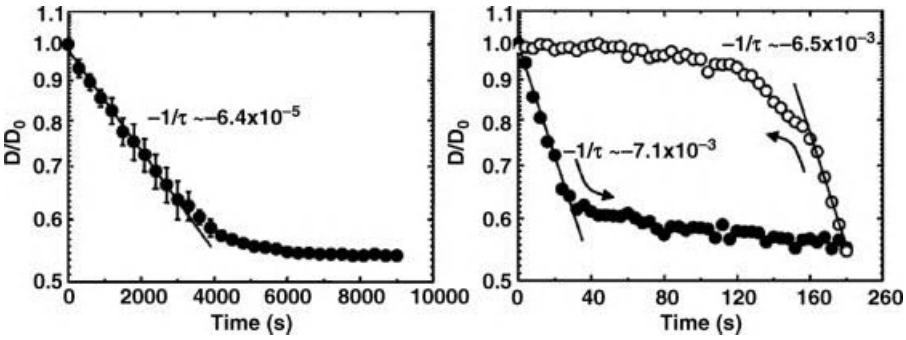

Figure 6.7 Variation of D/D_o (diameters of the cylindrical hydrogel during temperature ramping and that initially present) for (a) bulk hydrogel and (b) DX microgel based on poly (NIPAM). The temperatures were changed from 20 to 44 °C. (b) Also shows a reswelling experiment when the DX microgel was cooled back to 20 °C. Reproduced from [11] with permission from the American Chemical Society.

through the extent of aggregation (and porosity) formed during DX microgel preparation.

Values for Q_m were reported by Jha *et al.* [6] for their microgel-reinforced hydrogels. In that case the incorporation of microgel decreased Q_m compared to the parent hydrogel and values of about 38 were reported. The values for SF decreased with covalent attachment of the particles and decreased to about 0.10. The values for Q_m reported by Bencherif *et al.* [7] for their related materials were in the range of 22–21 depending on the microgel content. Again, incorporation of the microgels decreased Q_m compared to the parent hydrogel. Xia *et al.* [12] measured values for Q of up to 40 for their DX poly(NIPAM-*co*-AA) microgels. The highest Q values to be reported to date for DX microgels are those from Manchester [13]. In that work Q values of up to 55 at pH = 9.2 for DX GM-M-EGD microgels were reported. It is the high MAA content in the DX microgels that is responsible for the high extents of swelling for those systems.

In order to control the swelling of DX microgels the same parameters used for conventional hydrogels appear to apply. However, for DX microgels there are two types of crosslinking to consider. For example the DX GM-M-EGD microgel swelling could be decreased by increasing the extent of vinyl functionalization present for the microgel particles prior to double crosslinking. In that work [13] increasing the GM content by a factor of 3 decreased Q by a factor of about 1.8 at a pH of 7.4. As already mentioned above, the value for Q for microgel-reinforced hydrogels can be controlled by microgel loading if there is a difference in n for the microgel and hydrogel.

6.5.2
Optical Tuning

Arguably the best example of the photonic properties of microgel-crosslinked hydrogels is that published by Cai *et al.* [20] and reproduced in Figure 6.8. The image and graph are from the same data set. They show how temperature was used to tune the Bragg scattering maxima from periodic arrays of the microgel particles. Atomic force microscopy (AFM) images showed that the particles adopted a hexagonal close-packed arrangement. The color of the films was due to scattered light and the average plane separation and hence peak position was tunable using temperature. The authors also showed in related work [23] that the hydrogel color (and hence scattering) could be controlled through microgel particle concentration at fixed temperature.

6.5.3
Mechanical Properties of DX Microgels and Control

Table 6.1 summarizes modulus values reported for DX microgels in the literature to date. The modulus values for the microgel-reinforced hydrogels tend to be governed by the modulus values of the hydrogel phases themselves. However, this is not necessarily the case for DX microgels. The value for K for the microgel aggregates of Cho *et al.* [11] is at the lower end of the modulus values shown; however, this is

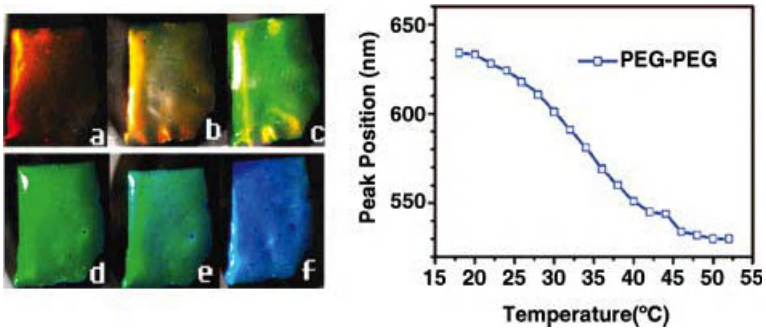

Figure 6.8 The images are from a poly (NIPAM-*co*-AAm) DX microgel as a function of temperature. For this system (a) to (f) correspond to 22, 24, 30, 34, 40 and 50 °C, respectively. The graph shows the absorption maximum peak positions as a function of temperature for the same DX microgels shown in the images. Reproduced from [20] with permission from the American Chemical Society.

consistent with the high porosity of those systems which will be largely responsible for the decreased modulus values. It is not possible to convert *E*, *K*, and *G* values without knowledge of their Poisson ratios. These values have not yet been reported for these systems.

Although there is considerable variation for these data, and direct comparison is difficult without the Poisson ratio, it can be seen that the DX GM(H)-M-EGD system stands out as the highest modulus value for a DX microgel reported to date. This may be due to differences in polymer concentration as not all of the concentrations were available for the studies cited in Table 6.1. However, the interpenetration method of preparation, which involves three-dimensional contact of the microgel particles, is likely to favor high modulus values.

It is instructive to consider how to control the modulus of DX microgels. For the pH-responsive DX microgels investigated at Manchester there are three parameters: pH, particle concentration, and extent of functionalization. For DX GM-M-EGD microgels prepared using SX GM-M-EGD microgels we have shown that the value for the storage modulus can be increased by a factor of six when the degree of GM

Table 6.1 Modulus values for selected hydrogels containing microgels.

System/hydrogel type	Modulus	Modulus/kPa	Reference
PEG–PEG/DX microgel	*E*	7.1	[20]
PEG–BIS/microgel reinforced hydrogel	*E*	10	[20]
Poly(NIPAM-*co*-AAm)/DX microgel	*K*	5 (at 20 °C)	[11]
HA-*co*-HGP/microgel-reinforced hydrogel	*K*	18.2	[6]
Poly(NIPAM-*co*-AAm)/DX microgel	*G*	0.5–1.3	[23]
DX GM(H)-M-EGD/DX microgel	*G*	19	[13]
HAGM microgel-reinforced hydrogels	*G*	35.6–37.8	[7]
HAADH microgel-reinforced hydrogels	*G*	0.16–2.0	[14]

functionalization increased by a factor of three. For these DX microgels it is expected that any process that leads to a higher n (Equation 6.5) will increase G'. It should be noted that the high-frequency value for G' can be approximated to G.

For pH-responsive DX microgels the pH used during preparation strongly affects the final modulus [13]. For this system the parent SX GM-M-EGD microgels had a pK_a of 7.1. DX microgels could not form until the pH exceeded this value. It was then that a physical gel and interpenetration of neighboring microgels occurred. The value for G' increased at higher pH values because of improved interpenetration and crosslinking. However, at pH values of about 9.6 hydrolysis and possibly particle deswelling (due to high electrolyte concentration) decreased G' (Figure 6.9a). We have also shown that the polymer volume fraction (ϕ_p) used during double crosslinking is an important factor. This can be seen for data for DX GM-M-EGD replotted [13] as a log–log plot in Figure 6.9b. An exponential increase of G' with ϕ_p occurs beyond a value of about 0.08. This was the value at which pronounced interpenetration of the particles was believed to occur. For these pH-responsive DX microgels the modulus values decreased upon swelling, which is expected since there are fewer elastically effective crosslinks per unit volume in the swollen state. These DX microgels show excellent potential for modulus tunability.

The ductility of the hydrogels is also an important issue because it governs the ability of these systems to withstand strain. The microgel crosslinked hydrogels of Cai *et al.* [20] had an ε_B of about 0.80. This is because of the relatively long linear polymer chains that existed between neighboring microgel particles. The DX GM-M-EGD microgels reported recently by our group [13] exhibited γ^* values of up to 0.65. Generally, the value for ε_B can be expected to increase with M_c because longer elastically effective chains will enable greater strain before rupture [40]. For the DX microgels this requires long elastically effective chains bridging the particles. This will in turn be controlled by the crosslink distribution within the microgel particles (especially near the particle surface) and also the nature and length of the interparticle

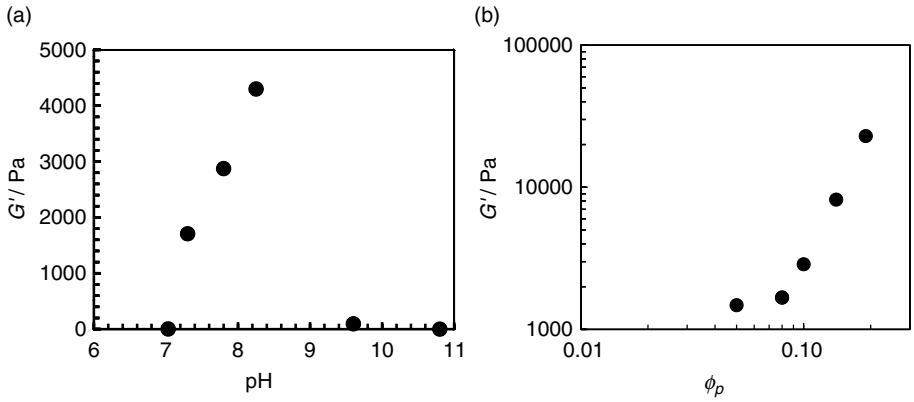

Figure 6.9 Variation of G' with (a) pH ($\phi_p = 0.1$) and (b) ϕ_p(at pH 7.8) for a DX GM-M-EGD microgel. Note that these are the pH values used during DX microgel preparation [13]. Reproduced by permission of the Royal Society of Chemistry.

crosslinking species. The data discussed above suggest that the microgel crosslinked hydrogel approach is currently best for high ε_B values.

6.5.4
Comparison of Properties with Microgels

Because DX microgels are constructed of microgels it is expected that that there will be a relationship between the swelling properties of the hydrogel and the parent microgels if no other structural factors are involved. Cho *et al.* [11] compared the temperature-dependent deswelling of their poly(NIPAM-*co*-AAm) microgels and the DX microgels. The deswelling data sets overlapped in the temperature range of 23–42 °C. This is not surprising given that their DX microgels were constructed by joining collapsed microgel particles at the interface through the aggregation method (Figure 6.2a).

The situation is not the same for DX microgels prepared using interpenetration. See Figure 6.10. The parent SX microgels (GM-M-EGD and GM(H)-M-EGD) had different extents of GM functionalization (Figure 6.10) but their pH-dependent swelling behaviors were not affected. However, the functionalization did have an effect for the DX microgels. At pH = 7.4 data points were available for each system. In both cases the DX microgels swelled more strongly than the parent microgels. This implies an overall decrease in the number density of elastically effective chains. The double crosslinking must have resulted in a longer average molar mass of elastically effective chains connecting the particles together compared to those present within the particles from microgel formation.

Figure 6.10 also shows that functionalization does affect DX microgel swelling. The swelling ratio was 24 for DX GM(H)-M-EGD (more highly functionalized)

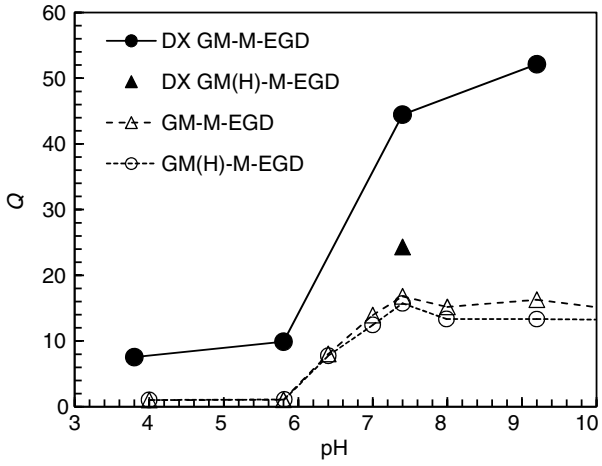

Figure 6.10 Swelling ratios for DX microgel and SX microgel particles as a function of pH. The GM(H)-M-EGD and GM-E-EGD had 5.8 and 1.8 mol% vinyl functionalization. Reproduced from [13] by permission of The Royal Society of Chemistry.

compared to 44 for DX GM-M-EGD at the same pH. This demonstrated that the overall number density of elastically effective chains increased as a consequence of increasing functionalization. The data also demonstrate that the pH-responsive swelling from the microgel prevails in the DX microgel.

6.5.5
Comparison of Properties with Conventional Hydrogels

The comparison of DX microgel properties with conventional hydrogels is an interesting topic. It is the ability to construct DX microgels using nanometer-sized "building blocks" that separates DX microgel structure from conventional hydrogels and provides new levels of design versatility. Indeed, this offers longer term potential to construct complex responsive hydrogels with distinct colloidal scale properties in three-dimensional space. This general theme of building heterogeneity on the nanometer-scale has been acted upon in the context of creating soft materials with heterogeneous morphologies related to cartilage [6].

The experimental results reported to date show that DX microgels prepared by the aggregation route provide much faster swelling/deswelling kinetics than conventional hydrogels [11]. The reasons for this were discussed above (Section 6.5.1). The mechanical properties of DX microgels and their conventional hydrogel analogs are difficult to compare at this stage. That is because an ideal comparison will require the same number density of elastically effective chains. The advantage of DX microgels is their ability to have two different types of tunable crosslinking. The more conventional analogy in this case is interpenetrating double network hydrogels [41]. Therefore, the unique feature for DX microgels is the physical separation of inter- and intraparticle crosslinking. A key difference between these systems is their dual networks being in series (DX microgels) and parallel (double network hydrogels).

6.6
Potential Applications

6.6.1
Photonic Applications

The potential photonic applications for DX microgels arise from their tunable scattering patterns, as pioneered by Hu *et al.* [22, 23, 26]. The applications envisaged include sensors, displays, and home decorations. The potential for biosensing also exists. However, in the case of their temperature-responsive systems the stimulus is limited. In the body the temperature is rigidly controlled. However, it is certainly conceivable that a temperature-responsive aqueous indicator of temperature could be developed from that technology. If coupled to a release mechanism there may be possibilities for an advanced external wound repair technology. This is because varying the temperature of surface regions of the body is already accepted clinical practice for specific therapies.

6.6.2 Biomedical Applications

It is in biomedical applications that DX microgels and microgel-reinforced hydrogels appear to have the greatest potential. In all cases the hydrogels must be nontoxic and should possess mechanical properties that can be tuned to match those of the tissue that they will replace [42]. Alternatively, the DX microgels can be designed so that they biodegrade *in vivo*. This is of course potentially advantageous because surgery will not be required for their removal. Generally, the use of GRAS materials (generally regarded as safe) is an advantage for DX microgel construction because this should reduce the regulatory barriers to approval for use in the body. It is for this reason that the DX microgels and microgel-reinforced hydrogels discussed below are based on poly(methyl methacrylate) or HA.

The work reported by Jia *et al.* [14] established DX microgels that match the mechanical properties of the vocal fold under the operating frequency range of human phonation. Those systems, which were found to be essentially nontoxic, are promising candidates for the treatment and repair of vocal fold scarring. Jha *et al.* [6] constructed a hierarchial microgel-reinforced hydrogel for cartilage repair. Their HA-based system degraded enzymatically, which provides a route for biodegradation *in vivo*. An important milestone established in that work was that it is possible to release a growth factor from the microgels during tissue culture experiments. This shows an added advantage for hydrogels that contain microgels. They can provide triggered or controlled release as well as the other benefits outlined above.

The work of Bencherif *et al.* [7] stands out as a potentially important biomedical development of microgel-reinforced hydrogels. In that case disulfide linkages were incorporated at the peripheries of the microgel particles which were reducible using glutathione (GSH). The latter is present in elevated concentrations in the intracellular environment. They demonstrated that GSH triggered release of a model active (FITC-dextran) from the microgel particles within the hydrogels. It was surprising that such large macromolecules were able to diffuse out of the hydrogel part of their system (the covalent microgel particle-to-hydrogel linkages were disrupted). Perhaps, the aggregates that were present (Figure 6.3b) provided a percolated, large-pore size pathway that allowed their removal once these linkages degraded.

Bencherif *et al.* [7] also demonstrated cell attachment to their hydrogels after copolymerization of a cell adhesion peptide (GRGDS) within their microgel particles and hydrogels. The results of live/dead assays are shown in Figure 6.11. The GRGDS was acrylated by reaction of acrylated-PEO-NHS with GRGDS. It can be seen from Figure 6.11a that the cells do not attach to unmodified hydrogels, although they remain alive (green). It is through incorporation of the cell adhesion peptide (GRGDS) into the hydrogel and microgel particles that attachment occurs. This is not surprising for hydrogels because they are highly swollen, which can make it difficult for cell attachment without scaffold modification.

At Manchester we have also investigated DX microgels for biomedical applications. The project originated in an effort to address degeneration of the intervertebal disc (DIVD). The latter is a major health problem that results in chronic pain for those

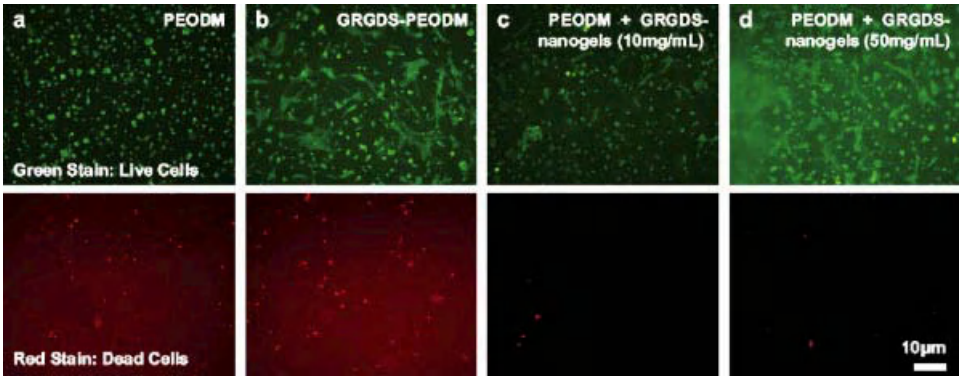

Figure 6.11 Mouse myoblast cells (C2C12) seeded on a series of 10 wt% hydrogels. The hydrogel control with and without peptide are shown in (a) and (b), respectively. The microgel-reinforced hydrogels with increasing levels of peptide are shown in (c) and (d). For all of the top images live cells are shown as green. The lower images show the dead cells (red). Reproduced from [7] with permission from Elsevier.

afflicted by the advanced stage of the disease and is a major drain on national health budgets. Surgical intervention usually involves spinal fusion, which is accompanied by considerable hospital and recovery time. We have explored using injectable pH-responsive microgels as a means for providing a minimally invasive solution to early-stage DIVD [43]. The early work demonstrated that a physically gelled SX E-BDD dispersion could restore the mechanical properties of degenerated intervertebal discs when subjected to biomechanically meaningful loads. However, those proof-of-concept measurements were only conducted over five load cycles. Because the physically gelled microgel particles were not held together, it was likely that migration of the particles under load would occur during potential application. In an effort to overcome this problem we have recently demonstrated that vinyl functionalized microgels can be covalently linked together. Figure 6.12 shows that the strategy resulted in macroscopic hydrogels that did not redisperse in pH 7.4 buffer, which is an important test for the

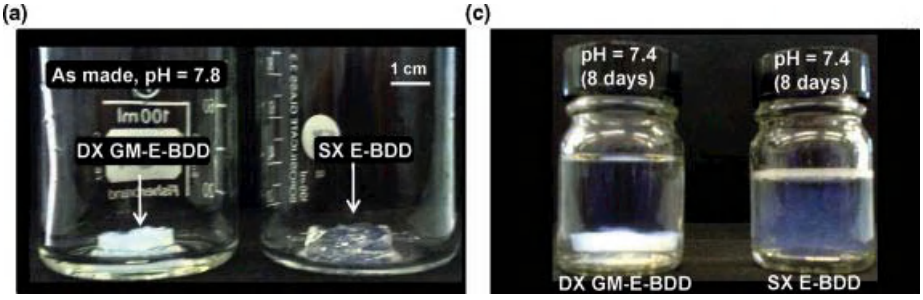

Figure 6.12 (a) Effect of addition of as-made DX GM-E-BDD and SX E-BDD microgels to (b) pH 7.4 buffers. Only the SX E-BDD microgel redispersed. Reproduced from [13] by permission of the Royal Society of Chemistry.

success of double crosslinking. The physically gelled single crosslinked microgel did redisperse. Importantly, these data showed that it was the presence of vinyl groups that were critical for preventing redispersion. Recently, we have established methods for achieving DX microgel formation using injectable dispersions and methods that could be used *in vivo*. That will be the subject of future publications.

6.7 Conclusion

DX microgels are a proven method for preparing responsive photonic hydrogels. DX microgels and microgel-reinforced hydrogels are both being actively pursued as a means for preparing biomaterials. Both systems have mechanical properties that are tunable and good biocompatibility has been demonstrated by several groups [6, 7, 14]. The morphology of DX microgels is an important consideration and care must be taken in determining morphology of DX microgels using freeze-fracture SEM as artifacts due to ice formation are possible. Cryo-SEM is the best method to use for high-resolution imaging; however, this is not always available.

The discussion presented here has shown that there are six distinct methods for preparing hydrogels containing covalently linked microgels. A definition of DX microgels has been presented which may be the first such definition. At least five distinct methods for preparing DX microgels have been reported. Microgel-reinforced hydrogels are distinguishable from DX microgels and tend to have mechanical and swelling properties that are related to the parent hydrogel; the similarity increases with decreasing microgel content. DX microgel mechanical and photonic properties can be tuned by intra- and interparticle crosslinking and as well as ϕ_p. DX microgels have additional tunability compared to conventional hydrogels. The modulus for DX microgels is strongly dependent on interparticle crosslink density. The ε_B value appears to be dependent on M_c. Both of these parameters are tunable. DX microgel swelling can be fast if aggregation is used for preparation. This provides new opportunities for tuning kinetics of hydrogel swelling. The swelling ratio for DX microgels is not necessarily be the same as the parent microgels, but depends on the method of preparation. Again, this gives increased opportunity for tunability.

DX microgels are a route to designer (heterogeneous) hydrogels with compartmentalized properties. They can be stimulus responsive and have excellent prospects for application in photonics and biomaterials. Because they have superior property tunability compared to conventional hydrogels they have excellent prospects for academic research and other new applications in the future.

Abbreviations

AA: Acrylic acid
AAm: Allylamine
BDD: Butanediol diacrylate

CLSM: Confocal laser scanning microscopy
DIVD: Degeneration of the IVD
DX: Doubly crosslinked
EA: Ethyl acrylate
E-BDD: Poly(EA-MAA-BDD) microgel
EGD: Ethyleneglycol dimethacrylate
GM: Glycidyl methacrylate
GM-E-BDD: GM functionalized E-BDD
GM-M-EGD: GM functionalized M-EGD
GM(H)-M-EGD: GM functionalized M-EGD (high GM content)
HA: Hyaluronic acid
HAGM: Hyaluronic acid glycidyl methacrylate
HEA: Hydroxyethyl acrylate
IVD: Intervertebral disk
MAA: Methacrylic acid
M-EGD: Poly(MMA-MAA-EGD) microgel
MMA: Methyl methacrylate
NIPAM: *N*-isopropylacrylamide
PCS: Photon correlation spectroscopy
SF: Sol fraction
SX: Singly crosslinked
VPTT: Volume phase transition temperature

References

1 Fernandez-Barbero, A., Suarez, I.J., Sierra-Martin, B., Fernandez-Nieves, A., de las Nieves, F.J., Marquez, M., Rubio-Retama, J., and Lopez-Cabarcos, E. (2009) *Adv. Colloid Interface Sci.*, **147–148**, 88.
2 Hoare, T. and Pelton, R. (2008) *Curr. Opin. Colloid Interface Sci.*, **13**, 413.
3 Lyon, L.A., Meng, Z., Singh, N., Sorrell, C.D., and John, A.St. (2009) *Chem. Soc. Rev.*, **38**, 865.
4 Saunders, B.R., Laajam, N., Daly, E., Teow, S., Hu, X., and Stepto, R. (2009) *Adv. Colloid Interface Sci.*, **147–148**, 251.
5 Kolmakov, G.V., Matyjaszewski, K., and Balazs, A.C. (2009) *ACSNano*, **3**, 885.
6 Jha, A.K., Manisha, S.M., Farach-Carson, M.C., Duncan, R.L., and Jia, X. (2010) *Soft Matter*, **6**, 5045.
7 Bencherif, S.A., Siegwart, D.J., Srinsvasan, A., Horkay, F., Hollinger, J.O., Washburn, N.R., and Matyjaszewski, K. (2009) *Biomaterials*, **30**, 5270.
8 Hu, Z., Lu, X., and Wang, C. (2000) *Adv. Mater.*, **12**, 1173.
9 Hu, Z., Lu, X., and Gao, J. (2001) *Adv. Mater.*, **13**, 1708.
10 Cho, E.C., Kim, J.-W., Hyun, D.C., Jeong, U., and Weitz, D.A. (2010) *Langmuir*, **26**, 3854.
11 Cho, E.C., Kim, J.-Y., Fernandez-Barbero, A., and Weitz, D.A. (2008) *Nano Lett.*, **8**, 168.
12 Xia, L.-W., Ju, X.-J., Liu, J.-J., Xie, R., and Chu, L.-Y. (2010) *J. Colloid Interface Sci.*, **349**, 106.
13 Liu, R., Milani, A.H., Freemont, T.J., and Saunders, B.R. (2011) *Soft Matter*, **7**, 4696.
14 Jia, X., Yeo, Y., Clifton, R.J., Jiao, T., Kohane, D.S., Kobler, J.B., Zeitels, S.M., and Langer, R. (2006) *Biomacromolecules*, **7**, 3336.

15 Flory, P.J. (1953) *Principles of Polymer Chemistry*, Cornell University, Ithaca, NY.
16 Brannon-Peppas, L. and Peppas, N.A. (1991) *Chem. Eng. Sci.*, **46**, 715.
17 Longo, G.S., de la Cruz, M., and Szleifer, I. (2011) *Macromolecules*, **44**, 147.
18 Capek, I. (2005) *Adv. Colloid Interface Sci.*, **118**, 73.
19 Anseth, K.S., Bowman, C.N., and Brannon-Peppas, L. (1996) *Biomaterials*, **17**, 1647.
20 Cai, T., Wang, G., Thompson, S., Marquez, M., and Hu, Z. (2008) *Macromolecules*, **41**, 9508.
21 Zhou, B., Gao, J., and Hu, Z. (2007) *Polymer*, **48**, 2874.
22 Hu, Z. and Huang, G. (2003) *Angew. Chem. Int. Ed.*, **42**, 4799.
23 Huang, G. and Hu, Z. (2007) *Macromolecules*, **40**, 3749.
24 Debord, S.B. and Lyon, L.A. (2000) *J. Phys. Chem. B*, **104**, 6327.
25 Wang, L., Wang, X., Xu, M., Chen, D., and Sun, J. (2008) *Langmuir*, **24**, 1902.
26 Zhou, J., Wang, G., Marquez, M., and Hu, Z. (2009) *Soft Matter*, **5**, 820.
27 Koel, B.E. (1992) in *Encyclopedia of Materials Characterization – Surfaces, Interfaces, Thin Films* (eds C.R. Brundle, C.A. Evans, and S. Wilson), Elsevier, Oxford.
28 Pygall, S.R., Whetstone, J., Timmins, P., and Melia, C.D. (2007) *Adv. Drug Deliv. Rev.*, **59**, 1434.
29 Yao, X., Yao, H., and Li, Y. (2009) *J. Mater. Chem.*, **19**, 6516.
30 Goodwin, J.W. and Hughes, R.W. (2000) *Rheology for Chemists: An Introduction*, RSC, Cambridge.
31 Tan, B.H., Hussain, H., and He, C.B. (2011) *Macromolecules*, **44**, 622.
32 Winter, H.H. (1987) *Polym. Eng. Sci.*, **27**, 1698.
33 Winter, H.H. and Chambon, F. (1986) *J. Rheol.*, **30**, 367.
34 Chougnet, A., Audibert, A., and Moan, M. (2007) *Rheol. Acta*, **46**, 793.
35 Lally, S., Cellesi, F., Freemont, T., and Saunders, B.R. (2011) *Colloid Polym. Sci.* doi: 10.1007/S00396-010-2366.8
36 Muniz, E.C. and Geuskens, G. (2001) *Macromolecules*, **34**, 4480.
37 Jenkins, P. and Snowden, M.J. (1996) *Adv. Colloid Interface Sci.*, **68**, 57.
38 Tanaka, T. and Fillmore, D.J. (1979) *J. Chem. Phys.*, **70**, 1214.
39 Okajima, T., Harada, I., Nishio, K., and Hirotsu, S. (2002) *J. Chem. Phys.*, **116**, 9068.
40 Friedrich, T., Tieke, B., Stadler, F.J., Bailly, C., Eckert, T., and Richtering, W. (2010) *Macromolecules*, **43**, 9964.
41 Gong, J.P. (2010) *Soft Matter*, **6**, 2583.
42 Uhrich, K.E., Cannizzaro, S.M., Langer, R.S., and Shakesheff, K.M. (1999) *Chem. Rev.*, **99**, 3181.
43 Saunders, J.M., Tong, T., LeMaitre, C., Freemont, A.J., and Saunders, B.R. (2007) *Soft Matter*, **3**, 486.

7
ATRP: A Versatile Tool Toward Uniformly Crosslinked Hydrogels with Controlled Architecture and Multifunctionality

Jeong Ae Yoon, Jung Kwon Oh, Wenwen Li, Tomasz Kowalewski, and Krzysztof Matyjaszewski

7.1
Incorporating Crosslinking Reactions into Controlled Radical Polymerization

Hydrogels are water-swellable polymer networks, typically with covalent crosslinks. The crosslinks can be incorporated into the hydrogel networks by reactions of crosslinkers which contain more than two vinyl groups with other unsaturated monovinyl compounds using radical (co)polymerization mechanisms. The radical polymerization method has benefits over other chain-growth polymerization mechanisms because of the wide range of applicable monomers, less stringent reaction conditions, and compatibility with a wide variety of functional groups. Despite such advantages, there are also limitations associated with conventional free radical polymerization (FRP). In macromolecular engineering aspects [1], these limitations come from difficulties in the precise control of molecular weight, preparation of polymers with broad molecular weight distributions, and difficulties in controlling molecular architectures. There are also limitations unique to crosslinked structures, such as in controlling the network size, crosslinkage distribution, and in predicting the critical gel point. These limitations have been successfully overcome by the application of controlled/living radical polymerization (CRP) [2, 3] to the preparation of uniformly crosslinked hydrogels. This success can be attributed to the nature of the controlled polymerization, that is, the even growth of all primary chains and the elongated propagation period to provide sufficient time for primary chains to relax. These phenomena lead to greater network homogeneity, as described below.

Theoretical prediction of branching and gelation in copolymerization was first described by Flory and Stockmayer [4, 5]. Their work predicts that the critical gel point is reached when the weight-average number of crosslinking units per primary chain (ν_c) is equal to unity. Thus, for a radical copolymerization with a divinyl crosslinker under ideal conditions (monodisperse primary chain, $DP_w/DP_n = 1$), the number-average number of crosslinking units per primary chain $\gamma_c = 1$ is the critical value required to reach the theoretical gel point. In other words, one half crosslinkage (crosslinker with both vinyl groups reacted, one crosslinkage contains two

Hydrogel Micro and Nanoparticles, First Edition. Edited by L. Andrew Lyon and Michael Joseph Serpe.
© 2012 Wiley-VCH Verlag GmbH & Co. KGaA. Published 2012 by Wiley-VCH Verlag GmbH & Co. KGaA.

crosslinking units) per primary chains is sufficient for the onset of theoretical gelation. This is due to a fact that crosslinking units are distributed randomly among all chains and some chains contain no crosslinking units and some contain several of them, sufficient to reach gelation [6].

Experimentally, crosslinking using FRP conditions shows a significant deviation in the moment of gelation from predicted values. Under typical polymerization conditions, the experimentally observed gel point occurs at conversions much higher than predicted. This significant deviation has been attributed to some assumptions in Flory and Stockmayer's theory, particularly the neglect of the presence of intramolecular cyclization reactions [7, 8]. In an FRP, due to the much faster propagation rate compared to initiation rate, a growing radical chain end has a greater chance of reacting with its own incorporated pendant vinyl groups to form a densely crosslinked polymer grain. This intramolecular cyclization does not contribute to expanding the network size and is thus considered to be a waste of incorporated functionalities. The eventual macrogelation occurs by the interconnection of the first formed polymer grains. Thus, the networks formed by FRP contain a significant portion of densely crosslinked domains, which lowers both network homogeneity and swellability.

Intramolecular cyclization reactions can be reduced under CRP conditions, as the extended propagation period of CRP provides sufficient time for the growing chains to be fully relaxed and diffused prior to subsequent activation steps. Consequently, an active polymer radical chain end has a higher probability of reacting with vinyl groups incorporated into vicinal molecules, forming a branching point rather than reacting with a pendant vinyl group on its own backbone. The expansion of the branched architecture leads to earlier macrogelation [9]. Therefore, networks formed by CRP contain a fewer dense polymer grains, and the network chains are more relaxed and homogeneous.

Hydrogels prepared by CRP (CRP gels) possess several advantages over gels prepared by FRP (FRP gels). For example, CRP gels exhibit higher swelling ratios due to the more homogeneous network structure, as discussed above [9, 10]. Moreover, the primary polymer chain ends in CRP preserve functional groups that can be further used for incorporation of other chemical species [11, 12]. CRP gels are also preferred when a degradable material is desired, because of the predetermined molecular weight and narrow molecular weight distribution of decomposed fragments which introduces the possibility of residues with a molecular weight below the renal threshold which is a desired feature in certain bioapplications [13, 14].

In this chapter, we discuss the successful use of atom transfer radical polymerization (ATRP) [15–18], one of the CRP methods [2, 3], for preparation of rapidly responsive hydrogels based on poly(oligo(ethylene oxide) monomethyl ether methacrylate) (POEOMA).

Rapidly responsive hydrogels have attracted attention due to their potential in a number of applications, such as artificial muscles/actuators, microfluidic parts, and responsive membranes. In particular, thermoresponsive hydrogels that can undergo a temperature-induced volume phase transition have been intensely studied because of the ease with which the stimulus (heat) can be controlled, and the suitability of gels in bio-related applications. Recently, POEOMA was highlighted as a successful

alternative to poly(*N*-isopropylacrylamide) (PNIPAM), the previously most often studied lower critical solution temperature (LCST) system. POEOMA systems are characterized by advantages of a controllable LCST, high biocompatibility/low cytotoxicity, commercially available monomers, and easy polymerization by both radical and anionic polymerization mechanisms.

In the first section of this chapter, the network homogeneity afforded by the ATRP crosslinking mechanism and the resulting impact on thermoresponsive hydrogel performance are compared to hydrogels prepared by FRP [19]. Above the LCST, macroscopically sized hydrogels prepared by ATRP formed a water-impermeable hydrophobic "skin layer" at the hydrogel surface that controlled the deswelling kinetics. In the following section, one example of network modification is introduced targeting suppression of "skin" layer formation [20]. In this modification, functionalized nanopores were incorporated into the uniform networks using ATRP techniques. The successful modification proves the versatility of ATRP in designing gel architecture to meet the requirements of a demanding application area.

In the last section, we describe the further use of ATRP toward the development of well-defined stimuli-responsive nanometer-sized hydrogels (called nanogels or microgels). They enable degradation to corresponding linear polymers in response to external stimuli, particularly reductive reactions based on thiol-disulfide exchange. Thus, their potential as multifunctional drug-delivery vehicles for biomedical applications is presented.

7.2
Effect of Network Homogeneity on Thermoresponsive Hydrogel Performance

Two types of LCST hydrogels were prepared using ATRP or FRP for the copolymerization of 2-(2-methoxyethoxy)ethyl methacrylate (MEO_2MA), 2-hydroxyethyl methacrylate (HEMA) and ethylene glycol dimethacrylate (EGDMA) (Scheme 7.1 and Table 7.1), in order to compare the effect of network homogeneity on hydrogel performance. In accordance with the polymerization mechanisms employed for

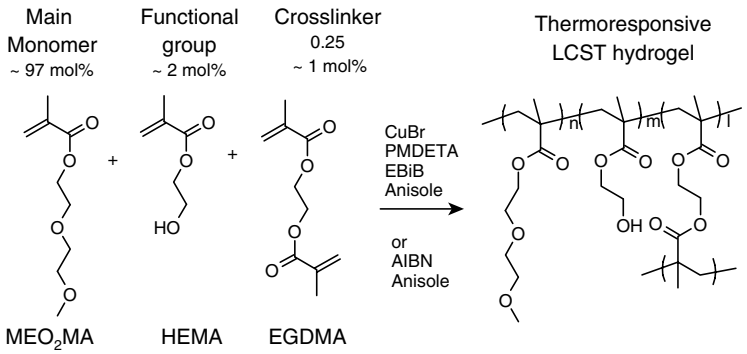

Scheme 7.1 Synthesis of a thermoresponsive LCST hydrogel based on MEO_2MA.

Table 7.1 Conditions for preparation of hydrogels.

Entry	Mechanism	Soln. composition Gel composition	Conditions	Conversion (%)[f]	SR[g]
AH	ATRP	500:10:5:1[a] (475:9.5:5:1)[e]	60 °C, 300 min	95	3.1
FH	FRP	500:10:5:1[b] (500:10:5:1)[e]	60 °C, 300 min	99	2.2
AL1	ATRP	625:12.5:1.56:1[c] (556:11.1:1.54:1)[e]	70 °C, 120 min	89	8.9
AL2	ATRP	625:12.5:1.56:1[c] (593:11.9:1.56:1)[e]	60 °C, 300 min	95	5.5
FL	FRP	625:12.5:1.56:1[d] (619:12.4:1.56:1)[e]	60 °C, 300 min	99	3.2

a) [MEO_2MA]/[HEMA]/[EGDMA]/[EBiB]/[PMDETA]/[CuBr] = 500/10/5/1/1/1.
b) [MEO_2MA]/[HEMA]/[EGDMA]/[AIBN] = 500/10/5/1.
c) [MEO_2MA]/[HEMA]/[EGDMA]/[EBiB]/[PMDETA]/[CuBr] = 625:12.5:1.56:1:1:1.
d) [MEO_2MA]/[HEMA]/[EGDMA]/[AIBN] = 625:12.5:1.56:1.
e) Gel composition based on monomer conversion.
f) Conversion of MEO_2MA measured by GC.
g) Swelling ratio at equilibrium measured at 4 °C. swelling ratio = (weight of absorbed water at 4 °C)/(weight of dried gel).

hydrogel synthesis, the ATRP and FRP hydrogels were named "A gels" or "F gels," respectively. Also, according to the mole ratios of the crosslinker EGDMA used for the synthesis, each hydrogel was classified as an "H gel" or "L gel" to describe hydrogels prepared with higher (1 mol% vs. MEO_2MA) or lower crosslinker content (0.25 mol% vs. MEO_2MA). Another potential modification of the gel structure was incorporation of HEMA at a molar ratio of 2:100 (to MEO_2MA).

7.2.1 Performance of Macroscopic Hydrogels

Table 7.1 displays the compositions of the prepared hydrogels, as well as gravimetrically measured swelling ratios. Clearly, the swelling ratios of ATRP gels are ca. 50% higher than the swelling ratios measured for FRP gels of similar composition. This can be attributed to the reduced formation of collapsed polymer grains in the gels prepared by the ATRP procedure [9, 10, 21].

In addition to examining the effect of polymerization procedure on swelling ratios, the deswelling kinetics of hydrogels above their LCST (~26 °C) is of interest for thermoresponsive hydrogels. The deswelling kinetics is often observed by following the rate of decrease of water retention (WR = (weight of retained water at time *t*)/(weight of initially absorbed water)) over time by gravimetric methods. In our studies, the water retention was determined by analyzing snapshot images taken during deswelling processes (Figure 7.1). The snapshot images were computationally analyzed to identify edge positions to calculate the areas within the edge positions.

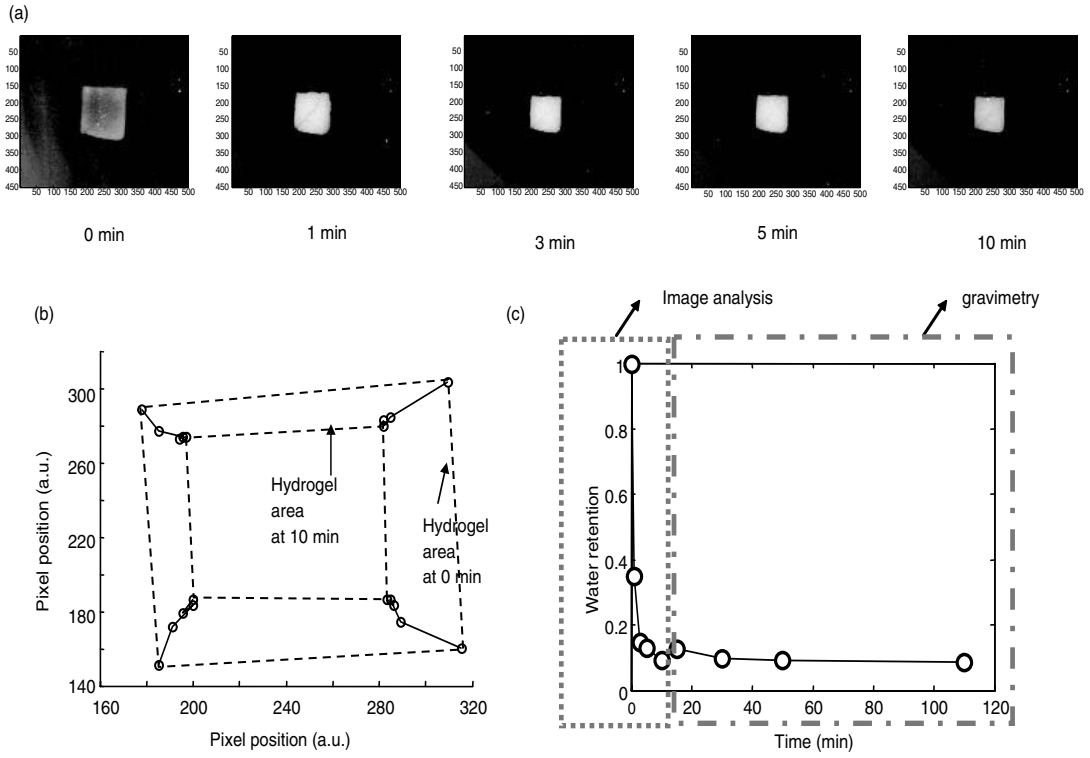

Figure 7.1 (a,b) The process of image analysis and (c) the combined data of image analysis and gravimetry (water retention). The images are side views of cylindrical hydrogels.

This method, called "image analysis," is advantageous in that the hydrogels remain immersed in water all the time and thus they do not experience any temperature changes during the measurement. Also, because of the absence of the time required to undertake the weighing process, this method is more useful in short time domains, for example, less than 10 min. In Figure 7.1, an example is shown which measured deswelling kinetics by a combination of image analysis and conventional gravimetric methods.

Figure 7.2 shows the deswelling kinetics measured by image analysis for 30 min at various temperatures. While the whole process progressed for a much longer period (i.e., over several hours), more than 40% of the deswelling process was completed within the observation period. The deswelling of the ATRP gel AH revealed a period of retardation at 45 and 60 °C, while the deswelling progressed without retardation at 30 °C (see inset, Figure 7.2a). This retardation in deswelling was attributed to the formation of a skin layer, a water-impermeable hydrophobic layer at the hydrogel surface. Moreover, although faster deswelling was expected at the higher temperature (60 °C), the deswelling was actually slower than at lower temperatures. This is because an even thicker skin layer formed at a very early stage of deswelling, further hindering the release of water. On the other hand, the LCST transition at the lower temperature, 30 °C, was relatively slow, hence skin formation was diminished. In contrast, the early retardation period at 45 or 60 °C was shorter for the FRP gel, FH, and the deswelling after the retardation period was faster than in the case of AH. This implies that the deswelling process of FH was not strongly affected by the formation of a skin layer. The lower tendency of the FRP gel to form a skin layer was attributed to its greater heterogeneity, and in particular to the presence of distributed densely crosslinked polymer grains. These densely crosslinked fractions within the gel have a higher LCST temperature than the other portions of the gel and retain their hydrophilic nature during the LCST transition for a longer time. Although these dense domains limit the absolute swelling ratio, they provide hydrophilic channels for water molecules to diffuse out of the hydrogel [22–24]. The slowest deswelling at 30 °C can be explained by the weaker hydrophobic aggregation.

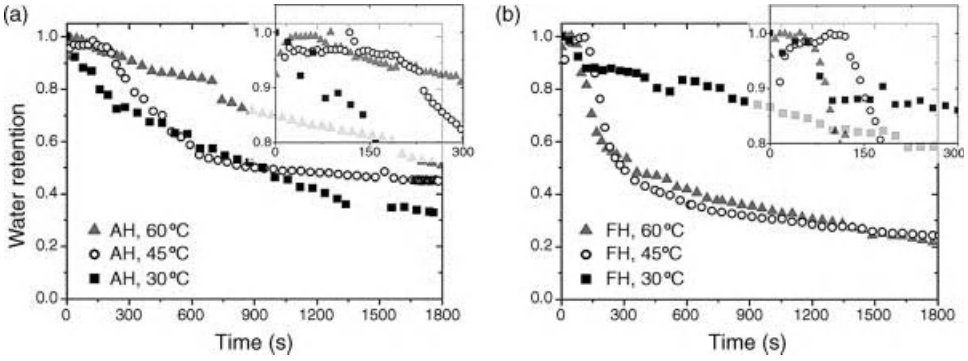

Figure 7.2 Comparison of water retention upon deswelling. (a) ATRP gel AH; (b) FRP FH.

7.2.2
Molecular Level Dehydration Kinetics

Variable-temperature time-lapse nuclear magnetic resonance (NMR) spectroscopy was studied in order to obtain molecular level insights into the kinetics of hydrogel dehydration. The NMR spectra of the lower crosslinking density L gels were more informative than those of the H gels, because the initial NMR spectra were generally better resolved for the L gels. The ^{1}H NMR spectra of the hydrogels were recorded in D_2O at a given temperature as a function of time for the kinetic studies. The spectra were then deconvoluted into four overlapping peaks. The decreasing peak height at 3.2 ppm was used as a measure of the extent of dehydration (Figure 7.3).

Figure 7.4a shows the decrease in the peak height of sample AL1 at temperatures ranging from 25 to 35 °C. The rate of dehydration increased with an increase of temperature and the overall level of dehydration after 10 min increased. Figure 7.4b compares the kinetics of dehydration of ATRP and FRP gels at 30 °C. The dehydration of sample AL2 was faster than FL, although the gel conversion values are quite comparable. The ATRP gel AL2 has a lower net crosslinking density because it has less dense polymer grains and, as a consequence of this lower crosslinking density, the hydrogen bonding in AL2 is more easily disrupted [25].

The most important comparison is the time scale of the macroscopic deswelling process and the molecular level dehydration. The dehydration of polymer chains assessed by ^{1}H NMR reached a plateau after 300 s, while the actual deswelling progressed over a longer time period. This apparent discrepancy can be resolved by recognizing the fact that collapse (dehydration) of the polymer chains does not immediately remove the water from the macroscopic network. Following chain collapse free water, which is unbound to the polymer network, still needs to reach the

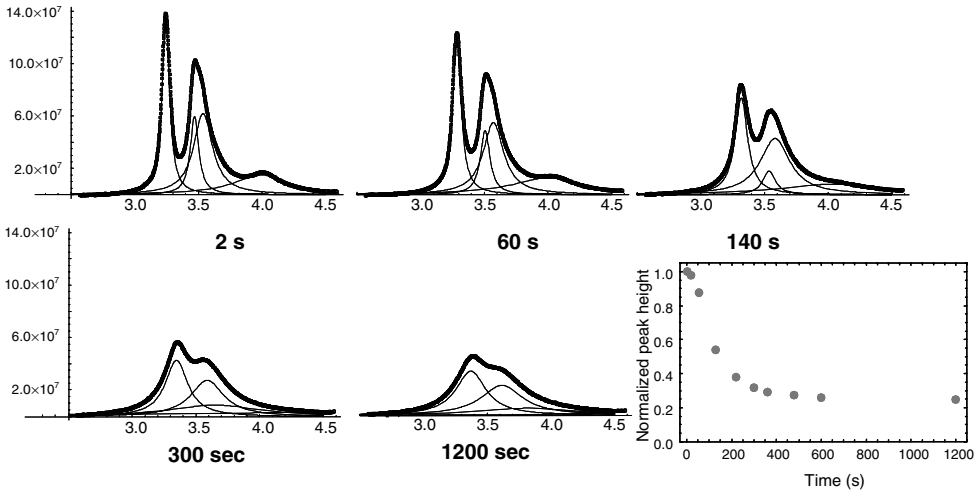

Figure 7.3 Deconvoluted ^{1}H NMR spectra of gel AL1 at 25 °C at selected times. Up field and down field are inverted for purpose of calculations.

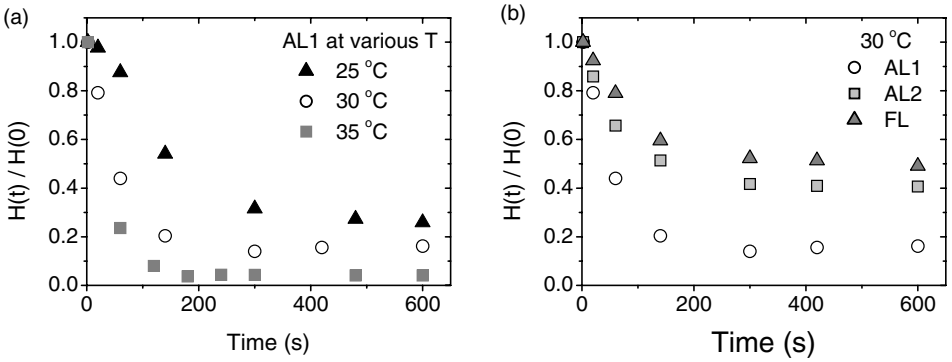

Figure 7.4 Decrease of peak height of variable-temperature time-lapse ^{1}H NMR spectra of low crosslink density gels (L gels). (a) ATRP gel AL1 at different temperatures; (b) L gels at 30 °C.

surface of the sample through "diffusion channels." Moreover, as discussed earlier, the final release of water from the gel may be significantly hindered through the formation of a dense skin at the surface of the sample.

The observation of a much slower deswelling process than polymer dehydration because of the skin effect indicates that the formation of a significant skin layer should be avoided if rapidly responsive hydrogels are required. The greater susceptibility of ATRP gels to the skin effect was attributed to the more homogeneous network structure, resulting in the formation of a uniformly collapsed skin layer and lack of water diffusion channels. This conclusion led us to incorporate designed heterogeneities into homogeneous ATRP hydrogels in order to obtain higher degrees of swelling coupled with rapid deswelling in thermoresponsive hydrogels.

7.3
Gel Networks Containing Functionalized Nanopores

This section discusses an example of gel architecture modification with predesigned heterogeneity. The selected approach involves incorporation of well-defined hydrophilic polymer-lined nanopores into the hydrogels which can serve as efficient water-release channels after network collapse.

The targeted gel architecture was achieved by synthesizing the gel network around a degradable star macro-initiator (dSM), Scheme 7.2. The well-defined dSM was prepared by ATRP using the "arm-first" method [6, 26, 27]. ATRP macro-initiators, which form the "arms," were chain extended with a degradable crosslinker, 2,2′-dimethacryloyloxyethyl disulfide (DSDMA) to form a core. The resulting dSMs were named dHSM and dTSM, respectively, based on the permanent hydrophilicity and thermal responsiveness provided by the arm chains.

The resulting $PMEO_2MA$ thermoresponsive hydrogels, with covalently embedded dSM particles are referred to as "S-gels." Controlled nanoporosity was introduced to

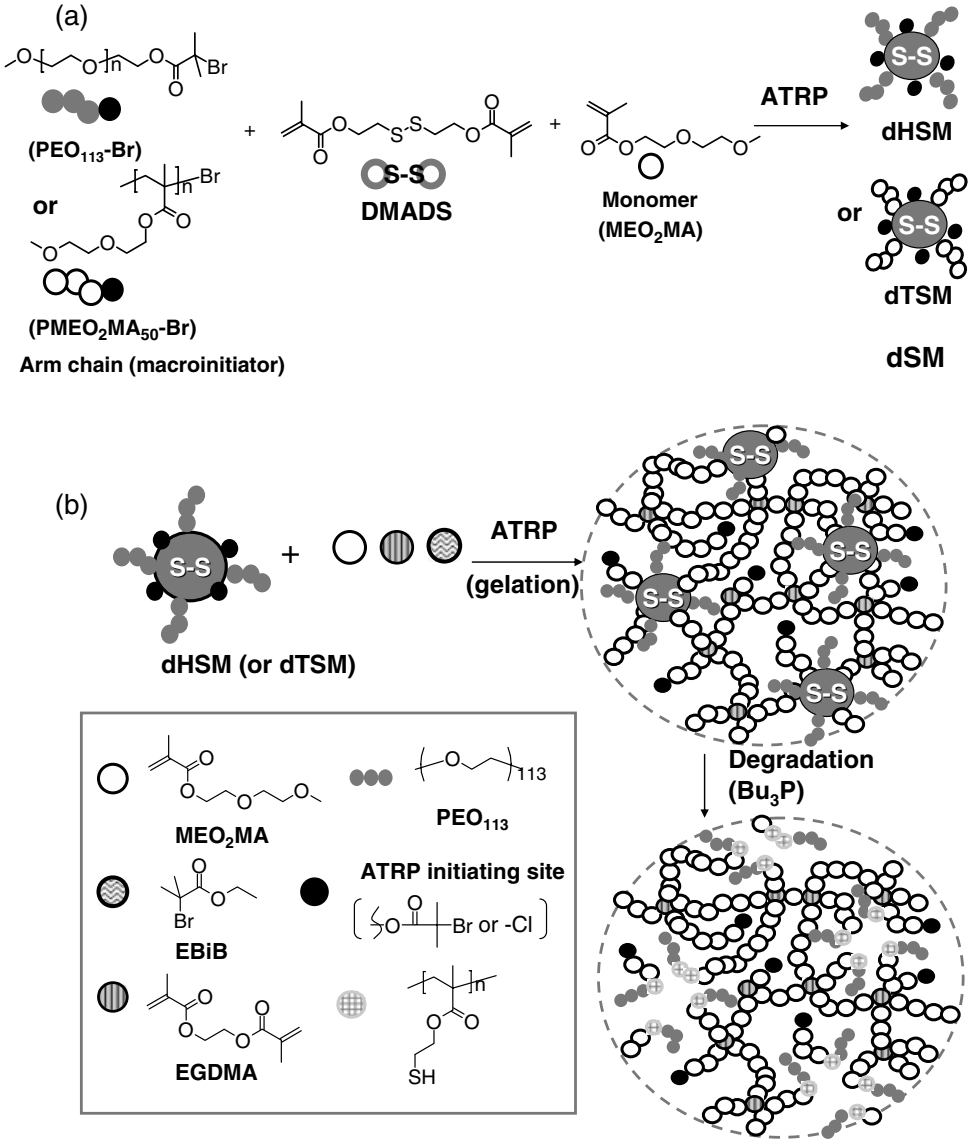

Scheme 7.2 (a) Synthesis of degradable star-branched macro-initiators (dHSM or dTSM). (b) The synthesis of a hydrogel in the presence of dHSM and the subsequent pore generation by degradation of the star core.

S-gels through reductive degradation of disulfide-crosslinked cores of the dSMs, yielding thermoresponsive nanoporous hydrogels referred to as "D-gels." Given the composition of dSMs used in the formation of the hydrogels the nanopores in the resulting D-gels were lined with either hydrophlic poly(ethylene oxide) (PEO) chains (dHSM) or thermoresponsive $PMEO_2MA$ chains (dTSM). In order to provide a

Table 7.2 Description of thermoresponsive hydrogels.

Hydrogel		dSM/%[a)]	Solvent[b)]	Conv/%[c)]	SR[d)]
R-gel[e)]		**0**	**anisole**	**95%**	**3.1 ± 0.07**
S-gel (Sxyz)[f)]	SH2a	1.9	Anisole	80%	4.1 ± 0.15
	SH5a	4.5	Anisole	92%	3.5 ± 0.15
	SH2d	1.9	DMSO	64%	14 ± 0.60
	SH5d	4.5	DMSO	24%	14 ± 0.80
	ST5d	4.5	DMSO	54%	7.1 ± 0.25
	ST9d	8.8	DMSO	39%	9.6 ± 0.16

a) Weight of dSM × 100/(weight of MEO_2MA + EGDMA).
b) Solvents used in gel formation.
c) Conversion of MEO_2MA measured by GC.
d) Swelling ratio = weight of absorbed water at an equilibrium at 4 °C/weight of dried gel, average of three measurements.
e) $[MEO_2MA]_0/[HEMA]_0/[EGDMA]_0/[EBiB]_0/[CuBr/PMDETA] = 500/10/5/1/1$, 60 °C, 5 h.
f) x = *H* or *T*, refers to the kind of dSMs, that is, dHSM or dTSM; y = *2*, *5*, or *9* refers to the weight fraction of dSM (1.9 wt%, 4.5 wt%, or 8.8 wt%, respectively); z = *a* or *d* indicating the solvent used in the synthesis (anisole or DMSO).
$[MEO_2MA]_0/[EGDMA]_0/[EBiB]_0/[CuBr/PMDETA] = 500/5/1/1$, 60 °C, 5 h.

reference sample, a homogeneous nondegradable hydrogel with no PEO chains was prepared by ATRP and is referred to as "R-gel" (Table 7.2).

7.3.1
Enhanced Swelling Ratios

The swelling ratios (SR) of a series of thermoresponsive hydrogels including R-, S-, and D-gels, were measured. The results presented in Table 7.2 show that higher swelling ratios were observed for hydrogels prepared in DMSO (SH2d, SH5d, ST5d, and ST9d). The most likely reason for this was the lower polymer conversion in this solvent as a result of enhanced chain termination resulting from higher ATRP equilibrium constants [28].

Degradation of dSM cores increased the swelling ratios of the resulting hydrogels with hydrophilic pores, and both dHSM and dTSM were found to be efficient macromolecular pore precursors for this purpose. This increase was particularly pronounced for already high-swelling S-gels prepared in DMSO, whereas the effect was not as clearly observed for S-gels prepared in anisole. The former gels were composed of networks of lower stiffness and were more susceptible to network expansion by pore generation (Figure 7.5).

7.3.2
Accelerated Deswelling Kinetics

The influence of additional nanopores on hydrogel deswelling kinetics was studied by measuring the water retention at 45 °C (Figure 7.6). The deswelling kinetics was

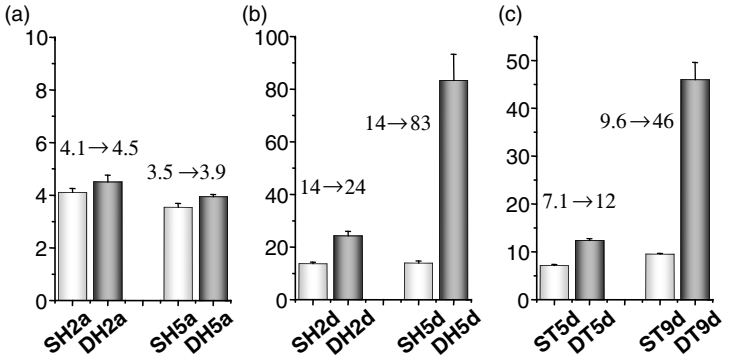

Figure 7.5 Changes in swelling ratio through pore generation. (a) Hydrogels prepared using dHSM as dSM in anisole as solvent. (b) Hydrogels prepared using dHSM as dSM and DMSO as solvent. (c) Hydrogels prepared using dTSM as dSM in DMSO as solvent.

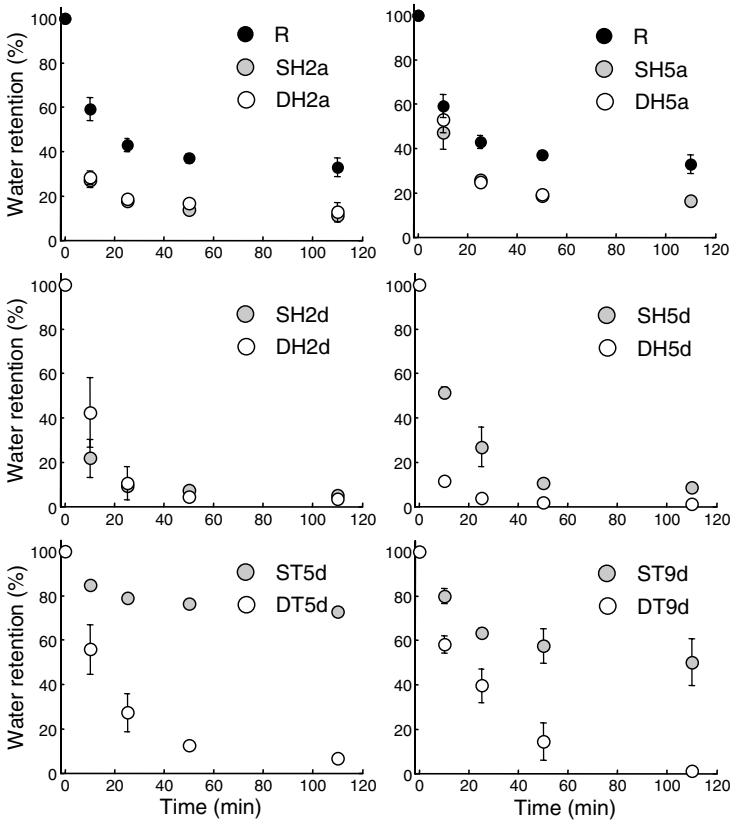

Figure 7.6 Deswelling kinetics at 45 °C expressed as the decrease of water retention with time.

not affected by the presence of additional pores in gels prepared in anisole. On the other hand, the introduction of pores significantly accelerated the deswelling kinetics of the gels prepared in DMSO. In particular, the percentage water retention of DH5d decreased to ~10% in 10 min, while that of DT5d or DT9d remained at ~60%. The accelerated deswelling after pore generation can be explained by the reduced hydrogel crosslinking density, since the crosslinks initially provided by the dSM cores were broken. However, the nature of generated pores should be considered to explain the significant difference in the deswelling kinetics observed for DH5d vs. DT5d or DT9d. The tethered PEO chains maintain their hydrophilicity at the experimental temperature of 45 °C, while the thermoresponsive $PMEO_2MA$ chains turn hydrophobic along with the hydrogel framework. Therefore, the presence of hydrophilic PEO chains on the surface of the pores ensured the open nature of the pores and effectively suppressed skin layer formation in sample DH5d. On the other hand, the pores provided by dTSM collapsed together with the gel framework and therefore could not serve as efficient water-diffusion channels. Thus, the hydrophilic pores were much more effective than the neutral pores in achieving a rapid deswelling process.

7.4 Toward Micro- and Nano-Sized Hydrogels by ATRP

Microgels are three-dimensionally crosslinked hydrogels confined in submicron-sized particles. When the size falls into the nanometer range, they can be considered to be nanogels. Like hydrogels, microgels/nanogels are often biocompatible, with high water content, and a tunable chemical and physical structure. In addition, they have a tunable size from submicron to tens of nanometers, a large surface area for multivalent bioconjugation, and an interior network for the incorporation of therapeutics. Because of these advantageous properties, microgels/nanogels hold great promise as effective polymer-based drug-delivery systems for biological and biomedical applications [29, 30].

For the preparation of microgels/nanogels through both chemical and physical crosslinking methods, several methods have been proposed; typically photolithographic, micro-molding, and microfluidic methods, as well as aqueous homogeneous gelation and spray-drying methods. Details are summarized in the recent review [31, 32]. The general method involves heterogeneous polymerization such as suspension, precipitation, inverse (mini)-emulsion, and inverse micro-emulsion polymerization. In particular, inverse mini-emulsion polymerization in an oil-in-water (o/w) heterogeneous process consists of aqueous submicron-sized droplets (including water-soluble monomers and difunctional crosslinkers) stably dispersed with an aid of oil-soluble surfactants, in organic solvents such as cyclohexane [33]. Upon addition of an water-soluble initiator, polymerization occurs in aqueous droplets yielding colloidally stable crosslinked hydrophilic microgels/nanogels. Their diameters are tuned by varying the concentration of surfactants and the weight ratio of aqueous to organic phases.

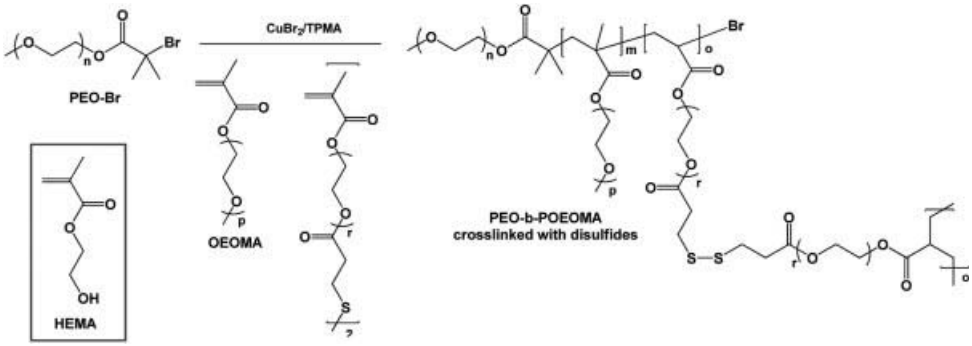

Figure 7.7 Scheme to synthesize thiol-responsive nanogels of PEO-*b*-POEOMA crosslinked with disulfide linkages in inverse mini-emulsion.

Recently, a new method employing ATRP, inverse mini-emulsion polymerization, and reductive degradation through disulfide-thiol exchange reaction has been developed. This method enables the preparation of well-defined thiol-responsive degradable microgels crosslinked with disulfide linkages (Figure 7.7). This section focuses on how to combine well-defined methods from polymer chemistry with biology to design and develop unique nanostructured materials for effective drug delivery applications.

There are a number of requirements to be met for conducting successful ATRP in inverse mini-emulsion [34]. First, the AGET (activator generated by electron transfer) process facilities inverse mini-emulsion ATRP with the use of oxidatively stable $CuBr_2$ deactivator species, which are reduced to CuBr active species in the presence of reducing agents [35]. Second, aqueous droplets consist of water-soluble ingredients, including poly(ethylene oxide)-2-bromoisobutyrate (PEO-Br) macro-initiator, oligo(ethylene glycol) monomethyl ether methacrylate (OEOMA), $CuBr_2$/TPMA (tris (2-pyridylmethyl)amine) complex, and ascorbic acid as a reducing agent [36]. The use of TPMA leads to the formation of an active water-soluble catalyst complex, with relatively low tendency toward dissociation in water. HEMA, a hydrophilic monomer, has also been successfully polymerized. Third, the selection of Span 80 as an oil-soluble surfactant ensures the preparation of aqueous droplets and microgels stably dispersed in cyclohexane.

Figure 7.8 illustrates the unique features of thiol-responsive biodegradable nanogels (also called ATRP nanogels) toward targeted drug-delivery applications [27]. A water-soluble disulfide-functionalized PEO-based dimethacrylate (DMA-SS) was used for the preparation of thiol-responsive biodegradable PEO-*b*-POEOMA nanogels, crosslinked with disulfide linkages. Their average diameter was 145 nm by dynamic light scattering (DLS) and 310 nm by atomic force microscopy (AFM) [31]. The larger diameter observed by AFM indicates that they are soft and flattened on the surface. These nanogels are nontoxic to cells from live/dead cell toxicity assay results. They could be internalized through clathrin-medicated endocytosis. The qualitative and quantitative analysis was carried out

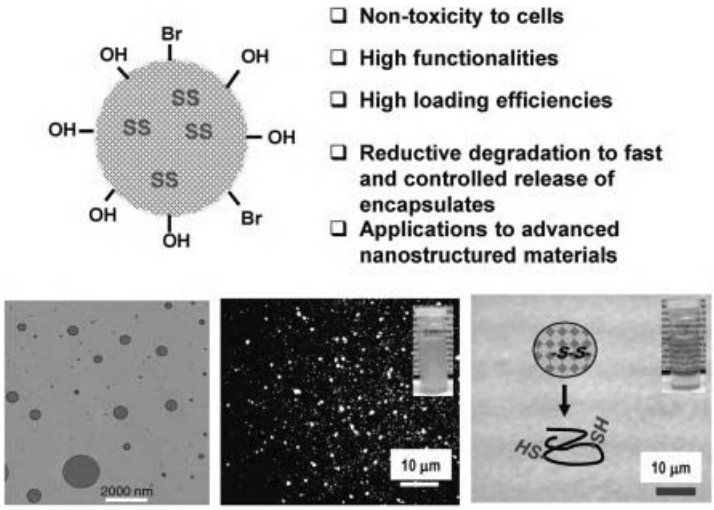

Figure 7.8 Illustration of unique features of thiol-responsive biodegradable nanogels toward targeted drug-delivery applications. The images are atomic force microscope (AFM) image of nanogels (left), fluorescence microscope image of R6G-loaded nanogels before (middle) and after (right) addition of DTT.

using laser confocal fluorescent microscopy (LCFM) and flow cytometry [37]. In addition, the nanogels have higher swelling ratios in both water and organic solvents such as toluene or tetrahydrofuran, compared to their counterparts prepared by the FRP method (FRP-nanogels) [34]. Similar to hydrogels described in the previous section, the high swelling ratio of ATRP nanogels is attributed to their uniform network.

Second, they are biodegradable in response to reductive reaction through thiol-disulfide exchange in the presence of thiols or in a reducing environment in the presence of reducing reagents. In biological environments, GSH (glutathione, a tripeptide-containing cysteine with a pendent thiol group), present in animal cells at millimolar concentrations, facilitates biodegradation [38, 39]. For polymer-based drug-delivery systems, the degradation enables fast and controlled release of encapsulated therapeutics from delivery vehicles in targeted cells. It also ensures the clearance of the original device after drugs are delivered in the body. Weight loss measurements and fluorescence microscopy of nanogels indicated that thiol-responsive nanogels were degraded in response to water-soluble dithiothritol (DTT) and GSH to corresponding linear polymers [13].

Third, these nanogels preserve high functionalities to enable further chain extension to form functional block copolymers and facilitate bioconjugation with cell-targeting agents such as peptides, proteins, and antibodies. In general, ATRP allows for well-defined polymers with terminal halide groups (typically bromide) which are used as ATRP-initiating species for block copolymerization and which are also chemically modified for further functions. Several other methods of preparation have been examined. One method employed copolymerization with functional

monomers such as HEMA to form functional nanogels with pendent OH groups, which reacted with biotin to form biotin-functionalized nanogels. The availability of biotin in nanogels was determined by HABA assay. Successful bioconjugation of biotin nanogels with fluorescein-labeled avidin was confirmed by fluorescence microscopy [13]. Another way to prepare functional nanogels relies on a functional initiator such as 2-hydroxyethyl 2-bromoisobutyrate (OH-iBuBr). OH-terminal nanogels were modified with biotin, pyrene, and GRGDS peptide to demonstrate their ease of (bio)conjugation [40]. These methods enable encapsulation of biomolecules by several routes. Anticancer drugs such as doxorubicin (DOX), fluorescent dyes, and gold nanoparticles (Au-NPs) were physically loaded into purified nanogels. High-molecular-weight carbohydrate and protein drugs were encapsulated by *in situ* physical loading during inverse mini-emulsion ATRP. The fast and controlled release of these drugs upon degradation of thiol-responsive nanogels was demonstrated in cellular environments. Rhodamine 6G (R6G), a fluorescent dye, was loaded at >30 wt% level in nanogels and released to stain C2C12 cells upon degradation of nanogels in the presence of DTT. DOX, an amphiphilic anticancer drug, was released to kill HeLa cancer cells in the presence of GSH. The cell viability was 52% in the presence of DOX-loaded nanogels determined from live/dead cytotoxicity assay [13]. In addition, rhodamine B isocyanate (RITC)-labeled dextran was released to interact with ConA through specific carbohydrate–protein interactions [41].

More recently, methods involving ATRP, inverse mini-emulsion, and biodegradation chemistry have been further explored to develop injectable nanostructured hydrogels. Acrylate-functionalized nanogels were synthesized from OH-functionalized nanogels by the reaction with acryloyl chloride. They reacted with thiolated hyaluronic acid to form *in situ* macroscopic gels by Michael-addition reaction [42]. Other examples include thermoresponsive degradable magnetic microgels for hyperthermia applications [43] and green florescent protein-loaded nanogels for protein–polymer hybrids [44, 45]. Very recently, a dual-responsive surfactant has been developed for the synthesis of functional nanocapsules in a mini-emulsion. The polymeric surfactant consists of a terminal azido ($-N_3$) group for further conjugation with a bio-related molecule using orthogonal click chemistry. Nanocapsules were crosslinked with degradable linkages, which degraded in response to low pH and reductive reactions [46].

In summary, ATRP is a versatile tool for the preparation of uniformly crosslinked hydrogels and small particles (microgels/nanogels) with controlled architecture and multifunctionality. These nanomaterials possess a number of interesting features, including a high swelling ratio and rapid thermoresponsiveness. They can contain various functionalities for bioconjugation, and enable encapsulation of biomolecules, including anticancer therapeutics. Consequently, they have great potential as multifunctional drug carriers, cellular imaging platforms, and thermosensitive tissue scaffolds for biological and biomedical applications. Furthermore, the living nature of chain ends and combined orthogonal chemistries such as click-type reactions could allow for ease of modification of well-defined polymers to meet requirements for advanced nanomaterials.

Acknowledgments

Financial support from NSF (DMR 09-69301) is gratefully acknowledged. JKO thanks NSERC Canada for a postdoctoral fellowship that permitted his 2-year stay at Carnegie Mellon University.

References

1 Matyjaszewski, K., Gnanou, Y., and Leibler, L. (2007) in *Macromolecular Engineering: From Precise Macromolecular Synthesis to macroscopic Materials Properties and Applications*, Wiley-VCH Verlag GmbH, Weinheim.

2 Braunecker, W.A. and Matyjaszewski, K. (2007) Controlled/living radical polymerization: Features, developments, and perspectives. *Prog. Polym. Sci.*, **32** (1), 93–146.

3 Matyjaszewski, K. and Mueller, A.H.E. (2006) 50 years of living polymerization. *Prog. Polym. Sci.*, **31** (12), 1039–1040.

4 Flory, P.J. (1953) *Principles of Polymer Chemistry*, Cornell University Press, Ithaca, NY, p. 672.

5 Flory, P.J. (1941) Molecular size distribution in three-dimensional polymers. I. Gelation. *J. Am. Chem. Soc.*, **63**, 3083–3090.

6 Gao, H.F. and Matyjaszewski, K. (2009) Synthesis of functional polymers with controlled architecture by CRP of monomers in the presence of cross-linkers: From stars to gels. *Prog. Polym. Sci.*, **34**, 317–350.

7 Gao, H., Polanowski, P., and Matyjaszewski, K. (2009) Gelation in living copolymerization of monomer and divinyl cross-linker: Comparison of ATRP experiments with monte carlo simulations. *Macromolecules*, **42** (16), 5925–5932.

8 Polanowski, P., Jeszka, J.K., and Matyjaszewski, K. (2010) Modeling of branching and gelation in living copolymerization of monomer and divinyl cross-linker using dynamic lattice liquid model (DLL) and Flory-Stockmayer model. *Polymer*, **51** (25), 6084–6092.

9 Yu, Q., Xu, S.H., Zhang, H.W., Ding, Y.H., and Zhu, S.P. (2009) Comparison of reaction kinetics and gelation behaviors in atom transfer, reversible addition-fragmentation chain transfer and conventional free radical copolymerization of oligo(ethylene glycol) methyl ether methacrylate and oligo (ethylene glycol) dimethacrylate. *Polymer*, **50** (15), 3488–3494.

10 Ide, N. and Fukuda, T. (1999) Nitroxide-controlled free-radical copolymerization of vinyl and divinyl monomers. 2. Gelation. *Macromolecules*, **32** (1), 95–99.

11 Tsarevsky, N.V. and Matyjaszewski, K. (2005) Combining atom transfer radical polymerization and disulfide/thiol redox chemistry: A route to well-defined (bio) degradable polymeric materials. *Macromolecules*, **38**, 3087–3092.

12 Taton, D., Baussard, J.F., Dupayage, L., Poly, J., Gnanou, Y., Ponsinet, V., Destarac, M., Mignaud, C., and Pitois, C. (2006) Water soluble polymeric nanogels by xanthate-mediated radical crosslinking copolymerisation. *Chem. Commun.*, **18**, 1953–1955.

13 Oh, J.K., Siegwart, D.J., Lee, H.-i., Sherwood, G., Peteanu, L., Hollinger, J.O., Kataoka, K., and Matyjaszewski, K. (2007) Biodegradable nanogels prepared by atom transfer radical polymerization as potential drug delivery carriers: Synthesis, biodegradation, in vitro release, and bioconjugation. *J. Am. Chem. Soc.*, **129** (18), 5939–5945.

14 Oh, J.K., Lee, D.I., and Park, J.M. (2009) Biopolymer-based microgels/nanogels for drug delivery applications. *Prog. Polym. Sci.*, **34** (12), 1261–1282.

15 Wang, J.-S. and Matyjaszewski, K. (1995) Controlled/"living" radical polymerization. atom transfer radical polymerization in the presence of

transition-metal complexes. *J. Am. Chem. Soc.*, **117** (20), 5614–5615.

16 Matyjaszewski, K., and Xia, J. (2001) Atom transfer radical polymerization. *Chem. Rev. (Washington, D. C.)*, **101** (9), 2921–2990.

17 Tsarevsky, N.V. and Matyjaszewski, K. (2007) "Green" atom transfer radical polymerization: From process design to preparation of well-defined environmentally friendly polymeric materials. *Chem. Rev.*, **107** (6), 2270–2299.

18 Matyjaszewski, K. and Tsarevsky, N.V. (2009) Nanostructured functional materials prepared by atom transfer radical polymerization. *Nat. Chem.*, **1** (4), 276–288.

19 Yoon, J.A., Gayathri, C., Gil, R.R., Kowalewski, T., and Matyjaszewski, K. (2010) Comparison of the thermoresponsive deswelling kinetics of poly(2-(2-methoxyethoxy)ethyl methacrylate) hydrogels prepared by ATRP and FRP. *Macromolecules*, **43** (10), 4791–4797.

20 Yoon, J.A., Bencherif, S.A., Aksak, B., Kim, E.K., Kowalewski, T., Oh, J.K., and Matyjaszewski, K. (2011) Thermoresponsive hydrogel scaffolds with tailored hydrophilic pores. *Chem. Asian J.*, **6** (1), 128–136.

21 Mespouille, L., Coulembier, O., Paneva, D., Degee, P., Rashkov, I., and Dubois, P. (2008) Novel biodegradable adaptive hydrogels: Controlled synthesis and full characterization of the amphiphilic co-networks. *Chem. Eur. J.*, **14** (21), 6369–6378.

22 Morimoto, N., Ohki, T., Kurita, K., and Akiyoshi, K. (2008) Thermo-responsive hydrogels with nanodomains: Rapid shrinking of a nanogel-crosslinking hydrogel of poly(N-isopropyl acrylamide). *Macromol. Rapid Commun.*, **29** (8), 672–676.

23 Kim, J.H., Lee, S.B., Kim, S.J., and Lee, Y.M. (2002) Rapid temperature/pH response of porous alginate-g-poly(N-isopropylacrylamide) hydrogels. *Polymer*, **43** (26), 7549–7558.

24 Van Durme, K., Van Mele, B., and Loos, W. (2005) and Du Prez. *F. _E.*, Introduction of silica into thermo-responsive poly(N-isopropyl acrylamide) hydrogels: A novel approach to improve response rates. *Polymer*, **46** (23), 9851–9862.

25 Dai, H.J., Chen, Q., Qin, H.L., Guan, Y., Shen, D.Y., Hua, Y.Q., Tang, Y.L., and Xu, J. (2006) A temperature-responsive copolymer hydrogel in controlled drug delivery. *Macromolecules*, **39** (19), 6584–6589.

26 Min, K., Gao, H., Yoon, J.A., Wu, W., Kowalewski, T., and Matyjaszewski, K. (2009) One-pot synthesis of hairy nanoparticles by emulsion ATRP. *Macromolecules*, **42** (5), 1597–1603.

27 Oh, J.K., Bencherif, S.A., and Matyjaszewski, K. (2009) Atom transfer radical polymerization in inverse miniemulsion: A versatile route toward preparation and functionalization of microgels/nanogels for targeted drug delivery applications. *Polymer*, **50** (19), 4407–4423.

28 Braunecker, W.A., Tsarevsky, N.V., Gennaro, A., and Matyjaszewski, K. (2009) Thermodynamic components of the atom transfer radical polymerization equilibrium: Quantifying solvent effects. *Macromolecules*, **42** (17), 6348–6360.

29 Hamidi, M., Azadi, A., and Rafiei, P. (2008) Hydrogel nanoparticles in drug delivery. *Adv. Drug Delivery Rev.*, **60** (15), 1638–1649.

30 Kabanov, A.V., and Vinogradov, S.V. (2009) Nanogels as pharmaceutical carriers: Finite networks of infinite capabilities. *Angew. Chem., Int. Ed.*, **48** (30), 5418–5429.

31 Oh, J.K. (2008) Recent advances in controlled/living radical polymerization in emulsion and dispersion. *J. Polym. Sci., Part A: Polym. Chem.*, **46** (21), 6983–7001.

32 Oh, J.K., Drumright, R., Siegwart, D.J., and Matyjaszewski, K. (2008) The development of microgels/nanogels for drug delivery applications. *Prog. Polym. Sci.*, **33** (4), 448–477.

33 Antonietti, M. and Landfester, K. (2002) Polyreactions in miniemulsions. *Prog. Polym. Sci.*, **27** (4), 689–757.

34 Oh, J.K., Tang, C., Gao, H., Tsarevsky, N.V., and Matyjaszewski, K. (2006) Inverse miniemulsion ATRP: A new method for

synthesis and functionalization of well-defined water-soluble/cross-linked polymeric particles. *J. Am. Chem. Soc.*, **128** (16), 5578–5584.

35 Jakubowski, W. and Matyjaszewski, K. (2005) Activator generated by electron transfer for atom transfer radical polymerization. *Macromolecules*, **38** (10), 4139–4146.

36 Oh, J.K., Min, K., and Matyjaszewski, K. (2006) Preparation of Poly(oligo(ethylene glycol) monomethyl ether methacrylate) by homogeneous aqueous AGET ATRP. *Macromolecules*, **39** (9), 3161–3167.

37 Siegwart, D.J., Srinivasan, A., Bencherif, S.A., Karunanidhi, A., Oh, J.K., Vaidya, S., Jin, R., Hollinger, J.O., and Matyjaszewski, K. (2009) Cellular uptake of functional nanogels prepared by inverse miniemulsion ATRP with encapsulated proteins, carbohydrates, and gold nanoparticles. *Biomacromolecules*, **10** (8), 2300–2309.

38 Carelli, S., Ceriotti, A., Cabibbo, A., Fassina, G., Ruvo, M., and Sitia, R. (1997) Cysteine and glutathione secretion in response to protein disulfide bond formation in the ER. *Science*, **277** (5332), 1681–1684.

39 Kim, E., Kim, D., Jung, H., Lee, J., Paul, S., Selvapalam, N., Yang, Y., Lim, N., Park, C.G., and Kim, K. (2010) Facile, template-free synthesis of stimuli-responsive polymer nanocapsules for targeted drug delivery. *Angew. Chem., Int. Ed.*, **49** (26), 4405–4408.

40 Siegwart, D.J., Oh, J.K., Gao, H., Bencherif, S.A., Perineau, F., Bohaty, A.K., Hollinger, J.O., and Matyjaszewski, K. (2008) Biotin-, pyrene-, and GRGDS-functionalized polymers and nanogels via ATRP and end group modification. *Macromol. Chem. Phys.*, **209** (21), 2179–2193.

41 Oh, J.K., Siegwart, D.J., and Matyjaszewski, K. (2007) Synthesis and biodegradation of nanogels as delivery carriers for carbohydrate drugs. *Biomacromolecules*, **8** (11), 3326–3331.

42 Bencherif, S.A., Washburn, N.R., and Matyjaszewski, K. (2009) Synthesis by AGET ATRP of degradable nanogel precursors for in situ formation of nanostructured hyaluronic acid hydrogel. *Biomacromolecules*, **10**, 2499–2507.

43 Dong, H., Mantha, V., and Matyjaszewski, K. (2009) Thermally responsive PM(EO)2MA magnetic microgels via activators generated by electron transfer atom transfer radical polymerization in miniemulsion. *Chem. Mater.*, **21** (17), 3965–3972.

44 Averick, S.E., Magenau, A.J.D., Simakova, A., Woodman, B.F., Seong, A., Mehl, R.A., and Matyjaszewski, K. (2011) Covalently incorporated protein-nanogels using AGET ATRP in an inverse miniemulsion. *Polym. Chem.*, **2** (7), 1476–1478.

45 Peeler, J.C., Woodman, B.F., Averick, S., Miyake-Stoner, S.J., Stokes, A.L., Hess, K.R., Matyjaszewski, K., and Mehl, R.A. (2010) Genetically encoded initiator for polymer growth from proteins. *J. Am. Chem. Soc.*, **132** (39), 13575–13577.

46 Li, W.W., Yoon, J.A., and Matyjaszewski, K. (2010) Dual-reactive surfactant used for synthesis of functional nanocapsules in miniemulsion. *J. Am. Chem. Soc.*, **132** (23), 7823–7825.

8
Nanogel Engineering by Associating Polymers for Biomedical Applications

Yoshihiro Sasaki and Kazunari Akiyoshi

8.1
Introduction

Nanogels (nanometer-sized hydrogel nanoparticles, diameter <100 nm, Figure 8.1) have attracted increasing interest in recent years because of their potential applications in drug-delivery systems (DDS) [1–3]. Unlike the nanocarriers usually used for DDS, such as nanospheres, which have a densely packed core structure, nanogels can take up a large amount of water and can incorporate bioactive compounds including drugs, proteins, and DNA within their nano-scale polymer networks in a relatively stable manner. Furthermore, molecules that are complexed with nanogels can be released by a change in the network structure or a gel-phase transition. These properties of nanogels, in comparison with other nanocarriers such as liposomes and polymer micelles, enable controlled release of the bioactive compounds by phase transition and a change in the network structure in response to specific environmental stimuli.

Nanogels can be classified as either chemically crosslinked nanogels or physically crosslinked nanogels. Chemically crosslinked nanogels are formed by crosslinking of polymers via covalent bonding. In contrast, noncovalent bonds (i.e., hydrogen bonds, ionic bonds, and hydrophobic interactions) link the polymers in physically crosslinked nanogels [4]. Typically, chemically crosslinked nanogels are synthesized under diluted conditions by a crosslinking reaction of polymers modified with reactive groups, such as vinyl and thiol groups. Nano- or micro-emulsion polymerization methods are often used to obtain nanogels with a well-controlled size. A variety of new synthetic techniques have been reported recently, including the block copolymer crosslinking method in which micelles composed of amphiphilic block copolymers or polyion complexes are crosslinked [5–7], the nano-template method, which exploits the internal water phase of liposomes [2] or the surface of silica or gold nanoparticles as templates for nanoreactions [8, 9], and the lithography-based top-down method [10, 11]. Various chemical crosslinking reactions have now been developed, including carbodiimide-mediated amide bond crosslinking [5–7], quaternization of amino groups [12], "click" chemistry [13], and

Hydrogel Micro and Nanoparticles, First Edition. Edited by L. Andrew Lyon and Michael Joseph Serpe.
© 2012 Wiley-VCH Verlag GmbH & Co. KGaA. Published 2012 by Wiley-VCH Verlag GmbH & Co. KGaA.

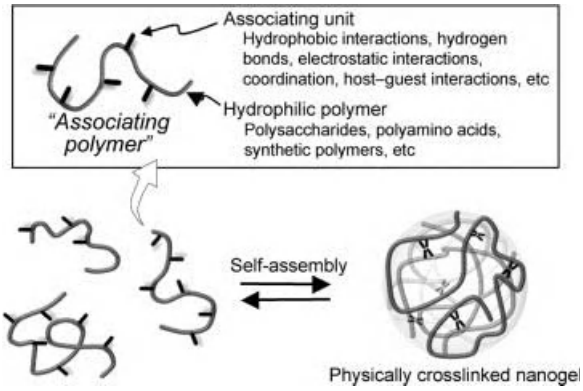

Figure 8.1 The associating polymers form physically crosslinked nanogels.

photo-crosslinking [14, 15]. Meanwhile, nanocarriers bearing disulfide bonds have been shown to be useful for efficient gene delivery [16]. Since many reports and excellent review articles have described the methods used to synthesize chemically crosslinked (non-associating polymer-based) nanogels [1], this method will not be discussed in detail here.

Noncovalent interactions, such as hydrogen bonds, van der Waals forces, and electrostatic and hydrophobic interactions are also available to prepare nanogels. However, it is difficult to obtain stable physically crosslinked nanogels with controlled sizes using noncovalent interactions because the bonds are relatively weak. In this chapter, we summarize the preparation and characteristics of associating polymer-based nanogels and discuss recent studies describing the applications of nanogels as DDS carriers. We also discuss recent advances in the development of nanogel-based biomaterials and their applications to regenerative medicine, along with our research achievements.

8.2
Preparation of Associating Polymer-Based Nanogels

8.2.1
Hydrophobically Modified Polysaccharide

In a recent study we reported the first physically crosslinked nanogels prepared by controlled association of hydrophobically modified polymers in a dilute aqueous solution [17]. Cholesterol-bearing pullulans (CHP), which are composed of hydrophilic pullulan partially modified with cholesteryl groups, self-assemble in an aqueous solution and form stable nanogels with a diameter of 30 nm (Figure 8.1) [18]. The association of hydrophobic cholesteryl groups provides crosslinking points via hydrophobic interactions. Nanogel formation is regarded as one of the most interesting functions of the associating polymers. The closed association of polymers

at the nanosize scale is governed by many factors, including the concentration of the associating polymers, the structure and concentration of the crosslinking points, and the characteristics of the associating polymers. Self-assembling nanogel formation from hydrophobically modified polymers has also been demonstrated with other associating polymers such as poly(aminoacids) [19] and hydrophilic synthetic polymers onto which associating groups are partly grafted [20, 21].

As a backbone polymer, polysaccharides (Figure 8.2) are often used to form nanogels because of their excellent biocompatibility and availability, which are favorable for DDS applications. Deoxycholic acid-modified glycol chitosan [22],

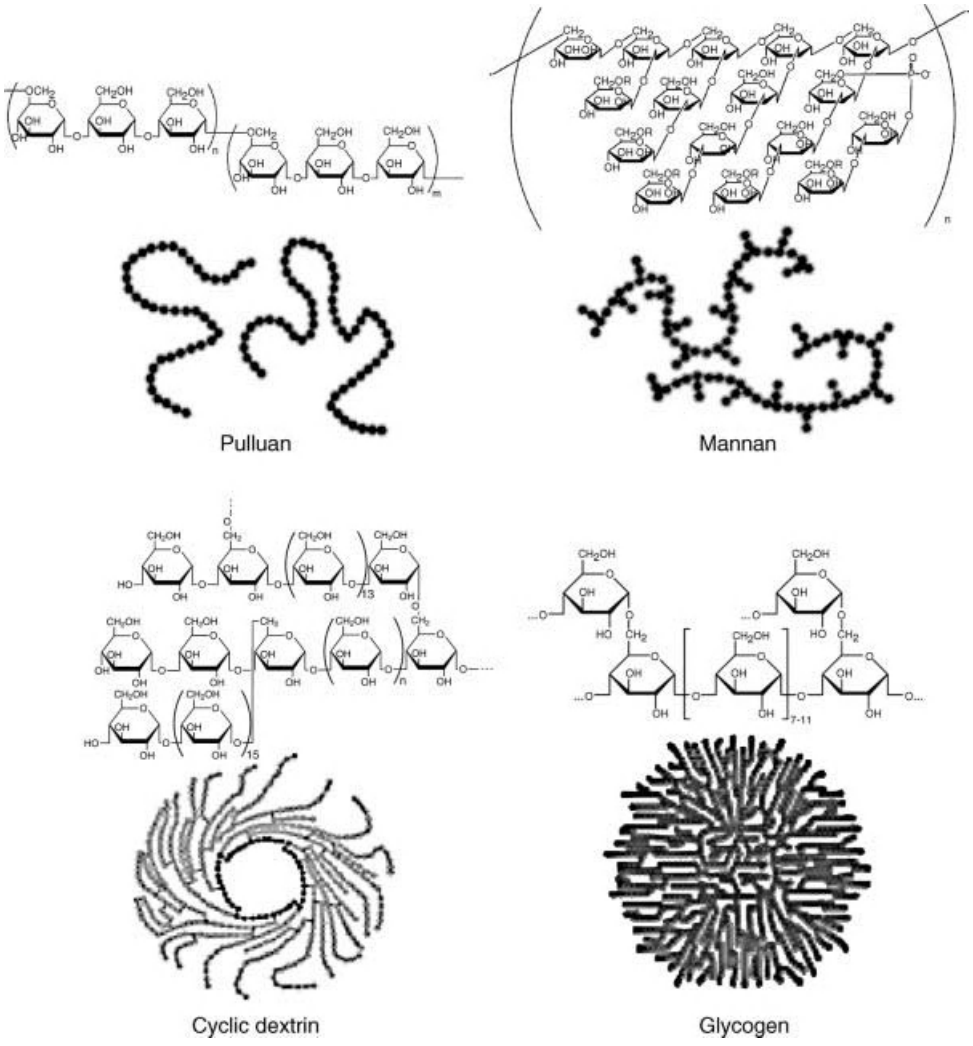

Figure 8.2 Structures of the parent polysaccharides commonly used for nanogel formation.

deoxycholic acid-modified heparin [23], bile acid-bearing dextran [24, 25], and cholesterol-modified dendritic dextrin [26] have been used as polysaccharides for nanogel formation. The effects of the hydrophobic structures and of the degree of substitution on the physicochemical properties of the resulting nanoparticles have been investigated in detail, leading to design rules with respect to the hydrophobic moieties. For example, cholesterol-modified highly branched mannan (CHM) formed highly hydrated nanogels in water through the association of cholesteryl moieties in a manner similar to that of other hydrophobically modified linear polysaccharides such as CHP [27]. A comparative study of the CHM and CHP nanogels revealed that the structure and level of hydration of the polysaccharide chain significantly affect the microscopic structure of the self-aggregates and the microviscosity of the hydrophobic domain within the nanogels [27]. We have also reported a novel amphiphilic nanoball in which a cholesterol group was introduced to enzymatically synthesized glycogen (ESG) [28]. ESG is a highly branched $(1 \rightarrow 4)$ $(1 \rightarrow 6)$-linked α-glucan and is a monodisperse spherical hyperbranched nanoparticle. Cholesterol-modified ESG assembled into a structure containing a few molecules in water to form a cluster of nanogels, which has great potential as a new building block for nanogel biomedical engineering.

One of the most significant characteristics of polysaccharide nanogels is their ability to incorporate proteins into nanogels and form stable complexes through hydrophobic interaction [29]. They can also protect proteins from irreversible aggregation to provide colloidal and thermal stability and release proteins in active forms from nanogels in response to external stimuli. These functions are described later in detail.

8.2.2
Photoresponsive Molecule-Modified Polysaccharides

In recent years, various stimulus-responsive materials have been developed and applied in biological and medical fields as DDS and for tissue engineering [31–37]. Stimulus-responsive nanogels have also attracted much attention because nanogels show an unusually rapid response to microenvironmental stimuli such as temperature and pH because of their nano-scaled dimensions. Associating polymers can be used to prepare stimulus-responsive nanogels because of the formation of noncovalent crosslinks, which can be easily modified by external stimuli. To date, several stimulus-responsive nanogels have been developed by introducing stimulus-responsive molecules to the polymers.

A photoresponsive nanogel was synthesized by substituting pullulan with a spiropyran molecule, a hydrophobic group that changes the polarity of the molecule in response to light and heat [30]. Spiropyrane molecules which isomerize from hydrophobic spiropyrane to hydrophilic merocyanine under photo- and thermo-stimulation are widely used to control the structure and function of biomaterials by exposure to light. Spiropyran-modified pullulan forms $\sim$75 nm nanogels in water. The assembly is controlled by changing the amphiphilicity of the spiropyrane molecule due to exposure to photo-irradiation or heat (Figure 8.3). In addition,

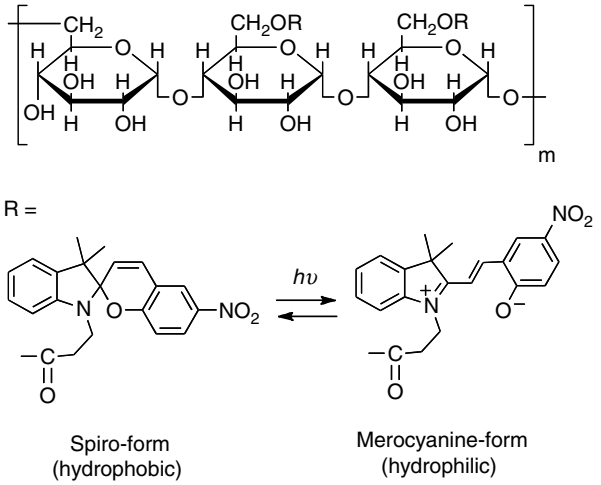

Figure 8.3 Structure of photoresponsive spiropyran-bearing pullulan.

refolding of the chemically denatured proteins after dilution of the protein solution is facilitated by photo-irradiation. Photoresponsive nanogels also act as novel photoresponsive artificial molecular chaperones.

8.2.3
Thermoresponsive Polymer-Grafted Polysaccharide

Thermoresponsive materials with low critical solution temperatures (LCSTs) in aqueous media have received much attention [38]. For example, some researchers have prepared thermoresponsive nanogels that enable heat-induced association and dissociation of polysaccharides partially grafted with short poly(*N*-isopropylacrylamide) (PNIPAM) chains [39]. These polymers readily dissolve in water at room temperature. Above the LCST, PNIPAM-*g*-polysaccharides form nanogels that are physically crosslinked by the hydrophobic nanodomains generated by dehydration of PNIPAM. Biocompatible heat-induced nanogels have also been obtained by grafting poly(2-isopropyl-2-oxazoline) (PIPOZ) [40], which is a biocompatible, thermoresponsive crystalline molecule, onto a polysaccharide (Figure 8.4). The assembly of the polymers is driven by the crystallization of PIPOZ chains following heat-induced dehydration of the chains in water heated above the LCST.

A dual stimuli-responsive nanogel that responds to changes in environmental temperature and redox potential has also been reported [41]. That nanogel was developed by associating a redox-responsive polymer containing a thiol group with the terminus of the PNIPAM chain, which forms a disulfide bond after nanogel formation. The formation of the nanogel is controlled by heating and cooling of the solution because the hydrophilic–hydrophobic transition of the PNIPAM side chains is temperature-dependent. Assembling the PNIPAM chain with a thiol group at its terminus provides nanogels that are chemically crosslinked via a disulfide bond after

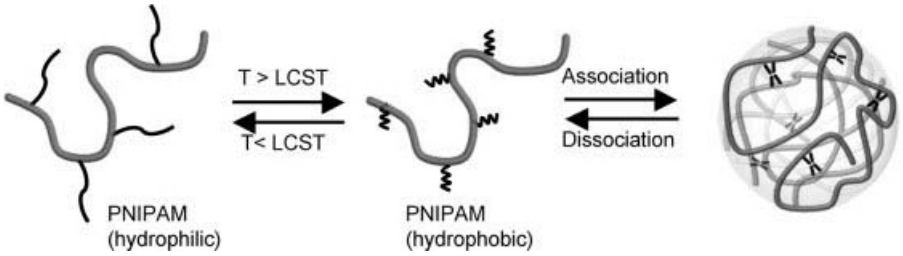

Figure 8.4 Nanogels enable heat-induced association of polysaccharides partially grafted with short poly(*N*-isopropylacrylamide) (PNIPAM) chains.

the nanogel is formed at a temperature above the LCST. Even after cooling the temperature to below the LCST, the structure of the nanogel is maintained as a swollen hydrophilic nanogel. In the presence of a reducing agent, the nanogel can be reduced to its thiol group to afford a dual-responsive nanogel that responds to both temperature and redox potential.

8.2.4
Metal–Ligand Modified Polysaccharides

Redox-sensitive nanogels have been found to be useful for efficient gene delivery [16]. As described above, redox-responsive nanogels can be obtained by using disulfide bonds as a crosslinking point [41]. More recently, redox-sensitive metal coordinative-crosslinked nanogels were prepared by introducing a metal–ligand to a hydrophilic polysaccharide and CHP (ImP and ImCHP, Figure 8.5) [42]. Metal-complexing and metal-containing polymers are fascinating research targets, particularly because such materials have properties that differ from their individual organic and inorganic components. These polymers offer a wide variety of applications that range from filtration to catalysis. The coordinating ability of the metal within the polymer chain enables their application in environmental metal sensing and as building blocks for supramolecular structures. We used metal ligands to prepare novel redox-responsive

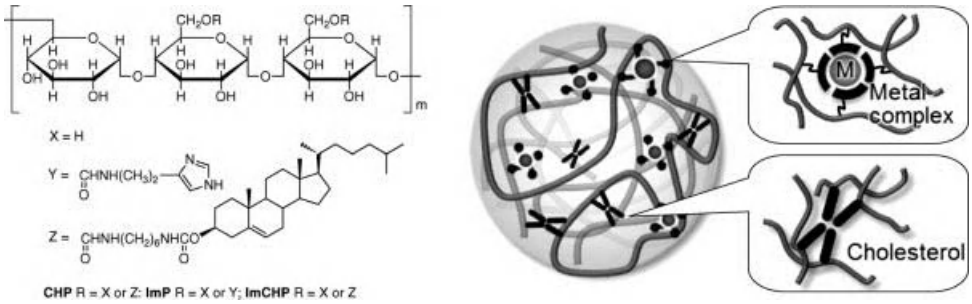

Figure 8.5 Structures of the metal–ligand-modified polysaccharide, CHP, and the metal-coordinative crosslinked nanogel.

nanogels [42]. As a metal–ligand, imidazolyl groups were conjugated with pullulan. The imidazolyl group has a high affinity for divalent transition metal ions and forms a complex. Complexation of more than one ligand group per metal ion can link two or more polymer chains at a metal-centered crosslink. In addition, the redox couple of Co(II) and Co(III) afforded this metal coordinative nanogel system with good redox sensitivity.

8.2.5
Siloxane-Modified Polysaccharides

The development of organic/inorganic hybrid nanomaterials is a fascinating research target in the fields of biosensing, bioimaging, and DDS [43, 44] because of the specific functionality of the organic part and the structural stability of the inorganic part. For example, hybrids consisting of polysaccharides with calcium phosphate and hydroxyapatite nanoparticles have been prepared [45, 46]. The hybrid nanogels are useful as intracellular protein carriers because of their excellent biocompatibility and biodegradability, in addition to their mechanical stability. In another example, hybrid nanogels were prepared by condensation of inorganic silanol groups (sol–gel reaction) grafted onto polysaccharides at ambient temperature and pH without any catalysts or organic solvents [47]. The hybrid nanogels were made rigid upon covalent crosslinking with inorganic siloxanes, which provides an additional platform for mineralization with other silane-coupling agents, titania and hydroxyapatite, for example. These stable hybrid nanogels are promising candidates for controlled-release DDS. In fact, using hybrid nanogels based on PNIPAM gels and tailored nanoporous silica, the carried drug can slowly diffuse out of the porous channels via a nanodiffusion mechanism [48].

8.2.6
Protein-Crosslinked Nanogels

Biomolecules such as oligopeptides [49], proteins [50], antibodies [51], and oligonucleotides [52] have been widely used as crosslinkers to prepare macroscale hydrogels. One of the main advantages of biomolecule-crosslinked hydrogels is that their response to stimuli is controlled and modulated by the complexed biomolecule [53]. Despite the promising utility of crosslinked biomolecules, there are few examples of biomolecule-crosslinked nanogels, perhaps because of the difficulty in conjugating the biomolecules with polymer chains in an aqueous environment. We recently prepared protein-crosslinked nanogels by introducing vitamin B_6 (pyridoxal) to hydrophilic polysaccharide [54]. One of the important chemical characteristics of the pyridoxal moiety is that it acts as an active aldehyde to form a Schiff base between the amine and the pyridoxal formyl group. By using the Schiff base, the pyridoxal-modified polysaccharides were held together to form nanogels that crosslinked with lysozyme containing six lysine residues (Figure 8.6). The pH-dependence of Schiff base formation was exploited to construct a pH-sensitive nanogel system. These pH-sensitive hybrid nanogels, upon Schiff base

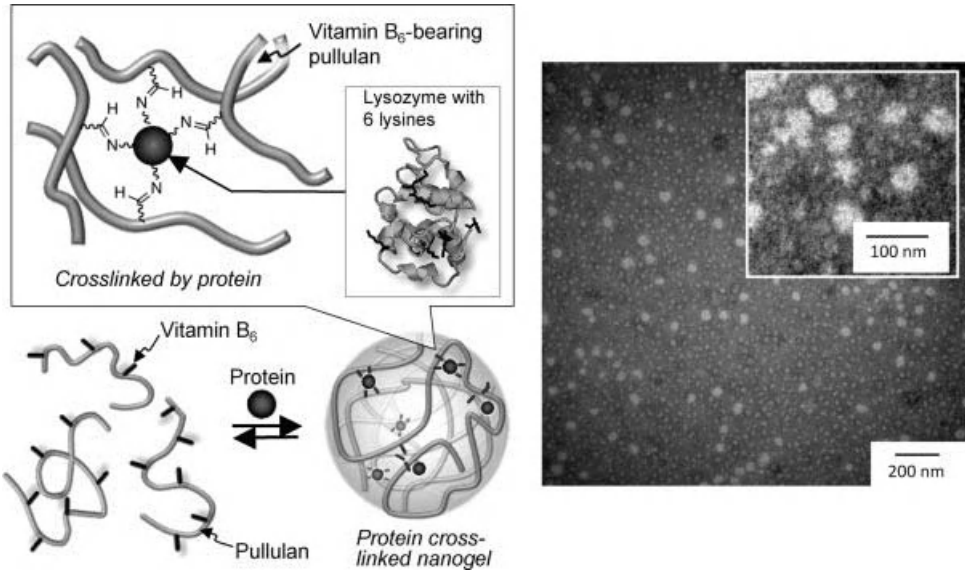

Figure 8.6 (Left) Formation of protein-crosslinked nanogels by introducing vitamin B_6 (pyridoxal) to hydrophilic polysaccharide. (Right) Transmission electroscopic image of the resulting nanogels.

formation with various biomolecules, are useful nanocarriers in DDS and could be used for cytosolic protein delivery.

8.3
Functions of Self-Assembled Nanogels

8.3.1
Nano-Encapsulation of Proteins by the Nanogel: Nanogels as Macromolecular Hosts

The design of a macromolecular host with a nano-cage that can bind macromolecular guests, such as proteins, and the ability to control uptake and release of the guest molecules are indispensable properties of effective DDS of biomacromolecules. The development of a macromolecular host that protects the accommodated biomolecule, particularly for proteins, DNA, and RNA, is essential because such molecules undergo rapid degradation by endolysosomal proteases and nucleases. One of the most notable characteristics of associating polymer-based nanogels is their dynamic properties, which enable them to spontaneously trap proteins in the relatively flexible nano-scale hydrogel matrix and protect them. For example, CHP nanogels were reported to selectively interact with various proteins, primarily through hydrophobic interactions [29, 55]. The nanogel–protein complexes showed excellent colloidal stability without any precipitation. One CHP nanogel complexed with approximately one bovine serum albumin (M_w 66 000), two α-chymotrypsin (M_w 25 000), two

myoglobin (M_w 17 800), four molecules of cytochrome *c* (M_w 12 500), and five molecules of insulin (M_w 5735). The maximum number of protein molecules complexed by CHP nanogels depends on the molecular weight (or size) and hydrophobicity of the protein. This is an interesting example of host–guest interactions in a macromolecular system.

In most cases, the activity of an enzyme is lost following complexation because of the induction of conformational changes in the enzyme due to the preferred hydrophobic interactions between the protein and the cholesterol groups of CHP. However, we found that complexation with a nanogel afforded high enzyme activity and thermal stabilization of lipase [56]. Lipases are key biocatalytic enzymes involved in the synthesis of bioactive molecules and biodegradable biopolymers. The thermostability of the lipase complex increased because the denaturation temperature of lipase increased by more than 20 °C after complexation with CHP nanogels. Lipase denaturation and aggregation upon heating was effectively prevented by complexation with CHP nanogels. Complexation with CHP nanogels also protected lipase from lyophilization-induced aggregation. Thus, nano-encapsulation with CHP nanogel as a macromolecular host is a useful method to achieve colloidal and thermal stabilization of an unstable enzyme.

8.3.2
Artificial Molecular Chaperones

In living systems, natural molecular chaperones such as GroEL/ES aid protein folding by preventing the aggregation of denatured proteins [57]. In general, native proteins partially unfold in response to stressors, such as heat, which expose the hydrophobic groups to the outer surface. Hydrophobic interactions between the exposed hydrophobic chains cause aggregation and the formation of insoluble aggregates in a (usually) irreversible manner. Molecular chaperones selectively trap the folding intermediate proteins or heat-denatured proteins via hydrophobic interactions to prevent irreversible aggregation. Then, with the aid of ATP and another co-chaperone, the chaperone releases the folded (refolded) proteins.

The use of polysaccharide nanogels as a macromolecular host can simulate these molecular chaperone systems because of the dynamic properties of the associating polymers [58]. As described above, CHP-based nanogels can interact with proteins. More interestingly, many enzymes and proteins can be captured within the nanogel network in a heat-denatured form above their denaturation temperatures [59]. Because the nanogel network is comparable with that of proteins, the nanogel can hold a protein molecule within a segregated nanomatrix. The ability of part of the nanogel network to isolate protein molecules is advantageous for stabilizing proteins, because protein–protein interactions and aggregation can be eliminated. Nanogels also prevented protein aggregation (e.g., carbonic anhydrase and citrate synthase) by forming nanogel–protein complexes during protein refolding after chemical denaturation by urea or guanidium hydrochloride [60, 61].

Fluorescence correlation spectroscopy (FCS) was recently used to evaluate the thermodynamic properties of the interaction between nanogels and proteins at

variable temperature [62], although preliminary thermodynamic studies were conducted using isothermal titration calorimetry at a single temperature [63]. FCS has been used to monitor the binding process by determining the diffusion of fluorescently labeled molecules. The van't Hoff plot showed that the CHP nanogels strongly complexed with heat-denatured proteins. The increased hydrophobicity of the denatured, unfolded protein may favor complexation with amphiphilic hydrogel nanoparticles over complexation with the completely folded native protein. Other thermodynamic parameters suggest that under the conditions studied the complexation is driven in an entropic rather than an enthalpic manner, indicating that the complexation is driven by hydrophobic interactions between proteins and nanogels.

Using a series of cyclodextrins (CDs), the polysaccharide nanogel system can simulate the release process controlled by molecular chaperones to afford folded active proteins. CHP nanogels can be dissociated by the addition of CD [64]. CD formed inclusion complexes with cholesteryl groups and dissociated the hydrophobic crosslinking points in the nanogel network. Indeed, we have reported the molecular chaperone-like activities of a CHP nanogel system using enzymes such as bovine carbonic anhydrase and porcine citrate synthase [59, 65, 66]. The nanogel–CD system has some superior features compared with other artificial chaperone systems. Similar two-step systems employing surfactants and CDs [67] are referred to as "artificial chaperone" techniques. However, it can be difficult to completely remove the surfactants, which may denature proteins after treatment with such systems. These polymers appear to act as a hydrophobic buffer by blocking the exposed hydrophobic surface on the denatured protein and thus preventing aggregation. In this polymer system, very strong binding to the intermediate would prevent folding to the native conformation. The current nanogel system can provide a delicate balance for the various folding processes and afford a high refolding efficiency with the broad specificity of natural molecular chaperones. In fact, the chaperone-like activity of CHP nanogels has been demonstrated in the refolding of acid-denatured green fluorescent protein (GFP) [68], the renaturation of the inclusion body of a recombinant protein [69], and the suppression of Aβ toxicity in primary cortical cultures and in microglial cell cultures [70].

8.3.3
Nanogel Chaperones in Cell-Free Protein Synthesis

Cell-free protein synthesis is a promising technique for the rapid production of proteins. However, the application of cell-free systems requires the development of artificial chaperones that prevent protein aggregation and support its correct folding. We reported that the CHP nanogel acted as an artificial chaperone in cell-free protein synthesis of GFP [71]. In this cell-free GFP system, GFP spontaneously folded with a relatively high yield in the absence of molecular chaperones so that the CHP nanogel–CD system did not improve folding efficiency. More recently, we showed that the nanogel-based artificial chaperone improves the folding efficiency of rhodanese produced in a cell-free system [72] (Figure 8.7). Rhodanese normally aggregates rapidly, but it was successfully expressed in the presence of the nanogel and folded

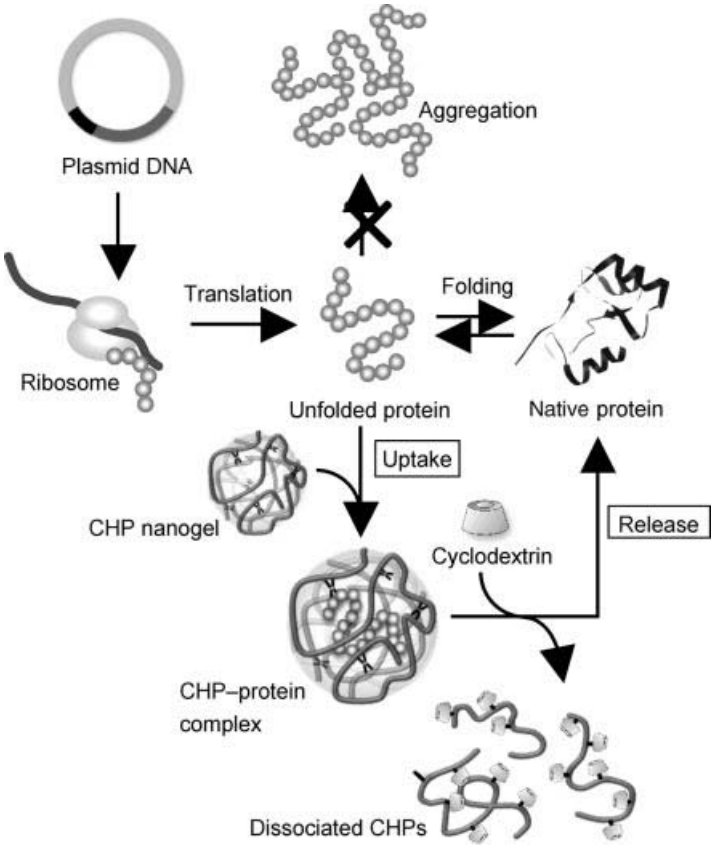

Figure 8.7 Schematic representation of the protein folding mediated by CHP nanogels. The CHP nanogel formed a complex with unfolded protein and the protein was released in its native form by the addition of methyl-beta-cyclodextrin.

to the enzymatically active form after the addition of CD. The general applicability of the nanogel-based molecular chaperone system was also demonstrated in the cell-free synthesis of 10 water-soluble proteins and it was concluded that the nanogel enables the high expression of proteins with a high tendency for aggregation [72].

8.4
Application of Polysaccharide Nanogels to DDS

Nanogels can be used as carriers in DDS by efficiently trapping not only hydrophobic and hydrophilic low-molecular-weight drugs, but also high-molecular-weight entities, including DNA, siRNA, peptides, and proteins, within the network [1–4, 17]. For example, amphiphilic nanogels with hydrophobic regions have been used for the incorporation and release of insoluble anticancer drugs. In this section, we describe

the biomedical applications of polysaccharide nanogels, particularly for the purpose of protein and nucleic acid delivery.

8.4.1 Protein Delivery

Biologically active proteins such as hormones, cytokines, growth factors, and antigenic proteins are effective for the treatment of various diseases. The development of technologies capable of efficiently delivering these proteins into the cells is also important in the fields of regenerative medicine and immunotherapy. However, there remain several issues to be overcome, including the instability of the carrier–protein complexes and difficulties in suppressing inactivation, aggregation and controlled release of proteins, which are less stable than low-molecular-weight drugs. The activity of molecular chaperones is an important concept that has led to significant breakthroughs in DDS, particularly for protein or peptide delivery [73, 74].

The main benefits of nanogels as protein carriers were recognized mainly in the field of immunotherapy for the treatment of cancer and HIV by stimulating or activating autoimmune function. Immunotherapy with cytokines and cancer vaccines is an important therapeutic modality because such treatments have minimal side effects and are capable of controlling the growth, recurrence, and metastasis of cancer cells over a prolonged time. CHP nanogels can form stable complexes with the protein antigens used to induce specific immune responses against tumor cells resulting in effective cancer immunotherapy [75–78]. For example, when CHP nanogels containing HER2 protein antigen (a cancer-related gene product) were subcutaneously injected into mice with cholangiocarcinoma, antitumor killer T cells and antibody-producing T helper cells were efficiently induced. A preliminary phase I clinical trial demonstrated the effect of the nanogel system, especially for treatment of esophageal cancer. Since then, CHP nanogels have been found to be effective as controlled-release carriers of interleukins for cytokine immunotherapy of cancer [79].

More recently, it was shown that cationic nanogels are effective carriers of mucosal (intranasal) vaccines [80]. Mucosal vaccines are expected to represent a new generation of vaccines that can prevent infection against pathogens, such as influenza virus, AIDS virus, and norovirus, which infect via the mucosal surfaces. A nontoxic subunit of *Clostridium botulinum* type A neurotoxin (BoHc/A) administered intranasally with a cationic nanogel adhered continuously to the nasal epithelium and was effectively taken up by the mucosal dendritic cells after its release from the cationic nanogel. Moreover, intranasally immunized tetanus toxoid with cationic nanogel induced systemic and mucosal immune responses. These results indicate that cationic nanogels can be used as a universal protein-based antigen-delivery vehicle for adjuvant-free intranasal vaccination.

The intracellular delivery of exogenous proteins is a topic of growing interest in bioscience and for medical applications [81]. Cationic liposomes [82, 83], cationic microparticles [84–86], and amphiphilic peptides containing protein transduction domains (PTD) [87] have been used as carriers for intracellular delivery. However, these DDS generally suffer from low delivery efficiency and poor specificity for a

particular cell type. We demonstrated that the intracellular protein delivery could be efficiently done using cationic nanogels with chaperone-like functions. For example, ethylenediamine was introduced to the CHP nanogel to form positively charged nanogels ~30 nm in size [73]. The cationic nanogels strongly interacted with a wide range of proteins to form stable nanogel–protein complexes, which were efficiently introduced into Hela cells. One advantage of nanogels is that they can form a colloidally stable complex with a protein with an overall complex size of several tens of nanometers, which is suitable for effective intracellular uptake. Indeed, it was shown that nanogels are capable of delivering an active enzyme (β-galactosidase) into the nucleus [73]. Protein-coated quantum dots (QDs) have also been effectively delivered into cells and hence can be used as an imaging reagent [88, 89]. We have also reported a new nanogel with a targeting function aimed at enhancing specific delivery via a ligand-conjugated nanocarrier (cell-specific peptide (Arg-Gly-Asp; RGD)-modified nanogel) [90].

8.4.2
Nucleic Acid Delivery

The gene-delivery system is an essential technology in both basic research and in clinical gene therapy [91]. Polymer-based carriers have received extensive attention because they are easier to prepare and have less toxicity than viral carriers. In particular, polysaccharide-based gene-delivery systems such as cationic dextran [92], cationic pullulan [93], cationic cycloamylose [94], chitosan [95], and schizophyllan [96] have been developed because of the low toxicity and high biocompatibility of the constituents. RNA interference has emerged as a new therapeutic pathway for delivering functional RNA, such as siRNA, to target cells. We reported a new siRNA-delivery system based on a functional cycloamylose nanogel [97]. Cholesterol-bearing cationic cycloamylose also formed nanogels by self-assembly in water. The nanogels formed 20–40 nm nanoparticles that bound to 21 bp siRNA. The complexes exerted an RNA-interfering effect on SCC7-GL3 cells stably expressing the luciferase gene.

We recently developed a hybrid gene-delivery system comprising a polysaccharide-based cationic nanogel and phospholipase A_2 (PLA_2) that was capable of endosomal disruption by hydrolyzing membrane phospholipids [98]. A cationic nanogel formed ternary complexes with PLA_2 and pDNA by hydrophobic and electrostatic interactions. Both pDNA and PLA_2 were internalized into cells by the nanogel. The ternary complex can disrupt the membrane when delivered into cells and triggers the release of pDNA from the endosome to the cytoplasm. Co-delivery of PLA_2 and pDNA using a nanogel may address an important issue in polymer-based gene-delivery systems – the need to overcome endosomal disruption produced by the polyion complex.

8.5
Integration of Nanogels

Effective control of the structure of the crosslinking points and the nano-domains in macro-scale hydrogels, which have been widely used as functional materials in

biotechnological and biomedical applications, is an important focus of research. We developed a method capable of forming novel gel materials using self-assembling nanogels as the building blocks (Figure 8.8). Specifically, we found that nanogels accumulate and form macrogels at a relatively high concentration [99]. We also developed polymerizable nanogels by synthesizing nanogels containing methacryloyl residues as reaction points [100]. When the nanogels were polymerized with various hydrophilic monomers, macrogels composed of crosslinked nanogels with immobilized artificial molecular chaperone functions [101] and quick thermoresponsiveness [102] were obtained. Macrogels consisting of a network of nanogels connected by biocompatible polymers can be formed by polymerization between nanogels and 2-methacryloyloxyethylphosphocholine at relatively high concentrations in an aqueous environment.

Recently, macroscopic hydrogels have been used as an artificial extracellular matrix capable of controlled release of a drug in regenerative medicine. Efficient tissue regeneration is possible by precisely controlling the release of multiple

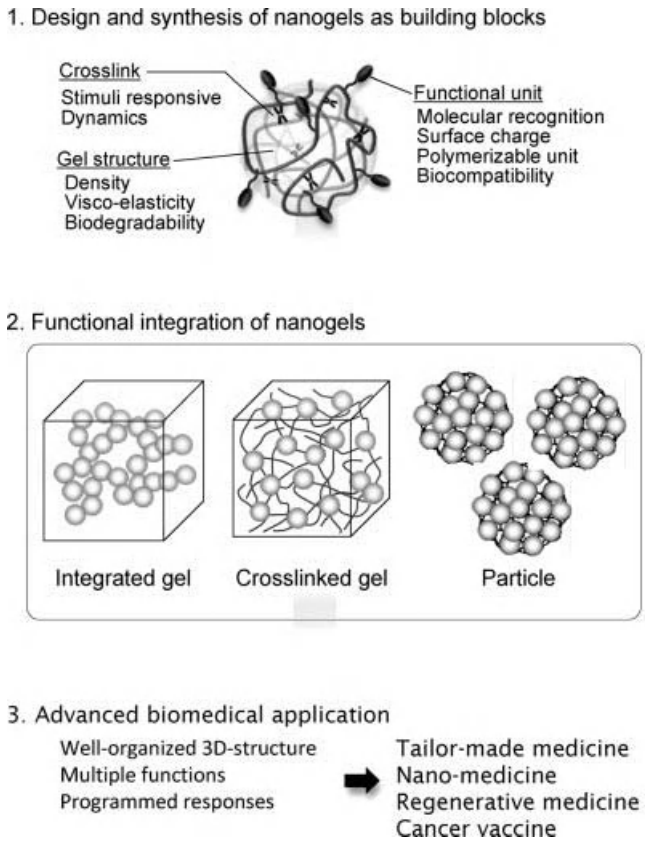

Figure 8.8 Bionanoengineering fabrication and applications of nanogel-based biomaterials.

cytokines and hormones. Therefore, development of a durable, long-lasting matrix is essential for applications in regenerative medicine. However, unfavorable rapid and bursts of drug release were observed in many cases because of the difficulty in controlling the crosslinking point in the gel, which leads to heterogeneity of the nano-scale structure. Another problem is the denaturation of proteins inside the hydrogels and their loss of function through irreversible aggregation. Biodegradable hybrid hydrogels consisting of acryloyl-substituted CHP and poly(ethylene glycol) (PEG) with four branched terminal thiol groups (CHP–PEG) were used as a matrix for bone regeneration. By allowing the acryloyl group-modified CHP nanogel to absorb prostaglandin E_2 (PGE_2), a PGE_2-encapsulated CHP–PEG hydrogel was prepared [103]. In that study, new bone formation was detected 4 weeks after implantation of the gel into the calvaria of mice. Furthermore, the CHP–PEG hydrogel system exhibited no side effects, such as increases in the cancellous bone of the femur, while bone formation was facilitated specifically at the target site. A CHP–PEG hydrogel encapsulating bone morphogenetic protein-2 within the nanogel markedly facilitated bone formation [104]. It was found that nanoparticles (~150 nm) consisting of several hundred nanogels (~30 nm) crosslinked with PEG-SH were formed when the nanogel-crosslinking reaction was performed at low nanogel concentration [105], a process termed "raspberry-like" nanogel assembly. The resulting raspberry-like nanoparticle was capable of encapsulating interleukin-12 as an immunostimulatory cytokine and was able to keep it even in the presence of BSA *in vitro*. More importantly, the raspberry-like nanoparticle had a protracted release profile after subcutaneous injection in mice because of hydrolytic degradation under physiological conditions to dissociate back to an original nanogel (Figure 8.9). Therefore, this system enables sustained release of proteins. The simplicity of the preparation and the high encapsulation efficiency will be very advantageous in practical applications.

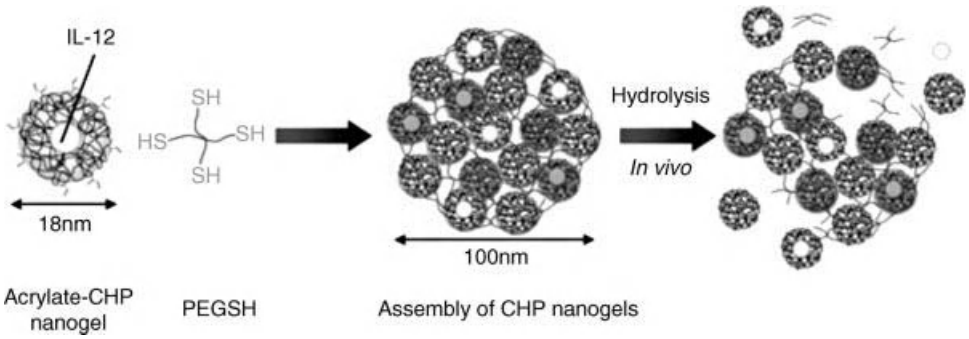

Figure 8.9 Formation of the raspberry-like assembly of nanogels by crosslinking reactions of PEG-SH. The protracted release profile is due to hydrolytic degradation of the raspberry-like nanogel under physiological conditions, which causes dissociation back to the original nanogel.

8.6 Conclusion and Perspectives

Research in the field of bioengineering on the biomedical applications of nanogels has rapidly progressed over the past 10 years. Their application to the DDS of various drugs has become possible because of the bioengineering techniques that allow us to control the size, stability, and surface properties of nanogels. A future objective of research is the delivery of drugs that are relatively unstable under physiological conditions, particularly proteins, antibodies, and nucleic acids. Nanogels with molecular chaperone functions may offer a promising approach to achieve this goal. Another objective of nanogel research should be the use of nanogels as individual components for building an integrated nanosystem using nanogel engineering. By integrating various functional nanogels using nanogel engineering techniques, the development of nanogel-based biomaterials with a well-organized three-dimensional structure, multiple functions, sensitivity to a range of different stimuli, and programmed responses that can be controlled temporally and spatially may become possible.

References

1 Oh, J.K., Drumright, R., Siegwart, D.J., and Matyjaszewski, K. (2008) The development of microgels/nanogels for drug delivery applications. *Prog. Polym. Sci.*, **33**, 448–477.

2 Reamdonck, K., Demeester, J., and De Smedt, S. (2009) Advanced nanogel engineering for drug delivery. *Soft Matter*, **5**, 707–715.

3 Hamidi, M., Azadi, A., and Rafiei, P. (2008) Hydrogel nanoparticles in drug delivery. *Adv. Drug. Deliv. Rev.*, **60**, 1638–1649.

4 Kabanov, A.V. and Vinogradov, S.V. (2009) Nanogels as pharmaceutical carriers: Finite networks of infinite capabilities. *Angew. Chem. Int. Ed.*, **48**, 5418–5429.

5 Huang, H.Y., Remsen, E.E., and Wooley, K.L. (1998) Amphiphilic core–shell nanospheres obtained by intramicellar shell crosslinking of polymer micelles with poly(ethylene oxide) linkers. *Chem. Commun.*, 1415–1416.

6 Zhang, Q., Remsen, E.E., and Wooley, K.L. (2000) Shell cross-linked nanoparticles containing hydrolytically degradable, crystalline core domains. *J. Am. Chem. Soc.*, **122**, 3642–3651.

7 Fujii, S., Cai, Y.L., Weaver, J.V.M., and Armes, S.P. (2005) Syntheses of shell cross-linked micelles using acidic abc triblock copolymers and their application as pH-responsive particulate emulsifiers. *J. Am. Chem. Soc.*, **127**, 7304–7305.

8 Shi, L. and Berkland, C. (2007) Acid-labile polyvinylamine micro- and nanogel capsules. *Macromolecules*, **40**, 4635–4643.

9 Singh, N. and Lyon, L.A. (2007) Au nanoparticle templated synthesis of pNIPAm nanogels. *Chem. Mater.*, **19**, 719–726.

10 Gratton, S.E.A., Ropp, P.A., Pohlhaus, P.D., Luft, J.C., Madden, V.J., Napier, M.E., and Desimore, J.M. (2008) The effect of particle design on cellular internalization pathways. *Proc. Natl. Acad. Sci. U.S.A.*, **105**, 11613–11618.

11 Glangchai, L.C., Caldorera-Moore, M., Shi, L. *et al.* (2008) Nanoimprint lithography based fabrication of shape-specific enzymatically-triggered smart nanoparticles. *J. Controlled Release*, **125**, 263–227.

12 Butun, V., Lowe, A.B., Billingham, N.C., and Armes, S.P. (1999) Synthesis of zwitterionic shell cross-linked micelles. *J. Am. Chem. Soc.*, **121**, 4288–4289.

13 Zhang, J., Zhou, Y., Zhu, Z., Ge, Z., and Liu, S. (2008) Polyion complex micelles possessing thermoresponsive coronas and their covalent core stabilization via "Click" chemistry. *Macromolecules*, **41**, 1444–1445.

14 Yusa, S., Sugahara, M., Endo, T., and Morishima, Y. (2009) Preparation and characterization of a pH-responsive nanogel based on a photo-cross-linked micelle formed from block copolymers with controlled structure. *Langmuir*, **25**, 5258–5265.

15 Shi, D., Matsusaki, M., Kaneko, T., and Akashi, M. (2008) Photo-cross-linking and cleavage induced reversible size change of bio-based nanoparticles. *Macromolecules*, **41**, 8167–8172.

16 Matsumoto, S., Christie, R.J., Nishiyama, N., Miyata, K., Ishii, A., Oba, M., Koyama, H., Yamasaki, Y., and Kataoka, K. (2009) Environment-responsive block copolymer micelles with a disulfide cross-linked core for enhanced siRNA delivery. *Biomacromolecules*, **10**, 119–127.

17 Sasaki, Y. and Akiyoshi, K. (2010) Nanogel engineering for new nanobiomaterials: From chaperoning engineering to biomedical applications. *Chem. Rec.*, **10**, 366–376.

18 Akiyoshi, K., Deguchi., S., Moriguchi., N. *et al.* (1993) Self-aggregates of hydrophobized polysaccharides in water. Formation and characteristics of nanoparticles. *Macromolecules*, **26**, 3062–3068.

19 Akiyoshi, K., Ueminami, A., Kurumada, S. *et al.* (2000) Self-association of cholesteryl-bearing poly(L-lysine) in water and control of its secondary structure by host–guest interaction with cyclodextrin. *Macromolecules*, **33**, 6752–6756.

20 Lee, K.Y., Jo, W.H., Kwon, I.C. *et al.* (1998) Structural determination and interior polarity of self-aggregates prepared from deoxycholic acid-modified chitosan in water. *Macromolecules*, **31**, 378–383.

21 Yusa, S., Kamachi, M., Morishima, Y. *et al.* (1998) Hydrophobic self-association of cholesterol moieties covalently linked to polyelectrolytes: Effect of spacer bond. *Langmuir*, **14**, 6059–6067.

22 Kim, K., Kwon, S., Park, J.H., Chung, H., Jeong, Y., and Kwon, I.C. (2005) Hydrophobically modified glycol chitosan nanoparticles as carriers for paclitaxel. *Biomacromolecules*, **6**, 1154–1158.

23 Park, K., Kim, K., Kwon, I.C., Kim, S.K., Lee, S., Lee, D.Y., and Byun, Y. (2004) Preparation and characterization of self-assembled nanoparticles of heparin-deoxycholic acid conjugates. *Langmuir*, **20**, 11726–11731.

24 Naeye, B., Raemdonck., K., Remaut, K., Sproat, B., Demeester, J., and De Smedt, S.C. (2010) PEGylation of biodegradable dextran nanogels for siRNA delivery. *Eur. J. Pharm. Sci.*, **40** (4), 342–351.

25 Nichifor, M., Lopes, A., Carpov, A. *et al.* (1999) Aggregation in water of dextran hydrophobically modified with bile acids. *Macromolecules*, **32**, 7078–7085.

26 Ozawa, Y., Sawada, S., Morimoto, N., and Akiyoshi, K. (2009) Self-assembled nanogel of hydrophobized dendritic dextrin for protein delivery. *Macromol. Biosci.*, **9**, 694–701.

27 Akiyama, E., Morimoto, N., and Kujawa, P. (2007) Self-assembled nanogels of cholesteryl-modified polysaccharides: Effect of the polysaccharide structure on their association characteristics in the dilute and semidilute regimes. *Biomacromolecules*, **8**, 2366–2372.

28 Takahashi, H., Sawada, S., and Akiyoshi, K. (2011) Amphiphilic polysaccharide nanoballs: a new building block for nanogel biomedical engineering and artificial chaperones. *ACS Nano*, **5** (1), 337–345.

29 Nishikawa, T., Akiyoshi, K., and Sunamoto, J. (1996) Macromolecular complexation between bovine serum albumin and the self-assembled hydrogel nanoparticle of hydrophobized polysaccharides. *J. Am. Chem. Soc.*, **118**, 6110–6115.

30 Hirakura, T., Nomura, Y., Aoyama, Y., and Akiyoshi, K. (2004) Photoresponsive nanogels formed by the self-assembly of spiropyrane-bearing pullulan that act as artificial molecular chaperones. *Biomacromolecules*, **5**, 1804–1809.

31 Stuart, M.A., Huck, W.T., Genzer, J., Müller, M., Ober, C., Stamm, M., Sukhorukov, G.B., Szleifer, I., Tsukruk, V.V., Urban, M., Winnik, F., Zauscher, S., Luzinov, I., and Minko, S. (2010) Emerging applications of stimuli-responsive polymer materials. *Nature Mater.*, **9**, 101–113.

32 Du, F.S., Wang, Y., Zhang, R., and Li, Z.C. (2010) Intelligent nucleic acid delivery systems based on stimuli-responsive polymers. *Soft Matter*, **6**, 835–848.

33 Asoh, T.A. and Akashi, M. (2009) Development of high-performance stimuli-responsive systems, in *Handbook of Hydrogels: Properties, Preparation & Applications (Chemical Engineering Methods and Technology Series)* (ed. D.B. Stein), Nova Science Publishers, Inc., Hauppauge, NY, pp. 633–648.

34 Li, M.H. and Keller, P. (2009) Stimuli-responsive polymer vesicles. *Soft Matter*, **5**, 927–937.

35 Xia, F., Zhu, Y., Feng, L., and Jiang, L. (2009) Smart responsive surfaces switching reversibly between super-hydrophobicity and super-hydrophilicity. *Soft Matter*, **5**, 275–281.

36 Cole, M.A., Voelcker, N.H., Thissen, H., and Griesser, H.J. (2009) Stimuli-responsive interfaces and systems for the control of protein-surface and cell-surface interactions. *Biomaterials*, **30**, 1827–1850.

37 Kloxin, M., Kloxin, C.J., Bowman, C.N., and Anseth, K.S. (2010) Mechanical properties of cellularly responsive hydrogels and their experimental determination. *Adv. Mater.*, **22**, 3484–3494.

38 Hirokawa, Y. and Tanaka, T.J. (1984) Volume phase transition in a non-ionic gel. *J. Chem. Phys.*, **81**, 6379–6380.

39 Akiyoshi, K., Kang, E.-C., Kurumada, S., Sunamoto, J., Principi, T., and Winnik, F.M. (2000) Controlled association of amphiphilic polymers in water: Thermosensitive nanoparticles formed by self-assembly of hydrophobically modified pullulans and poly(*N*-isopropylacrylamides). *Macromolecules*, **33**, 3244–3249.

40 Morimoto, N., Obeid, R., Yamane, S., Winnik, F.M., and Akiyoshi, K. (2009) Composite nanomaterials by self-assembly and controlled crystallization of poly(2-isopropyl-2-oxazoline)-grafted polysaccharides. *Soft Matter*, **5**, 1597–1600.

41 Morimoto, N., Qiu, X.P., Winnik, F.M., and Akiyoshi, K. (2008) Dual stimuli-responsive nanogels by self-assembly of polysaccharides lightly grafted with thiol-terminated poly(N-isopropylacrylamide) chains. *Macromolecules*, **41**, 5985–5987.

42 Sasaki, Y., Hirakura, T., Sawada, S., and Akiyoshi, K. (2011) Metal coordinative-crosslinked polysaccharide nanogels with redox sensitivity. *Chem. Lett.*, **40**, 182–183.

43 Katz, E. and Willner, I. (2004) Integrated nanoparticle–biomolecule hybrid systems: synthesis, properties, and applications. *Angew. Chem. Int. Ed.*, **43**, 6042–6108.

44 Parak, W.J., Gerion, D., Pellegrino, T., Zanchet, D., Micheel, C., Williams, S.C., Boudreau, R., Le Gros, M.A., Larabell, C.A., and Alivisatos, A.P. (2003) Biological applications of colloidal nanocrystals. *Nanotechnology*, **14**, R15.

45 Yamane, S., Sugawara, A., Sasaki, Y., and Akiyoshi, K. (2009) Nanogel–calcium phosphate hybrid nanoparticles with negative or positive charges for potential biomedical applications. *Bull. Chem. Soc. Jpn.*, **82**, 416–418.

46 Yamane, S., Sugawara, A., Watanabe, A., and Akiyoshi, K. (2009) Hybrid nanoapatite by polysaccharide nanogel-templated mineralization. *J. Bioact. Compat. Polym.*, **24**, 151–168.

47 Yamane, S., Sasaki, Y., and Akiyoshi, K. (2008) Siloxane-crosslinked polysaccharide nanogels for potential biomedical applications. *Chem. Lett.*, **37**, 1282–1283.

48 Shin, Y., Chang, J.H., Liu, J., Williford, R., Shin, Y., and Exarhos, G.J. (2001) Hybrid nanogels for sustainable positive

thermosensitive drug release. *J. Controlled Release*, **73**, 1–6.

49 Subr, V., Duncan, R., and Kopecek, J.J. (1990) Release of macromolecules and daunomycin from hydrophilic gels containing enzymatically degradable bonds. *J. Biomat. Sci. Polym. E*, **1**, 261–278.

50 Obaidat, A.A. and Park, K. (1996) Characterization of glucose dependent gel-sol phase transition of the polymeric glucose-concanavalin a hydrogel system. *Pharm. Res.*, **13**, 989–995.

51 Miyata, T., Asami, N., and Uragami, T. (1999) A reversibly antigen-responsive hydrogel. *Nature*, **399**, 766–769.

52 Nagahara, S. and Matsuda, T. (1996) Hydrogel formation via hybridization of oligonucleotides derivatized in water-soluble vinyl polymers. *Polym. Gels Networks*, **4**, 111–127.

53 Kopecek, J. (2007) Hydrogel biomaterials: a smart future? *Biomaterials*, **28**, 5185–5192.

54 Sasaki, Y., Tsuchido, Y., Sawada, S., and Akiyoshi, K. (2011) Construction of protein-crosslinked nanogels with vitamin B6 bearing polysaccharide. *Polym. Chem.*, **2**, 1267–1270.

55 Akiyoshi, K., Kobayashi, S., Shichibe, S., Mix, D., Baudys, M., Kim, S.W., and Sunamoto, J. (1998) Self-assembled hydrogel nanoparticle of cholesterol-bearing pullulan as a carrier of protein drugs: Complexation and stabilization of insulin. *J. Controlled Release*, **54**, 313–320.

56 Sawada, S. and Akiyoshi, K. (2010) Nano-encapsulation of lipase by self-assembled nanogels: induction of high enzyme activity and thermal stabilization. *Macromol. Biosci.*, **10**, 353–358.

57 Hartl, F.U. (1996) Molecular chaperones in cellular protein folding. *Nature*, **381**, 571–579.

58 Sasaki, Y. and Akiyoshi, K. (2010) Development of an artificial chaperone system based on cyclodextrin. *Curr. Pharm. Biotechnol.*, **11**, 300–305.

59 Akiyoshi, K., Sasaki, Y., and Sunamoto, J. (1999) Molecular chaperone-like activity of hydrogel nanoparticles of hydrophobized pullulan: Thermal stabilization with refolding of carbonic anhydrase B. *Bioconjug. Chem.*, **10**, 321–324.

60 Nomura, Y., Ikeda, M., Yamaguchi, N., Aoyama, Y., and Akiyoshi, K. (2003) Protein refolding assisted by self-assembled nanogels as novel artificial molecular chaperone. *FEBS Lett.*, **553**, 271–276.

61 Nomura, Y., Sasaki, Y., Takagi, M., Narita, T., Aoyama, Y., and Akiyoshi, K. (2005) Thermoresponsive controlled association of protein with a dynamic nanogel of hydrophobized polysaccharide and cyclodextrin: Heat shock protein-like activity of artificial molecular chaperone. *Biomacromolecules*, **6**, 447–452.

62 Sasaki, Y., Iida, D., Takahashi, H., Sawada, S., and Akiyoshi, K. (2011) Artificial chaperon polysaccharide nanogels for protein delivery: A physicochemical study of protein–nanogel interactions. *Curr. Drug Discov. Technol.*, **8**, 308–313.

63 Akiyoshi, K., Nishikawa, T., Mitsui, Y., Miyata, T., Kodama, M., and Sunamoto, J. (1996) Self-assembly of polymer amphiphiles: thermodynamics of complexation between bovine serum albumin and self-aggregate of cholesterol-bearing pullulan. *Colloid Surface A*, **112**, 91–95.

64 Akiyoshi, K., Sasaki, Y., Kuroda, K., and Sumanoto, J. (1998) Controlled association of hydrophobized polysaccharide by cyclodextrin. *Chem. Lett.*, **27**, 93–94.

65 Asayama, W., Sawada, S., Taguchi., H., and Akiyoshi, K. (2008) Comparison of refolding activities between nanogel artificial chaperone and GroEL systems. *Int. J. Biol. Macromol.*, **42**, 241–246.

66 Sawada, S., Nomura, Y., Aoyama, Y., and Akiyoshi, K. (2006) Heat shock protein-like activity of nanogel artificial chaperone for citrate synthase. *J. Bioact. Compat. Polym.*, **21**, 487–501.

67 Rozema, D. and Gellman, S.H. (1995) Artificial chaperones: protein refolding via sequential use of detergent and cyclodextrin. *J. Am. Chem. Soc.*, **117**, 2373–2374.

68 Asayama, W., Sawada, S., Taguchi, H., and Akiyoshi, K. (2008) Comparison of refolding activities between nanogel artificial chaperone and GroEL systems. *Int. J. Biol. Macromol.*, **42**, 241–246.

69 Ikeda, K., Okada, T., Sawada, S., Akiyoshi, K., and Matsuzaki, K. (2006) Inhibition of the formation of amyloid β-protein fibrils using biocompatible nanogels as artificial chaperones. *FEBS Lett.*, **580**, 6587–6595.

70 Boridy, S., Takahashi, H., Akiyoshi, K., and Maysinger, D. (2009) The binding of pullulan modified cholesteryl nanogels to Aβ oligomers and their suppression of cytotoxicity. *Biomaterials*, **30**, 5583–5591.

71 Sasaki, Y., Nomura, Y., Sawada, S., and Akiyoshi, K. (2010) Polysaccharide nanogel–cyclodextrin system as an artificial chaperone for in vitro protein synthesis of green fluorescent protein. *Polym. J.*, **42**, 823–828.

72 Sasaki, Y., Asayama, W., Niwa, T., Sawada, S.-I., Ueda, T., Taguchi, H., and Akiyoshi, K. (2011) Amphiphilic polysaccharide nanogels as artificial chaperones in cell-free protein synthesis. *Macromol. Biosci.*, **11**, 814–820.

73 Ayame, H., Morimoto, N., and Akiyoshi, K. (2008) Self-assembled cationic nanogels for intracellular protein delivery. *Bioconjug. Chem.*, **19**, 882–890.

74 Alles, N., Soysa, N.S., Mian, A.H., Tomomatsu, N., Saito, H., Baron, R., Morimoto, N., Aoki, K., Akiyoshi, K., and Ohya, K. (2009) Polysaccharide nanogel delivery of a TNF-alpha and RANKL antagonist peptide allows systemic prevention of bone loss. *Eur. J. Pharm. Sci.*, **37**, 83–88.

75 Ikuta, Y., Katayama, N., Wang, L., Okugawa, T., Takahashi, Y., Schmitt, M., Gu, X., Watanabe, M., Akiyoshi, K., Nakamura, H., Kuribayashi, K., Sunamoto, J., and Shiku, H. (2002) Presentation of a major histocompatibility complex class 1–binding peptide by monocyte-derived dendritic cells incorporating hydrophobized polysaccharide–truncated HER2 protein complex: implications for a polyvalent immunocell therapy. *Blood*, **99**, 3717–3724.

76 Gu, X.-G., Schmitt, M., Hiasa, A., Nagata, Y., Ikeda, H., Sasaki, Y., Akiyoshi, K., Sunamoto, J., Nakamura, H., Kuribayashi, K., and Shiku, H. (1998) A novel hydrophobized polysaccharide/oncoprotein complex vaccine induces in vitro and in vivo cellular and humoral immune responses against HER2-expressing murine sarcomas. *Cancer Res.*, **58**, 3385–3390.

77 Kageyama, S., Kitano, S., Hirayama, M., Nagata, Y., Imai, H., Shiraishi, T., Akiyoshi, K., Scott, A., Murphy, R., Hoffman, E., Old, L., Katayama, N., and Shiku, H. (2008) Humoral immune responses in patients vaccinated with 1-146 HER2 protein complexed with cholesteryl pullulan nanogel. *Cancer Sci.*, **99**, 601–607.

78 Shiku, H. (2004) Polyvalent cancer vaccines. *Exp. Med.*, **22**, 118–124.

79 Shimizu, T., Kishida, T., Hasegawa, U., Ueda, Y., Imanishi, J., Yamagishi, H., Akiyoshi, K., Otsuji, E., and Mazda, O. (2008) Nanogel DDS enables sustained release of a cytokine for tumor immunotherapy. *Biochem. Biophys. Res. Commun.*, **367**, 330–335.

80 Nochi, T., Yuki, Y., Takahashi, H., Sawada, S.I., Mejima, M., Kohda, T., Harada, N., Kong, I.G., Sato, A., Kataoka, N., Tokuhara, D., Kurokawa, S., Takahashi, Y., Tsukada, H., Kozaki, S., Akiyoshi, K., and Kiyono, H. (2010) Nanogel antigenic protein-delivery system for adjuvant-free intranasal vaccines. *Nat. Mater.*, **9**, 572–578.

81 Leader, B., Baca, Q.J., and Golan, D.E. (2008) Protein therapeutics: A summary and pharmacological. Classification. *Nat. Rev. Drug Discov.*, **7**, 21–39.

82 Zelphati, O., Wang, Y., Kitada, S., Reed, J.C., Felgner, P.L., and Corbeil, J. (2001) Intracellular delivery of proteins with a new lipid-mediated delivery system. *J. Biol. Chem.*, **276**, 35103–35110.

83 Dalkara, D., Zuber, G., and Behr, J.P. (2004) Intracytoplasmic delivery of anionic proteins. *Mol. Ther.*, **9**, 964–969.

84 Ravi Kumar, M.N. (2000) Nano and microparticles as controlled drug delivery devices. *J. Pharm. Pharm. Sci.*, **3**, 234–258.

85 Kwon, Y.J., Standley, S.M., Goh, S.L., and Frechet, M.J. (2005) Enhanced antigen presentation and immunostimulation of dendritic cells using acid-degradable cationic nanoparticles. *J. Controlled Release*, **105**, 199–212.

86 Futami, J., Kitazoe, M., Maeda, T., Nukui, E., Sakaguchi, M., Kosaka, J., Miyazaki, M., Kosaka, M., Tada, H., Seno, M., Sasaki, J., Huh, N.H., Namba, M., and Yamada, H. (2005) Intracellular delivery of proteins into mammalian living cells by polyethylenimine-cationization. *J. Biosci. Bioeng.*, **99**, 95–103.

87 Morris, M.C., Depollier, J., Mery, J., Heitz, F., and Divita, G. (2001) A peptide carrier for the delivery of biologically active proteins into mammalian cells. *Nat. Biotechnol.*, **19**, 1173–1176.

88 Hasegawa, U., Nomura, S.M., Kaul, S.C., Hirano, T., and Akiyoshi, K. (2005) Nanogel-quantum dot hybrid nanoparticles for live cell imaging. *Biochem. Biophys. Res. Commun.*, **331**, 917–921.

89 Toita, S., Hasegawa, U., Koga, H., Sekiya, I., Muneta, T., and Akiyoshi, K. (2008) Protein-conjugated quantum dots effectively delivered into living cells by a cationic nanogel. *J. Nanosci. Nanotechnol.*, **8**, 2279–2285.

90 Shimoda, A., Sawada, S.-I., and Akiyoshi, K. (2011) Cell specific peptide-conjugated polysaccharide nanogels for protein delivery. *Macromol. Biosci.*, **11**, 882–888.

91 Nguyen, D.N., Green, J.J., Chan, J.M., and Langer, R., and Anderson, D.G. (2009) Polymeric materials for gene delivery and DNA vaccination. *Adv. Mater.*, **21**, 847–867.

92 Azzam, T., Eliyahu, H., Makovitzki, A., Linial, M., and Domb, A.J. (2004) Hydrophobized dextran- spermine conjugate as potential vector for in vitro gene transfection. *J. Controlled Release*, **96**, 309–323.

93 Kanatani, I., Ikai, T., Okazaki, A., Jo, J., Yamamoto, M., Imamura, M., Kanematsu, A., Yamamoto, S., Ito, N., Ogawa, O., and Tabata, Y. (2006) Efficient gene transfer by pullulan-spermine occurs through both clathrin- and raft/caveolae-dependent mechanisms. *J. Controlled Release*, **116**, 75–82.

94 Toita, S., Morimoto, M., and Akiyoshi, K. (2010) Functional cycloamylose as a polysaccharide-based biomaterial: Application in a gene delivery system. *Bimacromolecule*, **11**, 397–401.

95 Huang, M., Fong, C.W., Khor, E., and Lim, L.Y. (2005) Transfection efficiency of chitosan vectors: effect of polymer molecular weight and degree of deacetylation. *J. Controlled Release*, **106**, 391–406.

96 Karinaga, R., Anada, T., Minari, J., Mizu, M., Koumoto, K., Fukuda, J., Nakazawa, K., Hasegawa, T., Numata, M., Shinkai, S., and Sakurai, K. (2006) Galactose-PEG dual conjugation of β-(1 → 3)-D-glucan schizophyllan for antisense oligonucleotide delivery to enhance cellular uptake. *Biomaterials*, **27**, 1626–1635.

97 Toita, S., Soma, Y., Morimoto, N., and Akiyoshi, K. (2009) Cycloamylose-based biomaterial: nanogel of cholesterol-bearing cationic cycloamylose for siRNA delivery. *Chem. Lett.*, **38** (11), 1114–1115.

98 Toita, S., Sawada, S., and Akiyoshi, K. (2011) Polysaccharide nanogel gene delivery system with endosome-escaping function: Co-delivery of plasmid DNA and phospholipase A2. *J. Controlled Release*, **155** (1), 54–59.

99 Kuroda, K., Fujimoto, K., Sunamoto, J. *et al.* (2002) Hierarchical self-assembly of hydrophobically modified pullulan in water: Gelation by networks of nanoparticles. *Langmuir*, **18**, 3780–3786.

100 Morimoto, N., Endo, T., Ohtomi, M. *et al.* (2005) Hybrid nanogels with physical and chemical cross-linking structures as nanocarriers. *Macromol. Biosci.*, **5**, 710–716.

101 Morimoto, N., Endo, T., Iwasaki, Y. *et al.* (2005) Design of hybrid hydrogels with self-assembled nanogels as cross-linkers: Interaction with proteins and chaperone-like activity. *Biomacromolecules*, **6**, 1829–1834.

102 Morimoto, N., Ohki, T., Kurita, K. *et al.* (2008) Thermo-responsive hydrogels with nanodomains: Rapid shrinking of a

nanogel-crosslinking hydrogel of poly(N-isopropyl acrylamide). *Macromol. Rapid Commun.*, **29**, 672–676.

103 Kato, N., Hasegawa, U., Morimoto, N. *et al.* (2007) Nanogel-based delivery system enhances PGE2 effects on bone formation. *J. Cell. Biochem.*, **101**, 1063–1070.

104 Hayashi, C., Hasegawa, U., Saita, Y. *et al.* (2009) Osteoblastic bone formation is induced by using nanogel-crosslinking hydrogel as novel scaffold for bone growth factor. *J. Cell Physiol.*, **220**, 1–7.

105 Hasegawa, U., Sawada, S., Shimizu, T. *et al.* (2009) Raspberry-like assembly of cross-linked nanogels for protein delivery. *J. Controlled Release*, **140**, 312–317.

9
Microgels and Biological Interactions

Michael H. Smith, Antoinette B. South, and L. Andrew Lyon

9.1
An Introduction to Polymer Biomaterials

Biomaterials have enabled profound contributions to medicine over the last several decades, from extracorporeal devices, such as contact lenses and kidney dialyzers, to implantable devices, including vascular grafts and pacemakers [1]. These materials are designed to interface with biological tissues and are capable of either augmenting, interacting with, or replacing natural functions in the body [1]. The diverse range of functionality of various biomaterials has led to the treatment of several diseases and has deeply impacted medicine as a whole.

As implantable devices, the impact of polymeric biomaterials has been especially significant in recent years. Some of the earliest applications of implantable polymers were developed by British ophthalmologist Harold Ridley. While observing wounds to the eyes of fighter pilots following World War II, Ridley noticed that imbedded shards of the Spitfire canopy (poly(methyl methacrylate)) had a tendency to heal without excessive inflammation and infection. These early observations led to the first intraocular device for the treatment of cataracts [2]. In present times, millions of these devices are used in the treatment of ocular disease each year.

The implementation of many other biomaterials also came in the post-war biomedicine boom. Like the implants inspired by the Spitfire canopy, these treatments typically used nonspecific, off-the-shelf components that were readily available. For example, the first artificial kidney employed in 1946 was inspired by the first hemodialysis machine invented by Dutch physician William Kolff. The Kolff machine employed cellulose acetate for dialysis tubing, a material commonly used at the time for sausage casing. Other significant medical devices also include commodity plastics in their design. Early vascular grafts used a common textile polymer known as Dacron, introduced in 1950 by DuPont. Although off-the-shelf materials were applied in these examples, the devices were effective in the treatment of medical problems. However, serious conflicts could also result from their use. Early dialysis tubing had an increased risk of platelet activation. Likewise, Dacron grafts were limited in their diameter and also increased the likelihood of clot

Hydrogel Micro and Nanoparticles, First Edition. Edited by L. Andrew Lyon and Michael Joseph Serpe.
© 2012 Wiley-VCH Verlag GmbH & Co. KGaA. Published 2012 by Wiley-VCH Verlag GmbH & Co. KGaA.

formation. These limitations have motivated the development of more specific materials that are safer and more efficient at the biological interface.

One of the principle limitations of early polymeric biomaterials was their lack of complete compatibility with living tissues, or biocompatibility. All biomaterials, whether implanted or injected, experience what is described as the "tissue response continuum" when administered to the body. This response occurs after injury, such as an incision, resulting in inflammatory and wound-healing responses, foreign body reactions, and fibrous encapsulation of the biomaterial, medical device, or prosthesis [3]. As safer and more effective biomaterials are developed for medical applications, their chemical, physical, and biological properties must be optimized to improve safety, biocompatible, and effectiveness in implementation. Hydrophilic polymers, specifically hydrogels, have great promise as biocompatible, responsive biomaterials.

9.1.1 Hydrogels

There are multiple reasons why hydrogels are a promising class of biomaterials for medical applications, including biological sensing, drug delivery, and tissue regeneration. These materials are generally very well-hydrated (absorbing up to 90–99% water by weight) and have an elastic structure [4]. This hydrated, or hydrophilic, property reduces the tendency for proteins to nonspecifically adsorb to the hydrogel, thus imparting "nonfouling" properties. The structure of a hydrogel is usually an elastic mesh, or network of polymers. The network is generally porous, where biological molecules and therapeutics can be incorporated or entrapped within. Through modification of the density of the network, the mechanical properties of the material can be changed to suit their application.

In addition, hydrogels may be designed to undergo a volume phase transition in response to an external stimulus such as temperature, light, small biomolecules, pH, electric field, or other triggers [5]. A volume phase transition is when the network transitions between a solvent swollen network and a hydrophobic collapsed state due to the presence of one of these triggers. As can be seen in Figure 9.1, in a collapsed or deswollen state, the polymer chain–chain interactions dominate and water is expelled

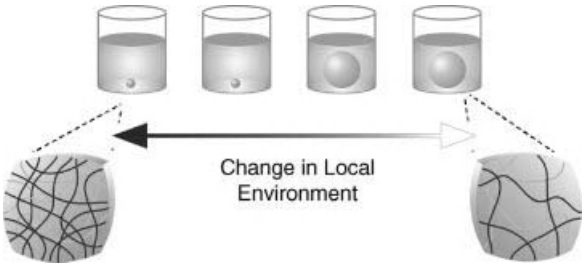

Figure 9.1 Schematic representing volume phase transition of responsive hydrogel materials.

from the network. In a swollen state the interactions between the solvent and the polymer chains dominate. In the case of hydrogels made of *N*-isopropylacrylamide (NIPAM), these materials undergo a transition with an increase in temperature from swollen in water to a deswollen state at approximately 31 °C. The temperature at which the transition occurs is known as the volume phase transition temperature (VPTT). The volume phase transition enables the material to be triggered to perform a particular function. For example, a hydrogel can be loaded with a drug and then upon the addition of heat will collapse and expel water along with the drug. The reverse mechanism can also be used to load hydrogel materials with small molecules; as the network reswells from a deswollen or dry state to a hydrated form it can pull drug from solution inside the network. Lastly, these polymeric networks can be easily chemically modified not only to add responsivity but also for attaching molecules such as peptides that can aid in properties such as tumor targeting or cellular attachment. Because hydrogels are tunable, responsive, and chemically versatile, they are a suitable platform in the design of many biomaterials where the properties of the polymer may be engineered to suit specific medical applications.

One method of classifying hydrogels is by their size. For example, macrogels are bulk gels whose dimensions are generally on the millimeter scale or larger. In contrast, hydrogels may be synthesized in a particulate form, where the dimensions of the resulting material are considerably smaller. This book chapter discusses the colloidal form of hydrogels, which are evenly distributed (or monodisperse) populations of particulates ranging in size from several micrometers down to tens of nanometers [6]. For the purposes of this chapter, the colloidal forms will be referred to as microgels or nanogels.

9.1.2 Hydrogels as Particles

There are two main approaches to materials fabrication; "top-down" manufacturing, where already existing materials are broken or milled down, while "bottom-up" fabrication utilizes the smallest components, or building blocks, to actually build a material in a desired fashion. Using a bottom-up approach has many advantages over a top-down approach, such as more control of the overall composition, size, morphology, and other desired properties of the final material. Microgels are an interesting building block because they are able to provide a spectrum of different functionalities, sizes (from nanometers to micrometers), morphologies, and responsivities. In terms of targeted drug delivery, a particulate form is necessary to effectively circulate the body. In addition, because these colloidal hydrogels can be modified, the particles can contain targeting moieties to more effectively guide them towards a particular region in the human body such as a tumor. Furthermore, nanogels can have incorporated molecules that elicit a certain response such as reduced or enhanced cellular or protein adhesion, or degradation of the particle. Lastly, the porous network is able to entrap molecules such as therapeutic drugs that can be released after the particle has been targeted towards a certain site or due to some triggering event. For thin films on surfaces, microgels of various nature can be

mixed to create a "mosaic interface" [7] on a surface. This mixture adds complexity to the interface which is needed to understand and manipulate the biological environment.

9.1.3 Hydrogel Particle Synthesis

There are a variety of ways in which microgels can be synthesized. The particular method chosen stems from the preferred characteristics needed in the final microgel. An important characteristic of microgels is their softness or porosity, which can be controlled by the amount of polymer or crosslinker that is incorporated in each particle during synthesis. Another critical attribute of microgels is their size, which is dictated by the synthetic environment during polymerization. Various different monomers can be copolymerized within a microgel to further give the particle functionality and the added capacity for chemoligation. Furthermore, the placement of different functional groups can be controlled by constructing a core–shell [8] type structure where different groups can be located within the interior or periphery of the particle. Interesting particle structures have been synthesized using the core–shell construct, such as biofunctionalized microgels [9, 10] and hollow nanocapsules [11].

Currently, the most widely used monomer for making microgels is NIPAM, which also renders microgels thermoresponsive. These microgels are commonly synthesized by free radical precipitation polymerization, otherwise known as surfactant-free emulsion polymerization. Philip Chibante was the first to demonstrate PNIPAM synthesis using this technique in 1978 [12, 13]. This process typically involves an aqueous mixture of monomers and one or more crosslinkers that has been purged free of oxygen. The solution is then heated to a temperature well above the VPTT of NIPAM (typically 70 °C). A free-radical initiator is then added to the solution, activating at the high temperature, which creates oligoradical species from the monomers that are in solution. The oligoradicals reach a critical chain length at which point the polymer chain is entropically driven to phase separate from the solvated state to a collapsed state where the polymer–polymer interactions dominate. The high temperature ensures that the chain collapses once it has reached its critical length. The collapsed oligoradical is termed a precursor particle that acts as a nucleating site for further growth of the microgel. The precursor particle aggregates with other precursor particles, existing particles, growing oligoradicals, or by addition of more monomer (see Figure 9.2) [14].

Surfactant, initiator, and temperature have been found to control the overall size of these microgels [15, 16]. A two-step free-radical polymerization process is used to synthesize a core–shell type hydrogel particle [8]. After fabrication of the core, the solution is then heated well above the VPTT once again with additional monomer. When initiator is added, the growing oligoradicals form once again and collapse. Because these oligoradicals are hydrophobic, they tend to aggregate with the collapsed core particles in solution, and thus contribute to the formation of a shell.

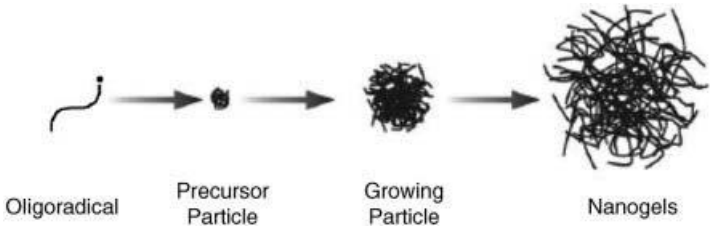

Figure 9.2 Precipitation polymerization of colloidal micro or nanogels from phase-separating polymers Taken from [14].

Hydrogel particles can also be synthesized using the self-assembly of block copolymers. Block copolymers typically have a hydrophobic and a hydrophilic end that allows them to self-assemble into spherical micelles depending on the concentration of polymer and type of solvent used. Micelles are typically unstable, but they can be crosslinked to form stable nanoparticles. The Wooley group has developed a class of crosslinked block copolymers known as shell crosslinked knedels (SCK), the first of which was made from a polystyrene and poly(4-vinylpyridine) block copolymer [17]. A number of additional synthesis approaches have been employed. The reader is directed to the contributions of Akiyoshi (Chapter 8), Ballauff (Chapter 2), and Matyjaszewski (Chapter 7) for alternate approaches to hydrogel colloids.

In the remainder of this chapter we discuss the study of colloidal hydrogels as biomaterials that come in contact with the biological environment. More specifically, we discuss the use of hydrogel particles as effective drug-delivery vehicles to target malignant tumors, as well as building blocks for biocompatible thin films for implantable devices.

9.2 Drug Delivery

The field of polymeric drug delivery has shown remarkable progress in recent years. The use of nanocarriers to specifically deliver drugs to cells is a revolutionary idea, and an exciting technology that may improve disease treatments of the future. Through the selective targeting of nanocarriers to malignant sites, drugs may be localized for the release of toxic or more potent therapeutics. This added specificity generally decreases the overall systemic dose needed for many therapeutics, while decreasing nonspecific damage that may otherwise occur elsewhere in the body. Additional treatment specificity can result from time or degradation-controlled release. The management of release properties may reduce unwanted side effects from circulation and the fluctuation of drug concentrations in the body. This chapter addresses the targeted delivery of a promising class of drug-delivery vehicles, the hydrogel nanoparticle (nanogel). Through selective targeting of nanogels to malignant cells, these carriers may increase the effectiveness of therapeutics, impart greater patient compliance, and improve the quality of life for many who suffer from disease.

9.2.1
Nanoparticles and the Mononuclear Phagocytic System

The intravenous administration of targeted nanocarriers is an attractive option for the treatment of cancer, where particles in circulation will reach malignant sites regardless of their location in the animal (e.g., metastatic tumors). However, the ability of a nanogel to effectively target and deliver its cargo depends on whether it can circulate long enough to reach its therapeutic site of action. Specifically, the dimensions of the polymeric material have a significant impact on blood circulation time and the overall bioavailability [18–24]. For example, materials below approximately 50 000 Daltons can be cleared through the kidney [25]. This mass correlates to a particle size of roughly 5–10 nm, resulting in rapid removal through organ extravasation and renal clearance. Particles above this regime are more likely cleared through an immune response, or the mononuclear phagocytic system (MPS) (also known as the reticuloendothelial system) [23].

The MPS is one of the largest biological barriers for virtually all long-circulating nanoparticles in development. This process involves monocytes and macrophages, which are primarily assembled in MPS-related organs like the spleen, liver, and lymph tissue. The primary function of these cells is in the recognition of foreign materials, in circulation. Nanoparticles are affected by the MPS almost immediately upon intravenous injection, where serum proteins begin interacting with the surface of the nanocarrier [26]. When a nanoparticle encounters blood serum proteins (opsonins), there is a tendency for the protein to stick to the particle through various attractive forces (including van der Waals, electrostatic, ionic, and hydrophobic) [25]. This process is known as opsonization, which makes the nanoparticles much more visible to phagocytic macrophages. In addition, integrin receptors on macrophages bind a variety of extracellular matrix (ECM) components and blood proteins (fibronectin, vitronectin) or immunoglobulin G (IgG) and IgM antibodies [27]. Finally, ligand–receptor complexation may be mediated by the presence of active cytokines and growth factors. Clearly this is a biologically complex process, in which the specific relationship between the physicochemical properties of the polymers, opsonins, macrophages, inflammatory cytokines, and growth factors is not fully understood [28].

In general, there are two types of mononuclear phagocytes responsible for MPS clearance: circulating monocytes of peripheral blood and fixed, non-circulating tissue macrophages found throughout the body. These non-circulating cells include Kupffer cells of the liver, histocytes in multiple tissues, and phagocytes of the spleen [29]. Once associated with opsonins, macrophages may engulf the foreign material by phagocytosis, resulting in enzyme secretion along with other oxidative-reactive chemical factors to break down the phagocytosed material.

9.2.2
Nanoparticle Size and Surface Modification for Enhanced Delivery

It is evident that particle size is an important factor in the biodistribution of the material. As previously described, materials with a hydrodynamic diameter less than

5 nm (or 50 000 Da, conservatively), will be removed from the body by the renal system. Particles with diameters significantly larger (~200 nm) demonstrate longer circulation times, with clearance occurring through spleen sequestration and mechanical filtration, and will eventually be removed by MPS [20, 24]. Particles in the range of 10–70 nm have been considered ideal for long circulation since they are large enough to penetrate smaller capillaries in various body tissues and typically have longer circulation times than similar materials of larger dimensions [19, 24, 30]. If we consider the fact that particles smaller than 100 nm may be enclosed within endocytic vesicles [31], it becomes clear that particles within the size range from 10 to 100 nm may be ideal for circulation, accumulation at sites of interest, and may participate in endocytosis at the tumor site.

The physical and chemical properties of the nanoparticle surface play an important role in protein adsorption. Extensive efforts have been made to elucidate the mechanism by which opsonins adhere to polymers, and techniques to minimize or slow the opsonization process. As described previously, opsonins adhere to nanoparticles through interactions of varying strengths [25]. The importance of the hydrophilic/hydrophobic nature of the particles has been observed; proteins seem to have a higher binding affinity for more hydrophobic surfaces [32, 33]. In addition, ionic character on the nanoparticle surface may dramatically affect opsonization. For example, Tabata *et al*. have demonstrated the role of nanoparticle surface charge density on the rate of phagocytosis *in vitro*. Phagocytosis is enhanced as the absolute value of zeta potential increases for both negative and positively charged surfaces on the delivery vehicle [34]. In consideration of nanogel circulation, the physicochemical properties of the particle must be considered if opsonin adhesion is to be reduced.

A common method used to slow opsonization is to graft certain polymers to the surface of the nanoparticle, shielding electrostatic and hydrophobic interactions. Multiple species of long hydrophilic polymer chains and non-ionic surfactants have been employed with varying success, including polysaccharides, polyacrylamide, poly(vinyl alcohol), poly(*N*-vinyl-2-pyrrolidone), and poly(ethylene glycol) (PEG) [25]. These polymers have a high hydrophilicity, are very flexible, and may be capable of shielding hydrophobic and charged particles from blood proteins. Of the multitude of polymers investigated for shielding properties, the most commonly employed and effective material is PEG and PEG-containing copolymers. PEG is an uncharged, hydrophilic, and non-immunogenic material that can be grafted, copolymerized, or adsorbed in the synthesis of polymeric materials [35, 36]. The incorporation of PEG may lead to an enhancement in biocompatibility and enhanced stabilization of colloid materials. The properties that PEG may impart on the nanomaterials is largely dependent on the molecular weight, density, conformation, and flexibility of the chains [37, 38]. As can be seen in Figure 9.3, the density of PEG on the periphery of a particle contributes to its conformation.

There have been several theories proposed to explain the mechanism of protein resistance and the described "stealth" effect caused by PEG incorporation. For example, the hydrophilic and flexible nature of the PEG chains allows them to take on an extended conformation in solution. As proteins interact with the surface of the particle they encounter extended surface PEG chains and attempt to compress them

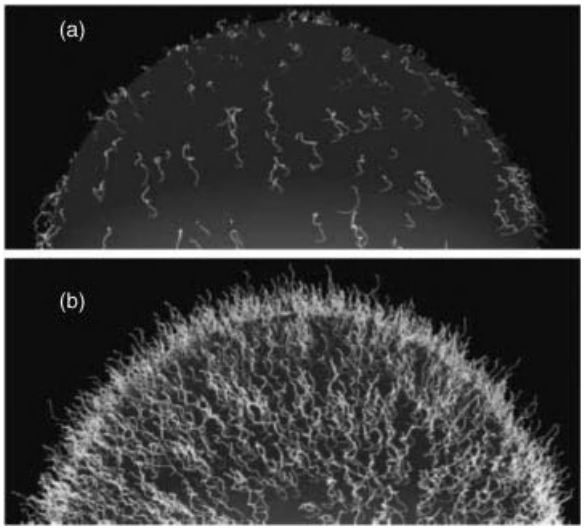

Figure 9.3 Schematic of PEG brushes on the periphery of a nanoparticle. Low coverage (a) leads to a "mushroom" topography, whereas high coverage (b) contributes to a "brush" configuration of PEG Taken from [25].

into the particle. The PEG chains are being forced into a higher energy, compressed conformation which causes an opposing repulsive force that effectively blocks or repulses the incoming protein [37, 38]. If the thickness of the PEG coating is sufficient, opsonization may be hindered *in vivo*.

9.2.3 Nanogel Cellular Targeting

Intravenously injected particles are commonly targeted to tumors through the enhanced permeability and retention effect (EPR) [15, 16, 18, 61]. Through EPR, the size of nanoparticles may allow their passage through characteristically leaky vasculature around tumor sites [39], and pores between endothelial cells may allow the extravasation of nanoparticles introduced systemically. Localization may be significantly enhanced by incorporation of targeting moieties on the surface of the carrier (e.g., peptides, aptamers, antibodies/antibody fragments, small molecules). Malignant cells may specifically recognize these ligands and imbibe the nanoparticle by receptor-mediated endocytosis. This section describes these targeting strategies, and methods to enhance localization and decreased accumulation in healthy tissues.

9.2.3.1 Passive Targeting: The Enhanced Permeability and Retention Effect

As cancerous cells replicate at a high rate, vascular tissue must also form rapidly to provide nutrients for the cancerous region. This process is known as angiogenesis, and is critical for the development of tumor mass. Before neovascularization, endothelial cells are barely dividing since only about 1 in 10 000 cells undergo

cellular division at any given time [40]. As angiogenesis occurs, the rate of endothelial cell division increases enormously (about 50-fold) [41]. During this process, endothelial cell growth will require the reorganization of the ECM, and cell growth will migrate toward the source of angiostimulatory molecules (e.g., tumor cells). For healthy cells, the growth of vasculature is self-limited through the production and release of angioinhibitory molecules. The regulated growth of healthy tissue results in a well-constructed tubular network of endothelium with very small pores between cells (~2 nm) [42]. However, this equilibrium between stimulatory and inhibitory molecules may be disrupted for tumors. The accelerated rate of growth of vasculature at tumors facilitates carcinogenesis, but also results in tissues that are physically very different from healthy cells.

Tumor vasculature [43] is characteristically highly permeable or "leaky", with pores ranging in size from 200 nm to 1.2 μm [44]. In addition, lymphatic drainage from the interstitial tissues within the tumor is commonly hindered [45]. This leaky nature of cancer was observed in the late 1980s by Maeda *et al.*, who noted that biocompatible macromolecules had a tendency to accumulate at higher concentrations at tumor sites than in healthy tissues [46, 47]. In their mechanistic explanation of the phenomenon, Maeda coined the term "enhanced permeability and retention effect" (EPR) [45, 47–49]. As a result, polymer drug carriers were designed to exploit EPR to selectively deposit at cancer sites. For example, particles of appropriate size and biocompatibility may circulate for extensive periods of time and deposit through leaky pores in neovasculature. As shown in Figure 9.4, accumulation is additionally promoted by poor lymphatic drainage from the region of tumor cells.

The result of the EPR effect is a possible outlet for passively targeting nanoparticle drug carriers to tumor sites. Through this targeting, the overall systemic dose needed for many therapeutics may be lowered. However, improved therapeutic efficacy and reduced toxicity may be achieved by targeting specific cell surface interactions. This is typically done through the surface conjugation of targeting ligands.

9.2.3.2 **Active Targeting: Nanoparticle Bioconjugation**

In addition to the vasculature environment, the surface of cancer cells is often unique and can be exploited by drug-delivery vehicles for more effective targeting. Solid tumors characteristically overexpress specific antigens or receptors on their surface, including epidermal growth factor (EGF) [50], TRAIL receptor [51], folate receptor [52], and others [53, 54]. By functionalizing the surface of nanoparticles with targeting molecules such as antibodies, peptides, or aptamers, the receptor-mediated uptake pathways of cancer cells may be exploited [55–59].

Folate Folic acid (or vitamin B9) plays an important role in the biosynthesis of nucleotide bases and is consumed rapidly during cellular proliferation. In general there are two mechanisms by which cells obtain folate, either through the folate carrier or by action of the folate receptor. While the folate carrier is present in virtually all cells and is the primary pathway for folate uptake, the folate receptor is typically on polarized epithelial cells and activated macrophages [60]. This receptor is responsible for preferentially binding and internalizing oxidized folates by receptor-mediated

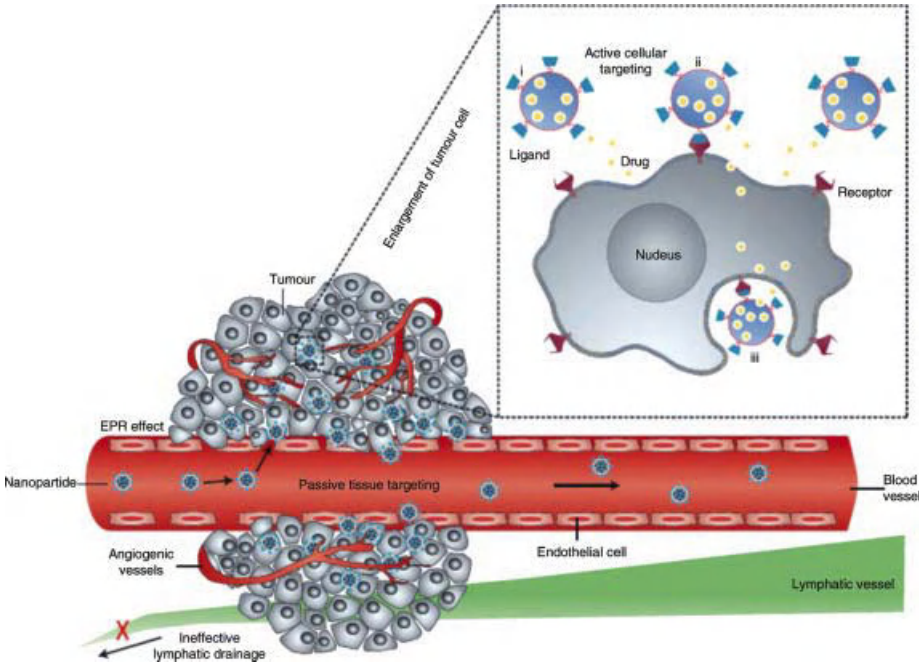

Figure 9.4 Schematic illustration of combined passive targeting (via EPR) and active targeting within tumor tissues Taken from [42].

endocytosis. Cancer cells frequently overexpress this receptor, which may enable diseased cells to compete for folate when scarce [61]. Folate is an attractive targeting molecule for several reasons, including its specificity to cancer cells, high binding affinity ($K_D \sim 10^{-10}$ M), small size, stability in storage, low cost, and availability [60, 62].

There are several examples of the targeting of macromolecules and nanoparticles utilizing folate bioconjugation [60, 63, 64]. For example, by decorating the surface of temperature-responsive PNIPAM-based nanogels with folate, uptake was readily observed *in vitro* in the presence cancer cells that overexpress the folate receptor (Figure 9.5) [64]. In this case, the targeting molecule was covalently tethered to the amines of the shell of a core–shell nanogel construct. Furthermore, these particles exhibited thermal cytotoxicity when at elevated temperatures (above their VPTT) [64]. Another example includes the folate nanogels recently developed by Vinogradov *et al.*, which also demonstrated the efficiency of folate targeting *in vitro* [65]. Transcellular transport of their folate-conjugated drug carrier was found to be four times more effective than using the drug alone in their cellular model system.

Galactose Like folate, galactose-based targeting of nanoparticles may be a promising route for active cell targeting, specifically for malignant tissues localized in the liver [66, 67]. This sugar has a specific binding affinity to asialoglycoprotein receptors in the HepG2 human hepatoblastoma cell line. By conjugating galactose to the

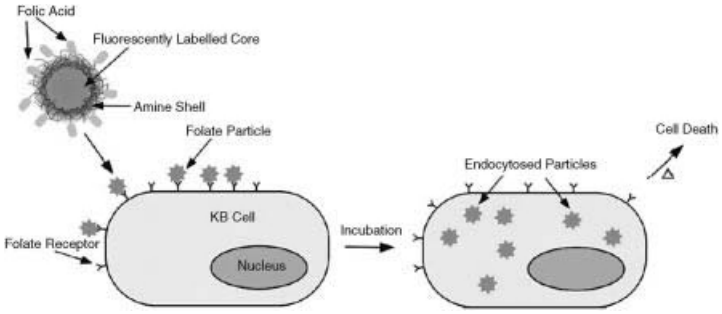

Figure 9.5 Folate-mediated cellular targeting of PNIPAM microgels Taken from [64].

surface of PNIPAM-*co*-AA nanogels, Choi *et al*. showed a drastic increase in uptake by receptor-mediated endocytosis into blastoma cells [68]. Because of particle temperature responsivity, this group also investigated the temperature-dependent uptake of their nanoparticles. The uptake efficiency was found to increase at elevated temperatures, which may be a result of particle deswelling above the VPTT of the polymer [68].

Transferrin Oligonucleotides have been attractive diagnostic and therapeutic agents for a variety of diseases, including cancer, neurodegenerative disorders, and lethal viral infections [69–72]. Unfortunately, oligonucleotides are highly unstable *in vivo*, with a high susceptibility to rapid clearance by renal excretion and enzymatic degradation. These therapeutics have also been limited in their application to the central nervous system because the blood–brain barrier (BBB) greatly restricts their passage. The use of small (∼100 nm) nanoparticles as carriers of oligonucleotide therapeutics may be a plausible option since they are injectable and may reach brain microvascular endothelial cells (BMVECs). Through conjugation of nanogels (nano-PEG-cross-PEI) bioconjugated with insulin and transferrin molecules, Vinagradov *et al*. demonstrated the efficient delivery of oligonucleotides across a model BBB [73]. Through incorporation of PEG, circulation times of nanogels was increased, resulting in an increased exposure to the BBB. Although the BBB is impermeable to macromolecules, it has been suggested that nanoparticles at this size scale may participate in receptor-mediated transcytosis in BBB without violating the integrity of the tight junctions of the BMVECs [73].

Peptides Small peptides (6–20 amino acids) are powerful targeting molecules when conjugated to nanoparticle drug carriers. Their ease of synthesis, well-defined and efficient chemical reactions for linkage to nanoparticle surfaces, and decreased likelihood of generating a harmful immune response make them an attractive alternative to some other targeting moieties [59, 74–76]. Certain peptides may mimic surface receptor ligands, allowing for direct targeting of nanoparticles to cells expressing the receptor target. This bioconjugation could promote the receptor–ligand-mediated endocytosis of nanoparticles and enable a pathway for uptake by target cells.

There are several examples of efficient targeting through peptide bioconjugation. Recently, Wolf *et al*. demonstrated the delivery of small interfering RNA molecules (siRNA) to tumor-bearing mice through the bioconjugation of RGD (Arg-Gly-Asp) to PEG–PEI nanoparticles [77]. In another example, Becker *et al*. bioconjugated the protein transduction domain (PTD) from the HIV-1 Tat protein to their polymer micelle drug-delivery vehicles [78, 79]. The bioconjugation employed in both examples increased the efficiency of cell penetration for the nanoparticles.

9.2.4
Degradation and Release of Encapsulated Cargo

In general, the release of therapeutics from the internal cavity of a nanogel may be influenced by either diffusion of drug through the gel or degradation of the encapsulating polymer network. This is of great interest in producing responsive microgels that selectively release therapeutics under specific cellular conditions. Through degradation of nanogels, the programmed release of encapsulated materials upon cellular uptake may be observed.

9.2.4.1 Release by Reduction

In consideration of biodegradable nanogels, materials that are responsive selectively to intracellular conditions may be of particular interest. For example, the efficient cellular uptake of heparin nanogels has been demonstrated, where a reductive intracellular environment may cause the release of heparin and apoptotic cell death [80].

These nanogels were nanocomplexes composed of thiolated heparin and PEG. When placed in organic solvent (DMSO), ultrasonication allows the formation of intermolecular disulfide bonds between the thiolated heparin. Through this method, stable heparin nanogels with an average size of ~250 nm were produced. However, when these particles are placed in reductive conditions, such as the intracellular cytosol, intermolecular disulfide bonds are destabilized and cause the release of heparin from the nanovector [80]. These nanoparticles have demonstrated excellent apoptotic activity *in vitro*, and may serve as promising materials to reduce cellular proliferation at malignant sites (Figure 9.6).

9.2.4.2 Release by pH Changes

Through the incorporation of acid-labile crosslinkers, nanogels may be synthesized which decompose under acidic conditions. An investigation of particular interest involved the polymerization of poly(hydroxyethlmethacrylate) (pHEMA), which is a hydrophilic and biocompatible polymer that has been used in several biomedical applications [81–84]. Monodisperse microgels in diameters ranging from 150 to 475 nm were produced through the inverse emulsion polymerization of pHEMA with various crosslinkers [85]. The hydrodynamic diameter and overall swelling of the particles were tuned through crosslinker concentration during synthesis. Under neutral pH conditions the particle retained a spherical morphology, but completely disintegrated after incubating at pH 5.5 overnight [85]. The destruction of microgels

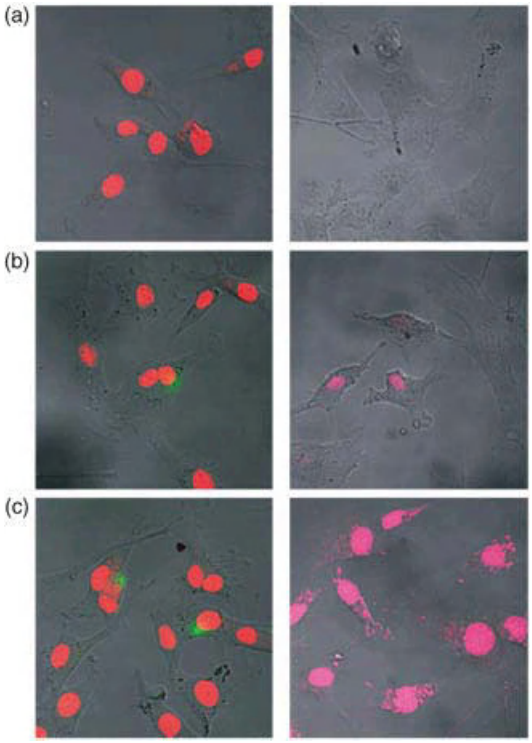

Figure 9.6 Confocal microscopy images of mouse melanoma cells untreated (a), incubated with heparin (b), and incubated with heparin nanogels (c). Nuclei are stained red, heparin is labeled green, while activation of caspases is labeled pink which signals apoptosis Taken from [80].

is attributed to hydrolysis of acetal bonds in the polymer network, where the half-life of degradation could be controlled for from 30 min to several hours depending on the nature of crosslinker used. Rhodamine B-labeled dextran was loaded into microgels and the release of these materials from the gel network was controlled by the pH of the environment, similar to the particle degradation [85]. These particles may be of interest for pH-controlled release of macromolecular therapeutics.

9.3 Biomaterial Films

The interface between the biological environment and a synthetic material has been of great interest for many years, and has been of importance for improving the state of medical implants. Implanted materials can serve as prosthesis, drug-delivery agents, or for sensing important molecules or signals throughout the body. It is estimated that currently one out of every ten Americans has some sort of medically implanted device. Whereas medical implants have come quite a long way over time due to

significant advancements in this arena, little still is understood as to what exactly occurs at the biological and material interface. Furthermore, most implants need to be replaced over time due to acute inflammation or chronic scar tissue formation; a problem that has yet to be solved effectively.

Medical implants have been in use for the last 2000 years. Some of the first materials to be used for implants were metals, which would corrode over time and therefore had to be replaced. Particular metals that could resist corrosion, such as stainless steel, aluminum, chromium and titanium alloys, and platinum then followed as materials for medical implants. For implants made from synthetic polymeric materials, polyesters and nylons were replaced by polymers that resisted degradation, such as poly(methyl methacylate) (PMMA), poly(ethylene), silicones, or polytetrafluoroethylene (PTFE) [86]. These materials do not produce any adverse affects to patients, nor do they degrade in the human body. Even though these materials are in use today, there is still a need for reducing and controlling the inflammatory response that occurs when any foreign material is implanted into a mammalian body.

9.3.1 The Foreign Body Response

A large portion of current biomedical research involving biological interfaces has focused on controlling protein or cellular adhesion to the surface of a biomaterial. Similar to the issue of the MPS to particles that circulate through the human body (as described in Section 9.2.1), implanted biomaterials experience a natural foreign body response [2] which is activated during inflammation and the wound-healing process when a foreign material is identified. As can be seen in Figure 9.7, this response first involves nonspecific protein adsorption, or biofouling, to the surface of the biomaterial within an hour. The adhered proteins provide a scaffold upon which white blood cells, which are present in high numbers during the wound-healing process, can attach and proliferate through mechanotransduction on the surface. Cells adhere, grow, and spread over the span of a few days. Eventually, after about a week has passed, the cells fuse together into a foreign giant body cell and these cells release small molecules called cytokines that initiate the wound-healing response. Over several weeks, a collagen capsule forms around the biomaterial that segregates the material from the rest of the body.

As one could imagine, a device such as an implanted glucose sensor would give false readings and need to be constantly recalibrated due to quick protein adhesion. A drug-eluting material would be rendered useless because it would become sealed off from the rest of the body due to the formation of a collagen capsule. The host's response to foreign materials decreases the lifetime and functioning of implanted materials.

Attempts at controlling inflammation and promoting wound healing has been aimed at taking what knowledge we have about the biological response to a foreign material and using that knowledge to modify the surface of biomaterials. It is evident that modification of the surface chemistry of a material impacts cellular adhesion

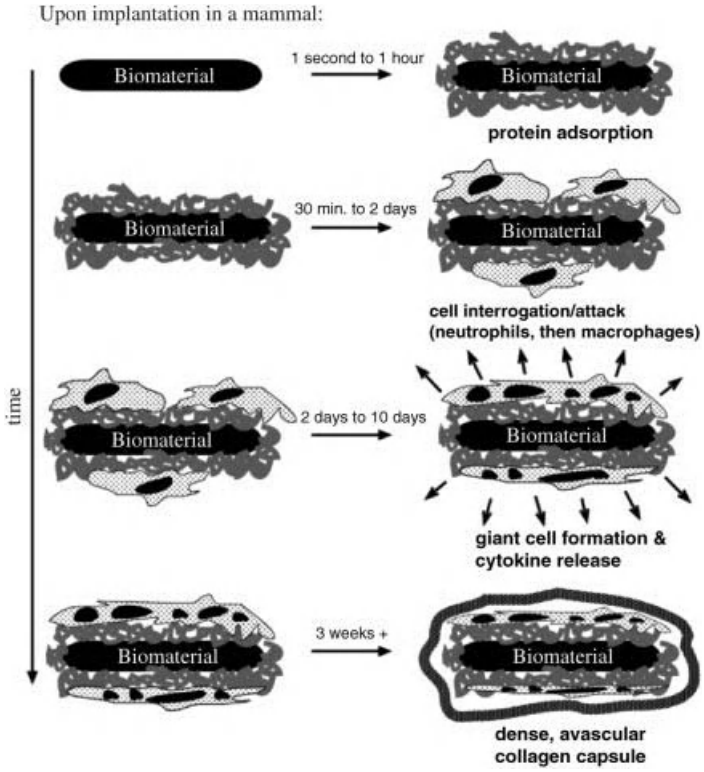

Figure 9.7 Host response to a foreign biomaterial Taken from [2].

in vitro [87]. However, unfortunately what is observed *in vitro* does not necessarily correlate to what occurs *in vivo* [88–90]. Therefore, approaches have become geared more towards controlling the first step of the host's response to foreign materials: protein adsorption, because it is ultimately proteins to which cells adhere. These surfaces are called "nonfouling" surfaces, and once nonspecific protein adsorption is under control, these materials can then be further built upon to contain proteins or peptides that can mitigate wanted cellular adhesion.

9.3.2
Hydrogels as a Biomaterial Interface

As mentioned above, hydrogels are an ideal construct for biomaterials because they are a water-swollen three-dimensional network and therefore conducive to a biological environment. Because of the wide range of materials that can be incorporated into a hydrogel, they can be finely tuned for various applications. Being able to finely tune a material is becoming increasingly more important as more knowledge is obtained about how cells interact with foreign interfaces. Hydrogel films may be modified to ultimately gain control over the foreign body response by exhibiting

nonfouling properties for protein adhesion along with further conjugation to promote controlled cellular adhesion as a tissue scaffold. Hydrogel materials can also serve as sensors or drug-releasing networks in addition to controlling protein and cellular adhesion. The versatility and responsiveness of hydrogel materials enables them to dynamically interact with biological environments.

There is a major advantage to using hydrogels in a particle form in place of a bulk gel for coating implants. A collection of many different kinds of microgels can be deposited on a surface to create mosaic multifunctional interfaces [7]. Such an interface that utilizes a bottom-up approach cannot be easily accomplished by bulk gels. In addition, colloids diffuse freely through solution and therefore can be deposited on a surface using simple techniques such as dip-coating or spin-coating. Microgel films can also be constructed in either crystalline ordered arrays [91–93] or in random assemblies such as a layer-by-layer approach [94], which allows for more complexity in these films.

9.3.3
Antifouling Surfaces

As described above, one of the first steps towards gaining control over a host's response to implanted biomaterials is preventing nonspecific protein adhesion. Proteins typically adhere better to hydrophobic surfaces than neutral hydrophilic ones, and therefore many efforts have focused on making the surface of biomaterials more hydrophilic. Surface modifications dictated by already existing biological components, such as phospholipids [95] and saccharides [96], have also been shown to resist biofouling. George Whitesides and coauthors surveyed chemically modified surfaces for their potential to reduce protein adhesion [97]. Using self-assembled monolayers of various terminally modified alkanes, four main characteristics were found to maximize antifouling behavior: (i) polar functional groups, (ii) hydrogen bond-accepting groups, (iii) a lack of hydrogen bond-donating groups, and (iv) charge neutrality. Whereas these discoveries are an important step for controlling protein adhesions *in vitro*, the proclaimed nonfouling surfaces need to show effective protein adhesion resistance *in vivo* as well.

One of the most accepted molecules used for the control of protein adhesion, which consequentially controls cellular adhesion, is PEG, alternatively known as poly (ethylene oxide) (PEO), which was also described previously (see Section 9.2.2). PEG is widely known to resist protein adhesion due to its highly hydrophilic and entropic nature. It is also biocompatible, nontoxic, nonimmunogenetic, and nondegradable. PEG is readily available and can be incorporated easily into various materials. Self-assembled monolayers of oligo(ethylene oxide) have been shown to dramatically decrease protein adhesion [98–100]. There has also been extensive work performed by Horbett and coworkers in using radiofrequency plasma deposition of tetraethyleneglycol dimethyl ether (tetraglyme) to modify a surface [101, 102]. These modified surfaces showed significant reduction in the adhesion of fibrinogen, albumin, and IgG, with concentrations found to be as low as $2\,\mathrm{ng\,cm^{-2}}$. However, when this promising material was plasma deposited on a fluorinated ethylene propylene (FEP)

copolymer surface and implanted into mice, a fibrous capsule had formed around all the implants after four weeks [103]. The capsule thickness was also no different from uncoated FEP. This illustrates the important point that promising protein resistance *in vitro* does not necessarily correlate to the outcome one would expect to observe *in vivo*.

While research is still ongoing on the use of PEG for protein resistance, work has also been involved in incorporating this important molecule into hydrogel films to serve as antifouling biomaterial interfaces [104–106]. PEG hydrogels have been used to prevent surgical adhesions at a wound site [107], to prevent protein and cellular adhesion to silicone rubber [108], and even as a network to house quantum dots for sensing in biological environments [109].

Gan and Lyon synthesized nanogels grafted with PEG, and demonstrated their ability to resist a common protein known as bovine serum albumin (BSA) [110]. In this work, PEG was also grafted onto the periphery of the nanogel using a core–shell construct (see Section 9.1.3), which further decreased BSA adhesion. Microgels have also been fabricated using PEG as a crosslinker [111]. An increase in PEG chain crosslinker length within the microgels resulted in a decrease in protein adsorption. Furthermore, these particles were spin-coated onto a glass substrate and a reduction in cell adhesion was observed.

Work was later conducted to permanently attach PEG-containing microgels to a model biomaterial, poly(ethylene terphthalate) (PET) (Figure 9.8) [112]. Antifouling microgels on PETs were studied both *in vitro* and *in vivo* as coatings for reducing protein and cellular adhesion [113]. These particles significantly reduced *in vitro* fibrinogen protein adsorption and also reduced primary human macrophage adhesion and spreading. The nonfouling microgel coatings also reduced leukocyte adhesion and expression of proinflammatory cytokines *in vivo*. Recently, Scott *et al*. has synthesized a macrogelation of star PEG polymers and albumin microgels to coat glass and PET substrates [114]. These materials also exhibited reduced protein and cellular adhesions.

9.3.4
Cellular Adhesion

Whereas PEG has been used successfully to generate implantable biomaterials that have a "stealth" surface, there is also interest in biomaterials that can be incorporated and integrated within the human body as opposed to being invisible. This can be accomplished by modulating the inflammatory response and controlling which cells ultimately adhere to the surface. Hydrogel films have been used to gain control over cellular adhesion in several ways. The thermoresponsivity of a hydrogel film has been utilized to create a reversible cell substrate [115]. At a physiological temperature of 37 °C, cells adhere to the hydrophobic collapsed film. When the incubation temperature is dropped below the lower critical solution temperature of the film, the cells experience a hydrophilic or swollen surface and consequently detach because cells do not adhere effectively to hydrophilic surfaces. Biologically relevant molecules can be attached to the hydrogel network, such as cellular adhesion moieties [116–119],

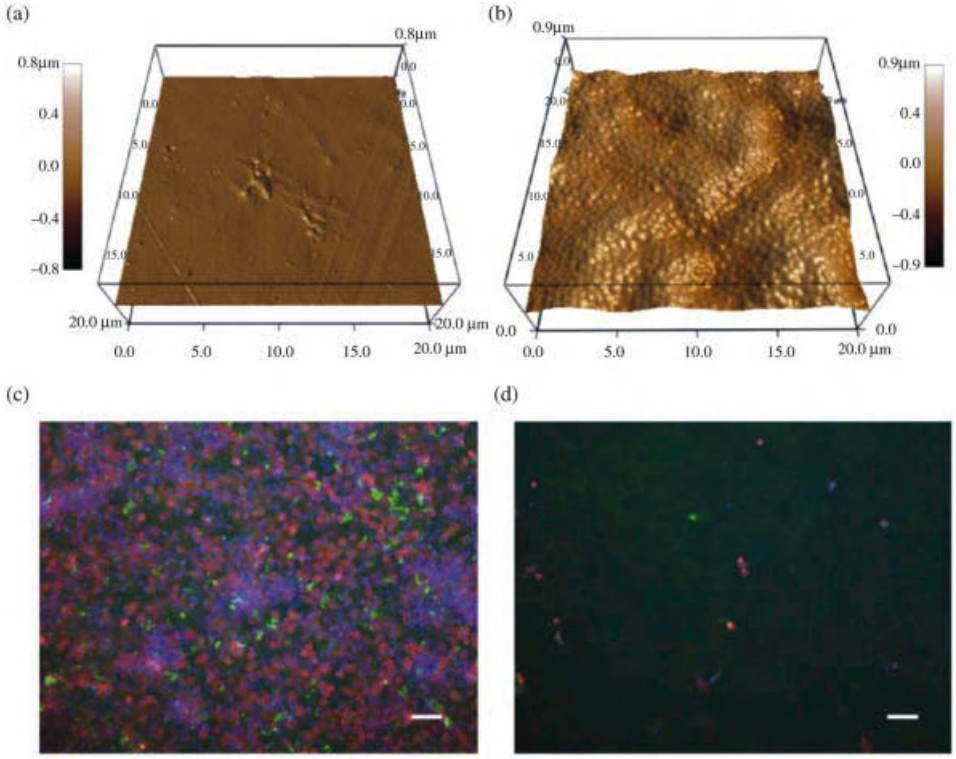

Figure 9.8 Atomic force microscopy of uncoated PET (a) and PEG-microgel coated PET (b). Immunostain showing *in vivo* leukocyte adhesion on uncoated PET (c) and PEG-microgel coated PET (d). A macrophage marker is shown in green, actin as red, and DNA as blue Taken from [112].

growth factors [106, 120], and ECM molecules [120–123]. One peptide adhesion sequence that is well known is RGD (arginine, glycine, aspartic acid) [124]. RGD is a sequence found in the ECM protein fibronectin. Cells adhere to RGD by integrin receptors, thus allowing them to attach to a surface and proliferate. Cells are also very sensitive to the conformation of this protein. Various ECM proteins have been covalently attached to a hydrogel to serve as a network for which cells can adhere, such as to repair broken bone [125]. Cellular adhesion and spreading can also be controlled by altering the topography of the film, which has been demonstrated by inducing a phase separation of microgels on the surface [126]. Dawson and coauthors used a depleting agent to induce attractions between particles (Figure 9.9). They then could observe how cells interact with surfaces that have a well-defined morphology.

Control over cellular adhesion gives one the tools to integrate biomaterials within the human body, bring the cells closer to the biomaterial surface to elicit a response, or build interesting morphologies and cellular architectures. Little has been demonstrated in using microgels that have these types of molecules attached as building blocks for interfaces. Nonetheless, there is a need for an interface that can be

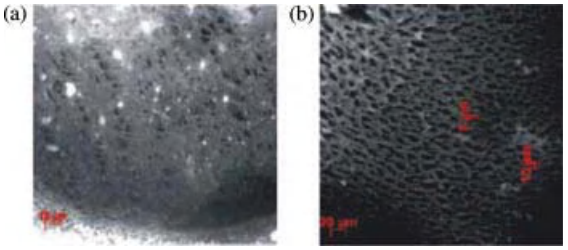

Figure 9.9 Microgel phase separation before (a) and after (b) depleting agent is added Taken from [126].

constructed using functionalized microgels so as to create a dynamic and versatile assembly. This type of assembly is conducive to adding more control and functionality to a biomaterial's surface.

9.3.5
Drug Release

Once the protein and cellular adhesion is under control, there is interest in also providing function to the implant coating. Hydrogel films can been used to encapsulate and release drugs, such as heparin for thromboresistance [127], or endothelial growth factors and inflammatory-reducing agents [128]. One important aspect of hydrogels is their ability to respond to an environment by swelling or deswelling. One early demonstration of this concept was by Peppas and coauthors in fabricating a glucose-responsive hydrogel [129]. A pH-responsive hydrogel was synthesized that had acidic side groups along with immobilized glucose oxidase. When there were high concentrations of glucose, glucose reacted with oxygen, which is catalyzed by glucose oxidase, and consequently gluconic acid was produced. The production of acid lowers the pH and the side chains within the hydrogel are neutralized and the network deswells. This reaction can expel small molecules, like insulin, into the outside biological environment. There is growing interest in using the stimulus-responsive nature of hydrogels films to induce the release of biopharmaceuticals [130].

Microgels have also been used for releasing drugs such as doxorubicin [131]. Doxorubicin is a potent anticancer therapeutic drug which induces apoptosis when taken up by tumor cells. In this work by Lyon and coauthors, polyelectrolyte multilayers of negatively charged thermoresponsive PNIPAM microgels were constructed using poly(allylamine) hydrochloric acid (PAH) as a cationic "glue."

As shown in Figure 9.10, with a change in temperature, the microgels swell and "breathe in" doxorubicin. In reverse, the microgels deswell with an increase in temperature and therefore expel the loaded drug. Other examples of using drug-loaded microgel films for drug delivery has been demonstrated using insulin [132] and antibacterial drugs [133]. As mentioned in Section 9.2.4, microgels can release molecules of interest over time as they degrade on a surface. However, while there

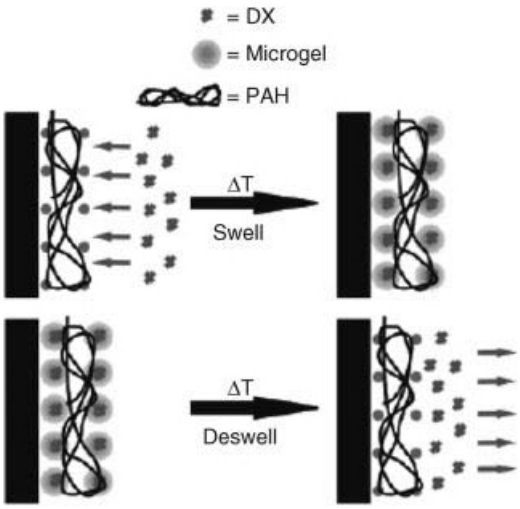

Figure 9.10 Schematic representation of the deswelling/swelling properties of a microgel multilayer thin film which enabled loading of doxorubicin (DX) Taken from [131].

have been extensive studies relating to the degradation of hydrogel films, little has been directly investigated about the degradation of microgel films on a surface.

9.4 Conclusion

Interest in polymeric biomaterials has been growing in importance for medicine in recent years because we are learning more and more about how our bodies react to these materials. Hydrogel materials can form nearly ideal materials for interactions with a biological environment. As described above, hydrogels are soft three-dimensional networks consisting mostly of water when swollen in an aqueous environment, and they also can be made to respond to many different stimuli. More importantly, they have the ability to be fine-tuned for various applications, which is imperative for both the manipulation and understanding of the interaction between the cellular milieu and a foreign material. Hydrogels can be synthesized in a particle form, known as a microgel or nanogel, which is more conducive for circulating in the human body and creating more complex colloidal films on the surface of an implant.

Upon reading this chapter, it should be apparent what parameters are needed to design a biomaterial that will meet particular needs. Because of this knowledge, we can construct the ideal hydrogel particle to obtain that goal. We can then use these particles, or microgels, as building blocks in a bottom-up approach towards constructing materials. Microgels can be fabricated and modified post-synthesis to aid with effective cellular targeting and drug delivery. In addition, microgels can be used to construct

interfaces that can minimize and control protein fouling, cellular attachment, and acute and chronic inflammatory responses to a medically implanted device. As our detailed understanding of how to design functionalized particles for predictable biological interactions improves, we can expect to produce truly functional and integrative biomaterials to address the enormous number of applications in which synthetic materials can positively impact and heal a damaged biological entity.

References

1 Langer, R. and Peppas, N.A. (2003) Advances in biomaterials, drug delivery, and bionanotechnology. *AIChE J.*, **49** (12), 2990–3006.

2 Ratner, B.D. and Bryant, S.J. (2004) Biomaterials: Where we have been and where we are going. *Annu. Rev. Biomed. Eng.*, **6**, 41–75.

3 Anderson, J.M. (2001) Biological responses to materials. *Annu. Rev. Mater. Res.*, **31**, 81–110.

4 Peppas, N.A., Hilt, J.Z., Khademhosseini, A., and Langer, R. (2006) Hydrogels in biology and medicine: From molecular principles to bionanotechnology. *Adv. Mater.*, **18** (11), 1345–1360.

5 Ulijn, R.V., Bibi, N., Jayawarna, V., Thornton, P.D., Todd, S.J., Mart, R.J., Smith, A.M., and Gough, J.E. (2007) Bioresponsive hydrogels. *Mater. Today*, **10** (4), 40–48.

6 Oh, J.K., Drumright, R., Siegwart, D.J., and Matyjaszewski, K. (2008) The development of microgels/nanogels for drug delivery applications. *Prog. Polym. Sci.*, **33** (4), 448–477.

7 Sorrell, C.D. and Lyon, L.A. (2008) Deformation controlled assembly of binary microgel thin films. *Langmuir*, **24** (14), 7216–7222.

8 Jones, C.D. and Lyon, L.A. (2000) Synthesis and characterization of multiresponsive core-shell microgels. *Macromolecules*, **33** (22), 8301–8306.

9 Nayak, S. and Lyon, L.A. (2004) Ligand-functionalized core/shell microgels with permselective shells. *Angew. Chem. Int. Ed.*, **43** (48), 6706–6709.

10 Gan, D. and Lyon, L.A. (2006) Amphiphilic, peptide-modified core/shell microgels. *Prog. Colloid Polym. Sci.*, **133** 1–8.

11 Nayak, S., Gan, D., Serpe, M.J., and Lyon, L.A. (2005) Hollow thermoresponsive microgels. *Small*, **1** (4), 416–421.

12 Pelton, R. (2000) Temperature-sensitive aqueous microgels. *Adv. Colloid Interface Sci.*, **85** (1), 1–33.

13 Pelton, R.H. and Chibante, P. (1986) Preparation of aqueous latexes with N-isopropylacrylamide. *Colloids Surf.*, **20** (3), 247–256.

14 Nayak, S. and Lyon, L.A. (2005) Soft nanotechnology with soft nanoparticles. *Angew. Chem. Int. Ed.*, **44** (47), 7686–7708.

15 Blackburn, W.H. and Lyon, L.A. (2008) Size-controlled synthesis of monodisperse core/shell nanogels. *Colloid Polym. Sci.*, **286** (5), 563–569.

16 Meng, Z., Smith, M.H., and Lyon, L.A. (2009) Temperature-programmed synthesis of micron-sized multi-responsive microgels. *Colloid Polym. Sci.*, **287** (3), 277–285.

17 Thurmond, K.B. II, Kowalewski, T., and Wooley, K.L. (1996) Water-soluble knedel-like structures: The preparation of shell-cross-linked small particles. *J. Am. Chem. Soc.*, **118** (30), 7239–7240.

18 Wichterle, O. and Lim, D. (1960) Hydrophilic gels for biological use. *Nature*, **185** (4706), 117–118.

19 Hawley, A.E., Davis, S.S., and Illum, L. (1995) Targeting of colloids to lymph-nodes - influence of lymphatic physiology and colloidal characteristics. *Adv. Drug Delivery Rev.*, **17** (1), 129–148.

20 Schiffelers, R.M., Bakker-Woudenberg, I., Snijders, S.V., and Storm, G. (1999)

Localization of sterically stabilized liposomes in *Klebsiella pneumoniae*-infected rat lung tissue: Influence of liposome characteristics. *Biochim. Biophys. Acta, Biomembr.*, **1421** (2), 329–339.

21 Ishida, O., Maruyama, K., Sasaki, K., and Iwatsuru, M. (1999) Size-dependent extravasation and interstitial localization of polyethyleneglycol liposomes in solid tumor-bearing mice. *Int. J. Pharm.*, **190** (1), 49–56.

22 Kong, G., Braun, R.D., and Dewhirst, M.W. (2000) Hyperthermia enables tumor-specific nanoparticle delivery: Effect of particle size. *Cancer Res.*, **60** (16), 4440–4445.

23 Alexis, F., Pridgen, E., Molnar, L.K.,and Farokhzad, O.C. (2008) Factors affecting the clearance and biodistribution of polymeric nanoparticles. *Mol. Pharm.*, **5** (4) 505–515.

24 Stolnik, S., Illum, L., and Davis, S.S. (1995) Long circulating microparticulate drug carriers. *Adv. Drug Delivery Rev.*, **16** (2–3), 195–214.

25 Owens, D.E. and Peppas, N.A. (2006) Opsonization, biodistribution, and pharmacokinetics of polymeric nanoparticles. *Int. J. Pharm.*, **307** (1), 93–102.

26 Gref, R., Minamitake, Y., Peracchia, M.T., Trubetskoy, V., Torchilin, V., and Langer, R. (1994) Biodegradable long-circulating polymeric nanospheres. *Science*, **263** (5153), 1600–1603.

27 Ward, P.A. (1997) Recruitment of inflammatory cells into lung: Roles of cytokines, adhesion molecules, and complement. *J. Lab. Clin. Med.*, **129** (4) 400–404.

28 Kao, W.Y.J. (1999) Evaluation of protein-modulated macrophage behavior on biomaterials: Designing biomimetic materials for cellular engineering. *Biomaterials*, **20** (23–24), 2213–2221.

29 Prokop, A. and Davidson, J.M. (2008) Nanovehicular intracellular delivery systems. *J. Pharm. Sci.*, **97** (9), 3518–3590.

30 Moghimi, S.M., Hedeman, H., Muir, I.S., Illum, L., and Davis, S.S. (1993) An investigation of the filtration capacity and the fate of large filtered sterically-stabilized microspheres in rat spleen. *Biochim. Biophys. Acta*, **1157** (3), 233–240.

31 Ogawara, K., Yoshida, M., Furumoto, K., Takakura, Y., Hashida, M., Higaki, K., and Kimura, T. (1999) Uptake by hepatocytes and biliary excretion of intravenously administered polystyrene microspheres in rats. *J. Drug Target.*, **7** (3), 213–221.

32 Muller, R.H., Wallis, K.H., Troster, S.D., and Kreuter, J. (1992) In vitro characterization of poly(Methyl-Methacrylate) nanoparticles and correlation to their in vivo fate. *J. Controlled Release*, **20** (3), 237–246.

33 Lynch, I. and Dawson, K.A. (2008) Protein-nanoparticle interactions. *Nano Today*, **3** (1–2), 40–47.

34 Tabata, Y. and Ikada, Y. (1988) Effect of the size and surface-charge of polymer microspheres on their phagocytosis by macrophage. *Biomaterials*, **9** (4), 356–362.

35 Gref, R., Domb, A., Quellec, P., Blunk, T., Muller, R.H., Verbavatz, J.M., and Langer, R. (1995) The controlled intravenous delivery of drugs using peg-coated sterically stabilized nanospheres. *Adv. Drug Delivery Rev.*, **16** (2–3), 215–233.

36 Otsuka, H., Nagasaki, Y., and Kataoka, K. (2003) Pegylated nanoparticles for biological and pharmaceutical applications. *Adv. Drug Delivery Rev.*, **55** (3), 403–419.

37 Jeon, S.I., Lee, J.H., Andrade, J.D., and Degennes, P.G. (1991) Protein surface interactions in the presence of polyethylene oxide. 1. Simplified theory. *J. Colloid Interface Sci.*, **142** (1), 149–158.

38 Jeon, S.I. and Andrade, J.D. (1991) Protein surface interactions in the presence of polyethylene oxide. 2. Effect of protein size. *J. Colloid Interface Sci.*, **142** (1), 159–166.

39 Monsky, W.L., Fukumura, D., Gohongi, T., Ancukiewcz, M., Weich, H.A., Torchilin, V.P., Yuan, F., and Jain, R.K. (1999) Augmentation of transvascular transport of macromolecules and nanoparticles in tumors using vascular endothelial growth factor. *Cancer Res.*, **59** (16), 4129–4135.

40 Hobson, B. and Denekamp, J. (1984) Endothelial proliferation in tumors and

normal-tissues – continuous labeling studies. *Br. J. Cancer*, **49** (4), 405–413.
41 Fox, S.B., Gatter, K.C., Bicknell, R., Going, J.J., Stanton, P., Cooke, T.G., and Harris, A.L. (1993) Relationship of endothelial-cell proliferation to tumor vascularity in human breast cancer. *Cancer Res.*, **53** (18), 4161–4163.
42 Maeda, H. (2001) The enhanced permeability and retention (Epr) effect in tumor vasculature: The key role of tumor-selective macromolecular drug targeting. *Adv. Enzyme Regul.*, **41**, 189–207.
43 Peer, D., Karp, J.M., Hong, S., Farokhzad, O.C., Margalit, R., and Langer, R. (2007) Nanocarriers as an emerging platform for cancer therapy. *Nat. Nanotechnol.*, **2** (12), 751–760.
44 Hobbs, S.K., Monsky, W.L., Yuan, F., Roberts, W.G., Griffith, L., Torchilin, V.P., and Jain, R.K. (1998) Regulation of transport pathways in tumor vessels: Role of tumor type and microenvironment. *Proc. Natl. Acad. Sci. U.S.A.*, **95** (8), 4607–4612.
45 Maeda, H. (2001) The enhanced permeability and retention (Epr) effect in tumor vasculature: The key role of tumor-selective macromolecular drug targeting. *J. Controlled Release*, **41**, 189–207.
46 Maeda, H. and Matsumura, Y. (1989) Tumoritropic and lymphotropic principles of macromolecular drugs. *Crit. Rev. Ther. Drug Carrier Syst.*, **6** (3), 193–210.
47 Matsumura, Y. and Maeda, H. (1986) A new concept for macromolecular therapeutics in cancer-chemotherapy – mechanisms of tumoritropic accumulation of proteins and the antitumor agent smancs. *Cancer Res.*, **46** (12), 6387–6392.
48 Maeda, H., Seymour, L.W., and Miyamoto, Y. (1992) Conjugates of anticancer agents and polymers – advantages of macromolecular therapeutics in vivo. *Bioconjugate Chem.*, **3** (5), 351–362.
49 Maeda, H., Wu, J., Sawa, T., Matsumura, Y.,and Hori, K. (2000) Tumor vascular permeability and the EPR effect in macromolecular therapeutics: A review. *J. Controlled Release*, **65** (1–2) 271–284.
50 Chaidarun, S.S., Eggo, M.C., Sheppard, M.C., and Stewart, P.M. (1994) Expression of epidermal growth-factor (EGF), its receptor, and related oncoprotein (Erbb-2) in human pituitary-tumors and response to EGF in-vitro. *Endocrinology*, **135** (5), 2012–2021.
51 Daniels, R.A., Turley, H., Kimberley, F.C., Liu, X.S., Mongkolsapaya, J., Ch'en, P., Xu, X.N., Jin, B.Q., Pezzella, F., and Screaton, G.R. (2005) Expression of trail and trail receptors in normal and malignant tissues. *Cell Res.*, **15** (6), 430–438.
52 Parker, N., Turk, M.J., Westrick, E., Lewis, J.D., Low, P.S., and Leamon, C.P. (2005) Folate receptor expression in carcinomas and normal tissues determined by a quantitative radioligand binding assay. *Anal. Biochem.*, **338** (2), 284–293.
53 Scholler, N., Fu, N., Yang, Y., Ye, Z.M., Goodman, G.E., Hellstrom, K.E., and Hellstrom, I. (1999) Soluble member(s) of the mesothelin/megakaryocyte potentiating factor family are detectable in sera from patients with ovarian carcinoma. *Proc. Natl. Acad. Sci. U.S.A.*, **96** (20), 11531–11536.
54 Bezwoda, W.R. (2000) C-Erb-B-2 expression and response to treatment in metastatic breast cancer. *Med. Oncol.*, **17** (1), 22–28.
55 Ryan, J.A., Overton, K.W., Speight, M.E., Oldenburg, C.M., Loo, L., Robarge, W., Franzen, S., and Feldheim, D.L. (2007) Cellular uptake of gold nanoparticles passivated with BSA-Sv40 large T antigen conjugates. *Anal. Chem.*, **79**, 9150–9159.
56 Vasir, J.K. and Labhasetwar, V. (2005) Targeted drug delivery in cancer therapy. *Technol. Cancer Res. Treat.*, **4** (4), 363–374.
57 Lee, R.J. and Low, P.S. (1994) Delivery of liposomes into cultured KB cells via folate receptor-mediated endocytosis. *J. Biol. Chem.*, **269** (5), 3198–3204.
58 Farokhzad, O.C., Cheng, J., Teply, B.A., Sherifi, I., Jon, S., Kantoff, P.W., Richie, J.P., and Langer, R. (2006) Targeted nanoparticle-aptamer bioconjugates for cancer chemotherapy in vivo. *Proc. Natl. Acad. Sci. U.S.A.*, **103** (16), 6315–6320.

59 Saad, M., Garbuzenko, O.B., Ber, E., Chandna, P., Khandare, J.J., Pozharov, V.P., and Minko, T. (2008) Receptor targeted polymers, dendrimers, liposomes: Which nanocarrier is the most efficient for tumor-specific treatment and imaging? *J. Controlled Release*, **130** (2), 107–114.

60 Lu, Y.J. and Low, P.S. (2002) Folate-mediated delivery of macromolecular anticancer therapeutic agents. *Adv. Drug Delivery. Rev.*, **54** (5), 675–693.

61 Toffoli, G., Cernigoi, C., Russo, A., Gallo, A., Bagnoli, M., and Boiocchi, M. (1997) Overexpression of folate binding protein in ovarian cancers. *Int. J. Cancer*, **74** (2), 193–198.

62 Reddy, J.A. and Low, P.S. (1998) Folate-mediated targeting of therapeutic and imaging agents to cancers. *Crit. Rev. Ther. Drug Carrier Syst.*, **15** (6), 587–627.

63 Kukowska-Latallo, J.F., Candido, K.A., Cao, Z.Y., Nigavekar, S.S., Majoros, I.J., Thomas, T.P., Balogh, L.P., Khan, M.K., and Baker, J.R. (2005) Nanoparticle targeting of anticancer drug improves therapeutic response in animal model of human epithelial cancer. *Cancer Res.*, **65** (12), 5317–5324.

64 Nayak, S., Lee, H., Chmielewski, J., and Lyon, L.A. (2004) Folate-mediated cell targeting and cytotoxicity using thermoresponsive microgels. *J. Am. Chem. Soc.*, **126** (33), 10258–10259.

65 Vinogradov, S.V., Zeman, A.D., Batrakova, E.V., and Kabanov, A.V. (2005) Polyplex nanogel formulations for drug delivery of cytotoxic nucleoside analogs. *J. Controlled Release*, **107** (1), 143–157.

66 Aarnoudse, C.A., Vallejo, J.J.G., Saeland, E., and van Kooyk, Y. (2006) Recognition of tumor glycans by antigen-presenting cells. *Curr. Opin. Immunol.*, **18** (1), 105–111.

67 Wu, J., Nantz, M.H., and Zern, M.A. (2002) Targeting hepatocytes for drug and gene delivery: Emerging novel approaches and applications. *Front. Biosci.*, **7**, D717–D725.

68 Choi, S.H., Yoon, J.J., and Park, T.G. (2002) Galactosylated poly(N-isopropylacrylamide) hydrogel submicrometer particles for specific cellular uptake within hepatocytes. *J. Colloid Interface Sci.*, **251** (1), 57–63.

69 Boado, R.J., Tsukamoto, H.,and Pardridge, W.M. (1998) Drug delivery of antisense molecules to the brain for treatment of Alzheimer's disease and cerebral aids. *J. Pharm. Sci.*, **87** (11) 1308–1315.

70 Seidman, S., Eckstein, F., Grifman, M., and Soreq, H. (1999) Antisense technologies have a future fighting neurodegenerative diseases. *Antisense Nucleic Acid Drug Dev.*, **9** (4), 333–340.

71 Stein, C.A. and Cheng, Y.C. (1993) Antisense oligonucleotides as therapeutic agents - is the bullet really magical. *Science*, **261** (5124), 1004–1012.

72 Wagner, R.W. and Flanagan, W.M. (1997) Antisense technology and prospects for therapy of viral infections and cancer. *Mol. Med. Today*, **3** (1), 31–38.

73 Vinogradov, S.V., Batrakova, E.V., and Kabanov, A.V. (2004) Nanogels for oligonucleotide delivery to the brain. *Bioconjugate Chem.*, **15** (1), 50–60.

74 Mok, H. and Park, T.G. (2008) Self-crosslinked and reducible fusogenic peptides for intracellular delivery of siRNA. *Biopolymers*, **89** (10), 881–888.

75 Kim, S., Jeong, J.H., Lee, S.H., Kim, S., and Park, T.G. (2008) Lhrh receptor-mediated delivery of siRNA using polyelectrolyte complex micelles self-assembled from sirna-peg-lhrh conjugate and pei. *Bioconjugate Chem.*, **19**, 2156–2162.

76 Jeong, J.H., Mok, H., Oh, Y.K., and Park, T.G. (2009) SiRNA conjugate delivery systems. *Bioconjugate Chem.*, **20** (1), 5–14.

77 de Wolf, H.K., Snel, C.J., Verbaan, F.J., Schiffelers, R.M., Hennink, W.E., and Storm, G. (2007) Effect of cationic carriers on the pharmacokinetics and tumor localization of nucleic acids after intravenous administration. *Int. J. Pharm.*, **331** (2), 167–175.

78 Becker, M.L., Remsen, E.E., Pan, D., and Wooley, K.L. (2004) Peptide-derivatized shell-cross-linked nanoparticles. 1. Synthesis and characterization. *Bioconjugate Chem.*, **15** (4), 699–709.

79 Becker, M.L., Bailey, L.O., and Wooley, K.L. (2004) Peptide-derivatized

shell-cross-linked nanoparticles. 2. Biocompatibility evaluation. *Bioconjugate Chem.*, **15** (4), 710–717.

80 Bae, K.H., Mok, H., and Park, T.G. (2008) Synthesis, characterization, and intracellular delivery of reducible heparin nanogels for apoptotic cell death. *Biomaterials*, **29** (23), 3376–3383.

81 Xu, F.J., Kang, E.T., and Neoh, K.G. (2006) Ph- and temperature-responsive hydrogels from crosslinked triblock copolymers prepared via consecutive atom transfer radical polymerizations. *Biomaterials*, **27** (14), 2787–2797.

82 Babensee, J.E. and Sefton, M.V. (2000) Viability of hema-mma microencapsulated model hepatoma cells in rats and the host response. *Tissue Eng.*, **6** (2), 165–182.

83 Abraham, S., Brahim, S., Ishihara, K., and Guiseppi-Elie, A. (2005) Molecularly engineered P(HEMA)-based hydrogels for implant biochip biocompatibility. *Biomaterials*, **26** (23), 4767–4778.

84 Xu, F.J., Zhong, S.P., Yung, L.Y.L., Tong, Y.W., Kang, E.T., and Neoh, K.G. (2005) Collagen-coupled poly(2-hydroxyethyl methacrylate)-Si(111) hybrid surfaces for cell immobilization. *Tissue Eng.*, **11** (11–12), 1736–1748.

85 Bulmus, V., Chan, Y., Nguyen, Q., and Tran, H.L. (2007) Synthesis and characterization of degradable P(HEMA) microgels: Use of acid-labile crosslinkers. *Macromol. Biosci*, **7** (4), 446–455.

86 Williams, D.F. (2008) On the mechanisms of biocompatibility. *Biomaterials*, **29** (20), 2941–2953.

87 Collier, T.O. and Anderson, J.M. (2002) Protein and surface effects on monocyte and macrophage adhesion, maturation, and survival. *J. Biomed. Mater. Res.*, **60** (3), 487–496.

88 Behling, C.A. and Spector, M. (1986) Quantitative characterization of cells at the interface of long-term implants of selected polymers. *J. Biomed. Mater. Res.*, **20** (5), 653–666.

89 Johansson, C.B., Albrektsson, T., Ericson, L.E., and Thomsen, P. (1992) A quantitative comparison of the cell response to commercially pure titanium and Ti-6al-4v implants in the abdominal wall of rats. *J. Mater. Sci. Mater. Med.*, **3** (2), 126–136.

90 Piglowski, J., Gancarz, I., Staniszewska-Kus, J., Paluch, D., Szymonowicz, M., and Konieczny, A. (1994) Influence of plasma modification on biological properties of poly(ethylene terephthalate). *Biomaterials*, **15** (11), 909–916.

91 Hellweg, T., Dewhurst, C.D., Bruckner, E., Kratz, K., and Eimer, W. (2000) Colloidal crystals made of poly(*N*-isopropylacrylamide) microgel particles. *Colloid Polym. Sci.*, **278** (10), 972–978.

92 Lyon, L.A., Debord, J.D., Debord, S.B., Jones, C.D., McGrath, J.G., and Serpe, M.J. (2004) Microgel colloidal crystals. *J. Phys. Chem. B*, **108** (50), 19099–19108.

93 Zhou, J., Wang, G., Marquez, M., and Hu, Z. (2009) The formation of crystalline hydrogel films by self-crosslinking microgels. *Soft Matter*, **5** (4), 820–826.

94 Serpe, M.J., Jones, C.D., and Lyon, L.A. (2003) Layer-by-layer deposition of thermoresponsive microgel thin films. *Langmuir*, **19** (21), 8759–8764.

95 Ishihara, K., Ziats, N.P., Tierney, B.P., Nakabayashi, N., and Anderson, J.M. (1991) Protein adsorption from human plasma is reduced on phospholipid polymers. *J. Biomed. Mater. Res.*, **25** (11), 1397–1407.

96 Holland, N.B., Qiu, Y., Ruegsegger, M., and Marchant, R.E. (1998) Biomimetic engineering of non-adhesive glycocalyx-like surfaces using oligosaccharide surfactant polymers. *Nature*, **392** (6678), 799–801.

97 Chapman, R.G., Ostuni, E., Takayama, S., Holmlin, R.E., Yan, L., and Whitesides, G.M. (2000) Surveying for surfaces that resist the adsorption of proteins. *J. Am. Chem. Soc.*, **122** (34), 8303–8304.

98 Pale-Grosdemange, C., Simon, E.S., Prime, K.L., and Whitesides, G.M. (1991) Formation of self-assembled monolayers by chemisorption of derivatives of oligo (ethylene glycol) of structure Hs(Ch2)11 (Och2ch2)Moh on gold. *J. Am. Chem. Soc.*, **113** (1), 12–20.

99 Prime, K.L. and Whitesides, G.M. (1993) Adsorption of proteins onto surfaces containing end-attached oligo(ethylene oxide): A model system using self-assembled monolayers. *J. Am. Chem. Soc.*, **115** (23), 10714–10721.

100 Balamurugan, S., Ista, L.K., Yan, J., Lopez, G.P., Fick, J., Himmelhaus, M., and Grunze, M. (2005) Reversible protein adsorption and bioadhesion on monolayers terminated with mixtures of oligo(ethylene glycol) and methyl groups. *J. Am. Chem. Soc.*, **127** (42), 14548–14549.

101 Lopez, G.P., Ratner, B.D., Tidwell, C.D., Haycox, C.L., Rapoza, R.J., and Horbett, T.A. (1992) Glow discharge plasma deposition of tetraethylene glycol dimethyl ether for fouling-resistant biomaterial surfaces. *J. Biomed. Mater. Res.*, **26** (4), 415–439.

102 Cao, L., Chang, M., Lee, C.-Y., Castner, D.G., Sukavaneshvar, S., Ratner, B.D., and Horbett, T.A. (2007) Plasma-deposited tetraglyme surfaces greatly reduce total blood protein adsorption, contact activation, platelet adhesion, platelet procoagulant activity, and in vitro thrombus deposition. *J. Biomed. Mater. Res. A*, **81A** (4), 827–837.

103 Shen, M., Martinson, L., Wagner, M.S., Castner, D.G., Ratner, B.D., and Horbett, T.A. (2002) PEO-like plasma polymerized tetraglyme surface interactions with leukocytes and proteins: In vitro and in vivo studies. *J. Biomater. Sci., Polym. Ed.*, **13** (4), 367–390.

104 Hubbell, J.A. (1997) PEG-based hydrogels for blocking, presenting and receiving information in the control of wound healing. *Polym. Prepr. (Am. Chem. Soc., Div. Polym. Chem.)*, **38** (1), 528.

105 Schmaljohann, D., Oswald, J., Jorgensen, B., Nitschke, M., Beyerlein, D., and Werner, C. (2003) Thermo-responsive PNIPAAM-G-PEG films for controlled cell detachment. *Biomacromolecules*, **4** (6), 1733–1739.

106 DeLong, S.A., Moon, J.J., and West, J.L. (2005) Covalently immobilized gradients of bfGf on hydrogel scaffolds for directed cell migration. *Biomaterials*, **26** (16), 3227–3234.

107 Lee, J.-H., Nho, Y.-C., Lim, Y.-M., and Son, T.-I. (2005) Prevention of surgical adhesions with barriers of carboxymethylcellulose and poly (ethylene glycol) hydrogels synthesized by irradiation. *J. Appl. Polym. Sci.*, **96** (4), 1138–1145.

108 Vladkova, T. (2004) Surface modification of silicone rubber with poly(ethylene glycol) hydrogel coatings. *J. Appl. Polym. Sci.*, **92** (3), 1486–1492.

109 Gattas-Asfura, K.M., Zheng, Y., Micic, M., Snedaker, M.J., Ji, X., Sui, G., Orbulescu, J., Andreopoulos, F.M., Pham, S.M., Wang, C., and Leblanc, R.M. (2003) Immobilization of quantum dots in the photo-cross-linked poly(ethylene glycol)-based hydrogel. *J. Phys. Chem. B*, **107** (38), 10464–10469.

110 Gan, D. and Lyon, L.A. (2002) Synthesis and protein adsorption resistance of peg-modified poly(N-isopropylacrylamide) core/shell microgels. *Macromolecules*, **35** (26), 9634–9639.

111 Nolan, C.M., Reyes, C.D., Debord, J.D., Garcia, A.J., and Lyon, L.A. (2005) Phase transition behavior, protein adsorption, and cell adhesion resistance of poly (ethylene glycol) crosslinked microgel particles. *Biomacromolecules*, **6** (4), 2032–2039.

112 Singh, N., Bridges, A.W., Garcia, A.J., and Lyon, L.A. (2007) Covalent tethering of functional microgel films onto poly (ethylene terephthalate) surfaces. *Biomacromolecules*, **8** (10), 3271–3275.

113 Bridges, A.W., Singh, N., Burns, K.L., Babensee, J.E., Lyon, L.A., and Garcia, A.J. (2008) Reduced acute inflammatory responses to microgel conformal coatings. *Biomaterials*, **29** (35), 4605–4615.

114 Scott, E.A., Nichols, M.D., Cordova, L.H., George, B.J., Jun, Y.-S., and Elbert, D.L. (2008) Protein adsorption and cell adhesion on nanoscale bioactive coatings formed from poly(ethylene glycol) and albumin microgels. *Biomaterials*, **29** (34), 4481–4493.

115 Von Recum, H.A., Kim, S.W., Kikuchi, A., Okuhara, M., Sakurai, Y., and Okano, T. (1998) Novel thermally reversible hydrogel as detachable cell culture

substrate. *J. Biomed. Mater. Res.*, **40** (4), 631–639.

116 Shin, H., Zygourakis, K., Farach-Carson, M.C., Yaszemski, M.J., and Mikos, A.G. (2004) Modulation of differentiation and mineralization of marrow stromal cells cultured on biomimetic hydrogels modified with Arg-Gly-Asp containing peptides. *J. Biomed. Mater. Res., Part A*, **69A** (3), 535–543.

117 Hall, H. (2007) Modified fibrin hydrogel matrices: Both, 3d-scaffolds and local and controlled release systems to stimulate angiogenesis. *Curr. Pharm. Des.*, **13** (35), 3597–3607.

118 Hayami, T., Matsumura, K., Kusunoki, M., Nishikawa, H., and Hontsu, S. (2007) Imparting cell adhesion to poly(vinyl alcohol) hydrogel by coating with hydroxyapatite thin film. *Mater. Lett.*, **61** (13), 2667–2670.

119 Takahashi, H., Emoto, K., Dubey, M., Castner, D.G., and Grainger, D.W. (2008) Imaging surface immobilization chemistry: Correlation with cell patterning on non-adhesive hydrogel thin films. *Adv. Funct. Mater.*, **18** (14), 2079–2088.

120 Von Recum, H., Kikuchi, A., Yamato, M., Sakurai, Y., Okano, T., and Kim, S.W. (1999) Growth factor and matrix molecules preserve cell function on thermally responsive culture surfaces. *Tissue Eng.*, **5** (3), 251–265.

121 Kirker, K.R., Luo, Y., Nielson, J.H., Shelby, J., and Prestwich, G.D. (2002) Glycosaminoglycan hydrogel films as bio-interactive dressings for wound healing. *Biomaterials*, **23** (17), 3661–3671.

122 Shu, X.Z., Liu, Y., Palumbo, F., and Prestwich, G.D. (2003) Disulfide-crosslinked hyaluronan-gelatin hydrogel films: A covalent mimic of the extracellular matrix for in vitro cell growth. *Biomaterials*, **24** (21), 3825–3834.

123 Zhu, A., Pan, Y., Liao, T., Zhao, F., and Chen, T. (2008) The synthesis and characterization of polymerizable and biocompatible N-maleic acyl-chitosan. *J. Biomed. Mater. Res. B Appl. Biomater.*, **85B** (2), 489–495.

124 Ruoslahti, E. (1996) Rgd and other recognition sequences for integrins. *Annu. Rev. Cell Dev. Biol.*, **12**, 697–715.

125 Lutolf, M.P., Weber, F.E., Schmoekel, H.G., Schense, J.C., Kohler, T., Mueller, R., and Hubbell, J.A. (2003) Repair of bone defects using synthetic mimetics of collagenous extracellular matrices. *Nat. Biotechnol.*, **21** (5), 513–518.

126 Lynch, I., Miller, I., Gallagher, W.M., and Dawson, K.A. (2006) Novel method to prepare morphologically rich polymeric surfaces for biomedical applications via phase separation and arrest of microgel particles. *J. Phys. Chem. B*, **110** (30), 14581–14589.

127 Goosen, M.F. and Sefton, M.V. (1983) Properties of a heparin-poly(vinyl alcohol) hydrogel coating. *J. Biomed. Mater. Res.*, **17** (2), 359–373.

128 Norton, L.W., Koschwanez, H.E., Wisniewski, N.A., Klitzman, B., and Reichert, W.M. (2007) Vascular endothelial growth factor and dexamethasone release from nonfouling sensor coatings affect the foreign body response. *J. Biomed. Mater. Res., Part A*, **81A** (4), 858–869.

129 Hassan, C.M., Doyle, F. III, and Peppas, N.A. (1997) Dynamic behavior of glucose-responsive poly(Methacrylic Acid-G-Ethylene Glycol) hydrogels. *Macromolecules*, **30** (20), 6166–6173.

130 Ehrbar, M., Schoenmakers, R., Christen, E.H., Fussenegger, M., and Weber, W. (2008) Drug-sensing hydrogels for the inducible release of biopharmaceuticals. *Nat. Mater.*, **7** (10), 800–804.

131 Serpe, M.J., Yarmey, K.A., Nolan, C.M., and Lyon, L.A. (2005) Doxorubicin uptake and release from microgel thin films. *Biomacromolecules*, **6** (1), 408–413.

132 Nolan Christine, M., Serpe Michael, J., and Lyon, L.A. (2004) Thermally modulated insulin release from microgel thin films. *Biomacromolecules*, **5** (5), 1940–1946.

133 Lin, S.Y., Chen, K.S., and Run-Chu, L. (2001) Design and evaluation of drug-loaded wound dressing having thermoresponsive, adhesive, absorptive and easy peeling properties. *Biomaterials*, **22** (22), 2999–3004.

10
Oscillating Microgels Driven by Chemical Reactions

Daisuke Suzuki

10.1
Introduction

Polymer hydrogel particles (i.e., microgels) have been attracting considerable attention as smart materials. Most microgels change their physicochemical properties in response to external stimuli such as pH, temperature, light, presence of biomolecules, and salt concentration. This stimulus-responsive property of microgels enables many applications such as drug or gene delivery, chemical or biological separation, photonic crystals, templates or stabilizers for inorganic nanoparticles, and smart particulate emulsifiers [1–45].

Probably the best known and most widely studied microgels are those made of poly (*N*-isopropylacrylamide) (PNIPAM), whose chain shows a thermoresponsive property. PNIPAM undergoes a coil–globule transition at a lower critical solution temperature (LCST) of around 32 °C in pure water [46, 47]. Thus, PNIPAM microgel shows a volume phase transition at around a LCST of PNIPAM liner chains [48]. Polyelectrolyte microgels have been synthesized in order to obtain pH-responsive microgels, and many researchers have already copolymerized charged monomers in microgels. For example, Kawaguchi *et al.* have reported that monodispersed and pH-responsive microgels have been obtained using acrylamide, methacrylic acid, and the crosslinker methylenebisacrylamide (BIS) by precipitation polymerization in several alcohols [49–51]. Naturally, because the presence of electrolytes in microgel dispersions affects electrostatic interactions between microgels, polyelectrolyte microgels also show a dependence on salt concentrations.

The aforementioned stimuli-responsive microgels are often called "smart" or "intelligent" because of their flexible response to their environment. In contrast with these conventional stimuli-responsive microgels, new microgels have been proposed whose physicochemical properties change periodically, as though automatically (i.e., the microgels undergo a swelling/deswelling volume oscillation that occurs without the on/off switch of external stimuli) [52–55]. In this chapter, we summarize the background and recent advances in this new class of microgels. Because this field of research is new, the contribution may place a disproportionate weight on personal opinion.

Hydrogel Micro and Nanoparticles, First Edition. Edited by L. Andrew Lyon and Michael Joseph Serpe.
© 2012 Wiley-VCH Verlag GmbH & Co. KGaA. Published 2012 by Wiley-VCH Verlag GmbH & Co. KGaA.

10.2 Types of Oscillating Microgels

Thus far, two different types of oscillating microgel systems have been reported. In the first type, a pH-oscillating reaction is coupled to pH-responsive microgels [53]. This scheme has recently been applied by Lagzi *et al.* in a rhythmic assembly/disassembly of Au or Ag nanoparticles [56] and in vesicle-to-micelle oscillations [57]. Several pH-oscillating chemical reactions have been reported by various groups [58–63]. In general, two main composite processes are necessary: autocatalytic production of H^+ (positive feedback) and consumption of H^+ (negative feedback). For the mixed Landolt reaction (iodate-sulfite-thiosulfate system) reported by Rabai and Beck [58, 59], the following simplified model, called the alternator, is demonstrated:

$$A + Y + X \rightarrow 2X + P_2 \tag{10.1}$$

$$A + B + X \rightarrow P_1 \tag{10.2}$$

$$A + B \rightarrow Y \tag{10.3}$$

where A corresponds to iodate, B to thiosulfate, Y to hydrogen sulfite, X to hydrogen ion, P_1 to tetrathionate, and P_2 to sulfate. Reaction 10.1 is an autocatalytic H^+ production, Reaction 10.2 is a H^+ consumption process, and Reaction 10.3 regenerates the reactant Y that serves as the source of X. A continuous-flow stirred tank reactor (CSTR) is often used, because Reaction 10.3 can be replaced by the input flow of the CSTR.

To achieve an oscillating microgel system by coupling to a pH-oscillating reaction, Varga *et al.* used a bromate–sulfite pH oscillator, which shows oscillations in a large pH range, from 3 to 7 [53]. The experimental setup is shown in Figure 10.1. These processes can be simply represented as follows:

$$BrO_3^- + 3H_2SO_3 \rightarrow 3SO_4^{2-} + Br^- + 6H^+ \tag{10.4}$$

$$BrO_3^- + 6HSO_3^- \rightarrow 3S_2O_6^{2-} + Br^- + 3H_2O \tag{10.5}$$

In the second type of oscillating microgel system, a reduction–oxidation (redox) oscillation of the Belousov–Zhabotinsky (BZ) reaction is coupled to thermoresponsive microgels in which a catalyst is covalently bound (Figure 10.2) [52, 54, 55]. The oscillating microgel has a cyclic reaction network and executes a periodic mechanical oscillation driven by the chemical energy of the BZ reaction. This differs from the abovementioned pH-oscillating system in that the redox oscillation can be realized in a closed solution (i.e., no CSTR is required).

Before introducing oscillating microgels coupled to the redox oscillation, the BZ reaction itself will be explained briefly. This reaction is widely known to exhibit spatial and temporal oscillating phenomena with periodic redox changes of the metal ion or metal ion complex catalyst [64–67]. The overall process of the BZ reaction is that an

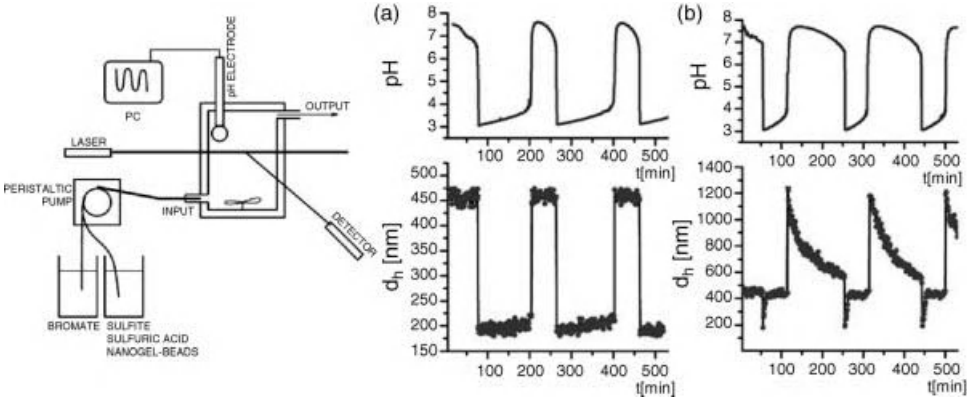

Figure 10.1 Experimental setup for oscillating microgels coupled to pH-oscillating chemical reaction. (a, b) The pH and the hydrodynamic size of the nanogel beads as a function of time in the pH-oscillating system. The concentrations in the input flow after mixing but prior to any reaction are $[BrO_3^-]_0 = 0.05\ mol\ dm^{-3}$, $[SO_3^{2-}]_0 = 0.05\ mol\ dm^{-3}$: (a) $[H_2SO_4]_0 = 0.0016\ mol\ dm^{-3}$, $[SDS]_0 = 0.4\ mmol\ dm^{-3}$; (b) $[H_2SO_4]_0 = 0.0010\ mol\ dm^{-3}$, $[SDS]_0 = 0.35\ mmol\ dm^{-3}$. Reproduced from [53] with permission.

organic substrate is oxidized by a reagent in the presence of the catalyst under acidic conditions. Many variants of the BZ reaction are known, due to changes of the metal ion catalyst and the other chemical species in the reaction. A substitution often leads to very peculiar results, and the reasons are not always clear. As the oxidizing reagent thus far, there appears to be no substitute for bromate ion, such as from sodium bromate ($NaBrO_3$) or potassium bromate ($KBrO_3$). Moreover, numerous experiments have been performed in attempts to find substitutes for the metal ion catalyst,

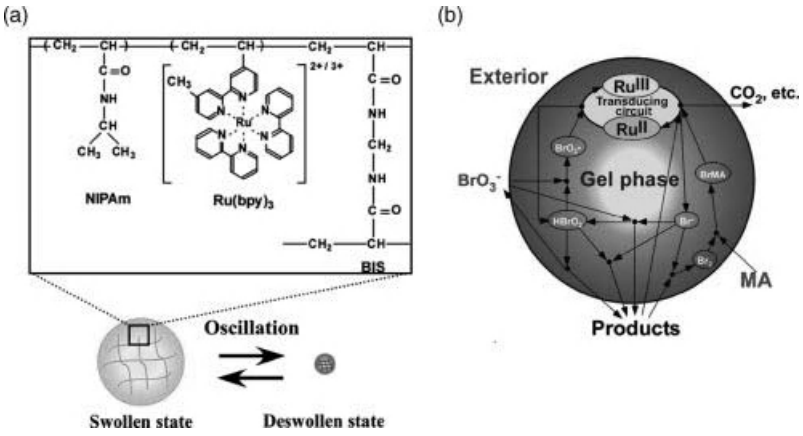

Figure 10.2 Schematic representation of oscillating microgels with chemical reaction cycle. (a) Chemical structure of the oscillating microgel. (b) Chemical reaction network of the BZ reaction in microgel.

inorganic acid, or organic substrate. Because various organic substrates are used, malonic acid (MA) or citric acid is often used. In almost every case, sulfuric acid (H_2SO_4) or nitric acid (HNO_3) is used as the inorganic acid. The sensitivity of the inorganic acid depends on the metal ion used. Because of the high redox potential (1–1.5 V/SCE), a metal ion such as cerium ion (Ce^{3+}), or a metal ion complex such as ferroin ($Fe(phen)_3^{2+}$) or ruthenium tris(2,2′-bipyridine) ($Ru(bpy)_3^{2+}$) is often used. In the course of the BZ reaction, the metal ion catalyst shows a redox oscillation that continues until the reagents are consumed to critical concentrations. While the solution is continuously stirred, the color of the solution changes periodically because of the redox oscillation of the metal ion catalyst. In contrast, when thin films of media such as hydrogels are soaked in the solution, a concentric or spiral wave pattern appears. The BZ reaction is a recognized cornerstone in the field of nonlinear chemical dynamics. The original BZ reaction occurred in a fluid, but hydrogels were later used as a medium to suppress hydrodynamic effects on the BZ reaction, especially when investigating dynamic patterns [68].

The kinetics of the BZ reaction are very complicated and involve more than 80 elementary reaction steps and two dozen chemical species. The oscillating mechanism of the BZ reaction has been developed primarily in terms of the Field–Körös–Noyes (FKN) mechanism [66, 69, 70], which can be divided into three basic processes as follows:

$$BrO_3^- + 2Br^- + 3H^+ \rightarrow 3HOBr \quad \text{(Process A)} \tag{10.6}$$

$$BrO_3^- + HBrO_2 + 2M_{red} + 3H^+ \rightarrow 2HBrO_2 + 2M_{ox} + H_2O \quad \text{(Process B)} \tag{10.7}$$

$$2M_{ox} + MA + BrMA \rightarrow f\ Br^- + 2M_{red} + \text{other products} \quad \text{(Process C)} \tag{10.8}$$

The stoichiometric factor f represents the number of bromide ions produced when two oxidized metal ions (M_{ox}) are reduced (M_{red}). To describe the FKN mechanism mathematically, the Oregonator model is widely used [70].

Both types of oscillating gels have been proposed initially as bulk hydrogels, which are coupled to either a pH-oscillating reaction [63, 71, 72] or a redox-oscillating reaction [73–77]. In particular, Yoshida *et al.* have proposed and developed an original idea for conversion of the redox oscillation of the BZ reaction into mechanical changes of bulk gels.

10.3
Synthesis and Fabrication of Oscillating Microgels

Key to the creation of oscillating microgels is that functional species whose properties are periodically changeable be anchored to microgels. In order to synchronize with pH-oscillating reactions, a carboxyl group or amine group should be chosen as the

functional group. For example, poly(NIPAM-*co*-acrylic acid (AA)) microgels prepared by precipitation polymerization were synchronized with the bromate–sulfite pH-oscillating reaction [53]. In addition, it may be possible to apply enzymatic reactions to the oscillating microgels as has been done for bulk hydrogels [78].

In our case, the metal ion catalyst of the BZ reaction was covalently bound to microgels in order to synchronize it with the redox oscillation of the BZ reaction [52, 54]. What is generally known is that aqueous free-radical precipitation polymerization is useful to synthesize stimuli-responsive microgels and that precipitation polymerization is beneficial to synthesize monodispersed microgels. Accordingly, ruthenium (4-methyl-4′-vinyl-2,2′-bipyridine)bis(2,2′-bipyridine)bis (hexafluorophosphate) monomer (denoted $Ru(bpy)_3$ monomer), NIPAM, and crosslinker BIS were dissolved in water, and the polymerization was started by injecting a cationic initiator solution (e.g., V-50) into the mixture at 70 °C [54, 55]. Usually, the polymerization required about 6 h to complete. During the polymerization, 50–60% of the $Ru(bpy)_3$ monomer was introduced into the resultant microgels, and the $Ru(bpy)_3$ moieties were fixed in the reduced $Ru(bpy)_3^{2+}$ state [79]. The amount of $Ru(bpy)_3$ monomer lost during the polymerization can be mainly attributed to its hydrophilicity. The LCST of highly charged PNIPAM liner chains was much higher than that of pure PNIPAM. This forced poly(NIPAM-*co*-$Ru(bpy)_3$) chains into a coiled state during the polymerization, even at 70 °C, and therefore those chains were not incorporated by microgels. Another feature of $Ru(bpy)_3$ monomer is that during the polymerization the hydrodynamic diameters of the microgels are decreased, which is an effect similar to that of ionic surfactants in precipitation polymerization [79]. Moreover, the microgel sizes obtained were controlled by changing the ionic strength, monomer concentration, initiator concentration, and so on. Until now, monodispersed microgels with hydrodynamic diameters of 100–800 nm have been prepared in their swollen states. At present, the metal catalyst of the BZ reaction must be immobilized within polymer chains composed of microgels. This is considered essential in order to achieve the swelling/deswelling volume oscillation.

Alternatively, Shen *et al*. took a different approach to fabricate poly(NIPAM-*co*-Ru $(bpy)_3$) microgels [80]. First, crosslinked poly(NIPAM-*co*-4-vinyl-4′-methyl-2,2′-bipyridine) microgels were synthesized. Then, the bipyridyl groups were converted into $Ru(bpy)_3$ through a coordination reaction with *cis*-$Ru(bpy)_2Cl_2$. The conversion percentage of this coordination reaction was estimated at $50 \pm 5\%$.

So far, $Ru(bpy)_3$ monomers have been incorporated into crosslinked microgels of PNIPAM only, but those of other chemical species (e.g., acrylamide) could also be employed. One reason for the selection of thermoresponsive PNIPAM is to increase the oscillation amplitude. Details of this are given below.

10.4 Control of Oscillatory Behavior

It is important to clarify how the oscillatory behavior of microgels is regulated. Basically, this depends on the conditions of the chemical reactions involved.

The reaction temperature and the concentrations of the chemical substrates in the reactions are key factors to determine the oscillatory characteristics of the chemical reaction itself (i.e., induction period, oscillation amplitude, oscillation period, waveform, etc.). In addition, the state of the microgel network structure (i.e., whether the polymer chain is coiled or globular) should dynamically affect the chemical reactions through a so-called feedback effect. In the next three subsections, the effects of the abovementioned key factors on the oscillatory behavior are summarized to clarify the features of oscillating microgels, especially those coupled to the BZ reaction. To simplify the discussion, assume that all reaction solutions are mechanically stirred, although mechanical stirring is another key parameter to determine the oscillatory behavior.

10.4.1
Effect on Induction Period

In general, the BZ reaction shows an induction period before oscillations are observed, as shown in Figure 10.3. For practical applications, there is a need to control the induction period of the oscillating microgels as precisely as possible. The induction period of the BZ reaction is determined by the types and concentrations of the chemical substrates (i.e., metal ion catalysts, oxidizing and reducing reagents, strong acids) as well as the temperature and stirring rate [66]. So far, the hypothesis most accepted to explain the induction period of the BZ reaction is that a critical concentration of the organic brominated species, mainly bromomalonic acid (BrMA), must be reached before the oscillation starts [66, 81].

The effect of the initial substrate concentrations on the induction period of the oscillating microgels is far more difficult to clarify. This has been investigated by varying the concentration of each substrate while keeping those of all others constant [82]. For oscillating microgels where metal ion catalysts are immobilized,

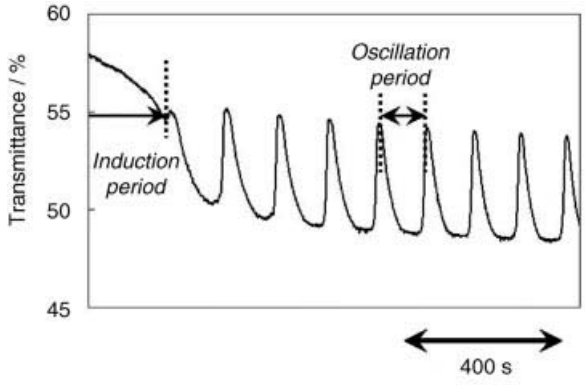

Figure 10.3 Typical oscillating profile of optical transmittance for the oscillating microgels. To observe transmittance changes originating with microgel oscillation, an isosbestic point (570 nm) of the Ru^{II} and Ru^{III} states was chosen for the measurement. Reproduced from [82] with permission.

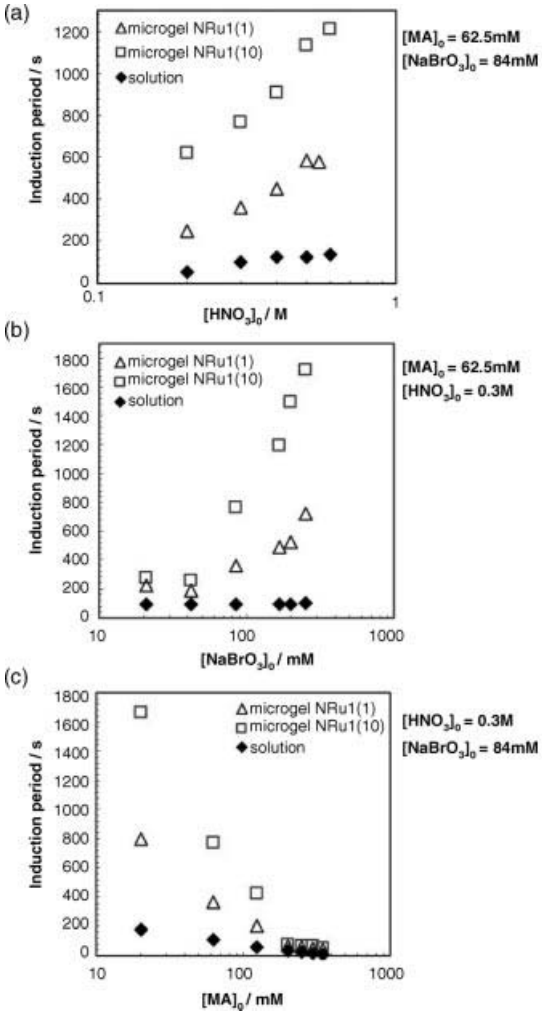

Figure 10.4 Effect of initial substrate concentrations on induction period for the bulk solution system (filled diamonds), the 1 mol% BIS crosslinked oscillating microgels (blue triangles), and the 10 mol% BIS crosslinked oscillating microgels (open squares). Reproduced from [82] with permission.

the network structure of the microgels is also an important parameter to determine the induction period. Figure 10.4 shows induction periods for microgel oscillations and the conventional BZ reaction (i.e., without microgels) at 25 °C. In all cases, MA, $NaBrO_3$, and HNO_3 were used as chemical reagents in the BZ reaction (initial concentrations are denoted by $[MA]_0$, $[NaBrO_3]_0$, and $[HNO_3]_0$, respectively). Both 1 and 10 mol% BIS crosslinked oscillating microgels were used. As their crosslink density increased, the induction period of the microgels became much longer. Given the popular hypothesis, the length of the induction period for a microgel system can

be related to the immobilization of the metal ion catalysts in the microgels. The rate of BrMA production must be lower than in the BZ reaction with non-immobilized catalysts, because the chemical substrates and intermediates in microgel networks have lower diffusion constants, which become lower still as the crosslink density increases.

In addition, trials [82] revealed that as $[NaBrO_3]_0$ was increased, for example, the induction period became longer for the oscillating microgels but remained almost constant for the bulk solution, as shown in Figure 10.4b. As mentioned above, the induction period is mainly related to a critical BrMA concentration, which in turn is known to depend on $[NaBrO_3]_0$ (i.e., critical BrMA concentration increases with initial $NaBrO_3$ concentration) [66, 81]. The difference between the induction period of the oscillating microgels and that of the bulk solution may be related to other factors, such as the concentrations of metal ion catalyst and MA. In fact, the tendency for the induction period to lengthen as $[NaBrO_3]_0$ increases became stronger as the metal catalyst diminished in the BZ reaction using non-immobilized cerium ions [81].

The dependence of induction period on temperature has also been investigated [79]. The induction period of the microgel system was longer than that of the conventional BZ reaction for all temperatures below the transition temperature of the microgels. Moreover, at all temperatures the induction period of the microgels became much longer as their crosslink density increased. The results can also be understood as the effect of $Ru(bpy)_3$ immobilization within microgels [82]. A similar dependence of induction period on temperature has been reported by Pullela *et al.* [83]. Further investigation is necessary to clarify the whole mechanism of the induction period of the microgel system, because of the complexity of the phenomenon.

10.4.2
Effect on Oscillation Amplitude

The short period of the swelling/deswelling volume oscillation of microgels is very difficult to follow by means of dynamic light scattering (DLS). Therefore, oscillation amplitudes with respect to hydrodynamic diameters were estimated from changes in diameter between the reduced Ru^{II} state and the oxidized Ru^{III} state at the same temperature [54, 79, 82]. As shown in Figure 10.5, hydrodynamic diameters of crosslinked poly(NIPAM-*co*-$Ru(bpy)_3$) microgels were measured as a function of temperature. Each solution contained more than 0.3 M of HNO_3 since the BZ reaction only proceeds at such high salt concentrations. The deswelling curves almost coincided when the amount of $Ru(bpy)_3$ monomer immobilized was low

Figure 10.5 Temperature dependence of the hydrodynamic diameters for the BIS crosslinked poly(NIPAM-*co*-$Ru(bpy)_3$) microgels with the reduced state Ru^{II} in solution with 1 mM Ce^{III} and 0.3 M HNO_3 (diamonds), as well as with the oxidized state Ru^{III} in solution with 1 mM Ce^{IV} and 0.3 M HNO_3 (squares) as measured by DLS. Samples contain (a) ~0.1 mol%, (b) ~0.6 mol%, and (c) ~1.0 mol% $Ru(bpy)_3$ monomer. Reproduced from [79, 89] with permission.

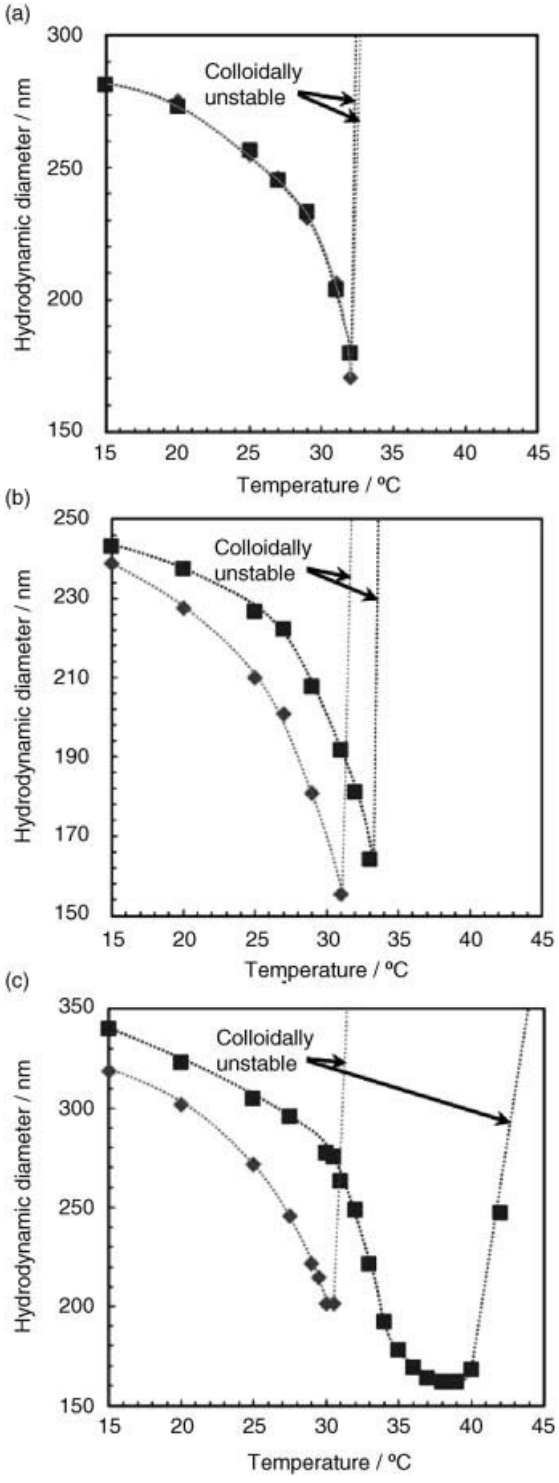
(a)
Hydrodynamic diameter / nm
300
250
200
150
Colloidally unstable
15
20
25
30
35
40
45
Temperature / °C
(b)
Hydrodynamic diameter / nm
250
230
210
190
170
150
Colloidally unstable
15
20
25
30
35
40
45
Temperature / °C
(c)
Hydrodynamic diameter / nm
350
300
250
200
150
Colloidally unstable
15
20
25
30
35
40
45
Temperature / °C

(below 0.12 mol%), as shown in Figure 10.5a. In contrast, when the $Ru(bpy)_3$ monomer incorporated into microgels was more than 0.34 mol%, the curve for the oxidized Ru^{III} state indicated a higher transition temperature than that for the reduced Ru^{II} state. A comparison of Figure 10.5b with c reveals that the shift in transition temperature grew larger when the amount of $Ru(bpy)_3$ monomer immobilized by microgels was increased from 0.56 to ~1 mol%. From these figures, we can roughly estimate the volume changes in the oscillations. For example, Figure 10.5c implies that for a constant temperature of 30 °C the microgels underwent a volume change of ~40%.

As shown in Figures 10.3 and 10.6, the changes in the optical transmittance of microgel dispersions are monitored to investigate oscillation amplitude, because

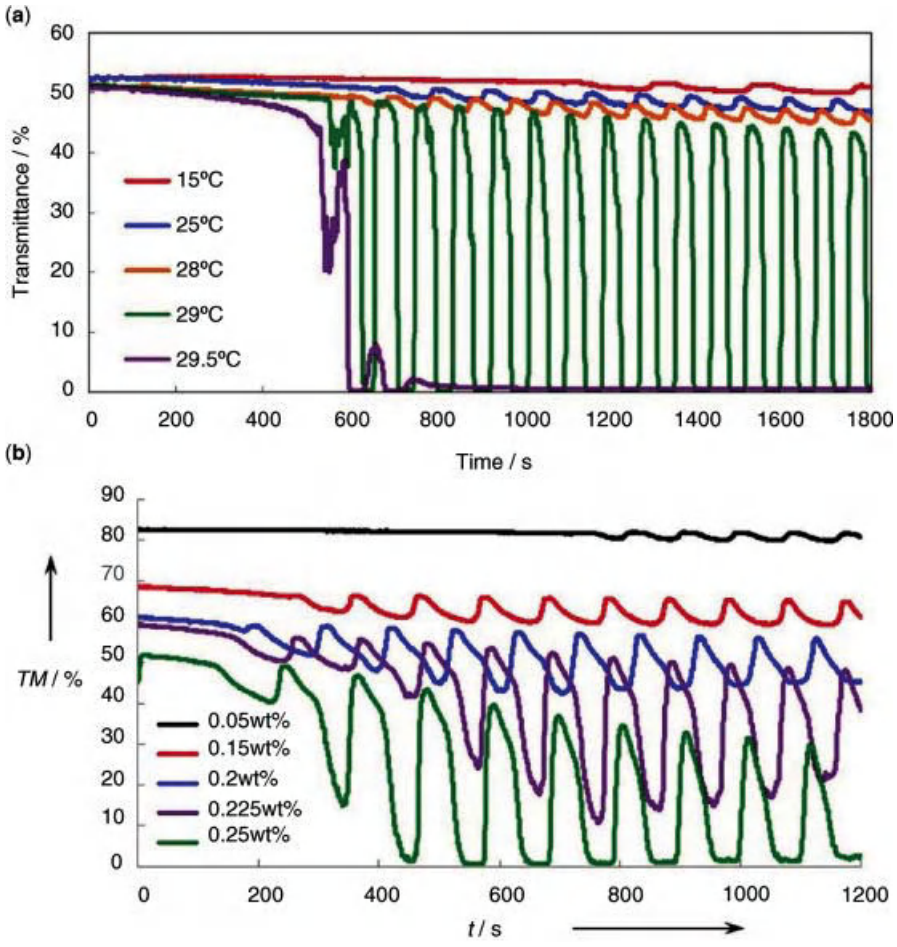

Figure 10.6 Oscillating profiles of optical transmittance for the BIS crosslinked oscillating microgel dispersions. (a) The profiles measured at different temperatures. (b) The profiles measured at different microgel concentrations. Reproduced from [54, 79] with permission.

real-time measurement of hydrodynamic diameters by DLS is difficult for oscillating microgels in terms of their concentrations, the measuring time, and so on. The oscillation amplitude of the microgel volume is related to that of the optical transmittance because the swelling determines the scattering intensity and thus the optical transmittance (i.e., transparent in swollen state but turbid in deswollen state). Below the transition temperature (e.g., 15–28 °C in Figure 10.6a), the oscillation amplitude of the optical transmittance became slightly greater with temperature. The increase in amplitude is mainly due to the increased deviation in hydrodynamic diameter between the Ru^{II} and Ru^{III} states, as shown in Figure 10.5b and c. (A remarkable change in waveform and amplitude at 29 °C in Figure 10.6a will be explained below.)

Note that the oscillation amplitude of the redox potential for the bulk solution of the BZ reaction depends on the initial substrate concentrations and the $Ru(bpy)_3$ catalyst concentration [84], so the $Ru(bpy)_3$ catalyst is not all in the reduced Ru^{II} state or oxidized Ru^{III} state at the same time. In addition, by means of isothermal titration calorimetry and ultrasensitive differential scanning calorimetry, Zhao *et al*. reported that less heat was released by the oscillating microgel system than by a bulk solution of the BZ reaction, because the chemical reaction was restricted by the presence of the hydrogel network structure [85]. Consequently, the amplitude of the volume oscillation must actually be lower than that estimated from Figure 10.5.

For the pH-oscillating system using a CSTR, an oscillation in hydrodynamic diameters between ∼200 and ∼450 nm for poly(NIPAM-*co*-AA) microgels was determined by controlling the concentrations of the chemical reaction and anionic surfactant (SDS) at a constant temperature of 35 °C [53]. Note that direct measurements of hydrodynamic diameters can be achieved for microgels in the pH-oscillating system because of the long oscillation period (∼200 min). As shown in Figure 10.1, the Brookhaven DLS equipment consisted of a BI-200SM goniometer and a BI-9000AT digital correlator [53].

10.4.3
Effect on Oscillation Period and Waveforms

Although the overall BZ reaction involves more than 80 elementary reactions, it would be useful to know how the overall oscillation period (P_{osc}) is affected by the conditions of the chemical reactions. Like the induction period mentioned above, the P_{osc} of the BZ reaction depends on the initial substrate concentrations, temperature, and stirring rate. Moreover, an effect of metal–catalyst immobilization on P_{osc} should appear for oscillating microgels. Therefore, the microgel oscillations were compared with the bulk solution of the BZ reaction in terms of the P_{osc}. As shown in Figure 10.7, the dependence of P_{osc} on the initial substrate concentrations (i.e., $[MA]_0$, $[NaBrO_3]_0$, and $[HNO_3]_0$) at a constant temperature of 25 °C was first determined. The average value of the period between the second and sixth oscillations was regarded as the P_{osc}. Figure 10.7 clearly shows that there are some differences in P_{osc} between the bulk solution and the microgel dispersion. In all cases reported here, P_{osc} became shorter as the initial substrate concentrations were increased. In comparison with the

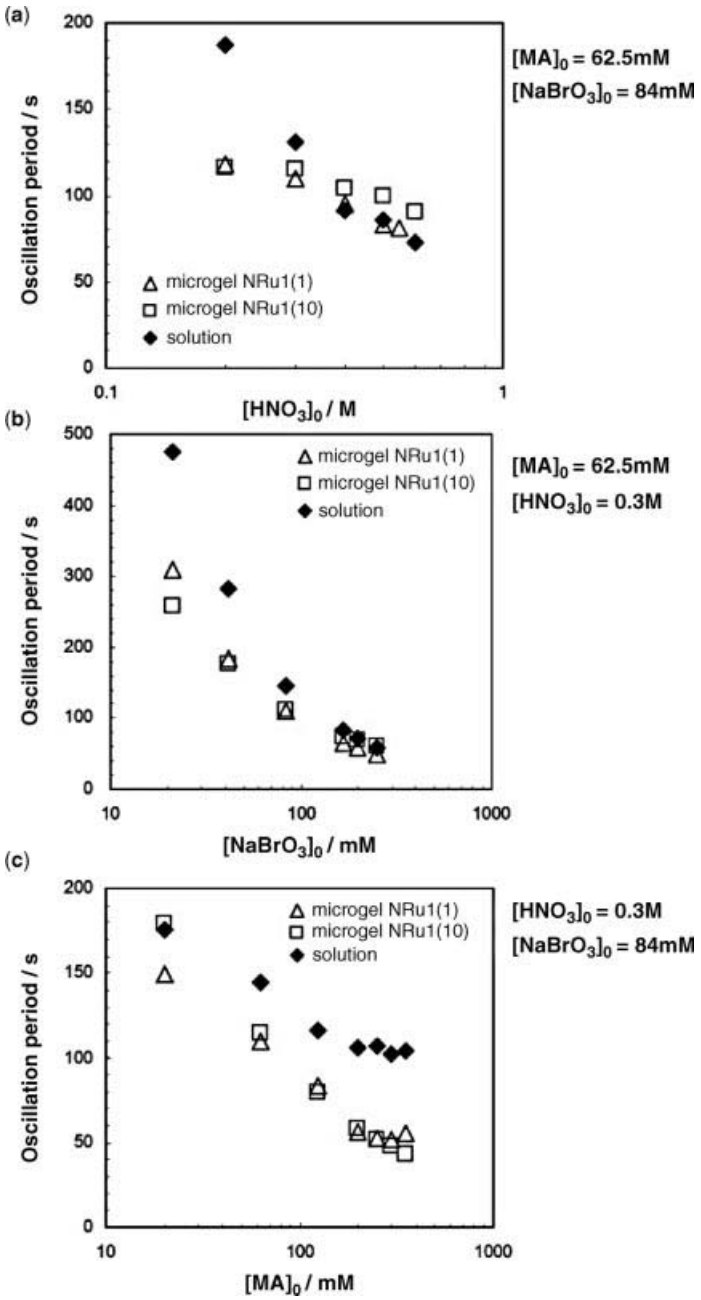

Figure 10.7 Effect of initial substrate concentrations on oscillation period for the bulk solution system (filled diamonds), the 1 mol% BIS crosslinked oscillating microgels (open triangles), and the 10 mol% BIS crosslinked oscillating microgels (open squares). Reproduced from [82] with permission.

concentration dependence of the bulk solution, that of the oscillating microgels was stronger in the case of MA but weaker in the case of HNO_3 or $NaBrO_3$. In addition, there are large differences in P_{osc} between the bulk solution and the oscillating microgels at high $[MA]_0$ and at low $[HNO_3]_0$ or $[NaBrO_3]$, but not at higher $[HNO_3]_0$ or $[NaBrO_3]_0$. Although the aforementioned results do not cover all of the phenomena, these may be useful indicators to qualitatively control the P_{osc}.

Next, effect of crosslink density on the P_{osc} is described. For that purpose, three types of oscillating microgels with different crosslink densities were used in the analysis. The oscillation frequency, F_{osc} ($= 1/P_{osc}$), was used for analysis, simply as a matter of convenience. As shown in Figure 10.8, the F_{osc} of the bulk solution for the BZ reaction tends to increase as the temperature increases, in accordance with the Arrhenius dependence [86, 87]. The oscillating microgels also exhibit the Arrhenius dependence below the transition temperature [79]. In contrast, the F_{osc} decreases near the transition temperature, and the corresponding plots deviate from the Arrhenius equation, as will be explained later. Clearly, the F_{osc} of the oscillating microgels became higher than that of the bulk solution. In addition, the F_{osc} became higher at low temperatures (see 15 °C), as the crosslink density of the microgels increased, but remained almost unchanged near the transition temperature (see 25 °C). This is a feature of thermosensitive microgels. That is, the mesh size of the microgel network structure may decrease monotonically as the BIS feed increases at 15 °C, with all the microgels highly swollen, whereas the mesh size may remain almost constant as the BIS feed changes at 25 °C, which is near the transition temperature. Therefore, the oscillation period of the microgels apparently depends on their crosslinked network structure. Note that the network structure also changes

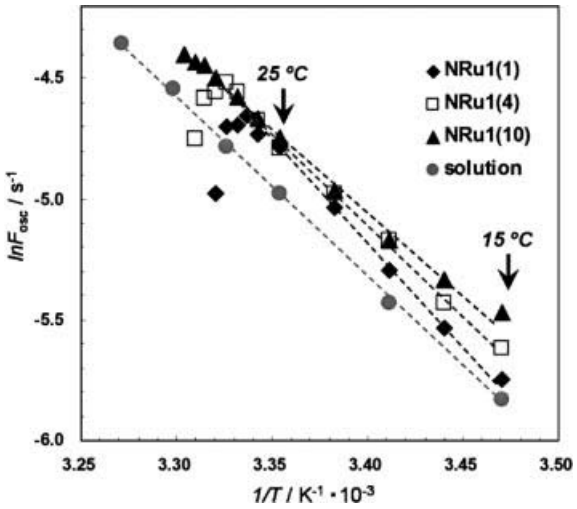

Figure 10.8 Arrhenius dependence of oscillation frequency (F_{osc}) using the 1 mol% (filled diamond), 4 mol% (open square), and 10 mol% BIS crosslinked oscillating microgels (filled triangles). Control experiments of the BZ reaction without microgels were performed (filled circles). Reproduced from [79] with permission.

while the microgels show the swelling/deswelling volume oscillation, so a feedback mechanism from mechanical changes to chemical changes should be considered. Although this effect has not been clarified yet, what is understood is that the network structure plays an important role in controlling the F_{osc} of the oscillating microgels.

In order to better understand the mechanisms of change in the oscillation period of the microgels, the waveforms observed for the bulk solution and the microgels were compared. In order to compare the oscillations, their waveforms were divided according to the three main processes of the FKN mechanism: consumption of bromide ion (process A), autocatalytic reaction of bromous acid with oxidation of the catalyst (process B), and organic reaction with reduction of the catalyst (process C) [69, 70]. Figure 10.9 illustrates this division of the waveforms. At the same temperature, the durations of processes B and C in relation to the oscillation period (i.e., B/P_{osc}, and C/P_{osc}) were larger for the oscillating microgels than for the bulk

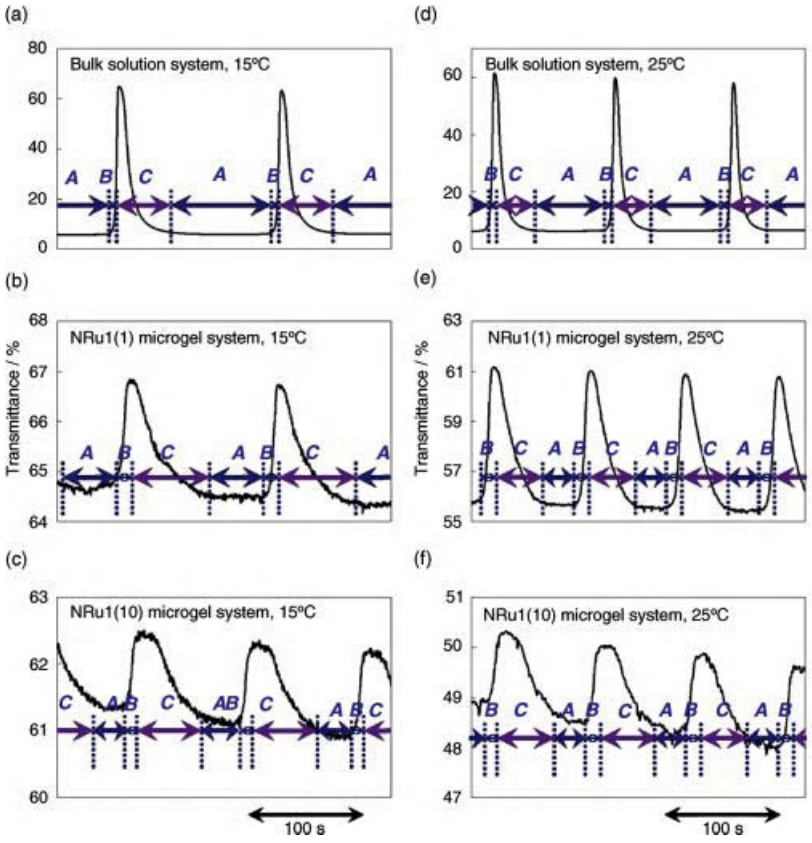

Figure 10.9 Typical oscillation waveforms of bulk solution (a, d), 1 mol% BIS crosslinked oscillating microgels (b, e), and 10 mol% BIS crosslinked oscillating microgels (c, f). The profiles were measured at temperatures of 15 °C (a–c) and 25 °C (d–f). Reproduced from [79] with permission.

solution. In addition, as the crosslink density of the oscillating microgels increased these ratios became larger at 15 °C but remained almost constant at 25 °C. These facts may be explained by the effect of $Ru(bpy)_3$ catalyst immobilization in microgels, because processes B and C involve catalytic reactions. The rate of an immobilized catalytic reaction is lower than that of one with the same amount of soluble catalyst. Contrastingly, the A/P_{osc} values for the oscillating microgels were smaller than those for the bulk solution, although the reason is unclear. As a result, the P_{osc} of the oscillating microgels was changed by the contrasting pair of effects mentioned above.

The waveforms of the volume oscillation and the bulk solution of the BZ reaction were also affected by the initial substrate concentrations [82]. In particular, the long duration of process C due to the crosslinking effect mentioned above [79] was greatly decreased as $[MA]_0$ increased, resulting in a different dependence for each substrate.

10.5 Flocculating/Dispersing Oscillation

This chapter has described how the oscillating microgels exhibit a swelling/deswelling oscillation (i.e., volume oscillation) that is synchronized with a chemical reaction such as the BZ reaction. However, another type of oscillating behavior, a flocculating/dispersing oscillation of microgels [54, 55], will now be explained. This type of oscillating behavior was also observed in the pH-oscillating system [53], as shown in Figure 10.1.

As shown in Figure 10.6a, the oscillation amplitude of the optical transmittance became larger as the temperature increased within the temperature range of 15–28 °C [54, 79]. The increase in amplitude is caused by the increased deviation in hydrodynamic diameter between the $Ru(bpy)_3^{2+}$ and $Ru(bpy)_3^{3+}$ states at a constant temperature, as shown in Figure 10.5. Then, a dramatic change in amplitude and waveform was observed at 29 °C. Eventually, at 29.5 °C, the oscillation was no longer detected. Taking into consideration the DLS data shown in Figure 10.5, the sudden change in amplitude and waveform could be due to the difference in colloidal stability between the $Ru(bpy)_3^{2+}$ and $Ru(bpy)_3^{3+}$ states. In this case, the microgels in the reduced $Ru(bpy)_3^{2+}$ state were flocculated due to a lack of electrostatic repulsion at high salt concentration. The microgels were in a deswollen state and lacked the repulsive interaction of steric hindrance that originates at the exterior of hydrated polymer chains.

Next, the effect of microgel concentration on the oscillations was investigated at a constant temperature, (Figure 10.6b) since colloidal stability is sensitive to microgel concentration [54]. Clearly, a dependence on microgel concentration was found. The sudden change in the amplitude and waveform of the optical transmittance was only observed at higher microgel concentrations, indicating that the microgels were flocculated and redispersed repeatedly.

In addition, the optical transmittance and redox potential of the microgel dispersion were measured simultaneously [79], as shown in Figure 10.10. In this case, an increase in the redox potential means an increased concentration of oxidized

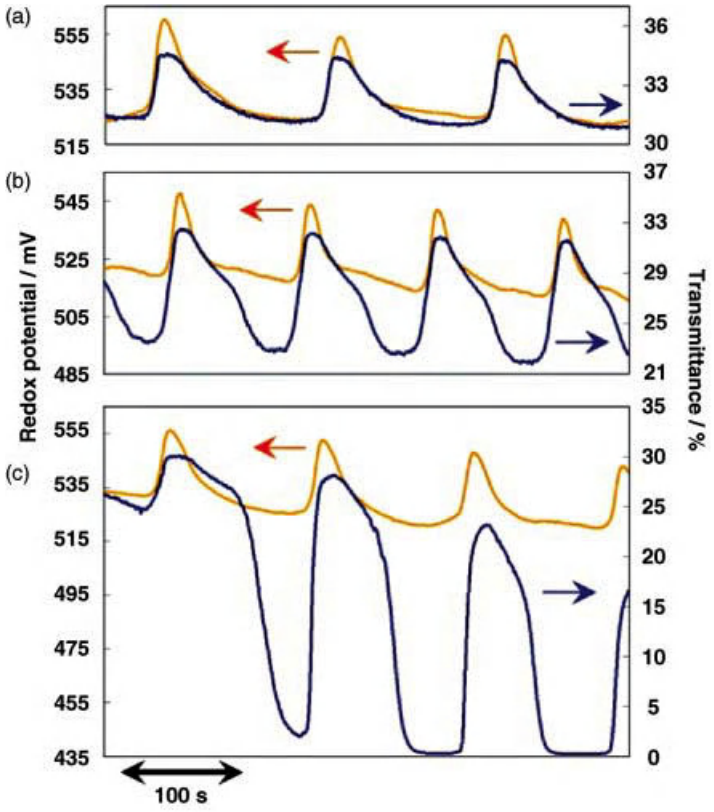

Figure 10.10 Simultaneous measurements of redox potential (orange) and transmittance (blue) of the 1 mol% BIS crosslinked oscillating microgel at temperatures of (a) 25 °C, (b) 27 °C, and (c) 27.5 °C. Reproduced from [79] with permission.

$Ru(bpy)_3^{3+}$ catalyst. As shown in Figure 10.10a, the transmittance curve and the redox potential curve agree well at low temperatures, indicating that the swelling/deswelling volume oscillation of the microgels is synchronized with the cyclic chemical reaction. In contrast, as shown in Figure 10.10b and c, the transmittance curve does not coincide with the redox potential curve at higher temperatures, indicating a flocculating/dispersing oscillation of the microgels. It is worthwhile mentioning that the large decreases in transmittance occur when the percentage of the reduced $Ru(bpy)_3^{2+}$ state is high, which is also proof that the large decreases were due to microgel flocculations. In this case, the redispersion from flocculation was because the microgel did not reside at a deep potential minimum, resulting in weak and reversible flocculation [88].

Both the flocculating/dispersing oscillation and the volume oscillation can be detected as the viscosity changes [55, 89], as shown in Figure 10.11. At low temperature (20 °C), the shape of the waveform is similar to that usually produced by the BZ reaction and detected by optical transmittance and redox potential changes

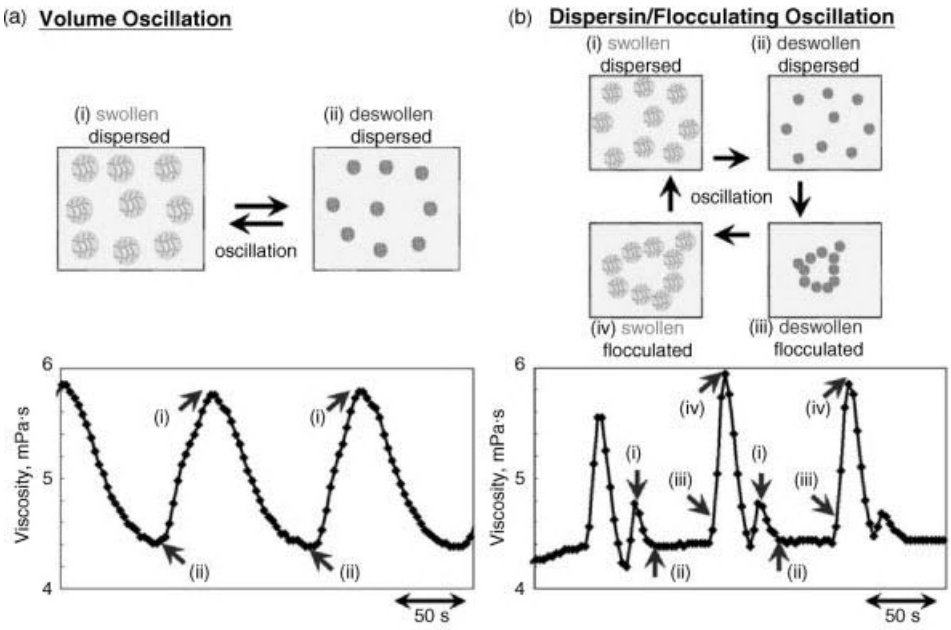

Figure 10.11 Oscillating profiles of viscosity in the oscillating microgel dispersions: (a) swelling/deswelling (volume) oscillation of microgels at 20 °C; and (b) dispersing/flocculating oscillation of microgels at 23 °C. Reproduced from [55] with permission.

(e.g., see Figure 10.10a). Therefore, the oscillating viscosity in the microgel dispersion is due to the swelling/deswelling volume oscillation of the microgels. In this case (Figure 10.11a), the viscosity is high when the microgels are in the swollen state at (i) and low when in the deswollen state at (ii). In contrast, the shape of the waveform was greatly changed at higher temperature (23 °C) (Figure 10.11b). Taking into consideration the abovementioned optical transmittance and redox potential experiments, it seems reasonable that the oscillating viscosity in the dispersion is due to the flocculating/dispersing oscillation of the microgels. In this case, the smaller peak is attributed to a simple volume oscillation of each microgel from (i) to (ii). The significant change in amplitude that follows is due to flocculation of the microgels at (iii), where the flocs become large enough to detect with an optical transmittance measurement. The flocculation continues until colloidal stability is recovered through hydrating and swelling at (iv). After that, the viscosity of the dispersion is decreased by redispersion of the flocs, which may be redispersed completely when the viscosity reaches a minimum. The swelling/deswelling oscillation of the microgels then repeats. Consequently, the behavior of the flocculating/dispersing oscillation was better revealed by the rheological measurements than by the transmittance ones [55]. In addition, a large viscosity oscillation amplitude was accomplished by inducing a large swelling/deswelling volume oscillation of microgels [89].

Considering the flocculating/dispersing oscillation of microgels, the changes in oscillating behavior (e.g., oscillation frequency) near the transition temperature can

be understood (see Figure 10.8). These are presumably related to the lower diffusion coefficients of the substrates and intermediates for chemical reactions in deswollen and flocculated microgels.

10.6 Concluding Remarks

In this chapter, the recently emerging research topic of oscillating microgels has been described. Examples have been given to demonstrate microgel oscillations that are synchronized with nonlinear chemical reactions. These covered swelling/deswelling oscillations as well as flocculating/dispersing oscillations. To develop the oscillating microgels further, construction of complex microgel structures would offer benefits. For example, core–shell-structured oscillating microgels show higher colloidal stability, which may lead to the creation of new technologies [90]. In fact, assembly of oscillating microgels may prove useful in the development of microdevices, such as microactuators for use in microfluidic devices. I believe that the work on oscillating microgels has only just begun and will contribute to progress in colloid, polymer, and materials chemistry, since there are many possibilities for both fundamental research and practical application.

Acknowledgments

The author acknowledges a Grant-in-Aid for Young Scientists (A) (22685024) from the Ministry of Education, Culture, Sports, Science, and Technology (MEXT) of Japan. This work was also partially supported by Special Coordination Funds for Promoting Science under the MEXT program "Promotion of Environmental Improvement for Independence of Young Researchers." The author would like to thank Prof. Haruma Kawaguchi and Prof. Ryo Yoshida for the inspiration to extend this kind of research.

References

1 Saunders, B.R. and Vincent, B. (1999) *Adv. Colloid Interface Sci.*, **80**, 1–25.
2 Pelton, R. (2000) *Adv. Colloid Interface Sci.*, **85**, 1–33.
3 Kawaguchi, H. (2000) *Prog. Polym. Sci.*, **25**, 1171–1210.
4 Nayak, S. and Lyon, L.A. (2005) *Angew. Chem. Int. Ed.*, **44**, 7686–7708.
5 Pich, A.Z. and Adler, H.J.P. (2007) *Polym. Int.*, **56**, 291–307.
6 Tan, B.H. and Tam, K.C. (2008) *Adv. Colloid Interface Sci.*, **136**, 25–44.
7 Oh, J.K., Drumright, R., Siegwart, D.J., and Matyjaszewski, K. (2008) *Prog. Polym. Sci.*, **33**, 448–477.
8 Lyon, L.A., Meng, Z., Singh, N., Sorrell, C.D., and John, A.S. (2009) *Chem. Soc. Rev.*, **38**, 865–874.
9 Ito, S., Ogawa, K., Suzuki, H., Wang, B.L., Yoshida, R., and Kokufuta, E. (1999) *Langmuir*, **15**, 4289–4294.
10 Hayashi, H., Iijima, M., Kataoka, K., and Nagasaki, Y. (2004) *Macromolecules*, **37**, 5389–5396.

11 Pelton, R.H. and Chibante, P. (1986) *Colloids Surf.*, **20**, 247–256.
12 Hoshino, F., Fujimoto, T., Kawaguchi, H., and Ohtsuka, Y. (1986) *Polym. J.*, **19**, 241–248.
13 Hoshino, F., Kawaguchi, H., and Ohtsuka, Y. (1986) *Polym. J.*, **19**, 1157–1164.
14 Sershen, S.R., Westcott, S.L., Halas, N.J., and West, J.L. (2000) *J. Biomed. Mater. Res.*, **51**, 293–298.
15 Nayak, S. and Lyon, L.A. (2004) *Chem. Mater.*, **16**, 2623–2627.
16 Kim, J., Nayak, S., and Lyon, L.A. (2005) *J. Am. Chem. Soc.*, **127**, 9588–9592.
17 Snowden, M.J., Chowdhry, B.Z., Vincent, B.G., and Morris, E. (1996) *J. Chem. Soc. Faraday Trans.*, **92**, 5013–5016.
18 Hsiue, G.H., Hsu, S.H., Yang, C.C., Lee, S.H., and Yang, I.K. (2002) *Biomaterials*, **23**, 457–462.
19 Nayak, S., Lee, H., Chmielewski, J., and Lyon, L.A. (2004) *J. Am. Chem. Soc.*, **126**, 10258–10259.
20 Bae, Y., Jang, W.D., Nishiyama, N., Fukushima, S., and Kataoka, K. (2005) *Mol. Biosyst.*, **1**, 242–250.
21 Tamura, A., Oishi, M., and Nagasaki, Y. (2009) *Biomacromolecules*, **10**, 1818–1827.
22 Morris, G.E., Vincent, B., and Snowden, M.J. (1997) *J. Colloid Interface Sci.*, **190**, 198–205.
23 Kawaguchi, H., Kisara, K., Takahashi, T., Achiha, K., Yasui, M., and Fujimoto, K. (2000) *Macromol. Symp.*, **151**, 591–598.
24 Weissman, J.M., Sunkara, H.B., Tse, A.S., and Asher, S.A. (1996) *Science*, **274**, 959–960.
25 Debord, J.D. and Lyon, L.A. (2000) *J. Phys. Chem. B*, **104**, 6327–6331.
26 Hu, Z., Lu, X., and Gao, J. (2001) *Adv. Mater.*, **13**, 1708–1712.
27 Lyon, L.A., Debord, J.D., Debord, S.B., Jones, C.D., McGrath, J.G., and Serpe, M.J. (2004) *J. Phys. Chem. B*, **108**, 19099–19108.
28 Tsuji, S. and Kawaguchi, H. (2005) *Langmuir*, **21**, 8439–8442.
29 Suzuki, D., McGrath, J.G., Kawaguchi, H., and Lyon, L.A. (2007) *J. Phys. Chem. C*, **111**, 5667–5672.
30 Okubo, T., Suzuki, D., Yamagata, T., Katsuno, A., Sakurai, M., Kimura, H., and Tsuchida, A. (2011) *Colloid Polym. Sci.*, **289**, 291–299.
31 Antonietti, M., Gröhn, F., Hartmann, J., and Brostein, L. (1997) *Angew. Chem. Int. Ed.*, **36**, 2080–2083.
32 Zhang, J., Xu, S., and Kumacheva, E. (2004) *J. Am. Chem. Soc.*, **126**, 7908–7914.
33 Gorelikov, I., Field, L.M., and Kumacheva, E. (2004) *J. Am. Chem. Soc.*, **126**, 15938–15939.
34 Pich, A., Bhattacharya, S., Lu, Y., Boyko, V., and Adler, H.-J.P. (2004) *Langmuir*, **20**, 10706–10711.
35 Pich, A., Hain, J., Lu, Y., Boyko, V., Prots, Y., and Adler, H.-J. (2005) *Macromolecules*, **20**, 10706–10711.
36 Suzuki, D. and Kawaguchi, H. (2005) *Langmuir*, **21**, 8175–8179.
37 Suzuki, D. and Kawaguchi, H. (2005) *Langmuir*, **21**, 12016–12024.
38 Suzuki, D. and Kawaguchi, H. (2006) *Colloid Polym. Sci.*, **284**, 1443–1451.
39 Lu, Y., Mei, Y., and Ballauff, M. (2006) *Angew. Chem. Int. Ed.*, **45**, 813–816.
40 Lu, Y., Mei, Y., Ballauff, M., and Drechsler, M. (2006) *J. Phys. Chem. B*, **110**, 3930–3937.
41 Akamatsu, K., Shimada, M., Tsuruoka, T., Nawafune, H., Fujii, S., and Nakamura, Y. (2009) *Langmuir*, **26**, 1254–1259.
42 Ngai, T., Behrens, S.H., and Auweter, H. (2005) *Chem. Commun.*, **3**, 331–333.
43 Fujii, S., Read, E., Binks, B.P., and Armes, S.P. (2005) *Adv. Mater.*, **17**, 1014–1018.
44 Tsuji, S. and Kawaguchi, H. (2008) *Langmuir*, **24**, 3300–3305.
45 Brugger, B. and Richtering, W. (2008) *Langmuir*, **24**, 7769–7777.
46 Heskins, M. and Guillet, J.E. (1968) *J. Macromol. Sci. Chem.*, **A2**, 1441–1455.
47 Schild, H.G. (1992) *Prog. Polym. Sci.*, **17**, 163–249.
48 Wu, C. and Zhou, S. (1997) *Macromolecules*, **30**, 574–576.
49 Kawaguchi, H., Yamada, Y., Kataoka, S., Morita, Y., and Ohtsuka, Y. (1991) *Polym. J.*, **23**, 955–962.
50 Kawaguchi, H., Fujimoto, K., Saito, M., Kawasaki, T., and Ohtsuka, Y. (1993) *Polym. Int.*, **30**, 225–232.

51 Kamijo, Y., Fujimoto, K., Kawaguchi, H., Yuguchi, Y., Urakawa, H., and Kajiwara, K. (1996) *Polym. J.*, **28**, 309–316.
52 Sakai, T. and Yoshida, R. (2004) *Langmuir*, **20**, 1036–1038.
53 Varga, I., Szalai, I., Mészaros, R., and Gilányi, T. (2006) *J. Phys. Chem. B*, **110**, 20297–20301.
54 Suzuki, D., Sakai, T., and Yoshida, R. (2008) *Angew. Chem. Int. Ed.*, **47**, 917–920.
55 Suzuki, D., Taniguchi, H., and Yoshida, R. (2009) *J. Am. Chem. Soc.*, **131**, 12058–12059.
56 Lagzi, I., Kowalczyk, B., Wang, D., and Grzybowski, B.A. (2010) *Angew. Chem. Int. Ed.*, **49**, 8616–8619.
57 Lagzi, I., Wang, D., Kowalczyk, B., and Grzybowski, B.A. (2010) *Langmuir*, **26**, 13770–13772.
58 Rabai, G. and Beck, M.T. (1988) *J. Phys. Chem.*, **92**, 2804–2807.
59 Rabai, G. and Beck, M.T. (1988) *J. Phys. Chem.*, **92**, 4831–4835.
60 Rabai, G., Kustin, K., and Epstein, I.R. (1989) *J. Am. Chem. Soc.*, **111**, 3870–3874.
61 Mori, Y. and Hanazaki, I. (1993) *J. Phys. Chem.*, **97**, 7375–7378.
62 Rabai, G. and Hanazaki, I. (1996) *J. Phys. Chem.*, **100**, 10615–10619.
63 Crook, C.J., Smith, A., Jones, R.A.L., and Ryan, A.J. (2002) *Phys. Chem. Chem. Phys.*, **4**, 1367–1369.
64 Zaikin, A.N. and Zhabotinsky, A.M. (1970) *Nature*, **225**, 535–537.
65 Zhabotinsky, A.M. and Zaikin, A.N. (1973) *J. Theor. Biol.*, **40**, 45–61.
66 Field, R.J. and Burger, M. (1985) *Oscillations and Traveling Waves in Chemical Systems*, John Wiley & Sons, Inc., New York.
67 Epstein, I.R. and Pojman, J.A. (1998) *An Introduction to Nonlinear Chemical Dynamics: Oscillation, Waves, Patterns, and Chaos*, Oxford University Press, New York.
68 Yamaguchi, T., Kuhnert, L., Nagy-Ungvarai, Z., Mueller, S.C., and Hess, B. (1991) *J. Phys. Chem.*, **95**, 5831–5837.
69 Field, R.J., Körös, E., and Noyes, R.M. (1972) *J. Am. Chem. Soc.*, **94**, 8649–8664.
70 Field, R.J. and Noyes, R.M. (1974) *J. Chem. Phys.*, **60**, 1877–1884.
71 Yoshida, R., Ichijo, H., Hakuta, T., and Yamaguchi, T. (1995) *Macromol. Rapid Commun.*, **16**, 305–310.
72 Yoshida, R., Yamaguchi, T., and Ichijo, H. (1996) *Mater. Sci. Eng. C*, **4**, 107–113.
73 Yoshida, R., Yamaguchi, T., Yamaguchi, T., and Ichijo, H. (1996) *J. Am. Chem. Soc.*, **118**, 5134–5135.
74 Yoshida, R., Tanaka, M., Onodera, S., Yamaguchi, T., and Kokufuta, E. (1999) *J. Phys. Chem. A*, **103**, 8573–8578.
75 Yoshida, R., Takei, K., and Yamaguchi, T. (2003) *Macromolecules*, **36**, 1759–1761.
76 Maeda, S., Hara, Y., Sakai, T., Yoshida, R., and Hashimoto, S. (2007) *Adv. Mater.*, **19**, 3480–3484.
77 Maeda, S., Hara, Y., Yoshida, R., and Hashimoto, S. (2008) *Angew. Chem. Int. Ed.*, **47**, 6690–6698.
78 Dhanarajan, A.P., Misra, G.P., and Siegel, R.A. (2002) *J. Phys. Chem. A*, **106**, 8835–8838.
79 Suzuki, D. and Yoshida, R. (2008) *Macromolecules*, **41**, 5830–5838.
80 Shen, J., Pullela, S., Marquez, M., and Cheng, Z. (2007) *J. Phys. Chem. A*, **111**, 12081–12085.
81 Cadena, A., Pérez, N., Ágreda, J.A., and Barragán, D. (2005) *J. Braz. Chem. Soc.*, **16**, 214–219.
82 Suzuki, D. and Yoshida, R. (2008) *J. Phys. Chem. B*, **40**, 12618–12624.
83 Pullela, S.R., Shen, J., Marquez, M., and Cheng, Z. (2009) *J. Polym. Sci., Part B: Polym. Phys.*, **47**, 847–854.
84 Yoshida, R., Tanaka, M., Onodera, S., Yamaguchi, T., and Kokufuta, E. (2000) *J. Phys. Chem. A*, **104**, 7549–7555.
85 Zhao, F., Ding, Y., Lu, Y., Liu, X., and Zhang, G. (2009) *J. Phys. Chem. B*, **113**, 6661–6665.
86 Ruoff, P. (1995) *Physica D*, **84**, 204–211.
87 Nagy, G., Körös, E., Oftedal, N., Tjelflaat, K., and Ruoff, P. (1996) *Chem. Phys. Lett.*, **250**, 255–260.
88 Rasmusson, M., Routh, A., and Vincent, B. (2004) *Langmuir*, **20**, 3536–3542.
89 Taniguchi, H., Suzuki, D., and Yoshida, R. (2010) *J. Phys. Chem. B*, **114**, 2405–2410.
90 Suzuki, D. and Yoshida, R. (2010) *Polym. J.*, **42**, 501–508.

11
Smart Microgel/Nanoparticle Hybrids with Tunable Optical Properties

Matthias Karg and Thomas Hellweg

11.1
Introduction

Inorganic nanoparticles have been the topic of countless studies in recent decades because of their unique behavior, which comprises interesting optical [1, 2], magnetic [3, 4], and/or catalytic [5, 6] properties. While a high catalytic activity may mainly be related to the enormous surface-to-volume ratio, optical properties result from surface plasmons in the case of metal nanoparticles or from the size dependence of the band gap in semi-conductor-based systems. Hence, for example, gold and silver nanoparticles with localized plasmon resonances are found.

However, the high surface energy of nanoparticles is a disadvantage with respect to their colloidal stability. Usually nanoparticles are sensitive towards aggregation if their surface is not protected by stabilizer molecules. A broad range of stabilizers has been used in the past, including surfactants, such as oleic acid [7, 8] and cetyl trimethylammonium bromide (CTAB) [9], block copolymers [10], polyelectrolytes [9], and highly charged acids like citric acid [1].

Recently, stabilization with responsive polymers such as gel networks, spherical polyelectrolyte brushes, or block copolymers has gained increasing interest. The advantage of this kind of organic/inorganic composite is that properties of both components are combined in one material. Hence, the resulting hybrid benefits from the organic and inorganic parts. Properties such as a responsivity towards temperature or pH due to the polymer and optical, magnetic, or catalytic ones stemming from the inorganic part can be realized. This allows the design of new, multifunctional materials, which are promising for a range of different applications such as drug delivery, optical devices, and sensors. The enormous interest in organic/inorganic hybrids is also reflected by several reviews [11–18]. The use of such hybrid materials in catalysis is discussed in Chapter 2.

The present chapter reviews recent developments in the field of microgel/nanoparticle hybrid materials with optical properties. These optical properties may be plasmon resonances due to metal nanoparticles or photoluminescence from semi-conductor particles.

Hydrogel Micro and Nanoparticles, First Edition. Edited by L. Andrew Lyon and Michael Joseph Serpe.
© 2012 Wiley-VCH Verlag GmbH & Co. KGaA. Published 2012 by Wiley-VCH Verlag GmbH & Co. KGaA.

In case of metal nanoparticles with localized plasmon resonances, the plasmon energy depends strongly on the particle size [2, 19] and shape [1, 9, 20–25] and also on the refractive index of the surrounding dielectricum [26–29]. Gold and silver nanoparticles have often been studied in particular. For semi-conductor materials the emission properties depend in the first place on the band gap of the material, but also a strong size and shape dependency is found since these parameters strongly affect the confinement geometry. Frequently studied semi-conductor nanocrystals (quantum dots) are composed of cadmium selenide (CdSe), cadmium sulfide (CdS), cadmium telluride (CdTe), or zinc sulfide (ZnS) [30–34], to mention only a few examples. Quantum dots are highly sensitive to their chemical environment which affects surface defects and therefore the photoluminescence [35, 36].

The reported organic components are built of monomers such as *N*-isopropylacrylamide (NIPAM) [37–39], *N*-isopropylmethacrylamide (NIPMAM) [40, 41], *N*-vinylcaprolactam (VCL) [43], and vinylpyridine (PVP) [43, 44]. Copolymerization has also been used, employing co-monomers like acetoacetoxyethyl methacrylate (AAEM) [45], maleic acid (MA) [46, 47], allylacetic acid (AAA) [48], acrylic acid (AA) [39, 49–52], and glycidyl methacrylate (GMA) [53].

Important aspects such as synthesis, characterization, and possible applications will be briefly discussed in this chapter [54]. Moreover, different hybrid structures as well as different compositions will be covered, but only focusing on systems with dimensions in the mesoscopic size range.

The structure of the present chapter is as follows. Section 11.2 gives an overview of different synthetic routines for the preparation of organic/inorganic hybrids, followed by frequently used methods of characterization briefly presented in Section 11.3. Sections 11.4 and 11.5 review new hybrid materials with either plasmonic or photoluminescent properties. Section 11.6 gives a summary and is also devoted to the discussion of future perspectives within this field of research.

11.2
Synthesis of Hybrid Gels

Composite materials combining organic and inorganic components can be prepared in different ways. Depending on the preparation routine used, different structures can be realized. Figure 11.1 compares three frequently used methods.

A simple and rather flexible way to attach inorganic nanoparticles to polymer materials is the use of electrostatic interactions. For example, positively charged gold nanorods have been attached to oppositely charged microgel particles [47, 55, 56]. This procedure leads to microgels which are randomly covered by inorganic nanoparticles. By the mixing ratio of polymer to nanoparticle, the surface coverage can be controlled over a rather broad range [56]. This allows the optical properties of the hybrid to be tuned and also the optical response in the case of particles with a responsive polymer component. If a higher surface coverage with nanoparticles is desired, chargeable co-monomers can be incorporated into the microgel [55].

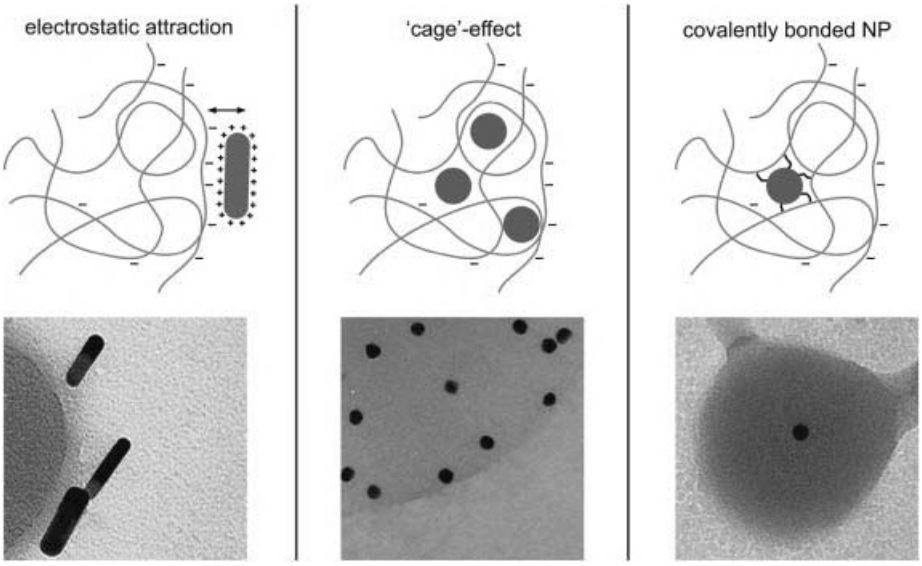

Figure 11.1 Three possible structures of organic/inorganic hybrid materials. Left: Inorganic nanoparticles are attached to organic polymers by electrostatic attraction. The TEM image shows positively charged gold nanorods on the surface of a negatively charged microgel. Middle: Inorganic nanoparticles are entrapped in meshes of a polymer network. The shown TEM example is a microgel with *in situ* grown gold nanoparticles embedded into the polymer network. Right: Inorganic nanoparticle covalently linked to a polymer network. The TEM image shows a core–shell microgel with a gold nanoparticle core.

A different approach for the preparation of hybrid materials uses the simple reduction of metal salts in the presence of polymer networks, which act as a scaffold. By this procedure, hybrid colloids with a random distribution of nanoparticles inside a polymer network can be prepared [15, 57–59]. Furthermore, the concentration of metal salt and reducing agent can be used to control the content and size of the embedded nanoparticles. It has also been shown that incorporated nanoparticles can be overgrown by either the same or a different metal [60].

While the latter approaches lead to hybrids with a rather random distribution of nanoparticles, the synthesis of core–shell systems stands out due to the unique, well-defined structure of core–shell particles. Here, we only discuss core–shell particles with inorganic cores. Particles with organic cores and responsive shells are reviewed in detail in Chapter 2.

To prepare core–shell structures with inorganic cores, functionalized nanoparticles are used as a seed particle and polymer shells are grown on the surface in a precipitation polymerization. Under appropriate synthetic conditions, core–shell hybrids with a high yield of single core particles can be prepared [61–63]. This has been shown using, for example, silica nanoparticles as a representative core material [62, 64].

In recent years, different methods of functionalizing the surface of inorganic nanoparticles in order to make them suitable for incorporation into polymer

materials have been developed. In general, the synthesis of core–shell hybrids comprises three steps: the preparation of the nanoparticles, their surface functionalization, and finally the polymerization leading to the desired composite. In addition, the inorganic core can be overgrown with control of not only size but also shape depending on the composition of the reactant solution [63, 65]. Based on such core–shell particles Singh and Lyon have shown that the nanoparticle core can be removed and a hollow capsule with a gel forming the wall can be made [66].

11.3 Characterization of Hybrid Gels

This section gives a brief overview of frequently used techniques for the characterization of the hybrid materials discussed in Section 11.2. A more detailed overview can be found in a recent review [12].

As the transmission electron microscopy (TEM) images in Figure 11.1 demonstrate, imaging methods are useful for the investigation of the structure of composites. While particles with dimensions below the micrometer scale are rather difficult to image with optical microscopes, electron microscopy is well suited for such samples. Hence, TEM and scanning electron microscopy (SEM) have often been used for the hybrids discussed within this article. Because of the large difference in electron density of metal nanoparticles and polymer components, even comparably small metal nanoparticles embedded in rather large polymers can be imaged with good resolution [67].

A different type of microscopy that is frequently used in the present field of research is atomic force microscopy (AFM) [68–73]. AFM allows samples to be imaged in a purely mechanic manner by scanning the desired sample with a probe of nanometer dimensions. This allows height profiles of the surface to be generated. AFM has been used to follow the volume phase transition of microgels under water. It is also a powerful way to image ordered two-dimensional arrangements of hybrid particles [74].

The latter microscopy techniques usually allow information on the size, shape, and polydispersity of particles to be obtained. In the case of organic/inorganic hybrids, these methods can also provide structural insights and, for example, the incorporation of inorganic nanoparticles in polymer networks can be investigated. However, microscopies give usually just an impression of a limited number of particles adsorbed on a substrate. If measures such as the size and polydispersity from an ensemble of particles are of interest, scattering methods have to be used. Dynamic light scattering (DLS) is frequently used to study the size of colloids in dispersion. Since parameters such as temperature, pH, and ionic strength of the dispersion medium can be varied easily, DLS is ideal for the investigation of the behavior of responsive systems. For example, for thermoresponsive microgels, swell curves are typically measured by DLS [75–77].

In contrast, small angle neutron scattering (SANS) and small angle X-ray scattering (SAXS) are techniques, which allow the study of structures on a local length

scale [76, 78, 79]. This is related to the much higher q-range available in experiments dealing with X-rays and neutrons, since their de Broglie wavelength is much smaller than the wavelength of lasers used in light scattering setups. Hence, light scattering is typically used to study overall particle size, while SANS and SAXS provide structural parameters in the nanometer scale. For example, SANS measurements of microgels can provide the network correlation length ξ [76, 80–83]. Moreover, SANS can be used to determine the size of inorganic cores of hybrids *in situ* if the contrast variation approach is applied [64, 74]. Internal motion inside the polymer network can be accessed using neutron spin-echo spectroscopy [84] or in the case of core–shell particles using depolarized dynamic light scattering (DDLS) [85] revealing the coupling of rotational motion with shape fluctuations.

The optical properties of hybrid particles are usually studied by UV-vis spectroscopy and/or fluorescence spectroscopy, providing absorbance and emission spectra.

11.4 Hybrid Microgels with Plasmon Properties

The physical properties of metal nanoparticles differ significantly from their bulk materials. For example, colloidal dispersions of nanoparticles of some metals (such as Cu, Ag, Au, and alkali metals) are strongly colored due to the absorption of light in the visible range. The latter phenomenon occurs when the dimensions of the individual particles are below the wavelength of visible light. Then, localized surface plasmon bands can be excited by the oscillating field of an incoming electromagnetic wave. The electromagnetic waves of the light cause a collective oscillation of electrons in the metal particles, which results in a strong absorption in a specific energy range. This unique optical property depends strongly on the size [2] and shape [1, 9, 23–25] of the metal particles. For isotropic particles, typically just one specific plasmon band is found. In the case of anisotropic particles a polarization-dependency occurs and different resonance frequencies are observed.

In addition, the energy of the plasmon resonance depends on the refractive index of the surrounding dielectric environment [26–29]. Therefore, the distance between individual metal nanoparticles is important. Below a certain distance, electronic coupling may occur and the plasmon resonance is affected. In the case of gold nanorods, much effort has been put into studying these coupling effects. Three different orientations have been found to be important: tip-to-tip, tip-to-side, and side-to-side interactions [86, 87]. Tip-to-tip interactions especially lead to remarkable changes in plasmon resonance. This was studied in gold nanorods in particular [29, 88, 89].

Most of the hybrid systems dealing with such nanoparticles presented in recent years contain either spherical gold or silver nanoparticles or gold nanorods.

In contrast to hybrids with randomly distributed metal nanoparticles and hybrids composed of polymers covered with metal nanoparticles, core–shell systems exhibit a well-defined structure.

Contreras-Cáceres *et al.* have studied a core–shell microgel with gold nanoparticle cores [65]. The authors have shown that gold nanoparticles of around 60 nm in diameter can be incorporated in a two-step protocol. The first step comprises the polystyrene coating of CTAB-stabilized gold nanoparticles. In the second step, these coated particles were added to a precipitation polymerization of the monomer NIPAM. The cores of these composites can be overgrown, leading to either spherical or branched cores with dimensions up to about 110 nm. Figure 11.2 shows UV-vis spectra for a system with spherical cores (59 nm in diameter) and with branched cores (110 nm in diameter) at different temperatures.

In addition, Figure 11.2 shows the shifts of the plasmon resonance as a function of temperature ($\Delta\lambda_{SPB}$) for core–shell microgels with spherical cores (59 nm in diameter) and different crosslinker densities of the polymer shell and for branched cores (110 nm in diameter) with 5% crosslinker. With increasing crosslinker density the magnitude of the shift decreases. The authors suggest possible applications of these core–shell microgels for quantitative analysis through sensing techniques such as surface-enhanced Raman scattering (SERS), as materials for the construction of photonic crystals, and for drug-delivery systems.

Another way to incorporate metal nanoparticles into a polymer network is the *in situ* reduction of metal salts in the presence of a polymer template. Microgels with different contents of gold nanoparticles were prepared by Pich *et al.* [90]. The authors have shown that the optical properties of the material depend strongly on the content of inorganic particles. Figure 11.3 displays a UV-vis spectrum of a pure poly(*N*-vinylcaprolactam–acetoxyethyl methacrylate) microgel and, in comparison, the spectra of microgels with gold contents from 1.5 to 15.2%. While the pure microgel shows no features in the absorbance spectrum except for the increase of absorbance towards

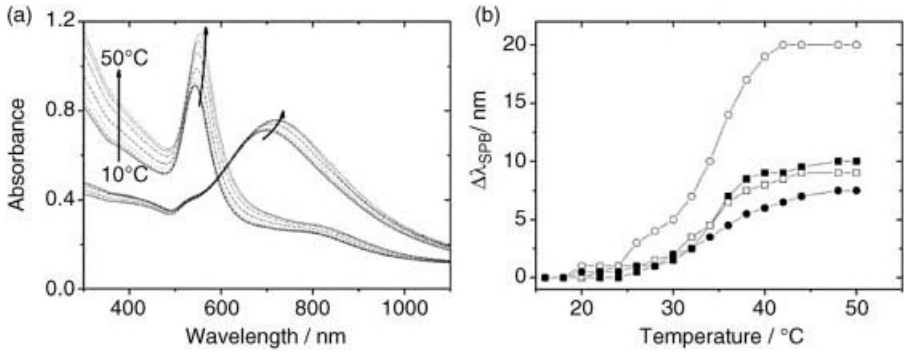

Figure 11.2 Gold–PNIPAM core–shell microgels. (a) UV-vis spectra of Au–PNIPAM hybrid microgels measured at different temperatures in a range of 10–50 °C. Spectra with maximum at about 540 nm: spherical cores with a diameter of 59 nm. Spectra with a maximum at about 700 nm: flower-like branched cores with a diameter of 110 nm. (b) Shifts of the surface plasmon band with the position at 15 °C (swollen state) as reference state. Filled rectangles: 5% BIS, open rectangles: 10% BIS, filled circles: 17.5% BIS for Au–PNIPAM with 59 nm spherical cores. Open circles: 5% BIS for branched, 110 nm cores. Reprinted with permission from [65]. Copyright (2009) Wiley-VCH.

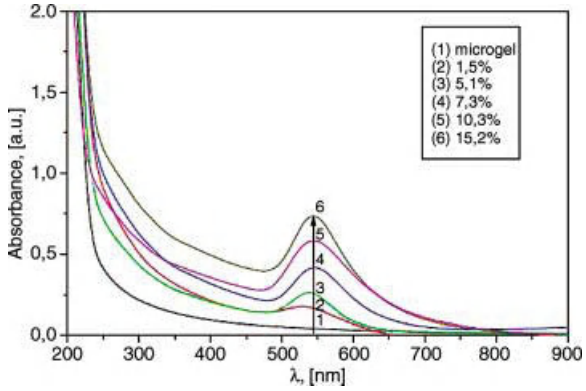

Figure 11.3 UV-vis spectra of hybrid microgels with different contents of Au. The polymer component is made of *N*-vinylcaprolactam (VCL) and acetoacetoxyethyl methacrylate (AAEM). Reproduced with permission from [90].

lower wavelength, which is caused by scattering, the composites show the typical resonance of gold nanoparticles (here around 540 nm). With increasing gold contents the plasmon resonance becomes more pronounced.

A similar approach has been used by Suzuki *et al.*, who incorporated multishell metal nanoparticles into thermoresponsive microgel particles [60]. First, gold nanoparticles were prepared *in situ* using a microgel as a template and then, in a second step, the gold particles were overgrown either with gold or with silver. In case of the silver-coated gold particles also a further overgrowing step with gold has been done, resulting in a Au/Ag/Au bimetallic multishell system. This approach results in composite microgels with adjustable optical properties, as the UV-vis spectra in Figure 11.4 show.

It has been suggested that these hybrid microgels are suitable for applications in biomedical and electronic devices.

As already mentioned before, rod-like nanoparticles are also of great interest for the preparation of hybrid materials (Figure 11.5). Das *et al.* presented a hybrid system with well-pronounced plasmon absorption obtained from gold nanorod-covered microgel particles [47]. In this work the idea was to use the plasmon absorption of the gold particles to transfer heat to the microgel carrier and this way to drive the deswelling transition. Such a material might be useful for drug-delivery applications.

Karg *et al.* investigated a similar system, which consists of PNIPAM microgels covered with polyelectrolyte-coated gold nanorods (Au-rods–PSS–PAH) [56]. In this study the microgel collapse is used to change the band position of the plasmon band of the rods. The longitudinal plasmon band in particular is found to be very sensitive with respect to changes in the degree of swelling of the carrier microgel. The microgel collapse can induce a shift in the position of the maximum of this band of up to 26 nm. An even more pronounced temperature-induced effect can be obtained when charged NIPAM copolymer microgels are used [55]. In addition, such hybrids show a responsivity towards changes of solution pH. Figure 11.6 shows the position of the

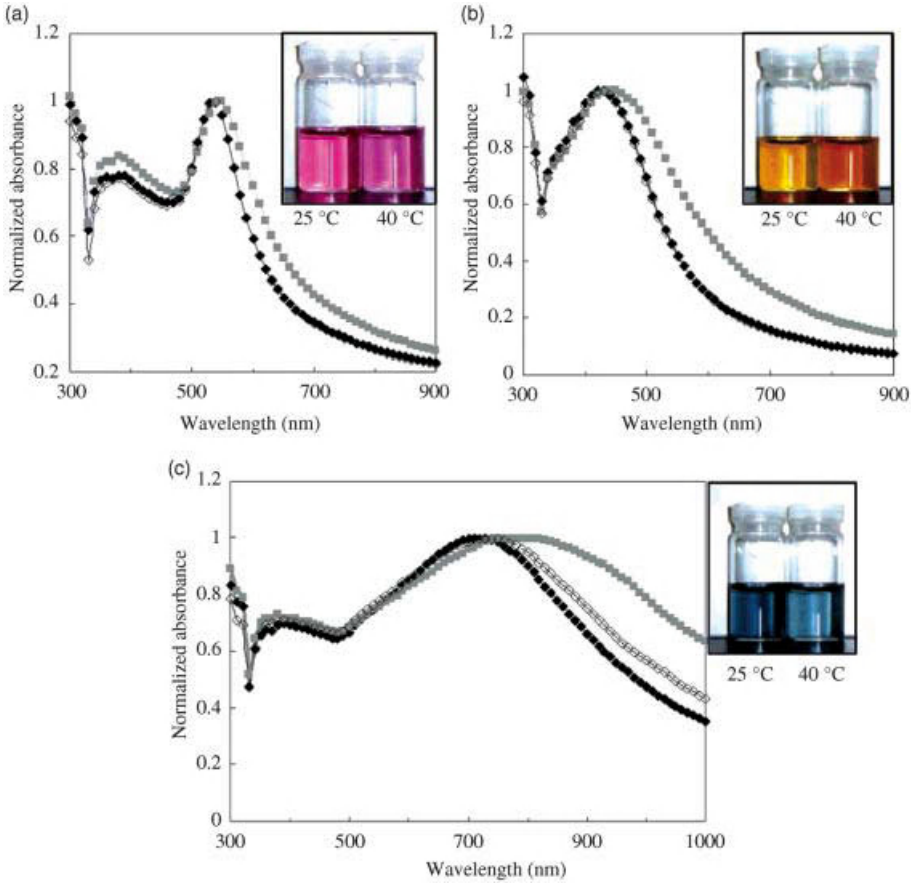

Figure 11.4 UV-vis spectra and photographs of composites of multishell nanoparticles and copolymer microgels made of NIPAM and glycidyl methacrylate (GMA). (a) Hybrid with gold-overgrown gold nanoparticles (Au/Au2). (b) Hybrid with silver–overgrown gold nanoparticles (Au/Ag). (c) Hybrids with gold–silver–gold nanoparticles (Au/Ag/Au). The spectra were recorded at 25 °C (filled diamonds) and 40 °C (open diamonds) and at 25 °C after 10 heating–cooling cycles (gray squares) [60]. Reprinted with permission from D. Suzuki and H. Kawaguchi, *Langmuir*, 22 (2006) 3818. Copyright (2006) American Chemical Society.

longitudinal plasmon band at pH 8 and pH 10 at three given temperatures for a copolymer system with 10 mol% allylacetic acid as co-monomer.

The results show that a small change in pH can lead to a remarkable shift of the plasmon band. These shifts are mainly related to interparticle coupling between the nanorods adsorbed on the microgels, which increases when the microgel core collapses and the surface area decreases dramatically. In consequence this leads to a decreasing interparticle distance between the gold nanorods. Based on these works Lu *et al.* recently reported the preparation of microgels filled with bimetallic nanorods consisting of gold with platinum tips [91]. The materials obtained are shown in Figure 11.7.

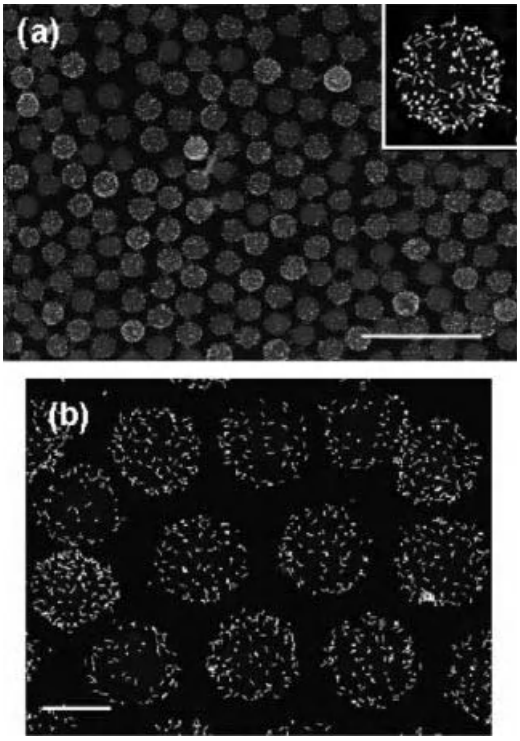

Figure 11.5 TEM images of different gold nanorod-covered microgels. (a) Poly-(*N*-isopropylacrylamide-*co*-maleic acid) microgels. The scale bar is 2 μm and the inset shows a magnification of a single hybrid particle. (b) Poly-(*N*-isopropylacrylamide-*co*-*N*-isopropylmethacrylamide)/poly-(acrylic acid) microgels with an interpenetrating network structure. The scale bar is 400 nm [47]. Reprinted with permission from M. Das, N. Sanson, D. Fava, and E. Kumacheva, *Langmuir*, 23 (2007) 196. Copyright (2007) American Chemical Society.

These particles seem to have interesting catalytic activity and also exhibit temperature-dependent shifts of the plasmon band positions upon shrinkage of the microgel core.

Silver nanoparticles also exhibit interesting optical properties [92]. In this context Pich *et al*. prepared new hybrid microgels with different contents of Ag nanoparticles by reduction of Ag^+ in the presence of poly(*N*-vinylcaprolactam-*co*-acetoacetoxyethyl methacrylate) (VCL–AAEM) microgel particles [93]. Figure 11.8a shows that the hydrodynamic dimensions of these hybrids depend strongly on the Ag nanoparticle content. Furthermore, it is shown that the responsive character of the particles decreases with increasing Ag nanoparticle content (Figure 11.8b).

The authors also studied the optical properties of films prepared from these hybrid microgels. UV-vis spectra show a well-pronounced plasmon resonance around 400 nm. The intensity of this plasmon band increases with increasing content of Ag nanoparticles in the microgels. Such films are suggested to be useful for

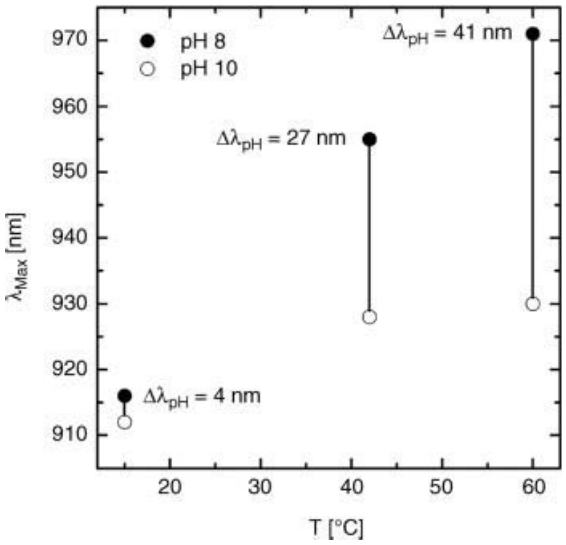

Figure 11.6 Position of the longitudinal plasmon band of poly(*N*-isopropylacrylamide-co-allylacetic acid) microgels covered with gold nanorods as a function of dispersion pH at three different temperatures. $\Delta\lambda_{pH}$ represents the difference in plasmon band position for pH 8 and pH 10 at a given temperature [55]. Reprinted with permission from M. Karg *et al.*, *Langmuir*, 25 (2009) 3163. Copyright (2009) American Chemical Society.

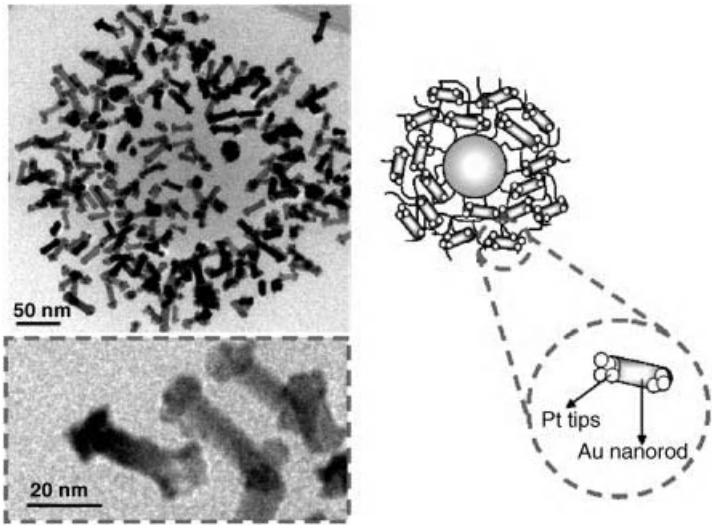

Figure 11.7 Cryo-TEM image of a polystyrene–PNIPAM core–shell microgel, where gold nanorods with Pt tips were grown inside the PNIPAM shell. The enlarged image shows the grown Pt tips in more detail [91]. Reprinted with permission from Y. Lu, J. Juan, F. Polzer, M. Drechsler, and J. Preussner, *ACS Nano*, 4 (2010) 7078. Copyright (2010) American Chemical Society.

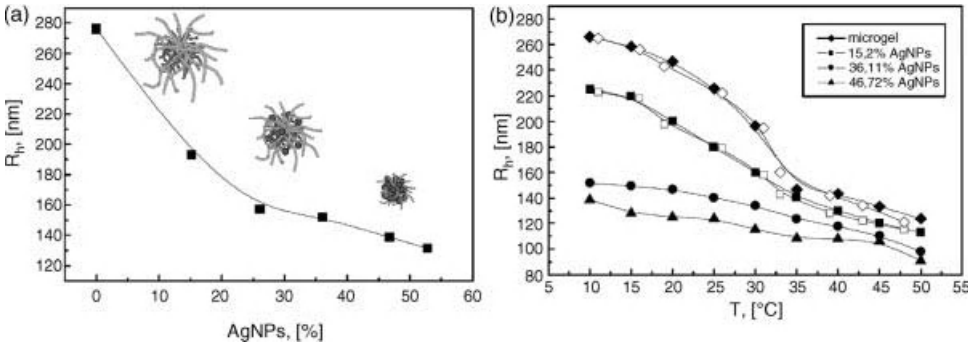

Figure 11.8 Results from DLS measurements on hybrid microgels with different contents of Ag nanoparticles. (a) Hydrodynamic radii at 10 °C. (b) Temperature evolution of the hydrodynamic radii. The filled symbols represent the heating run, whereas open symbols are the cooling run. Reproduced with permission from [93]. Copyright (2006) Wiley-VCH.

applications such as the fabrication of anti-inflammatory films for fast wound healing. Furthermore, the authors refer to potential applications of these hybrid microgels as smart catalysts and in medical use due to the antibacterial behavior of silver.

Contreras-Cáceres *et al*. have shown that core–shell hybrid microgels with spherical and rod-shaped Au cores can be used for the preparation of silver-coated gold nanoparticles inside a microgel network [94]. The cores were initially pure gold and could then be overgrown with either gold or silver. In Figure 11.9 the absorption spectra of these particles are presented for two temperatures.

Also in this case the observed plasmon spectra are shifting upon microgel collapse. In the same study the authors show that rod-like gold particles with silver coating in particular provide good amplification in SERS experiments and are well suited for *in situ* sensing of spurious amounts of chemicals.

Rodríguez-Fernández *et al*. have recently extended the approach of Das *et al*. [47]. In this work a single gold nanorod is used as core for the microgel synthesis. This core can afterwards be used to generate heat inside the hybrid using irradiation with a laser close to the adsorption maximum of the longitudinal plasmon band [95].

Figure 11.10 shows UV-vis/NIR spectra of the sample with and without laser illumination. It is obvious that the illumination-induced collapse of the PNIPAM shell leads to a shift of the absorption band position. A similar approach for light-induced changes in hybrid microgels was presented by Jones *et al*. in 2003 [96].

Hematite ellipsoids have also been incorporated into core–shell microgels [97]. Again, these particles have an intrinsic optical anisotropy, but in addition allow the interaction with the light to be controlled using external magnetic fields.

Besides PNIPAM-based systems, very few other polymers have been used for the preparation of hybrid microgels. One example is the recently published work by Akamatsu *et al*., who developed a composite microgel composed of lightly cross-linked poly-vinyl-2-pyridine (P2VP) and spherical gold nanoparticles [98]. The gold particles were prepared *in situ* by reduction of microgels doped with Au^{3+} ions using

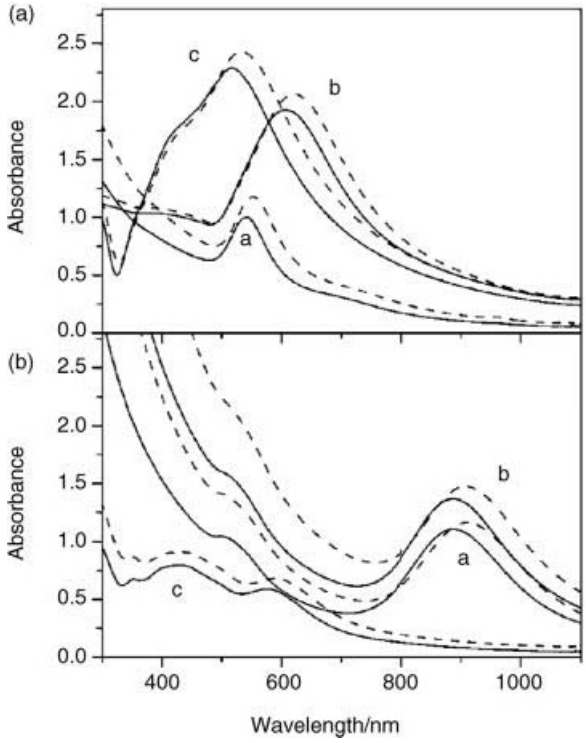

Figure 11.9 UV-vis-NIR absorption spectra of metal–PNIPAM core–shell particles in the swollen state, at 22 °C (solid lines) and in the collapsed state, at 44 °C (dashed lines). (A) Spherical cores: (a) 64 nm gold cores, (b) 103 nm gold cores, and (c) 100 nm Au–Ag core–shell spherical cores. (B) Rod-shaped cores: (a) gold nanorods, (b) overgrown gold nanorods, and (c) silver-coated gold nanorods. Reproduced with permission from [94]. Copyright (2010) Wiley-VCH.

dimethylamineborane (DMAB) as reducing agent. By the dropping-rate during the DMAB addition the authors were able to tune the size of the gold nanoparticles embedded in the microgel network to around 10–30 nm in diameter. The control in size which can be achieved by this method is in the range of a few tens of nanometers. Since the plasmon properties of gold nanoparticles are strongly size-dependent, the above mentioned controlled growing allows the optical properties of the final composites to be tuned with high precision. As well as the plasmonic properties of the Au–P2VP hybrids, a pH-responsive character is also found. The P2VP microgels swell at low pH (electrostatic repulsion), whereas they collapse at higher pH, where the pyridine functionalities are not protonated. This response to pH also influences the optical properties of the hybrid microgels. This is shown in Figure 11.11 where UV-vis spectra at two different pH values are compared for two composite systems with differently sized gold nanoparticles. At pH 8, when the microgel network is in the collapsed state, the interparticle distance between the

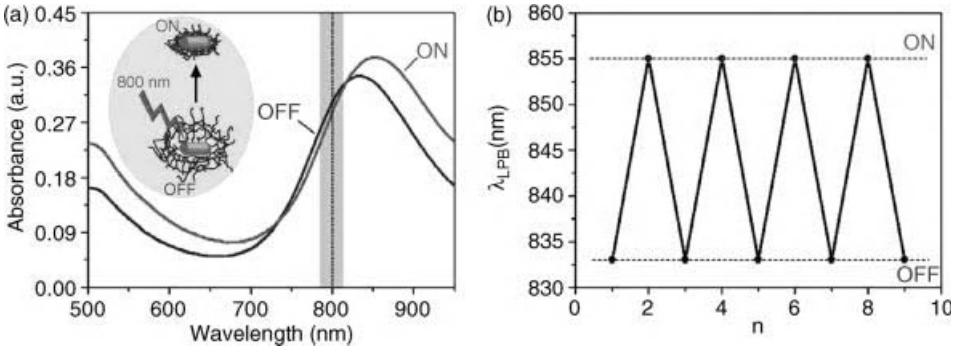

Figure 11.10 (a) Extinction spectra in the vis-NIR of gold nanorod–PNIPAM core–shell particles without (blue spectrum) and with (red spectrum) illumination with a continuous wave laser ($\lambda = 800$ nm, 880 kW cm^{-2}). (b) Response of the longitudinal plasmon band of the gold nanorod cores as a function of laser on and off events. Reproduced with permission from [95]. Copyright (2011) IOP Publishing.

individual metal nanoparticles is lowered significantly, leading to a well-pronounced redshift and broadening of the plasmon band.

These changes in the optical properties can be related to electronic coupling between the gold nanoparticles, which are close together. Because of this responsive behavior, the authors suggest that the presented material is suitable for materials employed in optical and biomedical applications.

A more quantitative description of the typical spectra from nanoparticle/microgel hybrids is given in [99]. In this study gold-PNIPAM core–shell particles were prepared with different shell thicknesses and different crosslinker concentrations. The optical properties were investigated by means of UV-vis spectroscopy. The scattering contribution from the PNIPAM carrier microgel is for the first time subtracted from absorption spectra, leading to spectra of the gold cores embedded in the refractive index matrix of the PNIPAM shell. This allows the molar mass of the core–shell particles to be calculated from simple UV-vis measurements.

11.5
Photoluminescent Hybrid Microgels

If semi-conductor nanoparticles are used as the inorganic component for the preparation of composites, materials with fluorescence properties can be obtained. Figure 11.12 shows fluorescence spectra (inset) of hybrid microgels with lanthanide nanoparticles. These composites were prepared by embedding europium-doped lanthanum fluoride (LaF_3:Eu) nanoparticles in poly(*N*-vinylcaprolactam-*co*-glycidyl methacrylate) (P(VCL-co-GMA)) microgels [53] with various contents of GMA. The microgel template used shows a thermoresponsive behavior due to the VCL and is considered to have a core–shell structure due to the much higher polymerization rate of the GMA. The authors claim that the microgels consist of a reactive

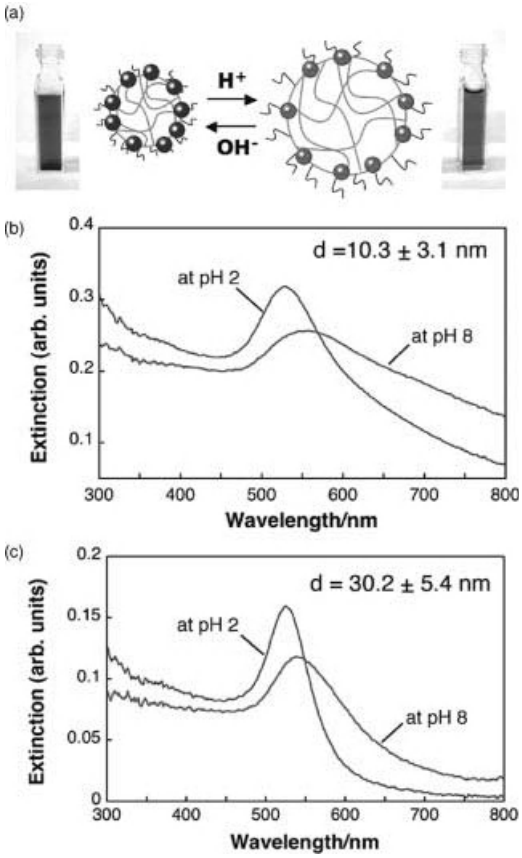

Figure 11.11 Composite microgels of lightly crosslinked polyvinylpyridine and gold nanoparticles. (a) Photographs and schemes of the composites at pH 8 (left) and pH 2 (right). (b) and (c) UV-vis spectra at pH 2 and pH 8 of composite microgels with different-sized gold nanoparticles. The respective size of the gold particles is indicated in the figures [98]. Reprinted with permission from K. Akamatsu *et al.*, *Langmuir*, 26 (2010) 1254. Copyright (2010) American Chemical Society.

GMA-rich core and a thermoresponsive VCL-rich shell. Different contents of GMA were investigated and the possible uptake of *in situ* deposited LaF_3:Eu nanoparticles was studied. The authors found that a lower GMA content leads to a higher content of inorganic material in the final hybrid system. This behavior is represented in Figure 11.12, where the peak area of the fluorescence signal ($\lambda = 612$ nm) is plotted against the GMA content.

The peak area clearly decreases with increasing GMA content, which indicates a lower content of lanthanides. Therefore, the authors expect the lanthanide particles to be localized preferably in the outer shell of the particles. This is also confirmed by light scattering and electron microscopy data.

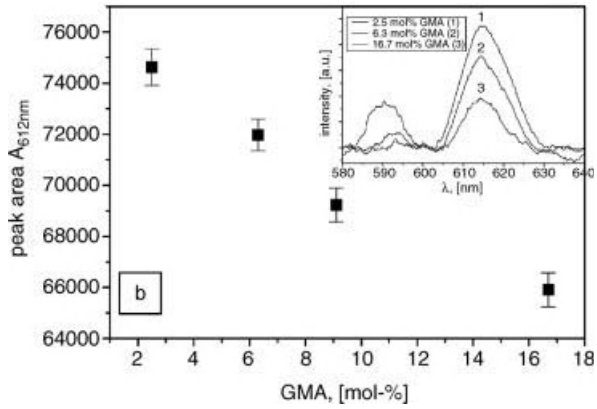

Figure 11.12 Hybrid microgels made of vinylcaprolactam (VCL) and glycidyl methacrylate (GMA) filled with lanthanide nanoparticles (LaF_3:Eu): Peak area calculated from the fluorescence spectra shown in the inset [53]. Reprinted with permission from N. Häntzschel *et al.*, *Langmuir*, 23 (2007) 10793. Copyright (2007) American Chemical Society.

Agrawal *et al.* covered PNIPAM microgels with CdTe nanocrystals [36]. The structure of the resulting system can be compared to the hybrids presented by Karg *et al.* and Das *et al.* in the previous section. While these authors investigated systems containing gold nanorods, which are attached to the microgel surface by charge interaction, the CdTe nanocrystals in the study of Agrawal *et al.* were covalently bond to the microgel surface. Figure 11.13 shows the intensity of the photoluminescence of the hybrid particles as a function of temperature.

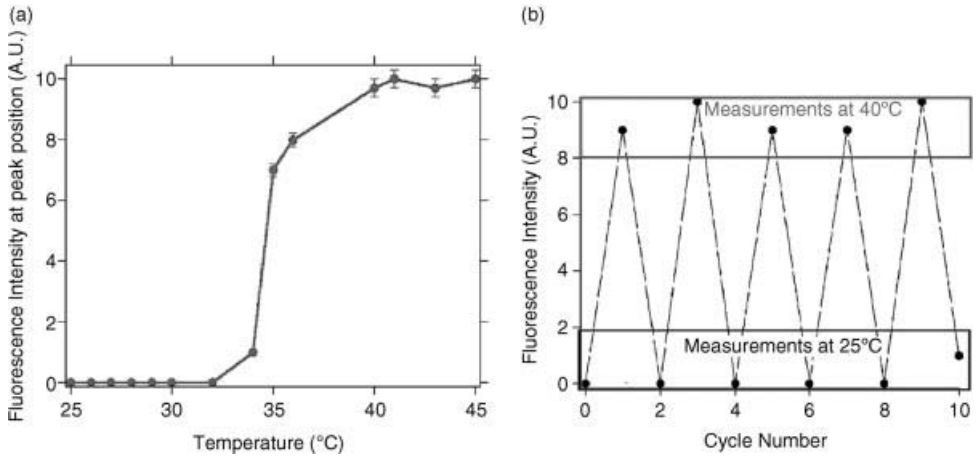

Figure 11.13 Photoluminescence intensities of PNIPAM microgels covered with CdTe nanocrystals. (a) Photoluminescence intensity at 620 nm as a function of temperature. (b) Photoluminescence intensities during a series of alternating cooling and heating steps [36]. Reprinted with permission from M. Agrawal *et al.*, *Langmuir*, 24 (2008) 9820. Copyright (2008) American Chemical Society.

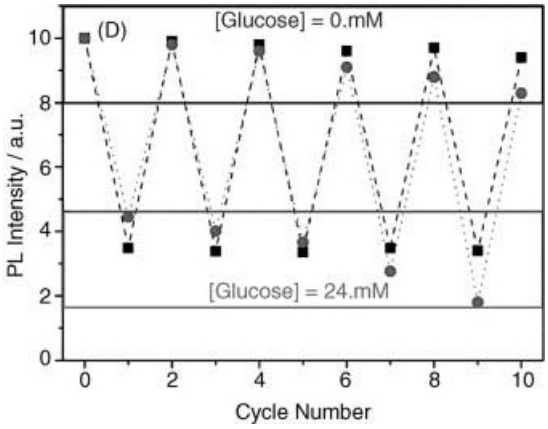

Figure 11.14 Glucose response of CdS quantum dot-loaded poly(NIPAM–acrylamide-2-acrylamidomethyl–5-fluorophenylboronic acid) copolymer microgels. The quenching and recovery of the photoluminescence of the CdS particles upon addition and removal of glucose (24.3 mM) is shown. Reprinted with permission from [100]. Copyright (2010) Elsevier B.V.

The temperature dependence of the photoluminescence shown in the left of Figure 11.13 nicely resembles the swelling behavior of the pure microgel used as core material for the hybrid preparation. The photoluminescence remains constant between 25 and 32 °C and then increases strongly until 40 °C. Alternating measurements between 25 and 40 °C (right image of Figure 11.13) demonstrate that this responsivity is reproducible. In other words, the presented hybrid system shows reversibly switchable luminescence.

Wu *et al.* have shown that the change in luminescence of microgel-borne CdS quantum dots can be used for sensing applications [100]. They have prepared glucose-sensitive copolymer microgels and the glucose binding is monitored by quenching of the emission of CdS quantum dots, which are incorporated in the microgels. Figure 11.14 shows the reversibilty of this quenching process.

11.6 Summary

Microgel/inorganic hybrid materials with well-pronounced optical absorption or emissions have been a hot research topic in recent years. As well as the preparation of new systems combining responsive polymer networks with inorganic nanoparticles, their characterization has also been a key aspect of several publications. A growing number of potential applications of these materials have been explored recently.

This chapter intended to give a brief overview of recent developments in the synthesis and characterization of hybrid materials with interesting optical properties.

Depending on the composition of the inorganic component either plasmonic or photoluminescence properties were achieved. At present research focuses mainly on two effects:

- The content of inorganic material in the organic/inorganic hybrid: In general, the optical properties become more pronounced with an increasing content of inorganic nanoparticles. Some authors have shown that the possible uptake of inorganic nanoparticles by the polymer component depends on the composition of the polymer.
- The change of optical properties as a function of an external stimulus for responsive hybrid systems: Depending on the size and shape of the incorporated nanoparticle, strong shifts of the absorbance/fluorescence behavior in terms of wavelength and intensity are observed.

The changes of optical properties induced by an external stimulus can be related to two effects:

- a change of the refractive index of the surrounding medium, for example caused by the collapse of a responsive polymer network surrounding the nanoparticle; and
- electronic interactions between individual nanoparticles, which appear when the distance between the particles is small enough.

The potential applications of the systems presented within this chapter range from biological and medical applications to their use as sensor material and for the design of electronic or optical devices. However, the possibilities arising from the combination of microgels with nanoparticles are still far from being fully exploited.

Some of the future perspectives are discussed below. The steady interest in the preparation of new multifunctional materials can be related to the increasing requirements for application purposes. Especially for biological or medical applications, strong requirements have to be fulfilled. For example, drug-delivery systems require biocompatibility and systems with sensitive/switchable properties which are appropriate for the conditions found in the human body.

From our point of view an important future challenge will be the combination of synthetic nanoparticle/microgel hybrids with biological building blocks (e.g., immunoglobulins). Also the use of hybrids inside living cells to monitor the microenvironment will be of great interest. Besides this, applications related to the use of surface-enhanced Raman scattering for sensing are very promising.

Acknowledgments

The authors acknowledge funding from the Deutsche Forschungsgemeinschaft within the framework of SFB840 TP A4. I. Pastoriza-Santos, J. Pérez-Juste and L. M. Liz-Marzán are acknowledged for fruitful collaboration within the last years. M.K. is grateful to the Alexander von Humboldt foundation for a Feodor-Lynen research fellowship.

References

1 Enüstün, B.V. and Turkevich, J. (1963) Coagulation of colloidal gold. *J. Am. Chem. Soc.*, **85**, 3317–3328.

2 Pérez-Juste, J., Pastoriza-Santos, I., Liz-Marzán, L.M., and Mulvaney, P. (2005) Gold nanorods: Synthesis, characterization and applications. *Coord. Chem. Rev.*, **249**, 1870–1901.

3 Shavel, A., Rodríguez-González, B., Spasova, M., Farle, M., and Liz-Marzán, L.M. (2007) Synthesis and characterization of iron/iron oxide core/shell nanocubes. *Adv. Funct. Mater.*, **17**, 3870–3876.

4 Guardia, P., Pérez, N., Labarta, A., and Batlle, X. (2010) Controlled synthesis of iron oxide nanoparticles over a wide size range. *Langmuir*, **26**, 5843–5847.

5 Carregal-Romero, S., Pérez-Juste, J., Hervés, P., Liz-Marzán, L.M., and Mulvaney, P. (2009) Colloidal gold-catalyzed reduction of ferrocyanate (III) by borohydride ions: A model system for redox catalysis. *Langmuir*, **26**, 1271–1277.

8 Mei, Y., Lu, Y., Polzer, F., Ballauff, M., and Drechsler, M. (2007) Catalytic activity of palladium nanoparticles encapsulated in spherical polyelectrolyte brushes and core-shell microgels. *Chem. Mater.*, **19**, 1062–1069.

9 Bao, Y., An, W., Turner, C.H., and Krishnan, K.M. (2009) The critical role of surfactants in the growth of cobalt nanoparticles. *Langmuir*, **26** (1), 478–483.

10 van Embden, J. and Mulvaney, P. (2005) Nucleation and growth of CdSe nanocrystals in a binary ligand system. *Langmuir*, **21**, 10226–10233.

11 Pastoriza-Santos, I., Pérez-Juste, J., and Liz-Marzán, L.M. (2006) Silica-coating and hydrophobation of CTAB-stabilized gold nanorods. *Chem. Mater.*, **18**, 2465–2467.

10 Boyer, C., Whittaker, M.R., Chuah, K., Liu, J., and Davis, T.P. (2010) Modulation of the surface charge on polymer-stabilized gold nanoparticles by the application of an external stimulus. *Langmuir*, **26** (4), 2721–2730.

11 Lu, Y. and Ballauff, M. (2011) Thermosensitive core-shell microgels: From colloidal model systems to nanoreactors. *Prog. Polym. Sci.*, **26**, 767–792.

12 Karg, M. and Hellweg, T. (2009) New smart poly(NIPAM) microgels and nanoparticle microgel hybrids: Properties and advances in characterisation. *Curr. Opin. Colloid Interface Sci.*, **14**, 438–450.

13 Karg, M. and Hellweg, T. (2009) Smart inorganic/organic hybrid microgels: Synthesis and characterisation. *J. Mater. Chem.*, **19**, 8714–8715.

14 Nayak, S. and Lyon, L.A. (2005) Soft nanotechnology with soft nanoparticles. *Angew. Chem. Int. Ed.*, **44**, 7686–7708.

15 Ballauff, M. (2007) Spherical polyelectrolyte brushes. *Prog. Polym. Sci.*, **32**, 1135–1151.

16 Pich, A.Z. and Adler, H.J.P. (2007) Composite aqueous microgels: an overview of recent advances in synthesis, characterization and application. *Polym. Int.*, **56**, 291–307.

17 Das, M., Zhang, H., and Kumacheva, E. (2006) Microgels: Old materials with new applications. *Annu. Rev. Mater. Res.*, **36**, 117–142.

18 Schmidt, A.M. (2007) Thermoresponsive magnetic colloids. *Colloid Polym. Sci.*, **285**, 953–966.

19 Sánchez-Iglesias, A., Pastoriza-Santos, I., Pérez-Juste, J., Rodriguez-González, B., de Abajo, F.J.G., and Liz-Marzán, L.M. (2006) Synthesis and optical properties of gold nanodecahedra with size control. *Adv. Mater.*, **18**, 2529–2534.

20 Harris, N., Ford, M.J., Mulvaney, P., and Cortie, M.B. (2008) Tunable infrared absorption by metal nanoparticles: The case for gold rods and shells. *Gold Bull.*, **41**, 5–14.

21 Grzelczak, M., Pérez-Juste, J., Mulvaney, P., and Liz-Marzán, L. (2008) Shape control in gold nanoparticle synthesis. *Chem. Soc. Rev.*, **37**, 1783–1791.

22 Grzelczak, M., Sánchez-Iglesias, A., Rodríguez-González, B., Alvarez-Puebla, R., Pérez-Juste, J., and Liz-Marzán, L. (2008) Influence of iodide ions on the growth of gold nanorods: Tuning tip curvature and surface plasmon resonance. *Adv. Funct. Mater.*, **18**, 616–621.

23 Lofton, C. and Sigmund, W. (2005) Mechanisms controlling crystal habits of gold and silver colloids. *Adv. Funct. Mater.*, **15**, 1197–1208.

24 Maldovan, M., Urbas, A.M., Yufa, N., Carter, W.C., and Thomas, E.L. (2002) Photonic properties of bicontiuous cubic microphases. *Phys. Rev. B*, **65** (16), 165 123/1-5.

25 Nehl, C.L., Liao, H., and Hafner, J.H. (2006) Optical properties of star-shaped gold nanoparticles. *Nano Lett.*, **6**, 683–688.

26 Novo, C., Funston, A.M., Pastoriza-Santos, I., Liz-Marzán, L.M., and Mulvaney, P. (2008) Influence of the medium refractive index on the optical properties of single gold triangular prisms on a substrate. *J. Phys. Chem. C*, **112**, 3–7.

27 Liz-Marzán, L.M., Giersig, M., and Mulvaney, P. (1996) Synthesis of nanosized gold-silica core-shell particles. *Langmuir*, **12**, 4329–4335.

28 Mulvaney, P. (1996) Surface plasmon spectroscopy of nanosized metal particles. *Langmuir*, **12**, 788–800.

29 Sudeep, P.K., Joseph, S.T.S., and Thomas, K.G. (2005) Selective detection of cysteine and glutathione using gold nanorods. *J. Am. Chem. Soc.*, **127**, 6516–6517.

30 Bullen, C.R. and Mulvaney, P. (2004) Nucleation and growth kinetics of CdSe nanocrystals in octadecene. *Nano Lett.*, **4** (12), 2303–2307.

31 Danek, M., Jensen, K.F., Murray, C.B., and Bawendi, M.G. (1996) Synthesis of luminescent thin-film CdSe/ZnSe quantum dot composites using CdSe quantum dots passivated with an overlayer of ZnSe. *Chem. Mater.*, **8** (1), 173–180.

32 Talapin, D.V., Rogach, A.L., Kornowski, A., Haase, M., and Weller, H. (2001) Highly luminescent monodisperse CdSe and CdSe/ZnS nanocrystals synthesized in a hexadecylamine-trioctylphosphine oxide-trioctylphospine mixture. *Nano Lett.*, **1** (4), 207–211.

33 Yu, W.W. and Peng, X. (2002) Formation of high-quality CdS and other II-VI semiconductor nanocrystals in noncoordinating solvents: Tunable reactivity of monomers. *Angew. Chem. Int. Ed.*, **41** (13), 2368–2371.

34 Yu, W.W., Qu, L., Guo, W., and Peng, X. (2003) Experimental determination of the extinction coefficient of CdTe, CdSe, and CdS nanocrystals. *Chem. Mater.*, **15**, 2854–2860.

35 Gaponik, N., Talapin, D.V., Rogach, A.L., Hoppe, K., Shevchenko, E.V., Kornowski, A., Eychmüller, A., and Weller, H. (2002) Thiol-capping of CdTe nanocrystals: An alternative to organometallic synthetic routes. *J. Phys. Chem. B*, **106**, 7177–7185.

36 Agrawal, M., Rubio-Retama, J., Zafeiropoulos, N.E., Gaponik, N., Gupta, S., Cimrova, V., Lesnyak, V., Lopez-Cabarcos, E., Tzavalas, S., Rojas-Reyna, R., Eychmüller, A., and Stamm, M. (2008) Switchable photoluminescence of CdTe nanocrystals by temperature-responsive microgels. *Langmuir*, **24**, 9820–9824.

37 Pelton, R.H. and Chibante, P. (1986) Preparation of aqueous latices with N-isopropylacrylamide. *Colloids Surf.*, **20**, 247–256.

38 Pankasem, S., Thomas, J.K., Snowden, M.J., and Vincent, B. (1994) Photophysical studies of poly(N-isopropylacrylamide) microgel structures. *Langmuir*, **10**, 3023–3026.

39 Kim, J., Serpe, M.J., and Lyon, L.A. (2004) Hydrogel microparticles as dynamically tunable microlenses. *J. Am. Chem. Soc.*, **126**, 9512–9513.

40 Duracher, D., Elaissari, A., and Pichot, C. (1999) Characterization of cross-linked poly(N-isopropylmethacrylamide) microgel latexes. *Colloid Polym. Sci.*, **277**, 905–913.

41 Berndt, I. and Richtering, W. (2003) Doubly temperature sensitive core-shell microgels. *Macromolecules*, **36**, 8780–8785.

42 Pich, A., Lu, Y., Boyko, V., Arndt, K.F., and Adler, H.J.P. (2003) Thermo-sensitive poly(N-vinylcaprolactam-co-acetoacetoxyethyl methacrylate) microgels: 2. incorporation of polypyrrole. *Polymer*, **44**, 7651–7659.

43 Fernandez-Nieves, A., Fernandez-Barbero, A., and de las Nieves, F.J. (2001) Salt effects over the swelling of ionized mesoscopic gels. *J. Chem. Phys.*, **115** (16), 7644–7649.

44 Chen, Q., Shen, X.H., and Gao, H.C. (2006) One-step synthesis of silver-poly (4-vinylpyridine) hybrid microgels by gamma-irradiation and surfactant-free emulsion polymerization. *Acta Polym. Sin.*, (5), 722–726.

45 Pich, A., Lu, Y., Boyko, V., Arndt, K.F., and Adler, H.J.P. (2004) Thermo-sensitive poly(N-vinylcaprolactam-co-acetoacetoxyethyl methacrylate) microgels: 3. incorporation of polypyrrole by selective microgel swelling in ethanol–water mixtures. *Polymer*, **45**, 1079–1087.

46 Frank, R.S., Downey, J.S., Yu, K., and Stöver, H.D.H. (2002) Poly (divinylbenzene-alt-maleic anhydride) microgels: Intermediates to microspheres and macrogels in cross-linking copolymerization. *Macromolecules*, **35**, 2728–2735.

47 Das, M., Sanson, N., Fava, D., and Kumacheva, E. (2007) Microgels loaded with gold nanorods: Photothermally triggered volume phase transition under physiological conditions. *Langmuir*, **23**, 196–201.

48 Karg, M., Pastoriza-Santos, I., Rodriguez-González, B., von Klitzing, R., Wellert, S., and Hellweg, T. (2008) Temperature, pH, and ionic strength induced changes of the swelling behavior of PNIPAM-poly(allylacetic acid) copolymer microgels. *Langmuir*, **24** (12), 6300–6306.

49 Snowden, M.J., Chowdhry, B.Z., Vincent, B., and Morris, G.E. (1996) Colloidal copolymer microgels of N-isopropylacrylamide and acrylic acid: pH, ionic strength and temperature effects. *J. Chem. Soc., Faraday Trans.*, **92** (24), 5013–5016.

50 Kim, J.H. and Ballauff, M. (1999) The volume transition in thermosensitive core-shell latex particles containing charged groups. *Colloid Polym. Sci.*, **277**, 1210–1214.

51 Kratz, K., Hellweg, T., and Eimer, W. (1998) Effect of connectivity and charge density on the swelling and local structural properties of colloidal PNIPA microgels. *Ber. Bunsenges. Phys. Chem.*, **102**, 1603–1608.

52 Debord, J.D. and Lyon, L.A. (2003) Synthesis and characterization of ph-responsive copolymer microgels with tunable volume phase transition temperatures. *Langmuir*, **19**, 7662–7664.

53 Häntzschel, N., Zhang, F., Eckert, F., Pich, A., and Winnik, M.A. (2007) Poly(N-vinylcaprolactam-co-glycidyl methacrylate) aqueous microgels labeled with fluorescent LaF_3:Eu nanoparticles. *Langmuir*, **23**, 10793–10800.

54 Karg, M., Lu, Y., Carbó-Argibay, E., Pastoriza-Santos, I., Pérez-Juste, J., Liz-Marzán, L.M., and Hellweg, T. (2009) Multi-responsive hybrid colloids based on gold nanorods and poly-(NIPAM-co-allyl-acetic acid) microgels: temperature- and pH-tunable plasmon resonance. *Langmuir*, **25**, 3163–3167.

55 Thorne, J., Vine, G., and Snowden, M. (2011) Microgel applications and commercial considerations. *Colloid Polym. Sci.*, **289**, 625–646.

56 Karg, M., Pastoriza-Santos, I., Perez-Juste, J., Hellweg, T., and Liz-Marzan, L.M. (2007) Nanorod-coated PNIPAM microgels: Thermoresponsive optical properties. *Small*, **3** (7), 1222–1229.

57 Lu, Y., Mei, Y., Ballauff, M., and Drechsler, M. (2006) Thermoresponsive core-shell particles as carrier systems for metallic nanoparticles. *J. Phys. Chem. B*, **110**, 3930–3937.

58 Bhattacharya, S., Eckert, F., Boyko, V., and Pich, A. (2007) Temperature-, pH-, and magnetic-field-sensitive hybrid microgels. *Small*, **3** (4), 650–657.

59 Suzuki, D., McGrath, J.G., Kawaguchi, H., and Lyon, L.A. (2007) Colloidal crystals of thermosensitive, core/shell hybrid microgels. *J. Phys. Chem. C*, **111**, 5667–5672.

60 Suzuki, D. and Kawaguchi, H. (2006) Hybrid microgels with reversibly changeable multiple brilliant color. *Langmuir*, **22**, 3818–3822.

61 Kim, D.J., Kang, S.M., Kong, B., Kim, W.J., Paik, H.J., and Choi, I.S. (2005) Formation of thermoresponsive gold nanoparticle/PNIPAAm hybrids by surface-initiated, atom transfer radical polymerization in aqueous media. *Macromol. Chem. Phys.*, **206**, 1941–1946.

62 Karg, M., Pastoriza-Santos, I., Liz-Marzan, L.M., and Hellweg, T. (2006) A versatile approach for the preparation of thermosensitive PNIPAM core-shell microgels with nanoparticle cores. *Chem. Phys. Chem.*, **7**, 2298–2301.

63 Contreras-Cáceres, R., Sánchez-Iglesia, A., Karg, M., Pastoriza-Santos, I., Pérez-Juste, J., Pacifico, J., Hellweg, T., Fernández-Barbero, A., and Liz-Marzán, L.M. (2008) Encapsulation and growth of gold nanoparticles in thermoresponsive microgels. *Adv. Mater.*, **20**, 1666–1670.

64 Karg, M., Wellert, S., Prevost, S., Schweins, R., Dewhurst, C., Liz-Marzán, L.M., and Hellweg, T. (2011) Well defined hybrid PNIPAM core-shell microgels: size variation of the silica nanoparticle core. *Coll. Polym. Sci.*, **289** (5), 699–709.

65 Contreras-Cáceres, R., Pacifico, J., Pastoriza-Santos, I., Pérez-Juste, J., Fernández-Barbero, A., and Liz-Marzán, L.M. (2009) Au@PNIPAM thermosensitive nanostructures: Control over shell cross-linking, overall dimensions, and core growth. *Adv. Funct. Mater.*, **19**, 3070–3076.

66 Singh, N. and Lyon, L.A. (2007) Au nanoparticle templated synthesis of PNIPAM nanogels. *Chem. Mater.*, **19**, 719–726.

67 Schrinner, M., Ballauff, M., Talmon, Y., Kauffmann, Y., Thun, J., Möller, M., and Breu, J. (2009) Single nanocrystals of platinum prepared by partial dissolution of Au-Pt nanoalloys. *Science*, **323**, 617–620.

68 Höfl, S., Zitzler, L., Hellweg, T., Herminghaus, S., and Mugele, F. (2007) Volume phase transition of smart microgels in bulk solution and adsorbed at an interface: A combined AFM, dynamic light, and small angle neutron scattering study. *Polymer*, **48**, 245–254.

69 Sorrell, C.D. and Lyon, L.A. (2007) Bimodal swelling responses in microgel thin films. *J. Phys. Chem. B*, **111**, 4060–4066.

70 Wiedemair, J., Serpe, M.J., Kim, J., Masson, J.F., Lyon, L.A., Mizaikoff, B., and Kranz, C. (2007) In-situ AFM studies of the phase transition behavior of single thermoresponsive hydrogel particles. *Langmuir*, **23**, 130–137.

71 FitzGerald, P.A., Dupin, D., Armes, S.P., and Wanless, E.J. (2007) In situ observations of adsorbed microgel particles. *Soft Matter*, **3**, 580–586.

72 Schmidt, S., Motschmann, H., Hellweg, T., and von Klitzing, R. (2008) Thermoresponsive surfaces by spin-coating of PNIPAM-co-PAA microgels. A combined AFM and ellipsometry study. *Polymer*, **49**, 749–756.

73 Schmidt, S., Zeiser, M., Hellweg, T., Duschl, C., Fery, A., and Möhwald, H. (2010) Adhesion and mechanical properties of PNIPAM microgel films and their potential use as switchable cell culture substrates. *Adv. Funct. Mater.*, **20** (19), 3235–3243.

74 Karg, M., Wellert, S., Pastoriza-Santos, I., Lapp, A., Liz-Marzán, L.M., and Hellweg, T. (2008) Poly(N-isopropylacrylamide) microgels with silica nanoparticle core: The volume phase transition/collapse of the polymer shell as seen by small angle neutron scattering and dynamic light scattering. *Phys. Chem. Chem. Phys.*, **10**, 6708–6716.

75 Kratz, K., Hellweg, T., and Eimer, W. (2001) Structural changes in PNIPA microgel particles as seen by SANS, DLS, and EM techniques. *Polymer*, **42** (15), 6531–6539.

76 Crowther, H.M., Saunders, B.R., Mears, S.J., Cosgrove, T., Vincent, B., King, S.M., and Yu, G.E. (1999) Poly (NIPAM) microgel particle de-swelling:

a light scattering and small-angle neutron scattering study. *Colloids Surf. A*, **152**, 327–333.

77 Xia, X. and Hu, Z. (2004) Synthesis and light scattering study of microgels with interpenetrating polymer networks. *Langmuir*, **20**, 2094–2098.

78 Dingenouts, N., Nordhausen, C., and Ballauff, M. (1998) The volume transition in thermosensitive micronetworks as observed by small-angle x-ray scattering. *Ber. Bunsenges. Phys. Chem.*, **102** (11), 1594–1596.

79 Seelenmeyer, S., Deike, I., Rosenfeldt, S., Norhausen, C., Dingenouts, N., Ballauff, M., Narayanan, T., and Lindner, P. (2001) Small-angle x-ray and neutron scattering studies of the volume phase transition in thermosensitive core-shell colloids. *J. Chem. Phys.*, **114** (23), 10471–10478.

80 Mears, S.J., Deng, Y., Cosgrove, T., and Pelton, R. (1997) Structure of sodium dodecyl sulfate bound to a poly(nipam) microgel particle. *Langmuir*, **13**, 1901.

81 Kratz, K., Lapp, A., Eimer, W., and Hellweg, T. (2002) Volume phase transition and structure of TREGDMA, EGDMA, and BIS cross-linked PNIPA microgels: A small angle neutron and dynamic light scattering study. *Colloids Surf. A*, **197** (1–3), 55–67.

82 Stieger, M., Pedersen, J.S., Lindner, P., and Richtering, W. (2004) Are thermoresponsive microgels model systems for concentrated colloidal suspensions? A rheology and small-angle neutron scattering study. *Langmuir*, **20**, 7283–7292.

83 Fernandez-Barbero, A., Fernandez-Nieves, A., Grillo, I., and Lopez-Cabarcos, E. (2002) Structural modifications in the swelling of inhomogeneous microgels by light and neutron scattering. *Phys. Rev. E*, **66** (5), 051 803/1-10.

84 Hellweg, T., Kratz, K., Pouget, S., and Eimer, W. (2002) Internal dynamics in colloidal PNIPAM microgel particles immobilised in a mesoscopic crystal. *Colloids Surf. A*, **202** (2–3), 223–232.

85 Bolisetty, S., Hoffrnann, M., Lekkala, S., Hellweg, T., Ballauff, M., and Harnau, L. (2009) Coupling of rotational motion with shape fluctuations of core-shell microgels having tunable softness. *Macromolecules*, **42** (4), 1264–1269.

86 Jain, P.K., Eustis, S., and El-Sayed, M.A. (2006) Plasmon coupling in nanorod assemblies: Optical absorption, discrete dipole approximation simulation, and exciton-coupling model. *J. Phys. Chem. B*, **110**, 18243–18253.

87 Funston, A.M., Novo, C., Davis, T.J., and Mulvaney, P. (2009) Plasmon coupling of gold nanorods at short distances and in different geometries. *Nano Lett.*, **9** (4), 1651–1658.

88 Gluodenis, M. and Foss, C.A. (2002) The effect of mutual orientation on the spectra of metal nanoparticle rod-rod and rod-sphere pairs. *J. Phys. Chem. B*, **106**, 9484.

89 Thomas, K.G., Barazzouk, S., Ipe, B.I., Joseph, S.T.S., and Kamat, P.V. (2004) Uniaxial plasmon coupling through longitudinal self-assembly of gold nanorods. *J. Phys. Chem. B*, **108**, 13066–13068.

90 Pich, A., Karak, A., Lu, Y., Ghosh, A.K., and Adler, H.J.P. (2006) Tuneable catalytic properties of hybrid microgels containing gold nanoparticles. *J. Nanosci. Nanotechnol.*, **6** (12), 3763–3769.

91 Lu, Y., Yuan, J., Polzer, F., Drechsler, M., and Preussner, J. (2010) In situ growth of catalytic active Au-Pt bimetallic nanorods in thermoresponsive core-shell microgels. *ACS Nano*, **4** (12), 7078–7086.

92 Hashimoto, N., Hashimoto, T., Teranishi, T., Nasu, N., and Kamiya, K. (2006) Cycle performance of sol-gel optical sensor based on localized surface plasmon resonance of silver particles. *Sens. Actuators, B*, **113**, 382–388.

93 Pich, A., Karak, A., Lu, Y., Ghosh, A.K., and Adler, H.J.P. (2006) Preparation of hybrid microgels functionalized by silver nanoparticles. *Macromol. Rapid Commun.*, **27**, 344–350.

94 Contreras-Cáceres, R., Pastoriza-Santos, I., Alvarez-Puebla, R.A., Pérez-Juste, J., Fernández-Barbero, A., and Liz-Marzán, L. (2010) Growing Au/Ag

nanoparticles within microgel colloids for improved surface-enhanced Raman scattering detection. *Chem. Eur. J.*, **16**, 9462–9467.

95 Rodríguez-Fernández, J., Fedoruk, M., Hrelescu, C., Lutich, A., and Feldmann, J. (2011) Triggering the volume phase transition of core–shell Au nanorod–microgel nanocomposites with light. *Nanotechnology*, **22, 245**, 708.

96 Jones, C.D., Serpe, M.J., Schroeder, L., and Lyon, L.A. (2003) Microlens formation in microgel/gold colloid composite materials via photothermal patterning. *J. Am. Chem. Soc.*, **125** (18), 5292–5293.

97 Dagallier, C., Dietsch, H., Schurtenberger, P., and Scheffold, F. (2010) Thermoresponsive hybrid microgel particles with intrinsic optical and magnetic anisotropy. *Soft Matter*, **6**, 2174–2177.

98 Akamatsu, K., Shimada, M., Tsuruoka, T., Nawafune, H., Fujii, S., and Nakamura, Y. (2010) Synthesis of pH-responsive nanocomposite microgels with size-controlled gold nanoparticles from ion-doped, lightly cross-linked poly (vinylpyridine). *Langmuir*, **26** (2), 1254–1259.

99 Karg, M., Jaber, S., Hellweg, T., and Mulvaney, P. (2011) Surface plasmon spectroscopy of gold-PNIPAM core-shell nanocrystals. *Langmuir*, **27**, 820–827.

100 Wu, W., Zhou, T., Aiello, M., and Zhou, S. (2010) Construction of optical glucose nanobiosensor with high sensitivity and selectivity at physiological pH on the basis of organic/inorganic hybrid microgels. *Biosens. Bioelectron.*, **25**, 2603–2610.

12
Macroscopic Microgel Networks

Todd Hoare

12.1
Introduction and Motivation

Hydrogels have a variety of distinct physical and chemical properties that have led to their widespread use in a range of applications. Hydrogels have a high capacity to bind water, maintain high transparency even at high thicknesses, exhibit unique mechanical and chemical properties intermediate to solids and liquids (and similar to soft tissues in the body), have a low interfacial tension with aqueous interfaces (leading to typically low protein adsorption, for example), and have large internal free volumes amenable to flow-based applications or high-capacity loading of analytes. However, hydrogels are also significantly limited in many applications, particularly biomedical applications, due to their lack of injectability and relatively slow response rates to changes in their environment.

Microgels address many of these issues, leading to many of the practical applications of microgels reported elsewhere in this volume. Microgels also have tremendous flexibility in terms of their composition, morphology (core–shell, interpenetrating network, etc.), or assembly (colloidal crystals, self-assembled films, etc.), enabling the production of multiple types of microgel-based materials with properties not accessible by conventional hydrogel fabrication techniques. However, while the small dimensions of microgels significantly improve the performance of hydrogel-based materials in many applications, they can also cause challenges. For example, submicron microgel particles can be readily engulfed by macrophages or other lymphatic cells *in vivo*, leading to rapid sequestering of microgels in the spleen, liver, or lungs either via circulation or lymphatic clearance away from an intended site of action. Similarly, for release applications, the small diffusional path length of a single microgel particle typically leads to rapid release relative to what could be achieved with a macroscopic hydrogel-based drug-delivery vehicle with a similar internal morphology.

In this respect, the development of materials that combine the advantageous properties of microgels and hydrogels together would address many outstanding challenges with the application of soft materials. In response, significant research

Hydrogel Micro and Nanoparticles, First Edition. Edited by L. Andrew Lyon and Michael Joseph Serpe.
© 2012 Wiley-VCH Verlag GmbH & Co. KGaA. Published 2012 by Wiley-VCH Verlag GmbH & Co. KGaA.

interest has been invested in the development of immobilized microgel networks, in which individual microgel particles are entrapped inside a macroscopic mesh or crosslinked to form a macroscopic object. Microgel networks formed in this way can exhibit several unique properties relative to hydrogels or microgels alone:

- **High strength**: Entrapment or crosslinking of microgel phases inside a bulk hydrogel phase has the potential to act as a reinforcing phase to enhance the strength of a hydrogel. The incorporation of dispersed particles in bulk hydrogels (and other bulk materials) for mechanical reinforcement has been widely reported in the literature [1, 2], with the effectiveness of such materials for mechanical reinforcement attributed primarily to a crack-pinning mechanism by which the energy of a propagating crack is pinned and dispersed over the full surface area of a particulate reinforcing phase. However, unlike the many nanocomposite hydrogels reported containing silica [3], clay [2], nanocrystalline cellulose [4], or other reinforcing phases, the incorporation of microgels as an embedded phase preserves the soft, water-penetrable properties of the entire network, offering significant advantages in terms of transparency and water binding capacity. In addition, if crosslinkable functional groups are incorporated on the surface of the microgel, more efficient crosslinking can occur between the microgel and bulk hydrogel phases; using this approach, microgels act as highly multivalent chemical crosslinkers for the overall hydrogel network. Mechanical strength enhancements of up to 100-fold (relative to the corresponding conventionally-crosslinked hydrogel) have been reported by incorporating a crosslinkable microgel inside a bulk hydrogel network [5, 6].
- **Kinetically frozen microstructures**: In some cases, post-crosslinking reactions to form microgel networks may be performed to freeze self-assembled microgel structures into permanent assemblies that cannot be disrupted by subsequent dissolution, drying, desorption, or physicochemical changes in the microgel environment. In some cases, equilibrium structures are first formed and then locked in by a post-gelation process. This approach is frequently used to freeze colloidal crystals into permanent ordered structures useful for optical applications, as will be described later in this chapter. In other cases, network formation can freeze non-equilibrium morphologies into the material, exploiting differences in the relative kinetics of phase separation and gelation. Even in the absence of distinct ordering of the constituent microgels, crosslinking or entrapment of microgels into randomly oriented macroscopic objects can also be useful, particularly in terms of applying microgels locally *in vivo*. Without external immobilization, microgels are typically quickly transported away from the injection site by the lymphatic system; indeed, the relative ease of circulation of nanogels relative to other types of "hard" nanoparticles is leading to significant interest in such particles for targeted drug delivery [7]. Entrapping or crosslinking microgels into a network prevents the engulfment of microgels by macrophages or the transport of microgels via convective mass transport in the circulatory system, facilitating long-term local activity at a targeted site. In addition, the degradation rate of the bulk hydrogel entrapping phase can be tuned to control the

residence time of the embedded microgels at a particular site, offering potential for controlled release of microgels over time or targeted hydrogel lifetimes *in vivo*.

- **Rapid swelling kinetics**: Scaling arguments, supported by experiment, have shown that the characteristic swelling time of an environmentally responsive microgel varies as the inverse of the particle dimension squared [8]. Thus, as the size of the swelling–deswelling unit is reduced, significantly faster swelling responses can be achieved relative to those achieved in bulk hydrogels. These reductions in swelling rates are typically on the order-of-magnitude level, even in cases where the bulk hydrogel phase comprises a large fraction of the overall volume fraction of the composite hydrogel [6]; indeed, significant enhancement of swelling kinetics has been observed even at microgel fractions as low as ~10 mol % [9]. Nanocomposite hydrogels based on thermoresponsive components also avoid or minimize the occurrence and the impact of the dense skin layer typically observed at the outer interface of bulk thermosensitive hydrogels, formed as a result of the surface layers of a hydrogel shrinking more rapidly than the internal gel. The collapsed skin layer significantly retards water diffusion out of a bulk hydrogel network, resulting in significantly slower deswelling kinetics and water transport out of the hydrogel. Microgel network-based hydrogels deswell more rapidly and more uniformly throughout the matrix, avoiding skin layer formation [9].
- **Well-defined compositional heterogeneity**: Microgel composites permit a single macroscopic hydrogel phase to contain multiple types of discrete hydrogel units. Indeed, by mixing different types of microgels together with a bulk hydrogel phase, any number of unique compositions of embedded phases may be incorporated into a single soft nanocomposite hydrogel. In this way, ordered or disordered gradients in chemical composition, charge, crosslink density, or any other physicochemical parameter can be introduced into a hydrogel material, introducing local gradients in the affinity for a particular target chemical, the diffusion of an analyte into or out of the hydrogel, or any other physicochemical parameter. Furthermore, given the variety of environmentally responsive hydrogels and microgels that have been reported, independent phase transitions may be engineered in the bulk and embedded phases of a microgel composite. Such functionality may, for example, be useful to induce a phase transition in the internal phase (and thus induce a change in the local affinity of the hydrogel for an analyte) without changing the bulk dimensions of the material. Conversely, a local hydrophilic embedded phase may be oriented inside a collapsed bulk hydrogel phase to, for example, protect entrapped proteins or enzymes from denaturation upon the hydrogel phase transition.

Each of these property changes are dependent on the chemical and physical composition of the two phases, the volume fraction of each phase (bulk and embedded) within the microgel composite, and the method used to assemble and immobilize the network. As such, a clear understanding of the different methods available to prepare microgel networks is required to best design the network for a particular application.

12.2
Preparation of Microgel Networks

12.2.1
Networking Strategies

Three principle approaches are used to form microgel networks: direct microgel crosslinking, microgel-mediated crosslinking, and physical microgel entrapment. These approaches are illustrated schematically in Figure 12.1. Direct microgel crosslinking may be achieved via physical (e.g., hydrophobic or ionic) interactions (Figure 12.1a) or covalent bonding (Figure 12.1b), providing microgel networks with the highest possible density of the microgel phase. Assembly of such networks demands that the microgels themselves have the physical or chemical properties to mediate microgel formation; multiple microgels with different charges or complementary reactive functional groups are often mixed together in order to provide the required crosslinking.

Alternately, microgels themselves can be used as crosslinking agents to crosslink reactive linear polymers into a network structure. In this case, the linear polymer may simply be mixed with the reactive microgel (Figure 12.1c) or may be grafted to the microgel (Figure 12.1d) to mediate network formation. In this approach, microgels act as multivalent crosslinkers to either directly mediate or enhance the crosslinking of the bulk hydrogel phase. This approach frequently results in high-strength materials, but reduces the overall volume fraction of microgels that can be incorporated into the final material.

A third potential morphology can be formed if the microgels have no mechanism to physically or chemical crosslink with the bulk hydrogel phase and instead become physically entrapped inside the hydrogel. In this case, microgels are essentially spectators in the bulk gelation process and become incorporated inside a hydrogel

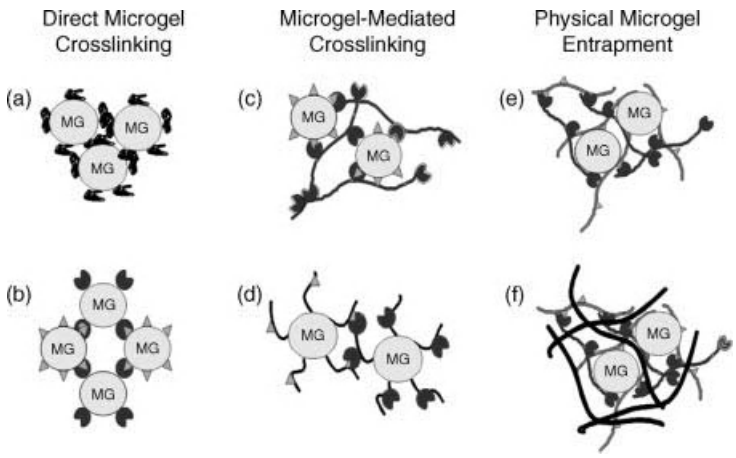

Figure 12.1 Methods of forming microgel networks. See text for explanations.

network only if they are well mixed with the polymerizing pre-hydrogel solution. Hydrogel formation occurs independently of the microgel phase and may occur based on polymerization from monomers, crosslinking of pre-polymers (Figure 12.1e), formation of interpenetrating networks (Figure 12.1f), or any other chemical or physical hydrogel crosslinking process. This approach tends to lead to lower volume fractions of microgels within the microgel composite network (otherwise entrapment would not occur); however, this approach also provides almost unlimited flexibility in terms of the types of chemistries and morphologies that can be achieved in either the bulk or entrapped phases, as no reactive functional groups need be incorporated on the microgel phase. Furthermore, since the two phases are not directly connected via covalent bonds, the bulk hydrogel and microgel phases can in some cases independently mediate their own swelling and/or the swelling of the other phase, leading to formation of potentially interesting and novel morphological features.

Within any of these general techniques, crosslinking (when required) can occur through any physical interaction or via covalent bond formation, facilitating the formation of hydrogel and/or microgel phases with targeted degradation profiles, chemistries, and elasticities. Strategies for preparing microgel networks of various morphologies using each of these techniques will be described below.

12.2.2 Direct Microgel Crosslinking

Direct microgel crosslinking can be used to prepare microgel networks mediated by physical (hydrophobic interactions, ionic interactions) or chemical (covalent bond formation) crosslinking approaches.

12.2.2.1 Hydrophobic Assembly

Hydrogels or microaggregates based on direct microgel–microgel interactions can be generated by exploiting the observed capacity of poly(*N*-isopropylacrylamide) (PNIPAM)-based microgels to thermally self-aggregate in high-concentration suspensions at temperatures above the phase transition temperature of the microgel, particularly under high-salt conditions. Microgel thermoaggregation differs from colloidal crystal formation via two main characteristics: (i) microgels typically deswell upon aggregation while colloidal crystals are typically formed with microgels in their fully hydrated states and (ii) microgel aggregates typically exhibit complete disorder or only short-range order on the length scale of the aggregate but long-range disorder across the whole sample, while colloidal crystals exhibit both short- and long-range order in three dimensions. Makino *et al*. first described this phenomenon by comparing the aggregation behavior of polystyrene core particles coated with PNIPAM compared to poly(NIPAM-*co*-acrylic acid (AA)) microgel layers [10]. Aggregation was shown to be a sensitive function of the volumetric charge density within the hydrogel. Microgels with high charge densities do not aggregate at any concentration or at any temperature. However, at low charge density, microgel aggregation is a function of the electrophoretic softness of the microgel particle,

defined by Ohshima [11] as the resistance to electro-osmotic flow within the microgel upon the application of an external electric field (and found to be a strong function of the polymer chain density in the outer shell of the microgel). High softness microgels remain colloidally stable, while low softness microgels tend to aggregate to form microgel clusters.

Several researchers have exploited similar approaches to form microgel aggregates based on thermogelation of PNIPAM-based microgel building blocks with different chemical and physical microstructures. For example, Hu *et al*. assembled interpenetrating network microgels consisting of poly(acrylic acid) and PNIPAM via reversible aggregation at ~33 °C [12] while Gan *et al*. showed similar aggregation phenomena using poly(NIPAM-*co*-AA) microgels [13] and poly(NIPAM-*co*-2-hydroxyethyl methacrylate (HEMA)) microgels [14] as the microgel building blocks. Using this approach, microgel networks with defined porosities (tunable according to the charge density of the constituent microgel building blocks) can be formed by simple heating in a high-ionic strength environment (Figure 12.2). Aggregation can also be used as a driving force for the assembly of non-PNIPAM-based hydrogel assemblies. For example, Yang *et al*. reported the self-assembly of a poly(ethylene glycol)–poly(propylene glycol)–poly(ethylene glycol) triblock copolymer into a micelle that was subsequently crosslinked to form a stabilized microgel and then heated (in a highly concentrated suspension) to form a fully thermoreversible microgel-based composite hydrogel [15].

Hydrophobic interactions also have considerable potential to generate self-healing microgel networks exhibiting labile interactions between individual microgel particles that can be disrupted by shear but be rapidly re-formed after the shear is removed. Using this approach, microgel networks may be prepared using a combination of stable and labile bonds to tune the shear responsiveness and thus the elastic strength of the microgel nanocomposite at both low and high shear. Modeling results indicate that only a small fraction (<5%) of labile bonds can result in a 25% increase in the stress required to induce fracture, indicating the utility of labile bonds in terms of improving the tensile strength of hydrogels [16]. While polystyrene-based microgels have been reported to form such networks in organic solvents due to

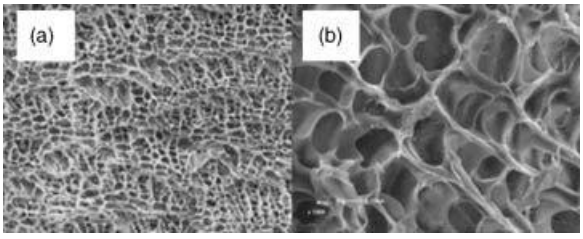

Figure 12.2 Scanning electron microscopy images of the cross section of thermogelled assemblies of (a) poly(NIPAM) and (b) 1 mol% AA poly(NIPAM-*co*-AA) microgels after equilibration for one week at 37 °C. Scale bar = 10 μm. Reproduced by permission of the Royal Society of Chemistry from Gan *et al.*, *Journal of Materials Chemistry*, 2010, 20, 5937 [13].

hydrogen-bonding interactions between diamidopyridine and thymine functional groups on the particle surface [17], hydrogen-bonding interactions are typically less effective in aqueous suspensions, making hydrophobic interactions a better candidate for such systems. While some shear thinning of hydrophobically associated microgels has been demonstrated, no true self-healing aqueous microgel formulation has yet been reported.

12.2.2.2 **Ionic Assembly**

Direct microgel–microgel networks can be assembled through electrostatic interactions by mixing microgels with different charges. For example, ionically networked mixtures of poly(ethylene glycol)–poly(sodium acrylate) microgels (anionic) and poly (ethylene glycol)–poly(vinylbenzyl trimethylammonium chloride) microgels (cationic) have been applied to produce colloidal gels with tunable rheological properties according to the ratios of the microgels added and the net surface charge on the microgel building blocks [18]. The microgel network exhibited improved resistance to external mechanical forces, improving the localization of vascular endothelial growth factor delivery while limiting host inflammation induced by isolated microgels. Similar materials were synthesized and fabricated by Karpushkin *et al.* [19] with larger (~100 μm) microgel particles. Both these studies suggest that the use of a variety of microgels with opposite charges but similar sizes can lead to strong network formation due to the increased probability of close packing in such systems.

Ionic assembly may be templated by an external agent or driving force to synthesize hydrogel-based materials with well-defined morphologies. An elegant example of this is the work of Yao *et al.*, who developed ionic-crosslinked microgel-based hydrogels with oriented structures by, using freeze drying to structure assemblies of poly(vinyl caprolactone) microgels functionalized to be cationic via copolymerization with *N,N*-diethylaminoethyl methacrylate and anionic via copolymerization with acrylic acid [20]. By mixing the charged microgels inside a syringe and flash-freezing the suspension by slowly submersing the syringe into liquid nitrogen, aligned porous scaffolds were formed as ice crystallized along the dipping direction and microgels clustered to form the scaffold walls (Figure 12.3). Such materials remained stable when rewarmed to room temperature. In this way, microgel networks with three levels of hierarchy can be formed: macrostructures (determined by ice crystallization), microstructures (determined by the microgel size and chemistry), and nanostructures (determined by the microgel crosslinking and/or internal morphology).

Ionic interactions have also been reported to prepare microgel networks made up of mixtures of microgels and "hard" nano-scale building blocks to generate composite hydrogels with unique properties. For example, assemblies based on cationically stabilized nanocrystalline cellulose and poly(NIPAM-*co*-AA) microgels have been reported that did not induce significant microgel deswelling upon ionic assembly, offering a significant advantage over other polyelectrolyte-based films [21]. Similar approaches could be applied to generate inorganic–organic microgel-based networks with clays, silica particles, ferrofluids, or other building blocks of

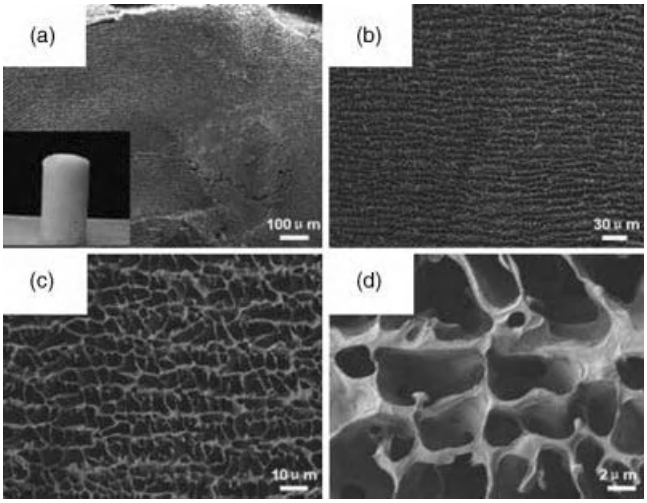

Figure 12.3 Scanning electron microscopy analysis in the direction of freezing of aligned pore hydrogels formed from ionic assemblies of cationic (poly(vinylcaprolactone-*co*-*N*,*N*-dimethylaminoethyl methacrylate) and anionic (poly(vinylcaprolactone-*co*-acrylic acid) microgel building blocks via directional freezing at different length scales: (a) 80× magnification; (b) 300× magnification; (c) 1000× magnification; (d) 5000× magnification. Reproduced by permission of the Royal Society of Chemistry from Yao *et al.*, *Journal of Materials Chemistry*, 2009, 19, 6516 [20].

interest, provided that the volume fraction of the "hard" phase is sufficiently low that the composite material formed maintains the mechanical properties of a hydrogel.

Divalent or trivalent salts or small molecule ionic crosslinkers (e.g., citric acid) may also be used to assemble networks of microgels with targeted swelling or interfacial properties. Don *et al.* prepared multifunctional networks made up of mixtures of poly (AA-*co*-sodium acrylate) (high water content), poly(AA-*co*-2-ethylhexyl acrylate) (adhesivity), and poly(NIPAM-*co*-AA) (thermosensitivity) microgels crosslinked by Al^{3+} ions [22]. This work specifically demonstrates the ease of making multifunctional hydrogel materials by simple mixing and/or self-assembly of functional microgel building blocks. Rapid ionic crosslinking can also be applied to pattern microgels using ink jet printing approaches. Nakamura demonstrated this mode of microgel network assembly by using an inkjet printer to print droplets of sodium alginate on to a substrate and then exposing the droplets to a calcium chloride gelling solution; the pattern of the inkjet droplets produced a microgel network with a defined pattern [23].

Ionic assembly can also be combined with other physical interactions to further direct assembly of the microgel building blocks. Specifically, bridging or depletion effects can be applied to create microgel networks with improved three-dimensional order. Cho *et al.* demonstrated such behavior by heating mixtures of poly(NIPAM-*co*-AA) and poly(NIPAM-*co*-allylamine) microgels in the presence of a small quantity of poly(AA). The inclusion of a depletion agent for the anionic poly(NIPAM-*co*-AA) microgel component (anionic poly(AA)) resulted in a more ordered ionically assembled morphology relative to simple mixing of the ionic microgel building blocks in

the absence of a depletant. The resulting, more highly ordered composite hydrogel exhibited faster and higher magnitude swelling–deswelling responses to thermal stimuli relative to the purely ionically structured hydrogel [24]. The crosslink density of the microgels does not significantly affect the swelling–deswelling kinetics of the bulk hydrogel network formed [25], permitting largely independent control over the macroscopic hydrogel properties and the internal microstructure of the hydrogel.

Microgel network films have also been reported based on polyelectrolyte layer-by-layer self-assembly. Serpe *et al.* demonstrated layer-by-layer deposition of 4-acrylamidofluorescein-modified poly(NIPAM-*co*-AA) microgels using polyallylamine hydrochloride as the polycation [26]. The films exhibited enhanced thermoresponsivity at low pH (microgel protonated) but a suppressed phase transition at high pH (microgel ionized), consistent with microgel phase transition temperature trends in suspension. Sorrell provided evidence that polyelectrolyte decomplexation at low pH (microgels protonated) also influences the properties of the films, providing an additional tunable parameter for engineering targeted film responses [27]. Similarly, Wang *et al.* demonstrated the utility of layer-by-layer techniques for forming microgel films based on polyampholyte microgels with excess cationic charge using poly (sodium 4-styrenesulfonate) as the structuring polycounterion [28]. In all these cases, structured microgel assemblies can be generated by using charge as both a crosslinking agent and an assembly agent.

12.2.2.3 **Covalent Assembly**

Direct chemical crosslinking between individual microgel particles (the morphology shown in Figure 12.1b) is relatively rare unless covalent crosslinking is coupled with a physical self-assembly process to bring the microgels close enough together that the relatively slow diffusivity of microgels relative to linear polymers does not significantly impede network formation. Several researchers have reported the use of centrifugation to produce close-packed microgel colloidal crystals from a concentrated monodisperse microgel suspension [29–33], as described more fully elsewhere in this volume. Such ordered and preconcentrated microgel arrays can subsequently be covalently crosslinked *in situ* to stabilize the colloidal crystal phase even upon dilution [34]. Similarly, ordered microgel networks created by phase separation (induced by addition of an organic solvent) [35] may be crosslinked via the addition of oil-soluble crosslinkers to covalently fix the network structure and enable the transfer of the microgel network into an aqueous solvent. Self-assembled films can also be crosslinked after assembly to form a covalently linked microgel film, as demonstrated by Zhou *et al.*'s work in forming a thin film of poly(NIPAM-*co*-*N*-hydroxymethylacrylamide (NMA)) microgels[36]; NMA groups self-crosslink in the absence of water to create a stable, hydrogen-bonded free-standing film that remained stable in water and demonstrated iridescent colors due to the fixed, self-assembly directed microgel array inside the film. In any of these cases, the otherwise unstable (due to dilution or solvent type) ordered arrays are stabilized into fixed arrays via covalent crosslinking of the self-assembled network. Such approaches can exploit the main advantages of both physical crosslinking (increased probability of order) and chemical crosslinking (permanence of the crosslinked network).

Covalent bond formation can also be used as a secondary crosslinking step following assembly of a microgel network based on physical interactions to produce dual physical–chemical crosslinked systems. Van Tomme *et al.* reported the synthesis of dextran microgels via copolymerization of methacrylated dextran with methacrylic acid (anionic) and dimethylaminoethyl methacrylate (cationic) in an aqueous two-phase system to generate a dextran-in-poly(ethylene glycol) suspension [37]. Instantaneous gelation was observed upon mixing the oppositely charged microgels. Rheological analysis indicated that the resulting hydrogel had a reversible yield point, in that the hydrogel can flow under high enough stress, and can be broken at either low pH or high ionic strength, making such systems efficiently injectable and reversible. After this initial, rapid ionic assembly step, residual acrylate groups could subsequently be photopolymerized to stabilize the structure at any pH or ionic strength. In this respect, covalent crosslinking is not required for the formation of the microgel network but can be used to change its mechanical strength and/or stability as desired.

12.2.3
Microgel-Mediated Crosslinking

Using microgel-mediated crosslinking to form a microgel network, microgels are functionalized with a reactive functional group and subsequently mixed with reactive polymers or monomers that can be polymerized through or from the reactive site on the microgel. In such systems, microgels behave as either initiators or crosslinkers that can mediate the formation of a bulk hydrogel network around them that may have the same or a different chemical composition relative to the microgels themselves. Several approaches can be used to create such networks.

12.2.3.1 Initiator-Grafted Microgels

By attaching initiator groups to the surface of a microgel, free radical polymerization can be initiated from the microgel surface to entrap microgels within a bulk network. The resulting microstructures resemble the schematic shown in Figure 12.1d, in which polymer is grafted from the microgel surface and then crosslinked in the inter-microgel space via the addition of a bifunctional crosslinker or free radical abstraction chemistries. He *et al.* demonstrated this approach using surface-peroxidased microgels based on gamma-irradiated alkylphenol polyoxyethylene ether micelles as microgel crosslinkers [38]; photopolymerization of acrylic acid initiated at the microgel surface created a bulk nanocomposite hydrogel with high compressive strength and high shape recoverability (Figure 12.4). The type of functional group incorporated on the surface of the microgel can be controlled to facilitate the incorporation of different surface-initiating functional groups. Xia *et al.* converted carboxylic acid groups on poly(NIPAM-*co*-AA) microgels to peracid groups via treatment with hydrogen peroxide; subsequent heating in the presence of NIPAM and AA monomer resulted in a microgel-crosslinked composite hydrogel structure [39]. Alternately, Xu *et al.* prepared PNIPAM core, poly(vinylamine) shell microgels and subsequently treated the microgels with potassium persulfate,

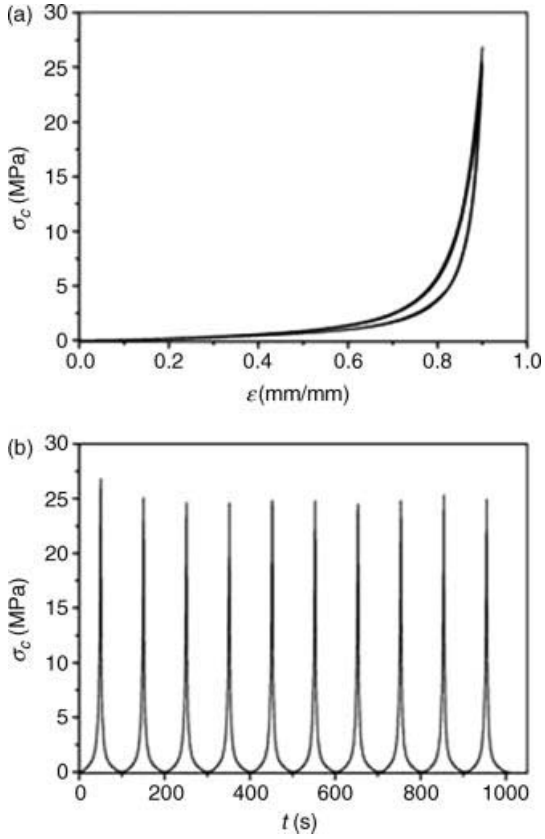

Figure 12.4 Cyclic compression tests of a poly (acrylic acid) hydrogel crosslinked with peroxidased alkylphenol polyoxyethylene ether microgels showing high elastic modulus and high shape recoverability: (a) stress–strain curves; (b) stress–time curves. Reproduced by permission of the Royal Society of Chemistry from He *et al.*, *Soft Matter*, 2011, 7, 2943 [38].

generating free radicals on the amine residues of poly(vinylamine) that initiated the synthesis of polyampholyte hydrogels composed of acrylic acid (anionic), acryloyloxyethyl trimethyl ammonium chloride (cationic), and acrylamide (neutral) monomers [6]. Surface initiation is highly effective for anchoring microgels within a free radical-polymerized bulk microgel network and may result in significant interpenetration between the bulk hydrogel and discrete microgel phases when such interpenetration is desirable for applications.

12.2.3.2 **Surface-Polymerizable Microgels**

Microgels functionalized with polymerizable functional groups on their surface can be used as multifunctional macromonomers in the polymerization of a bulk hydrogel phase. Allyl groups are most commonly used in conjunction with a thermal free

radical initiator and one or more monomer(s) and/or crosslinkers to form the bulk hydrogel phase. Matsumoto used benzoyl peroxide to crosslink poly(allyl methacrylate) microgels with pendant allyl groups together with diallyl terephthalate [40], while Tan *et al*. crosslinked starch-based microgels with allyl groups in the shell into a polyacrylamide [5] or poly(*N*-isopropylacrylamide) [41] hydrogel. In the case of the PNIPAM–starch system, the resulting microgel network exhibited extremely high enhancements in gel mechanical strength and significantly faster deswelling kinetics relative to bulk hydrogels, characteristic properties of microgel networks. Several examples of acrylated microgel-mediated crosslinking have also been reported. For example, Zhang *et al*. reported the use of surface-acrylated PNIPAM microgels as crosslinkers for a bulk PNIPAM network [42], Liu *et al*. demonstrated thermally initiated crosslinking of close-packed glycidyl methacrylate-functionalized poly (methyl methacrylate-*co*-methacrylic acid-*co*-ethylene glycol methacrylate) microgels to form a hydrogel network [43], and Morimoto *et al*. used self-assembled nanogels based on cholesteryl and methacryloyl-substituted pullulan with pendant polymerizable methacrylate groups as crosslinkers for a bulk PNIPAM network [44]. In the latter example, the resulting nanostructured hydrogel reached its equilibrium swelling state above the phase transition temperature in only two minutes, over 3000 times faster than a conventional *N*,*N*-methylenebisacrylamide-crosslinked PNIPAM hydrogel (Figure 12.5).

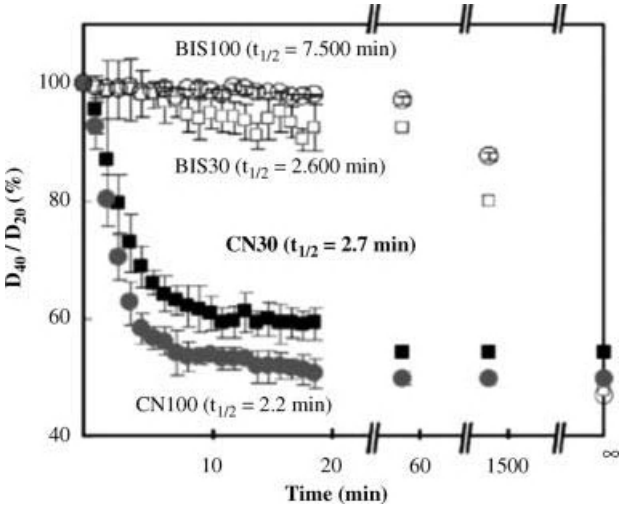

Figure 12.5 Shrinking kinetics of hydrogels as a function of temperature change from 40 to 20 °C. CN30 and CN100 are PNIPAM hydrogels crosslinked with self-assembled nanogels based on cholesteryl and methacryloyl-substituted pullulan with pendant polymerizable methacrylate groups (NIPAM : methacrylate molar ratio 30% and 100%, respectively); BIS30 and BIS100 are conventional PNIPAM microgels crosslinked with *N*,*N*-methylenebisacrylamide (NIPAM : acrylamido molar ratio 30% and 100%, respectively). Reprinted with permission from Morimoto *et al.*, *Macromolecular Rapid Communications*, 2008, 29, 672. Copyright 2008, John Wiley and Sons [44].

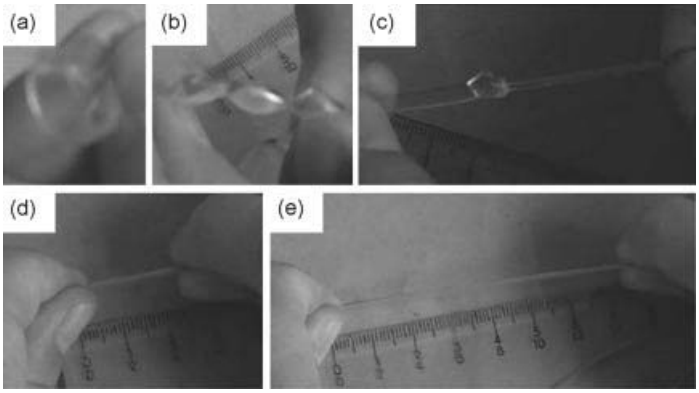

Figure 12.6 Photographs demonstrating the mechanical properties of microgel networks comprised of a polymerizable microgel covalently crosslinked in a bulk hydrogel; (a) bending; (b) torsion; (c) knotting; (d) original length; and (e) elongating (tensile). With kind permission from Springer Science + Business Media: *Colloid and Polymer Science*, 2009, 287, 621 [45].

Acrylamido-functionalized microgels have been applied using similar chemistry to generate extremely mechanically robust microgel networks. Qin *et al*. prepared acrylamido-functionalized microgels by a two-step reaction, first synthesizing poly(-acrylamide-*co*-(2-acrylamido-2-methylpropane sulfonic acid)) (poly(AAm-*co*-AMPS)) microgels via inverse emulsion polymerization and subsequently reacting them with *N*-methylolacrylamide to introduce polymerizable acrylamide residues to the microgel surface. Subsequent microgel network preparation by polymerizing acrylamide and AMPS in the presence of the acrylamido-functionalized microgels and a polymerization accelerator resulted in microgel networks with extremely elastic mechanical properties [45]. Tensile stresses of up to 4.6 MPa and strains of up to 90% could be elastically recovered in such networks (Figure 12.6), remarkably higher than that of a bulk hydrogel prepared with the same monomers crosslinked with *N,N*-methylenebis acrylamide (stress of 0.08 MPa and strain at break of 45%).

12.2.3.3 **Surface-Reactive Microgels**

Chemical crosslinking between the bulk and microgel phases can also be accomplished by incorporating non-polymerizable but chemically reactive functional groups on the microgel surface. Of particular interest in biomedical applications are a variety of *in situ* gelation chemistries, the most common of which are outlined in Figure 12.7. Using such chemistries is advantageous in that liquid-like precursors (linear polymer solutions and microgel suspensions) can be co-injected into the body and quickly gel *in situ*, eliminating the need for surgical insertion of a macroscopic hydrogel.

Michael reactions between amines/thiols and acrylate groups are most commonly applied in the literature. Bencherif *et al*. demonstrated this approach for forming

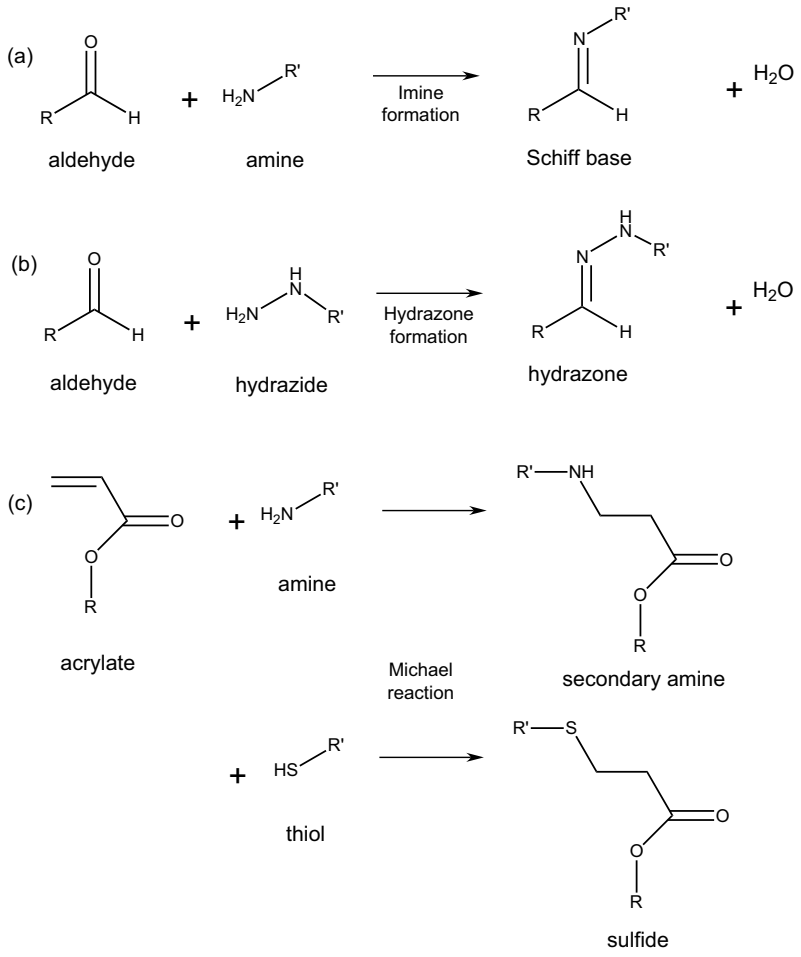

Figure 12.7 Common *in situ* gelation chemistries for microgel network formation. See text for explanations.

microgel networks by using acrylated poly(HEMA-*co*-polyethylene glycol methacrylate) microgels (prepared via inverse suspension polymerization) as a crosslinker for thiolated hyaluronic acid; simple mixing of the acrylated microgel and the thiolated hyaluronic acid resulted in the formation of a gel within 5–10 min under physiological temperature and pH [46]. Huang and Hu demonstrated the use of the imine reaction for the same purpose, using glutaraldehyde to crosslink poly(NIPAM-*co*-allylamine) microgels to form a stabilized microgel array using a similar method. However, their method would not be amenable to physiological use given the cytotoxicity of glutaraldehyde, a commonly used tissue fixative [47].

Other types of functional group reactions not amenable to *in situ* gelation inside the body may also be used to crosslink reactive linear polymers with multifunctional

reactive microgels to form microgel networks. Qin *et al*. demonstrated such an approach by mixing poly(acrylamide-*co*-(2-acrylamido-2-methylpropane sulfonic acid)-*co*-*N*-methylolacrylamide)(poly(AAm-*co*-AMPS-*co*-NMA)) microgels prepared via inverse emulsion copolymerization with a linear copolymer of AAm and AMPS [48]. Upon heating, hydroxymethyl groups on NMA residues (microgel phase) crosslink with amide groups on acrylamide residues (bulk phase) to form covalent crosslinks that fix the network in place. The advantage of this latent crosslinking approach is that microgels may be self-assembled into colloidal arrays or patterned on a surface and then networked spontaneously simply by changing the temperature, facilitating the freezing of ordered or complex microgel patterns in two or three dimensions if desired. Tensile strengths of up to 130 kPa and elongations of >500% could be achieved in some cases using this approach [48], both of which far exceed those typically achieved in conventional hydrogels. It should also be noted that composite networks with similar compositions prepared by polymerizing a mixture of AAm and AMPS monomers in the presence of the microgels and an accelerator and subsequently heating to perform the NMA–AAm crosslinking reaction resulted in weaker (tensile strength = 32 kPa) but more elastic (elongation >1000%) hydrogels [45]. This result suggests that the use of linear polymer precursors as opposed to monomeric precursors for the bulk hydrogel phase of a microgel network can result in a higher strength hydrogels, potentially due to the higher probability of linear polymer interpenetration into the microgel phase when the components are mixed prior to gelation.

12.2.4
Physical Microgel Entrapment

When hydrogel phases are polymerized around microgels that do not contain any polymerizable or reactive functional groups, microgel networks in which the microgel phase is simply physically entrapped inside a bulk hydrogel are formed (Figure 12.1e). There are two principle advantages to such an approach: (i) no specific surface chemistries need to be attached to the microgels, allowing the use of any microgel to form a microgel network and (ii) any deswelling transitions occurring within the microgel phase as a function of the gel environment can occur independently of the presence of the bulk hydrogel phase, offering the potential for dynamic macropore formation and/or dynamic switching inside the microgel without inducing a significant change in the bulk hydrogel properties. Stated in another way, physical entrapment of microgels within a continuous hydrogel phase allows the functionality and the mechanical strength of the overall network to be decoupled, leading to improved control over both the bulk and microstructural properties of the overall soft material.

12.2.4.1 **Entrapment to Form 3D Hydrogels**

Richtering's group has performed the most comprehensive comparison of the physical properties and morphologies of 3D microgel networks prepared using a chemical crosslinking versus physical entrapment approach [49, 50]. Microgel

networks consisting of a continuous polyacrylamide hydrogel phase and thermoresponsive PNIPAM microgel phase were made with two morphologies: (i) PNIPAM microgels were physically entrapped inside a polyacrylamide matrix; (ii) PNIPAM microgels were covalently attached to a polyacrylamide matrix, using gamma irradiation to crosslink the bulk phase with the microgel phase. Microgel-entrapped hydrogel networks were prepared both above and below the phase transition temperature of the PNIPAM microgels, at different microgel : hydrogel dry mass ratios, and using polyacrylamide hydrogels with different crosslink densities, with each of the resulting morphologies generated analyzed as a function of temperature.

The potential morphologies generated by physical entrapment of PNIPAM-based microgels in a bulk polyacrylamide hydrogel are demonstrated schematically in Figure 12.8. When microgels were physically entrapped in the polyacrylamide hydrogel at a temperature below their phase transition temperature (i.e., in the swollen state), the phase transition of the microgels was not affected by the presence of the encapsulating hydrogel phase, with the full thermoresponsiveness of the microgels retained independent of the formation of a microgel network (Figure 12.8a). On the other hand, when the hydrogel was polymerized around microgels at temperatures above the microgel phase transition temperature (i.e., in the collapsed state), the bulk hydrogel forms around the collapsed microgel and presents an elastic constraint to microgel swelling, even when the temperature is subsequently lowered below the phase transition temperature (Figure 12.8b). Similarly, when gamma irradiation was used to crosslink microgels directly to the bulk hydrogel phase, microgel deswelling upon heating was elastically restricted relative to the case where microgels are only physically entrapped in the bulk gel (Figure 12.8c).

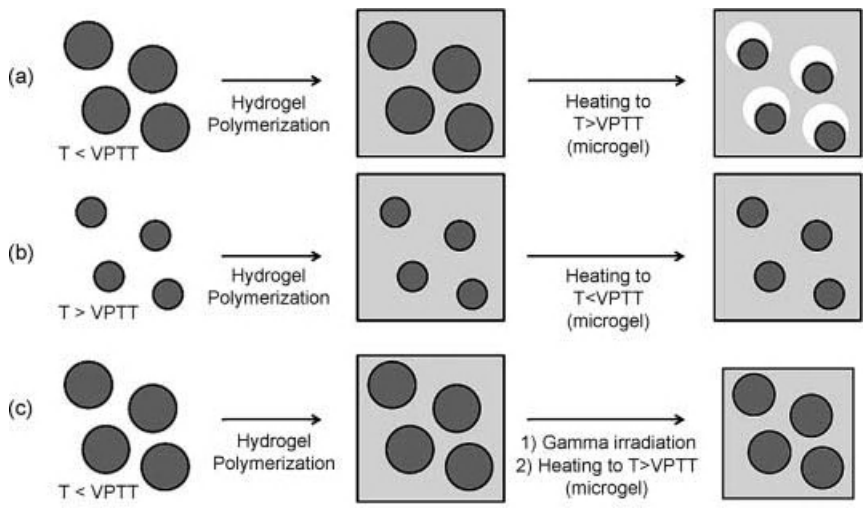

Figure 12.8 Phase transition behavior of PNIPAM-based microgels physically entrapped inside a polyacrylamide hydrogel as a function of the preparation conditions used to prepare the hydrogel. See text for explanations.

In either case, hydrogels with high crosslink densities can exert a corset-like constraint on microgel swelling–deswelling transitions, leading to partial dehydration of the microgel in its swollen state relative to its properties in free suspension.

The distribution of entrapped microgels within the hydrogel matrix is a strong function of the concentration of the microgels entrapped within the network [49, 50]. Microgel networks prepared at lower microgel concentrations result in microgel networks with uniform but at least partially disordered microgel distributions throughout the network, while networks prepared around close-packed, high-concentration microgel suspensions resulted in significant localization and partial aggregation of microgels within the network in response to the polymerization of the entrapping hydrogel phase. Thus, depending on the method used to entrap microgels within the bulk hydrogel, microgel networks with significantly different physical properties and morphologies were formed, demonstrating the flexibility of the physical entrapment approach for generating microgel networks.

As with microgel-crosslinked networks, physically entrapped microgel networks can be formed by polymerizing a bulk hydrogel phase around the microgels using either free radical or *in situ* gelation chemistries. Hirakura *et al*. reported the formation of a microgel nanocomposite consisting of 2-aminoethylmethacrylate-modified hyaluronic acid (crosslinked via a Michael addition reaction to form a bulk hydrogel) that entraps cholesteryl group-bearing pullulan nanogels [51]; the hydrogel degraded over over time due to the action of hyaluronidase enzyme naturally present *in vivo*. Our group has also recently reported a microgel nanocomposite in which poly(NIPAM-*co*-AA) microgels are physically entrapped inside an *in situ* gelling hydrogel formed by mixing hydrazide-functionalized carboxylmethyl cellulose with aldehyde-functionalized dextran; in this case, hydrogel degradation occurs via hydrolysis of hydrolytically labile hydrazone bonds used to crosslink the bulk hydrogel network [52].

Physical entrapment of microgels within bulk hydrogel networks has shown particular benefits in terms of improving the swelling–deswelling kinetics of microgel networks. Cai and Gupta entrapped poly(NIPAM-*co*-AA) microgels inside a PNIPAM hydrogel and observed higher swelling ratios and significantly faster swelling rates upon thermal or pH changes relative to conventional bulk hydrogels with similar compositions [53]. Similarly, Zhang *et al*. observed higher equilibrium swelling and faster swelling responses by entrapping PEG–diacrylate-crosslinked PNIPAM microgels inside a PNIPAM hydrogel [54]. By further tuning the chemistry of one or both phases, multiple types of environmental responses, diffusion resistances, solute affinities, or mechanical attributes can be engineered into the microgel networks, presenting novel and highly tunable properties for the design of functional soft materials.

Higher mechanical strength materials can also be produced using an entrapment approach, even in cases in which the bulk and microgel phase chemistries are identical. For example, entrapment of PNIPAM microgels inside a PNIPAM hydrogel continuous phase resulted in the fabrication of higher mechanical strength materials relative to hydrogel-only materials [54]. However, unlike with chemically crosslinked microgel networks in which each microgel present represents the of an

multivalent crosslinker to the hydrogel system, the improvement in composite hydrogel mechanical properties is a highly nonlinear function of microgel loading in entrapped microgel systems [54]. Indeed, if the microgel loading becomes too high, the mechanical strength of physically entrapped microgel networks can decrease relative to a bulk hydrogel with a similar composition; in such cases, the volume fraction of the continuous crosslinked network decreases to a point that the high (uncrosslinked) interfacial area between the embedded microgel and the bulk hydrogel phase reduces the overall elastic strength of the composite. Thus, in cases where mechanical strength enhancement is particularly desired for an application, chemical crosslinking between the microgel and hydrogel phase typically results in more mechanically robust microgel networks relative to physical entrapment.

Preparation of microgel networks via physical entrapment also permits remarkable control over the volume phase transitions observed within such materials. Lynch *et al.*, who dubbed such systems "plum pudding" gels due to their microstructural similarity to plum pudding, demonstrated the diversity of properties that can be achieved by physically entrapping fluorescently labeled PNIPAM microgels inside both thermoresponsive poly(NIPAM-*co*-*N*-*t*-butylacrylamide-*co*-*N*,*N*-dimethylacrylamide) (poly(NIPAM-*co*-BAM-*co*-DAM) hydrogels and non-responsive poly(DAM) hydrogels, polymerized via free radical polymerization around preformed microgels [9]. Unlike with bulk hydrogels, no skin layer was observed upon heating, resulting in rapid thermal responses in the PNIPAM bulk–PNIPAM microgel system. In addition, when the thermoresponsive microgels are entrapped inside a lightly crosslinked, non-thermoresponsive poly(DAM) hydrogel with a low elastic modulus, the bulk structure collapsed above the volume phase transition temperature (VPTT) even though the bulk phase was not itself thermoresponsive. In more highly crosslinked networks, this bulk gel collapse is avoided and a microgel phase transition happens independently of macroscopic gel swelling. Thus, by tuning the microgel fraction and the elasticity of the bulk hydrogel phase, nanocomposite microgel networks can be designed in which either the microgel or the bulk hydrogel phase primarily regulates the swelling of the overall composite material.

While the vast majority of examples of physically entrapped microgel networks involve the entrapment of a presynthesized microgel within a polymerizing bulk hydrogel phase, physically entrapped microgel networks have also been formed by using a macroporous hydrogel as a template for preparing the microgel phase. Such templating methods can generate highly ordered microgel arrays, with spacings different from those that would be achieved by electrostatically or sterically stabilized microgels. This approach also allows the production of microgel networks using different sizes or compositions of monodisperse microgel building blocks than can typically be synthesized using standard microgel polymerization techniques. Zhang and Jandt demonstrated this approach by preparing macroporous PNIPAM hydrogels using polydimethylsiloxane (PDMS) droplets stabilized by sodium dodecyl sulfate as porous templates; removal of the PDMS template resulted in large pores within the network which can subsequently be used to template microgel polymerizations *in situ* inside the macroporous hydrogel [55]. In this way, stable microgels need not be produced to act as embedded or crosslinked nanophases, as long as the

monomers or polymers used to assemble the microgels can partition selectively into the macropores within the templated hydrogel.

12.2.4.2 **Entrapment to Form 2D Films**

Both hydrogel and solid polymer films have been used to physically entrap microgels to form nanocomposite films. For hydrogel-based films, optical properties are typically the target of the network design. Nayak *et al.* reported the preparation of microgel thin films comprised of PNIPAM microgel particles inside a PNIPAM thin-film gel matrix, immobilized on a glass slide [56]. Unlike conventional PNIPAM hydrogel films, in which scattering increases and plateaus as the temperature is increased above the phase transition temperature, the microgel-impregnated hydrogel film increases in turbidity until the phase transition temperature is reached but then exhibits a large turbidity decrease above the phase transition temperature, with the rate of scattering decrease dependent on the microgel loading in the film.

Alternately, microgel entrapment within solid polymer films has been applied to enable triggered release of a particular analyte through the film. Typically, microgels are networked in disordered arrays in such devices but are incorporated at high enough concentrations that the random assembly of microgels provides a defined channel through which a solute can penetrate. The higher the microgel concentration within the film, the shorter the average percolation length and the faster the analyte flux through the membrane. Zhang and Wu first reported such systems, physically entrapping a poly(NIPAM-*co*-methacrylic acid (MAA)) microgel together with glucose oxidase and catalase in an ethyl cellulose film [57]. Glucose-responsive insulin delivery was achieved based on the pH-induced deswelling of the poly (NIPAM-*co*-MAA) microgels at high glucose concentrations (i.e., high glucose oxidase activity) inside the fixed-dimension pores defined by the dried, water-insoluble ethyl cellulose membrane support. Gordijo *et al.* improved this design by fabricating nanohybrid membranes consisting of a mixture of bovine serum albumin-manganese dioxide nanoparticle conjugates with glucose oxidase and catalase in the presence of poly(NIPAM-*co*-MAA) microgels [58]. The MnO_2 nanoparticle building blocks of the membrane enhance the mechanical strength of the membrane while also improving the long-term stability of the enzymes. The membrane enables a fully reversible fourfold increase in insulin permeation when insulin concentrations are increased from normal to hyperglycemic levels.

External triggers can also be applied to control flux within membrane network films "on demand." We recently demonstrated this concept by entrapping poly (NIPAM-*co*-*N*-isopropylmethacrylamide-*co*-acrylamide) microgels and magnetite nanoparticles within an ethyl cellulose film [59]. By applying an oscillating magnetic field, the magnetite nanoparticles generated heat via hysteresis losses, inducing a thermal phase transition in the microgels and opening the pores; subsequent removal of the magnetic field induced convective cooling of the membrane back to physiological temperature, causing the microgels to reswell and block the pores (Figure 12.9). Over 20-fold changes in drug flux were achieved upon the application and subsequent removal of a magnetic field.

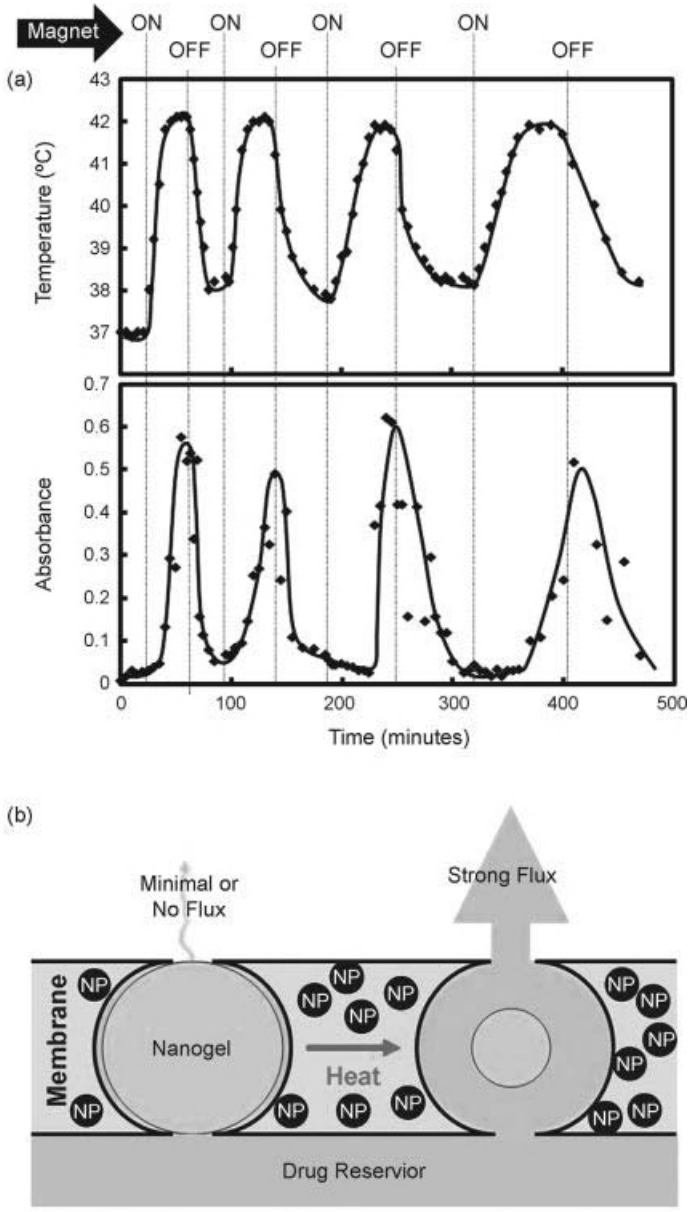

Figure 12.9 (a) Temperature profile in the sample chamber and differential flux of sodium fluorescein out of membrane-capped devices as a function of time over four successive on/off cycles using an external oscillating magnetic field. (b) Proposed mechanism of triggered drug release from microgel network composite membranes. Reprinted with permission from Hoare *et al.*, *Nano Letters*, 2009, 9, 3651. Copyright 2009, American Chemical Society [60].

12.3
Applications of Microgel Networks

The unique 3D microstructures possible using microgel networks, coupled with the faster swelling and higher mechanical strength of such networks relative to conventional hydrogels, have sparked considerable interest in applying microgel networks in a variety of applications.

12.3.1
Drug Delivery

The unique opportunity that microgel networks present for independently tuning the drug partitioning and diffusivity of drugs within each of the bulk and microgel phases has made microgel networks of considerable interest for controlling drug-delivery kinetics. In particular, by independently tuning the compositions, drug affinities, and rates of swelling of each of the bulk and microgel phases, significantly longer and (in some cases) more uniform drug release kinetics can be achieved with microgel networks relative to conventional bulk hydrogels. This is true even in cases where the compositions of the bulk and microgel phases are chemically similar. For example, Bako *et al*. entrapped poly(HEMA-*co*-poly(ethylene glycol dimethylacrylate) (PEGDMA)) microgels inside UV-photopolymerized poly(HEMA-*co*-PEGDMA) hydrogel of the same overall composition and observed prolonged release of chlorhexidine relative to the hydrogel alone (48 h compared to 24 h) [61]. This effect was attributed to slower overall hydration of the nanocomposite hydrogel (containing more highly crosslinked microgel embedded phases) compared to the bulk hydrogel alone.

The structure of the microgel network can have significantly different effects on the release of drugs according to the chemical properties of the target drug and the relative affinity of the drug for each of the two available phases inside the microgel network. Salvati *et al*. reported diffusion measurements for a series of PEG probes of different molecular weights through a microgel network consisting of PNIPAM microgels entrapped inside a DMA bulk hydrogel. The observed PEG diffusion coefficients depended almost entirely on the crosslink density of the bulk phase, with the addition of different quantities of microgels not significantly altering PEG diffusion [62]. In this case, the drug probe (PEG) has no particular affinity for the entrapped PNIPAM microgel phase; indeed, via simple mixing, it is likely that PEG would preferentially partition into the bulk (more hydrophilic) hydrogel phase upon microgel network formation. Hirakura *et al*. reached similar conclusions in investigating the delivery of glucagon-like peptide 1, insulin, and erythropoietin using cholesterol-bearing pullulan-based microgels entrapped in a hyaluronic acid-based hydrogel, with release controlled primarily by the crosslink density and degradability of the entrapping hyaluronic acid hydrogel [51]. In contrast, recent work in our lab has indicated that drug release from injectable microgel networks in which poly(NIPAM-*co*-AA) microgels with a high affinity to a target drug (bupivacaine hydrochloride, a cationic local anesthetic) are entrapped in an *in situ* gellable carbohydrate hydrogel is

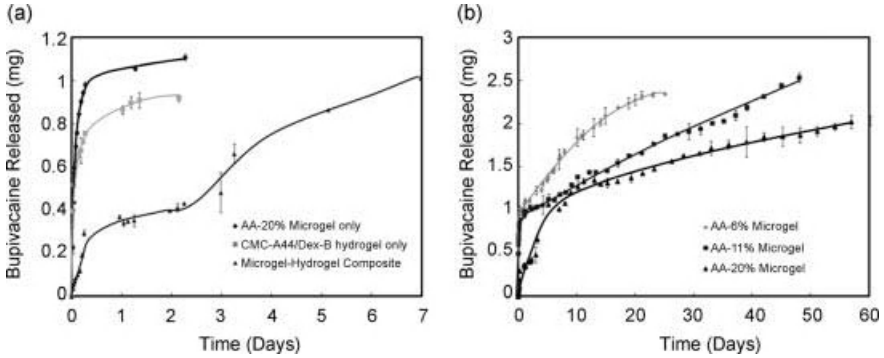

Figure 12.10 Drug release from poly(NIPAM-*co*-AA) microgels entrapped in an *in situ* gelling carboxymethyl cellulose (CMC)/dextran (Dex) hydrogel linked by hydrazone bonds: (a) comparison of bupivacaine release from CMC–Dex hydrogels alone, poly(NIPAM-*co*-AA) microgel (20 mol% AA, AA-20%) alone, and a 50 : 50 (by mass) nanocomposite hydrogel of the two components; (b) bupivacaine release from nanocomposite hydrogels consisting of a 50 : 50 (wt%) mixture of poly(NIPAM-*co*-AA) microgels with varying acrylic acid loadings (indicated by the % in the microgel legend) entrapped inside a hydrazone-crosslinked CMC–Dex injectable hydrogel. Reprinted with permission from Sivakumaran *et al.*, *Biomacromolecules*, 2011. Copyright 2011, American Chemical Society [52].

primarily controlled by the composition of the microgel phase [52]. Drug release could be extended from ~2 days with a bulk hydrogel without microgels to ~2 months in the presence of a 50% (dry polymer) mass fraction of microgels (Figure 12.10a), with successively slower drug release observed as the number of anionic functional groups in the microgel (i.e., cationic drug-binding sites) was increased (Figure 12.10b). Cho *et al.* similarly reported that the release of a model drug (rhapontin) loaded into the PNIPAM microgel phase occurred at a rate dependent only on the crosslink density of the microgel phase (i.e., independent of the inter-microgel crosslink density) [25]; here, the log *P* value of the drug chosen (~0.5) would suggest preferential partitioning of the drug into the microgel phase of the microgel network. Thus, drug partitioning between the microgel and bulk hydrogel phases appears to be the critical factor in terms of regulating drug release from microgel networks.

Multiple types of microgel phases may be entrapped inside a single bulk hydrogel phase to facilitate simultaneous delivery of multiple drugs from a single release vehicle. The ability to mix-and-match any number and any kind of embedded microgel phase within a single hydrogel represents a unique advantage of microgel networks in drug delivery, a key attribute for delivering controlled doses of synergistic drugs or drugs that have mutual incompatibility (e.g., hydrophobic and hydrophilic) from a single drug delivery device. Lynch and Dawson demonstrated this concept by embedding poly(NIPAM-*co*-BAM) microgels (hydrophobic microgels for uptake of hydrophobic solutes such as pyrene [63]) together with poly(NIPAM-*co*-AA) microgels (anionic microgels for uptake of cationic solutes such as rhodamine) inside a

single hydrogel, successfully releasing both drugs with controlled kinetics [64]. Wang *et al*. demonstrated a similar multidrug-delivery system using microgel networks based on polyampholyte microgels with both cationic and anionic charges; loading of anionic methyl orange and cationic rhodamine 6G into microgel multilayer films permitted simultaneous release of both target drugs. Further control over the relative rate of drug release was possible by introducing barrier layers of nondrug-loaded microgels with a single charge that can bind to, and thus retard release of, one of the two ionic drugs to be released [28].

Macromolecule drug delivery has also been demonstrated from microgel networks. Ramanan *et al*. entrapped bovine serum albumin (BSA)-loaded PNIPAM microgels in a PEG-diacrylate hydrogel phase polymerized *in situ* via photopolymerization [65]. Temperature-responsive BSA release was observed from the soft nanocomposite, with the crosslink density of the bulk hydrogel phase representing the major design parameter that can be tuned to effect changes in the drug-release kinetics.

Microgel networks have also been applied to significantly simplify drug loading by exploiting microgel self-assembly interactions to form a bulk hydrogel. Drugs of any chemistry, size, or even solubility can be entrapped either within or between the microgel building blocks, as the limitations on both the quantity and type (i.e., molecular weight or charge) of drug loading via diffusion into the bulk hydrogel network are minimized or eliminated when microgels are instead used as the assembly blocks. For example, thermogelled? microgel aggregates of poly(acrylic acid)–PNIPAM interpenetrating network microgels have be applied to spontaneously entrap macromolecules (e.g., dextran) upon gelation and subsequently release those macromolecules slowly over time [12]. In other cases, the drug itself may be used to drive microgel assembly via bridging [24] or crosslinking interactions, providing additional control over drug loading and release.

Effective drug delivery has been reported using multiple types of microgel assemblies. Microgel networks consisting of mixtures of highly hydrated and highly adhesive microgels (crosslinked via trivalent cation-mediated electrostatic interactions) have been investigated as transdermal drug delivery membranes with tunable drug-release properties; successful delivery of caffeine from such networks has been demonstrated [22]. Microgel membrane-based implantable devices have been fabricated for the delivery of insulin as a function of glucose levels (enabling the maintenance of normal blood glucose levels in diabetic rats) [66] as well as peptides [67] and small molecule drugs [59] using pH, temperature, and external magnetic fields as triggers. Electrostatic layer-by-layer assembled microgel films based on up to 30 layers of poly(NIPAM-*co*-AA) microgels immobilized by poly (allylamine hydrochloride) have shown repeated pulsatile bursts of insulin [68] and doxorubicin [69] over multiple cycles, with the potential to release constant pulses of insulin for more than one month. By tuning the structure of the network to suit the physicochemical properties of the target drug and the desired rate of drug release, microgel networks can offer unparalleled control over the release of a wide variety of clinically relevant therapeutics.

12.3.2
Cell Adhesion-Directing Coatings

Microgel networks have been reported to both resist cell adhesion to surfaces and direct cell adhesion (and subsequent growth) in ordered arrays, depending on the composition and assembly of the microgel building blocks.

The high water content yet near-zero net surface charge of most PNIPAM microgels below their VPTT (at which point the microgels are primarily sterically stabilized) makes such microgels of interest in cell-contacting applications. Assembly of these microgels into a bulk or 2D network permits the generation of conformal coatings of bulk biomaterial implants. Bridges demonstrated the utility of this approach by grafting PEGDMA-crosslinked PNIPAM microgels (VPTT $>37\,^{\circ}C$) to a polyethylene terephthalate surface. In the acute case, the surfaces reduced fibrinogen adsorption, reduced macrophage adhesion and spreading, and suppressed the expression of proinflammatory cytokines relative to the bare surface after a few days of implantation [70]; chronically, microgel-coated surfaces exhibited 22% thinner fibrous capsules and contained significantly lower macrophage levels relative to the uncoated controls [71] after several months of implantation. These results suggest the utility of such microgel network coatings as both short- and long-term antibiofouling interfaces.

Alternately, microgel assembly on a surface in an irregular pattern to generate micrometer-scale roughnesses instead of the nanometer-scale roughnesses typically achieved in ordered arrays can create a soft interface with the capacity to direct cellular adhesion. Lynch *et al*. described surfaces created by modifying the interactions between microgel particles to cause microgels to phase separate into microgel-rich and microgel-dilute domains which can subsequently be arrested on the interface via chemical crosslinking or physical interactions [72]. Changing the particle size alters the size of the pores formed and the distribution of microgels in the film, permitting localization of the cells in the pores (i.e., the microgel-dilute domains, Figure 12.11b) or along the ridges between pores (microgel-rich domains, Figure 12.11c), even using microgels with the same composition. Together with the demonstrated potential of PNIPAM-based grafted surfaces to adhere or release cell sheets as a function of the phase transition temperature [73], the capacity to structure microgel networks in ordered or disordered arrays with controlled morphologies offers unique potential to grow cells in defined patterns and subsequently release the resulting tissues from the surface for subsequent implantation or the construction of 3D cell scaffolds.

12.3.3
Tissue Engineering

Given the physical, mechanical, and chemical similarities between cells and microgels, the directed assembly of microgels in the presence of cells has potential to form tissue engineering matrices that provide the proper physical, chemical, and mechanical cues for tissue growth. By altering the microgel size, microgel stiffness

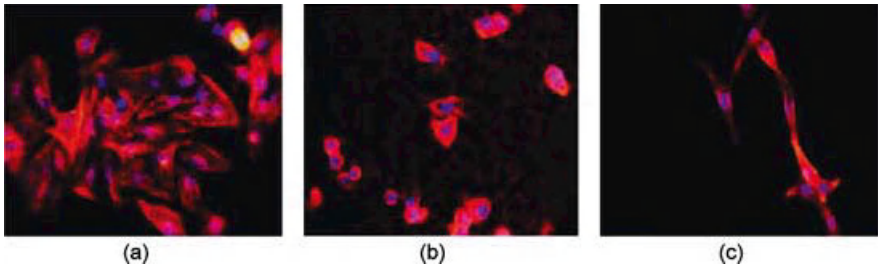

Figure 12.11 Fluorescence images (using rhodamine–phalloidin (red) and DAPI (blue) staining) of HeLa cells grown on (a) tissue culture polystyrene and (b) and (c) films made from 200 nm 50 : 50 poly(*N*-tert-butylacrylamide-*co*-NIPAM) microgel particles. In (b), the cells are confined to the pores; in (c), the cells are growing along the ridges between the pores. Magnification = 10×. Reprinted with permission from Lynch *et al.*, *J. Phys. Chem. B*, 2006, 110, 14581. Copyright 2006, American Chemical Society [72].

(i.e., crosslink density), or surface chemistry used to form the assembly, assemblies appropriate for the culturing and growth of different tissues may be generated [35]. Microgel self-assembly-based approaches may be tuned to either physically entrap cells or crosslink cells directly within the matrix; for example, ionic assembly approaches or covalent functionalization reactions using chemistries compatible with the extracellular matrix of cells can be used to form cell–microgel networks with directed cell growth and differentiation properties.

Microgel thermoaggregation via hydrophobic interactions has been identified as a particularly promising microgel network approach for generating tissue engineering matrices. Gan *et al.* demonstrated the use of poly(NIPAM-*co*-AA) microgel aggregation at physiological ionic strength to form injectable scaffolds for 3D cell culture [13]. The composition of the individual microgel building blocks can be tuned to change both the structure of the tissue engineering matrix (i.e., the pore structure) and the interaction strength between the matrix and the cells. Microgel networks which exhibited minimal deswelling upon thermoaggregation (i.e., microgels with high AA contents) facilitated the proliferation and formation of spheroid-like aggregates of HepG2 cells, while microgel networks exhibiting high deswelling upon particle aggregation (i.e., microgels with low AA contents) inhibited cell growth, presumably due to the smaller pore sizes in such networks. However, microgels with very high AA content (i.e., high hydrophilicities) could not support cell adhesion and thus resulted in low cell viability. Wang *et al.* demonstrated similar results, also using poly(NIPAM-*co*-AA) microgel networks for seeding HepG2 cells. In this case, the microgel network was demonstrated to support cell growth to spheroids over the course of several weeks (Figure 12.12) that could be subsequently released upon cooling as the microgels de-aggregated [74]. Subsequent plating of the microgel network-supported spheroid resulted in the growth of a stable cell culture. Cell growth and proliferation was also demonstrated in self-assembled microgel networks formed from poly(NIPAM-*co*-HEMA) microgels in the presence of a low concentration of calcium chloride [14].

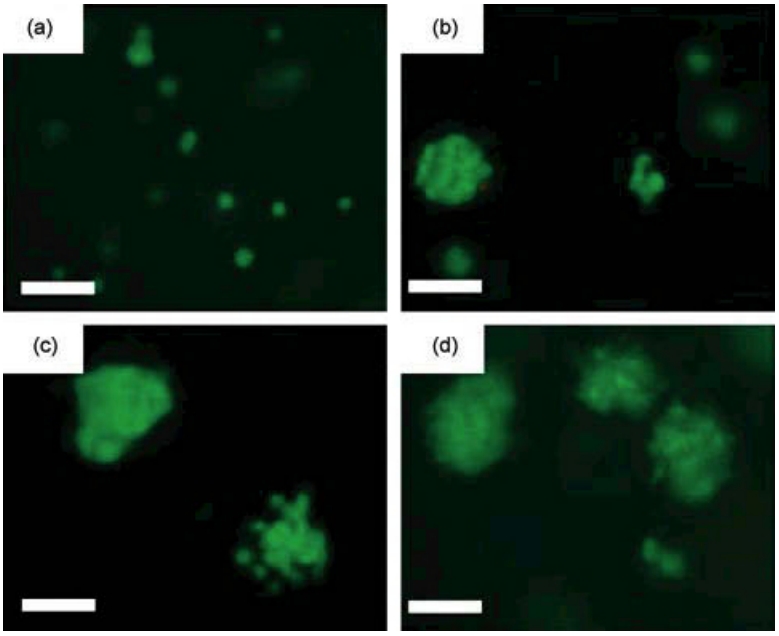

Figure 12.12 Fluorescence images of HepG2 cells (double stained with acridine orange and ethidium bromide) cultured in thermoaggregated poly(NIPAM-*co*-AA) (0.5 mol% AA) microgel-based hydrogel networks: (a) 0 days; (b) 7 days; (c) 14 days; (d) 21 days. Scale bar = 100 μm. Reprinted with permission from Wang *et al.*, *Biomacromolecules*, 2004, 25, 5281. Copyright 2004, American Chemical Society [74].

Further advantages may be achieved by combining the drug-delivery properties of microgel networks with their capacity to form a tissue engineering scaffold, enabling simultaneous support of cell growth through an interconnected porous matrix (interparticle structure) and delivery of drugs or growth factors to direct cell growth or differentiation (intraparticle structure). Hayashi *et al.* demonstrated the use of cholesterol-bearing pullulan nanogel-crosslinked hydrogels to simultaneously deliver bone morphogenic protein (BMP) and recruit and support osteoblasts to heal calvarial defects in bone [75]. Implantation of a microgel network disk seeded with BMP induced osteoblast stimulation and bone formation that did not occur in the absence of the microgel network. Combined delivery of a selective EP4 receptor agonist with BMP using the same microgel network resulted in improved performance, facilitating regeneration of both outer and inner cortical plates and bone marrow tissue required to fully reproduce a normal calvarial bone [76].

Cells may also be entrapped inside microgels to protect the cells from the strong, potentially denaturing physical interactions or chemical reactions used to crosslink microgels into a network. Using this approach, one can isolate the self-assembly or chemical crosslinking process used to form the network at the outside of the microgel without affecting the viability of the cell inside the microgel [35, 77]. Entrapment of cells inside microgels also enables the surface chemistry of the microgel to be

independently tuned relative to the bulk chemistry to enable controlled spatial assembly of microgels (and thus cells) in complex 2D or 3D arrangements without impacting the viability of the entrapped cells. Du *et al*. demonstrated this approach by patterning a glass surface with hydrophobic and hydrophilic regions to direct the assembly of microgels in a distinct 2D pattern directed by surface tension [77]. Ionic or chemical driving forces could similarly be applied to direct the formation of patterns containing multiple cell types, with subsequent post-crosslinking performed to fix the matrix in place if desired.

12.3.4 Biosensors

Ordered microgel networks templated by colloidal crystals or self-assembled films have particular utility for the design of optical sensors. Hu's group has made particular contributions in this field by fabricating a range of self-assembled microgel assemblies that are subsequently crosslinked to form iridescent microgel networks. Huang and Hu observed iridescent patterns in both covalently crosslinked and self-assembled arrays of poly(NIPAM) or poly(NIPAM-*co*-allylamine) microgel networks, observing changes in the Bragg diffraction from the nanocomposite hydrogels as a function of temperature (Figure 12.13), pH, and protein concentration not observed with individual microgel particles in suspension [47]. Entrapment or controlled growth of gold nanoparticles within the microgels facilitates the creation of tunable optical materials with refractive index periodicity on an environmentally tunable length scale, providing improved sensitivity of detection [78].

Doping a variety of sensing molecules within ordered microgel networks permits the use of microgel arrays as multistimulus detection sensors. For example, phosphorescent microgel network sensors have been reported by entrapping a water-soluble phosphorescent Au(I) complex (gold tris(3,3′,3″-trisulfonatophenyl)phosphine) into PNIPAM microgels and subsequently crosslinking the particles together to form a microgel network [79]. Up to 100-fold increases in sensitizations of the phosphorescent emission are achieved when the gold complex is entrapped inside the microgel or microgel network relative to being dissolved or suspended in aqueous solution, providing higher sensitivity detection of biological targets. Furthermore, the phase transition of the PNIPAM microgels is unaffected by the presence of the complex, permitting precise sensing of microgel deswelling (either as a function of temperature or as a function of a specific ligand–receptor interaction) by tracking the blue shift in the emission as the microgel is dehydrated.

Alternately, the analyte itself can be used to either increase or decrease the crosslinking between microgels within a network, facilitating highly sensitive analyte detection based on changes in microgel spacing within the network as the crosslink density changes. Kim *et al*. demonstrated the potential of poly(NIPAM-*co*-AA) microgels functionalized with biotin and assembled on a silane-modified glass substrate as a network-based sensor; brightfield optical microscopy could detect the multivalent binding of avidin and polyclonal antibiotin, both of which form functional

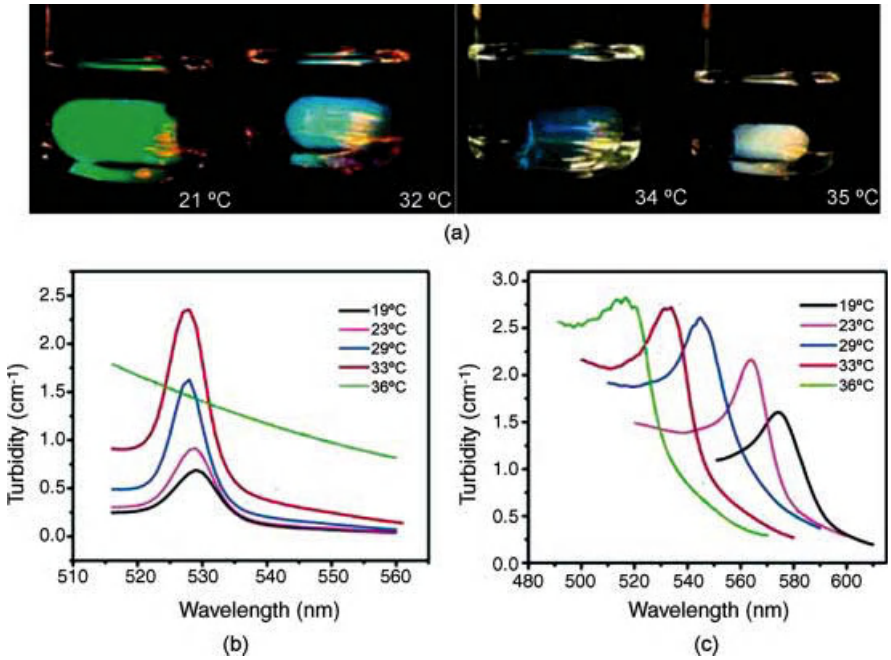

Figure 12.13 Temperature-tunable iridescence and turbidity of poly(NIPAM-*co*-allylamine) microgel networks: (a) color switch with the change of temperature; (b) turbidity of (uncrosslinked) poly(NIPAM-*co*-allylamine) microgels in suspension (concentration 4.5 wt%); (c) turbidity of (crosslinked) poly(NIPAM-*co*-allylamine) hydrogels (concentration 4.5 wt%). Reprinted with permission from Huang *et al.*, *Macromolecules*, 2007, 33, 1646. Copyright 2007, American Chemical Society [47].

crosslinks within the biotinylated microgels and thus alter the degree of swelling. The microgel network was observed to be highly specific for the target protein and, in the case of antibiotin, binding (and thus network formation) is reversible, permitting repeated or dynamic sensing of a target analyte [80]. Such systems have also been reported for antibody–antigen interactions, in which biotin–antibiotin crosslinks within an ordered microgel network are disrupted upon exposure to the free antigen in solution to induce network swelling and thus facilitate antigen detection [81].

Patterned microgel arrays containing different microgels with different responses to a targeted stimulus offer even more control over the types of responses that can be achieved in response to multiple stimuli. Chen *et al.* demonstrated such a system by using photolithography to graft azidophenyl-functionalized polyallylamine (basic) and poly(acrylic acid) (acidic) nano-thick microgel domains on a polystyrene plate, either as a monolayer of microgels or as a bilayer of both microgels stacked on top of each other in a network [82]. An increase in solution acidity resulted in swelling of the polyallylamine microgel, deswelling in the poly(acrylic acid) microgel, and minimal change in the overall swelling of the bilayer. Such an approach could also be used to rapidly detect multiple analytes using a single small microgel-based device.

12.3.5
Optical Materials

In addition to their applications in sensor technology, the optical properties of ordered colloidal crystals and microgel networks can be exploited in several different types of applications. The most widely investigated devices involve rapid, temperature-induced changes in light transmission upon the occurrence of a phase transition in a nanostructured hydrogel or ordered microgel film. For example, lightly crosslinked ordered assemblies of PNIPAM microgels respond to a laser temperature jump from 30 to 35 °C within 100 ns after the laser pulse, resulting in decreased light transmission through the crystal within 900 ns [34]. These nanosecond responses are several orders of magnitude faster than responses observed in bulk thermoresponsive hydrogels, making such materials of particular interest for rapid detection of environmental changes.

Lensing materials have also been developed based on microgel networks. Ravi *et al.* prepared intraocular lenses based on entrapment of a polyacrylamide nanogel (with a small size of ~40 nm to preserve optical clarity) inside a polyacrylamide-based hydrogel. Such materials exhibited an increased elastic modulus relative to a bulk hydrogel alone to better mimic the properties of a natural intraocular lens, improving the capacity of the lens to be auto-focused by the eye [83]. In this case, the rapid swelling responses that can be achieved with microgel networks relative to bulk hydrogels were key to the appropriateness of the material for the application; the significantly lower response rate of conventional macroscopic hydrogels is a challenge given the need for rapid accommodation of the hydrogel for focusing the eye.

12.3.6
Biomolecule Separation and Purification

Microgel networks have significant potential for the chromatographic or electrophoretic separation or purification of biological molecules such as proteins, DNA, or antibodies [84]. Three properties of composite microgel networks are particularly useful in this regard. First, the capacity to independently tune the crosslink densities and compositions of both the bulk hydrogel and microgel phases offers potential for targeted engineering of the pressure or electric field-driven flow of solutions through the bulk gel while still maintaining optimal crosslink densities (i.e., pore sizes) and analyte affinities in the microgel phase. In this way, the flow properties of a hydrogel column and the affinity properties of the column for the analyte can be decoupled, offering potential for improved performance. Second, the ability to entrap or crosslink microgels with multiple types of chemical reactivities or physical morphologies inside a single bulk matrix can facilitate more sensitive separation of complex mixtures of biomolecules. Third, the increased mechanical strength achievable with microgel networks relative to bulk hydrogels or nanoparticle/microparticle packings improves the robustness of the column over time. While Simhadri *et al.* have demonstrated the capacity of 3-acrylamidopropyltrimethylammonium chloride microgels entrapped in

a neutral acrylamide network as DNA separation columns [84], relatively little work has overall been performed in this field despite the significant opportunities that exist.

12.3.7
DNA Sequencing

Microgels and microgel networks offer advantages for capillary and microchip electrophoresis applications aimed at DNA sequencing. Relative to the conventional, linear polyacrylamide networks typically used for DNA sequencing, polyacrylamide microgels lightly crosslinked into a network using *N,N*-methylene bisacrylamide exhibit similar flow characteristics but significantly longer read lengths of DNA sequences, achieving reads of up to 726 bases with 98.5% accuracy while requiring 30% less polymer per unit volume [85]. In this case, the high interphase area between the hydrogel and bulk phase significantly enhances both the speed and accuracy of the DNA sequencing achieved.

12.4
Conclusions and Future Outlook

Microgel networks have tremendous potential to address many of the existing challenges with the use of both bulk hydrogels and free microgels in a variety of applications. The effective immobilization of microgels within a network structure, often in an ordered 2D or 3D array, provides a means of stabilizing self-assembled structures or trapping microgels at a desired location, key for the development of optimized sensors, optical materials, and local drug-delivery vehicles. The significantly more rapid swelling–deswelling kinetics achieved with microgel networks relative to bulk hydrogels alone has the potential to significantly enhance the detection limits and response times of hydrogel-based sensors. The orders-of-magnitude higher elasticities of some microgel networks relative to bulk hydrogels with similar compositions offer potential for use of such materials in load-bearing applications or as free-standing or extended membranes or columns for bioseparations. In addition, the unique capacity of microgel networks to have independently tuned chemical and physical properties within the bulk and microgel phases offers remarkable opportunities for designing controlled drug-release vehicles with extended or "on demand" kinetic profiles or bioseparation materials with independently tunable drug affinities and inlet flow properties. A range of additional applications may also be envisioned that take further advantage of these unique properties of microgel networks.

To extend the applications of microgel networks, several key research challenges should be addressed. First, the development of methods to enable the production of monodisperse microgel building blocks with sizes and/or compositions not easily achievable using existing methods would significantly expand the types of network morphologies that could be produced. Microfluidics offers significant potential in this regard, enabling the production of monodisperse microgels (based on template

monodisperse inverse emulsions) as well as the potential to assemble these building blocks into novel geometries by directing the interactions between these particles using hydrodynamic flow. Second, improving our understanding over the degree and mechanism of interpenetration between the bulk and microgel phases in physically entrapped microgel networks would enable improved control over the independence of the bulk hydrogel and microgel transitions that can be achieved, potentially leading to the development of (for example) transiently macroporous hydrogels with ordered macropore structures. Third, the development of new labile crosslinking chemistries would greatly expand control over the permanence of and/or the crosslink density within the microgel network, enabling (for example) the development of strong yet injectable microgel networks or microgel networks that can be degraded "on demand" according to the needs of the application. Finally, better exploitation of the modular, mix-and-match control over the size, chemistry, crosslink density, and environmental responsiveness of multiple types of microgels within a single microgel network may result in dramatically improved application performance without the need for developing new chemistries. Successfully addressing these and other outstanding challenges has significant potential for creating novel "smart" microgel networks with properties not yet achievable using existing materials.

References

1 Dai, Q.Z. and Kadla, J.F. (2009) Effect of nanofillers on carboxymethyl cellulose/hydroxyethyl cellulose hydrogels. *J. Appl. Polym. Sci.*, **114**, 1664–1669.

2 Sur, G.S., Lyu, S.G., and Chang, J.H. (2003) Synthesis and LCST behavior of thermosensitive poly (N-isopropylacrylamide)-clay nanocomposites. *J. Ind. Eng. Chem.*, **9**, 58–62.

3 Hernandez, J.C.R., Aroca, A.S., Ribelles, J.L.G., and Pradas, M.M. (2008) Three-dimensional nanocomposite scaffolds with ordered cylindrical orthogonal pores. *J. Biomed. Mater. Res. B*, **84**, 541–549.

4 Liang, S.M., Wu, J.J., Tian, H.F., Zhang, L.N., and Xu, J. (2008) High-strength cellulose/poly(ethylene glycol) gels. *Chemsuschem*, **1**, 558–563.

5 Tan, Y., Wang, P.X., Xu, K., Li, W.B., An, H.Y., Li, L.L., Liu, C., and Dong, L.S. (2009) Designing starch-based nanospheres to make hydrogels with high mechanical strength. *Macromol. Mater. Eng.*, **294**, 855–859.

6 Xu, K., Tan, Y., Chen, Q., An, H.Y., Li, W.B., Dong, L.S., and Wang, P.X. (2010) A novel multi-responsive polyampholyte composite hydrogel with excellent mechanical strength and rapid shrinking rate. *J. Colloid Interface Sci.*, **345**, 360–368.

7 Kato, N., Hasegawa, U., Morimoto, N., Saita, Y., Nakashima, K., Ezura, Y., Kurosawa, H., Akiyosh, K., and Noda, M. (2007) Nanogel-based delivery system enhances PGE(2) effects on bone formation. *J. Cell Biochem.*, **101**, 1063–1070.

8 Suarez, I.J., Fernandez-Nieves, A., and Marquez, M. (2006) Swelling kinetics of poly(N-isopropylacrylamide) minigels. *J. Phys. Chem. B*, **110**, 25729–25733.

9 Lynch, I. and Dawson, K.A. (2003) Synthesis and characterization of an extremely versatile structural motif called the "plum-pudding" gel. *J. Phys. Chem. B*, **107**, 9629–9637.

10 Makino, K., Kado, H., and Ohshima, H. (2001) Aggregation behavior of poly(N-isopropylacrylamide) microspheres. *Colloids Surf. B*, **20**, 347–353.

11 Ohshima, H. (2009) Theory of electrostatics and electrokinetics of soft particles. *Sci. Technol. Adv. Mater.*, **10**. 063001 doi:10.1088/1468-6996/10/6/063001

12 Hu, Z.B., Xia, X.H., Marquez, M., Weng, H., and Tang, L.P. (2005) Controlled release from and tissue response to physically bonded hydrogel nanoparticle assembly. *Macromol. Symp.*, **227**, 275–284.

13 Gan, T.T., Guan, Y., and Zhang, Y.J. (2010) Thermogelable PNIPAM microgel dispersion as 3D cell scaffold: effect of syneresis. *J. Mater. Chem.*, **20**, 5937–5944.

14 Gan, T.T., Zhang, Y.J., and Guan, Y. (2009) In situ gelation of P(NIPAM-HEMA) microgel dispersion and its applications as injectable 3D cell scaffold. *Biomacromolecules*, **10**, 1410–1415.

15 Yang, Z.G. and Ding, J.D. (2008) A thermosensitive and biodegradable physical gel with chemically crosslinked nanogels as the building block. *Macromol. Rapid. Commun.*, **29**, 751–756.

16 Kolmakov, G.V., Matyjaszewski, K., and Balazs, A.C. (2009) Harnessing labile bonds between nanogel particles to create self-healing materials. *ACS Nano*, **3**, 885–892.

17 Yu, X., Samanta, B., Xu, H., Arumugam, P., Ofir, Y., Jordan, B.J., and Rotello, V.M. (2009) Fabrication and functionalization of supramolecular microgel arrays through complementary hydrogen-bonding interactions. *Small*, **5**, 86–89.

18 DeVolder, R.J. and Kong, H.J. (2010) Three dimensionally flocculated proangiogenic microgels for neovascularization. *Biomaterials*, **31**, 6494–6501.

19 Karpushkin, E.A., Kechek'yan, A.S., and Zezin, A.B. (2006) Interpolyelectrolyte reaction between the particles of oppositely charged microgels. *Polym. Sci. Ser. B+*, **48**, 301–303.

20 Yao, X., Yao, H.W., and Li, Y.T. (2009) Hierarchically aligned porous scaffold by ice-segregation-induced self-assembly and thermally triggered electrostatic self-assembly of oppositely charged thermosensitive microgels. *J. Mater. Chem.*, **19**, 6516–6520.

21 Acciaro, R., Aulin, C., Wagberg, L., Lindstrom, T., Claesson, P.M., and Varga, I. (2011) Investigation of the formation, structure and release characteristics of self-assembled composite films of cellulose nanofibrils and temperature responsive microgels. *Soft Matter*, **7**, 1369–1377.

22 Don, T.M., Huang, M.L., Chiu, A.C., Kuo, K.H., Chiu, W.Y., and Chiu, L.H. (2008) Preparation of thermo-responsive acrylic hydrogels useful for the application in transdermal drug delivery systems. *Mater. Chem. Phys.*, **107**, 266–273.

23 Nakamura, M., Nishiyama, Y., Henmi, C., Iwanaga, S., Nakagawa, H., Yamaguchi, K., Akita, K., Mochizuki, S., and Takiura, K. (2008) Ink jet three-dimensional digital fabrication for biological tissue manufacturing: analysis of alginate microgel beads produced by ink jet droplets for three dimensional tissue fabrication. *J. Imaging Sci. Technol.*, **52**, 060201.

24 Cho, E.C., Kim, J.W., Fernandez-Nieves, A., and Weitz, D.A. (2008) Highly responsive hydrogel scaffolds formed by three-dimensional organization of microgel nanoparticles. *Nano Lett.*, **8**, 168–172.

25 Cho, E.C., Kim, J.W., Hyun, D.C., Jeong, U., and Weitz, D.A. (2010) Regulating volume transitions of highly responsive hydrogel scaffolds by adjusting the network properties of microgel building block colloids. *Langmuir*, **26**, 3854–3859.

26 Serpe, M.J., Jones, C.D., and Lyon, L.A. (2003) Layer-by-layer deposition of thermoresponsive microgel thin films. *Langmuir*, **19**, 8759–8764.

27 Sorrell, C.D. and Lyon, L.A. (2007) Bimodal swelling responses in microgel thin films. *J. Phys. Chem. B*, **111**, 4060–4066.

28 Wang, X., Zhang, L.B., Wang, L., Sun, J.Q., and Shen, J.C. (2010) Layer-by-layer assembled polyampholyte microgel films for simultaneous release of anionic and cationic molecules. *Langmuir*, **26**, 8187–8194.

29 Debord, J.D. and Lyon, L.A. (2000) Thermoresponsive photonic crystals. *J. Phys. Chem. B*, **104**, 6327–6331.

30 Debord, S.B. and Lyon, L.A. (2003) Influence of particle volume fraction on packing in responsive hydrogel colloidal crystals. *J. Phys. Chem. B*, **107**, 2927–2932.

31 Hellweg, T., Kratz, K., Pouget, S., and Eimer, W. (2002) Internal dynamics in colloidal PNIPAM microgel particles immobilised in mesoscopic crystals. *Colloids Surf. A*, **202**, 223–232.

32 Horecha, M., Senkovskyy, V., Synytska, A., Stamm, M., Chervanyov, A.I., and Kiriy, A. (2010) Ordered surface structures from PNIPAM-based loosely packed microgel particles. *Soft Matter*, **6**, 5980–5992.

33 Lally, S., Bird, R., Freemont, T.J., and Saunders, B.R. (2009) Microgels containing methacrylic acid: effects of composition on pH-triggered swelling and gelation behaviours. *Colloid Polym. Sci.*, **287**, 335–343.

34 Reese, C.E., Mikhonin, A.V., Kamenjicki, M., Tikhonov, A., and Asher, S.A. (2004) Nanogel nanosecond photonic crystal optical switching. *J. Am. Chem. Soc.*, **126**, 1493–1496.

35 Du, Y., Lo, E., Vidula, M.K., Khabiry, M., and Khademhosseini, A. (2008) Method of bottom-up directed assembly of cell-laden microgels. *Cell Mol. Bioeng.*, **1**, 157–162.

36 Zhou, J., Wang, G.N., Marquez, M., and Hu, Z.B. (2009) The formation of crystalline hydrogel films by self-crosslinking microgels. *Soft Matter*, **5**, 820–826.

37 Van Tomme, S.R., van Steenbergen, M.J., De Smedt, S.C., van Nostrum, C.F., and Hennink, W.E. (2005) Self-gelling hydrogels based on oppositely charged dextran microspheres. *Biomaterials*, **26**, 2129–2135.

38 He, C.C., Jiao, K.X., Zhang, X., Xiang, M., Li, Z.Y., and Wang, H.L. (2011) Nanoparticles, microgels and bulk hydrogels with very high mechanical strength starting from micelles. *Soft Matter*, **7**, 2943–2952.

39 Xia, L.W., Ju, X.J., Liu, J.J., Xie, R., and Chu, L.Y. (2010) Responsive hydrogels with poly(N-isopropylacrylamide-co-acrylic acid) colloidal spheres as building blocks. *J. Colloid Interface Sci.*, **349**, 106–113.

40 Matsumoto, A., Kawasaki, N., and Shimatani, T. (2000) Free-radical cross-linking polymerization of diallyl terephthalate in the presence of microgel-like poly(allyl methacrylate) microspheres. *Macromolecules*, **33**, 1646–1650.

41 Tan, Y., Xu, K., Wang, P.X., Li, W.B., Sun, S.M., and Dong, L.S. (2010) High mechanical strength and rapid response rate of poly(N-isopropylacrylamide) hydrogel crosslinked by starch-based nanospheres. *Soft Matter*, **6**, 1467–1471.

42 Zhang, J.T., Keller, T.F., Bhat, R., Garipcan, B., and Jandt, K.D. (2010) A novel two-level microstructured poly(N-isopropylacrylamide) hydrogel for controlled release. *Acta Biomater.*, **6**, 3890–3898.

43 Milani, A.H., Liu, R.X., Freemont, T.J., and Saunders, B.R. (2011) Doubly crosslinked pH-responsive microgels prepared by particle inter-penetration: Swelling and mechanical properties. *Soft Matter*, **7**, 4696–4704.

44 Morimoto, N., Ohki, T., Kurita, K., and Akiyoshi, K. (2008) Thermo-responsive hydrogels with nanodomains: Rapid shrinking of a nanogel-crosslinking hydrogel of poly(N-isopropyl acrylamide). *Macromol. Rapid Commun.*, **29**, 672–676.

45 Qin, X.P., Zhao, F., Liu, Y.K., Wang, H.Y., and Feng, S.Y. (2009) High mechanical strength hydrogels preparation using hydrophilic reactive microgels as crosslinking agents. *Colloid Polym. Sci.*, **287**, 621–625.

46 Bencherif, S.A., Washburn, N.R., and Matyjaszewski, K. (2009) Synthesis by AGET ATRP of degradable nanogel precursors for in situ formation of nanostructured hyaluronic acid hydrogel. *Biomacromolecules*, **10**, 2499–2507.

47 Huang, G. and Hu, Z.B. (2007) Phase behavior and stabilization of microgel arrays. *Macromolecules*, **40**, 3749–3756.

48 Qin, X.P., Zhao, F., and Feng, S.Y. (2011) Preparation of microgel composite hydrogels by polymer post-crosslinking method. *Express Polym. Lett.*, **5**, 460–469.

49 Meid, J., Friedrich, T., Tieke, B., Lindner, P., and Richtering, W. (2011) Composite hydrogels with temperature sensitive heterogeneities: influence of gel matrix on the volume phase transition of embedded poly-(N-isopropylacrylamide) microgels. *Phys. Chem. Chem. Phys.*, **13**, 3039–3047.

50 Musch, J., Schneider, S., Lindner, P., and Richtering, W. (2008) Unperturbed volume transition of thermosensitive poly-(N-isopropylacrylamide) microgel particles embedded in a hydrogel matrix. *J. Phys. Chem. B*, **112**, 6309–6314.

51 Hirakura, T., Yasugi, K., Nemoto, T., Sato, M., Shimoboji, T., Aso, Y., Morimoto, N., and Akiyoshi, K. (2010) Hybrid hyaluronan hydrogel encapsulating nanogel as a protein nanocarrier: New system for sustained delivery of protein with a chaperone-like function. *J. Controlled Release*, **142**, 483–489.

52 Sivakumaran, D., Maitland, D.M., and Hoare, T. (2011) Injectable microgel-hydrogel composites for prolonged small molecule drug delivery. *Biomacromolecules*, **12** (11), 4112–4120.

53 Cai, W.S. and Gupta, R.B. (2002) Fast-responding bulk hydrogels with microstructure. *J. Appl. Polym. Sci.*, **83**, 169–178.

54 Zhang, X.Z. and Chu, C.C. (2005) Fabrication and characterization of microgel-impregnated, thermosensitive PNIPAAm hydrogels. *Polymer*, **46**, 9664–9673.

55 Zhang, J.T. and Jandt, K.D. (2008) A novel approach to prepare porous poly(N-isopropylacrylamide) hydrogel with superfast shrinking kinetics. *Macromol. Rapid. Commun.*, **29**, 593–597.

56 Nayak, S., Debord, S.B., and Lyon, L.A. (2003) Investigations into the deswelling dynamics and thermodynamics of thermoresponsive microgel composite films. *Langmuir*, **19**, 7374–7379.

57 Zhang, K. and Wu, X.Y. (2002) Modulated insulin permeation across a glucose-sensitive polymeric composite membrane. *J. Controlled Release*, **80**, 169–178.

58 Gordijo, C.R., Shuhendler, A.J., and Wu, X.Y. (2010) Glucose-responsive bioinorganic nanohybrid membrane for self-regulated insulin release. *Adv. Funct. Mater.*, **20**, 1404–1412.

59 Hoare, T., Santamaria, J., Goya, G., Irusta, S., Lau, S., Lin, D., Padera, R., Langer, R., and Kohane, D.S. (2009) A magnetically-triggered composite membrane for on-demand drug delivery. *Nano Lett.*, **9**, 3651–3657.

60 Hoare, T., Santamaria, J., Goya, G., Irusta, S., Lau, S., Lin, D., Padera, R., Langer, R., and Kohane, D.S. (2009) A magnetically-triggered composite membrane for on-demand drug delivery. *Nano Lett.*, **9**, 3651–3657.

61 Bako, J., Szepesi, M., Veres, A.J., Cserhati, C., Borbely, Z.M., Hegedus, C., and Borbely, J. (2008) Synthesis of biocompatible nanocomposite hydrogels as a local drug delivery system. *Colloid Polym. Sci.*, **286**, 357–363.

62 Salvati, A., Soderman, O., and Lynch, I. (2007) Plum-pudding gels as a platform for drug delivery: Understanding the effects of the different components on the diffusion behavior of solutes. *J. Phys. Chem. B*, **111**, 7367–7376.

63 Lynch, I. and Dawson, K.A. (2004) Release of model compounds from "plum-pudding"-type gels composed of microgel particles randomly dispersed in a gel matrix. *J. Phys. Chem. B*, **108**, 10893–10898.

64 Lynch, I., de Gregorio, P., and Dawson, K.A. (2005) Simultaneous release of hydrophobic and cationic solutes from thin-film "plum-pudding" gels: A multifunctional platform for surface drug delivery? *J. Phys. Chem. B*, **109**, 6257–6261.

65 Ramanan, R.M.K., Chellamuthu, P., Tang, L.P., and Nguyen, K.T. (2006) Development of a temperature-sensitive composite hydrogel for drug delivery applications. *Biotechnol. Progr.*, **22**, 118–125.

66 Gordijo, C.R., Koulajian, K., Shuhendler, A.J., Bonifacio, L.D., Huang, H.Y., Chiang, S., Ozin, G.A., Giacca, A., and Wu, X.Y. (2011) Nanotechnology-enabled closed loop insulin delivery device: In vitro and in vivo evaluation of glucose-regulated insulin

release for diabetes control. *Adv. Funct. Mater.*, **21**, 73–82.

67 Zhang, K. and Wu, X.Y. (2004) Temperature and pH-responsive polymeric composite membranes for controlled delivery of proteins and peptides. *Biomaterials*, **25**, 5281–5291.

68 Nolan, C.M., Serpe, M.J., and Lyon, L.A. (2004) Thermally modulated insulin release from microgel thin films. *Biomacromolecules*, **5**, 1940–1946.

69 Serpe, M.J., Yarmey, K.A., Nolan, C.M., and Lyon, L.A. (2005) Doxorubicin uptake and release from microgel thin films. *Biomacromolecules*, **6**, 408–413.

70 Bridges, A.W., Singh, N., Burns, K.L., Babensee, J.E., Lyon, L.A., and Garcia, A.J. (2008) Reduced acute inflammatory responses to microgel conformal coatings. *Biomaterials*, **29**, 4605–4615.

71 Bridges, A.W., Whitmire, R.E., Singh, N., Templeman, K.L., Babensee, J.E., Lyon, L.A., and Garcia, A.J. (2010) Chronic inflammatory responses to microgel-based implant coatings. *J. Biomed. Mater. Res. A*, **94**, 252–258.

72 Lynch, I., Miller, I., Gallagher, W.M., and Dawson, K.A. (2006) Novel method to prepare morphologically rich polymeric surfaces for biomedical applications via phase separation and arrest of microgel particles. *J. Phys. Chem. B*, **110**, 14581–14589.

73 Okano, T., Yamada, N., Sakai, H., and Sakurai, Y. (1993) A novel recovery-system for cultured-cells using plasma-treated polystyrene dishes grafted with poly(N-isopropylacrylamide). *J. Biomed. Mater. Res.*, **27**, 1243–1251.

74 Wang, D.D., Cheng, D., Guan, Y., and Zhang, Y.J. (2011) Thermoreversible hydrogel for in situ generation and release of HepG2 spheroids. *Biomacromolecules*, **12**, 578–584.

75 Hayashi, C., Hasegawa, U., Saita, Y., Hemmi, H., Hayata, T., Nakashima, K., Ezura, Y., Amagasa, T., Akiyoshi, K., and Noda, M. (2009) Osteoblastic bone formation is induced by using nanogel-crosslinking hydrogel as novel scaffold for bone growth factor. *J. Cell Physiol.*, **220**, 1–7.

76 Kamolratanakul, P., Hayata, T., Ezura, Y., Kawamata, A., Hayashi, C., Yamamoto, Y., Hemmi, H., Nagao, M., Hanyu, R., Notomi, T. *et al.* (2011) Nanogel-based scaffold delivery of prostaglandin E-2 receptor-specific agonist in combination with a low dose of growth factor heals critical-size bone defects in mice. *Arthritis Rheum.*, **63**, 1021–1033.

77 Du, Y.A., Ghodousi, M., Lo, E., Vidula, M.K., Emiroglu, O., and Khademhosseini, A. (2010) Surface-directed assembly of cell-laden microgels. *Biotechnol. Bioeng.*, **105**, 655–662.

78 Suzuki, D., McGrath, J.G., Kawaguchi, H., and Lyon, L.A. (2007) Colloidal crystals of thermosensitive, core/shell hybrid microgels. *J. Phys. Chem. C*, **111**, 5667–5672.

79 Marpu, S., Hu, Z.B., and Omary, M.A. (2010) Brightly phosphorescent, environmentally responsive hydrogels containing a water-soluble three-coordinate gold(I) complex. *Langmuir*, **26**, 15523–15531.

80 Kim, J., Nayak, S., and Lyon, L.A. (2005) Bioresponsive hydrogel microlenses. *J. Am. Chem. Soc.*, **127**, 9588–9592.

81 Kim, J.S., Singh, N., and Lyon, L.A. (2006) Label-free biosensing with hydrogel microlenses. *Angew Chem. Int. Ed.*, **45**, 1446–1449.

82 Chen, G.P., Kawazoe, N., Fan, Y.J., Ito, Y., and Tateishi, T. (2007) Grid pattern of nanothick microgel network. *Langmuir*, **23**, 5864–5867.

83 Ravi, N., Aliyar, H.A., and Hamilton, P.D. (2005) Hydrogel nanocomposite as a synthetic intra-ocular lens capable of accommodation. *Macromol. Symp.*, **227**, 191–201.

84 Simhadri, J.J., Stretz, H.A., Oyanader, M., and Arce, P.E. (2010) Role of nanocomposite hydrogel morphology in the electrophoretic separation of biomolecules: A review. *Ind. Eng. Chem. Res.*, **49**, 11866–11877.

85 Doherty, E.A.S., Kan, C.W., Paegel, B.M., Yeung, S.H.I., Cao, S.T., Mathies, R.A., and Barron, A.E. (2004) Sparsely cross-linked "nanogel" matrixes as fluid, mechanically stabilized polymer networks for high-throughput microchannel DNA sequencing. *Anal. Chem.*, **76**, 5249–5256.

13
Color-Tunable Poly (*N*-Isopropylacrylamide) Microgel-Based Etalons: Fabrication, Characterization, and Applications

Michael J. Serpe, Courtney D. Sorrell, Matthew C.D. Carter, Ian N. Heppner, Janelle B. Smiley-Wiens, and Liang Hu

13.1
Introduction

Photonic materials interact with incident light (via reflection/refraction) to produce interesting properties, for example, color. A photonic material that is commonly found in nature is the opal gemstone. Opals have a refractive index order (periodicity) in three dimensions, which yields color, but many other examples come from nature as well (e.g., peacock feathers, sea-mouse whiskers, and butterfly wings). Color, while it can come from materials with 3D periodicity, can also result from structural periodicity in two dimensions and one dimension. For all the above materials, the color is caused by refractive index/dielectric periodicity at the length scale of the wavelength of light used [1–3], and not by the addition of dyes or pigments to the materials.

Of special interest to the work in this chapter are 1D optical materials (e.g., Bragg mirrors, Bragg reflectors, Bragg stacks). These constructs are the simplest of the photonic materials, and rely on periodic arrangement of dielectrics in only one dimension. For example, Bragg mirrors are generally composed of layers of materials of alternating refractive index, and the reflected/refracted light at the interface of each layer leads to constructive/destructive interference, which results in color. The refractive index and thickness of each of the layers contributes to the observed optical properties; as dielectric layer thickness or refractive index increases the color of the material red shifts, and vice versa [1, 4, 5].

Fabry–Pérot etalons, interferometers, and waveguides, although similar to Bragg stacks, are formed by creating a cavity containing a dielectric between two reflective surfaces. The "color" of these assemblies also depends on the thickness and refractive index of the cavity material, that is, increased thickness and refractive index yields a red shift [1]. A Fabry–Pérot etalon/interferometer, or simply etalon, is an optical device that consists of a dielectric layer between two reflective surfaces or mirrors as shown in Figure 13.1. Light impinging on the etalon enters the cavity between the mirrors, and resonates, causing light interference. This process yields a characteristic

Hydrogel Micro and Nanoparticles, First Edition. Edited by L. Andrew Lyon and Michael Joseph Serpe.
© 2012 Wiley-VCH Verlag GmbH & Co. KGaA. Published 2012 by Wiley-VCH Verlag GmbH & Co. KGaA.

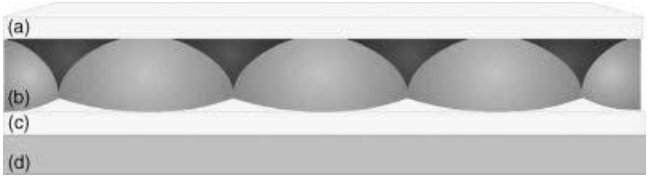

Figure 13.1 The Fabry–Pérot etalon depicting (a,c) two reflective surfaces sandwiching (b) a dielectric layer, all on (d) and glass base. Reprinted with permission from [26].

reflectance spectrum, and hence color. The resulting spectra can be defined by the equation for the interference of light in the optical cavity, and the maxima of reflected light intensity are described by the following equation:

$$\lambda m = 2nd\cos\theta \tag{13.1}$$

where λ is the wavelength maximum of the peak(s), m is the peak order, n is the refractive index of the dielectric, d is the spacing between the mirrors, and θ is the angle of incidence [6]. As stated above, and depicted in Equation 13.1, λ is directly proportional to n and d, therefore an increase in n or d results in a red shift of a peak of a given order m.

While photonic materials that exhibit "static" color are visually stimulating, and have enormous utility, photonic materials that change color in response to a stimulus (dynamic assemblies) are even more intriguing. Tunable photonic materials are useful as colorimetric sensor materials [4, 7–13], but are also used for laser applications, electronics, "smart" medical dressings [14], and environmentally friendly coatings for glass [15]. The Ozin group has made great strides in the construction of such materials, making Bragg stacks from inorganic materials like TiO_2 and SiO_2 films, inorganic nanoparticles, colloidal microspheres, and laponite clay [9, 16–18]. The Asher group has also made significant progress in this area, constructing tunable photonic structures by polymerizing crystalline colloidal arrays in a poly(*N*-isopropylacrylamide) (PNIPAM) matrix [11, 19–23].

Like the materials made in the Ozin and Asher labs, the color of the materials being developed in our lab is dynamically tunable. The "color" of our assemblies is tunable because these devices are constructed from responsive PNIPAM microgels sandwiched between two thin gold (Au) mirrors [24–26].

PNIPAM is a water-soluble thermoresponsive polymer, which undergoes a coil (swollen) to globule (collapsed) transition at $\sim$31 °C, expelling the majority of its solvating water in the process [27–31]. Hydrogels can be made from PNIPAM by incorporation of crosslinks to hold the PNIPAM chains together [29, 32, 33]. Now, the response on the PNIPAM chain length scale can propagate through the material to yield a macroscopic response, that is, the hydrogels contract (decrease size) and expand (increase size) with temperature variations. The addition of co-monomers to the hydrogel can influence its responsivity and can have a strong impact on the hydrogel structure and function by providing chemical handles to which one can attach proteins [34], small molecules [35–37], and other polymers [38]. One common co-monomer is acrylic acid (AA) [39–42]. AA has a pK_a of $\sim$4.25, so

when a PNIPAM-*co*-AA hydrogel is at a pH above the pK_a for AA the collapse transition is hindered. This is a result of Coulombic repulsion between the deprotonated AA in the hydrogel. Full thermoresponsivity can be recovered by simply lowering the pH to a value below 4.25.

The unique properties of PNIPAM can be used to synthesize a variety of colloidally stable, micro- or nano-sized hydrogel particles (microgels, and nanogels, respectively) with varying chemical and physical properties [37, 39, 43–50].

PNIPAM-based microgels and nanogels are colloidally stable hydrogel particles that, like their hydrogel counterparts, respond to temperature changes by changing their size (diameter). Again, this transition happens at ~31 °C. Specifically, when the temperature of the PNIPAM hydrogel particles is raised above ~31 °C, the microgels/nanogels deswell and expel the water solvating their structure. When the temperature is returned to below ~31 °C, the particles reswell with water and return to their initial diameter. PNIPAM-based microgels can also be made responsive to pH, ionic strength, glucose [35], protein binding [51], and DNA hybridization [52, 53]. As for the hydrogels, AA is the most popular co-monomer modification for PNIPAM-based microgels/nanogels. The AA not only renders the hydrogel particle responsive to pH, but it too can be utilized as a reactive group for microgel/nanogel modification [36, 42]. Microgels composed of PNIPAM can be modified to affect a myriad of material properties and functions, the most important aspect for our work is the potential to tune "lattice" spacing and color in ordered materials [24–26].

Our PNIPAM-based etalons can be fabricated to have a single bright color [24–26], and because the microgels exhibit a diameter that is dependent on temperature and pH, the mirror–mirror spacing can be dynamically tuned. The result is color tunability according to Equation 13.1; note also, that the change in refractive index has been found to be negligible for our etalons [24–26]. The materials exhibit multipeak spectra (as predicted from Equation 13.1, for the different reflection orders, m) that shift >300 nm spectrally in response to an increase in temperature of ~15 °C, with the majority of the shift occurring over ~7 °C. This high sensitivity makes microgel-based etalons excellent platforms for optical sensing applications. By incorporating analyte sensitive microgels into the etalon, the mirror–mirror distance can be engineered to change in the presence or absence of a specific analyte. The rest of the chapter is focused on microgel-based photonic materials, microgel-based etalons from our lab, and concludes with an example of glucose sensing from our lab.

13.2 Microgel-Based Photonic Materials

A mature field of microgel assemblies for optical applications is 3D crystalline assemblies of microgels, or colloidal crystals. This field has been pioneered by the work in the Lyon group, and others [54–62]. The Lyon group showed that microgel colloidal crystals can be assembled by concentrating the microgels into a viscous pellet, followed by thermal annealing, which allows the microgels to take on their thermodynamically preferred arrangement into crystals. The crystals reflect light of

specific wavelengths, dependent on the spacing between the microgels. The Lyon group has also extensively studied the fundamental properties of these assemblies; the results are published in multiple articles [54–59].

Of particular interest to this chapter are surface immobilized microgels. Various techniques have been used to immobilize microgels on surfaces such as glass, plastics, gold, and silicon [3, 24–26, 63–69]. The deposition approaches include: drying from aqueous solution [3, 68], dip coating [69], spin coating [63, 64, 70], adsorption [65, 67], and centrifugation [66]. These approaches have all been shown to yield surface-bound microgels with varying inter-microgel distances. However, these techniques can be time consuming, and they often yield inhomogeneous and/or sparse microgel coverage. For certain applications, such as drug delivery [71, 72], medical device coatings [73], solar cells [74], and batteries [75], it is desirable to generate *dense*, closely packed, "monolithic" and conformal polymer coatings. A unique property of colloidal microgels is that their assembly density can be controlled by modulating the softness and composition of the microgel, the solution ionic strength, pH, or temperature of the deposition medium, or the surface interactions at the solid–microgel interface [65].

Microgel thin films themselves are colored due to thin film interference, diffraction, or scattering [2]. Kawaguchi and coworkers [3] have shown that simple changes in the concentration of the particle solution deposited on a surface can result in drastic changes in the particle–particle spacing, and change the overall optical properties of the thin film. Kawaguchi's films were made simply by suspending microgels in solution at various concentrations and allowing them to dry into films on a substrate. Kawaguchi's work added significantly to the body of work by other researchers, who have used capillary forces [76, 77], the environment [78] and nature of the particle [79, 80], and the surface chemistry [81] to control the spacing and nature of the resultant microgel films. Subsequent work has further expanded this knowledge to include an understanding of how temperature [82, 83], charge or magnetic field [84, 85], pH [58], and hydrophobic/hydrophilic interactions [86] affect the formation of microgel films and their resultant behavior.

13.2.1
Microgel-Based Etalons

In our previous studies [25] we fabricated etalons by drying 775 μl of a 5% (v/v) solution of ~1.5 μm diameter PNIPAM-*co*-AA microgels onto an Au-coated glass coverslip (2 nm Cr was used as an adhesion layer followed by 15 nm Au). To make an etalon, a subsequent 2 nm Cr/15 nm Au overlayer was deposited on the initial microgel layer, a photograph of the etalon in air is shown in Figure 13.2a. Figure 13.2b,c shows differential interference microscopy (DIC) images of the resultant microgel film in Figure 13.1a, prior to the Cr/Au overlayer addition. As can be seen from the figure, the film's color and microgel packing density is not consistent from location to location. We experimented with drying more concentrated microgel solutions onto Au, but were never able to achieve *complete* coverage of the Au substrate with a dense, monolithic layer of microgels. The dense, monolithic

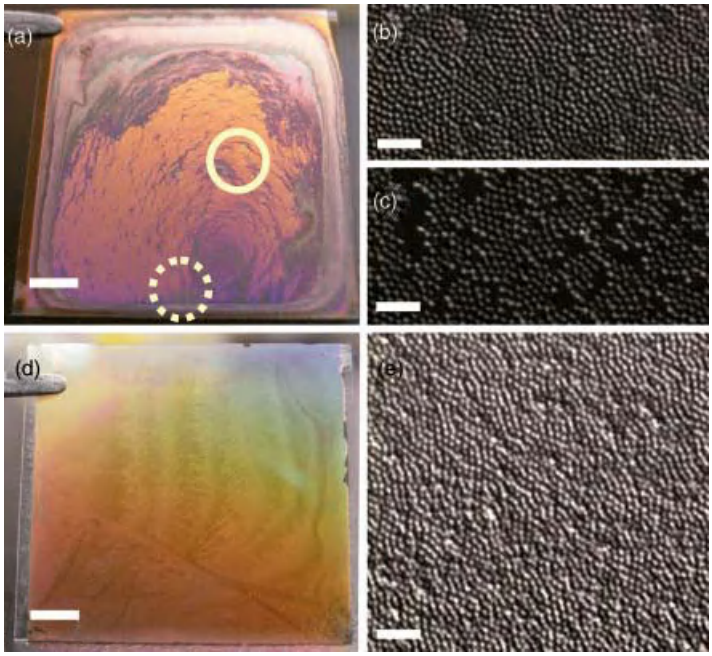

Figure 13.2 Photographs and DIC images of films fabricated using (a) the drying method and corresponding DIC images of an area that is an (b) etalon corresponding to the solid circle in (a) and an area that (c) is not an etalon corresponding to the dashed circle in (a). (d) A photograph of a film fabricated using the "paint-on" method and the corresponding (e) DIC image of the film. DIC images were taken using a 100× oil immersion objective before the addition of Cr/Au overlayer, scale bars are 5 μm. Scale bars in the photographs are 5 mm. Reprinted with permission from [24].

microgel coverage is necessary to make an etalon. The non-homogenous surface coverage is most likely a result of the so-called "coffee-ring effect" [87, 88].

Based on this result, we reasoned that a deposition technique that avoided this coffee-ring effect would be ideal. As a result, we developed the so-called "paint-on" method as depicted in Scheme 13.1 [24]. Here, concentrated microgels were continuously spread onto an annealed, clean, Au-coated glass substrate until the layer completely dried. Once completely dry, the film was rinsed with deionized water and soaked in a deionized water bath overnight at ∼30 °C. This was shown to remove any microgels not directly bound to the Au substrate, and was necessary to increase the quality of the resultant etalon. This technique yields an extremely robust, close-packed, monolithic layer of microgels on the Au.

Etalons made via this approach are far more visually, spectrally, and microscopically uniform, when compared to the air-dried films, see Figure 13.2d,e. The spectral quality of the etalons was determined by collecting reflectance spectra over random regions of the etalons. Figure 13.3a shows spectra obtained at three randomly selected regions of a "painted" etalon. As shown, reflectance peaks appear at very similar wavelengths, independent of the region being probed. For comparison,

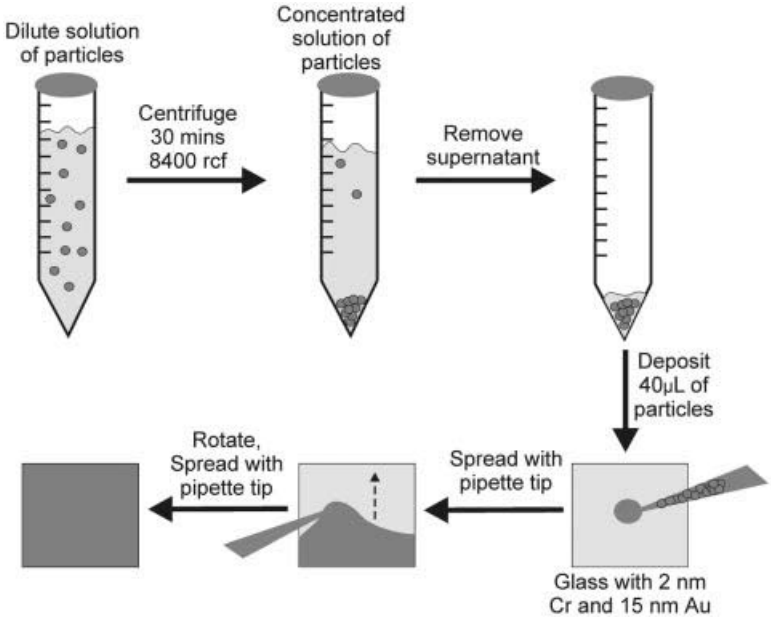
Dilute solution of particles
Centrifuge 30 mins 8400 rcf
Concentrated solution of particles
Remove supernatant
Deposit 40μL of particles
Spread with pipette tip
Rotate, Spread with pipette tip
Glass with 2 nm Cr and 15 nm Au

Scheme 13.1 The "paint-on" method used to fabricate etalons. Reprinted with permission from [24].

Figure 13.3b shows spectra obtained at three randomly selected regions of an air-dried etalon (775 μl of a 5% (v/v) microgel solution). In this case, the reflectance spectra are much more variable with position on the etalon. Moreover, only three out of four randomly chosen regions exhibited reflectance spectra because some regions do not have the jammed layer necessary to form an etalon.

The temperature-dependent optical properties of different regions on the painted etalon were also probed, and used as a measure for uniformity. Figure 13.3c shows a plot of the λ_{max} for one peak in a given painted etalon's spectrum as a function of temperature at three different areas on the etalon. It can be seen that all the regions exhibit the similar λ_{max} values at all temperatures investigated. In addition, the phase transition temperature is effectively constant from region to region. When the temperature-dependent optical properties are compared to those for the air-dried samples (Figure 13.3d), there is a clear improvement using the painting protocol. This procedure has also been shown to be useful for depositing microgels with differing functionalities [24] on a variety of metal surfaces, for example, Ti, Ni, Al, Fe, Ag, Cu.

To summarize, a "monolithic" film is necessary to suspend the Au overlayer some distance away from the Au-coated substrate. This effectively forms a cavity. At pH 3.0, when the solution temperature is raised above the lower critical solution temperature (LCST) of the microgels, and the microgels collapse, the Au layers approach one another uniformly, changing the interference properties of light, affecting the color of the etalon, as depicted in Figure 13.4. This is equivalent to changing the layer thickness between two mirrors in a traditional etalon, where the absorbance (reflectance) blue shifts as the two layers are brought closer to one another. If this

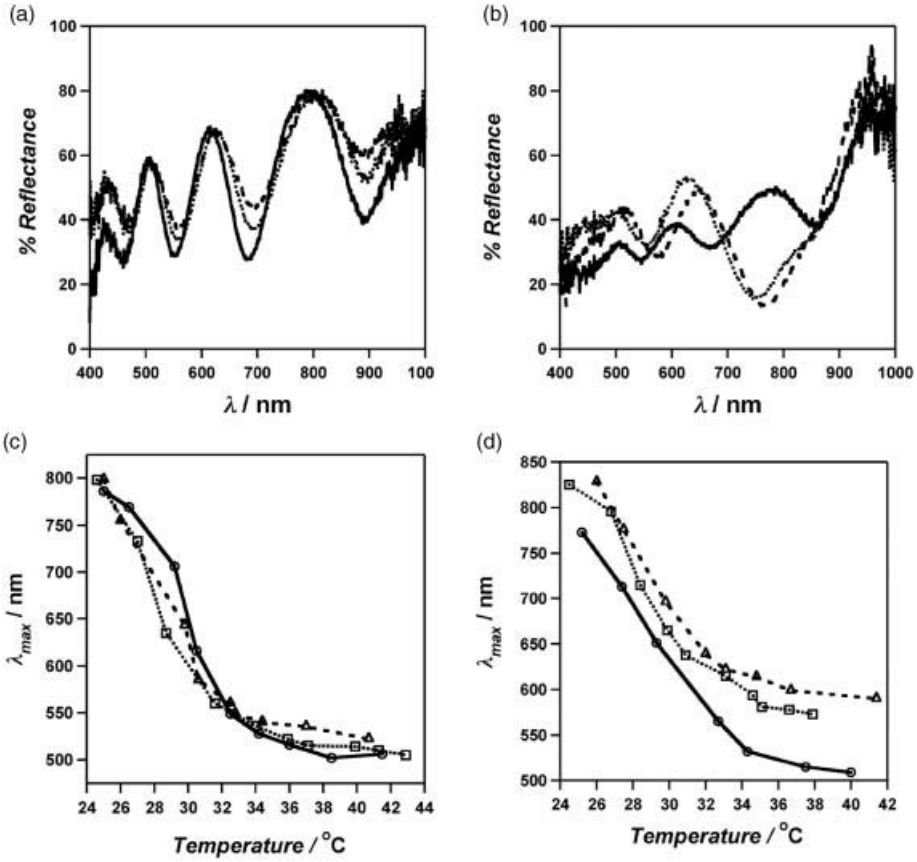

Figure 13.3 Reflectance spectra from three randomly selected areas of an etalon fabricated using (a) the "paint-on" method and (b) the overnight drying method. Plots of λ_{max} versus temperature for randomly selected regions (the three different curves on each plot) of film fabricated using (c) the "paint-on" method and (d) the overnight drying method. Reprinted with permission from [24].

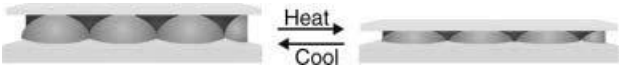

Figure 13.4 Uniform modulation of the mirror–mirror distance as a result of swelling–deswelling of microgel dielectric material with changes in temperature. Reprinted with permission from [25].

were a result of the particle refractive index changing, we would expect to see a red shift in the spectra.

13.2.2 Tuning the Reflection Order

Thus far, we have demonstrated that color-tunable materials can be generated, but the resulting spectra from these materials are quite peculiar in that they all have different

Table 13.1 Physical properties of microgels.

Microgel	PNIPAM-*co*-AA-1	PNIPAM-*co*-AA-2	PNIPAM-*co*-AA-3	PNIPAM-*co*-acrylamide	PNIPAM-*co*-vinylacetic acid
Hydrodynamic diameter, D_H [nm][a)]	1548 (± 69)	659 (± 21)	229 (± 10)	653 (± 10)	603 (± 17)
Etalon thickness [nm][b)]	1004 (± 98)	440 (± 36)	127 (± 16)	544 (± 56)	347 (± 46)

a) Determined by PCS (± standard deviation of five measurements).
b) Determined by AFM imaging (± standard deviation of height over 100 line scan averages on three areas each for three images).

numbers of peaks. We observed that the number of peaks in the reflectance spectra was dependent on the microgels that were used to make the assembly. While materials that have multiple spectral peaks in the visible region can be extremely beneficial for various types of sensing, we seek a configuration that produces a single reflectance peak. Materials that exhibit distinct, predictable colors can be used for point-of-care diagnostics and home testing applications. For example, an etalon can exhibit one color in the absence of analyte, but exhibit a different color when analyte is present.

As predicted from Equation 13.1, etalons that exhibit a single reflectance peak can be achieved by constructing etalons with the appropriate combination of dielectric thickness and refractive index [26]. By plugging in 1.37 for the refractive index of a solvent swollen hydrogel, we calculate that the dielectric layer thickness should be less than 400 nm to achieve a single reflectance peak in the visible. We constructed etalons from microgels with various hydrodynamic diameters (D_H) to yield etalons with variable dielectric thicknesses (see Table 13.1). For all assemblies, the etalon thickness corresponds to ~0.5–0.8 of the microgel diameter. Figure 13.5 shows the spectra for each etalon, along with photographs of the dry and hydrated assemblies. The thickest etalon Figure 13.5a was fabricated using PNIPAM-*co*-AA microgels with a nominal D_H of ~1.5 μm, which yielded a reflectance spectrum with five distinct peaks in the visible region of the electromagnetic spectrum. The etalon constructed from microgels with a D_H of ~660 nm yielded a reflectance spectrum with three peaks – fewer than the thicker etalon, as expected from Equation 13.1. Finally, etalons were constructed from microgels with a D_H of ~230 nm, which yielded one distinct peak at ~535 nm.

We went on to show that microgels of a similar D_H, but different mechanical properties could also be used to affect the number of reflectance peaks observed. For example, "soft" microgels yielded an etalon with a smaller dielectric thickness compared to "stiff" microgels, even though the initial D_H values were very similar (see Table 13.1). Figure 13.5 shows, as expected, that the thinner etalons have fewer peaks than the thicker etalons.

13.2.3
Mechanism of Etalon Deswelling

To study the deswelling kinetics, and to probe the deswelling mechanism, the microgels that make up the dielectric cavity of etalons were deswollen by exploiting

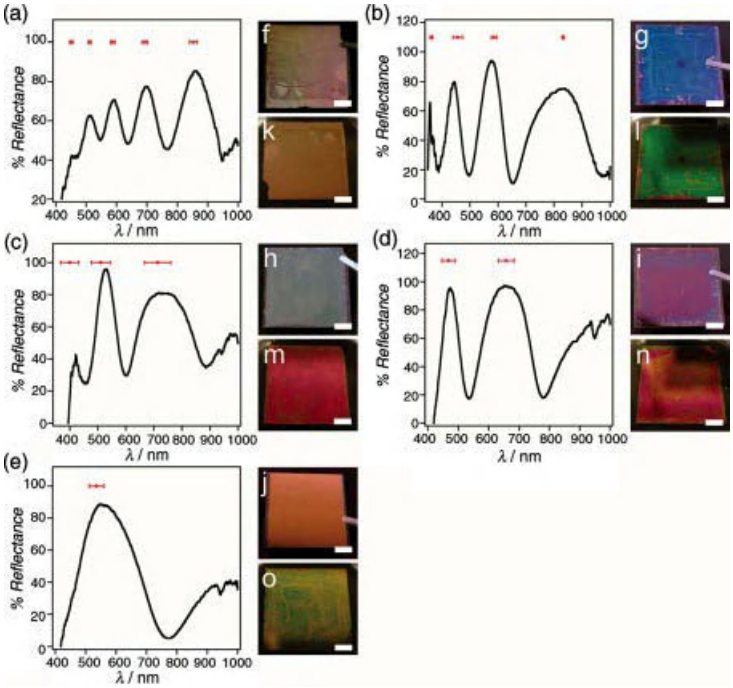

Figure 13.5 Representative spectra for etalons composed of (a) PNIPAM-*co*-AA-1, (b) PNIPAM-*co*-acrylamide, (c) PNIPAM-*co*-AA-2, (d) PNIPAM-*co*-vinylacetic acid, (e) PNIPAM-*co*-AA-3 microgels (see Table 13.1), obtained in pH 3 formate buffer. The average peak position (± one standard deviation) from six spectra shown in red above each spectrum. (f–j) Photographs for the etalons (a–e) in the dry state, respectively; (k–o) photographs for the etalons (a–e) hydrated in pH 3 formate buffer, respectively. Scale bars for photographs are 5 mm. Reprinted with permission from [26].

the "co-nonsolvency" effect [89–93]. Briefly, the phase transition temperature of PNIPAM has been shown to depend on the solvent they are immersed in. Here, a 30% (v/v) methanol MeOH:H_2O solution was used to lower the collapse temperature of the microgels to ∼18 °C. Since the experiments were conducted at a controlled temperature of 25 °C, in pH 3.0 water with an ionic strength of 2 mM, the microgels should instantly collapse and bring the Au mirrors close to each other. This Au layer approach should result in a spectral blue shift of a given reflectance peak, according to Equation 13.1.

The deswelling kinetics were monitored by monitoring the spectral shifts for etalons of different overlayer thickness during two independent experiments (set 1 and set 2). All etalons in this study were constructed from the same set of microgels. Since each etalon has a different absolute shift in wavelength, λ_{total}, the data were normalized by plotting the percentage shift versus time. The percentage shift for a particular data point with a wavelength peak value of λ_{max} is given by Equation 13.2:

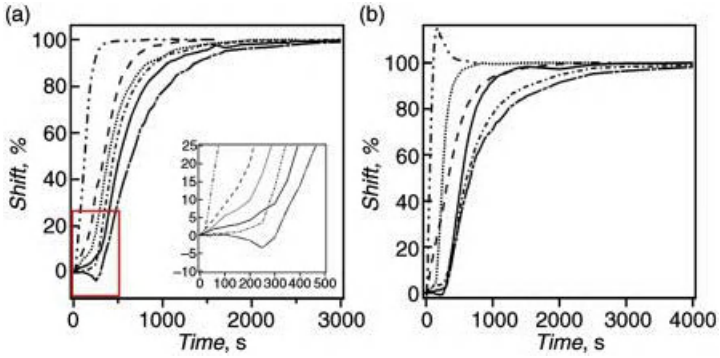

Figure 13.6 Deswelling curves for etalons in (a) set 1 and (b) set 2. The percent shift of the high wavelength peak is plotted as a function of time. Plots shown are: 5 nm (– –), 10 nm (— — —), 15 nm (···), 20 nm (solid), 25 nm (– · –), and 35 nm (—·—). Inset in (a) shows the expansion of the % shift versus time plot highlighted in the red box in panel (a). Deswelling was induced by introducing a 30% (v/v) MeOH:H_2O/Water solution (2 mM I.S.) held at 25 °C. Reprinted with permission Copyright (2011) American Chemical Society.

$$\%\ \text{Shift} = \frac{\lambda_{\max} - \lambda_{\text{initial}}}{\lambda_{\text{final}} - \lambda_{\text{initial}}} \cdot 100 \tag{13.2}$$

$\lambda_{\max}$ is the wavelength of the monitored peak at a particular time point, λ_{initial} is the initial peak position, and λ_{final} is the final peak position. For this section, $\lambda_{\max}$ was always the highest wavelength peak in each spectrum. Because the etalons were fabricated with the same microgels, and by the same fabrication method, it is an excellent assumption that the highest wavelength peaks in each spectrum are of the same order, therefore they can all be directly compared.

From the data in Figures 13.6a,b and 13.7 it is apparent that the deswelling time increases as a function of increasing overlayer thickness. Considering the work of Norrman *et al.* [94], which shows that the area of a substrate uniformly coated with Au increases with increasing thickness, this result is reasonable. For our system, we hypothesize that increased Au homogeneity translates to less porous overlayers slowing down the solvent exchange mechanism from the polymer layer to the bulk solution. Therefore, the thinner Au overlayers exchange solvent more easily when undergoing a transition, leading to faster deswelling kinetics. It is also apparent that the MeOH appears to enter the polymer layer primarily via diffusion through the Au overlayer. This is evident from Figure 13.6, as the lag phases for etalons with thicker overlayers are longer than those with thinner overlayers. It is also interesting to note that the etalons never fail to actuate, suggesting that either solvent can exchange through the edges, or that 35 nm is not entirely a bulk film that blocks the solvent exchange process [94]. Note that for the data in set 1, the etalon with an overlayer thickness of 25 nm does not fit the overall trend. We are unsure why this is the case, but hypothesize that it is due to slight differences inherently present in the fabrication method. That is, the Au overlayers may not be entirely uniform, and that some areas of the overlayer of a microgel etalon may have more pores than other areas.

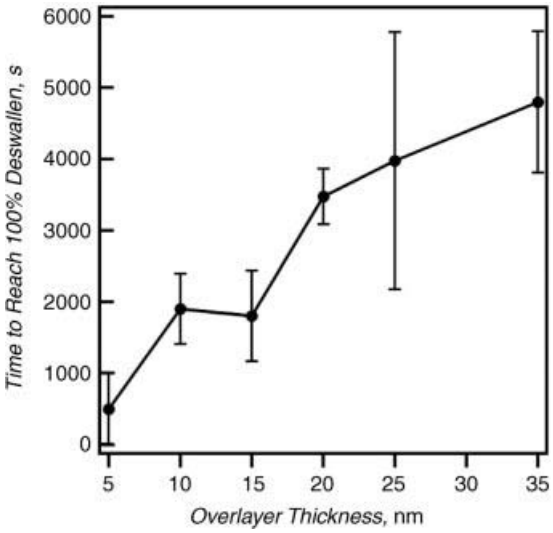

Figure 13.7 The time required for etalons of various overlayer thicknesses to reach 100% deswollen. Error bars are the standard deviations for the averages from two different sets of independently fabricated samples. Reprinted with permission Copyright (2011) American Chemical Society.

Nevertheless, the *general* trend of slower deswelling kinetics with increasing overlayer thickness holds.

Figure 13.6a,b can also be used to extract other relevant kinetic parameters, such as the maximum deswelling rate. We define this as the slope of the line in the deswelling phase in units of % shift per second (s^{-1}). Figure 13.8 reveals that the thinnest, 5 nm Au overlayer affords a much greater max rate than thicker overlayers, again suggesting the thin Au overlayers allow solvent to more easily exchange with the environment.

There are three possible mechanisms by which the etalons are triggered to actuate. MeOH can enter the structure and solvent can be exchanged: (i) *exclusively* through the edges; (ii) *exclusively* through the Au overlayer; or (iii) through a combination of diffusion through *both* the edges and the overlayer. The data suggest that the preferred route of solvent exchange with the microgel layer is through the overlayer. This conclusion was reached based on the observation that deswelling time increased with increasing overlayer thickness, with a concomitant decrease in the maximum deswelling rate. In addition, the lag and plateau phases increase with increasing overlayer thickness, as seen in Figure 13.6a,b, meaning that the thicker Au overlayers hinder solvent exchange through the overlayer, hence slowing the deswelling process down [94–96]. Taken together, the data suggest that the solvent exchange mechanism transitions from a state that is predominantly through the overlayer to one that proceeds less through the overlayer and potentially more through the sides.

To provide more evidence for our hypothesis (solvent exchange proceeding more through the sides of the film with increasing overlayer thickness), we probed the deswelling kinetics for a single etalon of different dimensions. An etalon from set 2

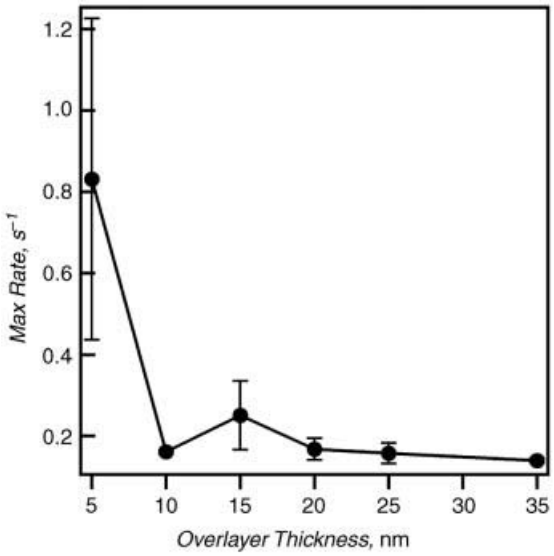

Figure 13.8 Plot of maximum rate of deswelling for different overlayer thicknesses. Data averaged from two sets of independently fabricated etalons, with standard deviation shown using error bars. Reprinted with permission Copyright (2011) American Chemical Society.

with a 25 nm Au overlayer of area 6.25 cm^2 (with dimensions of 2.5 × 2.5 cm) was deswollen. The kinetics of this larger etalon was compared to a smaller etalon cut from the larger one (with a glass-cutting tool), with an area of ∼2.5 cm^2 (dimensions of ∼1.0 × ∼2.5 cm). This etalon was then cut even smaller, ∼0.9 cm^2 (with dimensions of ∼0.9 × ∼1.0 cm) and the kinetics determined. It should be pointed out that the same etalon region was being probed for all the different sized etalons (the center region). The resultant deswelling curves are shown in Figure 13.9. From the data, it is apparent that the smaller the etalon becomes, the faster it reaches 100% deswollen. The lag phase for the smallest etalon is also significantly reduced. This is hypothesized to be a result of the solvent exchanging through the edges of the etalon, therefore there is less distance for the solvent to diffuse before it can contact the microgel layer and cause the desired response, resulting in a decrease in the total deswelling time. It also takes less time for the solvent inside the microgel layer to exit the etalon.

Taken together, we hypothesize that a microgel etalon will exchange its solvent primarily through the Au overlayer, however, solvent exchange does occur through the edges, and becomes more pronounced with increasing overlayer thickness.

To decouple the MeOH exchange from the water expulsion from the polymer layer, we evaluated etalon deswelling kinetics in response to a "temperature jump." To estimate the etalon's deswelling time in response to a temperature jump, the etalon was heated at different rates and the time to deswell by a given amount was determined. By extrapolating to the response time at high heating rate, it can be seen from Figure 13.10 that the etalon with the thinnest overlayer takes less time to expel water in response to a temperature jump than a film with a thicker overlayer. With the data in Figures 13.7 and 13.10, we can decouple the MeOH exchange kinetics from the kinetics associated with the polymer layer expelling its water.

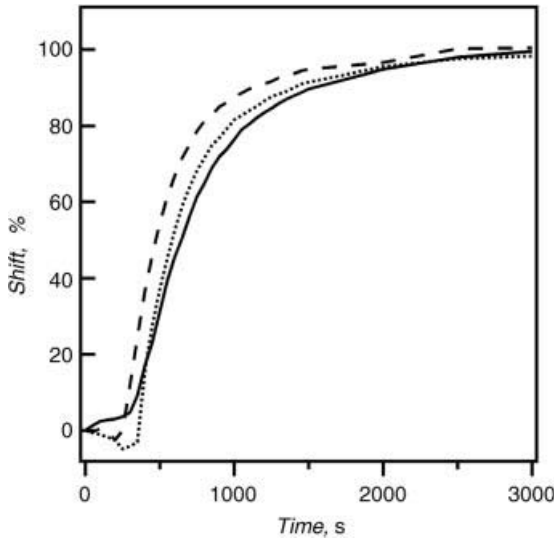

Figure 13.9 Plot of percent shift as a function of time for etalons with 25 nm overlayers and areas of (solid) 6.25 cm^2, (···) ~2.5 cm^2, and (— — —) ~0.9 cm^2. Reprinted with permission Copyright (2011) American Chemical Society.

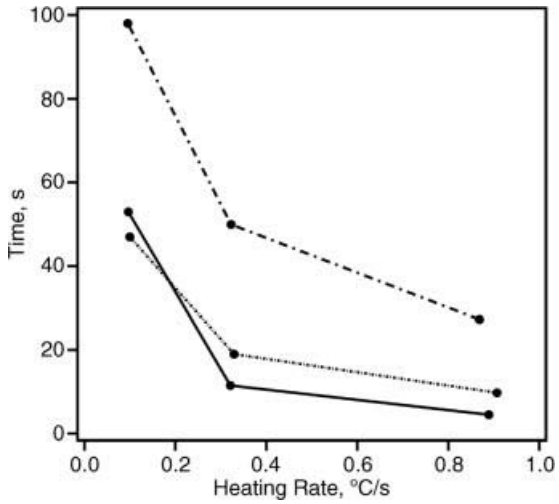

Figure 13.10 The time for etalons to deswell as a function of heating rate. Overlayer thicknesses, are: (solid) 5 nm, (···) 15 nm, and (— · —) 25 nm.

13.2.4
Applied Sensing

Applications of these materials are plentiful, although point-of-care (POC) sensing/diagnostics is a clear area that can benefit most immediately from this technology. To

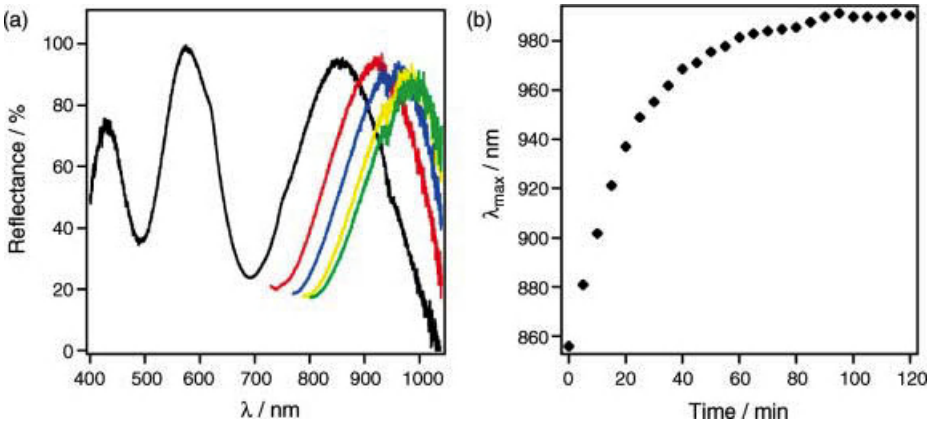

Figure 13.11 (a) Reflectance spectra over time after introduction of a 3 mg ml^{-1} glucose solution to an etalon constructed with APBA-modified microgels. The black line represents the initial spectrum, the red, blue, yellow, and green lines represent the spectrum after 15, 30, 60, and 120 min, respectively. (b) Plot of the high wavelength peak position in (a) as a function of time after glucose addition. Total spectral shift is ~134 nm. Reproduced with permission. Copyright 2012, Springer.

demonstrate their utility, we generated glucose-sensitive microgels by modification with 3-aminophenylboronic acid (APBA). APBA-modified microgels have been shown to increase their diameter in the presence of glucose. Using these APBA-modified microgels we generated etalons and exposed them to a 3 mg ml^{-1} solution of glucose in pH 9 carbonate buffer. By monitoring one reflection peak over time, we see a ~134 nm spectral shift in the most red-shifted peak starting at 856 nm and ending at 990 nm (Figure 13.11a). Figure 13.11b shows the peak position as a function of time, and it is apparent that the majority of the spectral shift occurs within 30 min of glucose introduction. Etalons not modified with APBA show virtually no response to glucose introduction. Interestingly, the visual color of the material can be differentiated before and after glucose introduction (Figure 13.12). In the case of the APBA-modified microgel-based etalons, the color changes from green to red, before and after glucose addition, respectively. On the other hand, the control substrates do not show any significant color change.

13.3 Conclusions and Future Directions

We describe a PNIPAM microgel-based assembly with reversible color tunability in the visible region of the electromagnetic spectrum; peaks blue shift in response to temperature. The transition temperature of the films was approximately equal to that of the microgels in solution; at pH 3.0, the film and the microgels collapse at ~31 °C.

We have developed a technique to generate etalons of high spectral and visual purity, in a reproducible fashion. This approach is advantageous because of its ease,

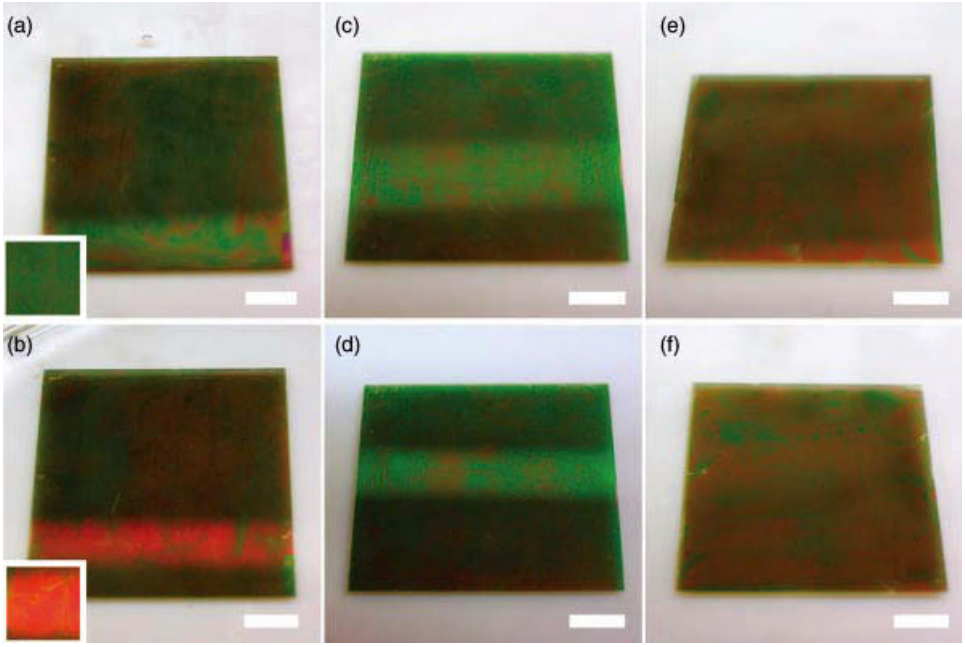

Figure 13.12 APBA-functionalized microgel etalons show visible color differences when they are soaked in (a) 5 mM pH 9 carbonate buffer versus (b) a pH 9 carbonate buffer containing 3 mg ml^{-1} glucose for 2 h. (c,f) Various etalon controls, for example, (c,d) etalons fabricated by exposure to APBA only, and (e,f) 1-Ethyl-3-(3-dimethylaminopropyl)carbodiimide hydrochoride only, show no significant color change (top) before and (bottom) after glucose exposure. Image insets show a cropped image of the approximate center ~1 cm^2 for each etalon, where the etalons were monitored spectrally, to better display the color change. To make the etalon's color more apparent, image processing software was used increase the image brightness of the select region. Scale bars are ~5 mm.Reproduced with permission. Copyright 2012, Springer.

simplicity, and apparent universality – it can be used to coat a variety of metal surfaces with microgels containing a variety of different microgel functionalities.

We show that we can control the number and order of reflection peaks a microgel etalon exhibits in the visible region of the electromagnetic spectrum by changing the size and/or softness of the microgels. This work has led toward a greater understanding of what dictates microgel etalon color and spectral behavior. It is a first step towards directed materials fabrication and the development of etalons that display a single visible color.

The mechanism by which microgel etalons exchange with their solvent was investigated by probing the deswelling kinetics as a function of overlayer thickness and etalons dimensions. The data strongly suggest that etalons exchange with their solvent through both the top and the edges. However, the route of exchange through the Au overlayer is favored, and an increase in overlayer thickness slows the rate of deswelling.

Etalons that respond to biologically significant concentrations of glucose can be generated by incorporating APBA into the microgels that are used to form the etalon.

The color and spectrum both shift significantly in the presence of 3.0 mg ml^{-1} glucose, while controls show virtually no response.

These materials have a promising future, ranging from light filtration applications to POC sensing. These etalons can also be coated on flexible substrates, which make them potentially useful for display technology. These systems, with their combined ease of fabrication, cost effectiveness, and sensitivity make them ideal for multiple applications.

References

1 Bonifacio, L.D., Lotsch, B.V., Puzzo, D.P., Scotognella, F., and Ozin, G.A. (2009) Stacking the nanochemistry deck: Structural and compositional diversity in one-dimensional photonic crystals. *Adv. Mater.*, **21** (16), 1641–1646.

2 Krieger, I.M. and Oneill, F.M. (1968) Diffraction of light by arrays of colloidal spheres. *J. Am. Chem. Soc.*, **90** (12), 3114–3120.

3 Tsuji, S. and Kawaguchi, H. (2005) Colored thin films prepared from hydrogel microspheres. *Langmuir*, **21** (18), 8439–8442.

4 Kang, Y., Walish, J.J., Gorishnyy, T., and Thomas, E.L. (2007) Broad-wavelength-range chemically tunable block-copolymer photonic gels. *Nat. Mater.*, **6** (12), 957–960.

5 Walish, J.J., Kang, Y., Mickiewicz, R.A., and Thomas, E.L. (2009) Bioinspired electrochemically tunable block copolymer full color pixels. *Adv. Mater.*, **21** (30), 3078–3081.

6 Brooker, G. (2003) Modern Classical Optics, Oxford University Press, Oxford.

7 Bonanno, L.M. and DeLouise, L.A. (2010) Integration of a chemical-responsive hydrogel into a porous silicon photonic sensor for visual colorimetric readout. *Adv. Funct. Mater.*, **20** (4), 573–578.

8 Bonanno, L.M. and DeLouise, L.A. (2010) Tunable detection sensitivity of opiates in urine via a label-free porous silicon competitive inhibition immunosensor. *Anal. Chem.*, **82** (2), 714–722.

9 Choi, S.Y., Mamak, M., von Freymann, G., Chopra, N., and Ozin, G.A. (2006) Mesoporous Bragg stack color tunable sensors. *Nano Lett.*, **6** (11), 2456–2461.

10 Ha, N.Y., Jeong, S.M., Nishimura, S., and Takezoe, H. (2010) Color- and reflectance-tunable multiple reflectors assembled from three polymer films. *Adv. Mater.*, **22** (14), 1617–1621.

11 Holtz, J.H. and Asher, S.A. (1997) Polymerized colloidal crystal hydrogel films as intelligent chemical sensing materials. *Nature*, **389** (6653), 829–832.

12 Lee, K. and Asher, S.A. (2000) Photonic crystal chemical sensors: pH and ionic strength. *J. Am. Chem. Soc.*, **122** (39), 9534–9537.

13 Alexeev, V.L., Sharma, A.C., Goponenko, A.V., Das, S., Lednev, I.K., Wilcox, C.S., Finegold, D.N., and Asher, S.A. (2003) High ionic strength glucose-sensing photonic crystal. *Anal. Chem.*, **75** (10), 2316–2323.

14 DeLouise, L.A., Fauchet, P.M., Miller, B.L., and Pentland, A.A. (2005) Hydrogel-supported optical-microcavity sensors. *Adv. Mater.*, **17** (18), 2199–2203.

15 Kurt, P., Banerjee, D., Cohen, R.E., and Rubner, M.F. (2009) Structural color via layer-by-layer deposition: layered nanoparticle arrays with near-UV and visible reflectivity bands. *J. Mater. Chem.*, **19** (47), 8920–8927.

16 Lotsch, B.V. and Ozin, G.A. (2008) Clay bragg stack optical sensors. *Adv. Mater.*, **20** (21), 4079–4084.

17 O'Brien, P.G., Puzzo, D.P., Chutinan, A., Bonifacio, L.D., Ozin, G.A., and Kherani, N.P. (2010) Selectively transparent and conducting photonic crystals. *Adv. Mater.*, **22** (5), 611–616.

18 Scotognella, F., Puzzo, D.P., Monguzzi, A., Wiersma, D.S., Maschke, D., Tubino, R., and Ozin, G.A. (2009) Nanoparticle one-dimensional photonic-crystal dye laser. *Small*, **5** (18), 2048–2052.

19 Asher, S.A., Holtz, J., Liu, L., and Wu, Z.J. (1994) Self-assembly motif for creating submicron periodic materials – Polymerized crystalline colloidal arrays. *J. Am. Chem. Soc.*, **116** (11), 4997–4998.

20 Asher, S.A., Kimble, K.W., and Walker, J.P. (2008) Enabling thermoreversible physically cross-linked polymerized colloidal array photonic crystals. *Chem. Mater.*, **20** (24), 7501–7509.

21 Zhang, J., Wang, L., Luo, J., Tikhonov, A., Kornienko, N., and Asher, S.A. (2011) 2-D array photonic crystal sensing motif. *J. Am. Chem. Soc.*, **133** (24), 9152–9155.

22 Wang, L. and Asher, S.A. (2009) Fabrication of silica shell photonic crystals through flexible core templates. *Chem. Mater.*, **21** (19), 4608–4613.

23 Reese, C.E., Mikhonin, A.V., Kamenjicki, M., Tikhonov, A., and Asher, S.A. (2004) Nanogel nanosecond photonic crystal optical switching. *J. Am. Chem. Soc.*, **126** (5), 1493–1496.

24 Sorrell, C.D., Carter, M.C.D., and Serpe, M.J. (2011) A "Paint-On" protocol for the facile assembly of uniform microgel coatings for color tunable etalon fabrication. *ACS Appl. Mater. Interface*, **3** (4), 1140–1147.

25 Sorrell, C.D., Carter, M.C.D., and Serpe, M.J. (2011) Color tunable poly (N-Isopropylacrylamide)-co-acrylic acid microgel-Au hybrid assemblies. *Adv. Funct. Mater.*, **21** (3), 425–433.

26 Sorrell, C.D. and Serpe, M.J. (2011) Reflection order selectivity of color-tunable poly (*N*-isopropylacrylamide) microgel based etalons. *Adv. Mater.*, **23** (35), 4088–4092.

27 Zhou, K., Lu, Y., Li, J., Shen, L., Zhang, G., Xie, Z., and Wu, C. (2008) The coil-to-globule-to-coil transition of linear polymer chains in dilute aqueous solutions: Effect of intrachain hydrogen bonding. *Macromolecules*, **41** (22), 8927–8931.

28 Schild, H.G. (1992) Poly (N-isopropylacrylamide) – Experiment, theory and application. *Prog. Polym. Sci.*, **17** (2), 163–249.

29 Shibayama, M. and Tanaka, T. (1993) Volume phase transition and related phenomena of polymer gels. *Adv. Polym. Sci.*, **109**, 1–62.

30 Xu, J., Zhu, Z.Y., Luo, S.Z., Wu, C., and Liu, S.Y. (2006) First observation of two-stage collapsing kinetics of a single synthetic polymer chain. *Phys. Rev. Lett.*, **96** (2).

31 Gong, X., Wu, C., and Ngai, T. (2010) Surface interaction forces mediated by poly(N-isopropylacrylamide) (PNIPAM) polymers: effects of concentration and temperature. *Colloid Polym. Sci.*, **288** (10–11), 1167–1172.

32 Tanaka, T., Fillmore, D., Sun, S.T., Nishio, I., Swislow, G., and Shah, A. (1980) Phase transitions in ionic gels. *Phys. Rev. Lett.*, **45** (20), 1636–1639.

33 Tanaka, T. and Fillmore, D.J. (1979) Kinetics of swelling gels. *J. Chem. Phys.*, **70** (3), 1214–1218.

34 Kim, J., Nayak, S., and Lyon, L.A. (2005) Bioresponsive hydrogel microlenses. *J. Am. Chem. Soc.*, **127** (26), 9588–9592.

35 Hoare, T. and Pelton, R. (2007) Engineering glucose swelling responses in poly(N-isopropylacrylamide)-based microgels. *Macromolecules*, **40** (3), 670–678.

36 Meng, Z., Hendrickson, G.R., and Lyon, L.A. (2009) Simultaneous orthogonal chemoligations on multiresponsive microgels. *Macromolecules*, **42** (20), 7664–7669.

37 Nayak, S. and Lyon, L.A. (2004) Ligand-functionalized core/shell microgels with permselective shells. *Angew. Chem. Int. Ed.*, **43** (48), 6706–6709.

38 Suzuki, A., Okabe, N., and Suzuki, H. (2005) Effects of guest microparticles of polyacrylamide gels on the swelling behavior. *J. Polym. Sci. B*, **43** (13), 1696–1704.

39 Jones, C.D. and Lyon, L.A. (2000) Synthesis and characterization of multiresponsive core-shell microgels. *Macromolecules*, **33** (22), 8301–8306.

40 Kratz, K., Hellweg, T., and Eimer, W. (1998) Effect of connectivity and charge density on the swelling and

local structural and dynamic properties of colloidal PNIPAM microgels. *Ber. Bunsen. Phys. Chem.*, **102** (11), 1603–1608.

41 Kratz, K., Hellweg, T., and Eimer, W. (2000) Influence of charge density on the swelling of colloidal poly(N-isopropylacrylamide-co-acrylic acid) microgels. *Colloid Surf. A*, **170** (2–3), 137–149.

42 Snowden, M.J., Chowdhry, B.Z., Vincent, B., and Morris, G.E. (1996) Colloidal copolymer microgels of N-isopropylacrylamide and acrylic acid: pH, ionic strength and temperature effects. *J. Chem. Soc., Faraday Trans.*, **92** (24), 5013–5016.

43 Pelton, R. (2000) Temperature-sensitive aqueous microgels. *Adv. Colloid Interface Sci.*, **85** (1), 1–33.

44 Sierra-Martin, B., Laporte, Y., South, A.B., Lyon, L.A., and Fernandez-Nieves, A. (2011) Bulk modulus of poly(N-isopropylacrylamide) microgels through the swelling transition. *Phys. Rev. E Stat. Nonlin. Soft Matter Phys.*, **84** (1–1), 011406.

45 Jones, C.D. and Lyon, L.A. (2003) Dependence of shell thickness on core compression in acrylic acid modified poly (N-isopropylacrylamide) core/shell microgels. *Langmuir*, **19** (11), 4544–4547.

46 Hu, X., Tong, Z., and Lyon, L.A. (2010) Multicompartment core/shell microgels. *J. Am. Chem. Soc.*, **132** (33), 11470–11472.

47 Jones, C.D. and Lyon, L.A. (2003) Shell-restricted swelling and core compression in poly(N-isopropylacrylamide) core-shell microgels. *Macromolecules*, **36** (6), 1988–1993.

48 Blackburn, W.H. and Lyon, L.A. (2008) Size-controlled synthesis of monodisperse core/shell nanogels. *Colloid Polym. Sci.*, **286** (5), 563–569.

49 Lyon, L.A., Meng, Z., Singh, N.U., Sorrell, C.D., and St. John, A. (2009) Thermoresponsive microgel-based materials. *Chem. Soc. Rev.*, **38** (4), 865–874.

50 Nayak, S., Gan, D.J., Serpe, M.J., and Lyon, L.A. (2005) Hollow thermoresponsive microgels. *Small*, **1** (4), 416–421.

51 Kim, J., Singh, N., and Lyon, L.A. (2007) Influence of ancillary binding and nonspecific adsorption on bioresponsive hydrogel microlenses. *Biomacromolecules*, **8** (4), 1157–1161.

52 Gao, M., Gawel, K., and Stokke, B.T. (2011) Toehold of dsDNA exchange affects the hydrogel swelling kinetics of a polymer-dsDNA hybrid hydrogel. *Soft Matter*, **7** (5), 1741–1746.

53 Gawel, K. and Stokke, B.T. (2011) Logic swelling response of DNA-polymer hybrid hydrogel. *Soft Matter*, **7** (10), 4615–4618.

54 Debord, J.D., Eustis, S., Debord, S.B., Lofye, M.T., and Lyon, L.A. (2002) Color-tunable colloidal crystals from soft hydrogel nanoparticles. *Adv. Mater.*, **14** (9), 658–662.

55 Debord, J.D. and Lyon, L.A. (2000) Thermoresponsive photonic crystals. *J. Phys. Chem. B*, **104** (27), 6327–6331.

56 St. John Iyer, A. and Lyon, L.A. (2009) Self-healing colloidal crystals. *Angew. Chem. Int. Ed.*, **48** (25), 4562–4566.

57 Lyon, L.A., Debord, J.D., Debord, S.B., Jones, C.D., McGrath, J.G., and Serpe, M.J. (2004) Microgel colloidal crystals. *J. Phys. Chem. B*, **108** (50), 19099–19108.

58 Meng, Z., Cho, J.K., Debord, S., Breedveld, V., and Lyon, L.A. (2007) Crystallization behavior of soft, attractive microgels. *J. Phys. Chem. B*, **111** (25), 6992–6997.

59 Suzuki, D., McGrath, J.G., Kawaguchi, H., and Lyon, L.A. (2007) Colloidal crystals of thermosensitive, core/shell hybrid microgels. *J. Phys. Chem. C*, **111** (15), 5667–5672.

60 Brijitta, J., Tata, B.V.R., Joshi, R.G., and Kaliyappan, T. (2009) Random hcp and fcc structures in thermoresponsive microgel crystals. *J. Chem. Phys.*, **131** (7), 074904.

61 Mohanty, P.S. and Richtering, W. (2008) Structural ordering and phase behavior of charged microgels. *J. Phys. Chem. B*, **112** (47), 14692–14697.

62 Tang, S.J., Hu, Z.B., Zhou, B., Cheng, Z.D., Wu, J.Z., and Marquez, M. (2007) Melting kinetics of thermally responsive microgel crystals. *Macromolecules*, **40** (26), 9544–9548.

63 Schmidt, S., Motschmann, H., Hellweg, T., and von Klitzing, R. (2008)

Thermoresponsive surfaces by spin-coating of PNIPAM-co-PAA microgels: A combined AFM and ellipsometry study. *Polymer*, **49** (3), 749–756.

64 Serpe, M.J., Jones, C.D., and Lyon, L.A. (2003) Layer-by-layer deposition of thermoresponsive microgel thin films. *Langmuir*, **19** (21), 8759–8764.

65 Sorrell, C.D. and Lyon, L.A. (2008) Deformation controlled assembly of binary microgel thin films. *Langmuir*, **24** (14), 7216–7222.

66 South, A.B., Whitmire, R.E., Garcia, A.J., and Lyon, L.A. (2009) Centrifugal deposition of microgels for the rapid assembly of nonfouling thin films. *ACS Appl. Mater. Interfaces*, **1** (12), 2747–2754.

67 Schmidt, S., Hellweg, T., and von Klitzing, R. (2008) Packing density control in p(NIPAM-co-AAc) microgel monolayers: Effect of surface charge, pH, and preparation technique. *Langmuir*, **24** (21), 12595–12602.

68 Sakai, T., Takeoka, Y., Seki, T., and Yoshida, R. (2007) Organized monolayer of thermosensitive microgel beads prepared by double-template polymerization. *Langmuir*, **23** (17), 8651–8654.

69 Nerapusri, V., Keddie, J.L., Vincent, B., and Bushnak, I.A. (2006) Swelling and deswelling of adsorbed microgel monolayers triggered by changes in temperature, pH, and electrolyte concentration. *Langmuir*, **22** (11), 5036–5041.

70 Zavgorodnya, O. and Serpe, M.J. (2011) Assembly of poly(N-isopropylacrylamide)-co-acrylic acid microgel thin films on polyelectrolyte multilayers: Effects of polyelectrolyte layer thickness, surface charge, and microgel solution pH. *Colloid Polym. Sci.*, **289** (5–6), 591–602.

71 Nolan, C.M., Reyes, C.D., Debord, J.D., Garcia, A.J., and Lyon, L.A. (2005) Phase transition behavior, protein adsorption, and cell adhesion resistance of poly (ethylene glycol) cross-linked microgel particles. *Biomacromolecules*, **6** (4), 2032–2039.

72 Nolan, C.M., Serpe, M.J., and Lyon, L.A. (2004) Thermally modulated insulin release from microgel thin films. *Biomacromolecules*, **5** (5), 1940–1946.

73 Singh, N., Bridges, A.W., Garcia, A.J., and Lyon, L.A. (2007) Covalent tethering of functional microgel films onto poly (ethylene terephthalate) surfaces. *Biomacromolecules*, **8** (10), 3271–3275.

74 Gratzel, M. (2001) Photoelectrochemical cells. *Nature*, **414** (6861), 338–344.

75 Song, J.Y., Wang, Y.Y., and Wan, C.C. (1999) Review of gel-type polymer electrolytes for lithium-ion batteries. *J. Power Sources*, **77** (2), 183–197.

76 Prevo, B.G. and Velev, O.D. (2004) Controlled, rapid deposition of structured coatings from micro- and nanoparticle suspensions. *Langmuir*, **20** (6), 2099–2107.

77 Cong, H.L. and Cao, W.X. (2004) Macroporous Au materials prepared from colloidal crystals as templates. *J. Colloid Interface Sci.*, **278** (2), 423–427.

78 Dimitrov, A.S. and Nagayama, K. (1996) Continuous convective assembling of fine particles into two-dimensional arrays on solid surfaces. *Langmuir*, **12** (5), 1303–1311.

79 Denkov, N.D., Velev, O.D., Kralchevsky, P.A., Ivanov, I.B., Yoshimura, H., and Nagayama, K. (1992) Mechanism of formation of 2-dimensional crystals from latex particles on substrates. *Langmuir*, **8** (12), 3183–3190.

80 Fudouzi, H. (2004) Fabricating high-quality opal films with uniform structure over a large area. *J. Colloid Interface Sci.*, **275** (1), 277–283.

81 Gu, Z.Z., Fujishima, A., and Sato, O. (2002) Patterning of a colloidal crystal film on a modified hydrophilic and hydrophobic surface. *Angew. Chem. Int. Ed.*, **41** (12), 2068–2070.

82 Suzuki, D. and Kawaguchi, H. (2006) Hybrid microgels with reversibly changeable multiple brilliant color. *Langmuir*, **22** (8), 3818–3822.

83 Zhou, M., Xing, F., Ren, M., Feng, Y., Zhao, Y., Qiu, H., Wang, X., Gao, C., Sun, F., He, Y., Ma, Z., Wen, P., and Gao, J. (2009) A facile method to assemble pNIPAM - containing microgel photonic crystals. *Chemphyschem*, **10** (3), 523–526.

84 Lu, Y. and Drechsler, M. (2009) Charge-induced self-assembly of 2-dimensional

thermosensitive microgel particle patterns. *Langmuir*, **25** (22), 13100–13105.
85 Miao, Y.H., Geng, D.L., and Helseth, L.E. (2006) Order-disorder transition in a quasi-two-dimensional colloidal system. *Langmuir*, **22** (13), 5572–5574.
86 Kuncicky, D.M. and Velev, O.D. (2008) Surface-guided templating of particle assemblies inside drying sessile droplets. *Langmuir*, **24** (4), 1371–1380.
87 Shmuylovich, L., Shen, A.Q., and Stone, H.A. (2002) Surface morphology of drying latex films: Multiple ring formation. *Langmuir*, **18** (9), 3441–3445.
88 Deegan, R.D., Bakajin, O., Dupont, T.F., Huber, G., Nagel, S.R., and Witten, T.A. (1997) Capillary flow as the cause of ring stains from dried liquid drops. *Nature*, **389** (6653), 827–829.
89 Winnik, F.M., Ottaviani, M.F., Bossmann, S.H., Garciagaribay, M., and Turro, N.J. (1992) Cononsolvency of poly (N-isopropylacrylamide) in mixed water-methanol solutions – A look at spin-labeled polymers. *Macromolecules*, **25** (22), 6007–6017.
90 Winnik, F.M., Ringsdorf, H., and Venzmer, J. (1990) Methanol water as a co-nonsolvent system for poly (N-isopropylacrylamide). *Macromolecules*, **23** (8), 2415–2416.
91 Schild, H.G., Muthukumar, M., and Tirrell, D.A. (1991) Cononsolvency in mixed aqueous – solutions of poly (N-isopropylacrylamide). *Macromolecules*, **24** (4), 948–952.
92 Anac, I., Aulasevich, A., Junk, M.J.N., Jakubowicz, P., Roskamp, R.F., Menges, B., Jonas, U., and Knoll, W. (2010) Optical characterization of co-nonsolvency effects in thin responsive pNIPAAm-based gel layers exposed to ethanol/water mixtures. *Macromol. Chem. Phys*, **211** (9), 1018–1025.
93 McPhee, W., Tam, K.C., and Pelton, R. (1993) Poly (N-isopropylacrylamide) latices prepared with sodium dodecyl-sulfate. *J. Colloid Interface Sci.*, **156** (1), 24–30.
94 Norrman, S., Andersson, T., Peto, G., and Somogyi, S. (1981) Quantitative evolution studies of particle separation, size, and shape for vapour-deposited ultrathin gold-films on glass substrates. *Thin Solid Films*, **77** (4), 359–366.
95 Golan, Y., Margulis, L., and Rubinstein, I. (1992) Vacuum-deposited glod-films. 1. Factors affecting the film morphology. *Surf. Sci.*, **264** (3), 312–326.
96 Roland, T., Khalil, A., Tanenbaum, A., Berguiga, L., Delichere, P., Bonneviot, L., Elezgaray, J., Arneodo, A., and Argoul, F. (2009) Revisiting the physical processes of vapodeposited thin gold films on chemically modified glass by atomic force and surface plasmon microscopies. *Surf. Sci.*, **603** (22), 3307–3320.

14
Crystals of Microgel Particles

Juan José Liétor-Santos, Urs Gasser, Jun Zhou, Zhibing Hu, and Alberto Fernández-Nieves

14.1
Introduction

Colloidal crystals have attracted attention due to their optical properties [1]. Because the characteristic size of the constituents is in the range of hundreds of nanometers, the associated lattice constants fall within the visible range of the electromagnetic spectrum and, therefore, these crystals Bragg diffract the incident light, very much as atomic crystals Bragg diffract X-rays. This makes them promising systems for applications like lithography [2] and optical detection [3–5]. They have also been proposed as candidates for photonic bandgap materials, which would exclude the propagation of photons with certain wavelengths, just as semiconductors exclude the propagation of electrons with certain energies [6].

For the particular case of hard spheres, crystallization results solely for entropic reasons. For a sufficiently high volume fraction, the system phase transitions from a liquid to a crystal phase. It is the gain in free volume per particle when these are arranged in a crystal which drives this phase transition. Colloids can be reminiscent of hard spheres and have provided model systems with which we can test predictions from statistical mechanics. In this case, the phase behavior is independent of temperature but depends on the volume fraction, as shown in Figure 14.1. Interestingly, since colloids are easy to see and move slowly [7] compared to atoms, they can be visualized with optical microscopy techniques [8–10]; this is an important advantage that has been exploited to study crystal nucleation and growth [11, 12], to measure and characterize defects structures like dislocations [13, 14] and stacking faults [15], to look at spherical crystallography [16], and to study melting [17–19].

Microgels are an interesting class of colloids whose size can be externally tuned with, for example, temperature [20–25] or hydrostatic pressure [26]. This provides an elegant way to modify the suspension volume fraction and thus to induce phase changes in colloidal suspensions. In addition, close-packed crystals made with microgel particles can change their characteristic lattice constant and thus exhibit Bragg diffraction at different wavelengths depending on the swelling degree of the particles [27]. Furthermore, since particle swelling is accompanied by a change in the

Hydrogel Micro and Nanoparticles, First Edition. Edited by L. Andrew Lyon and Michael Joseph Serpe.
© 2012 Wiley-VCH Verlag GmbH & Co. KGaA. Published 2012 by Wiley-VCH Verlag GmbH & Co. KGaA.

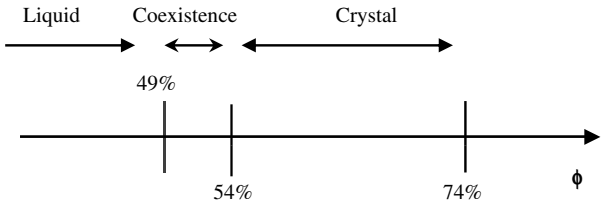

Figure 14.1 Phase equilibrium of hard-sphere suspensions.

refractive index of the particle, the intensity of the Bragg diffraction peaks can also be tuned [28, 29], allowing for ON and OFF optical switches [30–32]. Microgel crystals have indeed attracted a lot of interest in recent years [33–48].

At a fundamental level, microgel particles behave in many cases as hard spheres and this has been extensively exploited to experimentally study many of the properties of this relevant type of system [37, 49–53]. However, there is increasing evidence that in other cases, microgel particles behave quite differently from hard spheres [35]. Recent experimental results with binary microgel suspensions having a small fraction of large microgels and a majority of small microgels have been shown to crystallize as if these larger particles were not there; these larger microgels were forced to deswell to match the size of the small particles and become part of the crystal formed by them [54]. In addition, ionic microgel suspensions exhibit an increasingly different phase behavior compared to hard spheres as the charge within the particle and thus the microgel size increases; the range of the crystal region progressively narrows until it eventually disappears for sufficiently charged and swollen microgels [55]. Furthermore, recent theoretical predictions suggest that for slightly cross-linked and ionic microgel suspensions, the equilibrium phase at high particle densities is a crystal different from the usual face-centered cubic and body-centered cubic structures of most colloidal suspensions [56, 57].

The origin of this extremely rich behavior must be the particle softness. However, the detailed way in which this very general and, in a sense, ambiguous denomination affects the resulting phase behavior is not known. Interestingly, it is known that suspensions of microgel particles with high polydispersities, around 20%, can form beautiful crystals [34], which would not form if the suspensions were composed of hard spheres, since the maximum polydispersity allowing crystallization of hard spheres is 7% [58]. This suggests that microgel suspensions can change their size distribution spontaneously to allow crystallization in the approximate volume fraction range where hard spheres would crystallize. We further hypothesize that this can indeed happen without a significant change in the average particle size.

In this chapter, we will examine microgel crystals using small-angle neutron scattering (SANS) and interpret the data by considering whether the polydispersity can change without a change in the average particle size. We begin by briefly reviewing the solid-state theory of crystallization and crystal structure, and by giving a brief overview of SANS. We then determine the form factor of the particles, which we describe using a soft-sphere model. The central part of the chapter is dedicated to

the phase behavior of the microgel suspension and in particular to the crystal phase. We experimentally determine the structure factor of these crystals, fit them to possible crystal structures and discuss the possibility of polydispersity changes. At the end, we conclude and discuss directions for possible future work.

14.2
Theoretical Background and Experimental Methods

14.2.1
Crystal Nucleation and Growth

The ground state of atomic, molecular, or colloidal systems is often given by a crystalline state. The crystal structure that forms depends on the interaction between the particles forming the crystal as well as their environmental conditions such as temperature or particle density. The phase transition from a disordered liquid to a crystalline state occurs by nucleation. The formation of small crystals is hindered by the nucleation barrier; the rearrangement of particles from an unordered state into an ordered crystalline array needs a certain energy, which is given by the surface energy γA, where γ is the surface tension of the crystal surrounded by liquid, and A is the surface area of the small crystal. For very small crystals, γA exceeds the energy gain $\Delta\mu n V$ due to the formation of the energetically more favorable crystal state. Here, $\Delta\mu$ is the chemical potential difference of liquid and crystal, n is the number density in the crystal state, and V is the volume of the formed crystal. Due to this competition of a surface energy and a volume energy, there is a critical crystal nucleus size above which the crystal can reduce its energy by growing. Due to this free energy barrier for crystal nucleation,

$$\Delta G = \gamma A - \Delta\mu n V, \tag{14.1}$$

liquids can be supercooled before the formation of the crystalline state starts, and as a consequence the formation of crystals can be a very rare event depending on the degree of supercooling and other environmental conditions. The spontaneous formation of a crystal from random structural fluctuations in the bulk as described above is called homogeneous nucleation. Crystallization may occur, in addition, as a consequence of the presence of impurities in the sample or not in bulk, but rather on a surface due to the presence of a container wall. This process is called heterogeneous nucleation; it is often faster than homogeneous nucleation and can be exploited for a controlled formation of crystal with a defined orientation of the crystal lattice.

Once crystals larger than the critical size have formed, the system reduces its free energy by the growth of these crystals until either the free energy gain $\Delta\mu$ becomes 0 due to, for example, a density change in the liquid caused by the growing crystal or until the crystal grains begin to interact and no space for further growth is available. A material that is filled with crystal grains having different orientations is in the polycrystalline state and can continue to reduce its free energy by minimizing the area of the domain walls between the crystal grains. This process is called

coarsening and it leads to a shrinkage and disappearance of small crystal grains and the further growth of large grains.

14.2.2 Crystalline Structure

An ideal crystal is constructed by the repetition of a certain structure in space. This simple definition reveals the two most important concepts in the description of crystalline structures: the lattice and the basis. The lattice is a regular array of points in space that reflect the translational periodicity of the crystal. The basis, however, is the pattern which when placed on those points gives rise to the crystalline structure. This pattern could be a single object or a group of objects. As a result, we can establish the logical relationship [59]:

$$\text{Lattice} + \text{Basis} = \text{Crystal stucture} \tag{14.2}$$

A lattice is constructed by the linear combination of three linearly independent vectors, $\vec{a}_1$, $\vec{a}_2$ and $\vec{a}_3$. It is, thus, defined as the group of positions, $\vec{P}_i$, in space that fulfill the condition:

$$\vec{P}_i = n_1\vec{a}_1 + n_2\vec{a}_2 + n_3\vec{a}_3. \tag{14.3}$$

where n_1, n_2, and n_3 are integers. The vectors $\vec{a}_1$, $\vec{a}_2$ and $\vec{a}_3$ are called the primitive vectors, if the arrangement looks identical from any of the lattice points. These vectors also give rise to the primitive cell, which is defined as the minimum volume cell that will fill all space by repetition without either overlapping or leaving voids. A primitive cell only contains one lattice site. In 3D, there are 14 different types of lattices, referred to as Bravais lattices. These are summarized in Figure 14.2. They are classified into seven different systems according to the relationship between the primitive vectors and the angle between them. In this chapter, we will be concerned with cubic and hexagonal lattices mainly. There are three types of lattices within the cubic system, the simple cubic (SC), the body-centered cubic (BCC), and the face-centered cubic (FCC), as schematically shown in Figure 14.3; some of their properties are given in Figure 14.2. Whereas crystallization in the simple cubic lattice is extremely rare in nature, both crystallization in the FCC and BCC are ubiquitous in atomic and colloidal systems [60]. This is due to the efficient packing of the available space that is obtained with BCC and in particular with FCC structures. Dense packings are of primary importance for systems with isotropic interactions, which is the case in most colloidal systems.

14.2.2.1 Body-Centered Cubic

The BCC lattice can be described as a simple cubic cell with an additional position in the center of the cube, as shown in Figure 14.3. This cell, although very descriptive of the set of symmetries of the structure, is a conventional cell but not a primitive one. Each of the atoms in the vertices is shared by eight cells and thus, should be counted as 1/8. As a result, the total number of atoms within the cell is $8/8 + 1 = 2$. A primitive cell for the BCC structure is depicted in Figure 14.4a. The lattice

Bravais lattice	Parameters	Simple (P)	Volume centered (I)	Base centered (C)	Face centered (F)
Triclinic	$a_1 \neq a_2 \neq a_3$ $\alpha_{12} \neq \alpha_{23} \neq \alpha_{31}$				
Monoclinic	$a_1 \neq a_2 \neq a_3$ $\alpha_{23} = \alpha_{31} = 90^\circ$ $\alpha_{12} \neq 90^\circ$	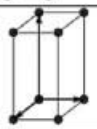	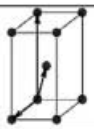		
Orthorhombic	$a_1 \neq a_2 \neq a_3$ $\alpha_{12} = \alpha_{23} = \alpha_{31} = 90^\circ$				
Tetragonal	$a_1 = a_2 \neq a_3$ $\alpha_{12} = \alpha_{23} = \alpha_{31} = 90^\circ$	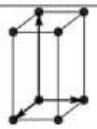	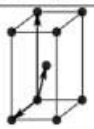		
Trigonal	$a_1 = a_2 = a_3$ $\alpha_{12} = \alpha_{23} = \alpha_{31} < 120^\circ$				
Cubic	$a_1 = a_2 = a_3$ $\alpha_{12} = \alpha_{23} = \alpha_{31} = 90^\circ$				
Hexagonal	$a_1 = a_2 \neq a_3$ $\alpha_{12} = 120^\circ$ $\alpha_{23} = \alpha_{31} = 90^\circ$				

Figure 14.2 The 14 Bravais lattices in three dimensions.

parameter is $\bar{l} = d(2/\sqrt{3})$, where d is the nearest neighbor distance. It is generated with the primitive vectors:

$$\vec{a}_1 = \frac{1}{2}\bar{l}(\hat{x} + \hat{y} - \hat{z}); \vec{a}_2 = \frac{1}{2}\bar{l}(-\hat{x} + \hat{y} + \hat{z}); \vec{a}_3 = \frac{1}{2}\bar{l}(\hat{x} - \hat{y} + \hat{z}) \tag{14.4}$$

Colloidal particles with repulsive interactions have been observed to crystallize in a BCC structure [61]. The maximum packing fraction of the BCC structure with spheres is $\phi = \sqrt{3}\pi/8 \approx 0.68$.

14.2.2.2 **Face-Centered Cubic**

The FCC structure can be described as a simple cubic lattice with atoms on the faces of the cube. This cell reflects the set of symmetries of the structure, yet it is not a primitive cell. In this case, in addition to the atoms of the vertices, the cell contains 6 atoms in the faces that are shared by two cells, thus the total number of atoms within

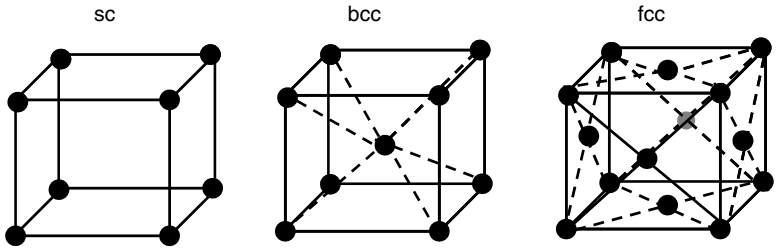

Figure 14.3 The three cubic lattices. The cells shown are conventional and not primitive cells.

one of these conventional cells is $8/8 + 6/2 = 4$. A primitive cell for the FCC is shown in Figure 14.4b. The lattice parameter is $\bar{l} = d\sqrt{2}$. The primitive cell can be generated using the vectors:

$$\vec{a}_1 = \frac{1}{2}\bar{l}(\hat{x}+\hat{y}); \vec{a}_2 = \frac{1}{2}\bar{l}(\hat{y}+\hat{z}); \vec{a}_3 = \frac{1}{2}\bar{l}(\hat{x}+\hat{z}) \tag{14.5}$$

The FCC structure is very common among crystals of colloidal particles, in particular for hard spheres that only interact when they come into direct contact. As a matter of fact, the FCC configuration together with the hexagonal close-packed (HCP) structure represents the most effective way of packing spheres. For both of them, the packing fraction is $\phi = \pi/(3\sqrt{2}) \approx 0.74$.

14.2.2.3 Hexagonal and Hexagonal Close-Packed

The hexagonal system is one of the seven crystal systems in three dimensions. It only has one Bravais lattice, which is obtained by stacking two-dimensional triangular nets at a distance c, as shown in Figure 14.5.

The primitive vectors are:

$$\vec{a}_1 = \bar{l}\hat{x}; \vec{a}_2 = \frac{\bar{l}}{2}\hat{x} + \frac{\sqrt{3}\,\bar{l}}{2}\hat{y}; \vec{a}_3 = c\hat{z} \tag{14.6}$$

The vectors $\vec{a}_1$ and $\vec{a}_2$ generate the triangular lattice and $\vec{a}_3$ allows for stacking the planes at a distance c from each other.

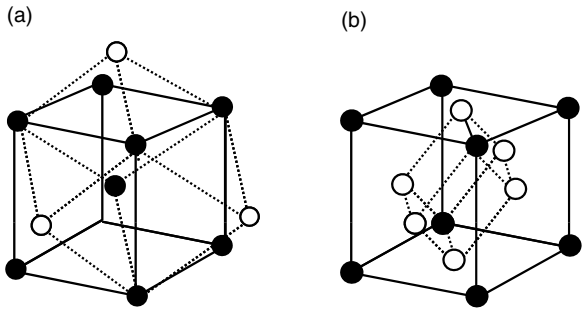

Figure 14.4 Primitive cell of the (a) BCC and (b) FCC structures.

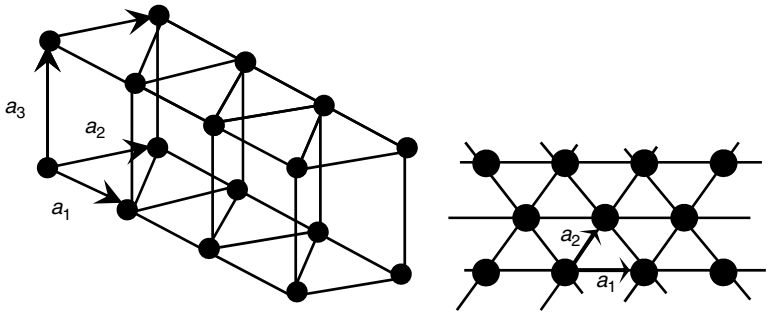

Figure 14.5 The simple hexagonal lattice (left) is obtained by stacking triangular nets (right) one on top of each other at a distance c.

The HCP structure is not a Bravais lattice. It is obtained by interlacing two hexagonal Bravais lattices, displaced from one another by $\vec{a}_1/3 + \vec{a}_2/3 + \vec{a}_3/2$. The arrangement follows that $\sqrt{8/3}\,\bar{l} = c$. In this case, it is easy to see that $\bar{l} = d$. As for the FCC, the maximum packing fraction of the HCP structure is $\phi \approx 0.74$.

Both the HCP and the FCC lattice consist of stackings of triangular planes, as shown on the right hand side of Figure 14.5. If one starts with a triangular plane, an additional triangular plane can be added in two different locations corresponding to the centers of gravity of the triangles shown in the figure. When the positions shown in the figure are labeled A and the two other positions are labeled B and C, the HCP lattice corresponds to a stacking of the type $ABAB\ldots$, while FCC corresponds to $ABCABC\ldots$. Due to stacking faults of the triangular planes, a HCP crystal, for example, can contain pieces of FCC-like stacking. In hard spheres, the ground state is known to be FCC, but stacking faults are very common such that hard-sphere crystals often grow as a random mixture of HCP- and FCC-like stackings. Such crystals are called random hexagonal close-packed (RHCP) [62, 63].

14.2.2.4 **A15**

Another important crystal arrangement is the A15 structure. It is obtained from a BCC lattice by decorating each of its faces with dimers, as shown in Figure 14.6. For this structure, $\bar{l} = \sqrt{(16/5)}d$. The A15 arrangement has been observed in certain types of polymer structures and it has been theoretically predicted to minimize the contact area between neighboring particles in systems with strong repulsions [64–67].

14.2.3
Scattering of Waves from Crystals

Following the discussion of the FCC and HCP structures, it is clear that crystals can be understood as stackings of planes of objects. A wave hitting a crystal can be reflected by these planes, which can give rise to strong scattering signals, if there is constructive interference between the reflections, as illustrated in Figure 14.7. This

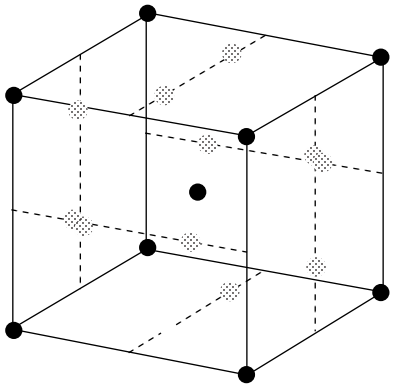

Figure 14.6 Conventional cell and basis for the A15 structure. Reproduced with permission of the American Chemical Society.

occurs when the path difference for waves reflected from adjacent planes, $2d\sin(\theta/2)$, with θ measured from the plane, is a multiple number of the wavelengths, λ:

$$n\lambda = 2d\sin(\theta/2), \tag{14.7}$$

where n is a natural number excluding 0. This equation can be rewritten as:

$$q = \frac{4\pi}{\lambda}\sin(\theta/2) \tag{14.8}$$

using the modulus $q = 2\pi/d$ of the scattering wave vector $\vec{q} = \vec{k}_s - \vec{k}_i$, with $\vec{k}_i$ and $\vec{k}_s$ the wave vectors of the incident and scattered waves, respectively. Such strong scattering peaks occur if a crystal plane happens to be oriented such that the Bragg

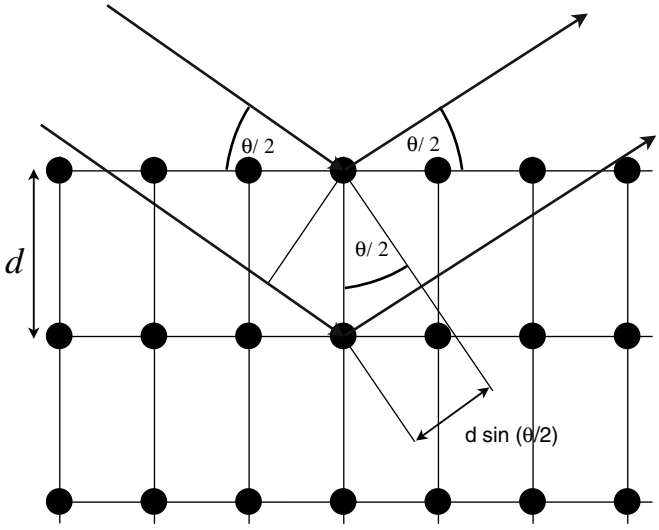

Figure 14.7 Lattice planes, incident rays, and reflected rays considered for the derivation of the Bragg condition.

condition (Equation 14.7) is fulfilled. All $\vec{q}$-vectors fulfilling the condition for constructive interference form a lattice called the reciprocal lattice [60]. It can be shown that this lattice is defined by the vectors:

$$\vec{b}_1 = \frac{2\pi}{V_c}\vec{a}_2 \times \vec{a}_3, \quad \vec{b}_2 = \frac{2\pi}{V_c}\vec{a}_3 \times \vec{a}_1, \quad \vec{b}_3 = \frac{2\pi}{V_c}\vec{a}_1 \times \vec{a}_2, \tag{14.9}$$

where $V_c = (\vec{a}_1 \times \vec{a}_2) \cdot \vec{a}_3$ is the volume of the corresponding cell. The $\vec{q}$-vectors of the reciprocal lattice can be expressed in terms of linear combinations of its lattice vectors:

$$\vec{q} = h\vec{b}_1 + k\vec{b}_2 + l\vec{b}_3 \tag{14.10}$$

where h, k, and l are integer numbers called Miller indexes. The reciprocal lattice is defined by the crystal lattice in real space. However, it can have different symmetry; for instance, the reciprocal lattice of a simple cubic lattice is again a simple cubic lattice, but that of a BCC is a FCC and vice versa, and that of a hexagonal lattice is again a hexagonal lattice but rotated with respect to the first.

The Miller indexes have a real space interpretation. Recall that the orientation of a particular family of lattice planes giving rise to a Bragg reflection can be determined by its intersection with the lattice axes in terms of the lattice constants a_1, a_2, and a_3. In order to provide the orientation of a lattice plane, it is customary to find its intercept with the three lattice axis, take the reciprocal of the result and find the smallest combination of integers that follow the same ratio. The three numbers are the Miller indexes (h, k, l) for the corresponding family of lattice planes [60], all having associated the reciprocal lattice vector $\vec{q}$ given by Equation 14.10. For example, if a crystal plane intercepts the lattice axes in (4, 3, 2), we would take the inverse of those numbers, (1/4, 1/3, 1/2), and find the smallest integers with the same ratio, (3, 4, 6). The corresponding reciprocal lattice vector would be $\vec{q} = 3\vec{b}_1 + 4\vec{b}_2 + 6\vec{b}_3$.

14.2.4
Small-Angle Neutron Scattering

Scattering of neutrons has been widely used as a method to determine static and dynamic properties of very different systems, taking advantage of the fact that thermal and cold neutrons have wavelengths, λ, in the range from 1 up to 20 Å, which is much larger than the dimension of the atomic nuclei that the neutrons interact with. As a consequence, the nuclei act like point scatterers and the neutrons are thus scattered as isotropic spherical waves. By contrast, recall that electromagnetic radiation interacts mainly with the much larger electronic cloud of the atoms. As a result, neutrons are able to penetrate deep inside the sample and are mostly singly scattered, except for extremely high concentrations of nuclei. This results from the small space occupied by the nuclei compared to the space occupied by the electron cloud of the atoms.

In a small-angle neutron experiment, a beam of collimated and fairly monochromatic radiation of flux, $I_0(\lambda)$, is directed at a sample, illuminating a small volume, V,

which depends on the area of the beam, A_{beam} and the width of the sample, d. Even though most of the radiation is transmitted, some is absorbed and some is scattered. If we place a detector with area A_{detector} at an angle θ and distance L from the sample, scattered radiation within the solid angle $d\Omega_{\text{d}} = A_{\text{detector}}/L^2$ will be collected. The flux of collected neutrons, $I_{\text{s}}(\lambda, \theta)$, can be expressed as [68, 69]:

$$I_s(\lambda, \theta) = I_0(\lambda) d\Omega_d \, \varepsilon Tr V \left(\frac{\mathrm{d}\sigma}{\mathrm{d}\Omega}\right)_\nu \tag{14.11}$$

where ε is the efficiency of the detector, Tr is the transmission coefficient of the sample and $(\mathrm{d}\sigma/\mathrm{d}\Omega)_\nu$ is the microscopic differential cross section, which contains information about the shape and size of the scatterers and about the interactions between them and their spatial organization. Whereas $I_0(\lambda)$, $d\Omega_{\text{d}}$, and ε depend on the source and particular arrangement of the experimental setup, Tr, V, and $(\mathrm{d}\sigma/\mathrm{d}\Omega)_\nu$ are sample-dependent and, therefore, need to be determined for each sample. Out of these three contributions, only $(\mathrm{d}\sigma/\mathrm{d}\Omega)_\nu$ depends on the scattering angle, θ, thus containing the desired structural information. Therefore, the main goal in a SANS experiment is the determination of $(\mathrm{d}\sigma/\mathrm{d}\Omega)_\nu$ as a function of the modulus of the scattering vector, $q = (4\pi/\lambda)\sin(\theta/2)$, if the sample is isotropic, where λ is the neutron wavelength.

Let us consider an incident neutron wave packet that encounters a single atomic nucleus, producing an emerging wave packet that contains a scattered wavelet and an incident wavelet that remains unscattered. The scattered wave can be described as a spherical wave [70]:

$$\Psi_{\text{s}} = \frac{f(\vartheta, \phi)}{r} A(x, y, z, t) \mathrm{e}^{i(\vec{k}_s \cdot \vec{r} - \omega t)} \tag{14.12}$$

with ϑ and ϕ the azimuthal and radial angles in spherical coordinates. If the wave function is properly normalized, it is easy to show that the differential cross section $\mathrm{d}\sigma/\mathrm{d}\Omega$, defined as the probability of finding the scattered particle within a solid angle $\mathrm{d}\Omega$ when one neutron is incident, can be written as [71]:

$$\frac{\mathrm{d}\sigma}{\mathrm{d}\Omega} = |f(\vartheta, \phi)|^2 \tag{14.13}$$

Note that we have dropped the subindex ν, as we are not referring to the scattering cross section per unit volume. From a quantum mechanical point of view, the problem we need to solve is that of an incident wave packet interacting with an atomic nucleus through a potential $V(r) = V_{\text{a}}\delta(\vec{r} - \vec{r}_{\text{a}})$, which we write in terms of a δ-function because the nucleus is much smaller than the neutron wavelength. $V(r)$ is called Fermi pseudo-potential. The corresponding Schröedinger equation can be written as:

$$i\hbar \frac{\partial}{\partial t} \Psi = \left[-\frac{\hbar^2}{2m} \nabla^2 + V(\vec{r}) \right] \Psi \tag{14.14}$$

where $\Psi = \Psi_i + \Psi_{\text{s}}$, with $\Psi_i = A(x_0, y_0, z_0, t) \mathrm{e}^{i(\vec{k}_i \cdot \vec{r} - \omega t)}$, and m is the mass of the neutron. This equation can be solved using the Born approximation [71]:

$$\Psi_s = -\frac{mA(x,y,z,t)e^{i(\vec{k}_s\cdot\vec{r}-\omega t)}}{2\pi\hbar^2 r}\iiint d^3\vec{r}\,' V_a\delta(\vec{r}\,'-\vec{r}_a)e^{-i(\vec{k}_s-\vec{k}_i)\cdot\vec{r}\,'} \tag{14.15}$$

which yields an expression for $f(\vartheta, \phi)$ after comparison with Equation 14.12:

$$f(\vartheta,\phi) = \frac{-m}{2\pi\hbar^2}\iiint d^3\vec{r}\,' V_a\delta(\vec{r}\,'-\vec{r}_a)e^{-i(\vec{k}_s-\vec{k}_i)\cdot\vec{r}\,'} \tag{14.16}$$

Using the properties of the delta function:

$$f(\vartheta,\phi) = \frac{-m}{2\pi\hbar^2}V_a = b \tag{14.17}$$

where we have written $V_a = -[(2\pi\hbar^2)/m]b$. The constant b is called the scattering amplitude and simply defines the strength of the interaction between a neutron and a nucleus. The differential cross section thus becomes:

$$\frac{d\sigma}{d\Omega} = b^2 \tag{14.18}$$

Let us now consider scattering from a collection of N nuclei, each characterized by its scattering amplitude, b_j. We can express the scattered wave from nucleus j in the detector at position $\vec{r}$ as:

$$\Psi_{s,j}(\vec{r}) \sim \frac{b_j}{r}e^{i(\vec{k}_s\cdot(\vec{r}-\vec{r}_1)+\Delta\Phi)} \tag{14.19}$$

where, on writing the denominator we have assumed that the distance to the detector is much larger than the distance between scatterers. The phase of this wave has been expressed in terms of the phase of the scattered wave from nucleus "1" plus a phase change, $\Delta\Phi = 2\pi\delta/\lambda$, related to the optical path difference between the scattered waves from nucleus "j" and nucleus "1", δ. From geometric considerations, $\delta = \overline{B1}-\overline{Aj} = \hat{k}_s\cdot\vec{r}_j-\hat{k}_i\cdot\vec{r}_j$, with $\vec{r}_j$ the position vector of scatterer "j" measured with respect to scatterer "1", as shown in Figure 14.8. Using this,

$$\Delta\Phi = \vec{k}_s\cdot\vec{r}_j-\vec{k}_i\cdot\vec{r}_j = \vec{q}\cdot\vec{r}_j \tag{14.20}$$

where $\vec{k}_s = 2\pi/\lambda\hat{k}_s$ and $\vec{k}_i = 2\pi/\lambda\hat{k}_i$. The total scattered wave at the detector is the superposition of all scattered waves:

$$\Psi(\vec{r}) = \sum_{j=1}^{N}\Psi_{s,j}(\vec{r}) \sim \sum_{j=1}^{N}\frac{b_j}{r}e^{i\vec{k}_s\cdot(\vec{r}-\vec{r}_1)}e^{i\vec{q}\cdot\vec{r}_j} \tag{14.21}$$

The probability of having a scattered neutron within the solid angle $d\Omega$ can be written as:

$$\frac{d\sigma}{d\Omega} = \langle\Psi\Psi^*\rangle = \left\langle\sum_{j=1}^{N}b_j e^{i\vec{q}\cdot\vec{r}_j}\sum_{k=1}^{N}b_k e^{-i\vec{q}\cdot\vec{r}_k}\right\rangle. \tag{14.22}$$

Under the assumption that there is no correlation between the scattering lengths from atom to atom, Equation 14.22 becomes [68]:

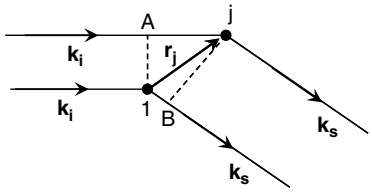

Figure 14.8 Geometry for obtaining the phase difference in Equation 14.19.

$$\frac{\mathrm{d}\sigma}{\mathrm{d}\Omega} = N\Delta b^2 + \langle b\rangle^2 \sum_{j,k=1}^{N} \left\langle \mathrm{e}^{-i\vec{q}\cdot(\vec{r}_k-\vec{r}_j)} \right\rangle \tag{14.23}$$

where $\langle b\rangle$ is the average scattering length and $\Delta b^2 = \langle b^2\rangle - \langle b\rangle^2$ the first term of this expression depends on the fluctuations of b for different nuclei, irrespective of their particular positions. This part of the scattering is called incoherent as it does not depend on θ or ϕ. It appears when there is a mixture of nuclei with different values of b. For elements with several isotopes, b can vary significantly from isotope to isotope, such that an incoherent background is usually observed in neutron scattering. Since incoherent scattering does not result from constructive interference between wave packets, it does not contain structural information about the distribution of nuclei. However, the second term in Equation 14.23 does depend on the arrangement of the nuclei and, thus, may give rise to interference. This term is usually called coherent scattering contribution and contains the structural information of the sample. This is the important quantity for a system with one component:

$$\left(\frac{\mathrm{d}\sigma}{\mathrm{d}\Omega}\right)_{coh} = \langle b\rangle^2 \sum_{j,k=1}^{N} \left\langle \mathrm{e}^{-i\vec{q}\cdot(\vec{r}_k-\vec{r}_j)} \right\rangle, \tag{14.24}$$

We can extend this to the case of a two-component system, comprising N_1 nuclei of species 1 with average scattering length b_1 and N_2 nuclei of species 2 with average scattering length b_2. Equation 14.24 can be generalized to:

$$\begin{aligned}\left(\frac{\mathrm{d}\sigma}{\mathrm{d}\Omega}\right)_{coh} &= b_1^2 \sum_{i_1,j_1=1}^{N_1} \left\langle \mathrm{e}^{-i\vec{q}\cdot(\vec{r}_{i_1}-\vec{r}_{j_1})} \right\rangle + b_2^2 \sum_{i_2,j_2=1}^{N_2} \left\langle \mathrm{e}^{-i\vec{q}\cdot(\vec{r}_{i_2}-\vec{r}_{j_2})} \right\rangle \\ &\quad + 2b_1b_2 \sum_{i_1}^{N_1}\sum_{j_2}^{N_2} \left\langle \cos(\vec{q}\cdot[\vec{r}_{i_1}-\vec{r}_{j_2}]) \right\rangle,\end{aligned} \tag{14.25}$$

which in the continuum limit becomes:

$$\begin{aligned}\left(\frac{\mathrm{d}\sigma}{\mathrm{d}\Omega}\right)_{coh} &= b_1^2 \int_V \mathrm{d}\vec{r} \int_{V'} \mathrm{d}\vec{r}' \langle \Delta n_1(\vec{r})\Delta n_1(\vec{r}')\rangle \mathrm{e}^{-i\vec{q}\cdot(\vec{r}-\vec{r}')} \\ &\quad + b_2^2 \int_V \mathrm{d}\vec{r} \int_{V'} \mathrm{d}\vec{r}' \langle \Delta n_2(\vec{r})\Delta n_2(\vec{r}')\rangle \mathrm{e}^{-i\vec{q}\cdot(\vec{r}-\vec{r}')} \\ &\quad + 2b_1b_2 \int_V \mathrm{d}\vec{r} \int_{V'} \mathrm{d}\vec{r}' \langle \Delta n_1(\vec{r})\Delta n_2(\vec{r}')\rangle \cos(\vec{q}\cdot[\vec{r}-\vec{r}']),\end{aligned} \tag{14.26}$$

where $\Delta n_\alpha(\vec{r})$ represents the fluctuations in the number density, $n_\alpha(\vec{r}) = \sum_{j=1}^{N_\alpha} \delta(\vec{r} - \vec{r}_j^{\,\alpha})$, $\alpha \in \{1, 2\}$; note that $\int n_\alpha d\vec{r} = N_\alpha$. This expression can be written as:

$$\left(\frac{d\sigma}{d\Omega}\right)_{coh} = b_1^2 F_{11}(\vec{q}) + b_2^2 F_{22}(\vec{q}) + 2b_1 b_2 F_{12}(\vec{q}), \tag{14.27}$$

where we define the partial structure factor, $F_{\alpha\beta}(\vec{q})$, as:

$$F_{\alpha\beta}(\vec{q}) = \int_V d\vec{r} \int_{V'} d\vec{r}' \langle \Delta n_\alpha(\vec{r}) \Delta n_\beta(\vec{r}') \rangle e^{-i\vec{q}\cdot(\vec{r}-\vec{r}')} \tag{14.28}$$

Note that the three partial structure factors are not independent. Since the system is incompressible, the total density is constant and thus:

$$\Delta n_1(\vec{r}) + \Delta n_2(\vec{r}) = 0, \tag{14.29}$$

which reflects that an increase in n_1 causes a decrease in n_2. Following this, Equation 14.27 becomes:

$$\left(\frac{d\sigma}{d\Omega}\right)_{coh} = (b_1 - b_2)^2 F_{11}(\vec{q}) + (b_1 - b_2)^2 F_{22}(\vec{q}) - (b_1 - b_2)^2 F_{12}(\vec{q}) \tag{14.30}$$

which can be further generalized for a system of $p + 1$ components [68]:

$$\left(\frac{d\sigma}{d\Omega}\right)_{coh} = \sum_{i=1}^{p} (b_i - b_0)^2 F_{ii}(\vec{q}) + 2 \sum_{i<j} (b_i - b_0)(b_j - b_0) F_{ij}(\vec{q}) \tag{14.31}$$

in which the component "0" is the one filling the vacancies to fulfill the incompressibility condition; this component is usually regarded as the solvent.

As a next step in our development, let us consider a system of N macromolecules, each comprised of z segments, which we consider as point scatterers with scattering length b. The partial structure factor for the system is:

$$F(\vec{q}) = \sum_{p=1}^{N} \sum_{q=1}^{N} \sum_{j=1}^{z} \sum_{k=1}^{z} \langle e^{-i\vec{q}\cdot(\vec{r}_{pj} - \vec{r}_{qk})} \rangle \tag{14.32}$$

We can extract the terms in which $p = q$, which correspond to interference within segments belonging to the same macromolecule. There are N terms of this type and they are all identical. The other terms will represent interference between pairs of segments in different macromolecules. There are $N(N-1)$ identical pairs of this type. As a result:

$$F(\vec{q}) = N \sum_{i_1=1}^{z} \sum_{j_1=1}^{z} \langle e^{-i\vec{q}\cdot(\vec{r}_{i_1} - \vec{r}_{j_1})} \rangle + N(N-1) \sum_{i_1=1}^{z} \sum_{j_2=1}^{z} \langle e^{-i\vec{q}\cdot(\vec{r}_{i_1} - \vec{r}_{j_2})} \rangle \tag{14.33}$$

By means of this rearrangement, we have separated the partial structure factor into one term that only depends on the particular properties of the macromolecules and another term that only depends on the distribution of the macromolecules. We note the first term as $P(\vec{q})$ and thus:

$$P(\vec{q}) = \frac{1}{z^2}\sum_{i_1=1}^{z}\sum_{j_1=1}^{z}\langle e^{-i\vec{q}\cdot(\vec{r}_{i_1}-\vec{r}_{j_1})}\rangle \tag{14.34}$$

This is the form factor of the macromolecule; it only contains information about interference of scattered waves from segments in the same macromolecule and contains information about the size and shape of the macromolecule. By contrast, the second term in Equation 14.33 depends on the interference of scattered waves from segments in different macromolecules. This term, which we note $Q(\vec{q})$, contains the structural information of the solution:

$$Q(\vec{q}) = \frac{1}{z^2}\sum_{i_1=1}^{z}\sum_{j_2=1}^{z}\langle e^{-i\vec{q}\cdot(\vec{r}_{i_1}-\vec{r}_{j_2})}\rangle \tag{14.35}$$

We can rewrite the partial structure factor $F(\vec{q})$ using $P(\vec{q})$ and $Q(\vec{q})$:

$$F(\vec{q}) = Nz^2P(\vec{q}) + N(N-1)z^2Q(\vec{q}) \tag{14.36}$$

We can still simplify the expression for $Q(\vec{q})$, by using the center of mass of each macromolecule:

$$\vec{r}_{i_1}-\vec{r}_{j_2} = \vec{r}_{i_1}-\vec{r}_{CM_1}+\vec{r}_{CM_1}-\vec{r}_{CM_2}+\vec{r}_{CM_2}-\vec{r}_{j_2} \tag{14.37}$$

where $\vec{r}_{CM_i}$ is the position vector of the center of mass of macromolecule i. Using this, Equation 14.35 becomes:

$$\begin{aligned} Q(\vec{q}) &= \langle e^{-i\vec{q}\cdot(\vec{r}_{CM_1}-\vec{r}_{CM_2})}\rangle \frac{1}{z^2}\sum_{i_1=1}^{z}\sum_{j_2=1}^{z}\langle e^{-i\vec{q}\cdot[\vec{r}_{CM_2}-\vec{r}_{j_2}-(\vec{r}_{CM_1}-\vec{r}_{i_1})]}\rangle \\ &= \langle e^{-i\vec{q}\cdot(\vec{r}_{CM_1}-\vec{r}_{CM_2})}\rangle P(\vec{q}) \end{aligned} \tag{14.38}$$

and the partial structure factor ends up written as:

$$F(\vec{q}) = Nz^2P(\vec{q})[1+(N-1)\langle e^{-i\vec{q}\cdot(\vec{r}_{CM_1}-\vec{r}_{CM_2})}\rangle] = Nz^2P(\vec{q})S(\vec{q}), \tag{14.39}$$

where $S(\vec{q}) = [1+(N-1)\langle e^{-i\vec{q}\cdot(\vec{r}_{CM_1}-\vec{r}_{CM_2})}\rangle]$ is the structure factor of the system of macromolecules. For a binary mixture of macromolecules and a solvent, we have (Equation 14.31):

$$\left(\frac{d\sigma}{d\Omega}\right)_{coh} = (b_1-b_0)^2Nz^2P(\vec{q})S(\vec{q}) \tag{14.40}$$

with component 1 the macromolecules and component 0 the solvent.

Given that each segment is treated as a singular scatterer, by further assuming its volume is identical to the volume of a solvent molecule, v_s, the volume of a single macromolecule can be written as $V_{mac} = zv_s$. Since each macromolecule is made of z segments and the scattering length of a macromolecule is $b_{mac} = zb_1$, then:

$$\frac{b_1}{v_s} = \frac{b_{mac}}{V_{mac}} \tag{14.41}$$

and thus:

$$\left(\frac{d\sigma}{d\Omega}\right)_{coh} = \nu_s^2 b_\nu^2 N z^2 P(\vec{q}) S(\vec{q}) \tag{14.42}$$

where $b_v = (b_{mac}/V_{mac}) - (b_0/\nu_s)$ is the difference in the scattering length density between the macromolecule and the solvent. Expressing Equation 14.42 per unit volume, we obtain:

$$\left(\frac{d\sigma}{d\Omega}\right)_{coh}/V = \left(\frac{d\sigma}{d\Omega}\right)_{coh,\nu} = b_\nu^2 \frac{N}{V} V_{mac}^2 P(\vec{q}) S(\vec{q}), \tag{14.43}$$

where we emphasize again that V_{mac} is the total volume of all segments in the macromolecule. Equation 14.43 shows that the differential cross section per unit volume depends on the number density of macromolecules, on their volume V_{mac}, on their shape and size through the particle form factor $P(\vec{q})$ and on the correlations between them, through the structure factor $S(\vec{q})$.

14.2.5 Experimental Details

We performed the SANS measurements on the SANS-I apparatus located at SINQ in Paul Scherrer Institute (Switzerland). Neutrons are generated in a spallation source and are cooled in a heavy water moderator and a cold source of 20 l of liquid deuterium at 25 K to produce thermal neutrons with energy $E \sim 2$ meV [72]. These neutrons are then guided towards a mechanical monochromator that selects those neutrons with wavelength λ; this is done with a resolution $\Delta\lambda/\lambda \sim 0.1$. The beam is collimated over 1 to 18 m and focused onto the sample cells, which are made of quartz and have a path length of 1 or 2 mm, using neutron lenses to reduce the uncertainty in the scattering angle [73, 74]. Therefore, $\Delta q/q \sim \Delta\lambda/\lambda$. The scattered neutrons are collected in a two-dimensional detector with 128×128 elements of $7.5 \times 7.5\ mm^2$, which can be placed at a distance ranging from 1.4 to 20 m away from the sample. In this way, we have access to three decades in scattering wave vector, from 5×10^{-3} nm^{-1} to $5.4\ nm^{-1}$. A simple schematic of the device is shown in Figure 14.9.

The measured scattered intensities from the sample, S, the corresponding sample background, B, and a calibration measurement, W, are all corrected according to:

$$M_f = \frac{I-D}{Tr_S} - \frac{B-D}{Tr_B} \tag{14.44}$$

$$I_f = \frac{S_f}{W_f}\frac{L_W}{L_S}, \tag{14.45}$$

where I represents either S or W, M_f stands for the corrected measurement, and I_f is the corrected and calibrated scattered intensity. In addition:

- The dark counts, D, of the detector are measured by blocking the incoming neutron beam with a cadmium plate. This measurement also detects stray neutrons that do not go through the sample.

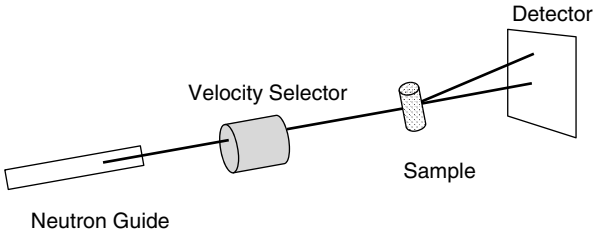

Figure 14.9 Schematic representation of a typical small-angle neutron scattering (SANS) layout.

- The efficiency of each pixel in the detector is calibrated with a measurement of H_2O, W, which is a predominantly incoherent scatterer, and the known path lengths of the sample, L_S, and water, L_W. The measurement W can be used to determine the scattering cross section in absolute units, although here we focus on the q-dependence of the scattered intensity; we will thus not perform this adjustment.
- Measurements of the solvent alone, B, are performed to account for the background scattering.
- Finally, the transmission through all samples, Tr, including the solvent, are determined. A measurement of the direct beam is used to determine the center of the direct neutron beam, which we use for radial averaging of the corrected data:

$$I_f(q) = \frac{1}{2\pi}\int_0^{2\pi} d\varphi I_f(q,\varphi). \tag{14.46}$$

14.2.6
Experimental System

The particles we use are made up of PNIPAM (poly-*N*-isoproprylacrylamide) and acrylic acid (AA). They are synthesized by emulsion polymerization [75] of NIPAM monomer, AA (2 mol%) and the crosslinker methylene-bis-acrylamide (5 mol%) in water at 70 °C using the surfactant sodium dodecyl sulfate (0.05 wt%) to control the particle size. This precursor solution is stirred and bubbled with nitrogen prior to the initiation of the reaction with potassium persulfate (0.06 wt%). The reaction is allowed to proceed for 4 h under a nitrogen blanket to ensure full reaction of the monomers. After cooling the products, the particles are exhaustively dialyzed against ultrapure water until the conductivity of the removed water matches the conductivity of the added water. Finally, we freeze-dry the particles and redisperse them in heavy water.

We use dynamic light scattering (DLS) to determine how the particle size of these microgels depends on temperature and hydrostatic pressure [76]. Since the miscibility of PNIPAM in water or heavy water decreases with temperature, the particle size also decreases with increasing temperature, as shown in Figure 14.10a and consistent with previous results [77–79]. It is important to note that for our PNIPAM

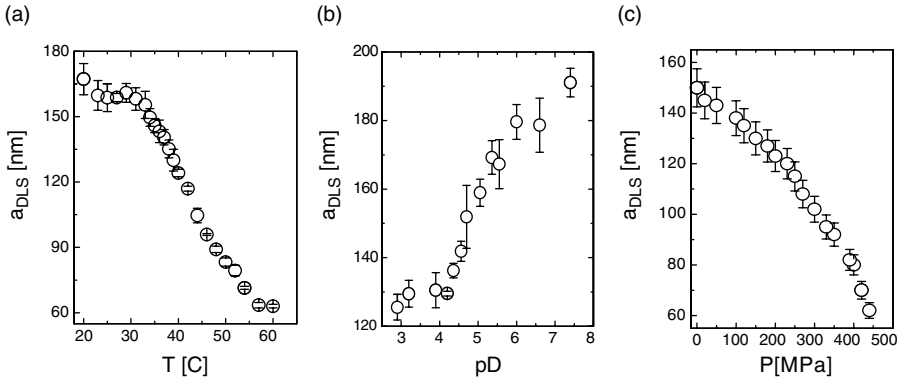

Figure 14.10 (a) Hydrodynamic radius, measured by dynamic light scattering, of PNIPAM–AA microgels in D_2O as a function of (a) temperature, (b) pD, and (c) hydrostatic pressure. The particle deswells with both increasing temperature and hydrostatic pressure and with decreasing pD.

particles the range of deswelling is considerably broadened in comparison with a pure PNIPAM microgel. This is due to the presence of AA on the polymer network, which affects the swelling behavior due to its dissociation; this changes the network charge and affects the ionic distributions inside and outside the particles. This, in turn, alters the osmotic equilibrium of the particles in the outside bath, favoring swelling and giving rise to the observed size-T broadening.

The particle size dependence with pD is shown in Figure 14.10b. We use pD instead of pH, because we use heavy water, D_2O, instead of water as solvent. Since the pK_a of polyacrylic acid is 4.5 [80], the system remains essentially uncharged at low values of pD, resulting in a constant particle size. However, as the pD is increased, the ionization of the acrylic acid becomes increasingly important and the particle swells due to the ionic osmotic pressure exerted by the counterions. This is observed for $pD > 4$, which is in agreement with previous results [81, 82]. Since the size–temperature measurements were performed at $pD = 4.5$, where the network is partially ionized, the deswelling transition becomes broader in temperature, consistent with previous results with charged gels [83, 84] and microgels [81, 82].

An alternative to temperature is to use hydrostatic pressure, P, to deswell the microgels, as shown in Figure 14.10c. In this case, it is the mixing between the polymer and the solvent that is modified as the hydrostatic pressure changes, resulting in the observed deswelling behavior [26]. Consistent with the results obtained with temperature, deswelling induced by hydrostatic pressure also results in a size change over a broad P-range.

14.3
Determining and Modeling the Particle Form Factor

To characterize the structural features of the microgel suspensions, we must first determine the form factor, $P(q)$. This is done by measuring the scattered intensity

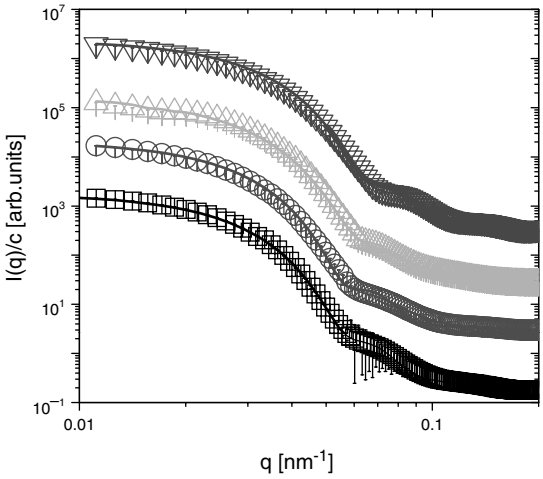

Figure 14.11 Experimental profiles for four different temperatures and their corresponding fits according to Equation 14.50. Open squares: $T = 25\,^{\circ}\mathrm{C}$ and $R_{av} = 83$ nm, $\sigma = 21$ nm, $\sigma_{pol} = 0.13$, $I_{chain}(0) = 2.0 \times 10^{-4}$, $\xi = 10.4$ nm; open circles $T = 27\,^{\circ}\mathrm{C}$ and $R_{av} = 82$ nm, $\sigma = 21$ nm, $\sigma_{pol} = 0.11$, $I_{chain}(0) = 9.0 \times 10^{-5}$, $\xi = 10.2$ nm; open triangles up: $T = 30\,^{\circ}\mathrm{C}$ and $R_{av} = 77$ nm, $\sigma = 23$ nm, $\sigma_{pol} = 0.13$, $I_{chain}(0) = 5.9 \times 10^{-4}$, $\xi = 9.8$ nm; open triangles down: $T = 35\,^{\circ}\mathrm{C}$ and $R_{av} = 73$ nm, $\sigma = 18$ nm, $\sigma_{pol} = 0.12$, $I_{chain}(0) = 1.3 \times 10^{-4}$, $\xi = 9.2$ nm. The data are vertically shifted by a factor of 10 with increasing temperature. Reproduced with permission of the American Institute of Physics.

of a dilute microgel suspension, since in this situation $S(q) \approx 1$. We find that the q-dependence of the scattered intensity is characterized by an initial decay at low q and by a shoulder at intermediate q, as shown in Figure 14.11 for different temperatures. At higher values of q, the intensity plateaus as a result of incoherent scattering resulting from the spin coupling between the neutrons and the hydrogen atoms in the sample. We find similar results at different hydrostatic pressures, as shown in Figure 14.12. With increasing pressure, the form factor shifts to higher q, consistent with particle deswelling. The presence of the shoulder observed in the intermediate q-region with temperature is, however, not as clear in this case due to the background scattering caused by the pressure cell and insufficient counting time.

The experimental profiles show the intrinsic structural richness of these particles. At high temperatures and pressures, the data agree well with the expectations for a polydisperse suspension of hard spheres with average size equal to the size measured by dynamic light scattering. In this case:

$$P_{HS,p}(q) = \int \mathrm{d}a D(a, \sigma_{\mathrm{pol}}) \left(\frac{3[\sin(qa) - q \cdot a \cdot \cos(qa)]}{(qa)^3} \right)^2 \tag{14.47}$$

where $D(a, \sigma_{\mathrm{pol}}) = \frac{1}{\sqrt{2\pi}\sigma_{pol} a_{av}} \exp\left[-(a - a_{av})^2 / (2\sigma_{pol}^2 a_{av}^2) \right]$, a_{av} is the average particle radius and σ_{pol} is the relative particle polydispersity, which in this case is ≈ 0.13. By contrast, at lower pressures or temperatures, the hard-sphere form factor is unable to

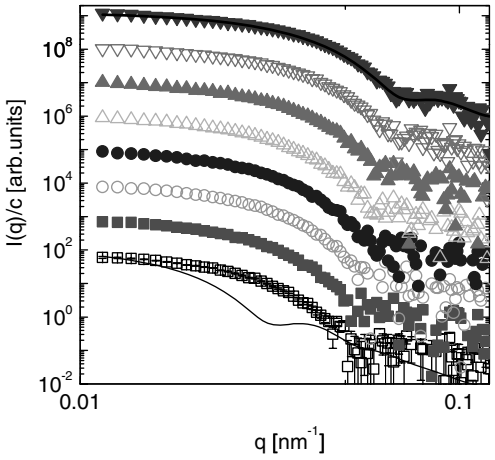

Figure 14.12 Experimental profiles for different hydrostatic pressure: Open squares: $P = 0$; filled squares: $P = 100$ MPa; open circles: P = 150 MPa; filled circles: $P = 175$ MPa; open triangles up: $P = 200$ MPa; filled triangles up: $P = 250$ MPa; open triangles down: $P = 300$ MPa; filled triangles down: $P = 350$ MPa. The data is vertically shifted by a factor of 10 with increasing hydrostatic pressure. The lines represent the expected form factor for hard spheres of average radius $R = 145$ nm (lower line) and $R = 70$ nm (upper line), and polydispersity $\sigma_{pol} = 12\%$. Data reproduced with permission of the American Institute of Physics.

describe the experimental results, as shown in Figure 14.12; this is the case irrespective of polydispersity. This highlights the intrinsic inhomogeneous structure of the particle in its swollen state, when the network is filled with water. A possible source for this inhomogeneous distribution of solid is an uneven distribution of the crosslink molecules inside the particles, which often decreases from the particle center towards its periphery [75, 85, 86]. Therefore, a more sophisticated model to describe the experimental results is needed. We use a model previously published by Stieger *et al.* [87–89] which considers the microgel as a hard-sphere core convoluted with a Gaussian to obtain a fuzzy polymer shell. In reciprocal space, the form factor is the product of the Fourier transforms of the hard-sphere core and the Gaussian shell [88]:

$$P_1(q) = \left[\frac{3(\sin qa - qa\cos qa)}{(qa)^3} e^{-[(\sigma q)^2/2]}\right]^2, \tag{14.48}$$

where a is now the radius of the core and σ the width of the fuzzy region. A similar version of this model was proposed by Pedersen to account for the scattering of block copolymer micelles [90]. In addition, the particle is further considered inhomogeneous at smaller length scales and an additional contribution to the form factor associated to internal chain correlations is incorporated [91]:

$$I_{chain}(q) = \frac{I_{chain}(0)}{1 + (\xi q)^2} \tag{14.49}$$

where $I_{chain}(0)$ is the intensity at zero q associated with this contribution and ξ is the mesh size of the network. This expression has been used to describe the structure of neutral gels [91] as well as the scattering of certain semi-dilute polyelectrolyte solutions [92]; thus, it can be considered as a reasonable approximation for the internal structure of our NIPAM–AA microgels. Finally, we incorporate polydispersity in the model. As a result:

$$P(q) = \int \mathrm{d}a D(a, \sigma_{pol}) P_1(q, a) + I_{chain}(q). \tag{14.50}$$

Using this model, we fit the experimental curves minimizing $\chi^2 = \sum_q [P_{exp}(q) - P(q)]^2$ [93], leaving a_{av}, σ_{pol}, σ, ξ, and $I_{chain}(0)$ as free parameters. The model successfully captures the different features of the experimental profiles, as shown in Figure 14.13 for $T = 25\,^{\circ}\mathrm{C}$ and $P = 0$. For this curve, we obtain $a_{av} = 83$ nm and $\sigma = 21$ nm, which gives a particle radius $a_{SANS} = a_{av} + 2\sigma = 124$ nm that is similar but slightly smaller than the particle size determined by DLS. The origin of this discrepancy is probably due to a very small number of peripheral chains, which contribute to the hydrodynamic radius but give a negligible contribution in the SANS experiment, thus rendering a_{DLS} slightly larger than a_{SANS} [87]. For the particle polydispersity we obtain $\sigma_{pol} = 0.12$ consistent with the result found for deswollen particles. However, the value for the mesh size, $\xi = 52$ nm, is unreasonably large given the particle size. This number can be estimated as the average distance between crosslink points:

$$\hat{\xi} = (N_p V_{1p} / N_{xlink})^{1/3} \tag{14.51}$$

where N_p is the number of particles, V_{1p} is the volume of one microgel, and N_{xlink} is the number of crosslink molecules. From the synthesis, we obtain $\hat{\xi} \approx 5$ nm, which is

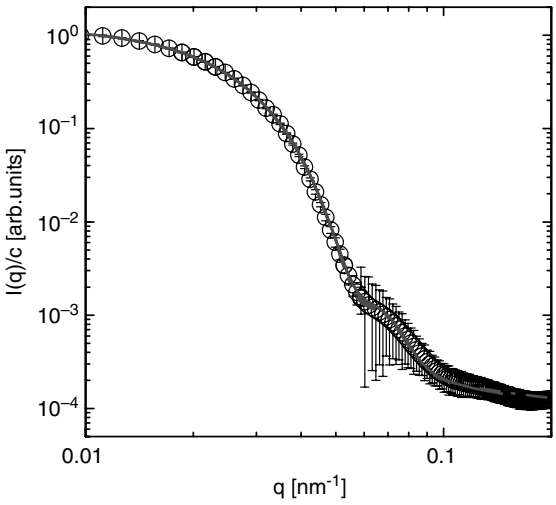

Figure 14.13 Intensity profile for $T = 25\,^{\circ}\mathrm{C}$ and $P = 0$. The two fits to the data are essentially identical. Reproduced with permission of the American Institute of Physics.

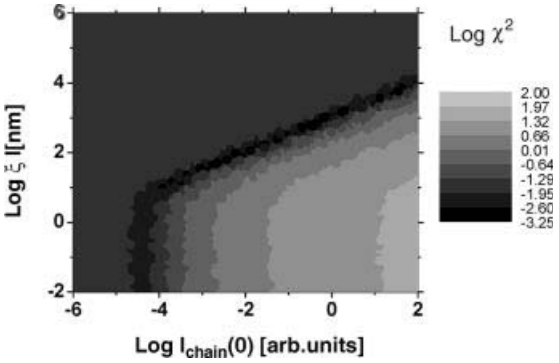

Figure 14.14 χ^2 as a function of $I_{chain}(0)$ and ξ for the sample at $T = 25\,^{\circ}C$ and $P = 0$. Reproduced with permission of the American Institute of Physics.

an order of magnitude smaller than the value that resulted from the fit. This disagreement can be traced back to the fitting procedure. In Figure 14.14, we plot the value of the statistical χ^2 parameter for different values of $I_{chain}(0)$ and ξ for constant values of the other free parameters. As shown by the figure, the selection of $I_{chain}(0)$ and ξ becomes degenerate since the parameter space contains many local minima of identical depth, which are shown as black points in Figure 14.14. Even if the value of χ^2 is similar for all of them, they correspond to very different values of $I_{chain}(0)$ and ξ. Sensible values can be obtained, however, if a careful spanning of the parameter space is achieved. To emphasize this, we show in Figure 14.13 two statistically equal fits with identical values of a_{av}, σ, and σ_{pol} but with $\xi = 10.4$ nm and $\xi = 52$ nm. Both fits are indistinguishable, but the lower value of the mesh size is in reasonable agreement with the expectations from the particle synthesis. Therefore, the selection of the best fit relies on both the value of χ^2 and on the known value of ξ. With these considerations in mind, we can fit the experimental data at other temperatures, as shown by the solid lines in Figure 14.11.

14.4
Structure Factor of Concentrated Suspensions

14.4.1
Phase Behavior

To characterize the state of our microgel suspensions, we use a generalized definition of volume fraction, $\zeta = nV_0$, where n is the particle number density and V_0 is the volume of the particles in dilute conditions. At low volume fractions, $\zeta = \phi$. However, ζ can be larger than 1 for sufficiently concentrated systems, reflecting the degree of particle interpenetration and/or compression at these high concentrations. We obtain ζ from the polymer concentration, c: $\zeta = kc$, where k is a proportionality constant determined from viscosity measurements [22]. We measure the viscosity, η,

in dilute samples at different concentrations and fit the data to the well-known Batchelor–Einstein equation [94]:

$$\frac{\eta}{\eta_0} = 1 + 2.5\zeta + 5.9\zeta^2 = 1 + 2.5(kc) + 5.9(kc)^2 \tag{14.52}$$

where η_0 is the viscosity of the solvent. We obtain $k = 24.2$ for our microgel suspensions.

There is a clear resemblance between the phase behavior of our system and that of hard spheres, for which the onset of crystallization occurs at $\phi = 0.495$ and the glass transition happens at $\phi = 0.58$ [95]. This is in close agreement with what we observe. Our samples are liquid for $\zeta < 0.484$ and form glasses for $\zeta > 0.638$, as shown in Figure 14.15. For volume fractions in between these ones, our suspensions exhibit clear signatures of crystal order: The samples Bragg diffract the incident white light and thus appear iridescent, as shown in Figure 14.16.

14.4.2
Analysis of the Structure Factor for Crystalline Samples

Visual inspection of the crystal samples indicates that the size of the crystals decreases as the volume fraction increases, as shown in Figure 14.16 and consistent with previous observations in hard-sphere suspensions [96]. This reflects that the increase in the particle concentration induces an increase of the nucleation rate, which further results in the formation of more, but smaller crystallites. We study the structure of the system using SANS and measure the scattered intensity, $I(q)$, as a function of the scattering wave vector (Figure 14.17a).

From $I(q)$ we obtain the structure factor of the system by normalizing with the model form factor described by Equation 14.50; we use the parameters obtained for $T = 25\,^{\circ}\mathrm{C}$ and $P = 0$, which correspond to the experimental conditions. Therefore, the structure factor is obtained as:

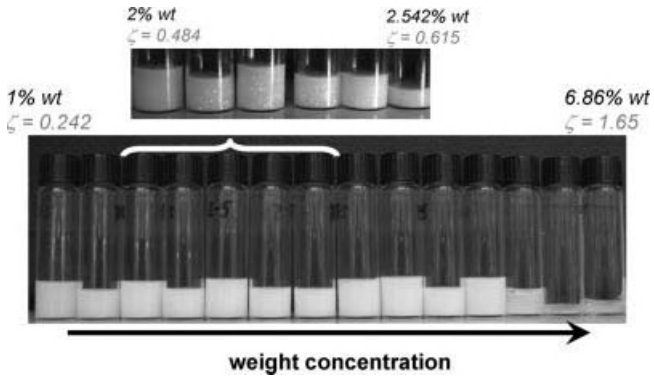

Figure 14.15 Phase behavior of the PNIPAM–AA system as a function of polymer concentration or generalized volume fraction, ζ. The samples with concentration above 2 wt% and below 2.542 wt% crystallize after some time, as shown by the upper series of images.

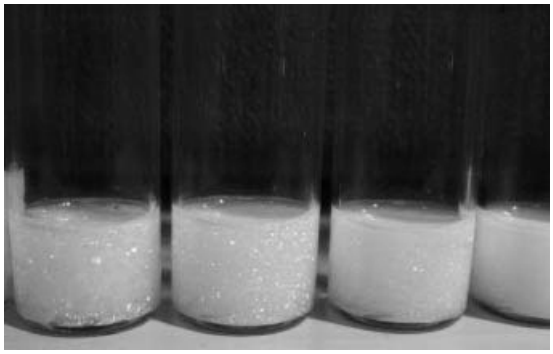

Figure 14.16 Close-up of several samples that form crystals. The volume fractions are, from left to right: $\zeta = 0.557$, $\zeta = 0.572$, $\zeta = 0.615$, and $\zeta = 0.638$. The size of the crystallites decreases with ζ.

$$S(q) = \frac{I(q)/c}{I(q)_{\text{dilute}}/c_{\text{dilute}}}. \tag{14.53}$$

where $I(q)_{\text{dilute}}$ is the best fit to the particle form factor, Equation 14.50, of the $I(q)$ data of a dilute sample at the experimental conditions of the concentrated sample. The calculation of $S(q)$ implicitly assumes that the form factor remains unaltered as the system is concentrated. The structure factor exhibits two distinctive peaks at all ζ, as shown in Figure 14.17b. As the sample shows Bragg reflections, a structure factor with sharp Bragg peaks is expected. The presence of two broad peaks can be attributed to the limited q-resolution of the SANS instrument, which results from the wavelength spread, $\Delta\lambda/\lambda = 0.1$, given by the neutron velocity selector and a smaller contribution due to the limited angular resolution of the detector. Therefore, in order

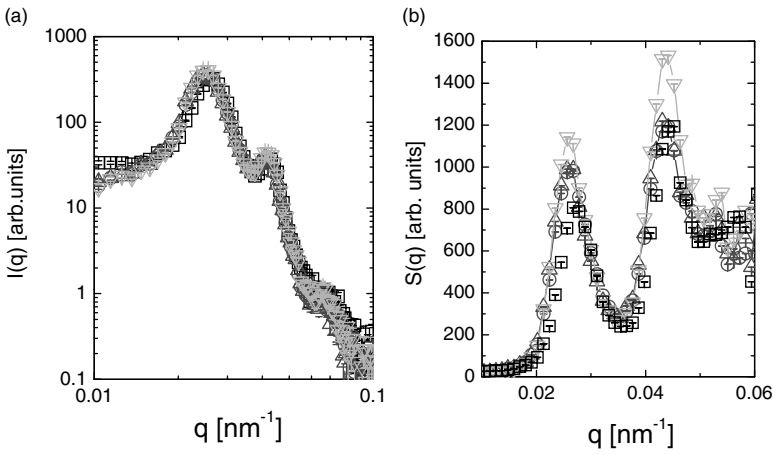

Figure 14.17 (a) Scattered intensity and (b) structure factor profiles for different crystalline samples: open triangle up: $\zeta = 0.516$, open circle: $\zeta = 0.547$, open triangle down: $\zeta = 0.558$, open square: $\zeta = 0.572$.

to perform a quantitative description of the data, we need to replace the structure factor of a polycrystal sample, which would exhibit sharp Bragg reflections at wave vectors fulfilling the Bragg condition, $q = q_{hkl}$, where q_{hkl} is the reciprocal lattice vector with Miller indexes (h, k, l), by a model that describes every Bragg peak as a Gaussian function, centered at q_{hkl} and whose width is determined by the q-resolution of the instrument $\Delta q/q \approx 0.1$ [52]. The structure factor then becomes:

$$S(q) = \sum_{(h,k,l)} \frac{1}{\sqrt{2\pi}\Delta q} e^{-\frac{(q-q_{hkl})^2}{2\Delta q^2}} \tag{14.54}$$

We then fit our experimental results to different crystalline lattices using Equation 14.54. The fit uses a single free parameter, the lattice constant $\bar{l}$, which we obtain by matching the position and height of the first peak in $S(q)$ to the experimental result. The rest of the curve follows thereafter without further adjustment. All fits very much describe the experimental results equally, as shown in Figure 14.18 for a particular sample at $\zeta = 0.574$. Perhaps, the fit to the BCC structure is the worst, as it predicts a narrower first peak than the other structures, failing to describe the experimental width. In any case, the limited resolution in q of the SANS instrument prevents the elucidation of the crystal structure [97].

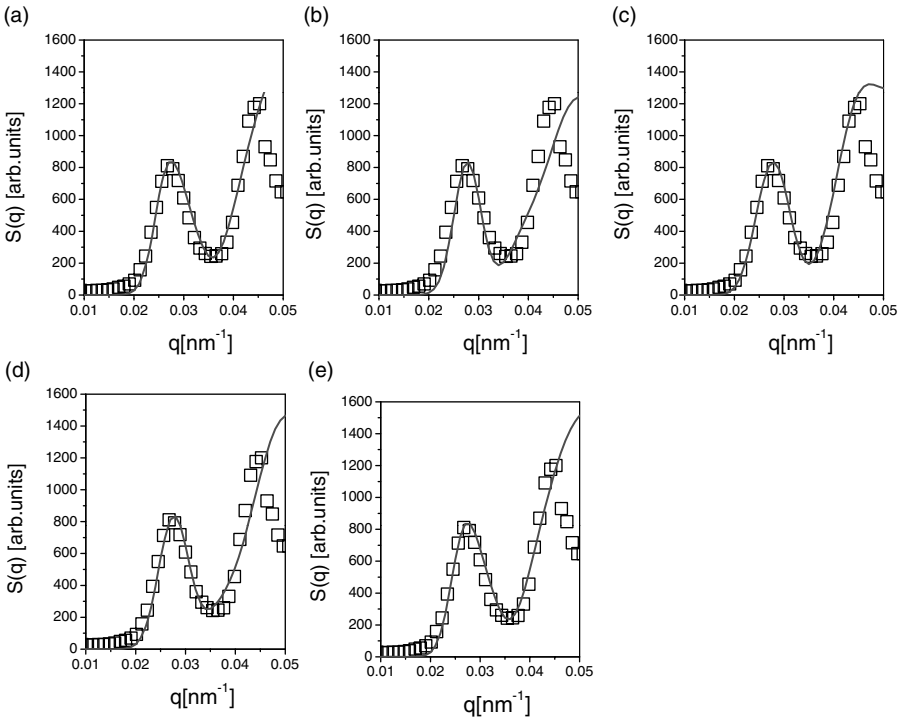

Figure 14.18 $S(q)$ for $\zeta = 0.574$ and corresponding fits to the (a) FCC, (b) BCC, (c) A15, (d) HCP, and (e) RHCP structures.

Table 14.1 Lattice constant, $\bar{l}$, obtained from the fits of the data at $\varsigma = 0.574$ to different structures and the the corresponding nearest neighbor distance, d.

	FCC	BCC	A15	HCP	RHCP
$\bar{l}$	410 nm	320 nm	520 nm	290 nm	290 nm
d	$= \frac{\bar{l}}{\sqrt{2}} = 290$ nm	$= \frac{\sqrt{3}\bar{l}}{2} = 277$ nm	$= \sqrt{\frac{5}{16}}\bar{l} = 290$ nm	$= \bar{l} = 290$ nm	$= \bar{l} = 290$ nm

FCC, face-centered cubic; BCC, body-centered cubic; HCP, hexagonal close-packed; RHCP, random hexagonal close-packed.

The values of $\bar{l}$ from the fits result in nearest-neighbor distances, d, that are in agreement with the particle diameter measured in dilute suspension, $2a = 285$ nm, as shown in Table 14.1. This suggests that particle deswelling does not take place in the range of volume fractions probed. In addition, this result emphasizes that the choice of form factor at these high ζ is reasonable. However, the high q region is not captured by our model $S(q)$, reflecting that some changes in the form factor at these high q might be happening at high ζ.

14.4.3 Tuning Polydispersity

The overall particle polydispersity obtained from the form factor fits was $\sigma_{pol} = 0.12$, which is larger than the usual 7% often reported as the upper limit for crystallization to occur in hard-sphere systems [58]. Since microgel particles are soft, it is possible that the suspension changes its overall polydispersity to allow the system to crystallize. Something similar has been recently reported for crystals of microgels doped with a small population of much larger microgels [54]. In this case, the larger particles deswell and become part of the crystal lattice formed by the smaller particles. In addition, it was also reported in the past that polydisperse suspensions of microgels where nevertheless able to form crystals [34]. These observations, as well as ours, suggest that it may be significant to explore the influence of particle polydispersity and account for it in the form factor used to obtain the suspension structure factor. We thus generate model form factors at $T = 25\,^{\circ}$C and $P = 0$, keeping all parameters constant except σ_{pol}. Using these form factors, we can obtain the experimental structure factors following the procedure we followed before. We can, then, compare the resulting $S(q)$ with the theoretical predictions of Equation 14.54. The high q region obtained in this way seems to better approach the theoretical expectations, particularly at high q, as shown in Figure 14.19. To quantify this, we calculate the χ^2-parameter:

$$\chi^2 = \sum_q [S_{\exp}(q) - S_{th}(q)]^2 \tag{14.55}$$

Remarkably, χ^2 changes with σ_{pol}. It has a minimum around 4–6% polydispersity, irrespective of the particular crystal structure considered, as shown in Figure 14.20. However, we are cautious in our judgment and simply conclude that

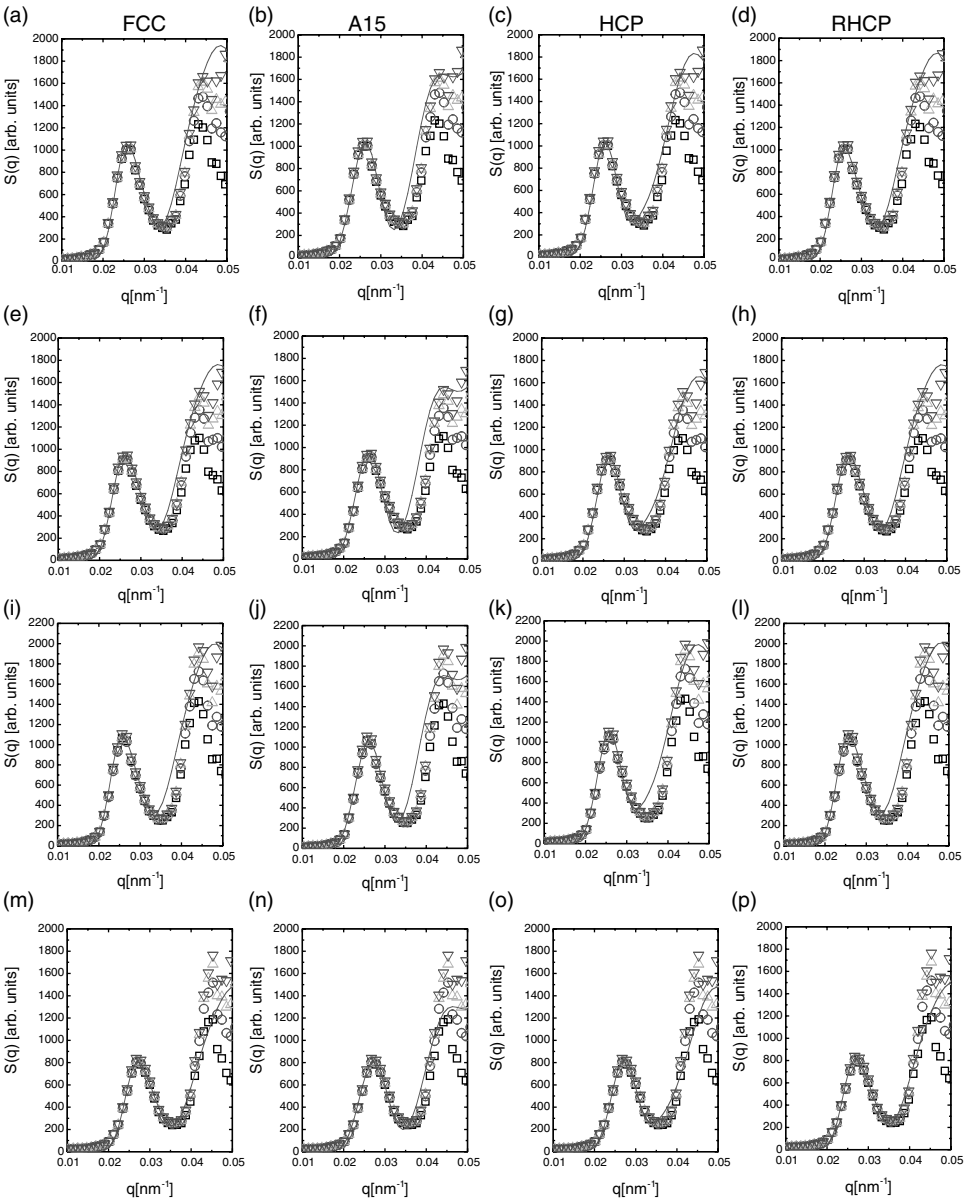

Figure 14.19 Influence of polydispersity in the particle form factor over the experimental structure factors of microgel suspensions at (a–d) $\zeta = 0.516$, (e–h) $\zeta = 0.558$, (i–l) $\zeta = 0.558$, and (m–p) $\zeta = 0.572$. The corresponding polydispersities in the form factor are: open squares: $\sigma_{pol} = 0.12$, open circles: $\sigma_{pol} = 0.08$, open triangles up: $\sigma_{pol} = 0.06$, and open triangles down: $\sigma_{pol} = 0.01$.

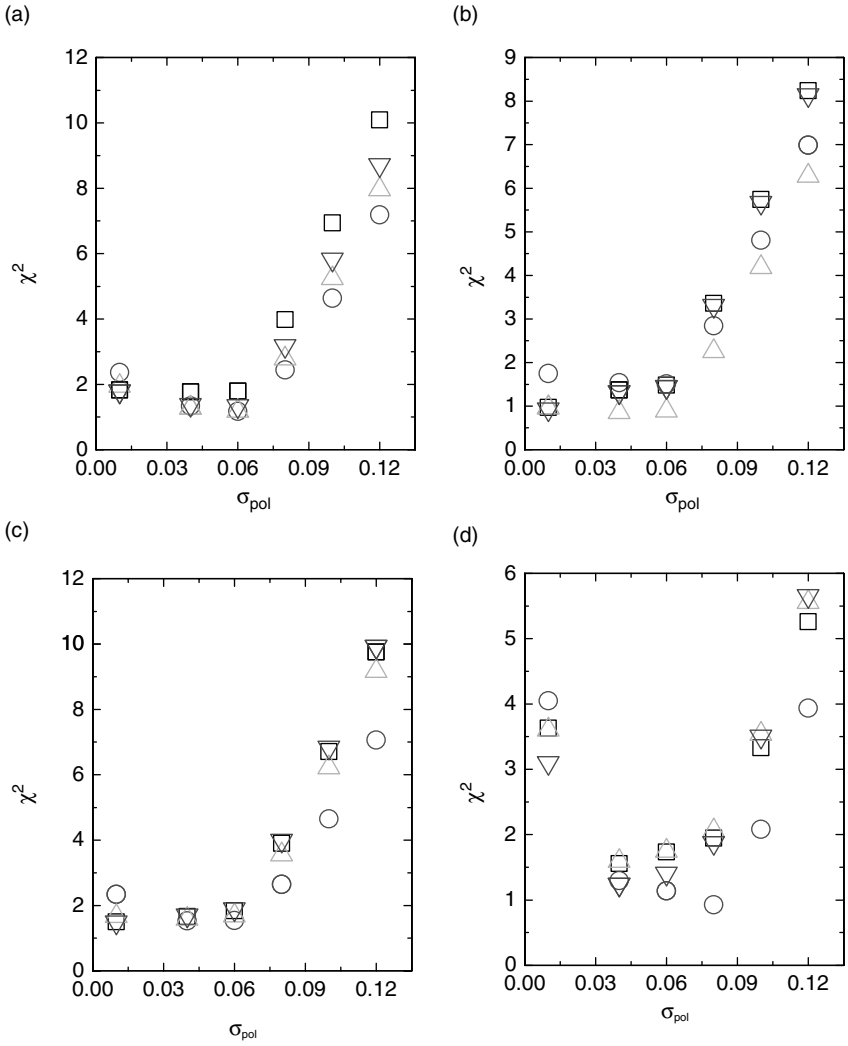

Figure 14.20 χ^2 parameter vs. σ_{pol} for (a) $\zeta = 0.516$, (b) $\zeta = 0.547$, (c) $\zeta = 0.558$, and (d) $\zeta = 0.572$. The symbols correspond to different crystal structures: open square: FCC, open circle: A15, open triangle up: HCP, open triangle down: RHCP.

our experimental results seem to point towards polydispersity changing as the system becomes more concentrated without an appreciable change in the average particle size. More detailed studies are needed, perhaps with small-angle X-ray scattering, which has a much better q-resolution than SANS, to support the interpretation of our results.

It is worth noting that a similar conclusion can be drawn when analyzing structure factors of concentrated microgel suspensions in a glassy state with

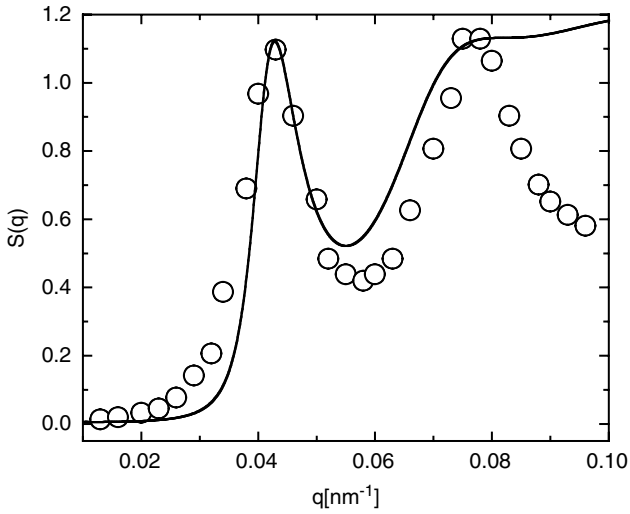

Figure 14.21 Experimental $S(q)$ of a glassy sample obtained by normalizing the scattered intensity by the form factor of a corresponding dilute suspension. The line is a fit to the theoretical $S(q)$ of polydisperse hard-sphere suspensions. The sample consists of microgels with radius $a = 84$ nm and is at a generalized volume fraction of $\zeta = 0.65$. The corresponding values of the parameters resulting from the fit are $\zeta = 0.71$, $a_{av} = 91$ nm, and a polydispersity of $\sigma_{pol} = 0.19$. Data reproduced with permission of the American Institute of Physics.

unusual characteristics [87], as shown in Figure 14.21 as an example; this $S(q)$ does not agree with the expectations for a system of monodisperse hard spheres. In the past, this has been sometimes attributed to the inability of the dilute form factor to correctly describe the concentrated form factor due to particle deswelling, which has been proposed to occur at volume fractions as low as $\phi \approx 0.3$ [87]. Based on our crystallization results, we propose an alternative interpretation consisting in attributing the unexpected shape of $S(q)$, with first and second liquid-like peaks of similar height, to polydispersity. We thus fit the experimental data to a polydisperse hard-sphere model [98]; the best fit is obtained for $\sigma_{pol} = 0.19$. The overall agreement between the model and the data is good; the model correctly captures the presence of the two peaks and the fact that the height of the second peak is similar to the height of the first peak. However, it fails to reproduce the decay of $S(q)$ at large q, as shown in Figure 14.21; this could very well reflect again that the high q region of the form factor does not accurately enough describe the internal structure of the microgels at these high ζ. The fit corresponds to a volume fraction $\zeta = 0.71$ and an average particle radius $a_{av} = 91$ nm, which should be compared with the values 0.65 and 84 nm provided for the data [87]. This comparison shows that polydispersity could indeed change at high ζ and play a role in the phase behavior and structural properties of microgel suspensions. In this case, in contrast to the analysis of our crystals, we consider polydispersity in $S(q)$ and not in $P(q)$.

14.5
Final Remarks and Future Directions

In this chapter we have presented experimental results on the crystallization of microgel particles studied by visual inspection, DLS, and SANS. In order to access the structural features of the suspension, we determined the particle form factor from measurements at various temperatures, T, and hydrostatic pressures, P. The obtained form factors, $P(q)$, reflect the structural richness of microgel particles. Whereas the form factor of the particles in their deswollen state can be approximately described using a hard-sphere model, the swollen state exhibits a completely different behavior. We model this by assuming an inhomogeneous distribution of polymer within the particle according to previous results for microgels and micelles. We obtain good agreement between the particle radius as determined by the model and the radius determined by independent dynamic light scattering measurements. From these studies, we obtain a suspension polydispersity $\sigma_{pol} = 12\%$.

With this model form factor, we determine the structure factor of the system by calculating the ratio between the scattered intensity in concentrated samples and the model $P(q)$. We explore the phase behavior of the system by visual inspection and observe that within a certain range of volume fractions, 0.484–0.635, the system crystallizes, as inferred from the Bragg reflections of the samples. We explore the structure factor of the crystalline samples and observe two distinctive peaks. In order to quantitatively describe the structure factor of the systems, we replace the expected sharp Bragg peaks by Gaussian-like peaks, where the width of the Gaussian is set equal to the q-resolution. We obtain a good description of the experimental $S(q)$ with different lattices although the particular structure cannot be elucidated due to the experimental uncertainty in q. Throughout the analysis, we assumed that the model form factor as obtained for dilute samples holds in a concentrated state. It is likely, however, that due to the soft character of the microgels there would be a disparity between the form factor in concentrated and dilute states. Indeed, we are observing crystallization for polydispersities beyond the maximum threshold required for crystallization in hard-sphere systems.

We hypothesize that the system crystallizes due to a polydispersity reduction. For hard spheres, crystallization is driven by the increase in entropy that results from the gain in free volume per particle. For soft, deformable objects, this entropy gain competes with the entropic penalty associated to changing the preferred equilibrium size of some microgels to reduce the suspension polydispersity. For sufficiently soft particles, this entropy penalty might be smaller than the entropy gained by crystallizing. As a result, these suspensions will change their polydispersity to allow the system to crystallize. We test this rationale by generating model form factors with reduced polydispersities and calculating the corresponding structure factors that we then compare with the theoretical ones. The general trend seems to show that the experimental curves and the theoretical ones better agree when the overall polydispersity of the suspension is reduced to 4–6%, as opposed to the original 12%. We also show the plausibility of our interpretation in other experimental systems in glassy, rather than crystal states.

This work demands more studies to fully and quantitatively address our proposal of polydispersity changes. The first question that needs to be addressed is the difference between the form factor in dilute and concentrated states. In order to access this, there are ongoing measurements with mixtures of hydrogenated and deuterated NIPAM. The idea is to render the deuterated NIPAM particles invisible from the neutron point of view and effectively measure the form factor of the hydrogenated NIPAM particles, even though from a structural point of view the system is concentrated.

This set of experiments will help us improve our description of the form factor in packed situations and, subsequently, our determination of the experimental structure factors. Furthermore, the role of the particle polydispersity and its change as the system is further concentrated needs to be explored. In the past, the description of the structural features of microgel suspensions has been done on the basis of hard-sphere behavior. Although, this has been proven successful in some occasions [49–52], we have increasing evidence that microgels can also behave differently from hard spheres [54–57]; at the origin of this difference is their softness, which affects their phase behavior in ways we do not yet fully understand.

Acknowledgment

This work was funded by the Petroleum Research Fund of the American Chemical Society (PRF 50603-DNI7), by the Ministerio de Ciencia y Tecnologia (DPI2008-06624-C03-03) and European Feder Funds, by the Swiss National Science Foundation (200021_132128) and the by National Science Foundation (DMR-0805089).

References

1 Pieranski, P. (1983) *Contemp. Phys.*, **24**, 25.
2 Hulteen, J.C., Treichel, D.A., Smith, M.T., Duval, M.L., Jensen, T.R., and Van Duyne, R.P. (1999) *J. Phys. Chem. B*, **103**, 3854.
3 Weissman, J.M., Sunkara, H.B., Tse, A.S., and Asher, S.A. (1996) *Science*, **274**, 959.
4 Pan, G.S., Kesavamoorthy, R., and Asher, S.A. (1997) *Phys. Rev. Lett.*, **78**, 3860.
5 Holtz, J.H. and Asher, S.A. (1997) *Nature*, **389**, 829.
6 Lyon, L.A., Hendrickson, G.R., Meng, Z., and Iyer, A.N.S. (2011) In *Microgel Suspensions* (eds A. Fernandez-Nieves, H. Wyss, J. Mattsson, and D.A. Weitz), Wiley-VCH Verlag GmbH, Weinheim.
7 Zahn, K. and Maret, G. (2000) *Phys. Rev. Lett.*, **85**, 3656.
8 Murray, C.A. and Grier, D.G. (1996) *Annu. Rev. Phys. Chem.*, **47**, 421.
9 Elliot, M.S. and Poon, W.C.K. (2001) *Adv. Colloid Interface Sci.*, **92**, 133.
10 Davidson., M.W. and Abramowitz, M. (2003) *Optical Microscopy*, Olympus America, New York.
11 van Blaaderen, A., Ruel, R., and Wiltzius, P. (1997) *Nature*, **385**, 321.
12 Gasser, U., Weeks, E.R., Schofield, A., Pusey, P.N., and Weitz, D.A. (2001) *Science*, **292**, 258.
13 Schall, P., Cohen, I., Weitz, D.A., and Spaepen, F. (2004) *Science*, **305**, 1944.
14 Ye., Y.H., LeBlanc, F., Hache, A., and Truong, V.V. (2001) *Appl. Phys. Lett.*, **78**, 52.
15 Hoogenboom, J.P., Derks, D., and van Blaaderen, A. (2002) *J. Chem. Phys.*, **117**, 11320.
16 Bausch, A.R., Bowick, M.J., Cacciuto, A., Dinsmore, A.D., Hsu, M.F., Nelson, D.R.,

Nikolaides, M.G., Travesset, A., and Weitz, D.A. (2003) *Science*, **299**, 1716.
17 Bubeck, R., Bechinger, C., Neser, S., and Leiderer, P. (1999) *Phys. Rev. Lett.*, **82**, 3364.
18 Zahn, K., Lenke, R., and Maret, G. (1999) *Phys. Rev. Lett.*, **82**, 2721.
19 Eisenmann, C., Keim, P., Gasser, U., and Maret, G. (2004) *J. Phys. Condens. Matter*, **16**, S4095.
20 Crowther, H.M. and Vincent, B. (1998) *Colloid Polym. Sci.*, **276**, 46.
21 Saunders, B.R. and Vincent, B. (1999) *Adv. Colloid Interface Sci.*, **80**, 1.
22 Senff, H. and Richtering, W. (1999) *J. Chem. Phys.*, **111**, 1705.
23 Pelton, R. (2000) *Adv. Colloid Interface Sci.*, **85**, 1.
24 Berndt, I. and Richtering, W. (2003) *Macromolecules*, **36**, 8780.
25 Ballauf, M. and Lu, Y. (2007) *Polymer*, **48**, 1815.
26 Lietor-Santos, J.J., Sierra-Martin, B., Vavrin, R., Hu, Z.B., Gasser, U., and Fernandez-Nieves, A. (2009) *Macromolecules*, **42**, 6225.
27 Gao, J. and Hu, Z.B. (2002) *Langmuir*, **18**, 1360.
28 Garcia, A., Marquez, M., Cai, T., Rosario, R. *et al.* (2007) *Langmuir*, **23**, 224.
29 Suzuki, D., McGrath, J.G., Kawaguchi, H., and Lyon, L.A. (2007) *J. Phys. Chem. C*, **111**, 5667.
30 Debord, J.D. and Lyon, L.A. (2000) *J. Phys. Chem. B*, **104**, 6327.
31 Reese, C.E., Mikhonin, A.V., Kamenjicki, M., Tikhonov, A., and Asher, S.A. (2004) *J. Am. Chem. Soc.*, **126**, 1493.
32 Zhang, J.G., Xu, S.Q., and Kumacheva, E. (2004) *J. Am. Chem. Soc.*, **126**, 7908.
33 Hellweg, T., Dewhurst, C.D., Bruckner, E., Kratz, K., and Eimer, W. (2000) *Colloid Polym. Sci.*, **278**, 972.
34 Debord, J.D., Eustis, S., Debord, S.B., Loyte, M.T., and Lyon, L.A. (2002) *Adv. Mater.*, **14**, 658.
35 Wu, J.Z., Zhou, B., and Hu, Z.B. (2003) *Phys. Rev. Lett.*, **90**, 048304.
36 Lyon, L.A., Debord, J.D., Debord, S.B., Jones, C.D., McGrath, J.G., and Serpe, M.J. (2004) *J. Phys. Chem. B*, **108**, 19099.
37 Alsayed, A.M., Islam, M.F., Zhang, J., Collings, P.J., and Yodh, A.G. (2005) *Science*, **309**, 1207.
38 Garcia, A., Marquez, M., Cai, T., Rosario, R., Hu, Z.B., Gust, D., Hayes, M., Vail, S.A., and Park, C.D. (2007) *Langmuir*, **23**, 224.
39 Suzuki, D., McGrath, J.G., Kawaguchi, H., and Lyon, L.A. (2007) *J. Phys. Chem. C*, **111**, 5667.
40 Huang, G. and Hu, Z.B. (2007) *Macromolecules*, **40**, 3749.
41 St John, A.N., Breedveld, V., and Lyon, L.A. (2007) *J. Phys. Chem. B*, **111**, 7796.
42 Wang, Y.L., Ming, G., Zheng, X.F., Tang, Q., and Gao, D.B. (2007) *Prog. Chem.*, **19**, 1475.
43 Clements, M., Pullela, S.R., Mejia, A.F., Shen, J., Gong, T., and Cheng, Z. (2008) *J. Colloid Interface Sci.*, **317**, 96.
44 Iacopini, S., Palberg, T., and Schoppe, H.J. (2009) *J. Chem. Phys.*, **130**, 084502.
45 Peng, Y., Wang, Z.R., Alsayed, A.M., Yodh, A.G., and Han, Y. (2010) *Phys. Rev. Lett.*, **104**, 205703.
46 Peng, Y., Wang, Z.R., Alsayed, A.M., Yodh, A.G., and Han, Y. (2011) *Phys. Rev. E*, **83**, 011404.
47 Quint, S.B. and Pacholski, C. (2011) *Soft Matter*, **7**, 3735.
48 Hu, Z.B. (2011) In *Microgel Suspensions* (eds A. Fernandez-Nieves, H. Wyss, J. Mattsson, and D.A. Weitz), Wiley-VCH Verlag GmbH, Weinheim.
49 Mohanty, P. and Richtering, W. (2008) *J. Phys. Chem. B*, **112**, 14692.
50 Purnomo, E.H., van den Ende, D., Vanapalli, S.A., and Mugele, F. (2008) *Phys. Rev. Lett.*, **101**, 238301.
51 Cloitre, M., Borrega, R., Monti, F., and Leibler, L. (2003) *Phys. Rev. Lett.*, **90**, 068303.
52 Gasser, U., Sierra-Martin, B., and Fernandez-Nieves, A. (2009) *Phys. Rev. E*, **79**, 051403.
53 Alsayed, A.M., Islam, M.F., Zhang, J., Collings, P.J., and Yodh, A.G. (2005) *Science*, **309**, 1207.
54 Iyer, A.S. and Lyon, L.A. (2009) *Angew. Chem. Int. Ed.*, **48**, 4562.
55 Meng, Z.Y., Cho, J.K., Debord, S., Breedveld, V., and Lyon, L.A. (2009) *J. Phys. Chem. B*, **111**, 6992.

56 Gottwald, D., Likos, C.N., and Kahl, G. (2004) *Phys. Rev. Lett.*, **92**, 068301.

57 Gottwald, D., Likos, C.N., and Kahl, G. (2005) *J. Chem. Phys.*, **122**, 074903.

58 Fasolo, M. and Sollich, P. (2003) *Phys. Rev. Lett.*, **91**, 068301.

59 Ashcroft, N.W. and Mermin, N.D. (1976) *Solid State Physics*, Thomson Learning, New York.

60 Kittel, C. (1996) *Introduction to Solid State Physics*, John Wiley & Sons, Inc., New York.

61 Sirota, E.B., Ouyang, H.D., Sinha, S.K., Chaikin, P.M., Axe, J.D., and Fujii, Y. (1989) *Phys. Rev. Lett.*, **62**, 1524.

62 Hendricks, S. and Teller, E. (1942) *J. Chem. Phys.*, **10**, 147.

63 Ackerson, B.J. *et al.* (1999) *Phys. Rev. E*, **59**, 6903.

64 Balagurusamy, S.K., Ungar, G., Percec, V., and Johansson, G. (1997) *J. Am. Chem. Soc.*, **119**, 1539.

65 Ziherl, P. and Kamien, R.D. (2000) *Phys. Rev. Lett.*, **85**, 3528.

66 Cagin, T., Wang, G., Martin, R., Zamanakos, G., Vaidehi, N., Mainz, D.T., and Goddard, W.A. III (2001) *Comput. Theor. Polym. Sci.*, **11**, 345.

67 Ziherl, P. and Kamien, R.D. (2001) *J. Phys. Chem. B*, **105**, 10147.

68 Higgins, J.S. and Benoit, H.C. (1996) *Polymers and Neutron Scattering*, Oxford Science Publications, New York.

69 Pethrick, R.A. and Dawkins, J.V. (eds) (1999) *Modern Techniques for Polymer Characterization*, John Wiley & Sons, Inc., New York.

70 Hobbie, R.K. (1962) *Am. J. Phys.*, **40**, 857.

71 Gasiorowicz, S. (1974) *Quantum Physics*, John Wiley & Sons, Inc., New York.

72 Squires, G.L. (1997) *Introduction to the Theory of Thermal Neutron Scattering*, Dover Publications, London.

73 Eskildsen, M.R., Gammel, P.L., Isaacs, E.D., Detlefs, C., Mortensen, K., and Bishop, D.J. (1998) *Nature (Lond.)*, **391**, 563.

74 Choi, S.M., Barker, J.G., Glinka, C.J., Cheng, Y.T., and Gammel, P.L. (2000) *Appl. Crystallogr.*, **33**, 793.

75 Wu, X., Pelton, R.H., Hamielec, A.E., Woods, D.R., and McPhee, W. (1994) *Colloid Polym. Sci.*, **272**, 467.

76 Lietor-Santos, J.J., Gasser, U., Vavrin, R., Hu, Z.B., and Fernandez-Nieves, A. (2010) *J. Chem. Phys.*, **133**, 034901.

77 Sierra-Martin, B., Choi, Y., Romero-Cano, M.S., Cosgrove, T., Vincent, B., and Fernandez-Barbero, A. (2005) *Macromolecules*, **38**, 10782.

78 McPhee, W., Tam, K.C., and Pelton, R.J. (1993) *J. Colloid Interface Sci.*, **156**, 24.

79 Varga, I., Gilanyi, T., Meszaros, R., Filipcsei, G., and Zrinyi, M. (2001) *J. Phys. Chem. B*, **105**, 9071.

80 Bradley, M., Ramos, J., and Vincent, B. (2005) *Langmuir*, **21**, 1209. 40, 1140, 2007.

81 Kratz, K., Hellweg, T., and Eimer, W. (2001) *Polymer*, **42**, 6631.

82 Snowden, M.J., Chowdhry, B.Z., Vincent, B., and Morris, G.E. (1996) *J. Chem. Soc. Faraday Trans.*, **92**, 5013.

83 Kawasaki, H., Sasaki, S., and Maeda, H.J. (1997) *J. Phys. Chem. B*, **101**, 4184.

84 Kawasaki, H., Sasaki, S., and Maeda, H.J. (1997) *J. Phys. Chem. B*, **101**, 5089.

85 Fernandez-Nieves, A., de las Nieves, F.J., and Fernandez-Barbero, A. (2004) *J. Chem. Phys.*, **120**, 374.

86 Mason, T.G. and Lin, M.Y. (2005) *Phys. Rev. E*, **71**, 040801.

87 Stieger, M., Pedersen, J.S., Linder, P., and Richtering, W. (2004) *Langmuir*, **20**, 7283.

88 Stieger, M., Richtering, W., Pedersen, J.S., and Linder, P. (2004) *J. Chem. Phys.*, **120**, 6197.

89 Richtering, W., Berndt, I., and Pedersen, J.S. (2011) In *Microgel Suspensions* (eds A. Fernandez-Nieves, H. Wyss, J. Mattsson, and D.A. Weitz), Wiley-VCH Verlag GmbH, Weinheim.

90 Pedersen, J.S., Svanenborg, C., Almdal, K., Hamley, I.W., and Young, R.N. (2003) *Macromolecules*, **36**, 416.

91 Shibayama, M., Tanaka, T., and Han, C.C. (1992) *J. Chem. Phys.*, **97**, 6829.

92 Prabhu, V.N., Muthukumar, M., Wignall, G.D., and Melnichenko, Y.B. (2001) *Polymer*, **42**, 8935.

93 Bulmer, M.G. (1979) *Principles of Statistic*, Dover Publications, New York.

94 Batchelor, G.K. (1977) *J. Fluid Mech.*, **87**, 97.

95 Pusey, P.N. and Van Megen, W. (1986) *Nature*, **320**, 340.

96 Harland, J.L. and Van Megen, W. (1997) *Phys. Rev. E*, **55**, 3054.

97 Dewhurst, C. (2008) *Meas. Sci. Technol.*, **19**, 1.

98 Ginoza, M. and Yasutomi, M. (1999) *J. Phys. Soc. Jpn*, **68**, 2292.

15
Dynamical Arrest and Crystallization in Dense Microgel Suspensions

Priti Mohanty, Divya Paloli, Jerome Crassous, and Peter Schurtenberger

15.1
Introduction

Colloidal suspensions have frequently been used as model systems to address phase transitions in condensed matter physics [1]. Their use as model atoms has been motivated primarily by the fact that the interaction between particles can be varied almost at will, quite in contrast to the situation when working with atomic or molecular systems. Moreover, the use of colloids also allows key physical properties, such as the static and dynamic structure factor or local lattice dynamics, to be investigated much more easily than in molecular systems. This is because the corresponding length and time scales are shifted by many orders of magnitude because of the much larger colloid size. Therefore, combinations of modern experimental techniques such as dynamic light scattering (DLS), X-ray photon correlation spectroscopy (XPCS), confocal laser scanning microscopy (CLSM), small-angle neutron scattering (SANS) and X-ray scattering (SAXS) enable colloid structure and dynamics to be monitored over a very broad range of length and time scales of many orders of magnitude [2–4].

In particular, CLSM has already made an enormous impact in this area [5–8]. Fast confocal scanners allow the observation of a small volume containing of the order of hundred particles in a colloidal suspension within short times of a few hundred milliseconds. This allows a time-resolved 3D reconstruction of the particle positions and thus gives access to particle dynamics with increasingly better time resolution thanks to high-speed cameras and significantly improved scanning techniques. CLSM thus provides quantitative information on quantities such as the pair-correlation function $g(r)$ and mean square displacement $\langle \Delta r^2(t) \rangle$. Moreover, the fact that CLSM provides information on particle dynamics on a single particle level has been instrumental investigating crystal nucleation and growth in 2D and 3D hard-sphere colloidal crystals. These studies have already resulted in unprecedented insights into nucleation, crystallization, and glass transition, topics that are not only relevant for a deeper understanding of soft matter in general, but crucial for many possible applications based on colloidal suspensions [9].

Hydrogel Micro and Nanoparticles, First Edition. Edited by L. Andrew Lyon and Michael Joseph Serpe.
© 2012 Wiley-VCH Verlag GmbH & Co. KGaA. Published 2012 by Wiley-VCH Verlag GmbH & Co. KGaA.

Initially, most of the investigations of self-assembly in colloids used relatively simple and well-defined model systems such as highly monodisperse spherical colloids interacting via hard-sphere-like or screened Coulomb (or Yukawa) repulsive interaction potentials [4]. However, the ability to control the colloidal interparticle interactions experimentally has recently begun to be extensively exploited [10]. The ability to create tunable interactions via external magnetic or electric fields or the fact that the addition of polymers induces an attraction with well-defined range and strength through the so-called "depletion effect" has resulted in a wealth of interesting data [3, 10–12]. A variety of intriguing phase transitions such as metastable fluid–fluid transitions in short-range attractive systems [3], crystal–crystal martensitic transitions in electrofluids [13], photonic crystals that are highly tunable in an external magnetic field [14], or a large variety of different binary crystal structures in mixtures of oppositely charged particles have been discussed [12].

The possibility of having not only passive control over interactions, but being able to actively tune them has important consequences not only for our ability to investigate phase transitions with colloids, but to design and create advanced materials whose functions and properties become switchable. It is here where microgel particles have added yet another degree of tunability that is extremely interesting in this context. Microgel particles are crosslinked polymeric structures based, for example, on poly(*N*-isopropylacrylamide) (PNIPAM) that can undergo reversible continuous or discontinuous volume transitions upon variations of external conditions such as temperature, pH, or ionic strength [15–18]. Moreover, the fact that soft microgels can become compressed and interpenetrate to a certain degree allows to create states with densities far above close packing, so-called squeezed states, with interesting structural and dynamic properties [19]. They have already been widely used as versatile model systems to investigate the phase behavior as a function of the nature and range of the interaction potential [20–25]. A number of studies using temperature-sensitive PNIPAM microgels at ultrahigh densities have clearly shown the existence of much richer phase behavior when compared to simple hard-sphere colloids [26, 27]. However, the exact nature of interaction potential between microgels and its dependence on volume fraction at high densities has not been unambiguously determined.

A particularly interesting class of microgels are ionic microgels, where charged groups are incorporated into neutral PNIPAM microgels. They exhibit multiresponsive properties with respect to pH, temperature, and ionic strength (Figure 15.1) [28–30]. With these particles it is possible to combine long-range electrostatic interactions with a high degree of particle softness and an ability to interpenetrate that opens up entirely new possibilities to create materials with extremely interesting structures and properties.

An important feature of these particles is that their interaction potential is strongly dependent upon the volume fraction and can be varied from soft long-range repulsive via a screened Coulomb electrostatic contribution at lower volume fractions to short-range soft repulsive through the steric repulsion between the partially interpenetrating particles at very high volume fractions (Figure 15.1). A model potential for ionic microgels has recently been derived which combines a long-range screened Coulomb

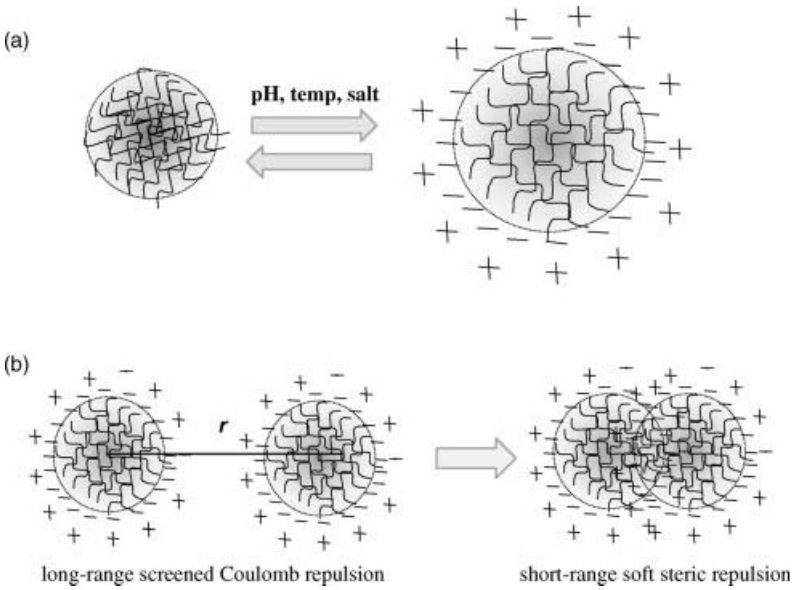

Figure 15.1 (a) Crosslinked microgel colloids undergo a reversible volume change with respect to parameters such as pH, temperature, and salt as illustrated by a schematic diagram. (b) Schematic description of the density-dependent interaction potential in ionic microgels that varies from soft long-range repulsive (screened Coulomb or Yukawa-like) at low densities and correspondingly large interparticle distances $r \gg 2R_h$ to short-range soft-repulsive at extremely high densities where $r \ll 2R_h$.

repulsion at longer distance and an ultrasoft counterion-dominated contribution above overlap [31]. These studies of charged soft particles indicated that at high concentrations and high charge densities a much more complex phase behavior with hexagonal, body-centered orthogonal, and trigonal crystalline structures accompanied by reentrant melting can be expected [31, 32]. However, there is currently a lack of systematic investigations with only a few qualitative experimental studies on this topic [33–35].

While the majority of previous studies have concentrated on the use of spherical colloids as model atoms, particles interacting via anisotropic interaction potentials have recently attracted an increasing amount of attention from the scientific community [36, 37]. The influence of anisotropic interactions in dipolar fluids has for example been investigated in numerous theoretical studies on the phase behavior of dipolar systems, recently reviewed by Teixeira *et al.* [38] and Huke and Lucke [39]. This recent focus on anisotropic interactions has been strongly motivated by attempts to copy nature's well-documented success in making regular structures such as virus capsids or photonic structures through the controlled self-assembly of biological molecules. It is clear that the design and fabrication of future materials and devices for photonics, molecular electronics, or drug delivery would enormously benefit if we were capable of self-assembling synthetic nanostructures with the precision and reliability found in biological self-assembly.

In this chapter, we will thus focus on the description and exploitation of the tunable interaction potential of neutral and ionic microgels. We will first describe the different available model systems and their intrinsic properties. We will then show how we can obtain quantitative information on the intrinsic short-range soft repulsion between neutral microgels and the resulting structural and dynamic properties of microgel suspensions at high and ultrahigh densities. Next we will demonstrate the possibilities of adding a long-range screened Coulomb repulsion, and how it influences the phase behavior of these systems. Finally, we show that we can utilize the high intrinsic polarizability of the ionic microgels in order to create strong and tunable dipolar interactions and investigate their influence on the self-assembly of microgels in the presence of an alternating electrical field (Figure 15.2).

15.2 Methods

All real-space studies were carried out on a Leica SP5 CLSM based on an inverted microscope (Leica DMI6000, Germany) using a fast resonance scanner (50 frames s^{-1} at 512×256 pixels). The fast resonance scanner allows us to track particles even at dilute concentrations. For the fluorescent studies, we use the green laser ($\lambda = 543$ nm) to excite the fluorescently labeled particle, and the emission wavelength is detected at 580 nm. Particular care is given to a well-controlled and stable sample temperature, and our confocal microscope is mounted in a thermostated enclosure which allows us to maintain the temperature with an accuracy of 0.2 degree. For our studies, we use a $63\times$ immersion objective (glycerol–water mixtures with a mixing ratio of 85:15) with a numerical aperture of 1.4.

The samples used for CLSM are prepared using either secure-seal imaging spacers (from Sigma-Aldrich) with a gap of 100 μm sandwiched between two cover glasses or

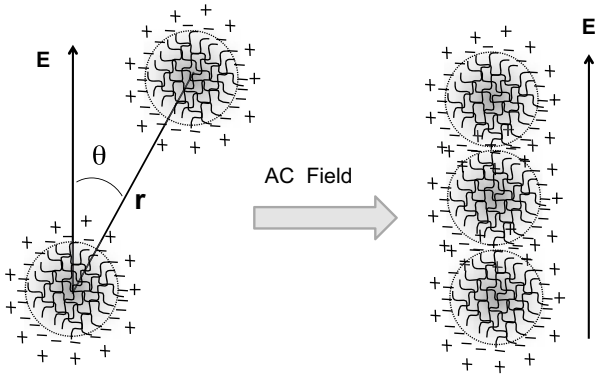

Figure 15.2 Schematic representation of electric field-induced dipole–dipole interactions between ionic microgels. Under the influence of an externally applied AC electric field, the particles experience an additional dipolar interaction that can for example lead to the formation of chains.

rectangular capillary tubes with an inner diameter of 0.1 × 2.0 mm (Vitrotubes Inc.). Crystallization studies and temperature- and time-dependent studies were made primarily using capillary tubes sealed with UV glue.

Very highly concentrated glassy samples were prepared by fast centrifugation of fluid samples. These highly concentrated glassy samples were first fluidized by heating them at temperatures around 28–29 °C and then loaded into the confocal cell.

All our measurements were carried out in bulk suspension far away from the cover glass in order to avoid wall and confinement effects. For dilute samples, we measured at a distance of 25 μm (≈35 times the particle diameter) away from the cover glass, and for the concentrated samples we measured 10 μm (≈14 times the particle diameter) from the cover glass in order to avoid multiple scattering.

Effective volume fractions were determined by measuring the particle number density n directly from extensive 3D scans with the CLSM, and then calculating the volume fraction using $\phi_{\mathrm{eff}} = n(4\pi/3)R_{\mathrm{h}}{}^3$, where R_{h} is the hydrodynamic radius determined by dynamic light scattering. For lower concentrations, volume fractions were estimated using the dilution factor with respect to the concentrated stock sample for which ϕ_{eff} had been determined using the CLSM.

Static light scattering (SLS) and dynamic light scattering (DLS) experiments were performed with a 3D LS goniometer system from LS Instruments (Switzerland) equipped with a 632.8 nm He–Ne laser with a maximum power of 20 mW. The 3D cross-correlation technique suppresses multiply scattered light, and thus allows for detecting scattered intensities and correlation functions which originate from singly scattered light only even for highly turbid suspensions. Suspensions were filled into 10 mm inner diameter cylindrical quartz glass tubes and placed in the temperature-controlled index-matching bath. The scattered light was detected within an angular range of 15° to 148°. In the 3D DLS instrument, the primary laser is split into two parallel beams, which are both focused into the same scattering volume within the sample cell. On the goniometer arm two optical fibers are placed exactly at the same q-vector relative to the incoming beams, and the scattered light is then detected by two avalanche photo diodes and processed by a flex correlator in cross-correlation mode. To correct for fluctuations in the primary laser intensity and calibrate the measured scattered intensity, a part of the incident laser is split off and detected separately by a power meter. Scattered intensities corrected for multiple scattering are then obtained following established procedures using the reduction in signal intercept as a measure of the degree of multiple scattering. For details of the 3D cross-correlation technique see ref.[40]. Apparent hydrodynamic radii R_{h} were determined from a second-order cumulant analysis of the cross-correlation functions.

Small-angle neutron scattering (SANS) experiments performed at the SANS I and SANS II facilities at the Swiss spallation neutron source, SINQ, Paul Scherrer Institute, Villigen, Switzerland. We used 1 mm Hellma quartz cells with a thermostated sample holder. Various combinations of wave length, sample-to-detector distance and collimation length were used to cover the required Q-range. The raw spectra were corrected for background from the solvent, sample cell, and electronic noise by conventional procedures. Furthermore, the 2D isotropic scattering spectra were corrected for detector efficiency by dividing with the incoherent

scattering spectra of pure water and azimuthally averaged. In the analysis of the data, the instrumental smearing was taken into account following the approach given in [41].

15.3 Synthesis and Responsive Properties

Different PNIPAM microgel particles were synthesized using free-radical precipitation polymerization and established recipes and procedures (see [18, 42] for details). NIPAM and BIS (*N,N′*-methylene-bis-acrylamide) were the monomer and crosslinker, respectively. Potassium persulfate (KPS) was used as the initiator to start the polymerization. For CLSM studies we prepared particles where we added the dye methacryloxyethyl thiocarbamoylrhodamine B (MRB) before the onset of polymerization in order to covalently label the microgels [43]. Charged and pH-sensitive microgels were synthesized by adding an ionic co-monomer such as acrylic acid or sulfonic acid [34].

Polymerization was typically performed in a 300 ml three-neck reactor immersed in a thermostated water bath and equipped with a reflux condenser, a N_2 or argon inlet and a thermometer. Initially, the required amounts of NIPAM and BIS were dissolved in water. This solution was then transferred into the reactor and purged with inert gas for 20–30 min. This mixture was then heated to 70 °C under N_2, and an aqueous solution of the initiator ($K_2S_2O_8$) was added to the above mixture in order to start the polymerization. The polymerization was stopped after 6 h to ensure complete conversion. The reaction mixture was slowly cooled to room temperature by overnight stirring, and the thus obtained dispersion was passed through a glass filter to remove the coagulum part. After the synthesis, the microgel suspension was purified by extensive dialysis using low conductivity ($<18\,\mu S$) water.

Generally, we adapted the size of the microgels according to the techniques used to probe the structural and dynamic properties of the suspensions. For scattering studies, we synthesized small microgel particles in the size range of 100–300 nm radius where we used the ionic surfactant sodium dodecyl sulfate in the synthesis. For real-space studies by means of CLSM, we synthesized large particles with radii around 350–500 nm without adding any surfactant. For fluorescence confocal microscopy studies, we used the dye MRB that can be covalently linked to the NIPAM monomer. For pH-responsive microgel, we have used acrylic acid (AA), where at high pH ($>pK_a$ of AA), the microgels are charged and accordingly exhibit a large degree of swelling. To further increase the charged density of the microgels, we have used a strong acid group such as sulfonic acid as a co-monomer. For all types of synthesized particles, the polydispersity is well below 5%.

The thermo- and pH-responsive properties of resulting microgels were then characterized using DLS on dilute samples. A typical temperature dependence of the average hydrodynamic radius R_h is shown in Figure 15.3a. At low temperature, water acts as a good solvent for the polymer and the microgel is fully swollen. At temperatures above 33 °C the solvent quality then changes and water now acts as a

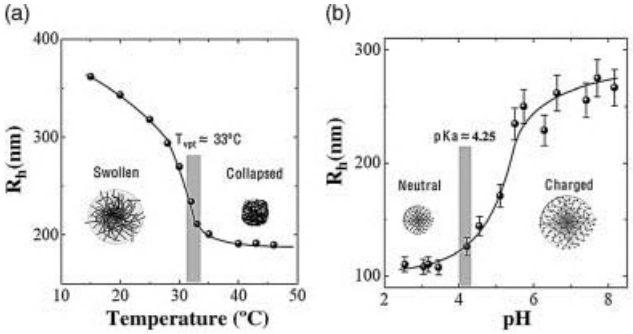

Figure 15.3 (a) Average hydrodynamic radius measured by DLS as a function of temperature for a thermoresponsive PNIPAM microgel with a crosslinking density of 5 mol%. The volume phase transition (VPT) occurs around the lower critical solution temperature (LCST) of PNIPAM at 33 °C. (b) Hydrodynamic radius as a function of increasing pH for a pH-responsive PNIPAM-*co*-PAA microgel at 1.55 mol% crosslinking density measured at a temperature $T = 25$ °C. At a pH below the pK_a (= 4.25) of the acidic group (COOH), the microgel behaves like a uncharged microgel, while for pH > pK_a, the microgel is charged and fully swollen.

poor solvent, leading to a complete collapse of the microgels at sufficiently high temperatures. For the given crosslink density of 5 mol%, we find a swelling ratio α defined as $\alpha = (R_h(20\,°C)/R_h(45\,°C))^3$ of 5.9.

Charged microgels based on weakly acidic monomer groups such as acrylic acid are particularly interesting model particles as this leads to an additional pH-responsiveness. Figure 15.3b shows the corresponding pH-dependence of the hydrodynamic radius for pH-responsive poly(*N*-isopropylacrylamide-*co*-acrylic acid) (PNIPAM-*co*-PAA) microgels with a crosslink density of 1.55 mol% synthesized using acrylic acid as a co-monomer [34]. For pH values below the pK_a (pK_a(AA) = 4.25), the AA groups are mostly undissociated and hence the microgel remains neutral, and for a given crosslink density its size is then determined by the temperature only. However, for pH > pK_a value, the AA groups starts dissociating and the microgel becomes charged. The swelling of the microgel is now dominated by two ionic contributions – a strong Coulomb repulsion between neighboring ionic groups that results in a rod-like conformation of the individual polymer chains, and the osmotic pressure of counter-ions. The data shown in Figure 15.3b reflect the low crosslink density of 1.55 mol%, which results in a much larger degree of swelling in its neutral state, that is, at pH < 4.25. At a pH = 3.1, we find $\alpha = 13.6$ compared to $\alpha = 5.9$ for a crosslink density of 5 mol%. This type of microgel is highly suitable for studying the phase behavior for particles interacting via ultrasoft potentials, as outlined below.

The charge density of the microgel also has a significant influence on the temperature-dependent swelling behavior. This is shown in Figure 15.4 for two different pH values in the charged state (above the pK_a of AA) and in the uncharged state (below the pK_a of AA), respectively. While at pH 3.1, where the majority of AA groups are protonated, the volume phase transition was observed around the lower critical solution temperature (LCST), 33 °C, we find that the volume phase transition

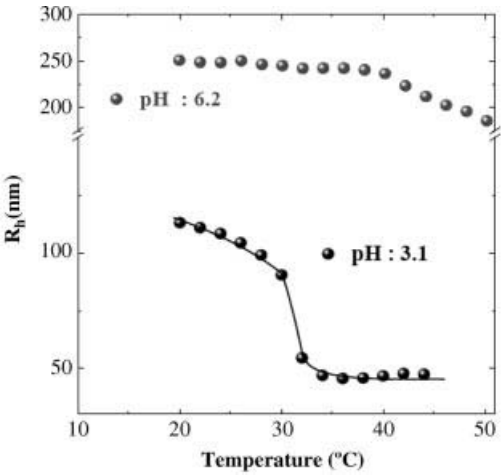

Figure 15.4 Hydrodynamic radius of a multiresponsive PNIPAM-*co*-PAA microgel with a crosslink density of 1.55 mol% measured as a function of temperature at two different pHs: in the charged state at pH = 6.2 and in the neutral state at pH = 3.1. The volume phase transition shifts towards higher temperatures for the charged case, while for the uncharged one VPT occurs around 33 °C, that is, similar to that of a pure thermoresponsive microgel shown in Figure 15.3a.

shifts towards higher temperatures for the strongly charged microgels. Moreover, the swelling behavior is now dominated by the ionic contributions, and while the overall size is much larger, the swelling ratio is reduced to $\alpha = 2.46$.

A key quantity in the investigation of the influence of the interaction potential on the phase behavior and the structural and dynamic properties of concentrated microgel suspensions is the number of charges per particle, as this will allow us to play with a combined and density-dependent interaction potential which will be dominated by the Yukawa-like soft repulsion at long distances (low densities) and the intrinsic (ultra)soft repulsion at and beyond overlap at short distances. We thus also estimated the total charges of a microgel due to the dissociation of its AA groups from titration and conductivity measurements [34]. Figure 15.5a,b show typical potentiometric and conductivity titration curves, respectively, for a weakly charged and weakly crosslinked microgel whose pH-dependent size has already been described in Figure 15.3b. The conductivity titration curve shows three distinct regimes. In regime I we see the effect of the neutralization of an excess of OH^- by H^+ ions. In regime II we observe the protonation of Na^+ counterions by H^+ ions. Finally, the rise in the conductivity in regime III is due to excess HCl. From the difference between the two neutralization points, we estimate the number of counter-ions present in the titrated microgel suspension, which results in about 10^4 dissociable charges per microgel particle.

While DLS allows us to characterize the temperature- and pH-dependence of the overall particle size, knowledge of the internal particle structure is of course essential when trying to understand the link between particle architecture, interaction

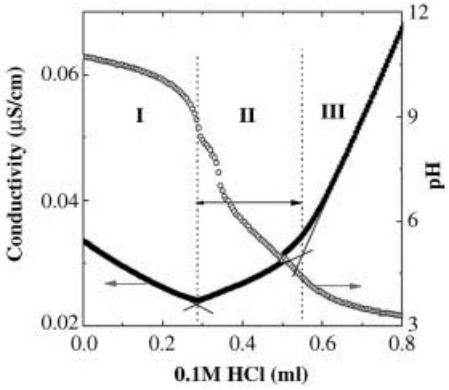

Figure 15.5 Results from potentiometric and conductivity titration measurements. The pH and the conductivity are measured as a function of increasing HCl concentration in a simultaneous potentiometric and conductivity titration, respectively. Before starting the titration with HCl, the microgels were completely deprotonated by adding 0.1 M NaOH until the pH of the solution reached pH = 11. Then titration with 0.1 M of HCl was performed. For details see [34].

potential and phase behavior. We thus also use SANS and SAXS experiments, which enables us to profit from the much higher spatial resolution of these techniques. Figure 15.6 shows two examples of SANS data obtained from a pH-responsive microgel at 1.55 mol% crosslinker measured at a temperature $T = 40\,^{\circ}\mathrm{C}$, that is, in the collapsed state, and at a temperature $T = 20\,^{\circ}\mathrm{C}$, that is, in the swollen state. The data shown in Figure 15.6 demonstrates the considerable effect that temperature has on the structure of the microgel.

In the analysis of the SANS data we can profit from the work of Stieger *et al.* [20], where the authors developed a model that takes into account the inhomogeneous nature of the microgels. A particle of radius R then consists of a dense core with high crosslinking density and a fuzzy shell with decreasing crosslink density. The radius of the high crosslink density core is given by $R-2\sigma_{\mathrm{shell}}$, where σ_{shell} describes the width of the fuzzy shell, and the overall particle size is given by $R_{\mathrm{SANS}} = R + 2\sigma_{\mathrm{shell}}$, which can directly be related to the average hydrodynamic radius R_{h} obtained by DLS [20]. We use an analogous approach where we also incorporate polydispersity using a Gaussian size distribution $D(R, \langle R\rangle, \sigma_{poly})$ characterized by an average radius $\langle R\rangle$ and a polydispersity σ_{poly}. The data are then analyzed using Equation 15.1:

$$I^{m}(Q) = n\Delta\varrho^{2}\int_{0}^{\infty}\int_{0}^{\infty} R(\langle Q\rangle, Q)D(R, \langle R\rangle, \sigma_{poly})V(R)^{2}P_{fuzzy}(Q, R)dRdQ + I_{fluct}(Q) + const_{back} \tag{15.1}$$

where $Q = (4\pi/\lambda)\sin\theta/2$ is the magnitude of the scattering vector, n is the number density of particles, $\Delta\varrho^{2}$ is their excess scattering length density, $V(R)$ is the volume of polymer in a particle with core radius R, $P_{\mathrm{fuzzy}}(Q,R)$ is the form factor of a microgel particle with radius R taking into account the core-fuzzy shell structure, $R_{res}(\langle Q\rangle, Q)$

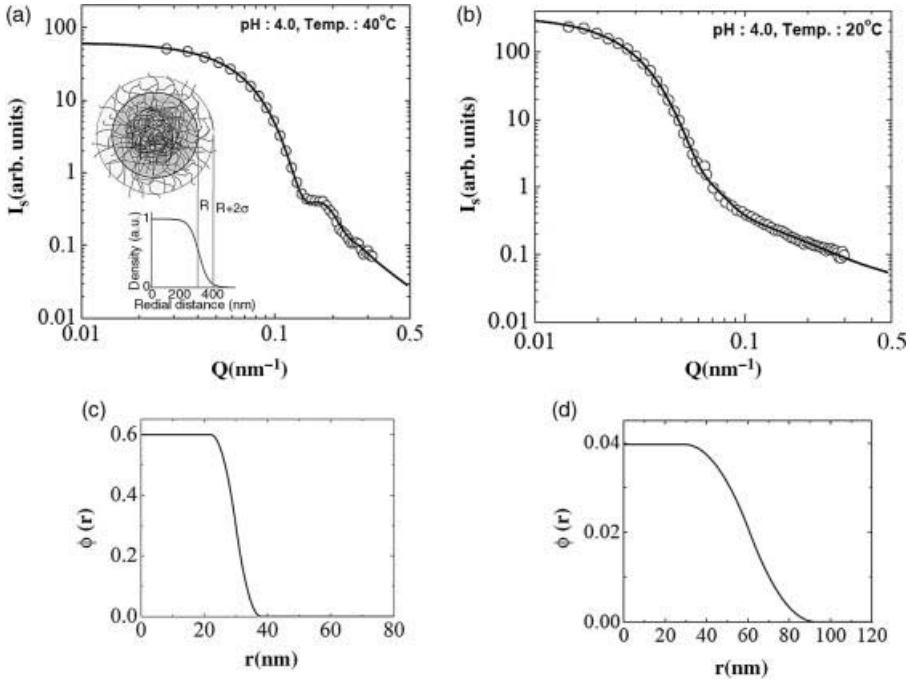

Figure 15.6 Scattering intensity, I_s vs. scattering vector Q measured by SANS for a pH-responsive PNIPAM-*co*-PAA microgel at 1.55 mol% crosslinker density and at a pH = 3.1 (a) measured at a temperature $T = 40\,^{\circ}\mathrm{C}$, that is, in the collapsed state, and at (b) measured at a temperature $T = 20\,^{\circ}\mathrm{C}$, that is, in the swollen state. The lines are the theoretical fits using the fuzzy sphere model (Equation 15.1) developed in [20]. Also shown as an inset in (a) is the underlying structural model used in the analysis of the data. The experimentally determined scattering length density profiles are shown in (c) for $T = 40\,^{\circ}\mathrm{C}$ and in (d) for $T = 20\,^{\circ}\mathrm{C}$, respectively.

describes the resolution function of the SANS instrument, $I_{\mathrm{fluct}}(Q)$ describes the scattering contributions arising from fluctuations of the microgel network and is represented by a Lorentzian function of the form $I_{\mathrm{fluct}}(Q) = I_{\mathrm{fluct}}(0)/(1 + \xi^2 Q^2)$, and $\mathrm{const}_{\mathrm{back}}$ is a constant background used to account for residual incoherent background.

A corresponding fit of the experimental data shown in Figure 15.6 thus allows for the determination of the amplitude of the form factor $P_{\mathrm{fuzzy}}(Q,R)$ and its relevant parameters R, σ_{shell} and σ_{poly}, and R_{SANS}. The parameters obtained from the data analysis are $R(40\,^{\circ}\mathrm{C}) = 30\,\mathrm{nm}$, $\sigma_{\mathrm{shell}}(40\,^{\circ}\mathrm{C}) = 4\,\mathrm{nm}$, and $R_{\mathrm{SANS}}(40\,^{\circ}\mathrm{C}) = 38\,\mathrm{nm}$ at $T = 40\,^{\circ}\mathrm{C}$, and $\mathrm{R}(20\,^{\circ}\mathrm{C}) = 61\,\mathrm{nm}$, $\sigma_{\mathrm{shell}}(20\,^{\circ}\mathrm{C}) = 16\,\mathrm{nm}$, and $R_{\mathrm{SANS}}(20\,^{\circ}\mathrm{C}) = 93\,\mathrm{nm}$ at $T = 20\,^{\circ}\mathrm{C}$, respectively. The data thus directly yield the strongly modified density profile from a clear core–shell structure with a fuzzy outer shell in the swollen state to a almost homogeneous sphere structure in the collapsed shell. The corresponding excess scattering length density profiles $\phi(r)$ are also shown in Figure 15.6. It is important to point out that R_{SANS} is the relevant length scale for determining the

effective volume fraction, the interaction potential and the resulting structural parameters such as the pair-correlation function $g(r)$ or the structure factor $S(Q)$ in the case of neutral microgels. We expect, however, that the drastically changed density profile as a function of temperature will have a significant effect on the interaction potential.

15.4
Structural and Dynamic Properties of Neutral Microgels

After having characterized the different particle types with respect to their responsive properties, overall sizes and particle structure, we next look at their phase behavior and the resulting structures in the various phases. First we concentrate on the behavior of suspensions from neutral microgels using a crosslink density of 5 mol%, that is, particles with swelling properties as shown in Figure 15.3a. As we want to directly visualize the samples in real space we use large and covalently labeled particles with an overall radius $R_h = 357$ nm as characterized by DLS at a temperature of $T = 15\,^{\circ}C$. Profiting from the fast resonant scanner of our CLSM, we can directly monitor the positional correlations between microgel particles at a low volume fraction of $\phi_{eff} = 0.06$. A single frame snapshot from such an experiment is shown in Figure 15.7a. Approximately 8000–10 000 frames were then used to determine the pair-correlation function $g(r)$ shown in Figure 15.7b. While $g(r)$ has been obtained from a large number of 2D frames without making any attempt to construct 3D

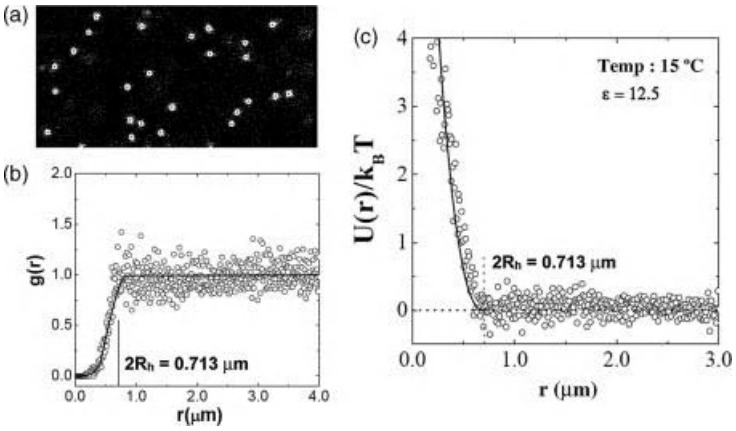

Figure 15.7 (a) Single-frame CLSM image of a dilute suspension of neutral and fluorescently labeled PNIPAM microgels with average radius $R_h = 357$ nm at an effective volume fraction of $\phi_{eff} = 0.06$. Particles in the plane of focus are marked by white circles. (b) Pair-correlation function $g(r)$ obtained from the CLSM images. About 8000–10 000 frames were used to determine $g(r)$. (c) The effective pair potential, $U(r)$ (in units of k_BT) obtained from the measured pair-correlation function. The particle diameter ($= 2R_h$ as obtained by DLS) of the microgel in the swollen state is shown as a vertical dotted line. Also shown as the solid line in (c) is the fit to a Hertzian potential given by Equation 15.2 with $\varepsilon = 12.5\ k_BT$ and $\sigma = 2R_h = 713$ nm.

images due to a lack of time resolution for these very low concentrations even with a fast resonant scanner, it is important to point out that bulk simulations have demonstrated that such an approach indeed yields the correct 3D $g(r)$ [45].

In general the pair-correlation function is related to the effective pair potential $U(r)$ via the Ornstein–Zernicke convolution integral equation, and a determination of $U(r)$ from $g(r)$ thus requires solving the convolution integral through the use of an appropriate closure relation [44]. However, under sufficiently dilute conditions we can use the so-called dilute gas approximation which directly relates $g(r)$ and $U(r)$ via the Boltzmann distribution as given in Equation 15.2 [45]

$$g(r) \approx \exp\left[-U(r)/k_B T\right] \tag{15.2}$$

The measured $g(r)$ shown in Figure 15.7b indeed demonstrates the absence of structural features, indicating a degree of positional correlation that resembles a dilute gas state. If we then use Equation 15.2, we can extract $U(r)$ as shown in Figure 15.7c. The resulting interaction potential between neutral microgels in the swollen state clearly demonstrates a significant degree of softness and strongly deviates from a hard-sphere potential. It is interesting to note that the repulsion sets in at contact given by the hydrodynamic diameter $d_h = 2R_h$ determined by DLS, and a significant degree of overlap is required before $U(r)$ reaches $1\,k_B T$. The distance at which $U(r) = 1\,k_B T$ is about $0.7d_h$, which corresponds to an overlap comparable to $2\sigma_{shell}/R_{SANS}$, that is, to a point where the radial density profile of the microgel has decreased to about 50% of its value in the core of the particle as determined from SANS for neutral particles with this crosslink density in the swollen state.

There has been a considerable interest in the interaction potential of neutral and charged microgels, primarily stirred by their ability to form solid-like phases at densities far above random closed packing. While the majority of the currently existing literature focuses on theoretical studies and indirect determinations based on various structural and dynamic data, there exist a few previous studies where CLSM-based direct measurements of $g(r)$ have been used to estimate $U(r)$. In contrast to our measurements, these authors used 2D conditions for pure PNIPAM microgels [46, 55] or quasi-2D conditions for core–shell PNIPAM microgels (polystyrene core and PNIPAM-*co*-PAA shell) [47]. Moreover, in these studies higher concentrations were used that resulted in stronger particle correlations that required the application of an approach based on the Ornstein–Zernicke integral equation scheme and an hypernetted chain (HNC) closure relationship. The thus obtained $U(r)$ were similar to the one obtained in the present study, although the potential appears to be less soft than in our case, with an effective interaction radius R_{eff} given by a value of $U(r) = 1\,k_B T$ which is about 10% smaller than the hydrodynamic radius. As the particles do not have identical composition such differences are not surprising, but the general trend clearly indicates that the potential may directly be related to the inhomogeneous particle structure that allows for interpenetration due to the fuzzy outer shell with its lower crosslink density and presence of dangling polymer chains.

Despite the considerable research effort devoted to crosslinked microgels and the fact that they have been proposed as models for soft colloids, the exact form of the effective interaction potential between them is still a matter of debate [48]. Various

model potentials such as an inverse power law [49], a Gaussian core [49], Hertzian [50, 51], harmonic [52] or based on polymer brush elasticity [27] have been considered. It is interesting to note that the measured potential in the dilute or gas-like state shown in Figure 15.7c can indeed be reproduced by a Hertzian model potential of the form

$$U(r) = \varepsilon(1-r/\sigma)^{2.5} \qquad r \leq \sigma \tag{15.3}$$

$$U(r) = 0 \qquad r > \sigma \tag{15.4}$$

where σ is the diameter of the particle and ε the strength of the repulsion, that is, it quantifies the softness of the particle. The fit of the experimental data to a Hertzian potential given by Equation 15.2 shown as the solid line in Figure 15.7c uses values of $\sigma = 713$ nm and $\varepsilon = 12.5\ k_BT$, respectively.

Having an explicit functional form for the potential that reasonably reproduces the measured $U(r)$, we can then try to establish an effective hard-sphere radius R_{eff} following the approach suggested by Barker and Henderson [53]

$$R_{eff} = \int_0^\infty [1-\exp(U(r)/k_BT)]dr \tag{15.5}$$

Using the potential shown in Figure 15.7c this leads to $R_{eff} = 270$ nm, which is close to the initial estimate $R_{eff}(1\ k_BT) = 250$ nm based on the distance between two particles that corresponds to a potential value of $U(r) = 1\ k_BT$.

A particularly important aspect of the interaction potential between microgel is its form at ultrahigh densities far above random closed packing, where we expect that the effective interaction radius as well as the overall size and shape of the microgels may change, and where no structural data exists to date. Here, the only information available is of indirect nature and comes either from neutron scattering measurements [54] or from rheological studies [18, 27]. However, the neutron scattering results available for example indicate that the concentration dependence of the scattering pattern can only be reproduced if the effective radius as a measure of the characteristic interparticle distance significantly decreases with increasing ϕ_{eff} [54].

It is thus clear that additional data on microgel interactions and interparticle correlations as well as on the size and shape of microgels at all densities will be required in order to arrive at a better understanding of $U(r)$. The data shown in Figure 15.7c represents only a starting point in our current attempt to systematically study positional correlations and microgel size and shape in suspensions at various effective volume fractions.

Having established the interaction potential between neutral microgels in the swollen state, we can next probe the structural ordering and the phase behavior of interacting suspensions at high effective volume fractions. A number of samples were prepared in range of volume fractions $0.3 \leq \phi_{eff} \leq 1.0$, that is, up to densities far above random closed packing. Typical confocal images of microgel suspension at different volume fractions are shown in Figure 15.8. We clearly see a transition from a liquid-like structure at the lowest $\phi_{eff} = 0.33$ to a crystalline structure (mixture of FCC

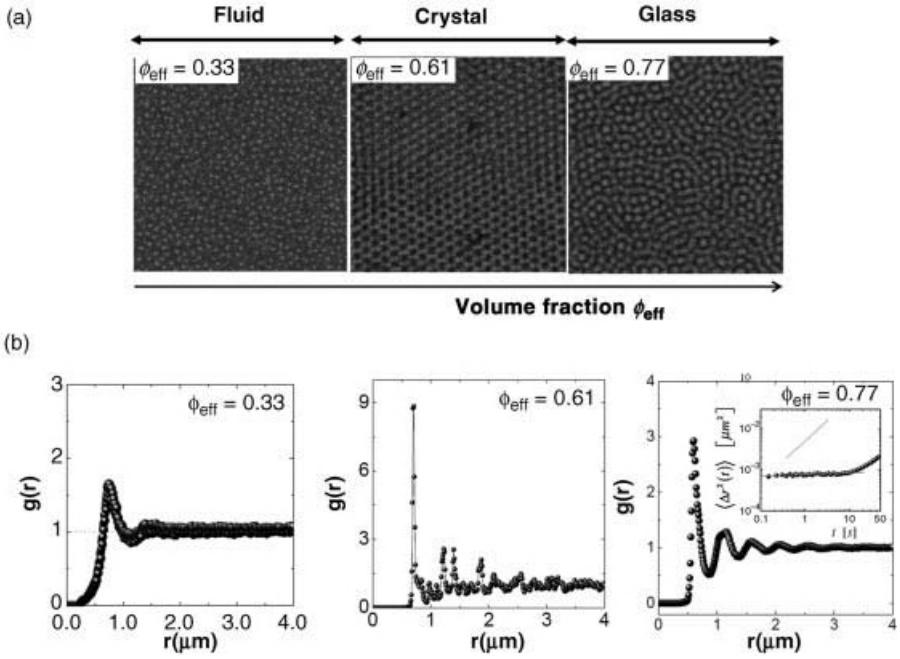

Figure 15.8 (a) Confocal images of rhodamine-labeled microgels in the swollen state at $T = 15\,^{\circ}C$ in the fluid ($\phi_{eff} = 0.33$), crystalline ($\phi_{eff} = 0.61$), and glassy state ($\phi_{eff} = 0.77$), respectively. (b) The calculated pair-correlation functions $g(r)$ from the confocal images obtained for the samples shown in (a) in the fluid (left), crystalline (middle), and glassy (right) state. The inset of the right figure shows the calculated mean square displacement $\langle \Delta r^2(t) \rangle$ (MSD) from time-series experiments where the particles are tracked in 3D. The MSD confirms that the microgel suspension at $\phi_{eff} = 0.77$ is in a glassy state.

and HCP) at $\phi_{eff} = 0.61$ and back to a disordered liquid-like structure, presumably a glass, at the highest $\phi_{eff} = 0.77$. The freezing transition is found to occur around a $\phi_{eff} \approx 0.5$, comparable to the value found for hard spheres.

From the images we then reconstruct the positional correlations of the particles in 3D and calculate the corresponding $g(r)$ values at different volume fractions using a large number of individual frames. The resulting $g(r)$ for the different states are shown in Figure 15.8. At volume fractions $\phi_{eff} < 0.5$, the measured $g(r)$ shows a pronounced first peak as a clear signature of a liquid-like state. However, the shape of $g(r)$ changes dramatically once the effective volume fraction is above the freezing line and crystallization sets in. This is demonstrated for a sample at $\phi_{eff} = 0.61$ in Figure 15.8. At even higher volume fractions, the suspension is once again found to show disordered or liquid-like structure as can be seen for the sample at $\phi_{eff} = 0.77$. Moreover, we can confirm that this sample is a colloidal glass by measuring the time dependence of the average mean square displacement placement $<\Delta r^2(t)>$ (MSD) (inset in the right hand panel of Figure 15.8b). It is interesting to look at the corresponding $g(r)$, which exhibits a pronounced first and second order peak as well as weak higher order peaks. The clearly visible distortions in the second order

peak of $g(r)$ are often considered as a signature for a glass-like ordering, and are also seen in colloidal as well as in atomic systems [6, 56, 57]. However, the amplitude g_{max} of the first peak in $g(r)$ is much lower than what would be expected for a hard-sphere fluid or glass (which could not of course exceed values of approximately 0.74 in this case) [58]. This clearly demonstrates the influence of the softness of the potential (see also [59] for soft spheres), which becomes even more obvious when going to effective volume fractions far above random close packing.

We also performed experiments where we suppressed crystallization by rapidly quenching the microgel suspensions to high densities using centrifugation. Figure 15.9a shows the resulting $g(r)$ values at very high densities $0.77 \leq \phi_{eff} \leq 0.97$. From this figure, two observations provide further direct experimental evidence for the soft-repulsive nature of the microgel interaction potential: (i) While below random closed packing ϕ_{rcp} the position of the first peak of $g(r)$ remains almost constant, it decreases with increasing ϕ_{eff} and follows a power law of the form $\phi_{eff}^{-1/3}$ in the high density regime (see Figure 15.9B). This indicates that the average interparticle separation distance a_s is determined not by the particle size as in the case of hard spheres, but by the number density only as it is the case for example in strongly correlated ionic colloids at low ionic strength. (ii) While in the fluid regime ($\phi_{eff} < \phi_{rcp}$) the height of the first peak, g_{max}, increases with increasing volume fraction, reflecting the increase in positional correlations, g_{max} starts to decrease again in the overlap regime ($\phi_{eff} > \phi_{rcp}$) as shown in Figure 15.10. This anomalous behavior of $g(r)$ is another result of the softness of the particles and has already been discussed previously in theoretical investigations of soft-repulsive colloids [59]. In low-volume fractions, the system has considerable available configurational space and thus behaves similar to hard spheres as it can easily minimize its free energy by avoiding energetically costly particle overlaps. However, at higher volume fractions ($\phi_{eff} > \phi_{rcp}$), it becomes more and more difficult entropically to find configurations with no overlap and to minimize the free energy. Hence to effectively create more space, the microgel particles can either shrink or interpenetrate and thus create a

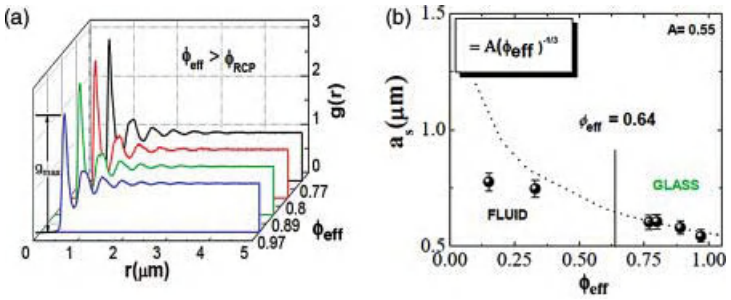

Figure 15.9 (a) The measured pair-correlation functions $g(r)$ in highly concentrated microgel suspensions, where $\phi_{eff} \gg \phi_{rcp} = 0.63$ is much larger than random closed packing ϕ_{rcp} in the swollen state at $T = 15\,^{\circ}C$. (b) The average interparticle separation distance a_s as given by the position of the first peak of $g(r)$ as a function of ϕ_{eff}. The dotted line corresponds to $\phi_{eff}^{-1/3}$, that is, an estimate of the average distance given by the number density only.

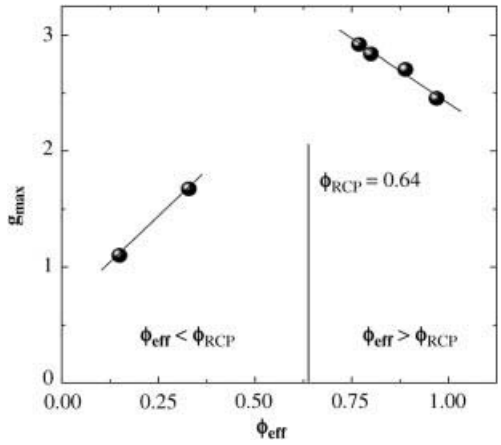

Figure 15.10 The height of the measured pair-correlation functions at the position of the first maximum g_{max} as a function of the effective volume fraction ϕ_{eff} for microgels with a crosslink density 5 mol% in the swollen state at $T = 15\,^{\circ}C$.

larger number of accessible configurations. This leads to a loss of positional correlation that is reflected in the decrease of the peak height g_{max} and also in peak width, which we clearly see in our experimentally measured $g(r)$ values. A recent theoretical study has, in fact, demonstrated this behavior for particles interacting via a Hertzian potential, and has even indicated the possibility for a reentrant fluid–glass transition, although at significantly softer potentials than what we believe to have for the particles used to generate the data shown in Figure 15.9 [59].

In this context it is also interesting to look at the position of the freezing line. While we currently have no precise value for the particles used here, we estimate that it is located around $\phi_{eff} \sim 0.5$, that is, close to the corresponding value for hard spheres. For the chosen crosslink density of 5 mol%, the potential thus seems to be soft enough to significantly alter the positional correlations in the glassy state at high and ultrahigh densities, but it does not yet seem to strongly modify the freezing line, quite in contrast to what has been observed for particles with much lower crosslink densities [18].

Having seen the importance of particle softness on the phase behavior and the structural properties of concentrated microgel suspensions, we extended our studies to softer particles with a lower crosslink density of 2.85 mol%. Theoretical studies of soft-repulsive systems based on an inverse power law or Gaussian core potential have predicted an extremely rich phase behavior [49]. With increasing density, freezing of a disordered fluid to a stable FCC and then to a BCC phase at intermediate density have been predicted. At very high concentrations, the theory then predicts a reentrant fluid transition. Recently, the phase diagram of soft-repulsive colloids based on Hertzian [51] and Harmonic [52] potentials have also predicted a variety of different crystal structures such as BCC, SC, BCT, and diamond-like in addition to the usual FCC and HCP structures which are commonly found for hard-sphere colloids. However, so far experimental verifications of these theoretical predictions are

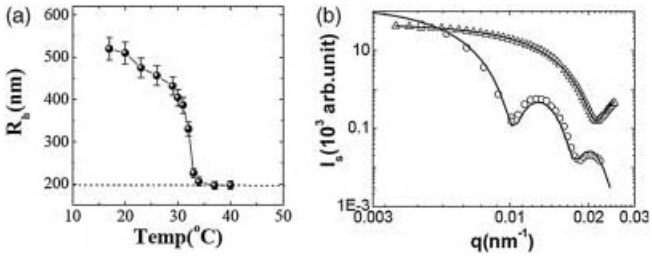

Figure 15.11 Structural properties of thermoresponsive PNIPAM microgels with a crosslinking density of 2.85 mol%. (a) Average hydrodynamic radius measured by DLS as a function of temperature. (b) Static light scattering data for two different temperatures $T = 15\,^{\circ}C$ (circles) in the swollen and $T = 40\,^{\circ}C$ (triangles) in the collapsed state. The lines are the corresponding fits to the data using a fuzzy sphere model.

missing. Here we thus concentrate on a discussion of the extent of the ordered phase and the underlying crystal structures found for these samples.

The responsive properties of the PNIPAM microgels with a crosslink density of 2.85 mol% were first characterized using static and dynamic light scattering. The temperature-dependent hydrodynamic radius of the microgels obtained from DLS is shown in Figure 15.11a. At this low crosslink density, the swelling ratio $\alpha = (R_h(20\,^{\circ}C)/R_h(45\,^{\circ}C))^3$ increases to 24. SLS experiments performed at two temperatures in the swollen and collapsed state, respectively, also demonstrate the enormous structural changes that go along with temperature for these more weakly crosslinked samples (Figure 15.11b).

We next investigated crystallization and glass formation using either slow and sequential increase of the effective volume fraction through controlled evaporation or sudden compression using high speed centrifugation, respectively. For the crystallization studies, we profit from the fact that these soft and thermoresponsive particles form stable crystalline phases over a large range of effective volume fractions that can easily be annealed at higher temperatures. All crystalline samples were thus annealed in order to make them defect free and monocrystalline as shown in Figure 15.12 for a selected example.

A number of samples at increasingly larger volume fractions in the range of $0.6 \leq \phi_{\mathrm{eff}} \leq 3.2$ were then prepared. Visual inspection of the samples after a sufficient equilibration time already indicates the existence of crystalline order in most of the samples due to the strongly iridescent colors caused by the Bragg diffraction of visible light as shown in Figure 15.13. Unfortunately, the fluorescently labeled microgels at this crosslinking density do not possess sufficient contrast to allow CLSM measurements at lower volume fractions in the dilute gas or fluid state, and we can thus neither produce a direct measurement of the interaction potential nor measure pair-correlation functions in the fluid state. It is only at high ϕ_{eff} that we can produce images of sufficient quality to calculate $g(r)$ in the brightfield mode of the microscope. Typical examples of pair-correlation functions thus obtained, together with the raw 2D images and the corresponding Fourier transformed diffraction pattern are shown in Figure 15.14a–g.

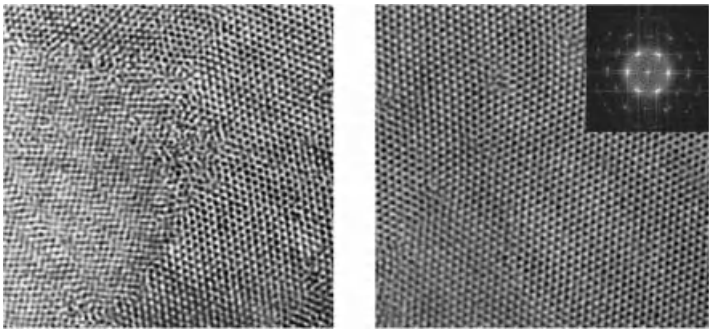

Figure 15.12 Temperature-induced annealing of a weakly crosslinked microgel sample at $\phi_{\text{eff}} = 0.71$. (Left) Confocal image of the initial microgel crystal before annealing. (Right) Confocal image of the microgel crystal after annealing for 2 days at 30 °C. The corresponding Fourier transformed diffractogram is shown as an inset.

Figure 15.14a,b shows the corresponding patterns for a sample at $\phi_{\text{eff}} = 0.71$ first after having shear molten the sample, and then again after letting it crystallize and having temperature-annealed it. In the shear molten fluid state, $g(r)$ exhibits fluid-like ordering, although the degree of correlation given by the value $g_{\max}$ at the first peak is significantly below what one would expect to find for a sample that is in the crystalline domain of the phase diagram. This changes dramatically after crystallization, and we now observe a typical $g(r)$ for a crystalline sample, and the crystalline order is also clearly visible from the 2D image and its Fourier transform. A closer look at the actual structure from a 3D reconstructed image reveals that the crystal structure is a mixture of FCC and HCP (Figure 15.15), similar to what has been found elsewhere [60]. When gradually increasing the concentration, we observe the formation of an ordered crystalline phase up to very high values of $\phi_{\text{eff}} = 2.23$. The resulting $g(r)$ values and diffraction patterns clearly indicate that the crystal structure remains unchanged. When quenching the sample to an even higher volume fraction $\phi_{\text{eff}} = 3.2$, no crystallization is observed even after prolonged equilibration, and the resulting $g(r)$ shows a fluid-like or amorphous structure (Figure 15.14g). The proposed fluid–crystal–glass sequence of the samples shown in Figure 15.14 is also supported

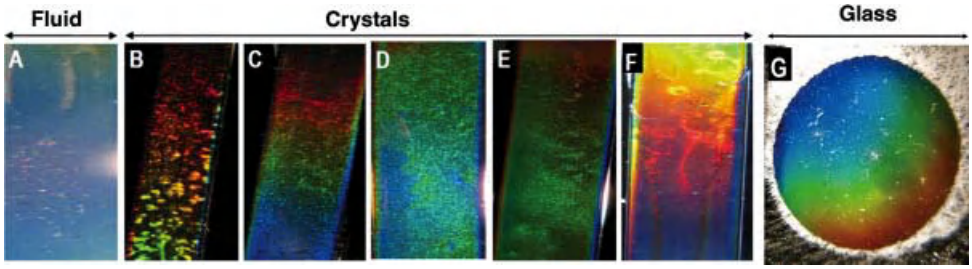

Figure 15.13 Digital photographs of microgel dispersions at different effective volume fractions ϕ_{eff}: (a) 0.6, (b) 0.71, (c) 0.837, (d) 0987, (e) 1.7, (f) 2.23, (g) 3.2.

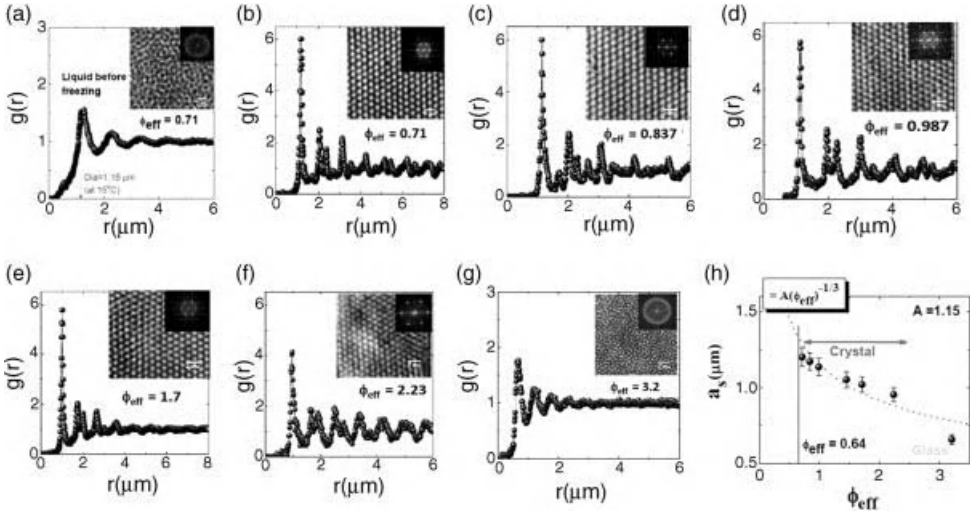

Figure 15.14 Pair-correlation function $g(r)$ at different ϕ_{eff} in fluid, crystal and glass states at $T = 15\,^{\circ}C$: (a) $\phi_{eff} = 0.71$ in a shear molten metastable fluid before freezing, (b) 0.71 in annealed crystal state, (c) 0.837, (d) 0.987, (e) 1.7, (f) 2.23, (g) 3.2. The raw 2D images and the corresponding fast Fourier transforms (FFTs) are shown as an inset. (h) Characteristic interparticle distance a_s calculated from the first peak position of $g(r)$ versus ϕ_{eff}. The dotted line corresponds to $\phi_{eff}^{-1/3}$.

through measurements of the particle mean square displacements shown in Figure 15.16.

It is interesting to note that no signs of dynamical arrest can be observed for the shear molten samples, and that only the sample at the highest volume fraction shows glassy behavior, while all other samples eventually crystallize. We observe

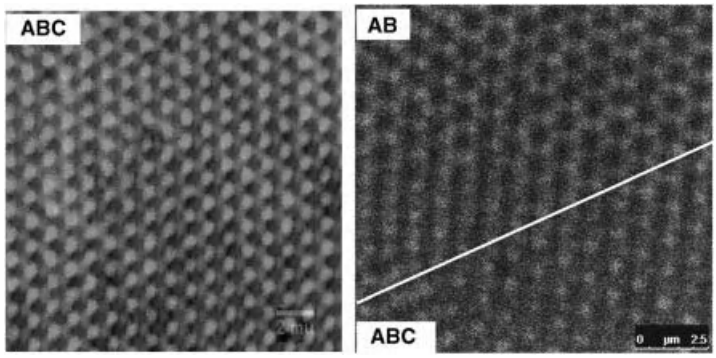

Figure 15.15 Crystalline order as obtained by merging the images from three consecutive layers in the microgel crystal at $\phi_{eff} = 0.71$ shown in Figure 15.14b. The three layers are distinguished through their assigned RGB pseudocolors. We see that the resulting crystal structure in this sample is a coexistence of FCC and HCP. (Left) ABC stacking (FCC). (Right) AB and ABC stacking (HCP and FCC).

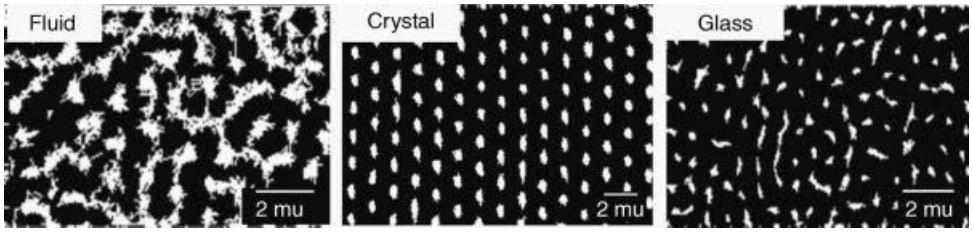

Figure 15.16 Particle trajectories observed during a period of 10 s in microgel suspensions at three different values of ϕ_{eff}: Shear molten sample at $\phi_{\text{eff}} = 0.71$ (left), crystalline sample at $\phi_{\text{eff}} = 0.71$ (middle), and glassy sample at $\phi_{\text{eff}} = 3.2$ (right).

well-ordered crystalline phases up to effective volume fractions of about 1.5. However, for even higher values of ϕ_{eff} the height of the first peak $g_{\max}$ decreases, and then a transition crystal-glass seems to occur. Analogous to the non-monotonic behavior of $g_{\max}$ for the glassy samples with 5 mol%, these findings are again in qualitative agreement with the predictions of a possible reentrant melting for soft potentials [59].

15.5
Structural and Dynamic Properties of Soft and Weakly Charged Microgels

Until now we have only looked at structural ordering in neutral microgels, where the soft potential reflects the particle structure with an outer fuzzy shell and a denser core. Based on previous theoretical studies [31], the combination of the intrinsic softness of the particles with a weakly screened Coulomb repulsion from the additional charges could give rise to a much richer phase diagram than previously encountered with neutral microgels. In this section, we will thus discuss the phase behavior of charged PNIPAM-*co*-PAA microgel suspensions in the deprotonated state with $\text{pH} = 6.2 > \text{p}K_a$. This system allows us to control the range and the strength of the interparticle interaction potential $U(r)$ over a very wide range, as the charges result in an additional soft repulsive contribution to $U(r)$ whose range can be controlled by the ionic strength of the suspensions. Giving the limited range of accessible Debye screening lengths in aqueous suspensions, smaller particles were synthesized in order to allow for a long-range Yukawa potential. These particles therefore require scattering methods to analyze the structural and dynamic features of the suspensions. The PNIPAM-*co*-PAA particles with a crosslink density of 1.55 mol% correspond to those already characterized in Figures 15.4–15.6. As shown in Figure 15.4, in the fully deprotonated state at $\text{pH} = 6.2$ they have a hydrodynamic radius of $R_h = 245$ nm. In order to achieve a long-range soft Yukawa-like repulsion, mixed bed ion-exchange resins were added to the dialyzed suspensions to keep the suspensions fully deionized. The number densities in the different suspensions were determined from the position $Q_{\max}$ of the first peak in the static structure factor measured for shear molten samples (Figure 15.17) following Palberg and

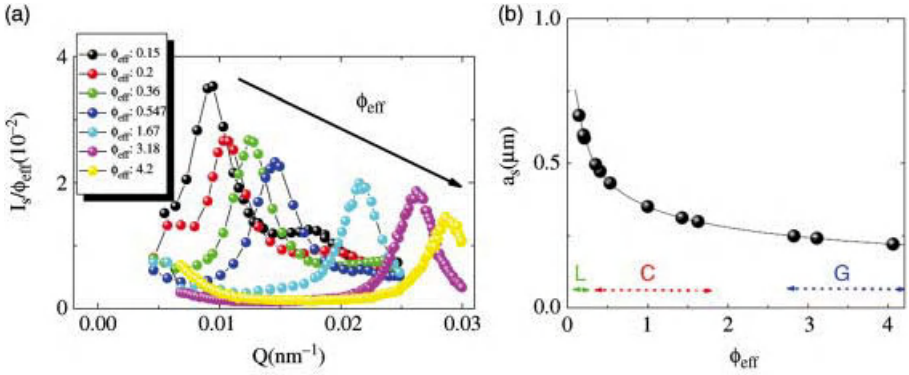

Figure 15.17 (a) Concentration-normalized scattered intensity $I(Q)/\phi_{eff}$ versus scattering vector Q for different values of ϕ_{eff} with $0.19 \leq \phi_{eff} \leq 4.15$. (b) Characteristic interparticle distance a_s calculated from the first peak position of $S(Q)$ versus ϕ_{eff}. The solid line corresponds to $\phi_{eff}^{-1/3}$. Also shown are the regions where liquid, crystalline and glass structures were observed.

collaborators [61]. The number density n is then given by $n \propto (Q_{max}/2\pi)^3$, with a proportionality constant of 0.75 for liquid-like samples.

Figure 15.18a shows samples prepared with increasing concentrations in the fully deionized state at pH 6.2. Samples with crystalline order exhibit strongly iridescent colors due to Bragg diffraction of visible light. At very high effective volume fractions the opal-like appearance vanishes and the samples now show quite uniform color with a concentration-dependent blue shift reflecting the decreasing average interparticle distance. The resulting $S(Q)$ and scattering intensities $I(Q)$ shown in Figure 15.18b–d unambiguously demonstrate the fluid–crystal–glass transition. The importance of the electrostatic repulsion is shown in Figure 15.18c, where we see a transition from a strongly correlated fluid to a very well-developed crystal after exposing the sample to an ion-exchange resin. Based on the diffraction pattern obtained for the crystalline samples, we find once again a coexistence of FCC and HCP. The diffraction pattern shown in Figure 15.18c corresponds for example to a FCC structure, where the crystallites are well oriented perpendicular to the scattering plane, which results in the sharp peaks seen.

At the two highest volume fractions investigated, the scattering intensity no longer has contributions from sharp Bragg reflexes, and we only observe a broad liquid-like peak in the structure factor. That the sample at $\phi_{eff} = 4.15$ is indeed glassy can be seen from the DLS experiments, where the obtained correlation functions are clearly non-ergodic, with a very well-developed plateau at a value of about 0.9.

In the fluid phase, we determined the number of effective charges Z from the structure factors in order to relate our microgels to the theoretical phase diagram published in [31]. For the given particles, we obtain $Z \approx 300$, which, following [31], would result in reentrant melting for the interaction potential they used, where the contributions are of electrostatic origin only. A fluid–FCC transition

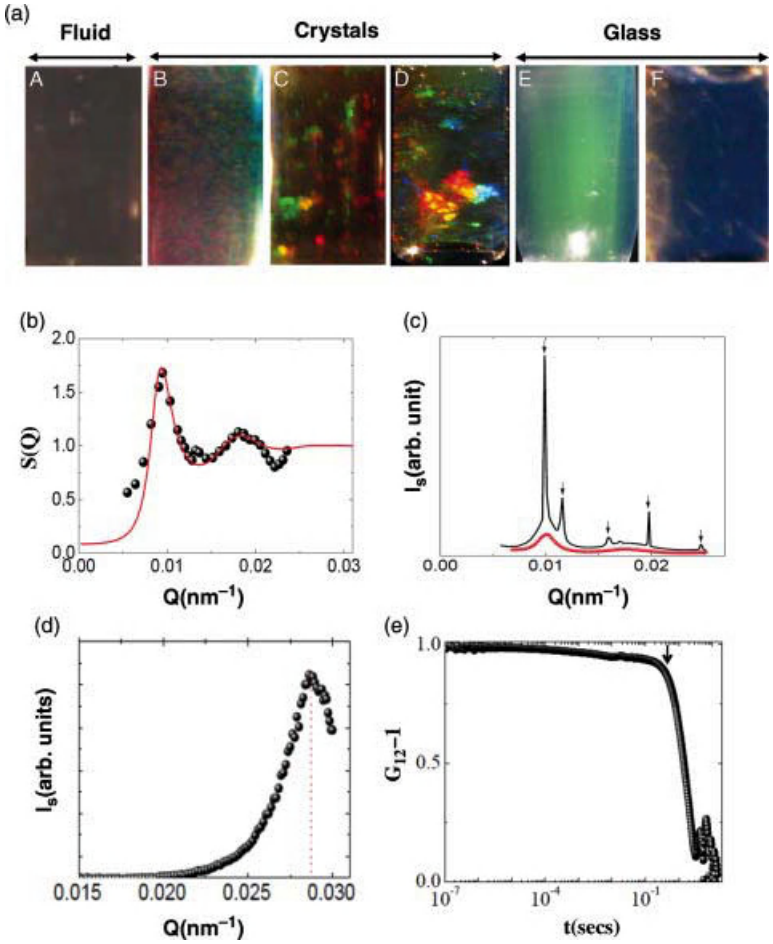

Figure 15.18 Charged microgels at different concentrations. (a) Digital photographs of fully deionized microgel dispersions at different effective volume fractions ϕ_{eff}: 0.145 (sample A), 0.2 (sample B), 0.533 (sample C), 1.63 (sample D), 4.05 (sample E), 9.5 (sample F). (b) Static structure factor $S(Q)$ determined from static light scattering for a fully deionized suspension at $\phi_{\text{eff}} = 0.19$. (c) Scattered intensity $I(Q)$ versus scattering vector Q for a suspension with $\phi_{\text{eff}} = 0.21$. Shown are results before (lower red line) and after deionization (upper black line). The peak positions (arrows) were assigned to the (111), (200), (220), (222), and (331) reflections from FCC crystals. (d) Scattered intensity $I(Q)$ versus scattering vector Q for a fully deionized suspension with $\phi_{\text{eff}} = 4.15$. (e) Ensemble averaged normalized intensity correlation function for the sample shown in (d) at the peak position. The ensemble average is obtained by rotating the sample cell slowly. The arrow indicates the artificial decay due to the sample rotation.

would be expected at $\phi_{\text{eff}} \approx 0.25$, and a crystal–fluid (or glass) transition should then occur around $\phi_{\text{eff}} \approx 1.2$. While we observe crystallization for $\phi_{\text{eff}} > 0.2$, that is, quite close to the predicted freezing line, crystals persist up to much larger volume fractions. While we do currently not have enough data points for clearly establishing

the upper limit for crystallization, it has to be at least higher than $\phi_{\text{eff}} \approx 1.7$ (Figure 15.18a). This discrepancy is not surprising as in the potential used by Gottwald *et al*. no (elastic) contribution from the polymer network is incorporated, and only electrostatic contributions from the bare interaction between two charged spheres and from the counter-ions (confinement entropy and screening effects) are taken into account. Although our microgels are weakly crosslinked, they nevertheless will also experience some direct repulsive interactions in the absence of charges, which will make the interaction potential less soft upon overlap.

The influence of an additional steric contribution has in fact also been studied by the same authors [31], and they have indeed demonstrated that depending on its strength the crystalline phases are stabilized and can extend all the way to $Z=0$. Moreover, they have also demonstrated that the presence of steric interactions broadens the stable FCC region at the expense of the BCC phase. Nevertheless, the sequence of phases remains liquid–FCC–BCC–liquid for effective volume fractions up to 1.5, and in the region of interest the reentrant melting is shifted only slightly to higher ϕ_{eff} values. Furthermore, based on the available data we have no evidence of a possible existence of a BCC phase at high volume fractions (see [34]), but due to the limited Q-range of light scattering we are unable to fully characterize the high-density crystalline phase. We are currently extending our work to SAXS and microgels with other charge densities in order to clarify this issue. It is clear that the interaction potential and the resulting phase behavior for charged soft microgels is by no means fully understood, and more systematic work is required.

15.6
Conclusions and Outlook: Probing Anisotropic Interactions

This series of experiments conducted with neutral and charged microgels clearly indicated the importance of the degree of softness of the interaction potential on the resulting phase behavior and the structures formed at high densities. Microgels have initially been used frequently as convenient model systems to study dynamical arrest, freezing and melting by exploiting their thermoresponsive nature that allows for a very convenient adjustment of the effective volume fraction ϕ_{eff}. However, our experiments summarized in Figures 15.9b, 15.14h and 15.17b also clearly indicate that ϕ_{eff} is only the relevant control parameter for neutral microgels below random close packing ($\phi_{\text{eff}} < \phi_{\text{rcp}}$), but for denser systems it is the number density n_{p} that together with the form of the interaction potential determines the resulting structural and dynamic properties. It is intriguing to see that once the effective volume fraction reaches ϕ_{rcp}, the characteristic distance a_{s} follows the classical $a_{\text{s}} \propto {\phi_{\text{eff}}}^{-1/3}$ seen for charged particles in the entire range of ϕ_{eff} studied, while the phase boundaries for the formation of crystalline and glassy phases then mainly depend on the charge density and intrinsic softness of the particles. These findings by themselves do not allow for an unambiguous interpretation, as the $a_{\text{s}} \propto {\phi_{\text{eff}}}^{-1/3}$ behavior and the underlying softness of the potential could be due to the ability of the particles to partially interpenetrate as well as because of a compression of the particles that will

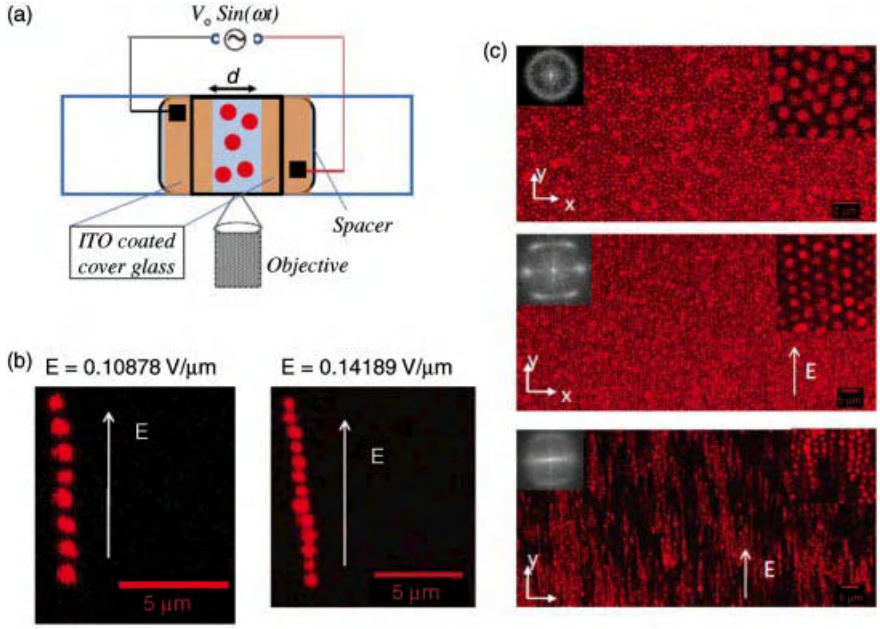

Figure 15.19 Charged microgels with a crosslink density of 5 mol% and additional sulfonic monomers in an externally applied oscillating electrical field at 100 kHz. (a) Schematic diagram of the CLSM cell used for the experiments. (b) Suspensions under dilute conditions at two different field strengths. (c) Concentrated microgel suspensions at $\phi_{\text{eff}} = 0.8$ under the external AC electric field. 2D confocal images: (top) no field, $E = 0\,\text{V}\,\mu\text{m}^{-1}$; (middle) $E_{\text{rms}} = 0.07\,\text{V}\,\mu\text{m}^{-1}$; (bottom) $E_{\text{rms}} = 0.15\,\text{V}\,\mu\text{m}^{-1}$. With increasing field, the initially glassy sample undergoes a glass–crystal transition, and at even higher field strengths we observe the formation of an inhomogeneous phase.

change the particle size in order to maintain a constant effective volume fraction that obeys $\phi_{\text{eff}} = \phi_{\text{rcp}}$ (or $\phi_{\text{eff}} = \phi_{\text{fcc}}$ for ordered structures). It is thus clear that additional experiments are required that allow us to characterize the particle size and internal structure as a function of ϕ_{eff} as well as further systematic measurements of the interaction potential for the different particles studied.

However, while there is still plenty of work required before we can fully understand the behavior of microgels at high densities, there are new and exciting developments in using microgels in order to study the effects of anisotropic or directed interactions on the phase behavior of colloids in suspensions. Yethiraj and van Blaaderen demonstrated a few years ago the enormous potential of inducing an additional anisotropic contribution to a purely isotropic repulsive potential between colloids by applying an alternating electric field [62]. Combined experimental and simulation studies have since then shown that the application of an alternating field results in the formation of a wealth of structures such as chains, vortex rings, or 2D crystals as a function of frequency and strength [63, 64].

However, these studies were mostly confined to hard-sphere and charged colloids, where the interparticle potential diverges at contact. For microgels, where their intrinsic softness results in an interaction potential that exhibits a finite repulsion even at or beyond contact, we can thus explore states with an effective volume fraction ϕ_{eff} much above ϕ_{rcp}, with enormous consequences for the resulting structural and dynamic properties. Moreover, ionic microgels with their soft and deformable polymeric structure and the large number of counterions trapped in the aqueous interior possess a very high polarizability, which allows us to generate large induced dipole moments. The use of an additional electric field as an external parameter to manipulate the crystalline structure and phase behavior of soft microgel colloids at different volume fractions thus allows us to access an even larger phase space and explore additional crystalline and amorphous structures. This is illustrated in Figure 15.19, where we see the effect of an alternating electrical field on microgel suspensions at different volume fractions and field strengths.

Figure 15.19b shows that for dilute samples the induced dipole moment results in the reversible formation of chains, where the interparticle distance changes with applied field strength, reflecting the modified balance between the soft repulsive force from the microgel potential and the added dipole attraction that is responsible for the chaining phenomenon. At higher volume fractions, we can then study the effect of an additional directed dipolar potential on the phase behavior. This is demonstrated in Figure 15.19c, where we see that the induced dipolar attraction induces a transition from a glass to a crystal and then to a new anisotropic phase with extended oriented chains. Figure 15.19 clearly demonstrates the enormous potential that microgels possess for the investigation of the effects of anisotropic interactions and their exploitation in controlled self-assembly of colloids into new crystalline structures. Here we are not constrained to the use of electric fields and ionic microgels, but recent developments in the synthesis of hybrid core-shell microgels will allow for even more versatility by using magnetic fields as well as combinations of different fields to generate more complex interaction potentials [65].

Acknowledgment

We acknowledge financial support by the Swiss National Science Foundation, the Adolphe Merkle Foundation, the Swiss State Secretariat for Education and Research and Cost Action D43. The small-angle neutron scattering experiments were performed at the instrument SANS I of the Swiss Neutron Source SINQ at the Paul Scherrer Institute (Villigen, Switzerland), the authors thank in particular J. Kohlbrecher, L. Almaszy, and U. Gasser for their expert help during the measurements. We gratefully acknowledge help from and fruitful discussions with H. Dietsch, J.-F. Dechezelles, M. Jenkins, S.U. Egelhaaf, M. Reufer, U. Gasser, and E. Zaccarelli at various stages of the project. PM thanks A. Yethiraj for hosting him and for his help during the initial experiments with AC electric fields applied to microgels.

References

1 Frenkel, D. (2002) *Physica A*, **313**, 1.
2 Poon, W. (2004) *Science*, **304**, 840.
3 Anderson, V.J. and Lekkerkerker, H.N.W. (2002) *Nature*, **416**, 811.
4 Pusey, P.N. (1991) In *Liquids, Freezing and the Glass Transition* (eds J.P. Hansen, D. Levesque, and J. Zinn-Justin), North-Holland, Amsterdam, p. 763.
5 Crocker, J.C. and Grier, D. (1996) *J. Colloid Interface Sci.*, **179**, 298.
6 Weeks, E.R., Crocker, J.C., Levitt, A.C., Schofield, A., and Weitz, D.A. (2000) *Science*, **287**, 627.
7 Kegel, W.K. and van Blaaderen, A. (2000) *Science*, **287**, 290.
8 Gasser, U., Weeks, EricR., Schofield, A., Pusey, P.N., and Weitz, D.A. (2001) *Science*, **292**, 258.
9 Gasser, U. (2010) *J. Phys.: Condens. Matter*, **21**, 203101.
10 Yethiraj, A. (2007) *Soft Matter*, **3**, 1099.
11 Pham, K.N. Puertas, A.M., Bergenholtz, J., Egelhaaf, S.U., Moussaïd, A., Pusey, P.N., Schofield, A.B., Cates, M.E., Fuchs, M., and Poon, W.C.K. (2002) *Science*, **296**, 104.
12 Leunissen, M.E., Christova, C.G., Hynninen, A.-P., Patrick Royall, C., Campbell, A.I., Imhof, A., Dijkstra, M., van Roij, R., and van Blaaderen, A. (2005) *Nature*, **437**, 235.
13 Dassanayake, U., Fraden, S., and van Blaaderen, A. (2000) *J. Chem. Phys.*, **112**, 3851.
14 Ge, J., Hu, Y., and Yin, Y. (2007) *Angew. Chem.*, **119**, 7572.
15 Cloitre, M. (2010) In *Microgel based Materials* (eds H. Wyss, A. Fernandez de las Nieves, J. Mattson, and D.A. Weitz), Wiley-VCH GmbH, Weinheim.
16 Bonnecaze, R. and Cloitre, M. (2010) *Adv. Polym. Sci*, **236**, 117.
17 Das, M., Zhang, H., and Kumacheva, E. (2006) *Annu. Rev. Mater. Res.*, **36**, 117.
18 Senff, H. and Richtering, W. (1999) *J. Chem. Phys.*, **111**, 1705.
19 Sessoms, D.D., Bischofberger, I., Cipelletti, L., and Trappe, V. (2009) *Phil. Trans. R. Soc. Am.*, **367**, 5013.
20 Stieger, M., Richtering, W., Pedersen, J.S., and Linder, P. (2004) *J. Chem. Phys.*, **120**, 6197.
21 Bartsch, E., Frenz, V., Baschnagel, J., Schartl, W., and Sillescu, H. (1997) *J. Chem. Phys.*, **120**, 6206.
22 Lyon, L.A., Debord, J.D., Byul Debord, S., Jones, C.D., McGrath, J.G., and Serpe, M.J. (2004) *J. Phys. Chem. B.*, **108**, 19099.
23 Crassous, J.J., Siebenburger, M., Ballauff, M., Drechsler, M., Hajnal, D., Henrich, O., and Fuchs, M. (2008) *J. Chem. Phys.*, **128**, 204902.
24 Alsayed, A.M., Islam, M.F., Zhang, J., Collings, P.J., and Yodh, A.G. (2005) *Science*, **309**, 1207.
25 Han, Y., Shokef, Y., Alsayed, A.M., Yunker, P., Lubensky, T.C., and Yodh, A.G. (2008) *Nature*, **456**, 898.
26 Wu, J., Zhou, B., and Hu, Z. (2003) *Phys. Rev. Lett.*, **90**, 048304.
27 Scheffold, F., Diaz-Leyva, P., Reufer, M., Ben Braham, N., Lynch, I., and Harden, J.L. (2010) *Phys. Rev. Lett.*, **104**, 128304.
28 Tan, B.H. and Tam, K.C. (2008) *Adv. Colloid Interface Sci.*, **136**, 25.
29 Karg, M., Pastoriza-Santos, I., Rodriguez-Gonzalez, B., von Klitzing, R., Wellert, S., and Hellweg, T. (2008) *Langmuir*, **24**, 6300.
30 Jones, C.D. and Lyon, L.A. (2000) *Macromolecules*, **33**, 8301.
31 Gottwald, D., Likos, C.N., Kahl, G., and Löwen, H. (2004) *Phys. Rev. Lett.*, **92**, 068301.
32 Gottwald, D., Likos, C.N., Kahl, G., and Löwen, H. (2005) *J. Chem. Phys*, **122**, 074903.
33 Gasser, U. and Fernandez-Nieves, A. (2010) *Phys. Rev. E.*, **81**, 052401.
34 Mohanty, P.S. and Richtering, W. (2008) *J. Phys. Chem. B.*, **112**, 14692.
35 Meng, Z., Cho, J.K., Breedveld, V., and Lyon, L.A. (2009) *J. Phys. Chem. B*, **113**, 4590.
36 Glotzer, S.C. and Solomon, M.J. (2007) *Nature Mater.*, **6**, 557.
37 Solomon, M.J. and Spicer, P.T. (2010) *Soft Matter*, **6**, 1391.

38 Teixeira, P.I.C., Tavares, J.M., and Telo da Gama, M.M. (2000) *J. Phys.: Condens. Matter*, **12**, R411.

39 Huke, B. and Lucke, M. (2004) *Rep. Prog. Phys.*, **67**, 1731.

40 Urban, C. and Schurtenberger, P. (1998) *J. Colloid Interface Sci.*, **207**, 150.

41 Pedersen, J.S. (1997) *Adv. Colloid Interface Sci.*, **70**, 171.

42 Stieger, M. and Richtering, W. (2003) *Macromolecules*, **36**, 8811.

43 Brugger, B., Rosen, B., and Richtering, W. (2008) *Langmuir*, **24**, 12202.

44 Hansen, J.P. and McDonald, I.R. (1976) *Theory of Simple Liquid*, Academic Press, London.

45 Tata, B.V.R., Mohanty, P.S., and Valsakumar, M.C. (2008) *Solid State Commun.*, **147**, 360.

46 Han, Y., Ha, N.Y., Alsayed, A.M., and Yodh, A.G. (2008) *Phys. Rev. E*, **77**, 0414061.

47 Cho, J.K., Zhiyong Meng, L., Lyon, A., and Breedveld, V. (2009) *Soft Matter*, **5**, 3599.

48 Heyes, D.M. and Branka, A.C. (2009) *Soft Matter*, **5**, 2681.

49 Prestipino, S., Saija, F., and Giaquinta, P.V. (2005) *J. Chem. Phys.*, **123**, 144110.

50 Yang, J. and Schweizer, K.S. (2011) *J. Chem. Phys.*, **134**, 204908.

51 Pàmies, J.C., Cacciuto, A., and Frenkel, D. (2009) *J. Chem. Phys.*, **131**, 044514.

52 Zhu, Y.-L. and Lu, Z.-Y. (2011) *J. Chem. Phys.*, **134**, 044903.

53 Barker, J.A. and Henderson, D. (1967) *J. Chem. Phys.*, **47**, 4714.

54 Stieger, M., Pedersen, J.S., Linder, P., and Richtering, W. (2004) *Langmuir*, **20**, 7283.

55 Zhang, Z., Xu, N., Chen, D.T.N., Yunker, P., Alsayed, A.M., Aptowicz, K.B., Habdas, P., Liu, A.J., Nagel, S.R., and Yodh, A.G. (2009) *Nature*, **459**, 230.

56 Ediger, M.D., Angell, C.A., and Nagel, S.R. (1996) *J. Phys. Chem.*, **100**, 13200.

57 van Blaaderen, A. and Wiltzius, P. (1995) *Science*, **272**, 1170.

58 Truskett, T.M., Torquato, S., Sastry, S., Debenedetti, P.G., and Stillinger, F.H. (1998) *Phys. Rev. E*, **58**, 3083.

59 Berthier, L., Moreno, A.J., and Szamel, G. (2010) *Phys. Rev. E*, **82**, 060501 (R).

60 Brijitta, J., Tata, B.V.R., Joshi, R.G., and Kaliyappan, T. (2009) *J. Chem. Phys.*, **131**, 074904.

61 Liu, J., Schöpe, H.-J., and Palberg, T. (2000) *Part. Part. Syst. Charact.*, **17**, 206.

62 Yethiraj, A. and van Blaaderen, A. (2003) *Nature*, **421**, 513.

63 Hynnien, A. and Dijkstra, M. (2005) *Phys. Rev. E*, **72**, 051402.

64 Zang, K. and Liu, X. (2009) *J. Chem. Phys.*, **130**, 184901.

65 Dagallier, C., Dietsch, H., Schurtenberger, P., and Scheffold, F. (2010) *Soft Matter*, **6**, 2174.

Index

a

acetoacetoxyethyl methacrylate (AAEM) 129, 130, 131, 258, 263
acrylamide 64, 87, 237, 291, 295, 310
acrylic acid (AA) 51, 64, 76, 89, 287, 290, 352, 353, 374, 375
aggregation
– number 6
– reversible 6
– spherical microgels 18–21
– SX microgels 146
– using poly(NIPAM-*co*-AA) microgels 286
– weaker hydrophobic 174
etalon 322
amines 218, 293
aminoethanethiol-hydrofluoride 73
aminoethyl phosphate (AEP) 133
3-aminophenylboronic acid (APBA) 330, 331
8-anilino-1-naphthalenesulfonic acid magnesium(II) salt 76
Antifouling surfaces 224, 225
artificial molecular chaperones 195, 196
associating polymer-based nanogels 188
– hydrophobically modified polysaccharide 188–190
– metal–ligand modified polysaccharides 192, 193
– photoresponsive molecule-modified polysaccharides 190, 191
– protein-crosslinked nanogels 193, 194
– siloxane-modified polysaccharides 193
– thermoresponsive polymer-grafted polysaccharide 191, 192
associating polymer-based nanogels 188
A15 structure, conventional cell and basis 344
atomic crystals Bragg diffract X-rays 337
atom-transfer radical polymerization (ATRP) 82–84, 147, 170, 171, 172, 176, 177, 178, 180, 182
Au/Ag/Au bimetallic multishell system 263
Au–P2VP hybrids 268
2-2′azobisisobutyronitrile (AIBN) 82

b

Batchelor–Einstein equation 358
Batchelor equation, for hard spheres 98
benzoic acid 118
binary microgel suspensions 338
biomaterial films 221, 222
– antifouling surfaces 224, 225
– cellular adhesion 225–227
– drug release 227, 228
– foreign body response 222, 223
– hydrogels as biomaterial interface (*See* hydrogels)
Bjerrum length 102
blood–brain barrier (BBB) 219
body-centered cubic (BCC) structures 338, 340, 343, 360, 391
bone morphogenic protein (BMP) 306
bovine carbonic anhydrase 196
bovine serum albumin (BSA)-loaded PNIPAM microgels 303
Bragg condition 360
– derivation of 344
Bragg diffraction 337, 338, 358
Bragg peaks 360, 365
Bragg reflections 345, 358, 365, 389
Bragg stacks 318
Bravais lattices 340, 341, 343
bromomalonic acid 242
Brownian motion 12, 21

c

Ca^{2+}/COO^{-} complexation 19
cadmium selenide (CdSe) 258
cadmium sulfide (CdS) 258

Hydrogel Micro and Nanoparticles, First Edition. Edited by L. Andrew Lyon and Michael Joseph Serpe.
© 2012 Wiley-VCH Verlag GmbH & Co. KGaA. Published 2012 by Wiley-VCH Verlag GmbH & Co. KGaA.

cadmium telluride (CdTe) 258
cage effect 43
carboxymethylcellulose (CMC) microgel 70
– graft polymerization of NIPAM from 71–73
– incorporation of PNIPAM into 71
– pH-sensitive swelling/shrinking behavior 71
– property of carboxyl groups 74
cation-induced aggregation, dynamics of 14. *See also* aggregation
– salt-induced complexation 14–18
CdTe nanocrystals 271
– PNIPAM microgels 271
cellular adhesion 225–227
cellulose derivatives 63, 82, 287, 302
ceric ion redox system 71
cetyl trimethylammonium bromide (CTAB) 257, 262
charged microgels 15, 16, 18
chitosan 71, 189, 199
cholesterol-bearing pullulans (CHP) 188
cholesterol-modified ESG 190
CLSM cell, schematic diagram 392
coffee-ring effect 321
coherent scattering 348
colloidal crystallization 45
colloidal suspensions 369
color-tunable poly (*N*-isopropylacrylamide) microgel-based etalons 317
– Fabry–Pérot etalon depicting 318
– future directions 330–332
– microgel-based photonic materials 319, 320
–– applied sensing 329, 330
–– etalon deswelling, mechanism 324–329
–– microgel-based etalons 320–323
–– tuning, reflection order 323, 324
comb-type grafted hydrogel 25
complexation
– between microgels and protein 18
– salt-induced 14
composite 133, 283, 298
concentrated suspensions 42, 44, 286
concentration-normalized scattered intensity 389
conductivity titration measurements 377
confocal laser scanning microscopy (CLSM) 149, 369, 374, 379, 385, 392
copolymerization 83
– cell adhesion peptide (GRGDS) within 163
– chemical synthesis of nanogels by 83
– *N*,*N*-diethylaminoethyl methacrylate 287
– divinyl crosslinker 169
– employing co-monomers 258
– free-radical 87
– free radical copolymerization of VCL and AAEM in 133
– glycidyl methacrylate with VCL 130
– HEMA 183
– hydrophobic and hydrophilic monomers 64
– ionic sodium acrylate (NaA) into PVCL 131
– kinetics 86
– for LCST hydrogels preparation using 171
– with linear copolymer of AAm and 295
– NIPAM with aminoethyl methacrylate hydrochloride 51
– polystyrene (PS) and PNIPAM 66
– styrene and acrylamide 64
– synthesis of dextran microgels via 290
– VCL and acetoacetoxy ethyl methacrylate 129
– VCL, itaconic acid dimethylester (IADME) 132
– VCL with *N*-isopropylacrylamide 129
– *N*-vinylcaprolactam and *N*-vinylpyrrolidone in 129
– vinyl-functionalized microgels with 146
copolymer PVCL microgels 129–133
core–shell hybrid microgels 259, 260, 267
core–shell microgels 33, 34
core–shell particles
– as carriers for catalysts 45
– defined 63
– emulsion polymerization 63
– preparation with temperature-sensitive shell 63–65
– soap-free emulsion polymerization 63–65
Coulomb repulsion 370, 372, 388
crystal–crystal martensitic transitions 370
crystallization
– 2D crystallization 41
– 3D crystallization 40
– for polydispersities 365
– solid-state theory 338
– two-dimensional 34
CTAB-stabilized gold nanoparticles 262
cyclodextrins (CDs) 196
4-cyclohepten-1-on 118
cyclohexane 180

d

de Broglie wavelength 261
Debye length 102
degradable star macro-initiator (dSM) 176
– synthesis 177

dense microgel suspensions, dynamical arrest/crystallization 369
– methods 372–374
– neutral microgels, structural/dynamic properties 379–388
– soft/weakly charged microgels, structural/dynamic properties 388–391
– synthesis and responsive properties 374–379
deoxycholic acid-modified glycol chitosan 189
depletion effect 370
depolarized dynamic light scattering (DDLS) 261
deswelling kinetics 325, 327
– plot of maximum rate 328
– time for etalons 329
dextran-in-poly(ethylene glycol) suspension 290
diallyl phthalate (DAP) 88
differential interference microscopy (DIC) images 320, 321
differential scanning calorimetry (DSC) 121, 129
diffusion-limited cluster–cluster aggregation (DLCA) 6
2,2′-dimethacryloyloxyethyl disulfide (DSDMA) 176
dimethylamineborane (DMAB) 268
1-(3-(dimethylamino) propyl)-3-ethyl-carbodiimide (EDC) 73
dipolar fluids, anisotropic interactions 371
dipole–dipole interactions 122, 372
direct microgel–microgel networks 287
DMA bulk hydrogel 301
DNA hybridization 319
DNA sequencing 310
doubly crosslinked microgels. *See* DX microgels
drug-delivery systems (DDS) 187, 213
DX microgels 141, 142
– aggregates 146
– biomedical applications 163–165
– comparison of properties
–– with conventional hydrogels 162
–– with microgels 161, 162
– compression modulus measurements 154
– confocal microscopy 149, 150
– crystals by small molecule addition 147
– dynamic rheology 153, 154
– general equations
–– governing hydrogel mechanical properties 144, 145
–– governing hydrogel swelling 143, 144
– history 142, 143
– ^{1}H nuclear magnetic resonance 148, 149
– interpenetrating DX microgels 148
– mechanical properties and control 158–161
– methods
–– of characterization 148
–– of preparation 145
– microgel crosslinked hydrogels 146
– microgel-reinforced hydrogels 146, 147
– morphology
–– control 156
–– types 155, 156
– optical properties 152
– optical tuning 158
– photonic applications 162
– property 143
– scanning electron microscopy 150
– self-crosslinked DX microgel crystals 147, 148
– stimulus-responsive 143
– swelling experiments 150–152
– swelling properties and control 157, 158
– swelling ratio 143, 144
– tensile testing 154, 155
dynamic light scattering (DLS) 89, 260, 352, 354, 369, 373, 375, 377

e

electrophoretic mobility 73–76, 91, 133
emulsion polymerization 63, 64, 82–84
encapsulated cargo, degradation and release 220
– release by pH changes 220, 221
– release by reduction 220
enhanced permeability and retention effect (EPR) 216
enzymatically synthesized glycogen (ESG) 190
enzymes 50–53
EP4 receptor 306
ergodic phenomena 21
etalons
– 3-aminophenylboronic acid (APBA) 330
– dielectric cavity 324
– fabricate 322
– photograph 320
– plot of percent shift 329
ethyl acrylate (EA) 82
ethylene glycol dimethacrylate (EGDMA) 171
ethylene glycol methacrylate phosphate (EGMAP) 134

f

Fabry–Pérot etalons 317, 318
face-centered cubic (FCC) structure 152, 338, 340, 341, 361
Fermi pseudo-potential 346
flocculating/dispersing oscillation of microgels 251–253
fluorescence confocal microscopy 374
fluorescence correlation spectroscopy (FCS) 195
fluorescence resonance energy transfer (FRET) particles 77, 78
fluorescent dye 76
fluorinated ethylene propylene (FEP) 224
folic acid 217, 218
– cellular targeting of PNIPAM microgels 219
Fourier transforms (FFTs) 386, 387
– diffraction pattern 385
free radical polymerization (FRP) 169
fuzzy sphere model 378, 385

g

galactose-based targeting of nanoparticles 218, 219
gas-to-liquid transition 33
Gaussian function 360
Gaussian-like peaks 365
Gaussian shell 355
Gaussian size distribution 377
gelatin/microgel molar ratio 18
gel networks, containing functionalized nanopores 176–178
– accelerated deswelling kinetics 178–180
– enhanced swelling ratios 178, 179
glutathione (GSH) 163
glutathione peroxidase (GPx) 52
glycidyl methacrylate (GMA) 130, 148, 258, 292
– multishell nanoparticles, and copolymer microgels 264
gold nanoparticles
– composite microgels of 270
– plasmon properties 268
gold nanorod–PNIPAM core–shell particles 269
gold–PNIPAM core–shell microgels 262, 269
graft polymerization of NIPAM 71–73

h

hairy particles
– attachment of hydrophilic polymer chains 73–75
– from block copolymer micelles 67, 68
– hair growth on core particles 68–71
– *in situ* formation of surface active material 68
– optical properties 76, 77
– with temperature-sensitive hair 66, 67
– trypsin-carrying PNIPAM hair 75
– two-dimensional assembly 76
hard-sphere suspensions, phase equilibrium 338
HCP structure 343
hematite ellipsoids 267
He–Ne laser 373
Hertzian model 381, 384
hexagonal close-packed (HCP) structure 342
homopolymer PVCL microgels 125–128
hybrid materials, organic/inorganic
– atomic force microscopy (AFM) 260
– hybrid gels 22
–– characterization of 260, 261
–– synthesis of 258–260
– scanning electron microscopy (SEM) 260
– structures of 259
– three possible structures of 259
– transmission electron microscopy (TEM) images 260
hybrid microgels 133–136
– DLS measurements 267
– photoluminescent 269–272
– with plasmon properties 261–269
– UV-vis spectra 263
hybrid particles, optical properties 261
hydrodynamic radius 5, 7, 14–17, 19, 35–37, 92, 126, 129, 356, 374–376, 385
– dynamic light scattering, measured by 353
hydrogels 2, 22, 281
– as biomaterial interface 223, 224
– conditions for preparation 172
– films, use of 225, 227
– ionic-crosslinked microgel-based 287
– LCST hydrogels 171
– macroscopic (*See* macroscopic hydrogels)
– made of NIPAM 211
– nanocomposite 283
– nano-sized, ATRP method 180, 181
– particles 211, 212
–– shell crosslinked knedels (SCK) 213
–– synthesis 212, 213
– phases 295
– prepared by CRP possess 170
– shrinking kinetics of 292
– synthesis, in presence of dHSM and 177
– thermoresponsive (*See* thermoresponsive hydrogel)
– volume phase transition 210, 211

hydrogen bonds 188
– interactions 287
hydrophobically modified alkali-soluble/swellable emulsions (HASE) 82
hydrophobically modified polysaccharide 188–190
hydrophobic polymer 25
hydrostatic pressure, experimental profiles 355
2-hydroxyethyl 2-bromoisobutyrate (OH-iBuBr) 183
hydroxyethyl cellulose 82
2-hydroxyethyl methacrylate (HEMA) 171, 172, 286

i

incoherent scattering 348
in situ polymerization 66
interactions
– anisotropic 391, 393
– dipole–dipole 372
– electrostatic 237, 370
– hydrophilic 320
– hydrophobic 188, 195, 196, 286, 287, 305
– noncovalent 188
internal motion 3, 4, 9
– in good solvent 9–11
– in poor solvents 11–14
interpenetrating polymer network (IPN) 11, 25
inverse mini-emulsion polymerization 180
ionic assembly 287, 288
ionic microgels. *See* microgel
ionic microgel suspensions 338
ionic strength, effect of 93–95
ionic surfactant sodium dodecyl sulfate 374
ion-selective electrode (ISE) 104
isoelectric points (IEP) 89
N-isopropylacrylamide (NIPAM) 51, 71, 72, 123, 258
itaconic acid dimethylester (IADME) 132, 133

k

Krieger–Dougherty equation 100

l

lightly crosslinked polyvinylpyridine
– composite microgels of 270
linear homopolymer 1
linear viscoelastic behavior 45
liquid–FCC–BCC–liquid phase 391
lower critical solution temperature (LCST) 1, 23, 63, 75, 76, 120, 322, 375
lymphatic system 282

m

MAA–EA nanogel systems 103–106
macromolecules
– distribution 349, 350
– drug delivery 303
– scattering length 350
macroscopic hydrogels, performance 172, 174
– deswelling kinetics 174
– drug-delivery vehicle 281
– image analysis 174
– LCST transition 174
– molecular level dehydration kinetics 175, 176
– water retention 172, 173
macroscopic microgel networks 281
– direct microgel crosslinking 285–290
–– covalent assembly 289, 290
–– hydrophobic assembly 285–287
–– ionic assembly 287–289
– high strength 282
– kinetically frozen microstructures 282, 283
– microgel-mediated crosslinking
–– initiator-grafted microgels 290, 291
–– surface-polymerizable microgels 291–293
–– surface-reactive microgels 293–295
– microgel networks, applications
–– biomolecule separation and purification 309, 310
–– biosensors 307, 308
–– cell adhesion-directing coatings 304
–– DNA sequencing 310
–– drug delivery 301–303
–– optical materials 309
–– tissue engineering 304–307
– networking strategies 284, 285
– physical microgel entrapment
–– entrapment to form 2D films 299
–– entrapment to form 3D hydrogels 295–299
– rapid swelling kinetics 283
– well-defined compositional heterogeneity 283
metal–ligand modified polysaccharides 192, 193
metal nanoparticles 45–50
metal–PNIPAM core–shell particles 268
– UV-vis-NIR absorption spectra 268
methacrylic acid (MAA) 82, 100, 102, 105, 148, 237, 290
2-methacryloyloxyethylphosphocholine 200
2-(2-methoxyethoxy)ethyl methacrylate (MEO_2MA) 171

methylenebisacrylamide 237
N,N-methylenebis acrylamide 293
Michael addition 293, 297
microgel 180, 281, 337, 364, 370
– acrylamido-functionalized 293
– APBA-modified 330, 331
– assemblies 304
–– for optical applications 319
– based etalons 319
– based photonic materials 319
– basic physics of 7–9
–– internal motion 9
–– volume phase transition 7
– borne CdS quantum dots, luminescence of 272
– carboxymethylcellulose (CMC) (*See* carboxymethylcellulose (CMC) microgel)
– charged 390
–– crosslink density 375, 392
– colloids 371
– crosslinked networks 297
– digital photographs 390
– dispersions, digital photographs of 386
– dynamics of 4–6
– films, formation 320
– interaction potential 383
– ionic 288, 338, 370, 372, 393
– lower critical solution temperature (LCST) 322
– macroscopic (*See* macroscopic microgel networks)
– membrane-based implantable devices 303
– nanoparticle hybrids, tunable optical properties 257
– networks 289, 297, 309
–– based hydrogels 283
–– drug-delivery properties 306
–– films 289
–– formation, *in situ* gelation chemistries for 294
–– mechanical properties 293
–– methods 284
–– multidrug-delivery system 303
–– preparation 298
– NIPAM–AA microgels 356
– NIPAM copolymer microgels 263
– oscillating (*See* oscillating microgels)
– pair-correlation functions 384
– phases, types of 302
– phase transition temperature 296
– pH-responsive 374
– physical properties 324
– self-assembly-based approaches 305
– size 374
– suspensions 338, 357, 383, 392
–– particle trajectories 388
–– polydisperse 361
–– structural features 353, 366
– swelling 144, 148, 158, 296, 297
–– magenetic field induced, convecting cooling, effect of 299, 300
– thermally sensitive 14
– thermoaggregation 285, 305
– thin films 320
– two-dimensional array formation 77
microgel particles, crystals 337, 338, 370
– A15 structure 343
– body-centered cubic (BCC) structure 340, 341
– concentrated suspensions, structure factor 357
–– phase behavior 357, 358
– crystalline samples, structure factor analysis 358–361
– crystalline structure 340
– crystal nucleation, and growth 339, 340
– experimental details 351, 352
– experimental system 352, 353
– face-centered cubic (FCC) structure 341, 342
– future directions 365, 366
– hexagonal and hexagonal close-packed structure 342, 343
– light scattering 343–345
– particle form factor, determining/ modeling 353–357
– small-angle neutron scattering 345–351
– structural richness 365
– suspensions 338
– tuning polydispersity 361–364
Miller indexes 345, 360
mirror–mirror distance 319
– uniform modulation of 323
mirror–mirror spacing 319
mode-coupling theory (MCT) 44, 45
monolithic film 322
mononuclear phagocytic system (MPS) 214, 215, 222

n

nanocrystalline cellulose 282
nanogel–protein complexes 194, 195
nanogels 187
– cellular targeting 216
–– active targeting 217–220
–– passive targeting 216, 217

– chaperones in cell-free protein synthesis 196, 197
– chemically crosslinked 187
– integration of 199–201
–– bionanoengineering fabrication, and applications 200
– photoresponsive 190
– pH-responsive
–– in colloidal suspensions, osmotic compressibility 106–109
–– crosslinking monomers, distribution of 85, 86
–– emulsion polymerization 82–84
–– functional group distributions in nanogels 82–87
–– ionic strength 93–95
–– preparation techniques for 82–85
–– properties, approach to model 97–106
–– rheological behavior of 96, 97
–– structural properties of 85–87
–– theory of swelling and elasticity 91–93
– raspberry-like assembly 201
– self-assembled, functions of 194–197
– thiol-responsive 181
nano/micro-emulsion polymerization 187
nanoparticles 214
– bioconjugation (*See* nanogels, cellular targeting)
– size and surface modification for enhanced delivery 214–216
nearest-neighbor distances 361
network-based sensor 307
neutron velocity selector 359
neutron wave packet 346
nitroxide-mediated polymerization (NMP) 84
NMA–AAm crosslinking reaction 295
non-ergodic phenomena 21
non-ergodic system 5–6
non-thermoresponsive poly(DAM) hydrogel 298
nucleation barrier 339

o

Ornstein–Zernicke convolution integral equation 380
oscillating microgels
– BIS crosslinked oscillating microgel 246
–– temperature dependence of hydrodynamic diameters 244, 245
– chemical reaction cycle 239
– effect on
–– induction period 242–244
–– oscillation amplitude 244–247
–– oscillation period, and waveforms 247–251
– experimental setup 239
– Field–Körös–Noyes (FKN) mechanism 240
– flocculating/dispersing oscillation 251–254
– oscillating profile, of optical transmittance 242
– oscillatory behavior, control of 241, 242
– synthesis, and fabrication 240, 241
– types of 238–240
osmotic deswelling 103, 104
– of soft particles 99
osmotic pressure 37, 82, 87, 88, 108, 109, 353, 375

p

paint-on method 321, 322, 323
pair-correlation function 387
particle–particle spacing 320
particle size 41, 75, 94, 97, 125, 214, 352, 356, 377, 392
particles on surfaces. *See* crystallization
Péclet number 44
PEG-diacrylate hydrogel phase polymerized 303
peptides 219, 220
phase transition temperature 7, 75, 121, 122, 147, 211, 285, 289, 296, 298, 299, 322, 325
photoluminescence, temperature dependence 272
photonic materials 317
photoresponsive molecule-modified polysaccharides 190, 191
plasticizing action of water molecules 121
P(MMA-co-AA) 87
PNIPAM-*co*-AA hydrogel 319
PNIPAM-*co*-AA microgels 324
– etalons composed, representative spectra 325
PNIPAM–AA system, phase behavior of 358
PNIPAM-based etalons 319
PNIPAM-based grafted surfaces 304
PNIPAM-based microgels. *See* poly(*N*-isopropylacrylamide) (PNIPAM)
PNIPAM-based systems 267
PNIPAM-block-poly(glycerol methacrylate) (PGLM) 67
PNIPAM hydrogels 81, 292, 297, 299, 319
PNIPAM-*co*-PAA particles 388
PNIPAM–starch system 292
point-of-care (POC) sensing 329
polyacrylamide-based hydrogel 309

poly(acrylic acid) microgel 308
poly(allylamine) hydrochloric acid (PAH) 227
poly(aminoacids) 189
polyampholyte nanogels 89
polydimethylsiloxane (PDMS) 298
polydispersity
– influence of 362
– reduction 365
poly(ε-caprolactone)-*b*-PAA copolymers 85
polyelectrolyte-coated gold nanorods 263
polyelectrolyte mediated protein adsorption 51
poly(ethyl acrylate-*co*-MAA) 87
poly(ethylene glycol)methacrylate (PEGMA) 89
poly(ethylene glycol) (PEG)-modified PVCL microgels 133
poly(ethylene glycol)–poly(sodium acrylate) microgels (anionic) 287
poly(ethylene oxide) (PEO) 224
poly(HEMA-*co*-poly(ethylene glycol dimethylacrylate) (PEGDMA)) microgels 301
poly (acrylic acid) hydrogel, cyclic compression tests of 291
poly(isoprene-*b*-acrylic acid) 85
poly(*N*-isopropylacrylamide) (PNIPAM) 33, 63, 84, 171, 352
– amino end group-carrying 73
– Au-PNIPAM core–shell particles 42, 262
– Brownian motion 9
– BSA-loaded 303
– CMC core–PNIPAM shell 74
– CMC–PNIPAM microgel 72
– folate-mediated cellular targeting of 219
– hydrodynamic radius, dynamic light scattering 353
– hydrophilic–hydrophobic transition 191
– lightly crosslinked 2
– matrix 318
–– water-soluble thermoresponsive polymer 318
– microgels (*See* poly(*N*-isopropylacrylamide) (PNIPAM) microgels)
– network 292
– phase transition behavior 296
– PNIPAM-*co*-allylacetic acid (AAA) microgel 47
– PNIPAM-block-poly(glycerol methacrylate) (PGLM) 67
– PNIPAM–starch system 292
– polystyrene–PNIPAM core–shell microgel 266
– properties 319
– relative viscosity 98
– representative spectra for etalons 325
– spherical swollen 22, 25
– temperature dependence 75
– temperature-sensitive FRET particle, compose of 78
– thermogelation 286
– trypsin-carrying 75
– water/heavy water 352
poly(*N*-isopropylacrylamide-*co*-acrylic acid) (PNIPAM-*co*-PAA) microgels 375
poly(*N*-isopropylacrylamide-*co*-allylacetic acid) microgels 266
poly-(*N*-isopropylacrylamide-*co*-maleic acid) microgels 265
poly(*N*-isopropylacrylamide) (PNIPAM) microgels 263, 271, 297, 307, 309, 319, 353, 370
– 2D conditions 380
– hydrodynamic radius 376
– lower critical solution temperature (LCST) 375
– phases 296, 301, 302
– self-assembled arrays of 307
– single-frame CLSM image 379
– temperature-sensitive 370
– thermogelled assemblies, cross section
–– scanning electron microscopy images 286
– thermoresponsive , structural properties 385
poly(2-isopropyl-2-oxazoline) (PIPOZ) 191
polymer-based drug-delivery systems 180
polymer biomaterials 209, 210
polymer gel–gelatin sheet 25
polymer–hydrate complexes 122
polymerization. *See* atom-transfer radical polymerization (ATRP); emulsion polymerization; free radical polymerization (FRP), nitroxide-mediated polymerization (NMP), RAFT; graft polymerization; precipitation polymerization
poly(methacrylic acid-co-ethylene glycol) (P(MAA-co-EG)) 87
poly(NIPAM-*co*-AA) microgels 247, 287
– aggregation, use of 305
– drug release 302
poly(NIPAM–acrylamide-2-acrylamidomethyl–5-fluorophenylboronic acid) copolymer microgels 272
poly(NIPAM-*co*-allylamine) microgels 288, 294
– networks, temperature-tunable 308
– self-assembled arrays of 307

poly(NIPAM-*co*-methacrylic acid (MAA)) microgel 299
poly(NIPAM-*co*-2-hydroxyethyl methacrylate (HEMA)) microgels 286, 305
poly(NIPAM-*co*-*N*-isopropylmethacrylamide-co-acrylamide) microgels 299
poly(NIPAM-*co*-Ru(bpy)3) microgels 244
poly(oligo(ethylene oxide) monomethyl ether methacrylate) (POEOMA) 170
polysaccharide nanogels, applications 197, 198
– nucleic acid delivery 199
– protein delivery 198, 199
polysaccharides 188, 190, 191
– for nanogel formation 189
polystyrene (PS) 9–11, 66, 84, 124
polystyrene-*b*-PAA copolymer 85
polystyrene core-PNIPAM shell particles 66, 77
– cryo-TEM image 266
polyvinyl alcohol 82
poly(vinylamine), amine residues 291
poly(*N*-vinylcaprolactam) (PVCL) 117–120
– amphoteric microgels 132
– copolymer microgels 129
– glass temperature of 122
– homopolymer microgels 125
– hydration mechanism 121
– hydrodynamic radius of 126, 131
– hydrophobic behaviour 14
– ingredients used for synthesis of 134
– Kuhn–Mark–Houwink equation 120
– microgels, with grafted amphiphilic chains 133
– molecular weights 119
– phase separation 124
– poly(ethylene glycol) (PEG)-modified 133
– SANS and NSE data 123
– temperature-sensitive 130
– types of interaction with water 123
poly(*N*-vinylcaprolactam-*co*-acetoacetoxyethyl methacrylate) (VCL–AAEM) microgel particles 265
poly(*N*-vinylcaprolactam–acetoxyethyl methacrylate) microgel 262
poly(*N*-vinylcaprolactam-*co*-glycidyl methacrylate) (P(VCL-*co*-GMA)) microgels 269
poly(vinylcaprolactone-*co*-*N*,*N*-dimethylaminoethyl methacrylate) 288
poly-vinyl-2-pyridine (P2VP) 267
porcine citrate synthase 196
pore sizes 52, 305, 309
potassium persulfate 352, 374
precipitation polymerization
– advantages of 124, 125
– batch surfactant-free 135
– of colloidal micro/nanogels from phase-separating polymers 213
– by free radical 212, 374
– limitations 125
– microgel formation by 124
– reaction mechanism 124
– synchronized with bromate–sulfite pH oscillating 241
– use of monomers 129, 131, 262
protein adsorption 76
protein-crosslinked nanogels 193, 194
PS–PNIPAM microgel 52
PVCL microgels. *See* poly(*N*-vinylcaprolactam) (PVCL)
PVCL–water system 122
1-pyrenebutyric acid *N*-hydroxysuccinimide ester (PBHS) 78

q
quantum dots 199

r
radius of gyration 5, 89, 119, 135
RAFT method 67, 84
random hexagonal close-packed (RHCP) 343, 360
Rayleigh ratio 4
reaction-limited cluster–cluster aggregation (RLCA) 18
α/β-relaxation 43
reversibly inflatable spheres 44
rheology 42–45, 290
rhodamine-labeled microgels, confocal images of 382
rhodamine–phalloidin, fluorescence images 305
rhodanese 196

s
salt-induced complexation 14–18
SANS. *See* small angle neutron scattering (SANS)
scattering amplitude 347
scattering angle, neutron lenses 351
scattering vector 5, 12, 19, 20, 38, 107, 346, 377, 378, 389, 390
Schröedinger equation 346
seeded polymerization 66
shell crosslinked knedel (SCK) nanoparticles 85
siloxane-modified polysaccharides 193

simple cubic (SC) system 340
singly crosslinked microgels. *See* SX microgel
small angle neutron scattering (SANS) 260, 338, 352, 369, 373
– data, analysis of 377
– instrument 360
– measurements 351
– SANS-I apparatus 351
sodium dodecyl sulfate 352
sodium fluorescein
– sample chamber and differential flux
–– temperature profile 300
sodium persulfate (NaPS) 82
soft-repulsive colloids
– theoretical investigations 383
sol–gel transition 21, 22
static light scattering (SLS) 4, 373
surface-acrylated PNIPAM microgels 292
surface-enhanced Raman scattering (SERS) 262
surfactant-free emulsion polymerization (SFEP) 84
suspensions, of colloidal spheres 40
swelling ratio 92, 93, 102, 103, 135, 143, 144, 152, 161, 170, 172, 178, 183, 375, 376, 385
Swiss spallation neutron source 373
SX microgels 141–143
– aggregation 146
– size 145
– swelling ratios 161

t

thermally sensitive polymer microgel sheet 26
thermodynamics, of volume phase transition 2
thermoresponsive hydrogel performance 171, 178
– effect of network homogeneity 171, 172
thermoresponsive polymer-grafted polysaccharide 191, 192
thermosensitive suspensions 43
– advantages 43, 44
thiol-responsive biodegradable nanogels 181
– features 181–183
– swelling ratios 182
– synthesis 181
transferrin 219
transition temperature 76

u

ultrasoft counterion-dominated contribution 371
UV glue 373

v

van der Waals forces 21, 188
VCL–AAEM microgel particles 130
– hydrodynamic radii 135, 136
– TEM images 136
vinylamides 118
N-vinylcaprolactam (VCL) 117, 121, 132, 258, 263, 271
– chemical structure 118
vinyl imidazole (VI) monomers 89
vinyl naphthalene (VN) 78
viscosity 98, 106
– measurements 357
volume phase transition 2, 3, 7, 9, 27, 52, 93, 170, 210, 211, 260, 298, 375, 376
– discontinuous 9
– response to external stimulus 210
– response to mono- or divalent electrolytes 93
– responsive hydrogel materials 210
– single particles 35–39
– temperature-sensitive shell and 75, 76
– theory 7
– thermodynamics 2, 3
volume phase transition temperature (VPTT) 75, 117, 129, 135, 147, 211, 212, 219, 298, 304
volume transition. *See* volume phase transition (VPT); volume phase transition temperature (VPTT).

w

water-soluble thermoresponsive polymer 318

x

X-ray photon correlation spectroscopy (XPCS) 369

y

Yukawa-like soft repulsion 376

z

zinc sulfide (ZnS) 258
zwitterionic behavior 89